Medical Radiology

Diagnostic Imaging

M.F. Reiser
H. Hricak
M. Knauth

Marc-André Weber
Editor

Magnetic Resonance Imaging of the Skeletal Musculature

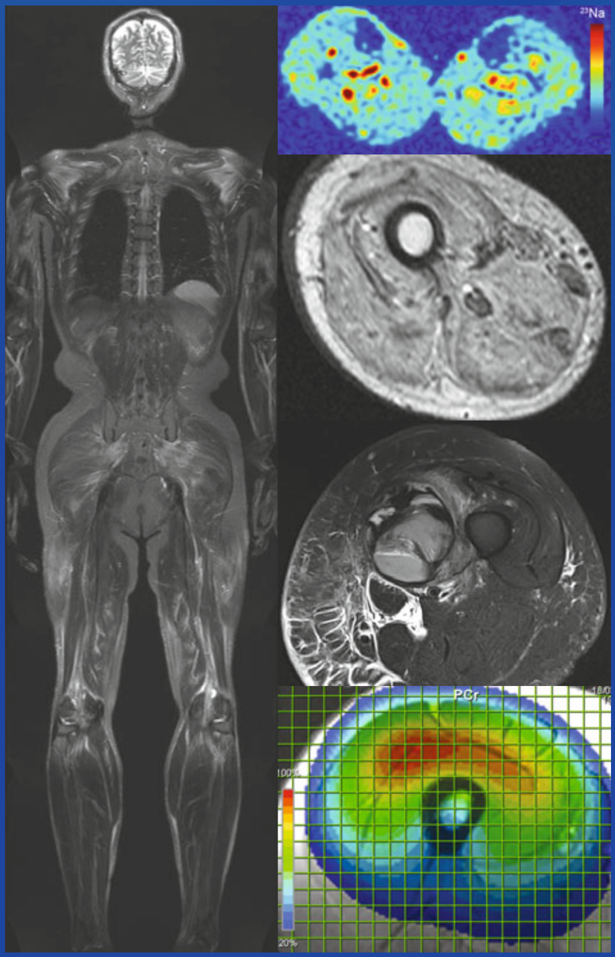

Springer

Medical Radiology

Diagnostic Imaging

Series editors

Maximilian F. Reiser
Hedvig Hricak
Michael Knauth

Editorial Board

Andy Adam, London
Fred Avni, Brussels
Richard L. Baron, Chicago
Carlo Bartolozzi, Pisa
George S. Bisset, Durham
A. Mark Davies, Birmingham
William P. Dillon, San Francisco
D. David Dershaw, New York
Sam Sanjiv Gambhir, Stanford
Nicolas Grenier, Bordeaux
Gertraud Heinz-Peer, Vienna
Robert Hermans, Leuven
Hans-Ulrich Kauczor, Heidelberg
Theresa McLoud, Boston
Konstantin Nikolaou, Munich
Caroline Reinhold, Montreal
Donald Resnick, San Diego
Rüdiger Schulz-Wendtland, Erlangen
Stephen Solomon, New York
Richard D. White, Columbus

For further volumes:
http://www.springer.com/series/4354

Marc-André Weber
Editor

Magnetic Resonance Imaging of the Skeletal Musculature

Springer

Editor
Prof. Dr. med. Marc-André Weber, M.Sc.
Diagnostic and Interventional Radiology
University Hospital Heidelberg
Heidelberg
Germany

ISSN 0942-5373 ISSN 2197-4187 (electronic)
ISBN 978-3-642-37218-6 ISBN 978-3-642-37219-3 (eBook)
DOI 10.1007/978-3-642-37219-3
Springer Heidelberg New York Dordrecht London

Library of Congress Control Number: 2013954837

© Springer-Verlag Berlin Heidelberg 2014
This work is subject to copyright. All rights are reserved by the Publisher, whether the whole or part of the material is concerned, specifically the rights of translation, reprinting, reuse of illustrations, recitation, broadcasting, reproduction on microfilms or in any other physical way, and transmission or information storage and retrieval, electronic adaptation, computer software, or by similar or dissimilar methodology now known or hereafter developed. Exempted from this legal reservation are brief excerpts in connection with reviews or scholarly analysis or material supplied specifically for the purpose of being entered and executed on a computer system, for exclusive use by the purchaser of the work. Duplication of this publication or parts thereof is permitted only under the provisions of the Copyright Law of the Publisher's location, in its current version, and permission for use must always be obtained from Springer. Permissions for use may be obtained through RightsLink at the Copyright Clearance Center. Violations are liable to prosecution under the respective Copyright Law.

The use of general descriptive names, registered names, trademarks, service marks, etc. in this publication does not imply, even in the absence of a specific statement, that such names are exempt from the relevant protective laws and regulations and therefore free for general use.

While the advice and information in this book are believed to be true and accurate at the date of publication, neither the authors nor the editors nor the publisher can accept any legal responsibility for any errors or omissions that may be made. The publisher makes no warranty, express or implied, with respect to the material contained herein.

Printed on acid-free paper

Springer is part of Springer Science+Business Media (www.springer.com)

To my wife, Daniela, and our daughters, Anna Sophie and Leonie Marie,
for making every day a special and joyful one

Foreword

Endorsement on behalf of the European Society of MusculoSkeletal Radiology (ESSR)

Muscle imaging is inherently complex and presents unique morphologic challenges and continuing integration of dynamic, pathophysiologic, and functional capabilities as imaging technology progresses. Compared to the several textbooks dedicated to imaging of the joints, an updated monography addressing muscle MRI is relatively rare. In this regard, this textbook provides a much-wanted survey and update of the current literature on the subject. This comprehensive work is written by internationally renowned experts in the field and is richly illustrated by well-selected high quality images. The work reads fluently and covers all technical issues related to the most advanced techniques for morphologic and functional imaging of the skeletal muscle, such as whole body MRI, diffusion-weighted and diffusion-tensor imaging, ^{23}Na MRI, muscle perfusion imaging and metabolite quantification in MR spectroscopy. Although emphasis has been placed on MRI as a diagnostic modality, correlation with ultrasound is provided in the first part of this book. All aspects of muscle pathology, including inherited disorders, sport-related conditions, inflammatory and ischemic disorders, tumors and non-neoplastic masses are well covered and extensively discussed.

We are convinced that this work will be a very useful tool for both certified general and musculoskeletal radiologists, as well as for orthopedic surgeons, geneticists, rheumatologists, sports physicians, physiatrists, neurologists, and all other colleagues involved in the diagnosis and management of muscle disorders. On behalf of the ESSR, we wish to congratulate the editor, Prof. Marc-André Weber, most warmly on this superb work, and it is our great privilege to recommend this book as a reference standard in modern muscle imaging.

Antwerp Filip M. Vanhoenacker, Secretary ESSR
Genoa Carlo Martinoli, Chairman of the Educational Committee ESSR

Preface

The muscular system is one of the largest organ systems of the human body. In almost every MR image, skeletal muscles are also displayed. Although muscular diseases encompass a huge and heterogeneous group of both hereditary and acquired disorders, in most cases of progressive disease, myopathy presents with focal or general muscle weakness, which is, however, an unspecific symptom. Since the clinical presentation of these disorders may be quite similar, there is a need for ancillary testing. Therefore, in principle, imaging techniques that offer differential diagnostic clues are urgently needed. The ancillary testing in cases of suspected myopathy has traditionally included, besides clinical data, electrodiagnostic, histopathologic, and genetic information, whereas imaging of the peripheral nerves and skeletal muscles was in the past not routinely included in this integrated approach to diagnosis and treatment.

There is increasing evidence, however, that MRI has many advantages for imaging the skeletal muscle, e.g., it can image both superficial and deep structures with equal efficacy (better than ultrasonography), and it can image large areas of the body and is thus ideal for describing patterns of muscle involvement. Moreover, MRI provides excellent differentiation between the skeletal muscle, fat, and adjacent tissues, including bones and tendons. Quantitative MRI measures are valuable for monitoring disease progression. Thus, by virtue of the excellent contrast that it offers between healthy and diseased tissues, MRI is currently the most sensitive imaging modality for displaying the skeletal muscle and its pathologic changes. To date, nevertheless, MRI has often been assigned a subsidiary role in the diagnostic work-up of muscular diseases since routine MRI protocols frequently reveal no pathognomonic findings. This is because morphologic alterations such as edema-like or lipomatous changes are sensitive indicators of disease but are not very disease specific and do not visualize the underlying (patho) physiologic changes.

Now, however, exciting new advances in modern MRI technology make possible the acquisition of functional images that provide deeper insights into the muscle metabolism and even allow for dynamic assessment of the muscular motion. Surrogate pathophysiologic parameters, such as muscular microcirculation, sodium homeostasis, energy and lipid metabolism, and muscle fiber architecture, can now be investigated using these functional MR techniques. Therefore, a much higher level of acceptance and also demand by clinicians are to be expected for these new techniques in the near future, and radiologists will have to face up to the increasing value of MRI in imaging the skeletal musculature.

In order to help in meeting these demands, this book provides a comprehensive overview of the potential of MRI of the skeletal musculature. Recognized authors from all around the world present their experiences regarding the current role of MRI in imaging the skeletal musculature and the diagnostic work-up of myopathies.

The book starts with three chapters on the role of MRI in imaging the skeletal musculature, with a focus on clinical needs, the correlation of imaging to anatomy, and when to use MRI and when to use ultrasonography.

The next six chapters present cutting-edge research findings obtained using modern morphologic and functional MRI techniques for assessment of the skeletal musculature and give some examples of the added value offered by these techniques in the evaluation of muscular diseases. A wide range of topics are covered, from whole-body MRI for evaluation of the entire muscular system to the insights into muscle cell metabolism provided by spectroscopic imaging. Furthermore, promising techniques for the skeletal muscle that have already been introduced in other organ systems, such as diffusion and perfusion imaging and dynamic MRI techniques, are thoroughly discussed.

The last part of the book describes the value of MRI in the diagnostic work-up of different pathologies of the skeletal musculature. In detail, the role of MRI is elucidated in muscle injuries, in neurogenic myopathies, and in establishing the cause of muscle denervation. Of course, the MRI findings in the large fields of muscle dystrophies, inflammatory myopathies, and autoimmune-mediated myositis, as well as muscle channelopathies, are presented and the added value provided by MRI in relation to clinical examination is described. Moreover, the role of MRI alongside electrodiagnostic and genetic testing in the diagnostic work-up is discussed. The MRI characteristics of tumors of the muscle and their sheaths are discussed in detail in the final chapter.

To sum up, “Magnetic Resonance Imaging of the Skeletal Musculature” addresses the increasingly rapid advances in modern MR techniques for imaging of the skeletal musculature and gives a comprehensive overview of the cutting-edge value of MRI for the assessment of normal and diseased skeletal muscle, as well as helpful guidance on the role of alternative imaging techniques, such as ultrasonography. I hope that this book will be a useful and an insightful tool for all physicians with an interest in muscular diseases and that it will aid them in their clinical practice and patient care.

I very much thank the series’ editor, Prof. Maximilian F. Reiser, for inviting me to edit this issue and for his valuable suggestions, and my academic teacher, Prof. Hans-Ulrich Kauczor, for his continuous support and encouragement. Moreover, I am especially grateful to all contributing authors, who are internationally known experts in their field, and I would like to acknowledge their great efforts and their outstanding contributions. I am also very grateful for the constant support and encouragement of Springer, especially Mrs. Corinna Schäfer for all her useful advice and untiring efforts in helping me to collect and edit the book chapters, which deserves special recognition. Last, but not least, a special word of thanks goes to my family for their unstinting encouragement and loving support.

Finally, I hope that readers will share my enthusiasm for the interesting and rapidly developing role of MRI in visualizing the skeletal musculature and will enjoy this textbook.

Heidelberg Marc-André Weber

Contents

Part I Role of MRI in Imaging the Skeletal Musculature

Imaging of Skeletal Muscle in Neuromuscular Disease: A Clinical Perspective . . . 3
Craig M. Zaidman and Lisa D. Hobson-Webb

Correlation of Skeletal Muscle Anatomy to MRI and US Findings . . . 27
Alberto Tagliafico, Bianca Bignotti, Sonia Airaldi and Carlo Martinoli

Imaging the Skeletal Muscle: When to Use MR imaging and When to Use Ultrasound . . . 41
Carlo Martinoli, Sonia Airaldi, Bianca Bignotti and Alberto Tagliafico

Part II Modern MRI Techniques for Assessment of the Skeletal Musculature

Whole-Body MRI for Evaluation of the Entire Muscular System . . . 55
Nicolai Schramm, Sabine Weckbach, Stephen Eustace and Niamh M. Long

Diffusion-Weighted and Diffusion Tensor Imaging: Applications in Skeletal Muscles . . . 69
Usha Sinha and Shantanu Sinha

Assessment of Skeletal Muscle Microperfusion Using MRI . . . 87
Sasan Partovi, Bjoern Jacobi, Yaron Gordon, Lisa Zipp, Anja-Carina Schulte, Sasan Karimi, Rolf Huegli and Deniz Bilecen

Skeletal Muscle MR Imaging Beyond Protons: With a Focus on Sodium MRI in Musculoskeletal Applications . . . 115
Armin M. Nagel, Marc-André Weber, Arijitt Borthakur and Ravinder Reddy

MR Spectroscopy and Spectroscopic Imaging for Evaluation of Skeletal Muscle Metabolism: Basics and Applications in Metabolic Diseases . . . 135
Chris Boesch

Dynamic MR Imaging of the Skeletal Musculature: From Static Measures to a Dynamic Assessment of the Muscular (Loco-) Motion . . . 165
Shantanu Sinha and Usha Sinha

Part III MRI in the Diagnostic Work-up of the Skeletal Musculature

MRI of Muscle Injuries 187
Simon Dimmick, Christoph Rehnitz, Marc-André Weber and James M. Linklater

MRI of Muscle Denervation in Central and Peripheral Nervous System Disorders 221
Mirko Pham, Marcel Wolf, Philipp Bäumer, Martin Bendszus and Gregor Kasprian

MRI in Muscle Dystrophies and Primary Myopathies 241
Dirk Fischer and Mike P. Wattjes

MRI in Inflammatory Myopathies and Autoimmune-Mediated Myositis 255
Umesh A. Badrising, Hermien E. Kan and Jan JGM Verschuuren

MRI in Muscle Channelopathies 271
Karin Jurkat-Rott, Marc-André Weber and Frank Lehmann-Horn

MRI in Muscle Tumors and Tumors of Fasciae and Tendon Sheaths 289
F. M. Vanhoenacker, M. E. A. P. M. Adriaensen-van Roij and A. M. De Schepper

Index 309

Contributors

M. E. A. P. M. Adriaensen-van Roij Department of Radiology, Atrium Medical Center Parkstad, Henri Dunantstraat 5, Heerlen, The Netherlands

Sonia Airaldi Radiology Department – DISSAL, University of Genova, Via Pastore 1, Genoa, Italy

Umesh A. Badrising Department of Neurology, K5-Q, Leiden University Medical Center, Albinusdreef 2, Leiden, The Netherlands, e-mail: u.a.badrising@lumc.nl

Philipp Bäumer Department of Neuroradiology, University Hospital Heidelberg, Im Neuenheimer Feld 400, Heidelberg, Germany

Martin Bendszus Department of Neuroradiology, University Hospital Heidelberg, Im Neuenheimer Feld 400, Heidelberg, Germany

Bianca Bignotti Department of Health Sciences – DISSAL, Università di Genova, Via Pastore 1, Genoa, Italy

Deniz Bilecen Department of Radiology and Nuclear Medicine, University Hospital Bruderholz, Bottmingen, Switzerland, e-mail: deniz.bilecen@unibas.ch

Chris Boesch AMSM (DKF and DIPR), University and Inselspital Bern, Pavilion 52A Inselspital, P.O. Box 35, Bern, Switzerland, e-mail: chris.boesch@insel.ch

Arijitt Borthakur Department of Radiology, School of Medicine, Center for Magnetic Resonance and Optical Imaging, University of Pennsylvania, Philadelphia, PA, USA

A. M. De Schepper Department of Radiology, University Hospital Antwerp, Wilrijkstraat 10, Edegem, Belgium

Simon Dimmick Castlereagh Imaging, 60 Pacific Highway, St Leonards, NSW, Australia

Stephen Eustace Departments of Radiology, Mater Misericordiae University Hospital and Cappagh National Orthopaedic Hospital, University College Dublin, Dublin, Ireland

Dirk Fischer Department of Neurology, University Hospital of Basel, Basel, Switzerland; Division of Neuropediatrics, University Children's Hospital of Basel, Basel, Switzerland, e-mail: Dirk.Fischer@ukbb.ch

Yaron Gordon Department of Diagnostic and Interventional Radiology, University Hospital Heidelberg, Heidelberg, Germany

Lisa D. Hobson-Webb Department of Neurology, Duke University Medical Center, DUMC 3403, Durham, NC, USA

Rolf Huegli Department of Radiology and Nuclear Medicine, University Hospital Bruderholz, Bottmingen, Switzerland

Bjoern Jacobi Third Department of Medicine-Hematology, Oncology, Pneumology, University Medical Center of Johannes Gutenberg University, Mainz, Germany

Karin Jurkat-Rott Department of Neurophysiology, Ulm University, Albert-Einstein-Allee 11, Ulm, Germany, e-mail: karin.jurkat-rott@uni-ulm.de

Hermien E. Kan Department of Neurology, K5-Q, Leiden University Medical Centre, Albinusdreef 2, P.O. Box 9600, Leiden, The Netherlands

Sasan Karimi Department of Neuroradiology, Memorial Sloan-Kettering Cancer Center, New York, NY, USA

Gregor Kasprian Division of Neuroradiology and Musculoskeletal Radiology, Department of Biomedical Imaging and Image-guided Therapy, Medical University of Vienna, Währinger Gürtel 18–20, Vienna, Austria

Frank Lehmann-Horn Department of Neurophysiology, Ulm University, Albert-Einstein-Allee 11, Ulm, Germany

James M. Linklater Castlereagh Imaging, 60 Pacific Highway, St Leonards, NSW, Australia, e-mail: JamesLinklater@casimaging.com

Niamh M. Long Department of Radiology, Cappagh National Orthopaedic Hospital, Dublin, Finglas, Ireland

Carlo Martinoli Department of Health Sciences – DISSAL, Università di Genova, Via Pastore 1, Genoa, Italy, e-mail: carlo.martinoli@unige.it

Armin M. Nagel Medical Physics in Radiology, German Cancer Research Center (DKFZ), Heidelberg, Germany, e-mail: a.nagel@Dkfz-Heidelberg.de

Sasan Partovi Department of Radiology and Nuclear Medicine, University Hospital Bruderholz, Bottmingen, Switzerland; Department of Radiology, University Hospitals Case Medical Center, Case Western Reserve University, Cleveland, OH, USA

Mirko Pham Department of Neuroradiology, University Hospital Heidelberg, Im Neuenheimer Feld 400, Heidelberg, Germany, e-mail: Mirko.Pham@med.uni-heidelberg.de

Ravinder Reddy Department of Radiology, School of Medicine, Center for Magnetic Resonance and Optical Imaging, University of Pennsylvania, Philadelphia, PA, USA

Nicolai Schramm Institute for Clinical Radiology, Ludwig-Maximilians-University Hospital Munich, Marchioninistr. 15, Munich, Germany, e-mail: nicolai. schramm@med.uni-muenchen.de

Anja-Carina Schulte Department of Radiology and Nuclear Medicine, University Hospital Bruderholz, Bottmingen, Switzerland

Shantanu Sinha Department of Radiology, University of California, San Diego, CA, USA, e-mail: shsinha@mail.ucsd.edu

Usha Sinha Department of Physics, San Diego State University, San Diego, CA, USA, e-mail: usinha@sciences.sdsu.edu

Alberto Tagliafico Department of Experimental Medicine (DIMES), University of Genoa, Via L.B. Alberti, Genoa, Italy, e-mail: albertotagliafico@gmail.com

F. M. Vanhoenacker Department of Radiology, University Hospital Antwerp, Wilrijkstraat 10, Edegem, Belgium; General Hospital Sint-Maarten Duffel-Mechelen, Rooienberg 25, Duffel, Belgium; Faculty of Medicine and Health Sciences, University of Ghent, Ghent, Belgium, e-mail: filip.vanhoenacker@telenet.be

Jan JGM Verschuuren Neuromuscular Division and Division of Child Neurology, Department of Neurology, School of Medicine, Washington University, St. Louis, MO, USA

Mike P. Wattjes Department of Radiology and Nuclear Medicine, VU University Medical Center, Amsterdam, The Netherlands

Marc-André Weber Department of Diagnostic and Interventional Radiology, University Hospital Heidelberg, Heidelberg, Germany, e-mail: marcandre.weber@med.uni-heidelberg.de

Sabine Weckbach Department of Diagnostic and Interventional Radiology, University Hospital Heidelberg, Heidelberg, Germany

Marcel Wolf Department of Neuroradiology, University Hospital Heidelberg, Heidelberg, Germany

Craig M. Zaidman Neuromuscular Division and Division of Child Neurology, Department of Neurology, School of Medicine, Washington University, St. Louis, MO, USA, e-mail: zaidmanc@neuro.wustl.edu

Lisa Zipp Department of Radiology and Nuclear Medicine, University Hospital Bruderholz, Bottmingen, Switzerland; Department of Pediatrics, Rainbow Babies and Chidren's Hospital, Cleveland, OH, USA

Part I

Role of MRI in Imaging the Skeletal Musculature

Imaging of Skeletal Muscle in Neuromuscular Disease: A Clinical Perspective

Craig M. Zaidman and Lisa D. Hobson-Webb

Contents

1 Introduction 4

2 Overview of Neuromuscular Disease 4

3 Clinical Presentations 4
3.1 Myopathy 4
3.2 Neuropathy 5
3.3 Motor Neuron Disease 5
3.4 Disorders of the Neuromuscular Junction 5
3.5 Ion Channel Disorders 6

4 Evaluation of Neuromuscular Disorders 6
4.1 Patient History 6
4.2 Physical Examination 6
4.3 Serological Investigations 7
4.4 Electrodiagnostic Testing 8
4.5 Nerve and Muscle Biopsy 9
4.6 Genetic Testing 10

5 Imaging of Muscle 10
5.1 MRI of Skeletal Muscle 10
5.2 Ultrasound Imaging 12
5.3 Computed tomography and Radiographs 14

6 Muscle Imaging in Neuromuscular Disorders 14
6.1 Overview 14
6.2 Denervation 16
6.3 Myopathy 17
6.4 Immune and Inflammatory Myopathies 18
6.5 Hereditary Myopathies 19
6.6 Congential Myopathies 20
6.7 Glycogen Storage Disorder Myopathies 20
6.8 Muscular Dystrophies 21

7 Diagnostic Utility of Imaging in Neuromuscular Disease 21

8 Conclusions 22

References 22

Abstract

Neuromuscular diseases result from pathologic processes affecting the peripheral nerve, neuromuscular junction, or muscle. The clinical phenotypes of these differing disorders may overlap, creating difficulty in making an exact diagnosis. Skeletal muscle imaging offers a noninvasive means of obtaining detailed information on the presence and pattern of pathology that may augment the evaluation. In addition to diagnosis, imaging of muscle may prove valuable for longitudinal study of individual patients. While computed tomography (CT) and ultrasonography (US) are utilized, magnetic resonance imaging (MRI) provides a superior view of muscle. Additional studies will determine the best methods of imaging and their exact role in the care of patients with neuromuscular disease.

Key Points

1. Neuromuscular disease encompasses a wide range of disorders involving the peripheral nerve, neuromuscular junction, and muscle. The current standard of care involves clinical examination, serological studies, electrodiagnostic testing, and pathological examination. Muscle imaging is underutilized in the evaluation of patients of suspected neuromuscular disorders.
2. Muscle imaging, particularly with US and MRI augments the clinical and electrodiagnostic evaluation by providing detailed anatomic information on the presence and pattern of pathology that can impact the differential diagnosis and aid in site selection for biopsy.
3. Muscle MRI may be a valuable tool for monitoring progression of disease and response to therapeutic interventions.

C. M. Zaidman (✉)
Department of Neurology, Neuromuscular Division and Division of Child Neurology, Washington University in Saint Louis School of Medicine, St. Louis, USA
e-mail: zaidmanc@neuro.wustl.edu

L. D. Hobson-Webb
Department of Neurology, Duke University Medical Center, DUMC 3403, Durham, NC 27710, USA

M.-A. Weber (ed.), *Magnetic Resonance Imaging of the Skeletal Musculature*, Medical Radiology. Diagnostic Imaging,
DOI: 10.1007/174_2013_846, © Springer-Verlag Berlin Heidelberg 2013
Published Online: 6 July 2013

1 Introduction

Neuromuscular diseases encompass a broad and diverse array of disorders affecting the nerve, neuromuscular junction, and muscle. The clinical presentation of these disorders may be quite similar, creating a need for ancillary testing. The approach to diagnosis and treatment requires an integrated approach that merges clinical, electrodiagnostic, pathologic, and genetic data. Imaging of the peripheral nerve and muscle has traditionally not been routinely performed. However, there is increasing evidence that peripheral nerve and muscle imaging is uniquely informative in the evaluation of patients with suspected neuromuscular disease. Imaging studies, including ultrasound (US) and magnetic resonance imaging (MRI), can accurately depict alterations in nerve and muscle structure and inform the differential diagnosis. MRI is particularly well suited for evaluation of muscle as it can similarly visualize both deep and superficial tissues, offering excellent contrast between healthy and diseased tissues. This chapter will serve as an introduction to the categorization, clinical presentation, and evaluation of neuromuscular disorders with an emphasis on the radiologic findings of MRI in healthy and diseased muscle.

2 Overview of Neuromuscular Disease

The term “neuromuscular disease” encompasses a broad, heterogeneous spectrum of processes arising from pathology in the nerve, muscle, or neuromuscular junction. This umbrella includes disorders as common as diabetic polyneuropathy and as rare as congenital myasthenia gravis. Many of these disorders have some effect upon muscle, most often resulting in variable degrees and patterns of weakness. Subtle differences in the clinical symptoms of disease, the presence of comorbidities, and anatomical distribution of involvement aid in diagnosis. Additional information on nerve and muscle function, garnered from nerve conduction studies (NCS) and electromyography (EMG) is also valuable, but often lacks specificity. Muscle biopsy, nerve biopsy, and increasingly genetic testing are performed to better define the etiology of disease. Although powerful diagnostic tools, biopsies are invasive and genetic testing requires a relatively narrow differential diagnosis. While whole-exome sequencing is now available to avert the need for a specific genetic question, interpretation of results remains challenging (Goh and Choi 2012). Muscle imaging, in select cases, is a valuable technique to identify pathology and guide further testing (Lovitt et al. 2006).

3 Clinical Presentations

3.1 Myopathy

Myopathy encompasses both hereditary and acquired disorders of muscle and typically present with muscle weakness as the defining feature. Myalgias, stiffness, cramps, and fatigue are also common complaints. Weakness may be absent, or so mild as to go unnoticed by patients with the problem first detected by incidental discovery of elevated creatine phosphokinase (CK or CPK) levels. Myopathies are not associated with paresthesias or loss of sensation. The physical examination findings of myopathy are variable. “Typical” myopathy is characterized by symmetric, proximal more than distal extremity weakness with depression of tendon reflexes in proportion to the degree of weakness. Variable degrees of facial and bulbar weakness can be present. The sensory examination should be normal. Certain myopathies may deviate from the usual limb girdle pattern of weakness, resulting in extraocular muscle weakness (mitochondrial disorders (Schrier and Falk 2011)), deep finger flexor weakness (inclusion body myopathy (Dimachkie and Barohn 2013)), or asymmetric face and shoulder weakness (facioscapulohumeral dystrophy (Orrell 2011)).

Hereditary myopathies can present at any age, from birth or early childhood (congenital myopathy) through late adulthood. Onset at birth or early childhood suggests a genetic cause, but acquired myopathies such as dermatomyositis are also well-known to occur in childhood. In addition to weakness, congenital or hereditary myopathies may present with symptoms affecting other organ systems, including musculoskeletal, cardiac, and central nervous system abnormalities. Arthrogryposis, elongated facial features, scoliosis, and a high arched palate may all be the result of early weakness. Joint contractures feature prominently in select congenital myopathies and muscular dystrophies (e.g., Bethlem myopathy, Emery-Dreifuss muscular dystrophy (Bonnemann 2011; Puckelwartz and McNally 2011)), while cardiomyopathy is also noted frequently. Hepatomegaly may be present in glycogen storage disorders (Prater et al. 2012; Hobson-Webb et al. 2010) and hearing loss is often noted in association with mitochondrial disease (Marti et al. 2010).

Acquired myopathies, such as polymyositis and dermatomyositis, commonly present with insidious, progressive proximal, symmetric weakness with elevated CK levels, and are sometimes accompanied by a rash or other cutaneous manifestation (Callen 2010). Identifying and distinguishing acquired from hereditary myopathies is essential as acquired myopathies often respond to immune-modulating therapies. In addition, involvement of other organ systems is common and can impact care. Acquired myopathies have been associated with interstitial lung disease, connective tissue disorders, and hematologic disturbances (e.g., hemolytic anemia) (Andrews and Hall 2002; Mimori et al. 2012). Myocarditis may occur in fulminant myositis (Bazzani et al. 2010). Weakness from an acquired inflammatory myopathy is sometimes the presenting feature of a paraneoplastic disorder and should prompt a search for underlying malignancy (Zahr and Baer 2011).

3.2 Neuropathy

The term “neuropathy” in its broadest sense refers to both mononeuropathy (affecting a single nerve i.e., carpal tunnel) and polyneuropathy (affecting multiple nerves). The most common variant, often termed “peripheral neuropathy”, is a length-dependent sensorimotor polyneuropathy, in which patients commonly present with tingling, pain, numbness, and/or weakness in the distal feet that may ascend to involve the lower legs and hands. In peripheral neuropathy, sensory symptoms usually predominate with weakness occurring in more advanced disease. Ankle dorsiflexion and the intrinsic foot musculature are typically affected. Peripheral neuropathy can be inherited (Charcot-Marie-Tooth Disease) or acquired. Common causes of acquired peripheral neuropathy include diabetes mellitus, monoclonal gammopathy, nutritional deficiencies, infection, and connective tissue disorders. Immune-mediated sensorimotor polyneuropathies present in a more precipitous fashion with weakness being a more prominent feature than in other acquired peripheral neuropathies. These neuropathies are often responsive to immune-modulating therapies.

The physical examination of typical sensorimotor peripheral neuropathy reveals loss of sensation in a length-dependent pattern. Preferential small fiber nerve loss leads to impairment of temperature and pinprick sensation. Involvement of larger nerve fibers presents with reduced vibratory sense or proprioception. The motor examination may reveal reduced muscle bulk and atrophy in the distal lower extremities, with relative sparing of proximal muscle groups. Toe extensor and ankle dorsiflexor strength are commonly impaired. In peripheral neuropathies, the achilles reflex is preferentially lost, while demyelinating polyneuropathies may result in loss of all tendon reflexes. Only in the most severe cases will there be involvement of respiratory or cranial nerve function.

3.3 Motor Neuron Disease

Lower motor neuron disease (MND) is a disorder of the anterior horn cell and, as it affects the motor but not sensory nerve, results in weakness without altered sensation. Lower motor neuron degeneration creates muscle atrophy and progressive, severe loss of strength affecting cranial, truncal, and limb musculature. Unlike peripheral neuropathy, MNDs do not show a length dependent pattern and affect bulbar, proximal, and distal muscle groups. The two most common MNDs are amyotrophic lateral sclerosis (ALS) (Ludolph et al. 2012), which typically presents in adulthood, and spinal muscular atrophy (SMA) (D’Amico et al. 2011), an autosomal recessive disorder which presents at birth or childhood through early adulthood depending on the degree of weakness. Unlike SMA, ALS is a disease of both the central and peripheral nervous system, and therefore presents with a combination of upper (hyperreflexia, spasticity, and increased tone) and lower motor neuron findings, which are often asymmetric. ALS is typically sporadic, although heritable causes of ALS represent approximately 5–10 % of cases (Pratt et al. 2012).

Patients with MND typically present with painless weakness or, in ALS, onset of dysarthria. Fasciculations and cramps are commonly present. Muscle atrophy is typically noted in association with limb weakness. In SMA, the examiner is confronted with an attentive, alert child with variable degrees of proximal, distal, and bulbar weakness and muscle atrophy with diffusely reduced reflexes. Respiratory insufficiency is common and can be life threatening. In older children with SMA, truncal weakness results in scoliosis that often requires bracing and surgical intervention (D’Amico et al. 2011). In ALS, central nervous system involvement is reflected in spastic speech, hyperactive tendon and gag reflexes, and pseudobulbar affect (Ludolph et al. 2012). Frontotemporal dementia is increasingly recognized as part of the disease spectrum in ALS (Achi and Rudnicki 2012). Respiration ultimately becomes impaired and is the frequent cause of death.

3.4 Disorders of the Neuromuscular Junction

Neuromuscular junction disease results from a disturbance in pre- or post-synaptic communication between the motor nerve terminal and the muscle endplate. Neuromuscular junction disorders result in weakness that may mimic myopathy or motor neuron disease, but differ in that weakness often affects the bulbar muscles and is typically fatigable. A relatively common neuromuscular junction disorder is myasthenia gravis, an autoimmune disorder of the post-synaptic neuromuscular junction that can affect patients of any age. Myasthenia gravis classically presents with asymmetric ptosis and fluctuating diplopia. Chewing fatigue, dysarthria, dysphagia, respiratory difficulties, and proximal extremity weakness are other common symptoms. On clinical examination, fatigable ptosis, extraocular dysmotility, and proximal weakness may be dominant features (Juel and Massey 2007). Lambert–Eaton myasthenic syndrome (LEMS), an acquired disorder of presynaptic transmission associated with malignancies, congenital myasthenic syndromes, and botulism are less frequent etiologies of disordered neuromuscular transmission. Sluggishly reactive pupils may be found in both LEMS and botulism with the former having milder degrees of weakness and more insidious onset. Tendon reflexes may be depressed or absent in LEMS with facilitation noted after a brief period of exercise (Sanders and Juel 2008). Congenital myasthenic syndromes can present in childhood or adulthood with bulbar and ocular symptoms similar to myasthenia gravis or with a limb-girdle pattern of weakness that mimics myopathy.

3.5 Ion Channel Disorders

Ion channel disorders represent a distinct class of neuromuscular disease that include periodic paralysis, neuromyotonia, and the nondystrophic myotonias (Abou-Zeid et al. 2012; Burge and Hanna 2012; Matthews et al. 2010). Disruptions in the normal functioning of the chloride, calcium, potassium, and sodium channels create phenotypes that range from attacks of near total paralysis to states of near continuous muscle activity. These disorders are diagnosed through a careful clinical history and examination augmented by electrodiagnostic and genetic testing. The physical examination is often normal in periodic paralysis, while muscle hypertrophy and myotonia are found in myotonia congenita. Muscle biopsy may be abnormal, but is often nonspecific. Electrodiagnostic and molecular genetic testing are typically used to confirm the diagnosis.

4 Evaluation of Neuromuscular Disorders

4.1 Patient History

The clinical history and physical examination are essential in guiding the evaluation of neuromuscular disorders. The patient's chief complaint, most often weakness or numbness, can occur from any number of causes. To narrow the differential diagnosis, a detailed history must be taken. A key component of the history is to establish the time course and distribution of the symptoms. Questioning should be directed toward determining if symptoms were monophasic, progressive or fluctuating. In acquired neuromuscular disorders, the onset of symptoms can usually be defined. Patients with a chronic, slowly progressive disorder are often unable to recall the time of onset or note any recent evidence of progression. In these situations, identifying the loss of a particular skill, such as difficulty arising from a chair or ascending stairs, can provide a more defined timeline of the disorder. For inherited disorders like Charcot-Marie-Tooth and hereditary muscular dystrophies, it is helpful to elicit a developmental history. Difficulties with feeding or breathing after birth suggest involvement in the neonatal period. Delayed motor milestones, incoordination, or difficulty performing at the level of other children at play or during sports is also informative. A careful family history is also needed, keeping in mind that the patient or other family members often harbor symptoms they may not identify as related to the neuromuscular system. It is useful to ask specifically about family members with difficulties with ambulation, an unusual gait, the need for assistive devices like walkers or wheelchairs, and a family history of cardiomyopathy or sudden cardiac death.

After establishing the temporal course of disease, the history can focus on associated symptoms. Paresthesias are likely to occur in neuropathy, but not myopathy. Episodes of dark, tea-colored urine are most suggestive of a metabolic myopathy. Muscle atrophy and fasciculations and a change in affect heighten suspicion for motor neuron disease. As neuromuscular disorders often affect other organ systems, it is critical to elicit a detailed review of systems of the patient and potentially affected family members. For instance, cataracts and diabetes mellitus can be seen in myotonic dystrophy while dementia can be seen in patients or family members with familial ALS. Thus, a thorough history provides tremendous guidance and, along with the physical exam, are the hallmarks of evaluating a patient with suspected neuromuscular disorder.

4.2 Physical Examination

A complete physical examination should be performed in each patient presenting with possible neuromuscular disease. The examiner should not overlook nonneurologic segments of the exam, as critical findings may be missed. Hepatomegaly may indicate a glycogen storage disease causing myopathy or be found in patients with amyloidosis and polyneuropathy. Cardiomyopathy and cardiac arrhythmias are found in many hereditary myopathies, while the ophthalmologic examination may hold clues in myotonic dystrophy or mitochondrial disorders. Skeletal deformities, like pectus excavatum, are indicative of some congenital myopathies mediated by mutations in the ryanodine receptor gene. Contractures are a common feature of Emery–Dreifus muscular dystrophy (Puckelwartz and McNally 2011). Scoliosis is common in many neuromuscular disorders, can lead to impaired respiration when severe, and can be improved with bracing or surgical intervention.

The neurological examination should begin with an assessment of mental status. Hereditary disorders may be associated with cognitive impairment, particularly mitochondrial disease and myotonic dystrophy. ALS is associated with frontotemporal dementia, which may be more apparent from the history than on bedside cognitive tests like the mini-mental status examination (MMSE) or the montreal cognitive assessment (MOCA) (Achi and Rudnicki 2012). Detailed neuropsychological testing may be needed to discern the extent of impairment in these cases. Following examination of mentation, a complete cranial nerve examination should be performed. For all cases, an assessment of facial and bulbar strength is needed. This not only serves to narrow the differential diagnosis, but to identify patients at risk for swallowing and/or respiratory impairment. The presence of extraocular motility abnormalities should raise concern for mitochondrial and neuromuscular junction disorders. Ptosis and facial weakness may also be seen in these conditions, along with myopathies.

The motor examination should focus on identifying the presence and pattern of weakness. Careful observation of the relative distribution of weakness will go far in narrowing the differential diagnosis. The relative involvement of distal versus proximal muscles may help differentiate several hereditary disorders. Preferential and early involvement of the quadriceps or deep finger flexors is common in inclusion body myopathies. Scapular winging can point toward facioscapulohumeral muscular dystrophy (FSHD) or ryanodine receptor myopathies among others. Muscle bulk and tone is also a critical component of the motor examination. Calf pseudohypertrophy is common in several muscular dystrophies, including Duchenne muscular dystrophy. Muscle atrophy is common in neurogenic disorders, while preserved muscle bulk with weakness argues in favor of a myopathy. Increased tone or spasticity in the setting of weakness informs the examiner of concurrent upper motor neuron involvement. Examination of tendon reflexes should be included and interpreted in the context of the motor examination. Most myopathies, neuropathies, and other neuromuscular disorders are associated with either normal or depressed tendon reflexes. Hyperreflexia in a weak muscle supports upper motor neuron involvement as in ALS, while absent reflexes in a strong muscle suggests a neurogenic etiology with sensory involvement.

Evaluation of cerebellar function and gait is also extremely important and can inform the differential diagnosis of neuromuscular disorders. Ataxia is typically absent in most myopathies, although weakness may mimic ataxia. Some neuropathies present with ataxia from impairment of the sensory system, for example neuropathy from vitamin B12 deficiency (Rudnicki 2010). Other disorders, such as Friedreich's ataxia, present with sensory neuropathy and ataxia stemming from involvement of both the cerebellum and peripheral nervous system. Other abnormalities of gait can be further informative. Hyperlordosis and pelvic instability (Trendelenburg gait) is indicative of proximal, hip-girdle weakness. Watching a child arise from the floor can reveal the need to push off or climb up the leg to stand (Gower's maneuver). Foot drop, the result of moderate to severe ankle dorsiflexor weakness, is often found in neuropathies. Rarely, patients with myopathy can present with foot drop as a sign of distal more than proximal weakness. This narrows the differential diagnosis considerably, as "distal predominant myopathies" are relatively uncommon compared to limb-girdle myopathies with proximal weakness. Other findings evident on gait analysis include ankle and elbow contractures (Emery-Dreifuss muscular dystrophy (Puckelwartz and McNally 2011)), scoliosis, and kyphosis.

The sensory examination and evaluation of deep tendon reflexes completes the physical assessment. Sensory loss usually indicates the presence of a neuropathy, with a stocking-glove pattern of abnormalities being most common. Loss of sensation in a multifocal pattern corresponding to individual peripheral nerve territories suggests mononeuritis multiplex, while a dermatomal pattern of loss may indicate radiculopathy. Sensory loss is typically absent in myopathies, motor neuron disease, and disorders of the neuromuscular junction. Co-morbidities like diabetes mellitus may result in sensory loss and can complicate the assessment. Again, identifying the distribution of symptoms and signs is critical in forming differential diagnosis. Myopathy tends to affect the proximal more than distal muscle groups. Neuropathy tends to progress in a length dependent fashion, and typically begins in the distal most regions.

4.3 Serological Investigations

Serological studies can be valuable in the assessment of neuromuscular disease. These tests are ordered based on the history and physical examination, serving to provide more information on the suspected diagnosis. As with the history and examination, the serological studies of interest depend on the suspected illness. In disorders of muscle, it is common to evaluate the serum level of CK. CK is an enzyme produced by several tissues, including muscle, and can be elevated in many myopathic disorders. The degree and persistence of elevation in the CK can impact the differential diagnosis. Duchenne muscular dystrophy, for instance, typically has chronic, marked elevations in the CK in the tens of thousands. Acute, marked elevation of CK levels (>10,000 U/L) in the presence of myoglobinuria is indicative of rhabdomyolysis. This can occur after exposure to sustained, high intensity exercise, often in association with heat and dehydration, in patients with metabolic

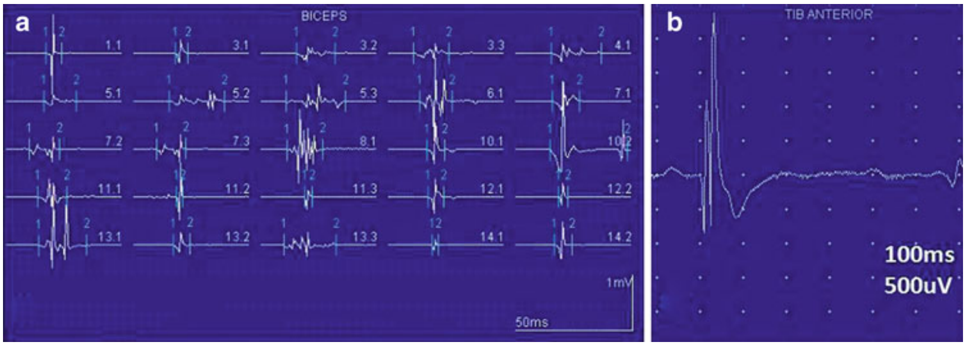

Fig. 1 Myopathic and neuropathic motor unit potentials (MUPs) on electromyography (EMG). **a** Short duration, polyphasic, low amplitude MUPs are seen in this quantitative EMG study of a patient with myopathy. **b** A tall, long duration MUP indicates chronic reinnervation in a patient with neuropathy

disorders of muscle metabolism (e.g., McArdle's disease), or myositis resulting from a viral illness or toxin exposure. CK can also be increased in otherwise healthy, asymptomatic subjects, particularly following strenuous physical activity (Gojanovic et al. 2011; Pantoja et al. 2009). Thus, in the asymptomatic patient with mild to moderately elevated CK, a repeat evaluation after sustaining from activity can be highly informative. Two other features of CK are particularly noteworthy. One, the absence of an elevated CK does not exclude a myopathy, and two, the presence of an elevated CK in a weak patient, particularly if mildly elevated, is not specific for myopathy and can occur from denervation (e.g., SMA). Importantly, in addition to CK, muscle disease can result in elevations of other serologic markers including aldolase, aspartate aminotransferase (AST), alanine aminotransferase (ALT), and lactate dehydrogenase (LDH). It is therefore important to evaluate the CK in patients who have unexpectedly elevated AST and ALT in order to avoid unnecessary investigations (e.g., liver biopsy).

Additional testing is usually tailored toward the suspected diagnosis. In patients with suspected inflammatory myopathy, myositis antibody profiles and markers of connective tissue disorders are requested. Depending on the type of inflammatory myopathy and the age of the patient, additional investigation for malignancy or involvement of other organ systems (e.g., interstitial lung disease) is often warranted. Myasthenia gravis commonly results in elevated acetylcholine receptor or, more rarely, anti-MuSK antibody titers (Meriggioli and Sanders 2012). Anti-ganglioside antibodies (GM1 or Ns6s antibodies) are found in patients with multifocal motor neuropathy, a relatively rare, but treatable autoimmune disorder affecting motor nerves (Muley and Parry 2012; Galban-Horcajo et al. 2013). In patients with distal symmetric polyneuropathy, blood glucose levels, serum protein electrophoresis with immunofixation, and vitamin B12 measures are the recommended first line of testing (England et al. 2009), but are far from comprehensive. These are but a few examples of some relatively common serologic markers of neuromuscular disease. Ultimately, testing must be tailored to the individual patient and interpreted in the context of the history and physical exam.

4.4 Electrodiagnostic Testing

Electrodiagnostic (EDx) testing, consisting of NCS and EMG is an essential part of evaluating the patient with a suspected neuromuscular disorder. In nerve conduction studies, the motor or sensory nerve is electrically stimulated and the speed and amplitude of the response, from either the muscle or the sensory nerve, is recorded. In EMG, a needle is inserted into the muscle and the presence and patterns of electrical activity of the muscle fiber and motor units are observed. Trained, experienced clinicians should perform the testing, as it is technically demanding and operator dependent. For instance, cool skin temperature can result in falsely normal sensory amplitudes or falsely slowed conduction velocities (Herrera et al. 2010). Interpretation of motor unit morphology and patterns on EMG also requires a high level of expertise, as the characteristics of denervation, reinnervation, and myopathy can vary significantly depending on the duration and severity of disease. It is therefore essential to validate the quality and experience of the electrodiagnostic laboratory to ensure that patients are receiving quality testing and accurate interpretation.

When performed properly, EDx testing can differentiate neuropathies, myopathies and neuromuscular junction disorders (Fig. 1). Neuropathies can be divided into axonal or demyelinating, based upon the NCS results, while EMG can help refine the characteristics and distribution of disease. In myopathies, the EMG is most helpful, both for characterizing the pattern of involvement and the level of muscle membrane instability present. For instance, the presence of abnormal spontaneous activity (fibrillations, positive sharp

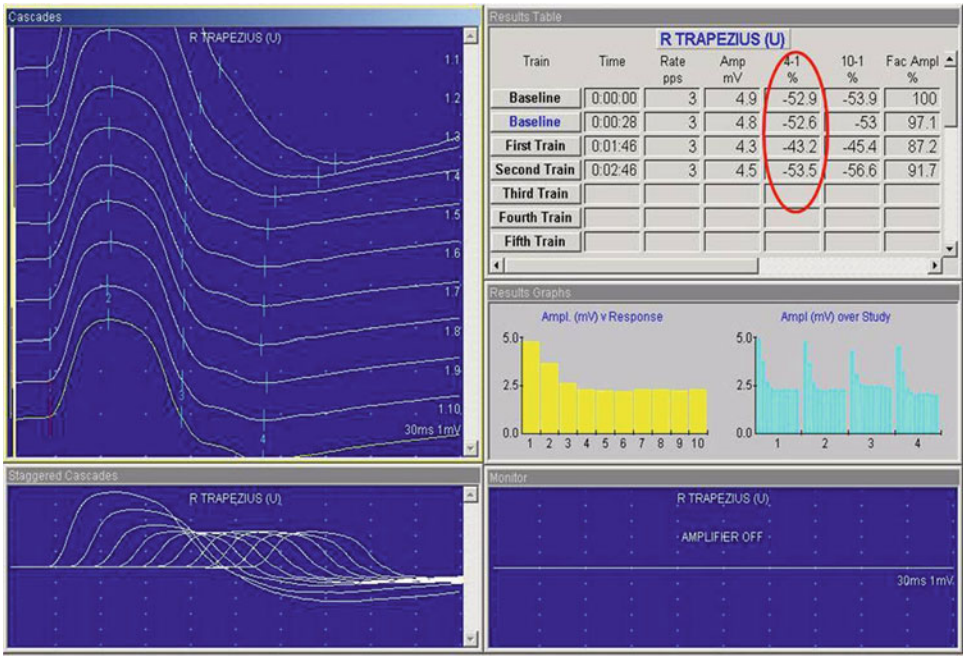

Fig. 2 Repetitive nerve stimulation (RNS) of the right trapezius in a patient with myasthenia gravis. In healthy controls, there should be no decline in the size of the nerve response. In this patient, the amplitude declines by 43–54 %, indicating a disorder of the neuromuscular junction

R TRAPEZIUS (U)

Train	Time	Rate pps	Amp mV	4-1 %	10-1 %	Fac Ampl %
Baseline	0:00:00	3	4.9	-52.9	-53.9	100
Baseline	0:00:28	3	4.8	-52.6	-53	97.1
First Train	0:01:46	3	4.3	-43.2	-45.4	87.2
Second Train	0:02:46	3	4.5	-53.5	-56.6	91.7
Third Train						
Fourth Train						
Fifth Train						

waves) signifies muscle membrane instability and is typically seen in inflammatory myopathies and muscular dystrophies. Neuromuscular junction disorders are identified by special testing (i.e., repetitive nerve stimulation and single fiber electromyography) that is designed to reveal dysfunction at the pre- and post-synaptic levels (Fig. 2). Together, the combination of NCS and EMG can identify and differentiate irritable from nonirritable myopathy, axonal from demyelinating neuropathy, and pre- and post-synaptic disorders of neuromuscular junction transmission. In addition, by quantifying the level of response, EMG and NCS can describe the pattern of disease, identifying asymmetry and grading degree of involvement of different body regions. Thus, EDx is not only essential to narrowing the differential diagnosis but can determine the need for and location of nerve and muscle biopsy.

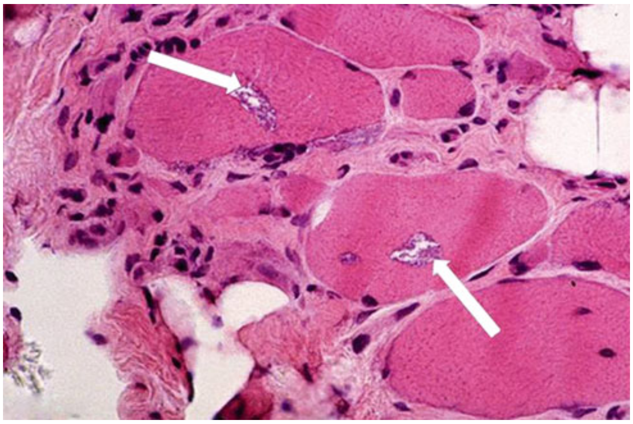

Fig. 3 Muscle biopsy in a patient with inclusion body myositis. In this patient, the characteristic rimmed vacuoles are seen (*arrows*). However, several biopsies are often needed to confirm the diagnosis secondary to the heterogeneous pattern of involvement

4.5 Nerve and Muscle Biopsy

Tissue biopsy is often necessary to provide an exact diagnosis (Fig. 3). Both muscle and nerve can be biopsied for histopathology and molecular studies. Muscle biopsy is indicated in patients with weakness, fatigue, myalgia, cramping, or persistently high CK. Muscle biopsy is typically performed following EDx testing, and, if possible, in a muscle not examined by EMG to avoid artifact from needle insertion. Some conditions, such as myasthenia gravis, are better diagnosed by NCS while other conditions (e.g., Duchenne muscular dystrophy), have such well-characterized genotypes that genetic testing is increasingly replacing muscle biopsy as the diagnostic test of choice. Muscle biopsy can be particularly helpful when evaluating patients with suspected systemic disorders, such as mitochondrial disorders as enzyme levels of mitochondrial function can be measured directly from muscle tissue. Additionally, systemic conditions, including amyloidosis (Chuquilin and Al-Lozi 2011) and sarcoidosis (Fujita et al. 2011; Le Roux et al. 2007), may involve the muscle, which allows for relatively accessible tissue for biopsy. Finally, molecular analysis, immunohistochemistry, and electron microscopy, allow for investigation of specific structural or immunologic elements that are either diagnostic or can direct specific genetic testing.

Like muscle, biopsy of nerve can be highly informative to the diagnosis and can impact treatment. Indications for nerve biopsy include asymmetric neuropathies, sensory loss in an easily accessible nerve, abnormal nerve conduction studies in an accessible nerve, or when the differential diagnosis suggests a potentially treatable disorder with high morbidity (e.g., vasculitis). Pathology may be present in only a portion of the nerve or muscle and may not affect all regions equally. Therefore, it is important to select a nerve or muscle that is clearly symptomatic. Unlike a muscle biopsy, nerve biopsy carries the potential for loss of function. Therefore, if possible, an affected sensory nerve at an easily accessible site is typically chosen for biopsy. If not, fascicular biopsy of an affected motor nerve may be performed in hopes of preventing any permanent loss of strength in affected muscles. Fascicular biopsies are becoming more common, as they can provide adequate diagnostic information without resulting in severe motor or sensory impairments (Campbell et al. 2009; Lyons 2009). Regardless of the technique utilized the patchy nature of some nerve and muscle diseases results in a significant number of false-negative biopsies. One study revealed that combined nerve and muscle biopsy yielded a diagnosis of vasculitis in only 50 % of cases (Collins et al. 2000) and it is well recognized that several muscle biopsies may be required to confirm the presence of inclusion body myositis (Dahlbom et al. 2002). Neuromuscular imaging could better inform the site selection for biopsy and therefore could improve the diagnostic yield of biopsies in these disorders.

4.6 Genetic Testing

A wide range of commercial genetic testing is now available. For some disorders, specifically Duchenne muscular dystrophy and spinal muscular atrophy (D'Amico et al. 2011), gene tests have largely replaced EDx testing and muscle biopsies. A directed, stepwise approach to testing is recommended in most cases. Batched testing is available to check for many limb-girdle muscular dystrophies (LGMD) or Charcot-Marie-Tooth disease. However, this broad approach to genetic testing is expensive and often includes conditions that are not only clinically distinct but also often exceedingly rare. The preceding elements of the evaluation (clinical history, physical examination, EDx results, and biopsy) should be combined to direct genetic testing toward a specific diagnosis. This minimizes the cost of testing and potential for misdiagnosis resulting from changes of unknown significance in genes that are clinically unrelated to the patient's presentation. For the most unusual of cases, whole-exome sequencing is now available, but due to the high rate of polymorphisms of unknown significance, typically requires the assistance of a geneticist for accurate interpretation (Goh and Choi 2012).

5 Imaging of Muscle

While imaging of the arms and legs is commonly employed for evaluation of trauma or joint disease, and imaging of the brain and spine is commonly employed for evaluation of central nervous system disease, imaging in the evaluation of neuromuscular disease is not routinely performed. While imaging can be utilized to inform our understanding of neuromuscular disorders, it often identifies patterns of disease that can be clearly discerned from the history, physical exam, and EDx testing. However, with greater utilization and improved technical capabilities, it is increasingly apparent that in some neuromuscular disorders, imaging is uniquely informative and critical to the appropriate management of the patient. Imaging with MRI, US, and CT scans is most often performed. The following section is a brief introduction to the advantages and limitations of these different imaging modalities.

5.1 MRI of Skeletal Muscle

The signal characteristics of MRI are based upon the interaction between magnetic forces and the composition of tissues. Images are created from changes in the energy state of protons induced by magnetization. The time for return to equilibrium (the resting state) of protons is recorded. Fat has shorter T1 relaxation time relative to muscle and pure water or cerebrospinal fluid. Thus fat appears bright on T1 weighted images, while muscle appears intermediate and water appears dark (Fig. 4). T1 sequences are good for detecting fat deposition in chronic myopathies but are not sensitive for detecting increased intramuscular fluid that might be present in acute disease. T2 images display a different pattern. Here, muscle and tendons have a short T2 relaxation time, while water, cerebrospinal fluid, and edematous or inflamed tissues have a long relaxation time. Also, compared to muscle, fat takes longer to return to the resting state and thus appears brighter than normal muscle tissue. On T2 sequences, water will appear bright, making this the preferred sequence for visualizing acute or subacute muscle changes that may be related to edema or increased blood flow. In summary, the T1-weighted sequence is best for imaging fatty replacement of muscle seen in chronic neuromuscular disease and T2-weighted sequences are better for detecting acute or inflammatory changes of muscle.

Short tau inversion recovery (STIR) sequences are also helpful in muscle imaging (Fig. 5). STIR uses a short

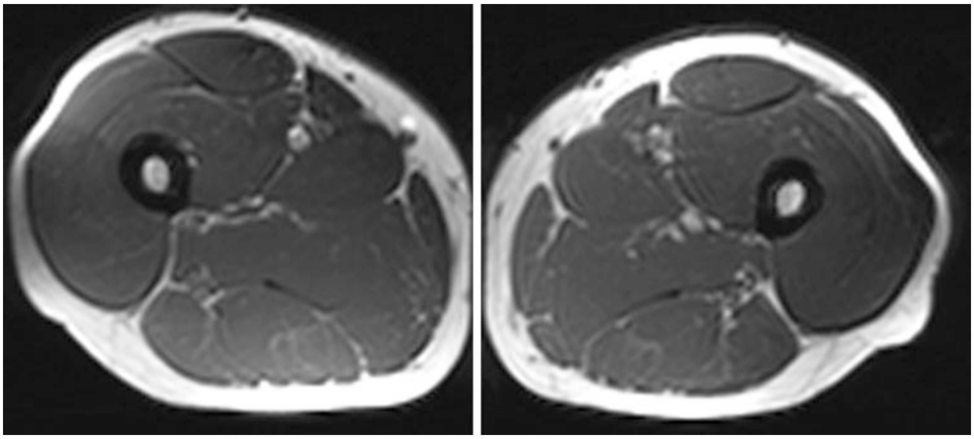

Fig. 4 Normal MRI of muscle in a healthy 32-year-old sports instructor. Axial T1-weighted images of the bilateral thighs reveals normal muscle without fatty infiltration (images courtesy of Prof. Dr. M. A. Weber, Heidelberg)

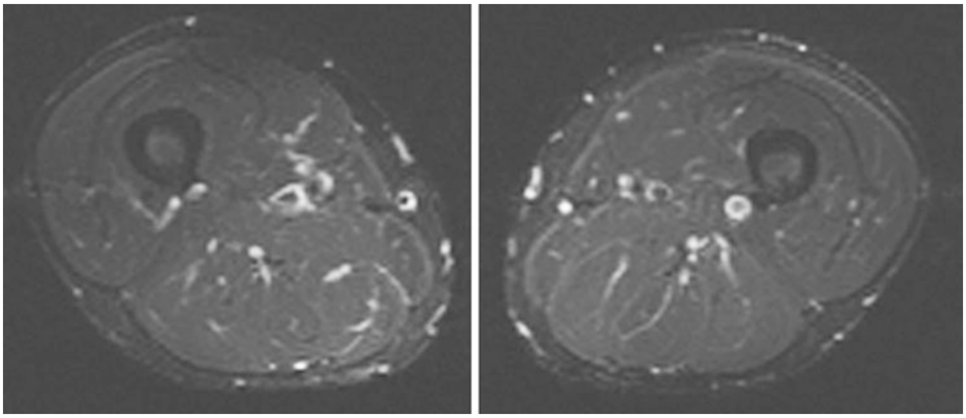

Fig. 5 Normal MRI of muscle (same subject as in Fig. 1.4). Axial STIR MRI of the bilateral thighs demonstrates no evidence of edema-like changes (images courtesy of Prof. Dr. M. A. Weber, Heidelberg)

inversion time to suppress fat signal. Thus the sequence will suppress signal from fat as well as any tissue with a relaxation time similar to that of fat, such as gadolinium (STIR sequences are not used with contrast agents for this reason) while allowing for signal from water. Some have advocated STIR as a replacement for T2 imaging for investigations of muscle injury (Evans et al. 1998). STIR sequences are faster than T2 sequences, and can therefore shorten the imaging time. This is extremely important for patients who have difficulty remaining immobile in the scanner and for whole body imaging studies, which are highly informative for determining patterns of muscle involvement (Schramm et al. 2008) and guiding muscle biopsy (Connor et al. 2007).

Diffusion-weighted imaging (DWI) sequences are also used to examine muscle. DWI sequences provide information on fluid motion in tissues and are commonly employed to detect acute stroke. DWI can identify post-exercise muscle edema (Morvan 1995) and radiation injury to skeletal muscle (Baur and Reiser 2000). Quantification of edema-like changes in DWI sequences of inflammatory myopathies has potential applications for measuring disease progression and response to treatment (Qi et al. 2008).

Gadolinium, which shortens the T1 relaxation time, is not typically required to identify neuromuscular pathologies. Although the addition of gadolinium contrast can aid in the visualization of intramuscular pathology on T1 sequences, it does not appear to provide additive benefit in the evaluation of neuromuscular disease (Reimers et al. 1994a; Stiglbauer et al. 1993). In traumatic muscle injury, however, gadolinium may aid in diagnosis. A single prior study recommended the combination of STIR sequences and gadolinium contrast in cases of suspected muscle injury (el-Noueam et al. 1997). The authors reported four cases where both STIR and T2 sequences were negative for muscle strain, but the injury became apparent after the addition of contrast. For most purposes, the addition of contrast is limited to suspected cases of muscle tumors, abscess or other focal injury (Fig. 6).

MRI has many advantages for muscle imaging. MRI can image superficial and deep structures with equal efficacy and is not highly operator dependent. It is possible to image tissue from multiple and large areas of the body and is thus ideal for describing patterns of muscle involvement. It provides excellent differentiation between the muscle, fat, and adjacent tissues, including bone and tendon. New

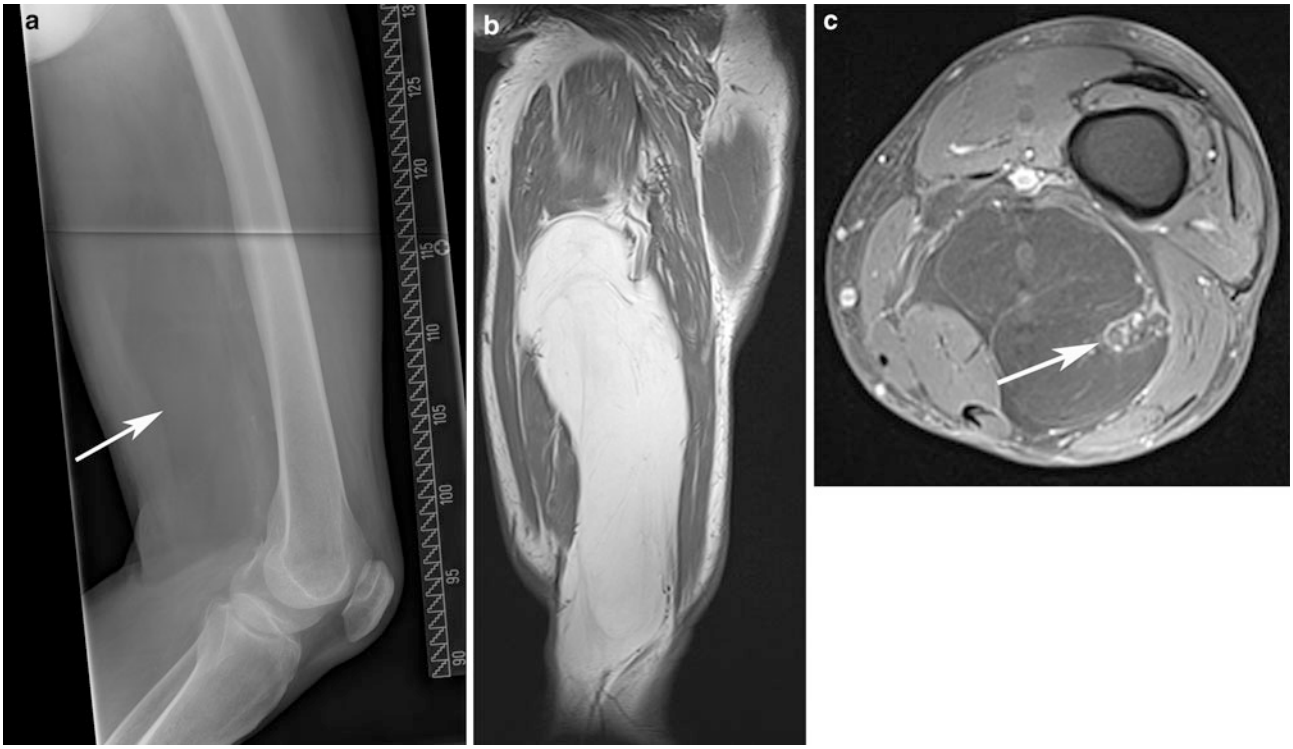

Fig. 6 Large (about 20 cm) lipoma of the thigh with encasement of the sciatic nerve in a 74-year-old man. The lipoma is seen as radiolucency in the projection radiograph (*arrow* in **a**), appears homogeneous on the T1-weighted sagittal MR image **b** and encases the sciatic nerve on the fat-saturated contrast enhanced, axial T1-weighted MR image (*arrow* in **c**). There are no areas of avid contrast enhancement and no thickened septae that are suspicious of a liposarcoma (images courtesy of Prof. Dr. M. A. Weber, Heidelberg)

advances in MRI technology are now generating functional images that may provide additional information on muscle metabolism (see Chaps. 5–9 of this book). Quantitative measures are also potentially valuable for monitoring disease progression.

Despite these many advantages, MRI does have its limitations. It cannot provide dynamic images under standard circumstances, making it a less than ideal choice in select cases compared to ultrasonography as a real-time examination. Pediatric patients and other patients who are unable to remain still for the examination may require sedation, increasing the risk of the procedure. Finally, MRI carries a higher cost that either ultrasound or CT scans, a factor that cannot be overlooked in an increasingly cost-conscious health care environment. Analysis of the most cost-effective approaches to imaging as an ancillary test in neuromuscular disorders is needed.

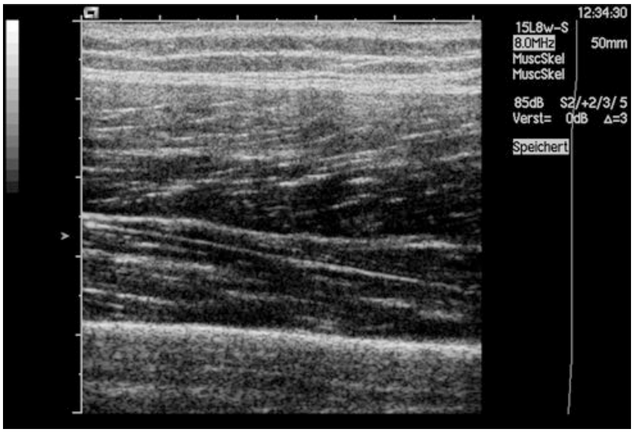

Fig. 7 US image of healthy thigh muscle displaying normal vastus lateralis and vastus intermedius muscle overlying the femur (same subject as in Figs. 4 and 5) (image courtesy of Prof. Dr. M. A. Weber, Heidelberg)

5.2 Ultrasound Imaging

Ultrasound (US) imaging is based upon the interaction of sound waves with tissues that they encounter. The ultrasound transducer emits sound waves that travel through body tissues and these are reflected, refracted, scattered, or absorbed. Only the sound waves that are reflected back to the transducer are displayed on the resulting image. Objects like bone that reflect most sounds waves appear bright, or hyperechoic, on US imaging (Fig. 7). Structures that are fluid-filled transmit rather than reflect most of the sound waves and appear dark (hypoechoic).

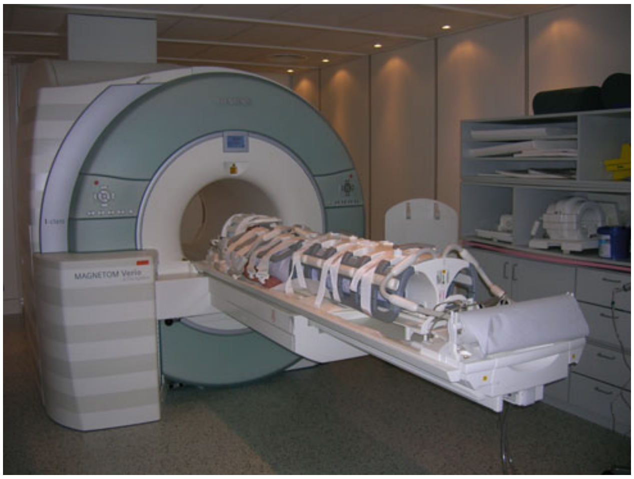

Fig. 8 Whole-body MRI. To obtain whole body MRI images, the entire body is covered in coils (image courtesy of Prof. Dr. M. A. Weber, Heidelberg)

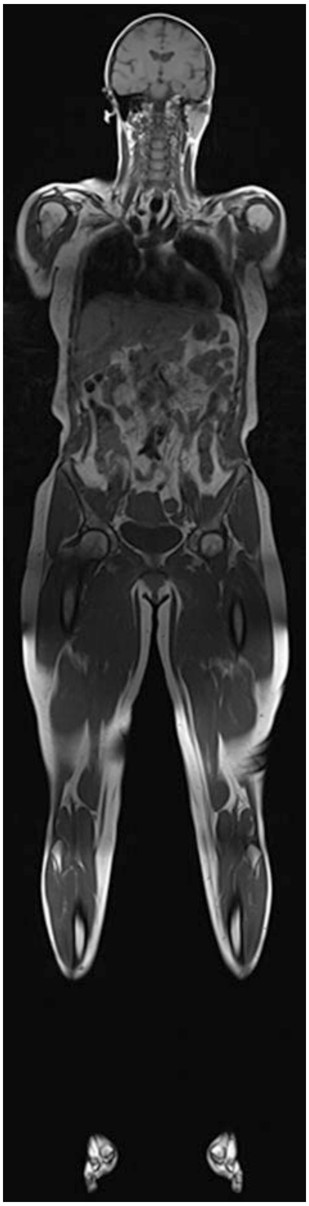

Fig. 9 Whole-body T1-weighted MR images of a healthy 50-year-old (image courtesy of Prof. Dr. M. A. Weber, Heidelberg)

Ultrasound carries many advantages in imaging muscle. It is less expensive than MRI or CT and there are no contraindications to testing. It can be performed without sedation in children and is painless. Clinicians can perform the test at the patient's bedside, eliminating the need for additional referrals. US has high spatial resolution, making it ideal for visualizing small structures. Its major advantage over MRI or CT in muscle imaging is the ability to image and rapidly examine and compare multiple body regions (side to side comparisons, proximal to distal and arm to leg comparisons) and its ability to visualize the muscle in motion. This provides the opportunity to visualize fasciculations and other abnormal muscle movements. For comparison, in whole-body MRI, the patient is completely covered with coils (Figs. 8, 9) making this examination not suited for children or incompliant adults.

Newer US technologies are expanding its diagnostic repertoire. Contrast-enhanced ultrasound refers to the use of microbubbles that are injected into the vascular system. High-energy ultrasound pulses create oscillations of these microbubbles, permitting the visualization of capillary perfusion within skeletal muscle (Amarteifio et al. 2011). This functional imaging technique can be performed at rest, during or after muscle contraction. Contrast-enhanced ultrasound will provide insight into microvascular disturbances that occur in muscular dystrophies and myositis (Fig. 10), aiding understanding of the underlying pathophysiology, while possibly serving as a biomarker for monitoring therapeutic response.

Ultrasound elastography is another promising tool that is currently in development. Elastography permits measurement of tissue rigidity or stiffness and is already being utilized in the assessment of liver disease and breast masses. For muscle, its use remains investigational, as researchers continue to devise reliable and accurate means of quantifying muscle stiffness. Different methods include manual compression and measuring tissue strain (Chino et al. 2012; Palmeri et al. 2011). Newer methods of US elastography include delivery of a high frequency pulse followed by measurement of movement in the tissue region of interest (known as acoustic radiation force imaging). Elastography techniques may permit detection of structural changes that alter the stiffness of skeletal muscle. As many myopathies are characterized by increased intramuscular fat and fibrous tissue, elastography is a promising technique for detecting the pathology associated with muscle disease.

Ultrasound is not always the optimal choice for imaging. Deeper muscles cannot be well depicted by most structures. Bone impedes the view of any structure that lies behind it,

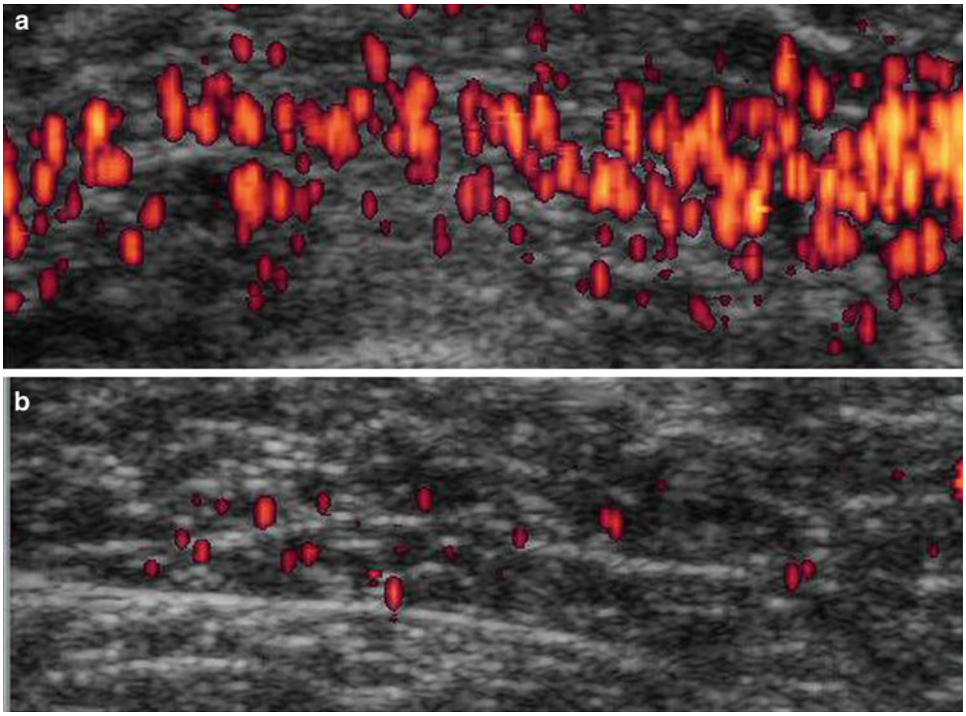

Fig. 10 Contrast-enhanced power doppler ultrasound reveals increased intramuscular blood flow in muscle of a woman with polymyositis **a** than in a woman with scleroderma **b** (modified from Weber et al. (2007))

limiting views of some muscles. Obesity can impede optimal visualization of proximal or deep muscles. Acute pathology that results in increased edema like signal on MRI may be undetectable or subtle on ultrasound. Severe chronic pathology, with replacement of muscle with fat and fibrosis, may prevent identification of muscle borders or intramuscular architecture on ultrasound.

5.3 Computed tomography and Radiographs

In a nutshell, computed tomography (CT) scans use X-ray images taken from multiple directions that are then compounded to make a cross-sectional image. CT scans provide axial images with high resolution and good detail of the soft tissues. Newer technologies are available and CT now has multiplanar imaging capabilities (Kuo and Carrino 2007). The use of CT imaging for evaluation of muscle is limited. While it is able to distinguish bones, tendons, ligaments, and other structures associated with muscle, it is not very sensitive in detecting inflammation or edema. It can detect fatty changes, along with abnormal mineralization of the soft tissues (Calo et al. 1986; Swash et al. 1995).

With increasing use of MRI, CT is less often used for the assessment of neuromuscular disorders. It exposes patients to ionizing radiation and is not the optimal test for detecting the edema and/or inflammation in muscle. The same may be said for plain radiographs, which can identify calcinosis of soft tissues, but does not provide detail on the muscle itself (Kuo and Carrino 2007). CT scans are, however, much faster to obtain than MRI and offer improved contrast resolution and imaging of deep tissue compared to ultrasound.

6 Muscle Imaging in Neuromuscular Disorders

6.1 Overview

Imaging of injured and diseased muscle can reveal a diverse array of alterations. Abnormal muscle typically shows changes in signal characteristics, and can also show changes in size, shape, movement, metabolism, and blood flow. The choice of imaging modality, typically either MRI or US, affects which abnormal property of muscle will be best appreciated. For instance, while MRI yields superior imaging of deep tissue and identification of signal changes from increased water content compared to US, sonography is superior for identifying abnormal muscle movements. The differential diagnosis, and the suspected underlying pathology, must drive the decision of when and how to image a patient with a suspected neuromuscular disorder.

Unique to neuromuscular disorders is the relative importance of the pattern and distribution of muscle pathology within and between muscle groups (Costa et al. 2012). Muscle pathology, when identified, should be described as focal, patchy, or diffuse. Focal changes or space occupying lesions suggest most often a traumatic or infectious etiology including herniation, strain, hematoma, and infection, but rarely also a tumor of the muscle or muscle sheath (see "MRI in Muscle Tumors and Tumors of Fasciae and Tendon Sheaths" of this book). Myositis ossificans, a focal area of heterotopic bone formation within the muscle, is a sign of chronicity and can occur following myositis, trauma, or bleeding (Tyler and Saifuddin 2010). Sheets of heterotopic intramuscular bone suggest a diagnosis of myositis ossificans progressiva, a rare inherited disorder characterized by recurrent, transient focal enlargements of muscle, and progressive ossification of connective tissues. Patchy or diffuse involvement of muscle can be seen with inherited or acquired myopathies and infectious or inflammatory myositis. Myonecrosis or ischemic myositis, sometimes occurring in diabetes mellitus, can cause patchy involvement of a single muscle or muscle groups. Diffuse, symmetric, and proximal muscle involvement suggest a myopathic process, as opposed to neuropathy which affects the distal most muscles of the legs and, in advanced cases, arms. It is important to note that inherited myopathies can show highly selective and variably stereotyped patterns of muscle involvement, as discussed in following sections.

Muscle shape and size can be quantified using many imaging modalities, and can assist in the identification of disease (Heckmatt et al. 1988a; Hudash et al. 1985). In asymmetric disorders, comparison to the less or unaffected limb can be helpful in identifying the presence and degree of abnormality in muscle size. With more diffuse disorders, thickness measurements should be compared to appropriate reference values. It is important to note that muscle thickness varies with age and gender, and pathologic processes often do not affect all muscles equally (Ota et al. 2012; Arts et al. 2007). Exercise and body habitus can also affect muscle size. These factors must be considered when referencing normative values.

In neuromuscular disorders, muscle can be normal in size, atrophic, hypertrophic, or pseudohypertophic. *Atrophy* is histologically defined by small muscle fiber size and results in reduced muscle bulk. In isolation, atrophy of muscle is nonspecific and can occur from disease of the nerve or muscle or from disuse. The combination of atrophy and abnormal muscle signal makes disuse much less likely. Denervation is more likely to result in muscle atrophy than myopathy. In many myopathies, muscle bulk is relatively preserved despite abnormal muscle signal and, often, weakness. *Hypertrophy* of muscle can occur from compensation due to weakness of neighboring muscle groups or in response to disease. Muscle can also appear hypertrophic following tendon tear, as the retracted muscle belly will thicken. Myotonia congenita, acromegaly, or space occupying lesions in the muscle (e.g., infection, tumor, or inflammation) can also increase muscle size. In the acute phase of myositis, mild muscle hypertrophy can be seen, presumably related to increased blood flow and/or water content or from inflammation within the muscle (Pillen et al. 2008b). *Pseudohypertrophy*, as opposed to true hypertrophy, occurs when increased intramuscular fat leads to enlarged muscle bulk. Thus, the thickened appearing muscle in pseudohypertrophy stems not from true muscle hypertrophy but from infiltration and replacement with fat (De Beuckeleer et al. 1999; Lovitt et al. 2006). This is classically seen in the calves of patients with Duchenne muscular dystrophy, but is not specific for this disorder (Reimers et al. 1996a).

Changes in muscle signal properties are perhaps the most common abnormalities noted in neuromuscular disorders. MRI has an advantage to CT scan and US as MRI sequences can best detect and differentiate increased fat from edema-like changes (May et al. 2000). Increased T1 signal in muscle suggests increased fat content of muscle, as often seen in muscular dystrophy, chronic myopathies, or severe, long-standing denervation. Early fatty replacement in muscle appears as patchy or marbled increased T1 signal, whereas diffuse or complete fatty infiltration of muscle reflects more chronic, longstanding, or severe disease (Fig. 11). Alternative etiologies of increased T1 signal include methemoglobin, highly proteinaceous fluid, early calcinosis, scar formation, or mass occupying lesions. Increased T2 signal is often detected in myopathic or denervated muscle. The pathogenic etiology of the increased T2 signal is unknown and may result from inflammation, increased blood flow, or increased water content. Again, the pattern of muscle involvement affects the differential diagnosis (Costa et al. 2012). Focal increased T2 signal within the muscle typically results from trauma. Diffusely increased T2 signal limited to a single muscle suggests severe strain or denervation. Increased T2 signal in an isolated group of adjacent muscles suggests infectious myositis, deep vein thrombosis, compartment syndrome, or, when sharply demarcated, radiation injury. Increased T2 signal in symmetric nonadjacent muscles suggests a myopathy and is particularly informative in the identification and management of inflammatory myopathies, as T2 signal changes appear early and revert with successful treatment, although resolution of changes in MRI with treatment may lag clinical changes by months. Decreased T1 or T2 signal can results from calcifications and fibrosis (Reimers 2000).

Imaging with ultrasound and CT also can be helpful in assessing suspected neuromuscular disorders. Increased fatty or fibrotic tissue is readily detected with CT or US scan but may not detect edema-like pathology seen only on T2 or STIR MR sequences. Muscle echogenicity on US increases with greater amounts of intramuscular fat and fibrosis (Heckmatt et al. 1989; Pillen et al. 2009). In the authors' experience, US of inflammatory myopathies shows increased echogenicity without the attenuation seen in

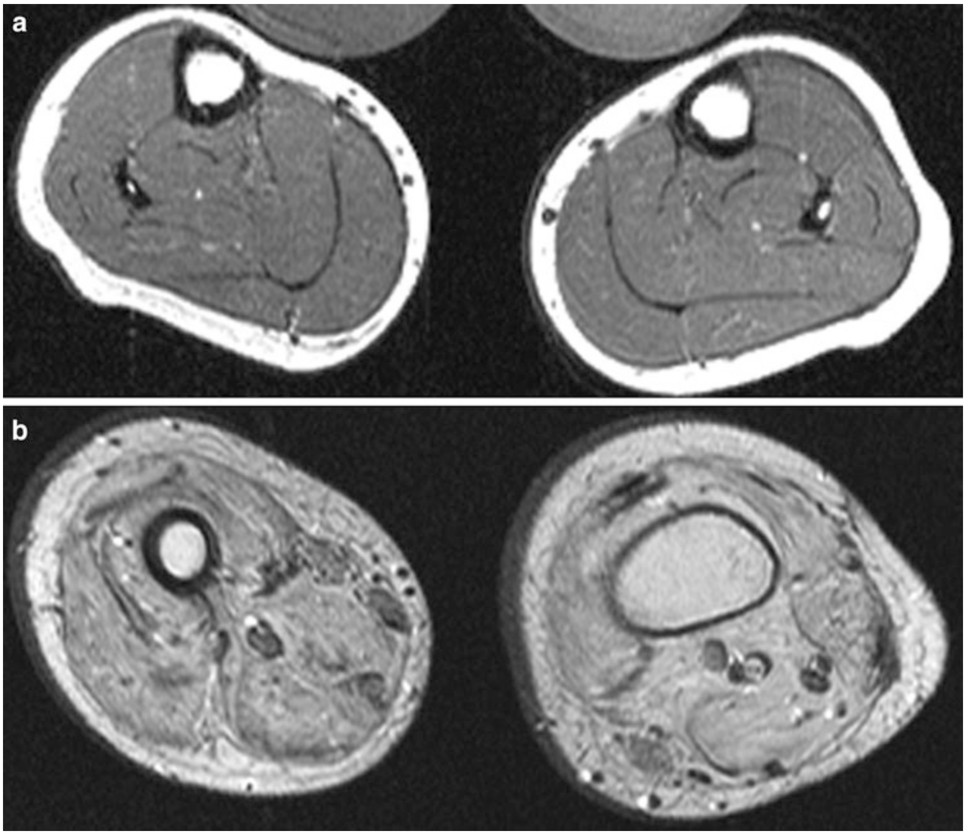

Fig. 11 T1-weighted MR images from a 7-year-old (**a**) and 14-year-old (**b**) boys with Duchenne muscular dystrophy demonstrate increased fat content within the muscl e, worse in **b** with more severe pathology (images courtesy of Prof. Dr. M. A. Weber, Heidelberg)

disorders characterized by fatty replacement of muscle. Thus, a highly echogenic muscle with a well-preserved bone reflection suggests an inflammatory myopathy over a muscular dystrophy.

One advantage of ultrasound over other imaging modalities is that evaluation in real time permits the identification of pathologic muscle movement, particularly fasciculations. Fasciculations are more readily detected with ultrasound than EMG or the clinical exam (Reimers et al. 1996b). Fasciculations are fast, random, nonrhythmic movements in a portion of the muscle that deform its shape but typically do not cause movement of the joint. Care must be taken to assure the imaged muscle is fully relaxed. In healthy individuals, fasciculations often are limited to muscles in the distal leg and are known to increase in frequency with age (Fermont et al. 2010). Other factors, including caffeine consumption, certain medications (e.g. pyridostigmine), and recent exercise may temporarily increase the frequency as well (Fermont et al. 2010; Simon and Kiernan 2013). Frequent and/or widespread fasciculations can occur in benign cramp-fasciculation syndrome or following denervation and are of particular diagnostic significance in amyotrophic lateral sclerosis (Misawa et al. 2011; de Carvalho and Swash 2013). Denervation is the likely etiology when fasciculations are seen in conjunction with weakness, reduced muscle thickness and increased signal intensity. However, denervation cannot be excluded in an otherwise normal appearing muscle with fasciculations. It is the authors' practice to obtain electromyography to further evaluate for denervation when fasciculations are detected, particularly when they are not restricted to the distal leg and more frequent than 1–2 every 10 seconds. Fibrillation potentials can also cause abnormal muscle movement detected with ultrasound. Previously identified only by electromyography, the tiny movements generated by profuse fibrillation potentials can also be detected using ultrasound, although their detection is neither sensitive nor specific (van Alfen et al. 2011). Muscle tremor may also be recorded, but in the authors' experience this adds little to the clinical examination.

6.2 Denervation

Denervation of muscle results in changes in the shape, size, and composition of muscle. These changes can be detected using both ultrasound and MRI (Kullmer et al. 1998). On MRI, denervated muscles is characterized by increased T2 signal, but the etiology is of this change is unknown. Although often attributed to edema, there is no supporting histopathologic evidence. Increased blood flow and extracellular fluid are two alternative mechanisms that could explain T2 signal change (Kamath et al. 2008; Wessig et al. 2004). Increased T2 signal in muscle is not specific for denervation. A recent study of 23 patients with forearm trauma demonstrated transient, increased signal in nondenervated hand musculature (Viddeleer et al. 2011). This study emphasizes the nonspecific nature and uncertain origin of fluid weighted signal change on muscle MRI following trauma or denervation. Despite this lack of understanding, clear patterns of evolving signal change on US and MRI follow denervation. These have been described in both experimental and, less commonly, clinical settings and when applied correctly, could be beneficial for patient care.

Following experimental denervation, increased relaxation time of fluid weighted sequences such as T2 and STIR may occur within 2 days of injury. Over time, replacement of chronically denervated muscle with fat and fibrotic tissue results in hyperintensity on T1-weighted sequences. With reinnervation, T2 signal changes begin to resolve and ultimately disappear. Wessig and colleagues found that that T2 relaxation time of muscle showed a high temporal concordance with electrodiagnostic findings of denervation and reinnervation after experimental denervation (Wessig et al. 2004). T2 signal acutely increased following denervation and then returned to normal as regeneration and voluntary activity of denervated muscle reappeared. Increases in T2 signal closely paralleled increases in the total capillary area identified on histologic examination of the affected muscle. Following reinnervation, both capillary size and T2 signal decreased, suggesting that increased blood volume is a strong contributor to T2 signal changes following denervation.

Similar to MRI, muscle ultrasound can be used to evaluate the presence and extent of denervation. High resolution ultrasound detects nerve transection immediately after injury and can influence clinical decision making (Cartwright et al. 2007; Padua et al. 2013). Changes in muscle are also seen on ultrasound following denervation, but not as quickly as with MRI. Increased echogeneity and loss of normal intramuscular architecture can appear approximately 2 weeks following acute nerve lesions. Muscle echointensity increases along with the severity and chronicity of denervation (Gunreben and Bogdahn 1991). As with MRI, the onset of sonographic changes parallels electrodiagnostic evidence of denervation. In contrast with MRI, ultrasound can detect abnormal movements in denervated muscle with fasciculations seen most prominently. In conjunction with electrodiagnostic studies, this dynamic assessment may improve the diagnostic sensitivity for lower MNDs, including amyotrophic lateral sclerosis (Misawa et al. 2011).

Both MRI and ultrasound can monitor changes in muscle size following denervation (Kullmer et al. 1998). While muscle atrophy is most commonly associated with denervation, both muscle hypertrophy and pseudohypertrophy may also occur (Petersilge et al. 1995). Alterations in muscle size following denervation are of particular prognostic interest. Zaidman et al. performed a study using ultrasound in 51 infants with newborn brachial plexus palsy. They compared each infant's affected limb with the unaffected opposite side and found that muscle thickness, but not muscle signal, correlated with function and increased with functional recovery overtime (Zaidman et al. 2012). Relative to the uninjured limb, muscle hypertrophy (mean increase 17 %) was also seen more frequently in children with moderately impaired strength. In contrast, in muscles with severely impaired strength, atrophy was seen, being 15 % thinner than the normal side. Another recent study of muscle cross-sectional area in 31 infants with obstetrical brachial plexus lesions used MRI. In general, both elbow flexors and extensors had reduced areas as compared to the unaffected side. However, this was not true in each individual. The authors demonstrated that muscle hypertrophy occurred in 17 of 31 patients following denervation, but found no correlation between muscle size and function (Ruoff et al. 2012).

A study by Viddeleer et al. (2011) provides evidence for the potential value of monitoring muscle signal change following denervation. Twenty-three patients with traumatic transection of the median or ulnar nerve, who had also undergone nerve repair, were enrolled. MRI of the affected hand was performed, including short inversion time inversion recovery (STIR) sequences. Patients underwent imaging at 1, 3, 6, 9 and 12 months after nerve repair. The authors found that STIR MRI could differentiate between denervated and reinnervated muscles up to 1 year after repair. Normalization of signal intensity correlated with good functional recovery, while persistently elevated signal was seen in those with poor hand function at 12 months. Prospective studies are required to determine the diagnostic and prognostic value of serial changes in muscle size and signal on patient care and recovery following denervation (Berciano et al. 2012).

6.3 Myopathy

Muscle imaging, particularly with MRI, can be incorporated into the clinical assessment of myopathies. Appropriately directed imaging can augment the diagnostic and clinical assessment of patients with myositis, muscular dystrophies, and other myopathies. Imaging is particularly helpful in ascertaining involvement of muscles that cannot be easily assessed on physical or electrodiagnostic testing. Whole-body MRI techniques allow for relatively rapid image acquisition not limited to the upper or lower limbs (Quijano-Roy et al. 2012) and for identification of patterns of muscle involvement that inform the differential diagnosis (reviewed by Pillen et al. (2008a) and Mercuri et al. (2005a), see also Chap. 4 of this book). Although additional investigation is needed, quantitative imaging techniques in MRI or US could potentially be used to monitor disease progression.

Algorithms for deducing specific genetic etiologies using patterns of radiologically determined muscle involvement have been described (Wattjes et al. 2010). The success of these strategies is variable and depends upon the specific type of myopathy. One study compared visual analysis of MRI patterns in 83 patients with rigid spine muscular dystrophy caused by SEPN1 mutations, Bethlem and Ulrich congenital muscular dystrophy (COL6A1, COL6A1, and COL6A1), Emery–Dreifuss muscular dystrophy (LMNA mutations) and limb-girdle muscular dystrophy 2A (CAPN3). These were compared with a control group of 25 other patients with other forms of muscular dystrophy. All subjects underwent conventional T1-weighted spin echo MRI. The authors found that compared to other myopathies, these disorders have highly specific (0.96) and sensitive (0.90) patterns of myopathology. Rigid spine muscular dystrophy and LGMD2A were most easily identified, but there was high interobserver agreement for all scans (Mercuri et al. 2010). Another study of other myopathies and using CT scan was not as promising. Four evaluators reviewed the imaging of 188 patients with seven different types of limb-girdle muscular dystrophy and found that the sensitivity of patterns of myopathology was high in Bethlem myopathy (90 %) and Becker muscular dystrophy (BMD) (91 %), but not for other limb-girdle muscular dystrophies (Ten Dam et al. 2012). This is likely in part because some genotypes share overlapping features. Additionally, the study had poor overall interobserver agreement ($\kappa = 0.27$), raising concern for reproducibility of the results. This highlights the need for prospective studies to determine the diagnostic utility of imaging in the evaluation of suspected hereditary myopathies.

Although these studies raise questions regarding routine imaging of patients with suspected myopathies, in particular instances, it is clear that muscle imaging can reveal patterns of abnormalities or involvement of muscles not easily detected on the physical exam. For instance, a hereditary form of inclusion body myopathy is typically characterized clinically as having “quadriceps sparing”, because knee extension strength is relatively preserved compared to sporadic inclusion body myositis. However, US of six patients with hereditary “quadriceps sparing” inclusion body myositis and homozygous glucosamine (UDP-*N*-acetyl)-2-epimerase/*N*-acetylmannosamine kinase (GNE) mutations revealed severe, selective involvement of the rectus femoris with relatively sparing of the vastus medialis, vastus lateralis, and vastus intermedius (Adler et al. 2008). Thus, imaging can detect abnormalities within muscles or groups of muscles that may not be apparent clinically.

The following sections highlight examples of neuromuscular disorders in which imaging has been shown to impact the diagnostic work-up or to identify muscle involvement that could aid in diagnosis or monitoring of disease progression.

6.4 Immune and Inflammatory Myopathies

Immune and inflammatory myopathies (IIM) are a group of heterogeneous myopathies that are classically subdivided based on clinicopathologic features into dermatomyositis (juvenile and adult), polymyositis, and inclusion body myositis. The heterogeneous clinical and pathologic features of these disorders complicate their categorization and an alternate classification based on myopathologic features has recently been proposed (Pestronk 2011). Most imaging studies rely on the traditional classification conventions. To reflect the most widely accepted nomenclature and avoid confusion, we will organize this section according to the classic terminology with the realization that disparate disorders may be termed “polymyositis” despite having variable clinical and pathologic features.

Dermatomyositis and polymyositis are immune-mediated disorders that result in muscle inflammation and weakness. Muscle weakness is typically proximal, symmetric, and progressive. Patients describe functional impairment in rising from chairs, stair climbing, or lifting objects overhead. In severe cases, dysphagia and respiratory weakness may occur. Myalgias are reported in a considerable number of patients. Creatine kinase levels are typically elevated; when absent, an elevated aldolase can suggest the diagnosis (Casciola-Rosen et al. 2012).

Dermatomyositis is associated with several cutaneous manifestations (Bohan and Peter 1975a, b; Khan and Christopher-Stine 2011). These include a violaceous, erythematous rash about the periorbital region (heliotrope), symmetrically about the neck and shoulders (shawl sign), or a linear erythema over the limb extensor regions or joints. Gottron’s papules, flat topped violet colored papules over the extensor joints of the fingers are highly common. Scaling and hyperkeratosis of the hands (mechanic’s hands) can also occur. Cutaneous manifestations of the disease can occur concurrently with or precede the onset of weakness. These skin findings can occur in the absence of identifiable muscle symptoms, a process termed amyopathic dermatomyositis.

Electromyography readily identifies inflammatory myopathies, but is not particularly specific or helpful in differentiating subtypes of diseases. Abnormal spontaneous activity (fibrillations, positive sharp waves, and complex repetitive discharges) is accompanied by short duration,

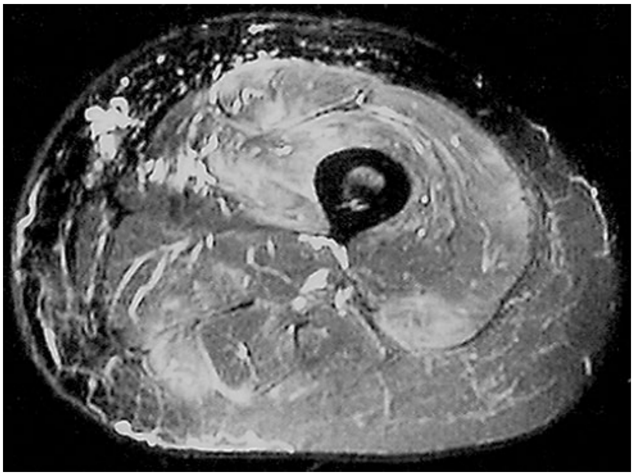

Fig. 12 MRI of thigh using a fat-suppressed T2-weighted short tau inversion recovery sequence demonstrates increased edema-like signal in the muscle of this woman with polymyositis (modified from Weber et al. (2007))

polyphasic motor unit potentials, and early recruitment. Unfortunately, these changes may be patchy with some areas of muscle appearing entirely normal. Myopathologic findings display the heterogeneous nature of these disorders and include myovasculopathy in juvenile more than adult dermatomyositis, perifascicular inflammation, and myofiber necrosis and regeneration (Pestronk 2011). Serum antibody markers (e.g. anti-Jo-1, anti-SRP, etc.) also aid in the diagnosis of inflammatory myopathies, but are not present in all patients (Casciola-Rosen et al. 2012).

MRI investigations of the IMMs have been well documented (Del Grande et al. 2011). Muscle MRI demonstrates increased edema-like changes within and surrounding the muscle (Fig. 12), along with fatty infiltration and calcification (Reimers et al. 1994b; Hernandez et al. 1990, 1993). Increased edema-like changes on MRI are more prominent than increased signal on fat sensitive sequences, especially in dermatomyositis. Edema-like changes are more commonly seen during the acute phase of illness, when they correlate with the degree of weakness and inflammatory infiltrate seen on biopsy (Reimers et al. 1994b; Tomasova Studynkova et al. 2007). In some cases, MRI abnormalities were detected more frequently than elevated creatine kinase levels and revealed muscle disease in patients with apparent amyopathic dermatomyositis (Reimers et al. 1994b; Lam et al. 1999; Stonecipher et al. 1994). Given the patchy distribution of muscle pathology in IIMs, pre-biopsy MRI can improve the diagnostic yield of muscle biopsy. In one study of MRI and IIM (Schweitzer and Fort 1995), a false-negative biopsy occurred in only 1 of 14 patients randomized to MRI before biopsy compared to 5 of 11 who did not have an MRI. Those randomized to MRI also had lower total average medical costs.

Several case studies of IIM, mainly juvenile dermatomyositis, have described the serial assessment of disease using MRI. These studies have shown general resolution of edema-like abnormalities with treatment and time, but reveal a variable temporal correlation between clinical improvement and MRI abnormalities following initiation of treatment (Chapman et al. 1994; Huppertz and Kaiser 1994; Keim et al. 1991; Hernandez et al. 1993). Semi-quantitative scoring systems have been proposed but are limited by suboptimal inter-rater reliability, even when comparing between musculoskeletal radiologists at the same institution (Davis et al. 2011). One promising technique for quantifying MR signal is measuring the T2 signal relaxation time. T2 signal relaxation time is increased in muscles of children with active compared to inactive juvenile dermatomyositis and to controls and correlates with measures of function and strength (Maillard et al. 2004). Additional studies of the utility of serial MRI and improved, reliable quantification schemes for MRI findings are needed to determine the role of MRI as a marker for monitoring efficacy of treatment in IIM.

Inclusion body myopathy, most often occurring in later adulthood, is characterized by weakness of the quadriceps and flexor digitorum profundus. The most common form is sporadic inclusion body myopathy (sIBM). It shares some clinical and pathologic features with immune mediated myopathies (polymyositis) in that the electromyography reveals an irritable myopathy and inflammatory features may be present on histologic examination. It differs, however, in that is does not respond to treatment with immunomodulation. MRI features that differentiate sIBM from polymyositis are related to the chronicity of sIBM and pattern of muscle involvement (Dion et al. 2002). As compared to polymyositis, MRI of sIBM is less likely to have isolated edema-like changes and instead more frequently shows chronic changes of fatty infiltration and atrophy. Asymmetry and preferential involvement of the anterior thigh and foreleg were also more common in sIBM than polymyositis. However, patterns of muscle involvement in sIBM can be highly variable (Phillips et al. 2001), highlighting the importance of correlation with clinical and histopathologic diagnosis. It is our clinical experience that sIBM is often apparent based upon the clinical examination alone, limiting the need for diagnostic muscle imaging.

6.5 Hereditary Myopathies

Hereditary myopathies are a large group of heterogeneous disorders that include the metabolic, mitochondrial, and congenital myopathies and muscular dystrophies. Diagnosis and classification is determined by the clinical findings, histopathology, pattern of inheritance, and genetic mutation.

In some disorders, such as facioscapulohumeral dystrophy, the pattern of weakness and autosomal dominant inheritance pattern is highly suggestive of the diagnosis. In others, such as the LGMD, patterns of proximal, symmetric limb weakness are nonspecific. This homogenous clinical phenotype makes molecular histopathology of muscle tissue and genetic testing essential in obtaining a specific diagnosis. The following are descriptions of specific hereditary myopathies in which muscle imaging may also contribute to the diagnosis.

6.6 Congential Myopathies

Myopathies associated with abnormalities of collage VI have undergone MRI characterization. These myopathies include the autosomal dominant Bethlem myopathy and the more severe, autosomal recessive Ullrich congenital muscular dystrophy. They are characterized by contractures typically affecting the fingers and elbows with spine rigidity that is out of proportion of the degree of weakness. Additional clinical features include "cigarette paper" scar formation, hyperkeratosis pilaris, and distal joint laxity early in the disease course. Imaging with either MRI or US shows a characteristic "outside-in" pattern of myopathology affecting the concentric, outer rim of muscle with relative sparing of the central portion of the muscle belly (Bonnemann et al. 2003; Mercuri et al. 2002a, 2005b). There is also thickening in the connective tissues between muscles, particularly the soleus and gastrocnemius. In Bethlem myopathy, the central fascia that vertically divides the superficial half of the rectus femoris is thickened, creating a "central-shadow" sign within this region of the rectus femoris. Ullrich myopathy shows similar, but more severe findings with thickening of the superficial rim and central sparing seen more prominently in the vastus lateralis than rectus femoris (Mercuri et al. 2005b).

Other myopathies with contractures and rigid spines also have typical and specific patterns of muscle involvement identifiable using MRI (Mercuri et al. 2010). Myopathies caused by SEPN1 gene mutations present with weakness in childhood, respiratory weakness and early onset of contractures. MRI shows selective involvement of the sartorius with sparing of the other thigh muscles. LGMD 2A (calpain-3) presents in childhood with a limb-girdle or scapulohumeral pattern of weakness, contractures, and prominent involvement of the posterior thigh and adductor magnus muscles on MRI. Emery–Dreifuss muscular dystrophy caused by a mutation of the lamin A/C (LMNA) gene results in symmetric scapuloperoneal weakness, cardiomyopathy, arrythmias, and prominent contractures. MRI reveals selective involvement of the vastus lateralis, vastus intermedius, and the medial gastrocnemius (Mercuri et al. 2002b).

Congenital myopathies associated with mutations of the ryanodine receptor (RYR1) further highlight the potential of MRI for describing selective and highly characteristic patterns of muscle pathology. In a study of 37 patients with RYR1 mutations, MRI revealed a typical pattern of selective involvement of the vasti, sartorius, adductor magnus, soleus, gastrocnemius, and peroneal muscle groups with relative sparing of rectus femoris, gracilis, adductor longus, and tibialis anterior (Jungbluth et al. 2004). This pattern is specific for RYR1 mutations (Klein et al. 2011). Thirty-four of the patients with autosomal dominant or recessive RYR1 mutations, but none of 23 control patients with other myopathies, demonstrated this pattern of muscle involvement. Furthermore, slight differences were seen between patients with autosomal recessive RYR1 mutations and ophthalmoplegia who showed more diffuse muscle involvement than those with autosomal dominant inheritance patterns. This highlights how some MRI patterns may be highly specific for particular genotypes.

6.7 Glycogen Storage Disorder Myopathies

Acid maltase deficiency (Pompe disease) is an autosomal recessive disorder of lysosomal glycogen degradation caused by a deficiency of alpha-glucosidase (GAA) activity. It presents in a classic, infantile form that is characterized by cardiomyopathy, respiratory weakness or a milder, and late-onset variant appearing after 1 year of age. Diagnosis is often delayed because of its highly heterogeneous phenotype and variable pattern of weakness can mimic other myopathies or other conditions (Hobson-Webb and Kishnani 2012; Hagemans et al. 2005). A timely diagnosis is important as treatment with enzyme replacement therapy can modify the course of Pompe disease (van der Ploeg et al. 2010). One study of ultrasound in patients with Pompe disease showed a specific pattern of muscle involvement not seen in other myopathies. This pattern includes increased echointensity of the biceps but not triceps brachii, sparing of the superficial but not deep portion of the biceps brachii, and differential involvement of the vastus intermedius more than the rectus femoris (Zaidman et al. 2011). Studies of MRI in patients with acid maltase deficiency have shown similar patterns. These studies showed relative sparing of the rectus femoris, sartorius, gracilis, and superficial vastus lateralis, prominent and early involvement of the tongue, adductor magnus, and anterior arm muscles, and demonstrated higher fat content in muscles and more diffuse patterns of muscle with worsening disease severity (Del Gaizo et al. 2009; Pichiecchio et al. 2004; Carlier et al. 2011).

6.8 Muscular Dystrophies

Imaging studies of Duchenne muscular dystrophy (DMD), the most common form of muscular dystrophy, highlight the potential of quantitative imaging as a marker of disease activity and progression. DMD, and the less severe BMD, are X-linked muscular dystrophies caused by mutations of the dystrophin gene. Boys affected with DMD typically present by age 5 years with progressive, symmetric weakness, and calf pseudohypertrophy. Most will lose the ability to ambulate by the age of 14 and death often occurs in early adulthood due to respiratory failure or cardiomyopathy. Tendon reflexes are reduced or absent in weak muscles. Creatine kinase is markedly elevated and electromyography yields small, narrow motor unit potentials with early recruitment patterns. Genetic testing is typically ordered as the confirmatory diagnostic test, but muscle biopsies are still occasionally performed. Myopathology of DMD is characterized by small, rounded muscle fibers with increased endomysial connective tissue, and prominent degenerating and regenerating muscle fibers. Increased connective tissue and fatty replacement of muscle fibers are seen in increasing amounts at more advanced stages of the disease.

DMD rarely presents a diagnostic dilemma as its clinical, histopathologic, and genetic features are well defined. However, as with many slowly progressive diseases in children, objective outcome measures for clinical trials have been difficult to define. Markers that are sensitive to pathologic changes, but that do not rely on the cooperation or ability of the child, are needed to avoid exclusion of the very young or weak child. While the 6-min walk test can be used to monitor treatment efficacy in clinical trials in ambulatory children, no comparable alternative exists for older, nonambulatory children. As an alternative, both MRI and ultrasound have been utilized to describe the patterns of muscle pathology and quantitate disease progression in DMD. Ultrasound reveals diffusely increased intramuscular echointensity thought to reflect increased quantities of intramuscular fat (Heckmatt et al. 1989) and fibrosis (Pillen et al. 2009) and is frequently abnormal in children by the time they are 2 years of age (Heckmatt et al. 1988b, 1989; Pillen et al. 2007). Muscle echointensity in DMD is higher with increasing age and worsening strength, and increases with disease progression over time (Zaidman et al. 2010; Jansen et al. 2012). MRI abnormalities in DMD demonstrate patterns of predominantly proximal limb muscle involvement with increased intramuscular fat composition and edema-like signal in fluid-weighted sequences possibly resulting from inflammation (Marden et al. 2005). Unlike ultrasound images, MRI allows for quantification of the degree of both fat and edema-like signal abnormalities in DMD (reviewed in Finanger et al. (2012)). Increased fatty infiltration as well as increased edema-like changes correlate with worse functional status in DMD and are promising techniques for quantifying longitudinal changes (Torriani et al. 2012; Kim et al. 2010; Wren et al. 2008).

7 Diagnostic Utility of Imaging in Neuromuscular Disease

Imaging with MRI or ultrasound is appealing as a screening tool for evaluation of patients with suspected neuromuscular disease as they are painless, noninvasive technologies that do not require ionizing radiation. The diagnostic utility of imaging has been most extensively studied using ultrasound in children and its success appears to depend upon the type and severity of the underlying disorder (reviewed by Pillen et al. (2008a)). In studies of children with suspected neuromuscular disorders, ultrasound has sensitivities of 78–81 % and specificity of 91–96 % for discriminating neuromuscular disease from other disorders (Brockmann et al. 2007; Zuberi et al. 1999). The diagnostic utility of ultrasound varies with age, disease, and severity. Ultrasound is less sensitive in children under age 3 years, in children with mitochondrial disorders, and is nonspecific when mildly abnormal. Only 7 of 13 children with a mildly abnormal ultrasound scan had a neuromuscular disorder. In contrast, all of the children with moderate or severely abnormal ultrasounds had a neuromuscular disorder. Similarly, nearly all (62 of 69) children with a normal ultrasound did not have a neuromuscular disorder (Zuberi et al. 1999).

Despite increasing evidence that imaging studies can detect pathology in neuromuscular conditions, MRI and ultrasound are rarely used in the diagnostic evaluation. This may be due to reduced efficacy in comparison to EMG for distinguishing myopathic from neuropathic disorders, but also due to clinicians' lack of familiarity with the available evidence. While electromyographic patterns of neurogenic and myogenic disease are well described, differentiation of these etiologies with imaging is less established and often identifies patterns of involvement that can be discerned clinically. Myopathic processes typically cause symmetric abnormalities preferentially affecting proximal muscles with preserved muscle bulk. Neurogenic etiologies result in atrophic muscles that are most severe distally. Muscle echogenicity on ultrasound is typically increased diffusely throughout the muscle in myopathy and heterogeneously in denervation. These imaging patterns for differentiating myogenic and neurogenic etiologies are specific when present but are not highly sensitive (Brockmann et al. 2007; Pillen et al. 2007; Maurits et al. 2003). In children, one study of ultrasound showed higher specificity than sensitivity for detecting myogenic (92 vs. 67 %) and neurogenic

(98 vs. 77 %) etiologies (Brockmann et al. 2007), while another study using quantitative ultrasound techniques found that a pattern of distal predominant echogenicity and reduced muscle thickness was 94 % specific but only 67 % sensitive for neurogenic disease. Of note, this method could not distinguish myopathic disease from controls (Pillen et al. 2007).

There are even fewer studies examining the diagnostic efficacy of imaging for neuromuscular disorders in adults. One study of ultrasound in adults found that increased echointensity of the biceps brachii (increased grey-scale values) was 94 % sensitive and 93 % specific for myopathy, while increased signal heterogeneity was 100 % sensitive and 93 % specific for neuropathy (Maurits et al. 2003). These patterns did not differentiate myogenic from neurogenic etiologies in children (Maurits et al. 2004). For these reasons, it is unlikely that imaging will supplant electrodiagnosis in the evaluation of patients with suspected neuromuscular disease. Imaging findings that not only identify the presence of disease but also discriminate myogenic from neurogenic etiologies are needed if imaging is to play a more valued role in the evaluation of suspected neuromuscular diseases.

8 Conclusions

In neuromuscular medicine, there is considerable overlap between the clinical phenotypes of various disorders. Standard laboratory and electrodiagnostic testing are not always helpful in narrowing the differential diagnosis. The current standard of care for neuromuscular disorders does not involve imaging. It is the authors' opinion that muscle imaging is underutilized and that in select instances its use will improve patient care. Muscle imaging may be helpful to verify the presence of neuromuscular disease, especially early in the course of disease. When abnormalities are present, they serve in guiding the site of biopsy, increasing the diagnostic yield of the testing. In some disorders, a specific, characteristic pattern of muscle involvement may be diagnostic. Additional research will determine how imaging may be best used to evaluate patients for neuromuscular disorders in both clinical trials and clinical practice.

References

Abou-Zeid E, Boursoulian LJ, Metzer WS, Gundogdu B (2012) Morvan syndrome: a case report and review of the literature. J Clin Neuromuscul Dis 13(4):214–227. doi:10.1097/CND.0b013e31822b1977

Achi EY, Rudnicki SA (2012) ALS and frontotemporal dysfunction: a review. Neurol Res Int 2012:806306. doi:10.1155/2012/806306

Adler RS, Garolfalo G, Paget S, Kagen L (2008) Muscle sonography in six patients with hereditary inclusion body myopathy. Skeletal Radiol 37(1):43–48. doi:10.1007/s00256-007-0367-6

Amarteifio E, Nagel AM, Kauczor HU, Weber MA (2011) Functional imaging in muscular diseases. Insights Imaging 2(5):609–619. doi:10.1007/s13244-011-0111-6

Andrews J, Hall MA (2002) Dermatomyositis-scleroderma overlap syndrome presenting as autoimmune haemolytic anaemia. Rheumatology (Oxford) 41(8):956–958

Arts IM, Pillen S, Overeem S, Schelhaas HJ, Zwarts MJ (2007) Rise and fall of skeletal muscle size over the entire life span. J Am Geriatr Soc 55(7):1150–1152. doi:10.1111/j.1532-5415.2007.01228.x

Baur A, Reiser MF (2000) Diffusion-weighted imaging of the musculoskeletal system in humans. Skeletal Radiol 29(10):555–562

Bazzani C, Cavazzana I, Ceribelli A, Vizzardi E, Dei Cas L, Franceschini F (2010) Cardiological features in idiopathic inflammatory myopathies. J Cardiovasc Med (Hagerstown) 11(12):906–911. doi:10.2459/JCM.0b013e32833cdca8

Berciano J, Gallardo E, Fernandez-Torre JL, Gonzalez-Quintanilla V, Infante J (2012) Magnetic resonance imaging of lower limb musculature in acute motor axonal neuropathy. J Neurol 259(6):1111–1116. doi:10.1007/s00415-011-6309-1

Bohan A, Peter JB (1975a) Polymyositis and dermatomyositis (first of two parts). N Engl J Med 292(7):344–347. doi:10.1056/NEJM197502132920706

Bohan A, Peter JB (1975b) Polymyositis and dermatomyositis (second of two parts). N Engl J Med 292(8):403–407. doi:10.1056/NEJM197502202920807

Bonnemann CG (2011) The collagen VI-related myopathies Ullrich congenital muscular dystrophy and Bethlem myopathy. Handb Clin Neurol 101:81–96. doi:10.1016/b978-0-08-045031-5.00005-0

Bonnemann CG, Brockmann K, Hanefeld F (2003) Muscle ultrasound in Bethlem myopathy. Neuropediatrics 34(6):335–336. doi:10.1055/s-2003-44665

Brockmann K, Becker P, Schreiber G, Neubert K, Brunner E, Bonnemann C (2007) Sensitivity and specificity of qualitative muscle ultrasound in assessment of suspected neuromuscular disease in childhood. Neuromuscul Disord 17(7):517–523. doi:10.1016/j.nmd.2007.03.015

Burge JA, Hanna MG (2012) Novel insights into the pathomechanisms of skeletal muscle channelopathies. Curr Neurol Neurosci Rep 12(1):62–69. doi:10.1007/s11910-011-0238-3

Callen JP (2010) Cutaneous manifestations of dermatomyositis and their management. Curr Rheumatol Rep 12(3):192–197. doi:10.1007/s11926-010-0100-7

Calo M, Crisi G, Martinelli C, Colombo A, Schoenhuber R, Gibertoni M (1986) CT and the diagnosis of myopathies. Preliminary findings in 42 cases. Neuroradiology 28(1):53–57

Campbell CA, Turza KC, Morgan RF (2009) Postoperative outcomes and reliability of "sensation-sparing" sural nerve biopsy. Muscle Nerve 40(4):603–609. doi:10.1002/mus.21347

Carlier RY, Laforet P, Wary C, Mompoint D, Laloui K, Pellegrini N, Annane D, Carlier PG, Orlikowski D (2011) Whole-body muscle MRI in 20 patients suffering from late onset Pompe disease: involvement patterns. Neuromuscul Disord 21(11):791–799. doi:10.1016/j.nmd.2011.06.748

Cartwright MS, Chloros GD, Walker FO, Wiesler ER, Campbell WW (2007) Diagnostic ultrasound for nerve transection. Muscle Nerve 35(6):796–799. doi:10.1002/mus.20761

Casciola-Rosen L, Hall JC, Mammen AL, Christopher-Stine L, Rosen A (2012) Isolated elevation of aldolase in the serum of myositis patients: a potential biomarker of damaged early regenerating muscle cells. Clin Exp Rheumatol 30(4):548–553

Chapman S, Southwood TR, Fowler J, Ryder CA (1994) Rapid changes in magnetic resonance imaging of muscle during the treatment of juvenile dermatomyositis. Br J Rheumatol 33(2): 184–186

Chino K, Akagi R, Dohi M, Fukashiro S, Takahashi H (2012) Reliability and validity of quantifying absolute muscle hardness using ultrasound elastography. PLoS One 7(9):e45764. doi: 10.1371/journal.pone.0045764

Chuquilin M, Al-Lozi M (2011) Primary amyloidosis presenting as "dropped head syndrome". Muscle Nerve 43(6):905–909. doi: 10.1002/mus.22049

Collins MP, Mendell JR, Periquet MI, Sahenk Z, Amato AA, Gronseth GS, Barohn RJ, Jackson CE, Kissel JT (2000) Superficial peroneal nerve/peroneus brevis muscle biopsy in vasculitic neuropathy. Neurology 55(5):636–643

Connor A, Stebbings S, Anne Hung N, Hammond-Tooke G, Meikle G, Highton J (2007) STIR MRI to direct muscle biopsy in suspected idiopathic inflammatory myopathy. J Clin Rheumatol 13(6):341–345. doi:10.1097/RHU.0b013e31815dca0a

Costa AF, Di Primio GA, Schweitzer ME (2012) Magnetic resonance imaging of muscle disease: a pattern-based approach. Muscle Nerve 46(4):465–481. doi:10.1002/mus.23370

Dahlbom K, Lindberg C, Oldfors A (2002) Inclusion body myositis: morphological clues to correct diagnosis. Neuromuscul Disord 12(9):853–857

D'Amico A, Mercuri E, Tiziano FD, Bertini E (2011) Spinal muscular atrophy. Orphanet J Rare Dis 6:71. doi:10.1186/1750-1172-6-71

Davis WR, Halls JE, Offiah AC, Pilkington C, Owens CM, Rosendahl K (2011) Assessment of active inflammation in juvenile dermatomyositis: a novel magnetic resonance imaging-based scoring system. Rheumatology (Oxford) 50(12):2237–2244. doi:10.1093/rheumatology/ker262

De Beuckeleer L, Vanhoenacker F, De Schepper A Jr, Seynaeve P, De Schepper A (1999) Hypertrophy and pseudohypertrophy of the lower leg following chronic radiculopathy and neuropathy: imaging findings in two patients. Skeletal Radiol 28(4):229–232

de Carvalho M, Swash M (2013) Fasciculation potentials and earliest changes in motor unit physiology in ALS. J Neurol Neurosurg Psychiatry. doi:10.1136/jnnp-2012-304545

Del Gaizo A, Banerjee S, Terk M (2009) Adult onset glycogen storage disease type II (adult onset Pompe disease): report and magnetic resonance images of two cases. Skeletal Radiol 38(12):1205–1208. doi:10.1007/s00256-009-0797-4

Del Grande F, Carrino JA, Del Grande M, Mammen AL, Christopher Stine L (2011) Magnetic resonance imaging of inflammatory myopathies. Top Magn Reson Imaging 22(2):39–43. doi:10.1097/RMR.0b013e31825b2c35

Dimachkie MM, Barohn RJ (2013) Inclusion body myositis. Curr Neurol Neurosci Rep 13(1):321. doi:10.1007/s11910-012-0321-4

Dion E, Cherin P, Payan C, Fournet JC, Papo T, Maisonobe T, Auberton E, Chosidow O, Godeau P, Piette JC, Herson S, Grenier P (2002) Magnetic resonance imaging criteria for distinguishing between inclusion body myositis and polymyositis. J Rheumatol 29(9):1897–1906

el-Noueam KI, Schweitzer ME, Bhatia M, Bartolozzi AR (1997) The utility of contrast-enhanced MRI in diagnosis of muscle injuries occult to conventional MRI. J Comput Assist Tomogr 21(6): 965–968

England JD, Gronseth GS, Franklin G, Carter GT, Kinsella LJ, Cohen JA, Asbury AK, Szigeti K, Lupski JR, Latov N, Lewis RA, Low PA, Fisher MA, Herrmann DN, Howard JF, Lauria G, Miller RG, Polydefkis M, Sumner AJ (2009) Practice parameter: the evaluation of distal symmetric polyneuropathy: the role of laboratory and genetic testing (an evidence-based review). Report of the American Academy of Neurology, the American Association of Neuromuscular and Electrodiagnostic Medicine, and the American Academy of Physical Medicine and Rehabilitation. PM R 1 (1):5–13. doi:10.1016/j.pmrj.2008.11.010

Evans GF, Haller RG, Wyrick PS, Parkey RW, Fleckenstein JL (1998) Submaximal delayed-onset muscle soreness: correlations between MR imaging findings and clinical measures. Radiology 208(3):815–820

Fermont J, Arts IM, Overeem S, Kleine BU, Schelhaas HJ, Zwarts MJ (2010) Prevalence and distribution of fasciculations in healthy adults: Effect of age, caffeine consumption and exercise. Amyotroph Lateral Scler 11(1–2):181–186. doi:10.3109/17482960903062137

Finanger EL, Russman B, Forbes SC, Rooney WD, Walter GA, Vandenborne K (2012) Use of skeletal muscle MRI in diagnosis and monitoring disease progression in Duchenne muscular dystrophy. Phys Med Rehabil Clin N Am 23 (1):1–10, ix. doi:10.1016/j.pmr.2011.11.004

Fujita H, Ishimatsu Y, Motomura M, Kakugawa T, Sakamoto N, Hayashi T, Kohno S (2011) A case of acute sarcoid myositis treated with weekly low-dose methotrexate. Muscle Nerve 44(6):994–999. doi:10.1002/mus.22222

Galban-Horcajo F, Fitzpatrick AM, Hutton AJ, Dunn SM, Kalna G, Brennan KM, Rinaldi S, Yu RK, Goodyear CS, Willison HJ (2013) Antibodies to heteromeric glycolipid complexes in multifocal motor neuropathy. Eur J Neurol 20(1):62–70. doi:10.1111/j.1468-1331.2012.03767.x

Goh G, Choi M (2012) Application of whole exome sequencing to identify disease-causing variants in inherited human diseases. Genomics Inform 10(4):214–219. doi:10.5808/gi.2012.10.4.214

Gojanovic B, Feihl F, Liaudet L, Gremion G, Waeber B (2011) Whole-body vibration training elevates creatine kinase levels in sedentary subjects. Swiss Med Wkly 141:w13222. doi:10.4414/smw.2011.13222

Gunreben G, Bogdahn U (1991) Real-time sonography of acute and chronic muscle denervation. Muscle Nerve 14(7):654–664. doi: 10.1002/mus.880140709

Hagemans ML, Winkel LP, Hop WC, Reuser AJ, Van Doorn PA, Van der Ploeg AT (2005) Disease severity in children and adults with Pompe disease related to age and disease duration. Neurology 64(12):2139–2141. doi:10.1212/01.wnl.0000165979.46537.56

Heckmatt JZ, Pier N, Dubowitz V (1988a) Assessment of quadriceps femoris muscle atrophy and hypertrophy in neuromuscular disease in children. J Clin Ultrasound 16(3):177–181

Heckmatt JZ, Pier N, Dubowitz V (1988b) Real-time ultrasound imaging of muscles. Muscle Nerve 11(1):56–65. doi:10.1002/mus.880110110

Heckmatt J, Rodillo E, Doherty M, Willson K, Leeman S (1989) Quantitative sonography of muscle. J Child Neurol 4(Suppl):S101–S106

Hernandez RJ, Keim DR, Sullivan DB, Chenevert TL, Martel W (1990) Magnetic resonance imaging appearance of the muscles in childhood dermatomyositis. J Pediatr 117(4):546–550

Hernandez RJ, Sullivan DB, Chenevert TL, Keim DR (1993) MR imaging in children with dermatomyositis: musculoskeletal findings and correlation with clinical and laboratory findings. AJR Am J Roentgenol 161(2):359–366

Herrera E, Sandoval MC, Camargo DM, Salvini TF (2010) Motor and sensory nerve conduction are affected differently by ice pack, ice massage, and cold water immersion. Phys Ther 90(4):581–591. doi:10.2522/ptj.20090131

Hobson-Webb LD, Kishnani PS (2012) How common is misdiagnosis in late-onset Pompe disease? Muscle Nerve 45(2):301–302. doi: 10.1002/mus.22296

Hobson-Webb LD, Austin SL, Bali DS, Kishnani PS (2010) The electrodiagnostic characteristics of Glycogen Storage Disease

Type III. Genet Med 12(7):440–445. doi:10.1097/GIM.0b013e3181cd735b

Hudash G, Albright JP, McAuley E, Martin RK, Fulton M (1985) Cross-sectional thigh components: computerized tomographic assessment. Med Sci Sports Exerc 17(4):417–421

Huppertz HI, Kaiser WA (1994) Serial magnetic resonance imaging in juvenile dermatomyositis–delayed normalization. Rheumatol Int 14(3):127–129

Jansen M, van Alfen N, Nijhuis van der Sanden MW, van Dijk JP, Pillen S, de Groot IJ (2012) Quantitative muscle ultrasound is a promising longitudinal follow-up tool in Duchenne muscular dystrophy. Neuromuscul Disord 22(4):306–317. doi:10.1016/j.nmd.2011.10.020

Juel VC, Massey JM (2007) Myasthenia gravis. Orphanet J Rare Dis 2:44. doi:10.1186/1750-1172-2-44

Jungbluth H, Davis MR, Muller C, Counsell S, Allsop J, Chattopadhyay A, Messina S, Mercuri E, Laing NG, Sewry CA, Bydder G, Muntoni F (2004) Magnetic resonance imaging of muscle in congenital myopathies associated with RYR1 mutations. Neuromuscul Disord 14(12):785–790. doi:10.1016/j.nmd.2004.08.006

Kamath S, Venkatanarasimha N, Walsh MA, Hughes PM (2008) MRI appearance of muscle denervation. Skeletal Radiol 37(5):397–404. doi:10.1007/s00256-007-0409-0

Keim DR, Hernandez RJ, Sullivan DB (1991) Serial magnetic resonance imaging in juvenile dermatomyositis. Arthritis Rheum 34(12):1580–1584

Khan S, Christopher-Stine L (2011) Polymyositis, dermatomyositis, and autoimmune necrotizing myopathy: clinical features. Rheum Dis Clin North Am 37(2):143–158. doi:10.1016/j.rdc.2011.01.001

Kim HK, Laor T, Horn PS, Racadio JM, Wong B, Dardzinski BJ (2010) T2 mapping in Duchenne muscular dystrophy: distribution of disease activity and correlation with clinical assessments. Radiology 255(3):899–908. doi:10.1148/radiol.10091547

Klein A, Jungbluth H, Clement E, Lillis S, Abbs S, Munot P, Pane M, Wraige E, Schara U, Straub V, Mercuri E, Muntoni F (2011) Muscle magnetic resonance imaging in congenital myopathies due to ryanodine receptor type 1 gene mutations. Arch Neurol 68(9):1171–1179. doi:10.1001/archneurol.2011.188

Kullmer K, Sievers KW, Reimers CD, Rompe JD, Muller-Felber W, Nagele M, Harland U (1998) Changes of sonographic, magnetic resonance tomographic, electromyographic, and histopathologic findings within a 2-month period of examinations after experimental muscle denervation. Arch Orthop Trauma Surg 117(4–5):228–234

Kuo GP, Carrino JA (2007) Skeletal muscle imaging and inflammatory myopathies. Curr Opin Rheumatol 19(6):530–535. doi:10.1097/BOR.0b013e3282efdc66

Lam WW, Chan H, Chan YL, Fung JW, So NM, Metreweli C (1999) MR imaging in amyopathic dermatomyositis. Acta Radiol 40(1):69–72

Le Roux K, Streichenberger N, Vial C, Petiot P, Feasson L, Bouhour F, Ninet J, Lachenal F, Broussolle C, Seve P (2007) Granulomatous myositis: a clinical study of thirteen cases. Muscle Nerve 35(2):171–177. doi:10.1002/mus.20683

Lovitt S, Moore SL, Marden FA (2006) The use of MRI in the evaluation of myopathy. Clin Neurophysiol 117(3):486–495. doi:10.1016/j.clinph.2005.10.010

Ludolph AC, Brettschneider J, Weishaupt JH (2012) Amyotrophic lateral sclerosis. Curr Opin Neurol 25(5):530–535. doi:10.1097/WCO.0b013e328356d328

Lyons MK (2009) Nerve rootlet and fascicular biopsy in patients with hypertrophic inflammatory neuropathy. Neurologist 15(1):40–41. doi:10.1097/NRL.0b013e31817882c8

Maillard SM, Jones R, Owens C, Pilkington C, Woo P, Wedderburn LR, Murray KJ (2004) Quantitative assessment of MRI T2 relaxation time of thigh muscles in juvenile dermatomyositis. Rheumatology (Oxford) 43(5):603–608. doi:10.1093/rheumatology/keh130

Marden FA, Connolly AM, Siegel MJ, Rubin DA (2005) Compositional analysis of muscle in boys with Duchenne muscular dystrophy using MR imaging. Skeletal Radiol 34(3):140–148. doi:10.1007/s00256-004-0825-3

Marti R, Nascimento A, Colomer J, Lara MC, Lopez-Gallardo E, Ruiz-Pesini E, Montoya J, Andreu AL, Briones P, Pineda M (2010) Hearing loss in a patient with the myopathic form of mitochondrial DNA depletion syndrome and a novel mutation in the TK2 gene. Pediatr Res 68(2):151–154. doi:10.1203/PDR.0b013e3181e33bbe

Matthews E, Fialho D, Tan SV, Venance SL, Cannon SC, Sternberg D, Fontaine B, Amato AA, Barohn RJ, Griggs RC, Hanna MG (2010) The non-dystrophic myotonias: molecular pathogenesis, diagnosis and treatment. Brain 133(Pt 1):9–22. doi:10.1093/brain/awp294

Maurits NM, Bollen AE, Windhausen A, De Jager AE, Van Der Hoeven JH (2003) Muscle ultrasound analysis: normal values and differentiation between myopathies and neuropathies. Ultrasound Med Biol 29(2):215–225. doi: S0301562902007585 [pii]

Maurits NM, Beenakker EA, van Schaik DE, Fock JM, van der Hoeven JH (2004) Muscle ultrasound in children: normal values and application to neuromuscular disorders. Ultrasound Med Biol 30(8):1017–1027. doi: 10.1016/j.ultrasmedbio.2004.05.013

May DA, Disler DG, Jones EA, Balkissoon AA, Manaster BJ (2000) Abnormal signal intensity in skeletal muscle at MR imaging: patterns, pearls, and pitfalls. Radiographics 20 Spec No: S295-315

Mercuri E, Cini C, Counsell S, Allsop J, Zolkipli Z, Jungbluth H, Sewry C, Brown SC, Pepe G, Muntoni F (2002a) Muscle MRI findings in a three-generation family affected by Bethlem myopathy. Eur J Paediatr Neurol 6(6):309–314. doi: S1090379802906185 [pii]

Mercuri E, Counsell S, Allsop J, Jungbluth H, Kinali M, Bonne G, Schwartz K, Bydder G, Dubowitz V, Muntoni F (2002b) Selective muscle involvement on magnetic resonance imaging in autosomal dominant Emery-Dreifuss muscular dystrophy. Neuropediatrics 33(1):10–14. doi: 10.1055/s-2002-23593

Mercuri E, Jungbluth H, Muntoni F (2005a) Muscle imaging in clinical practice: diagnostic value of muscle magnetic resonance imaging in inherited neuromuscular disorders. Curr Opin Neurol 18(5):526–537. doi: 00019052-200510000-00008 [pii]

Mercuri E, Lampe A, Allsop J, Knight R, Pane M, Kinali M, Bonnemann C, Flanigan K, Lapini I, Bushby K, Pepe G, Muntoni F (2005b) Muscle MRI in Ullrich congenital muscular dystrophy and Bethlem myopathy. Neuromuscul Disord 15(4):303–310. doi: S0960-8966(05)00024-6 [pii]

Mercuri E, Clements E, Offiah A, Pichiecchio A, Vasco G, Bianco F, Berardinelli A, Manzur A, Pane M, Messina S, Gualandi F, Ricci E, Rutherford M, Muntoni F (2010) Muscle magnetic resonance imaging involvement in muscular dystrophies with rigidity of the spine. Ann Neurol 67(2):201–208. doi: 10.1002/ana.21846

Meriggioli MN, Sanders DB (2012) Muscle autoantibodies in myasthenia gravis: beyond diagnosis? Expert Rev Clin Immunol 8(5):427–438. doi: 10.1586/eci.12.34

Mimori T, Nakashima R, Hosono Y (2012) Interstitial lung disease in myositis: clinical subsets, biomarkers, and treatment. Curr Rheumatol Rep 14(3):264–274. doi: 10.1007/s11926-012-0246-6

Misawa S, Noto Y, Shibuya K, Isose S, Sekiguchi Y, Nasu S, Kuwabara S (2011) Ultrasonographic detection of fasciculations markedly increases diagnostic sensitivity of ALS. Neurology 77(16):1532–1537. doi: 10.1212/WNL.0b013e318233b36a

Morvan D (1995) In vivo measurement of diffusion and pseudo-diffusion in skeletal muscle at rest and after exercise. Magn Reson Imaging 13(2):193–199

Muley SA, Parry GJ (2012) Multifocal motor neuropathy. J Clin Neurosci 19(9):1201–1209. doi: 10.1016/j.jocn.2012.02.011

Orrell RW (2011) Facioscapulohumeral dystrophy and scapuloperoneal syndromes. Handb Clin Neurol 101:167–180. doi: 10.1016/b978-0-08-045031-5.00013-x

Ota M, Ikezoe T, Kaneoka K, Ichihashi N (2012) Age-related changes in the thickness of the deep and superficial abdominal muscles in women. Arch Gerontol Geriatr 55(2):e26–e30. doi: 10.1016/j.archger.2012.03.007

Padua L, Di Pasquale A, Liotta G, Granata G, Pazzaglia C, Erra C, Briani C, Coraci D, De Franco P, Antonini G, Martinoli C (2013) Ultrasound as a useful tool in the diagnosis and management of traumatic nerve lesions. Clin Neurophysiol. doi: 10.1016/j.clinph.2012.10.024

Palmeri ML, Wang MH, Rouze NC, Abdelmalek MF, Guy CD, Moser B, Diehl AM, Nightingale KR (2011) Noninvasive evaluation of hepatic fibrosis using acoustic radiation force-based shear stiffness in patients with nonalcoholic fatty liver disease. J Hepatol 55(3):666–672. doi: 10.1016/j.jhep.2010.12.019

Pantoja PD, Alberton CL, Pilla C, Vendrusculo AP, Kruel LF (2009) Effect of resistive exercise on muscle damage in water and on land. J Strength Cond Res 23(3):1051–1054. doi: 10.1519/JSC.0b013e3181a00c45

Pestronk A (2011) Acquired immune and inflammatory myopathies: pathologic classification. Curr Opin Rheumatol 23(6):595–604. doi: 10.1097/BOR.0b013e32834bab42

Petersilge CA, Pathria MN, Gentili A, Recht MP, Resnick D (1995) Denervation hypertrophy of muscle: MR features. J Comput Assist Tomogr 19(4):596–600

Phillips BA, Cala LA, Thickbroom GW, Melsom A, Zilko PJ, Mastaglia FL (2001) Patterns of muscle involvement in inclusion body myositis: clinical and magnetic resonance imaging study. Muscle Nerve 24(11):1526–1534

Pichiecchio A, Uggetti C, Ravaglia S, Egitto MG, Rossi M, Sandrini G, Danesino C (2004) Muscle MRI in adult-onset acid maltase deficiency. Neuromuscul Disord 14(1):51–55

Pillen S, Verrips A, van Alfen N, Arts IM, Sie LT, Zwarts MJ (2007) Quantitative skeletal muscle ultrasound: diagnostic value in childhood neuromuscular disease. Neuromuscul Disord 17(7):509–516. doi: 10.1016/j.nmd.2007.03.008

Pillen S, Arts IM, Zwarts MJ (2008) Muscle ultrasound in neuromuscular disorders. Muscle Nerve 37(6):679–693. doi: 10.1002/mus.21015

Pillen S, Tak RO, Zwarts MJ, Lammens MM, Verrijp KN, Arts IM, van der Laak JA, Hoogerbrugge PM, van Engelen BG, Verrips A (2009) Skeletal muscle ultrasound: correlation between fibrous tissue and echo intensity. Ultrasound Med Biol 35(3):443–446. doi: 10.1016/j.ultrasmedbio.2008.09.016

Prater SN, Banugaria SG, DeArmey SM, Botha EG, Stege EM, Case LE, Jones HN, Phornphutkul C, Wang RY, Young SP, Kishnani PS (2012) The emerging phenotype of long-term survivors with infantile Pompe disease. Genet Med 14(9):800–810. doi: 10.1038/gim.2012.44

Pratt AJ, Getzoff ED, Perry JJ (2012) Amyotrophic lateral sclerosis: update and new developments. Degener Neurol Neuromuscul Dis 2:1–14. doi: 10.2147/dnnd.s19803

Puckelwartz M, McNally EM (2011) Emery-Dreifuss muscular dystrophy. Handb Clin Neurol 101:155–166. doi: 10.1016/b978-0-08-045031-5.00012-8

Qi J, Olsen NJ, Price RR, Winston JA, Park JH (2008) Diffusion-weighted imaging of inflammatory myopathies: polymyositis and dermatomyositis. J Magn Reson Imaging 27(1):212–217. doi: 10.1002/jmri.21209

Quijano-Roy S, Avila-Smirnow D, Carlier RY (2012) Whole body muscle MRI protocol: pattern recognition in early onset NM disorders. Neuromuscul Disord 22(Suppl 2):S68–S84. doi: 10.1016/j.nmd.2012.08.003

Reimers CD (2000) Imaging in myology: a neurologist's perspective. Semin Musculoskelet Radiol 4(4):367–373. doi: 10.1055/s-2000-13161

Reimers CD, Schedel H, Fleckenstein JL, Nagele M, Witt TN, Pongratz DE, Vogl TJ (1994a) Magnetic resonance imaging of skeletal muscles in idiopathic inflammatory myopathies of adults. J Neurol 241(5):306–314

Reimers CD, Schedel H, Fleckenstein JL, Nagele M, Witt TN, Pongratz DE, Vogl TJ (1994b) Magnetic resonance imaging of skeletal muscles in idiopathic inflammatory myopathies of adults. J Neurol 241(5):306–314

Reimers CD, Schlotter B, Eicke BM, Witt TN (1996a) Calf enlargement in neuromuscular diseases: a quantitative ultrasound study in 350 patients and review of the literature. J Neurol Sci 143(1–2):46–56

Reimers CD, Ziemann U, Scheel A, Rieckmann P, Kunkel M, Kurth C (1996b) Fasciculations: clinical, electromyographic, and ultrasonographic assessment. J Neurol 243(8):579–584

Rudnicki SA (2010) Prevention and treatment of peripheral neuropathy after bariatric surgery. Curr Treat Options Neurol 12(1):29–36. doi: doi:10.1007/s11940-009-0052-2

Ruoff JM, van der Sluijs JA, van Ouwerkerk WJ, Jaspers RT (2012) Musculoskeletal growth in the upper arm in infants after obstetric brachial plexus lesions and its relation with residual muscle function. Dev Med Child Neurol 54(11):1050–1056. doi: 10.1111/j.1469-8749.2012.04383.x

Sanders DB, Juel VC (2008) The Lambert-Eaton myasthenic syndrome. Handb Clin Neurol 91:273–283. doi: 10.1016/s0072-9752(07)01509-6

Schramm N, Born C, Weckbach S, Reilich P, Walter MC, Reiser MF (2008) Involvement patterns in myotilinopathy and desminopathy detected by a novel neuromuscular whole-body MRI protocol. Eur Radiol 18(12):2922–2936. doi: 10.1007/s00330-008-1071-1

Schrier SA, Falk MJ (2011) Mitochondrial disorders and the eye. Curr Opin Ophthalmol 22(5):325–331. doi: 10.1097/ICU.0b013e328349419d

Schweitzer ME, Fort J (1995) Cost-effectiveness of MR imaging in evaluating polymyositis. AJR Am J Roentgenol 165(6):1469–1471

Simon NG, Kiernan MC (2013) Fasciculation anxiety syndrome in clinicians. J Neurol. doi: 10.1007/s00415-013-6856-8

Stiglbauer R, Graninger W, Prayer L, Kramer J, Schurawitzki H, Machold K, Imhof H (1993) Polymyositis: MRI-appearance at 1.5 T and correlation to clinical findings. Clin Radiol 48(4):244–248

Stonecipher MR, Jorizzo JL, Monu J, Walker F, Sutej PG (1994) Dermatomyositis with normal muscle enzyme concentrations. A single-blind study of the diagnostic value of magnetic resonance imaging and ultrasound. Arch Dermatol 130(10):1294–1299

Swash M, Brown MM, Thakkar C (1995) CT muscle imaging and the clinical assessment of neuromuscular disease. Muscle Nerve 18(7):708–714. doi: 10.1002/mus.880180706

Ten Dam L, van der Kooi AJ, van Wattingen M, de Haan RJ, de Visser M (2012) Reliability and accuracy of skeletal muscle imaging in limb-girdle muscular dystrophies. Neurology 79(16):1716–1723. doi: 10.1212/WNL.0b013e31826e9b73

Tomasova Studynkova J, Charvat F, Jarosova K, Vencovsky J (2007) role of MRI in the assessment of polymyositis and dermatomyositis. Rheumatology (Oxford) 46(7):1174–1179. doi:10.1093/rheumatology/kem088

Torriani M, Townsend E, Thomas BJ, Bredella MA, Ghomi RH, Tseng BS (2012) Lower leg muscle involvement in Duchenne muscular dystrophy: an MR imaging and spectroscopy study. Skeletal Radiol 41(4):437–445. doi: 10.1007/s00256-011-1240-1

Tyler P, Saifuddin A (2010) The imaging of myositis ossificans. Semin Musculoskelet Radiol 14(2):201–216. doi: 10.1055/s-0030-1253161

van Alfen N, Nienhuis M, Zwarts MJ, Pillen S (2011) Detection of fibrillations using muscle ultrasound: diagnostic accuracy and identification of pitfalls. Muscle Nerve 43(2):178–182. doi: 10.1002/mus.21863

van der Ploeg AT, Clemens PR, Corzo D, Escolar DM, Florence J, Groeneveld GJ, Herson S, Kishnani PS, Laforet P, Lake SL, Lange DJ, Leshner RT, Mayhew JE, Morgan C, Nozaki K, Park DJ, Pestronk A, Rosenbloom B, Skrinar A, van Capelle CI, van der Beek NA, Wasserstein M, Zivkovic SA (2010) A randomized study of alglucosidase alfa in late-onset Pompe's disease. N Engl J Med 362(15):1396–1406. doi: 10.1056/NEJMoa0909859

Viddeleer AR, Sijens PE, van Ooijen PM, Kuypers PD, Hovius SE, Oudkerk M (2011) MR intensity measurements of nondenervated muscle in patients following severe forearm trauma. NMR Biomed 24(7):895–901. doi: 10.1002/nbm.1647

Wattjes MP, Kley RA, Fischer D (2010) Neuromuscular imaging in inherited muscle diseases. Eur Radiol 20(10):2447–2460. doi: 10.1007/s00330-010-1799-2

Weber MA et al (2007) Quantitative evaluation of muscle perfusion with CEUS and with MR. Eur Radiol 17:2663–2674

Wessig C, Koltzenburg M, Reiners K, Solymosi L, Bendszus M (2004) Muscle magnetic resonance imaging of denervation and reinnervation: correlation with electrophysiology and histology. Exp Neurol 185(2):254–261

Wren TA, Bluml S, Tseng-Ong L, Gilsanz V (2008) Three-point technique of fat quantification of muscle tissue as a marker of disease progression in Duchenne muscular dystrophy: preliminary study. AJR Am J Roentgenol 190(1):W8–W12. doi: 10.2214/AJR.07.2732

Zahr ZA, Baer AN (2011) Malignancy in myositis. Curr Rheumatol Rep 13(3):208–215. doi: 10.1007/s11926-011-0169-7

Zaidman CM, Connolly AM, Malkus EC, Florence JM, Pestronk A (2010) Quantitative ultrasound using backscatter analysis in Duchenne and Becker muscular dystrophy. Neuromuscul Disord 20(12):805–809. doi: 10.1016/j.nmd.2010.06.019

Zaidman CM, Malkus EC, Siener C, Florence J, Pestronk A, Al-Lozi M (2011) Qualitative and quantitative skeletal muscle ultrasound in late-onset acid maltase deficiency. Muscle Nerve 44(3):418–423. doi: 10.1002/mus.22088

Zaidman CM, Holland MR, Noetzel MJ, Park TS, Pestronk A (2012) Newborn brachial plexus palsy: Evaluation of severity using quantitative ultrasound of muscle. Muscle Nerve. doi: 10.1002/mus.23518

Zuberi SM, Matta N, Nawaz S, Stephenson JB, McWilliam RC, Hollman A (1999) Muscle ultrasound in the assessment of suspected neuromuscular disease in childhood. Neuromuscul Disord 9(4):203–207

Correlation of Skeletal Muscle Anatomy to MRI and US Findings

Alberto Tagliafico, Bianca Bignotti, Sonia Airaldi, and Carlo Martinoli

Contents

1 **Key Points** 27

2 **Introduction** 28

3 **Microscopical Anatomy** 28
3.1 Muscle Fibers Classification 28

4 **Macroscopical Anatomy** 29

5 **Physiological Notes on Muscular Contraction** 30

6 **Tendons** 31

7 **Aponeuroses** 33

8 **Muscle–Tendon Junction** 33

9 **Imaging** 33

10 **Anatomical Variants** 35

References 39

Abstract

Muscles are anatomical structures with the capability to reduce their length if stimulated appropriately. In this chapter the anatomy of the skeletal muscle and of its imaging appearance are briefly reviewed. The anatomic description starts from the microscopical anatomy to reach the macroscopical anatomy. Biomechanical principles of levers and muscular contraction are also reviewed. Imaging features are described with an emphasis on ultrasound and magnetic resonance imaging. Moreover, a brief overview on accessory muscles is presented.

1 Key Points

1. The muscles are anatomical structures with the capability to reduce their length if stimulated appropriately.
2. According to the famous anatomist of the past Bichat, muscles are divided into two main groups: muscles of animal life and muscles of vegetative life. The first group is characterized by the capability to react under one person’s will, and their contraction is quite fast. The other group, the “visceral muscles” are not dependent on the will of the individual.
3. Microscopical anatomy: the smallest contractile unit of the skeletal muscle is the muscle fiber or myofiber, which is a long cylindrical cell that contains multiple nuclei, several mitochondria, and sarcomeres.
4. Muscle fibers classification: individual muscle fibers are classified by their histologic appearance and by their ability to use energy deposits.
5. Classification based on the relationship between muscle and tendon: considering the relationship between the muscle and the tendon, the muscle may be divided into those having a direct insertion and those having a lateral

Electronic supplementary material The online version of this article (doi: 10.1007/174_2013_924) contains supplementary material, which is available to authorized users.

A. Tagliafico (✉)
Department of Experimental Medicine (DIMES),
University of Genova, Via L.B. Alberti, Genoa, Italy
e-mail: albertotagliafico@gmail.com

B. Bignotti · S. Airaldi · C. Martinoli
Department of Health Sciences (DISSAL),
University of Genova, Via Pastore 2, Genoa, Italy

M.-A. Weber (ed.), *Magnetic Resonance Imaging of the Skeletal Musculature*, Medical Radiology. Diagnostic Imaging,
DOI: 10.1007/174_2013_924, © Springer-Verlag Berlin Heidelberg 2013
Published Online: 31 October 2013

insertion, or according to its general shape and predominant orientation of fibers.
6. Ultrasound, magnetic resonance imaging and computed tomography are widely used with different purposes to visualize the normal anatomy of the musculoskeletal system.
7. Anatomical variants: muscular anatomical variants are more common than normally thought. Muscular anatomical variants include not only supernumerary or accessory muscles, but also their absence, their deviation from a normal course, and an anomalous origin or insertion.

2 Introduction

Muscles are anatomical structures with the capability to reduce their length if stimulated appropriately. According to Bichat, the famous anatomist of the past, they are divided into two main groups: muscles of animal life and muscles of vegetative life. The first group is characterized by the capability to react under a person's will, and their contraction is quite fast. The other group, the "visceral muscles" are not dependent on the will of the individual. The muscles of animal life are characterized by several fibers which are arranged in "striae." For this reason the term "striated muscle" may be used to describe the muscles of animal life, or also called voluntarily controlled. The term "striated muscle" is sometimes used to describe the cardiac muscle.

3 Microscopical Anatomy

The smallest contractile unit of the skeletal muscle is the muscle fiber or myofiber, which is a long cylindrical cell that contains multiple nuclei, several mitochondria, and a lot of sarcomeres (Boron and Boulpaep 2009). Muscle fibers are long and cylindrical and they range in size from 10 to 100 µm. In general, larger fibers are found in big and powerful muscles such as the muscles of the thigh. However, fibres are small in muscles which have the task to perform quick and precise movements, such as the extrinsic muscles of the eye. The functional subunit of the muscle fiber is called sarcomere. Sarcomeres contain two types of protein filaments: a thick filament (myosin) and a thin filament (actin, troponin and tropomyosin). The movement of these filaments with respect to each other guarantees movement.

Microscopically, a muscle fiber presents transversely orientated bands called Z-lines which constitute the limits of the sarcomere. In classical textbooks they are also described as A-bands and I-bands. The A-bands consist of thick filaments with interdigitation; the I-bands consist of two adjacent sarcomeres with no interdigitation. A more detailed description of these bands is beyond the scope of this chapter. Muscle fibers have multiple nuclei and adjacent to the myofibrils there are the Golgi apparatus, the ribosomes, and the mitochondria in sufficient numbers, which depend on the main function of the muscle (prevalence of aerobic or anaerobic metabolism). A single muscle fiber is surrounded by a thin layer of connective tissue named endomysium. Approximately a number, ranging from 20 to 80, of these muscle fibers are grouped together in a parallel arrangement. These groups of fibers form a muscle fascicle or fiber bundle. A muscle fascicle or a fiber bundle is encapsulated by another layer of connective tissue called the perimysium. The perimysium is thicker than the epimysium enclosing each of the bundled muscle fibers. A single distinct muscle is formed by a large number of muscle fascicles enveloped in a thick collagenous external sheath extending from the tendons called the epimysium (Korthuis 2011; Standrings 2005).

3.1 Muscle Fibers Classification

Individual muscle fibers are classified by their histologic appearance and by their ability to use energy deposits. Type I fibers are generally slow-twitch fibers, which are thinner, invested by a denser capillary network; on microscopy they are red due to the presence of a large amount of the oxygen-binding protein myoglobin. These fibers are resistant to fatigue, relying on oxidative metabolism for energy, and thus they have a high mitochondrial number and oxidative enzyme content opposed to a low glycogen presence and to a low glycolytic activity. On the other hand, type II fibers are fast-twitch fibers that differ among themselves with regard to resistance to fatigue. They are divided into type IIa and type IIb (Armstrong 1996). Type IIa muscle fibers contain abundant glycogen and more mitochondria to generate an adequate ATP content to balance the high rate of ATP hydrolysis. Type IIb fibers depend on glycogen storage and phosphocreatine: they contain few mitochondria, low content of myoglobin (for this reason they are called white muscles), and low levels of oxidative enzymes: for this reason type IIb muscle fibers are fast but easily fatigable. Type IIx, and 1–2 % type IIc fibers have also been described and they should be fast glycolytic fibers; they represent only 1 or 2 % of the total number of muscle fibers (Exeter and Connell 2010). Moreover, different muscle fibers receive different patterns of innervation by their motor neurons: the innervation pattern is different for different muscles. For example, the extrinsic muscles of the eyes have several motor units, whereas the powerful muscles of the back have a lower number of motor units with one motor neuron innervating a huge number of muscle fibers.

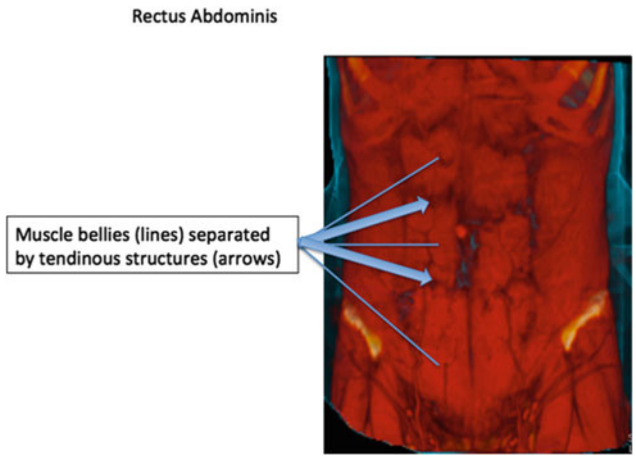
Rectus Abdominis
Muscle bellies (lines) separated by tendinous structures (arrows)

Fig. 1 Volume rendering computed tomography in false colors showing the macroscopical anatomy of the muscles of the abdominal wall, including the rectus abdominis muscle

4 Macroscopical Anatomy

Muscles can macroscopically be described and classified according to the following characteristics:

I. *Localization.* Muscles are divided into two big classes: superficial and deep, in relation to the position occupied regarding the superficial fascia.

II. *Number and mass.* It is difficult to count the total number of the muscles contained in the human body, because it is not clear how to classify a single muscular body. In the past the total number of muscles was reported to range from 346 by THEILE to 501 by SAPPEY. Their mass is approximately 3/7 of the entire human body.

III. *Classification based on the relationship between muscle and tendon.* Considering the relationship between the muscle and the tendon, the muscle may be divided into those having a direct insertion and those having a lateral insertion (Gray 2000), or according to its general shape and predominant orientation of fibers (Standring 2005).

The macroscopical shape and function of a skeletal muscle is determined by the internal arrangement of the fascicles.

Some muscles are strap-like (e.g., the sartorius muscle) and their fibers are parallel to the long axis of the muscle. The rectus abdominis muscle is a particular muscle where the muscle bellies are separated by tendinous structures oriented transversally (Fig. 1). Fusiform muscles, such as biceps, have fascicles that are orientated parallel to each other in the mid-portion, whereas at the end, near the myotendinous junction, the fibers converge. Pennate muscles have fascicles that are obliquely oriented relative to the line of traction. These muscles are called pennate because their aspect resembles a feather. From the biomechanical point of view these muscles contract against great loads (e.g., the soleus-gastrocnemius complex).

Pennate muscles include triangular-shaped (e.g., adductor longus), unipennate or semipennate (e.g., flexor pollicis longus), bipennate (e.g., rectus femoris), multipennate (e.g., deltoid), and circumpennate (e.g., tibialis anterior) muscles.

Some muscles are bipennate and their fascicles join a single central tendon; multipennate muscles have more than one tendon coursing through the muscle substance. Fascicles may also present a curved spiral arrangement between the origin and the insertion (e.g., pectoralis major, supinator). Several muscles are composed of a single belly or may have a complex internal architecture made up of multiple heads with a different origin (e.g., two heads for the biceps brachii and the biceps femoris; three heads for the triceps brachii and the triceps surae) and join together to generate a distal tendon (Fig. 2a–d).

From the biomechanical point of view, during muscle contraction, the force is transmitted to the skeleton by the tendon or aponeurosis and may or may not result in joint motion. Skeletal muscle contractions may be divided into three types: isometric, when the muscle contracts, but there is no change in its length; isotonic or concentric, when the muscle contracts and simultaneously shortens; and eccentric, when the muscle contracts and at the same time lengthens.

When a muscle is activated by the nervous system and it is required to lift a load which is less than the maximum tetanic tension the muscle can generate, the muscle is able to shorten. Contractions that permit the muscle to shorten are referred to as concentric or isotonic contractions. An example of a concentric contraction is the lifting of a weight during a biceps curl. In concentric contractions, the force generated by the muscle is always less than the muscle's maximum force. As the load the muscle is required to lift decreases, contraction velocity increases. This occurs until the muscle finally reaches its maximum contraction velocity.

In eccentric contractions the muscle actively lengthens. During normal activity, muscles are often active while they are lengthening. Classic examples of this are walking, when the quadriceps (knee extensors) are active just after heel strike while the knee flexes, or setting an object down gently (the arm flexors must be active to control the fall of the object).

As the load on the muscle increases, it finally reaches a point where the external force on the muscle is greater than the force that the muscle can generate. Thus even though the muscle may be fully activated, it is forced to lengthen due to the high external load. This is referred to an eccentric contraction. There are two main features to remark regarding eccentric contractions. First, the absolute tensions achieved are very high relative to muscle's maximum

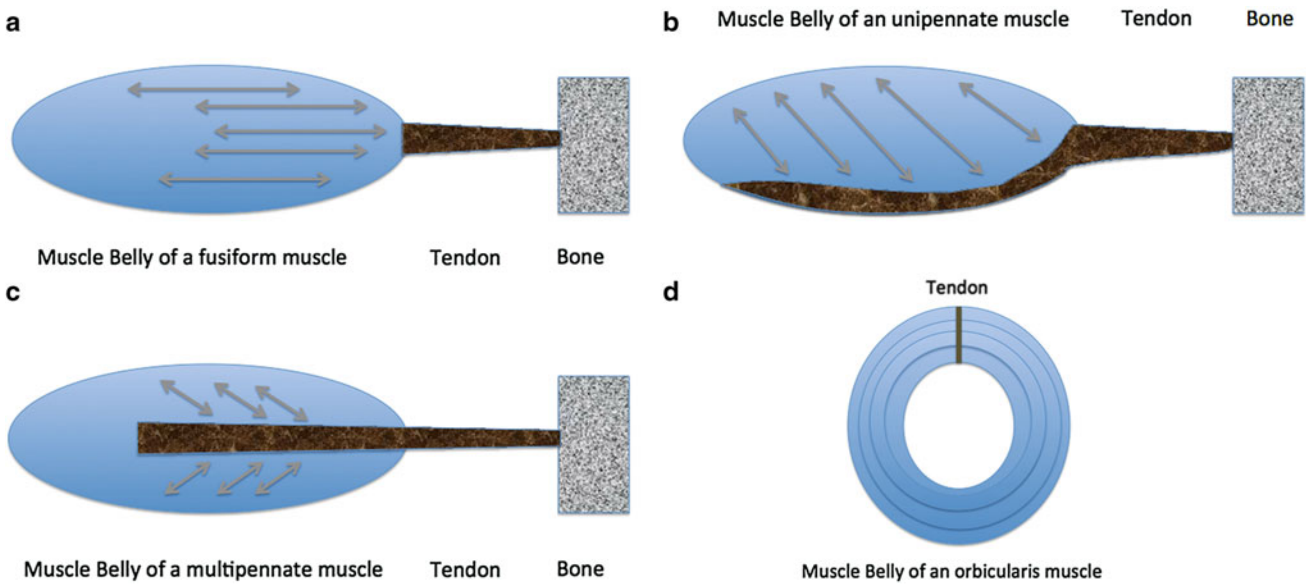
a
Muscle Belly of a fusiform muscle
Tendon
Bone
b
Muscle Belly of an unipennate muscle
Tendon
Bone
c
Muscle Belly of a multipennate muscle
Tendon
Bone
d
Tendon
Muscle Belly of an orbicularis muscle

Fig. 2 Schematic drawing of common skeletal muscle anatomy. **a** Fusiform muscle. The fascicles are parallel to the mid-portion of the muscle belly (low strength but high velocity and range of movement). **b** Unipennate muscle. The fascicles insert on one side of the aponeurosis (great strength but low range of shortening). **c** Bipennate muscle. The fascicles insert on two sides of a central aponeurosis (great strength but low range of movement). **d** Orbicularis muscles. These muscles contract concentrically and may not have a real bony insertion but a strong tendinous insertion

tetanic tension generating capacity (you can set down a much heavier object than you can lift). Second, the absolute tension is relatively independent of lengthening velocity. This suggests that skeletal muscles are very resistant to lengthening. The basic mechanics of eccentric contractions are still a source of debate, since the cross-bridge theory, which so nicely describes concentric contractions, is not as successful in describing eccentric contractions. Many muscle injuries and delayed soreness are often associated with eccentric contraction. Moreover, muscle strengthening may be greater using exercises that involve eccentric contractions. It has been recently demonstrated that eccentric contractions that normally determine an injury may stimulate the activation and proliferation of satellite stem cells to guide skeletal muscle regeneration. For this reason therapeutic strategies to combat disuse muscle atrophy may be implemented by the use of eccentric contractions in a rehabilitative setting (Valero et al. 2012). During isometric contraction the muscle is activated, but instead of being allowed to lengthen or shorten, it is held at a constant length. An example of an isometric contraction would be carrying an object in front of you. The weight of the object would be pulling downward, but your hands and arms would be opposing the motion with equal force going upwards. Since your arms are neither raising nor lowering, your biceps will be isometrically contracting. The force generated during an isometric contraction is dependent on the length of the muscle while contracting. Maximal isometric tension is produced at the muscle's optimum length, where the length of the muscle's sarcomeres is on the plateau of the length-tension curve.

Sometimes, a fourth type of muscle "contraction," known as passive stretch, is described. As the name implies, the muscle is being lengthened in a passive state (i.e., not being stimulated to contract) (Fig. 3a–d). An example of this would be the pull one feels in their hamstrings while touching their toes. The usefulness of stretching is still a controversial topic. Several studies investigated optimal stretching techniques causing confusion among researchers and clinicians. Further investigations may be useful to determine how passive and active muscular stretch may improve muscular function as a whole and eventually prevent musculoskeletal derangements (Williams et al. 2013). Examples of muscular contractions on ultrasound (US) examinations are demonstrated in three video clips (VIDEO 1–3) which can be accessed and downloaded via www.extras.springer.com. Representative snapshots of the video clip for isometric contraction are given in Fig. 4.

5 Physiological Notes on Muscular Contraction

From the physiological point of view the musculoskeletal system moves the different segments with respect to each other following the principle of levers. Each muscle is able to provide stability and to produce movement of the levers (bone) around the fulcrum (joint).

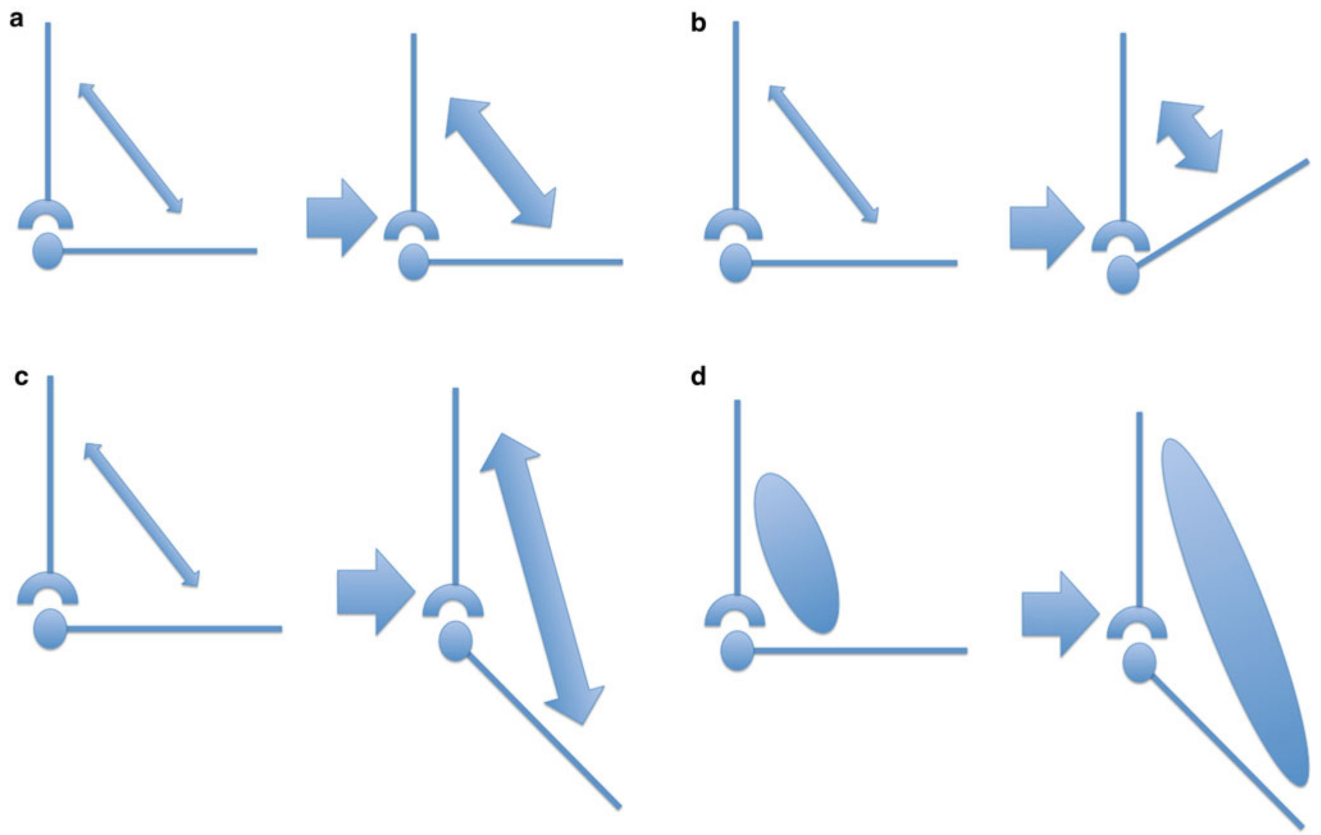

Fig. 3 **a** Isometric contraction. The length of the muscle does not change during contraction. **b** Isotonic contraction. The muscle shortens as it contracts. A typical example of isotonic contraction is the flexion of the arm on the forearm. **c** Eccentric contraction. The muscle lengthens during contraction. **d** Passive stretching. The muscle is lengthened in a passive state without active contraction

The system of levers is divided into three types on the basis of the organization and the distance between the fulcrum to the point of effort and to the load point. We can find all three classes of levers in body muscles.

First Class: The fulcrum lies between the effort and the load. In the human body, a lever of the first class can be found at the level of the head, for example. The weight of the face and of the head may be considered the resistance. The contraction of the posterior neck muscles may be considered the effort to lift the weight. A lever of the first class has a twofold purpose: to increase the speed of movement and to overcome the resistance. In this case the resistance (load) is moved in the opposite direction.

Second Class: The load lies between the fulcrum and the effort. The classical example reported in several textbooks is the principle of the wheelbarrow. A small upward force applied to the handles can overcome a much larger force (weight) acting downwards in the barrow. Similarly, a relatively small muscular effort is required to raise the body weight. In the human body, a lever of the second class can be found in our feet when we stand on our toes and lift our heels off the ground. The resistance (load) is the weight of our body resting on the arch of the foot. The effort is brought about by the contraction of the calf muscle attached to the heel. This leverage allows us to walk. The main purpose of a lever of the second class is to overcome the resistance.

Third Class: The effort lies between the fulcrum and the load. In the human body, a typical example of a lever of the third class is when the biceps contracts, allowing us to lift an object. The elbow may be considered the fulcrum, the object is the resistance (or load), and the biceps muscles contraction is the effort. The load can be moved rapidly over a large distance, while the point of application moves over a relatively short distance. The main purpose of this type of lever is to obtain rapid movement. Human skeletal muscles are shaped also according to their action as levers (Fig. 5a–c).

6 Tendons

Tendons are non-contractile collagenous structures with the function of connecting the muscle to its bony insertion. Tendons are important to transmit forces generated by muscle contraction, to facilitate and to maintain the posture.

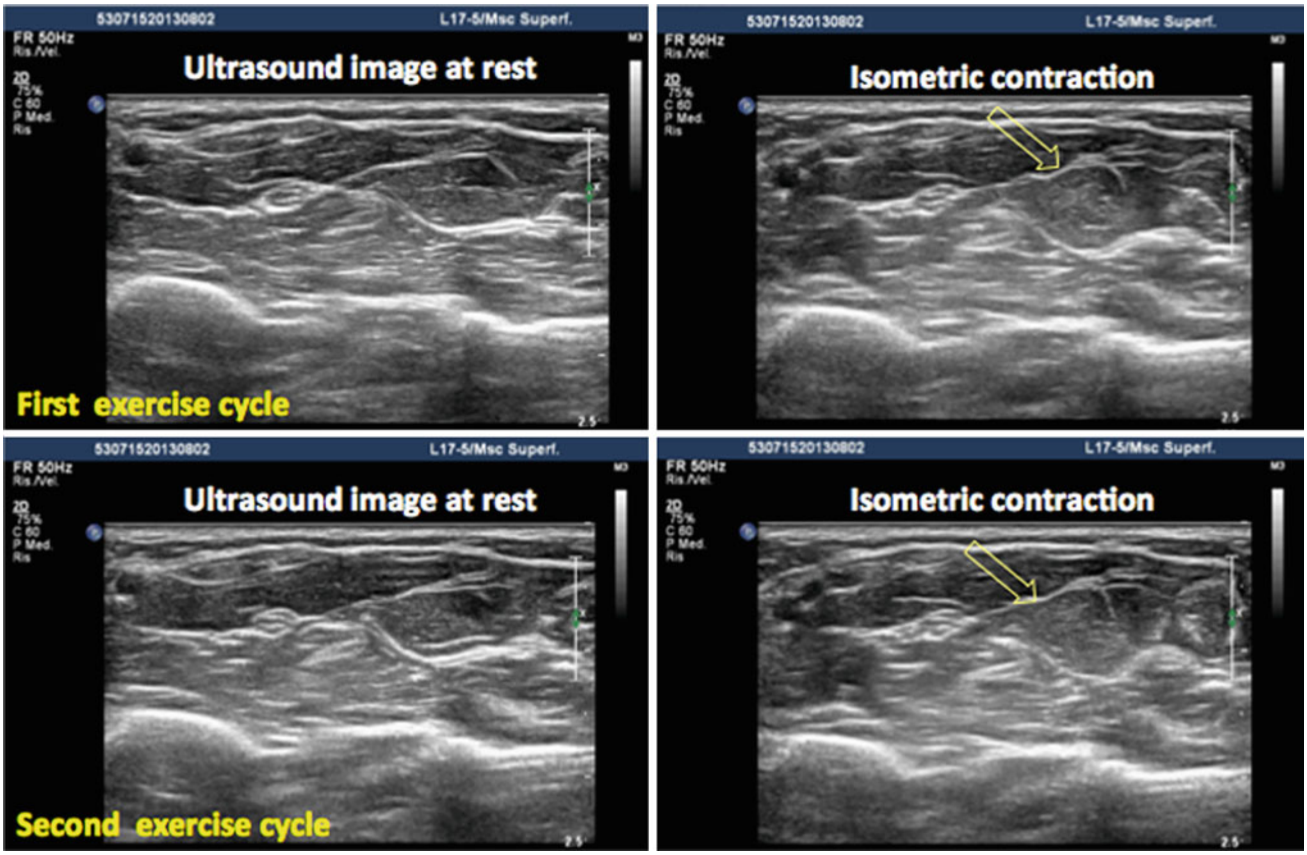
53071520130802
L17-5/Msc Superf.
FR 50Hz
Ultrasound image at rest
First exercise cycle
Isometric contraction
Ultrasound image at rest
Second exercise cycle
Isometric contraction
2.5

Fig. 4 Examples of different forms of muscular contractions on real-time ultrasound examinations are demonstrated in the three video clips (isometric contraction, isotonic contraction, and passive stretching) which can be accessed and downloaded via www.extras.springer.com. Representative snapshots of the video clips are given for isometric contraction on two subsequent exercise cycles to show the potential of ultrasound to show muscular motion in real-time. The *open arrows* show the time point of contraction

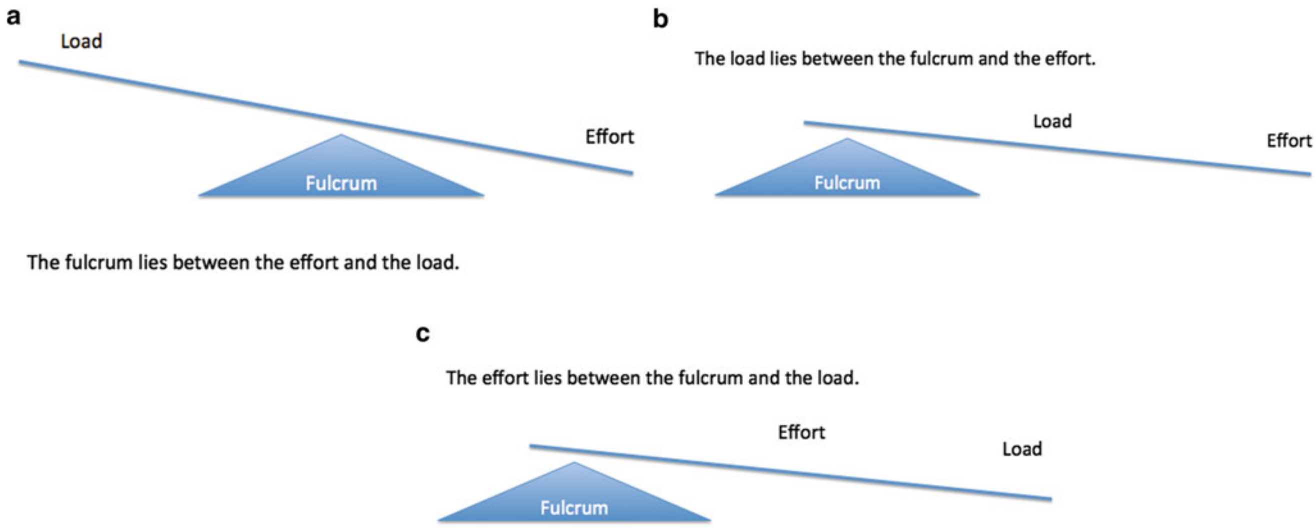
a
Load
Effort
Fulcrum
The fulcrum lies between the effort and the load.
b
The load lies between the fulcrum and the effort.
Load
Effort
Fulcrum
c
The effort lies between the fulcrum and the load.
Effort
Load
Fulcrum

Fig. 5 Principle of levers. **a** First class lever. **b** Second class lever. **c** Third class lever

Several skeletal muscles have both a tendinous insertion and a tendinous origin. Tendons are round or oval in cross-section and are made mainly of type I collagen fibers. These collagen fibers have the task to transmit the force with the minimum area, therefore the fibers are orientated parallel to the long axis of the tendon. Vessels and nerves course within loose connective tissue between the tendon fascicles. Some tendons are surrounded by a synovial sheath, especially when the corresponding muscle has the function to move bony segments for long distances (for example at the level of the fingers). Tendons attach to the periosteum of the bone through fasciculi that continue directly into the cortex of the bone. A plate of fibrocartilage at the site of bony attachment serves to cushion and reinforce the site of attachment. In general, tendons have a variable length according to the muscle of origin. Some tendons may have an intramuscular component or a superficial component resulting in a variable length of the myotendinous junction. Type I collagen fibers of the tendon are accompanied by a few amount of elastic fibers. These elastic fibers are important to increase the resilience and resistance of the tendon. The elastic properties of the tendons allow an elongation up to 6 % during maximum loads preventing damages during movements. Concerning the vascular supply of the tendons it is well known that they have a limited blood supply. This anatomical feature predisposes certain tendons to some typical injuries (e.g., the supraspinatus and the Achilles tendon). Each tendon receives its vascular supply from segmental vessels arising from the surrounding peritendon or, from folds of the mesotendon for those tendons with synovial sheaths (http://www.wheelessonline.com).

7 Aponeuroses

Aponeuroses are connective structures that may be considered flattened tendons. Aponeuroses may be considered separate structures emerging from or within a muscle belly or its surface (for example the tendons of latissimus dorsi and pectoralis major or the aponeurosis of the quadriceps femoris muscle).

8 Muscle–Tendon Junction

The muscle–tendon junction (musculotendinous or myotendinous junction) is the anatomical site where the muscular tissue becomes tendon. This site may be considered a weak area since the majority of traumatic lesions occur at this site. From the microscopical point of view, at this level tendon fibrils insert into deep recesses between finger-like processes of skeletal muscle cells covered by a thick layer of basement membrane. The tendon fibrils attach to the basement membrane of the skeletal muscle cells. Myocytes and tendons fibrils are linked by means of interdigitation to have an increased contact area able to distribute the tensile forces during contraction. The muscle–tendon junction has negligible elastic content and for this reason it has a lower resistance to loads during movement.

9 Imaging

Diagnostic imaging commonly available in clinical practice is able to study the muscles, the tendons, and the bone from a macroscopical point of view in normal and pathological conditions. US, MRI, and CT are widely used with different purposes to visualize the normal anatomy of the musculoskeletal system. Moreover, in recent years, new and technologically advanced imaging techniques have been introduced to study the musculoskeletal anatomy from a physiological and microscopical point of view. For example, elastography has been introduced to assess the elastic properties of tendons and muscles. Using MRI, diffusion tensor imaging (DTI) has been introduced to study the architecture of the skeletal muscle (see also "Correlation of Skeletal Muscle Anatomy to MRI and US Findings" of this book). The DTI technique is based on the measurement of the apparent diffusion of water in a (biological) tissue (Van Donkelaar et al. 1999). It is concluded that DTI fiber directions resemble fascicle directions visible in high-resolution images very well. Moreover, on DTI images it is possible to observe and study specific features of the skeletal muscle such as the pennate insertion on the aponeuroses and the pennation angle. DTI has the potential to be introduced in biomechanical research on skeletal muscle function.

On ultrasound, the evaluation of the skeletal muscle should be made with small-sized probes working in general at high frequencies (frequency band 7–15 MHz). If a large and deep muscle should be evaluated, for example, at the level of the thigh it should be better to use low-frequency probes with high penetration of the US-beam (frequency band 3.5–10 MHz). During the US-machine setting, it is useful to set the focal zone in the appropriate position to improve image quality over the region examined. To depict the normal anatomy of a large wide muscle, such as the rectus femoris and the sartorius, it is possible to use an extended field-of-view. The advantage of US over MRI is that the muscle may be studied "in vivo" in a relaxed status and during contraction. Ultrasound may be used to perform quantitative evaluation of the skeletal muscle. The usefulness of these measurements is reinforced by the observation that muscle size correlates with muscle force (during isometric contractions). Muscular echogenicity may be calculated with US as well as other parameters such as muscle thickness and pennation angle. It has been recently demonstrated that measurement of vastus medialis muscle thickness with US is a reliable, bedside method for monitoring the extent of sarcopenia (Strasser et al 2013). Moreover, it has been demonstrated that US is a highly reproducible method to quantify muscle thicknesses of all muscles both in young people and old sarcopenic individuals. It has been proposed that US muscle thickness measurement, especially of the vastus intermedius muscle and the vastus medialis muscle, could be an accurate and bedside tool for diagnosis and course of sarcopenia in neuromuscular unimpaired patients (Strasser et al. 2013). Muscular hypotrophy or hypertrophy can be easily assessed on short-axis US planes (US probe perpendicular to the main axes of the muscle): during these measurements, care should be taken, however, to avoid any pressure with the probe that can reduce the muscular thickness. It is useful to use the contralateral muscle to increase accuracy. Till date there are many papers suggesting that US can be considered a valuable alternative to MR imaging for cross-sectional area measurements. From the ultrasonographic point of view the echotexture of normal skeletal muscles consists of a relatively hypoechoic background reflecting muscle fascicles and clearly demarcated linear hyperechoic lines related to fibroadipose septa (perimysium). The intramuscular tendons and aponeuroses appear as hyperechoic bands, which are usually better assessed on short-axis images of the muscle. From a histologic point of view, the relative amount of hypoechoic and hyperechoic components of muscle reflects the proportion between connective tissue and muscle fascicles (Fig. 6). This ratio may be variable and depends on the muscle evaluated and it also differs among muscles. On short-axis scans, the muscle echotexture consists of small dot-like reflectors representing fibroadipose septa. As for tendons, muscular fascicles and fibroadipose septa are responsible for muscular anisotropy (Fig. 7). This artifact is clearly visible when a muscle is examined on transverse planes. This artifact depends on the angle between the US beam and the muscle. An angle that deviates from the perpendicular causes the muscle to appear artificially hypoechoic. The arrangement of muscle fibers and fibroadipose septa is important to differentiate semipennate, unipennate, bipennate, or multipennate muscles. On US it is possible to demonstrate intramuscular vessels. Depiction of intramuscular vessels is important in several clinical situations. For example, color Doppler US resulted accurate for the pre-surgical assessment of deep inferior epigastric perforator procedure for breast reconstruction and US was able to assess the intramuscular course of the perforator vessel and in identifying superficial venous communications (Cina et al. 2010). Moreover, color Doppler US was superior for measuring perforator artery calibers, and CT angiography was superior for estimating the intramuscular course of the perforator vessel and for identifying superficial venous communications (Cina et al. 2010). US has the big advantage to reduce the role of CT and thus the exposure of patients with radiation only to selected cases (Cina et al. 2010). On US the outer muscle fascia (epimysium) normally appears as a well-delineated echogenic envelope circumscribing the hypoechoic muscular tissue. In complex muscles, an individual hyperechoic fascial sheath surrounds each muscle belly, thus helping the examiner to recognize the different heads. Sometimes, it is possible to demonstrate focal interruptions of the muscle fascia found at the points where nerves, veins, and arteries (perforating vessels) enter the muscles.

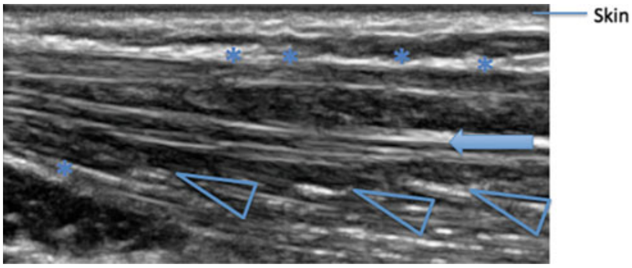

Fig. 6 Skeletal muscle anatomy. Individual muscle fibers are arranged in fascicles. Loose connective tissue strands envelope the fibers (endomysium), the fascicles (perimysium), and the whole muscle (epimysium). On the long-axis 17-5 MHz US image of flexor tendons of the forearm there are multiple hyperechoic lines (*arrowheads*) consistent with perimysium. Some lines converge to form the aponeurosis (*arrow*). The epimysium (*asterisks*) demarcates the outer boundaries of the muscle

Conventional MRI uses gyration of protons (^{1}H) basically of water and carbohydrate compounds for image acquisition. At ^{1}H MRI muscular tissue has a different appearance according to the specific sequences adopted. In general the muscle is isointense on T1-weighted sequences, whereas tendons and aponeuroses are hypointense on both T1-weighted and T2-weighted sequences due to the low water content and high collagen content (Fig. 8). Fat has a shorter T1 relaxation time relative to muscle and pure water, so that fat appears bright on T1-weighted images and thus the T1-weighted sequence is best for imaging fatty replacement of muscle seen in chronic disease. On T2-weighted images muscle and tendons have a short T2 relaxation time, while water and therefore also edematous or inflamed tissues have a long relaxation time and T2-weighted sequences, especially with additional fat suppression techniques, which are better for detecting acute or inflammatory changes of muscle that may be related to edema or increased blood flow. Also, the MRI signal on T1- and T2-weighted images is susceptible to blood degradation products and, of note, the appearance of muscular hematomas on MRI is primarily dependent on the age of the hematoma and on the imaging sequence or parameters (Fig. 9). Therefore, muscle trauma sequelae like muscular hematomas after blunt trauma can nicely be verified and monitored using MRI. Detailed descriptions of muscular MRI techniques (see "Whole-Body MRI for Evaluation of the Entire Muscular System", "Skeletal Muscle MR Imaging Beyond Protons: With a Focus on Sodium MRI in Musculoskeletal Applications", "MR Spectroscopy and Spectroscopic Imaging for Evaluation of Skeletal Muscle Metabolism: Basics and Applications in Metabolic Diseases") and MRI applications (see "MRI of Muscle

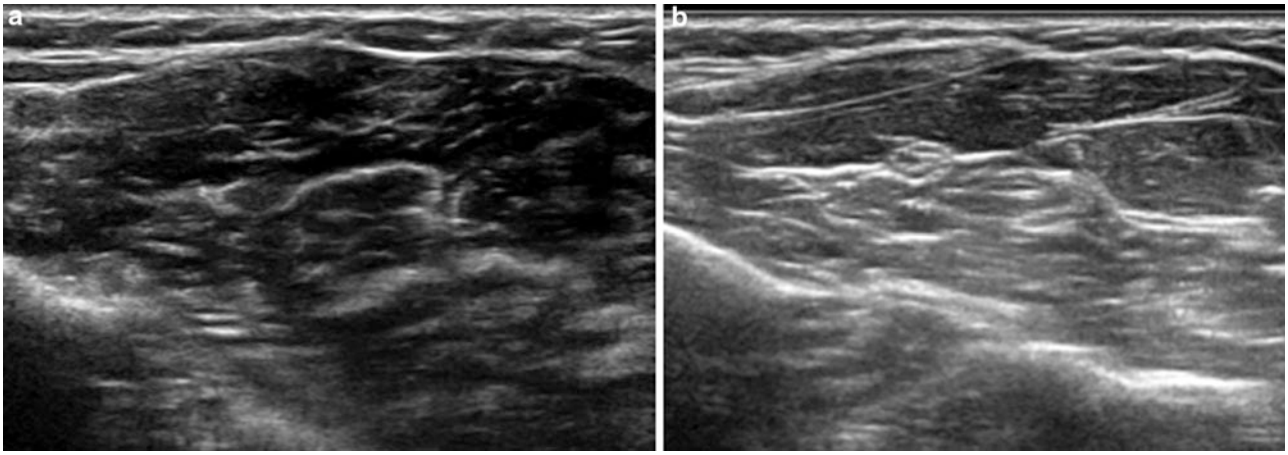

Fig. 7 Muscle anisotropy. Short-axis 17–5 MHz US images of the flexor muscles of the forearm examined with an almost perpendicular angle (**a**) between the transducer and the muscle fibers and an oblique angle (**b**). In (**b**), the muscle appears diffusely hyperechoic owing to the highest specular reflectivity from the perimysium interfaces. Artificial hypoechoic patterns should be differentiated from mild strains

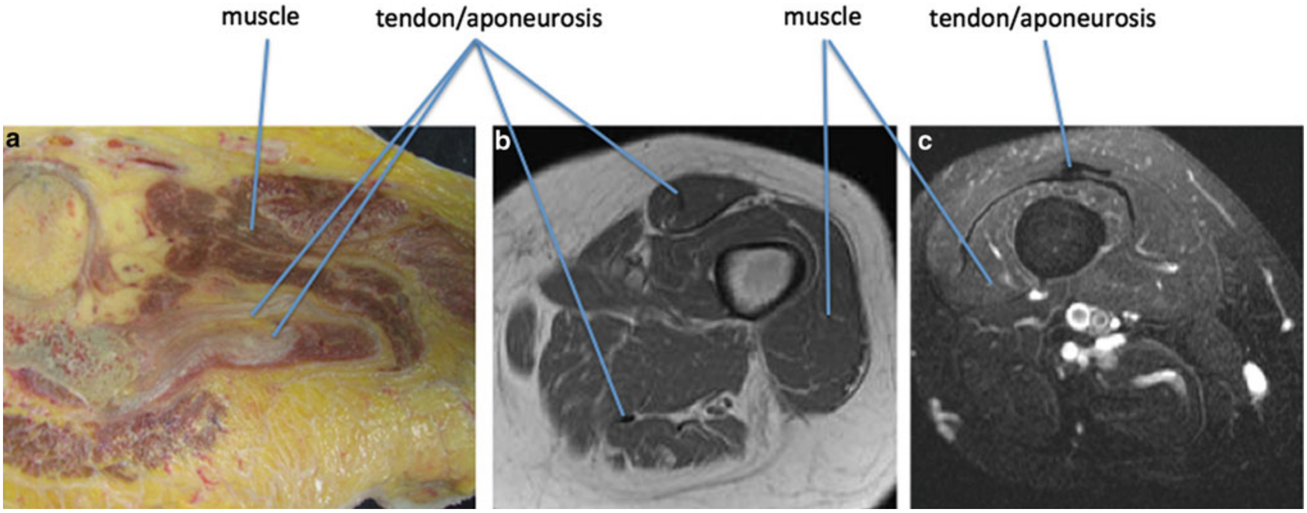

Fig. 8 Gross anatomy (**a**), transverse T1-weighted fast spin-echo (**b**) and T2-weighted fast spin echo (**c**) with fat saturation of the human thigh showing the appearance of muscle, tendons, and aponeuroses

Injuries", "MRI in Muscle Dystrophies and Primary Myopathies", "MRI in Inflammatory Myopathies and Autoimmune-Mediated Myositis", "MRI in Muscle Channelopathies", "MRI in Muscle Tumors and Tumors of Fasciae and Tendon Sheaths") are reported in the second and third parts of this book.

10 Anatomical Variants

Muscular anatomical variants are more common than normally thought. Muscular anatomical variants include not only supernumerary or accessory muscles, but also absence, deviation from a normal course, and an anomalous origin or insertion (Sookur et al. 2008).

Among these variants, the absences of a muscle, a supernumerary muscle, or a deviation from the normal course (anomalous origin or insertion) are the most frequent abnormalities amenable of diagnostic imaging evaluation. Accessory muscles are distinct muscles that are generally not present in the population and may be encountered in adjunct to the normal muscles generally described in anatomical textbooks.

The first report dealing with accessory muscles was based on cadaveric dissection or on surgical reports. With the increased use of medical imaging, both US and MRI are

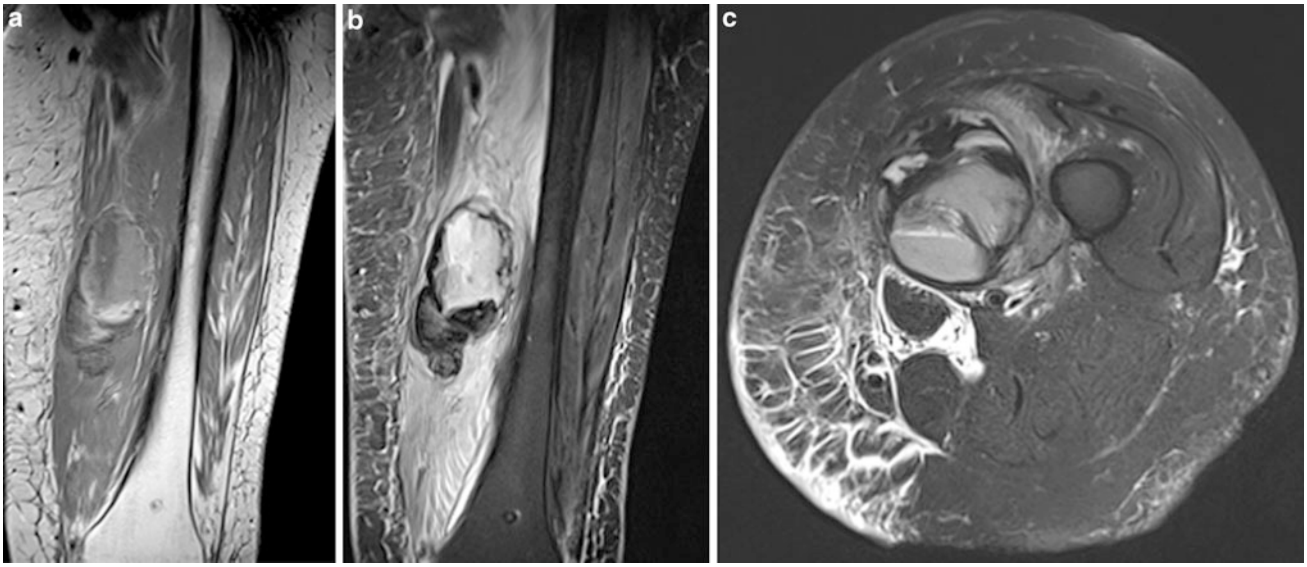

Fig. 9 78-year old-woman under anticoagulatory therapy with phenprocoumon and presentation with sudden swelling and pain of left thigh. Coronal STIR sequence (**a**), coronal T1-weighted (**b**), and axial fat-suppressed T2-weighted 3 Tesla MR images of the left thigh demonstrate large, subacute, muscular hematoma of the vastus medialis muscle (images courtesy of Prof. Dr. M.-A. Weber, Heidelberg)

Table 1 Accessory muscles or anatomical variants amenable of imaging evaluation at the level of the six major joints

	First choice	Second choice	Accessory muscles or variants to be detected	Notes
Shoulder	MRI	US/CT	Additional heads of the biceps brachii (three- or four-headed variant)	MRI is the first choice due to its panoramic characteristics. CT has low contrast resolution
			Axillopectoral muscle	
			Chondroepitrochlearis (Chondrohumeralis)	
Elbow	US	MRI	Anconeus epitrochlearis	The anconeus epitrochlearis may be associated with cubital tunnel syndrome
			Accessory brachialis	
Wrist and Hand	US	MRI	Accessory abductor digiti minimi	US is usually used as first choice technique
			Anomalous flexor digitorum superficialis of the index finger	
			Palmaris profundus	
			Extensor digitorum brevis manus	
Knee	MRI	US	Accessory slips of the medial and lateral gastrocnemius muscle	MRI may be better due to the deep location of the structures to be evaluated
Foot/ Ankle	US	MRI	Accessory peroneal muscles (lateral)	US is generally used as first choice technique
			Flexor digitorum accessorius longus (medial)	
			Peroneocalcaneus internus	
			Accessory soleus	
			Tibiocalcaneus internus	

able to detect anatomical variants related to the accessory musculature, thus helping to differentiate normal variants from pathological findings such as a soft tissue mass. From the clinical point of view, accessory muscles are often asymptomatic and non-visible at clinical examination. However, they may be responsible for clinical symptoms in case of hypertrophy or associated lesions. The mass effect produced by the additional muscle belly, possibly mimicking a soft tissue tumor, a compression or displacement of adjacent structures, such as nerves, vessels, and tendons near osteofibrous tunnels and exercise-related pain as a probable result of localized compartment syndrome or inadequate blood supply received by the muscle are the three main causes of complaints among patients having accessory muscles (Martinoli et al. 2010).

Accessory muscles and anatomical variants are commonly overlooked at imaging evaluation, but the appropriate use of US and MRI may be useful to detect these abnormalities.

In Table 1 is reported the most frequent anatomical variants amenable for imaging evaluation and for each of them is reported the best imaging technique that should be used for detection and appropriate diagnosis.

At the level of the shoulder the axillopectoral muscle crosses the axilla as a triangle arising from the external border of the latissimus dorsi; the chondroepitrochlearis or chondrohumeralis muscle is an extremely rare muscle variant that arises from either the ventral edge of the pectoralis major muscle, the osteochondral junction of the fifth and sixth costal cartilages, or the aponeurosis of the external oblique muscle and inserts into the medial intermuscular septum or the medial epicondyle (Figs. 10 and 11) after crossing the axilla and the upper arm (Martinoli et al. 2010). Additional heads of the biceps brachii resulting in a three- or four-headed variant are extremely rare, and the data are limited to case reports. In a case report reporting a four-headed biceps (Vazquez et al. 2003), the first supernumerary was located between the lesser tuberosity and the coracobrachialis and brachialis muscles and joined the long head of the biceps at the level where the short head joined. The second supernumerary head originated from the humerus at the site of insertion of the coracobrachialis and joined the biceps tendon at the bicipital aponeurosis in the distal third of the arm.

At the level of the elbow the most commonly encountered accessory muscle is the anconeus epitrochlearis (Fig. 12). The anconeus epitrochlearis or accessory anconeus is a small accessory muscle of the posteromedial aspect of the elbow that extends from the medial epicondyle to the olecranon with an almost transverse course. Sometimes the anconeus epitrochlearis may substitute the cubital tunnel retinaculum (Osborne ligament).

At the wrist and hand there are four most relevant accessory muscles: the accessory abductor digiti minimi, the anomalous flexor digitorum superficialis of the index finger, the palmaris profundus, and the extensor digitorum brevis manus. These muscles are in close relationship with non-muscular structures belonging to osteofibrous tunnels. These muscles may cause symptoms of ulnar neuropathy (Guyon tunnel syndrome), or median neuropathy (carpal tunnel syndrome). The extensor digitorum brevis manus and the anomalous flexor digitorum superficialis of the index finger may mimic a palpable soft tissue mass (Martinoli et al. 2010).

At the knee, variations of the origin of the medial and lateral heads of the gastrocnemius consist of anomalous origins and accessory slips. The medial head of the

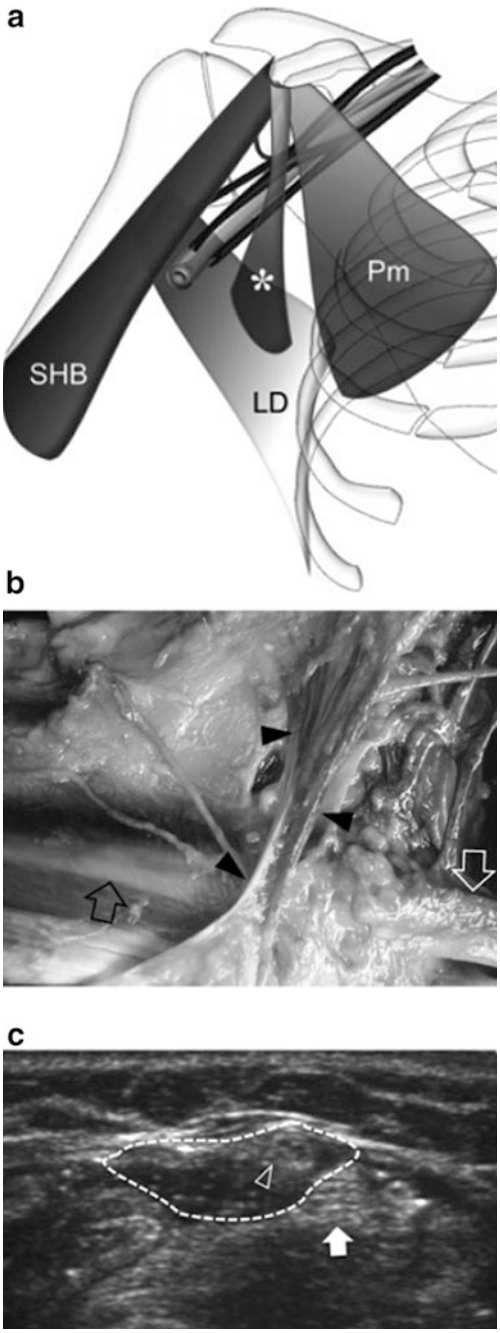

Fig. 10 Axillary arch muscle. **a** Schematic drawing of the axilla illustrates an axillary arch muscle (*asterisk*) originating from the latissimus dorsi (LD) and inserting into the coracoid after bridging the axillary artery and the nerve cords of the brachial plexus. The short head of the biceps (SHB) and the pectoralis minor muscle (Pm) also arise from the coracoid. **b** Cadaveric image of the axilla shows the axillary arch muscle (*arrowheads*) as a slender myotendinous band crossing over the nerve cords and the axillary artery (*arrows*). **c** Transverse 10–5 MHz ultrasound image shows the axillary muscle (*dashed line*) in its cross section, adjacent to the median nerve (*arrow*). Note the intramuscular tendon (*void arrowhead*) of the accessory muscle. Printed with permission of Thieme from Martinoli et al. (2010)

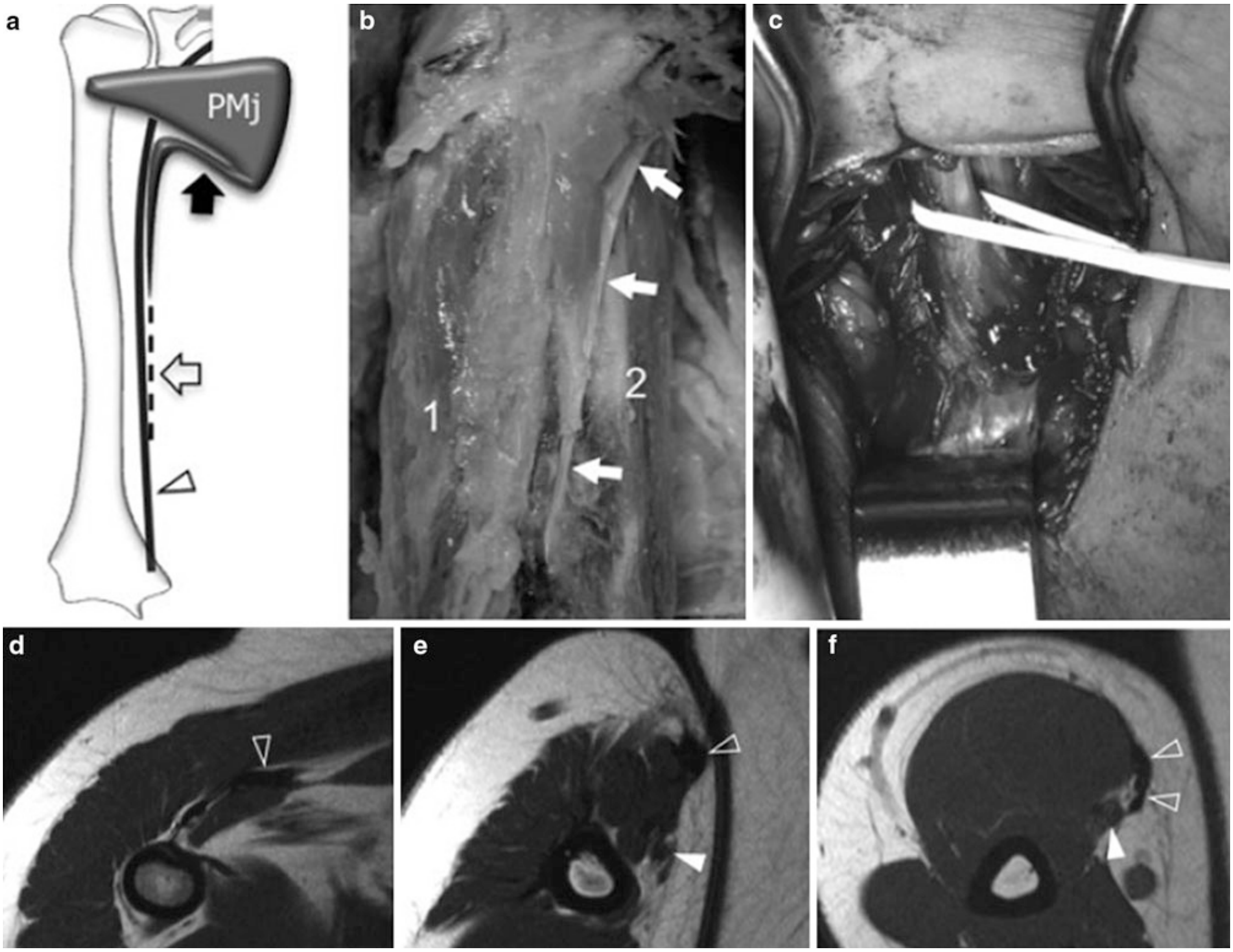

Fig. 11 Chondroepitrochlearis muscle. **a** Schematic drawing with **b** cadaveric and **c** surgical correlation illustrates the chondroepitrochlearis muscle (*black arrow*) arising from the lowest fibers of the pectoralis major (PMj) and descending the medial aspect of the arm with a slender tendon (*white arrow*), between the biceps (1) and the triceps (2). The chondroepitrochlearis tendon travels alongside the medial neurovascular bundle (*arrowhead*) of the arm. **d–f** Axial T1-weighted magnetic resonance imaging of the upper arm obtained from (**d**) cranial to (**f**) caudal demonstrate a hypointense cord (*void arrowheads*) descending the arm in close relationship with the neurovascular bundle (*white arrowheads*) reflecting the long tendon of a chondroepitrochlearis muscle. Printed with permission of Thieme from Martinoli et al. (2010)

gastrocnemius may have an aberrant origin, arising from the region of the intercondylar notch rather than the medial femoral condyle. The lateral head of the gastrocnemius may have an aberrant origin, arising more medially from the posterior femur but maintaining its position lateral to the popliteal artery. An accessory slip of the medial head of the gastrocnemius may arise from the intercondylar notch, passing between the popliteal artery and vein and inserting into the medial head of the muscle. An accessory slip of the lateral head of the gastrocnemius has also been described originating from the posterior cortex of the distal femur, medial to the lateral head. The slip courses anterolateral to the popliteal vessels, inserting into the lateral head of the gastrocnemius. From the clinical point of view, an anomalous relationship between the popliteal artery and the proximal gastrocnemius may be responsible to manifest clinically with popliteal artery entrapment syndrome (Sookur et al. 2008).

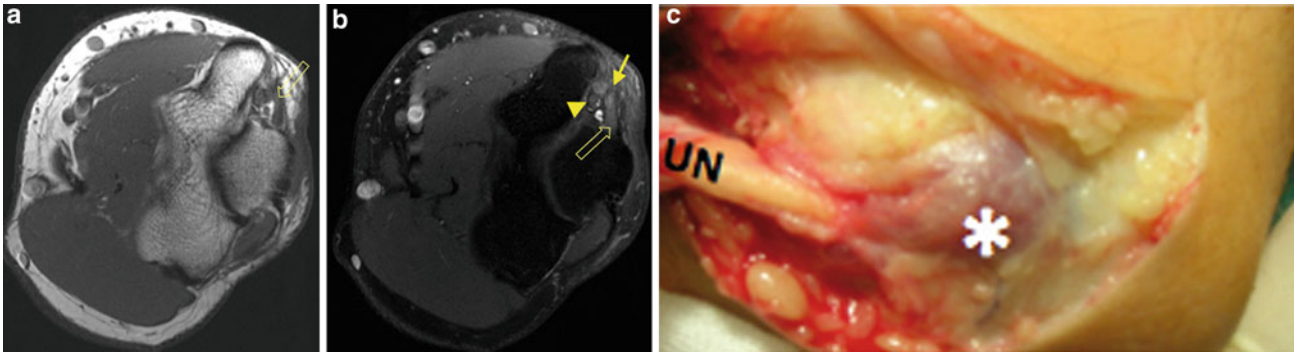

Fig. 12 38-year-old man with anconeus epitrochlearis muscle that has led to a cubital tunnel syndrome. The T1-weighted 3 Tesla MR images **a** show the accessory anconeus epitrochlearis muscle next to the cubital tunnel (*open arrows*). To cure the irritation of the ulnar nerve, the muscle has been split surgically (*closed arrow*). The fat-saturated contrast-enhanced T1-weighted MR image **b** demonstrates that the nerve exhibits no pathologic enhancement (arrowhead) and that the accessory muscle shows postoperative subtle enhancement. Furthermore, the intraneural T2 signal of the ulnar nerve was normal (image not shown). The anconeus epitrochlearis or accessory anconeus muscle is thought to represent an atavistic muscle that is usually found as a remnant in form of the epitrochleoanconeus ligament. It can be found intact in ~5 to ~35 % of cadavers **c** and in a recent MRI study this accessory muscle has been reported in about 25 % of patients (Husarik et al. 2009) (images courtesy of Dr. J. Kollmer, Heidelberg) *UN* ulnar nerve, *asterisk* anconeus epitrochlearis muscle. Part Figure c is printed with permission of Springer from Tagliafico et al. A Radiologically Guided Approach to Musculoskeletal Anatomy

Accessory muscles are fairly common about the ankle. They include the accessory peroneals (peroneus quartus and peroneus tertius), the accessory flexors (flexor digitorum accessorius longus, peroneocalcaneus internus), and the accessory soleus.

References

Armstrong RB (1996) Properties, distribution, and functions of mammalian skeletal muscle fibers. In: Cerretelli P, Whipp BJ (eds) Exercise bioenergetics and gas exchange. Elsevier/North-Holland Biomedical Press, Amsterdam, pp 137–146

Boron WF, Boulpaep EL (2009) Medical physiology: a cellular and molecular approach. Saunders/Elsevier, Philadelphia

Cina A, Salgarello M, Barone-Adesi L, Rinaldi P, Bonomo L (2010) Planning breast reconstruction with deep inferior epigastric artery perforating vessels: multidetector CT angiography versus color doppler US. Radiology 255(3):979–987

Exeter D, Connell DA (2010) Skeletal muscle: functional anatomy and pathophysiology. Semin Musculoskelet Radiol 14(2):97–105

Gray H. (2000) Anatomy of the human body. lea and febiger 1918, Philadelphia, Bartelby

Husarik DB, Saupe N, Pfirrmann CW, Jost B, Hodler J, Zanetti M (2009) Elbow nerves: MR findings in 60 asymptomatic subjects-normal anatomy, variants, and pitfalls. Radiology 252:148–156

Martinoli C, Perez MM, Padua L, Valle M, Capaccio E, Altafini L, Michaud J, Tagliafico A (2010) Muscle variants of the upper and lower limb (with anatomical correlation). Semin Musculoskelet Radiol 14:106–121. doi:10.1055/s-0030-1253155

Korthuis RJ (2011) Skeletal muscle circulation. Morgan and Claypool Life Sciences, San Rafael

Standring S (2005) Gray's anatomy: the anatomical basis of clinical practice, 39th edn. Elsevier, Edinburgh

Strasser EM, Draskovits T, Praschak M, Quittan M, Graf A (2013) Association between ultrasound measurements of muscle thickness, pennation angle, echogenicity and skeletal muscle strength in the elderly. Age (Dordr) Mar 2

Sookur PA, Naraghi AM, Bleakney RR, Jalan R, Chan O, White LM (2008) Accessory muscles: anatomy, symptoms, and radiologic evaluation. Radiographics 28:481–499. doi:10.1148/rg.282075064

Strasser EM, Draskovits T, Praschak M, Quittan M, Graf A (2013) Association between ultrasound measurements of muscle thickness, pennation angle, echogenicity and skeletal muscle strength in the elderly. Age (Dordr) Mar 2

Valero MC, Huntsman HD, Liu J, Zou K, Boppart MD (2012) Eccentric exercise facilitates mesenchymal stem cell appearance in skeletal muscle. PLoS ONE 7(1):e29760. doi:10.1371/journal.pone.0029760

Van Donkelaar CC, Kretzers LJ, Bovendeerd PH, Lataster LM, Nicolay K, Janssen JD et al (1999) Diffusion tensor imaging in biomechanical studies of skeletal muscle function. J Anat 194(1):79–88

Vazquez T, Rodriguez-Niedenfuhr M, Parkin I, Sanudo JR (2003) A rare case of a four-headed biceps brachii muscle with a double piercing by the musculocutaneous nerve. Surg Radiol Anat 25:462–464

Williams JG, Laudner KG, McLoda T (2013) The acute effects of two passive stretch maneuvers on pectoralis minor length and scapular kinematics among collegiate swimmers. Int J Sports Phys Ther 8(1):25–33

Imaging the Skeletal Muscle: When to Use MR imaging and When to Use Ultrasound

Carlo Martinoli, Sonia Airaldi, Bianca Bignotti, and Alberto Tagliafico

Contents

1 Key Points ... 41
2 Introduction ... 42
3 Muscle Strains and Tears ... 42
4 Delayed Onset Muscle Soreness ... 44
5 Myositis Ossificans ... 44
6 Muscle Hernia ... 45
7 Compartment Syndrome ... 46
8 Inflammatory and Infectious Disorders ... 47
9 Muscle Tumors ... 49
References ... 50

Abstract

Muscle imaging is inherently complex and presents unique morphologic challenges and continuing integration of dynamic, physiologic and functional capabilities as imaging technology progresses. This chapter is focused on the optimal use of US and MR imaging in the evaluation of a variety of muscle disorders, including muscle strains and tears, delayed onset muscle soreness, myositis ossificans, muscle hernia, acute and chronic exertional compartment syndromes, inflammatory and infectious diseases, tumors and non-neoplastic masses. The value of US and MR imaging in each muscle disorder will be weighted up to find strengths and weaknesses of the techniques and understand the appropriate place of modern imaging in the clinical management of patients with muscle disease.

1 Key Points

1. US and MR imaging have intrinsic advantages and disadvantages in muscle evaluation and need to be viewed as complementary rather than adversarial.
2. In the acute phase, US has nearly equal sensitivity to MR imaging to diagnose muscle strains and tears, except in the first few hours after the injury, when fresh hemorrhage and edema have similar echogenicity to normal muscle.
3. Dynamic US scanning during muscle contraction can be valuable to improve the conspicuity of muscle hernias and to assess the biomechanical dysfunction caused by posttraumatic scars.
4. In elite athletes, MR imaging plays a pivotal role in management of muscle injury, particularly when decisions regarding the time at which the patient can return to play are required.

C. Martinoli (✉) · S. Airaldi · B. Bignotti
Radiology Department – DISSAL, Università di Genova,
Via Pastore 1, 16132 Genoa, Italy
e-mail: carlo.martinoli@unige.it

A. Tagliafico
Department of Experimental Medicine – DIMES,
Università di Genova, Genoa, Italy

M.-A. Weber (ed.), *Magnetic Resonance Imaging of the Skeletal Musculature*, Medical Radiology. Diagnostic Imaging,
DOI: 10.1007/174_2013_925, © Springer-Verlag Berlin Heidelberg 2013

Published Online: 11 October 2013

5. MR imaging has definite advantages over US to diagnose compartment syndromes, inflammatory and infectious disorders due to its wider panoramicity and higher sensitivity to detect muscle edema and perfusional changes.
6. In muscle tumors, contrast-enhanced MR imaging is the unquestioned gold standard for diagnosis and staging. US plays a limited role in follow-up studies and for characterization of specific lesions (e.g., intramuscular lipoma, ganglion, myxoma, desmoids).

2 Introduction

Ultrasound (US) and magnetic resonance (MR) imaging are currently touted for assessment of muscle pathology. Considering the imaging literature, however, these techniques have followed parallel paths with insufficient comparison each other and lack of definite validation studies to draw undisputed guidelines on their optimal use in muscle imaging. Intrinsically, each modality has "pros & cons" that are not only related to accuracy concerns but also involve availability problems, costs, operator- and equipment-dependency. High-end technology, scanning optimization, firm grasp of anatomy and in-depth understanding of pathologic processes are essential prerequisites to rationalize the use of US and MR imaging in this field depending on clinical needs and environmental settings. In this chapter, an overview on the rational use of US and MR imaging in skeletal muscle evaluation will be presented with the aim to introduce the reader to the respective advantages and limitations of these two modalities.

3 Muscle Strains and Tears

Muscle injuries are common in recreational and sporting activities (Järvinen et al. 2005). Four major muscle groups of the lower extremity are affected in the large majority (>90 %) of cases, such as the hamstrings, adductors, quadriceps and gastrocnemius (Ekstrand et al. 2011). The accuracy of information provided by US and MR imaging varies with time depending on the stages of blood products and amount of muscle fibers disruption as well as on the healing process (Koh and McNally 2007) (Table 1). In Grade-1 injuries (strain), muscle injuries may look normal or show ill-defined hyperechoic appearance on US as a result of interfascial hemorrhage (Lee and Healy 2004; Blankenbaker and Tuite 2010). At this stage, this technique may not be as sensitive and reliable as MR imaging to identify the abnormality because changes are often subtle and possibly confused with muscle anisotropy (Allen and Wilson 2007; Koh and McNally 2007) (Fig. 1). On the contrary, MR imaging is very accurate to detect even minimal strains in the acute stage using fluid-sensitive sequences, by showing a feathery edema-like pattern along the affected myotendinous junction (Kneeland 1997; Blankenbaker and Tuite 2010). In Grade-2 injuries (partial tear), US demonstrates a definite discontinuity of muscle fibers with surrounding hypoechoic hematoma and loss of perimysium pattern close to the injured myotendinous junction (El-Koury et al. 1996; Koh and McNally 2007; Blankenbaker and Tuite 2010). Edema and hemorrhage at the site of injury are also readily recognized on MR imaging using fluid-sensitive sequences but this modality is less accurate to distinguish Grade-2 from Grade-1 strains due to a similar hyperintense appearance (Lee and Healy 2004; Blankenbaker and Tuite 2010). Basically, muscle tear details are better visualized on US given a better contrast resolution in the acute phases of trauma. Problems may be encountered with this technique if the injury is deep-seated, while scanning very thick thighs and if the hemorrhage filling the gap has echogenicity similar to that of muscle or if it mixes with the normal echotexture of fibro-fatty strands. In Grade-3 injuries (complete tear), US and MR imaging depict complete discontinuity of muscle fibers (Lee and Healy 2004). A large hematoma surrounding the retracted muscle end (clapper-in-bell sign) may make the diagnosis more obvious (Campbell and Wood 2002). In case of extensive edema and hemorrhage, US and MR imaging may have difficulties to distinguish partial from complete tears in absence of muscle retraction. Dynamic US scanning during active muscle contraction and passive motion to check if the gap widens may help to confirm the diagnosis of a complete tear and decide operative management.

Table 1 Comparison of US and MR imaging performance in muscle strain injuries

	Ultrasound	MR imaging
Strain—early acute phase (<6 h)	+	+++
Strain—late acute phase (>24 h)	++	+++
Muscle scar detection	++	+
Recovery time prediction	+	++
Delayed onset muscle soreness	+	++

In the sporting setting, selection of the most appropriate imaging modality may be greatly influenced by accuracy concerns, workflow and costs (please see also "MRI of Muscle Injuries"). If US is performed sideline at the sporting event within the first few hours after the injury using portable machines, the risk of missing muscle tears should be taken into account because fresh hemorrhage (within 1-day after trauma) looks echogenic and may be quite similar to normal muscle. This problem may be compounded by two factors: (i) the image quality of portable US equipments may be suboptimal at the sideline of

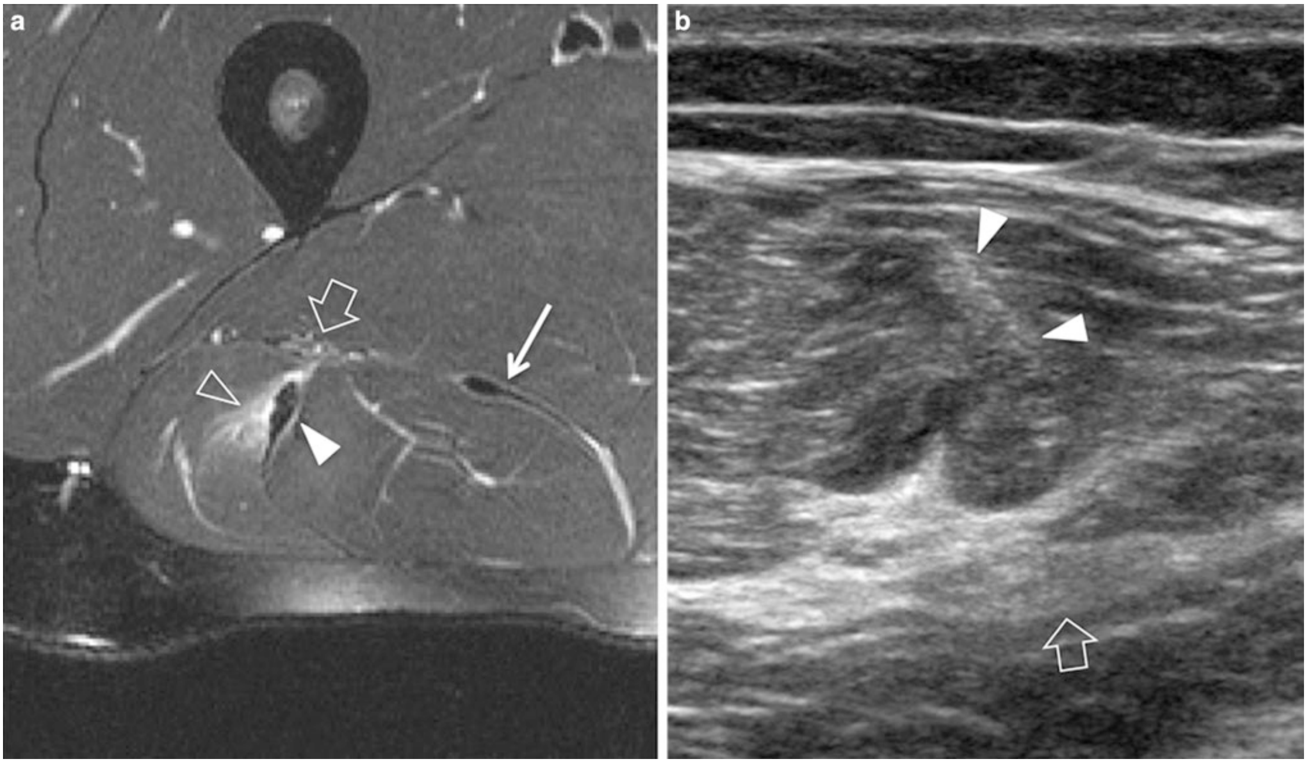

Fig. 1 Acute Grade-1 muscle injury. **a** Axial fat-suppressed T2-weighted MR image of the proximal thigh shows disruption of muscle fibers (*void arrowhead*) as they arise from the conjoined intermuscular tendon (*white arrowhead*) of the biceps femoris and semitendinosus. Note the sciatic nerve (*large arrow*) and the aponeurosis of the semimembranosus (*narrow arrow*). **b** Corresponding transverse 12-5 MHz US image reveals the conjoined aponeurosis as a sagittal hyperechoic band (*white arrowheads*) located superficial to the sciatic nerve (*arrow*). The injury in the surrounding muscle fibers is not visualized due to the relatively poor contrast of US

the sporting event to disclose minimal echotextural changes or does not have enough penetration to recognize deep-seated injuries; (ii) the examiner in charge of the event and the team is more likely to have learnt US as an adjunct to clinical work and to be less skilled to recognize the injury in a difficult operating setting (Allen and Wilson 2007). In the few hours after trauma, signs of a significant injury may be, in fact, subtle placing great demand on machine quality and operator experience. On the other hand, MR imaging is more reliable and easy to perform, but there may be problems of access and the cost may not be sustained by minor sports clubs systematically. Given some reservations, a wised use of US with selection of an appropriate timing of examination later than 1 day from trauma, when the hematoma starts to liquefy and collect becoming increasingly hypoechoic and conspicuous, might reduce the number of MR imaging examinations (Allen and Wilson 2007). This seems particularly true in the instance of mild trauma and outside the context of the highest professional levels.

When trauma occur in a professional sporting setting, the coaching staff of the club typically faces pressure to ensure a quick return of the athlete to play in order to avoid too many lost games, but a premature return to competition in an incompletely assessed and rehabilitated athlete has a high risk of reinjury and may result in a longer time removed from activity (Koulouris et al. 2007). Under these circumstances, US and MR imaging are extensively used, sometimes redundantly and in combination, to better prognosticate lay-off, healing time, mid-term outcome, as well as to guide rehabilitation and assess risk of late complication such as posttraumatic fibrosis, herniation and ossification (Connell et al. 2004; Gibbs et al. 2004; Schneider-Kolsky et al. 2006; Koulouris et al. 2007; Slavotinek 2010). Outside the high-performance context, muscle injuries often occur in the general population engaged in amateur athletic and non-athletic trivial activities. In these cases, imaging is basically directed to focus on more essential information, such as confirming the injury, defining its location and severity without the need to speculate on the exact time of return to play (Peetrons 2002). The need for serial follow-up examinations is also less. Given these considerations, one can imagine that the choice of the most appropriate imaging modality to perform is not only based on accuracy concerns but it may change depending on non-clinical factors such as level of the team, league requirements and budget (Allen and Wilson 2007). In the hamstrings, the percentage cross-sectional area (or volume) of injured muscle has been found to be a promising parameter

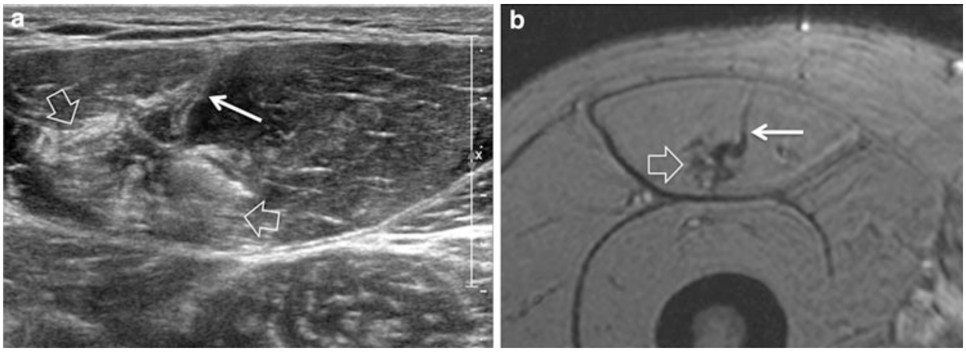

Fig. 2 Posttraumatic fibrous scar. **a** Transverse 12-5 MHz US image of the rectus femoris muscle with **b** correlative GRE T1-weighted MR imaging reveals an irregular hyperechoic image (*large arrows*) around the deep end of the central aponeurosis (*narrow arrow*) related to intramuscular fibrous scar. This finding appears more conspicuous on US

to predict outcome, somewhat reflecting the proportion of myofibrils that have been disrupted at the level of measurement. An association between longer recovery time (>6 weeks) and involved muscle cross-sectional area >55 % has also been found (Slavotinek et al. 2002; Slavotinek 2010; Ekstrand et al. 2012). However, the strongest correlation with prognosis is given by the craniocaudal extension of muscle abnormality, as an estimate of the number of muscle units separated from the aponeurosis at the time of injury (Connell et al. 2004). Despite noticeably improvement in US technology with introduction and refinement of 3D systems and wide-FOV algorithms, size parameters are measured more simply and reproducibly on MR imaging rather than on US. In addition, the extent of the injury appears consistently smaller on US than on MR imaging, both in longitudinal and cross-sectional views, due to a lower sensitivity of US to depict edematous changes (Connell et al. 2004). Similarly, abnormalities tend to resolve sooner on US than on MR imaging during the healing process, thus making US less accurate in predicting the exact time to return to full competition.

US seems to have some advantages over MR imaging to depict posttraumatic scars (Fig. 2). They typically appear as a linear or stellate hyperechoic areas attached to the affected aponeurosis or the epimysium and cause distortion of the surrounding pennate pattern (Koh and McNally 2007). Local abnormal contraction of the muscle fibers can be revealed around the scar. From the biomechanical point of view, the local amount and severity of architectural distortion in a scarred muscle can be nicely estimated with US due to its dynamic capability. Scar conspicuity is also greater with US (Allen and Wilson 2007). On MR imaging, fresh scar may be possibly confused with an acute tear/retear due to a high signal on fluid-sensitive sequences, whereas old scars may be missed or underestimated in their extension as they are associated with low signal intensity in all sequences. Differently, a fresh retear on an old scar is more conspicuous on MR imaging due to its higher sensitivity in edema detection.

4 Delayed Onset Muscle Soreness

Delayed onset muscle soreness is a peculiar form of self-limiting injury related to muscle strain that typically does not cause serious clinical consequences (Cleak and Eston 1992). This condition is secondary to repeated eccentric contractions and its severity is proportional to the duration and intensity of the exercise (Shellock et al. 1991). One-two days following exertion, local pain, soreness, and soft-tissue swelling appear with a peak at 2–3 days and reduce until gone over the course of one week. In the early phase, the appearance of the muscle is similar to Grade-1 strain injury with a feathery-like pattern seen on fluid-sensitive sequences related to interfascicular edema (Blankenbaker and Tuite 2010). Some perifascial fluid can also be found. Compared with Grade-1 strains, delayed onset muscle soreness affects more extensive patches of the muscle, irrespective of the location of aponeuroses (Fig. 3). In cases with severe pain, imaging studies may be required to rule out a strain. Due to its ability to reveal intramuscular edematous changes, MR imaging is intrinsically more sensitive than US to detect this condition (Dierking et al. 2000) (please see also "MRI of Muscle Injuries"). In the late phase, edematous changes may persist far longer than the resolution of symptoms (Shellock et al. 1991).

5 Myositis Ossificans

In early stages, myositis ossificans is a challenging diagnosis on both imaging and histopathology, because it exhibits a non-specific appearance at its onset and may often mimic an infiltrative malignant soft-tissue mass (please see also "MRI in Muscle Tumors and Tumors of Fasciae and Tendon Sheaths"). In approximately 40 % of cases, myositis ossificans cannot be linked to a specific injury and this may create difficulties in the differential diagnosis. Imaging is able to reveal the phasic changes of the process. In the initial precalcified stage, the

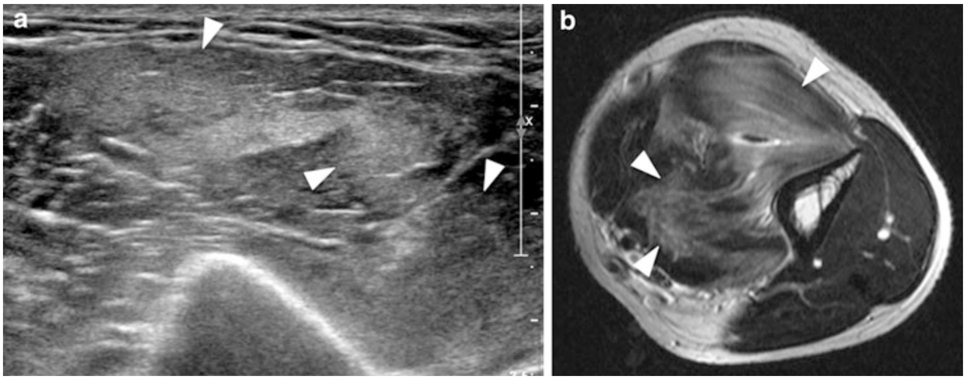

Fig. 3 Delayed onset muscle soreness. **a** Transverse 12-5 MHz US image of the brachialis muscle with **b** correlative Turbo-Spin-Echo T2-weighted MR imaging correlation demonstrates patches of muscle tissue (*arrowheads*) characterized by loss of fibrillar pattern and hyperechoic appearance. Diffuse feathery edema is shown on MR imaging

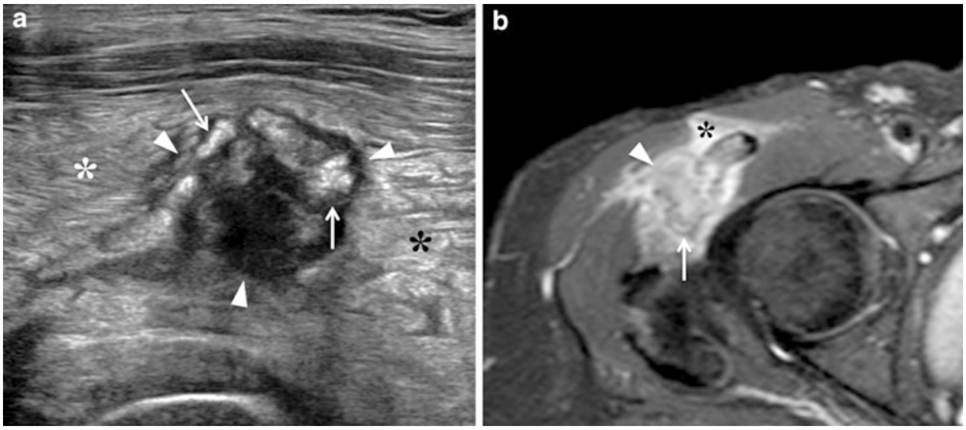

Fig. 4 Myositis ossificans, early stage. **a** Transverse 12-5 MHz US image over the anterolateral right hip with **b** correlative fat-suppressed Turbo-Spin-Echo T2-weighted MR image demonstrates a heterogeneous soft-tissue mass (*arrowheads*) with peripheral calcified deposits (*arrows*) surrounded by intense inflammatory changes (*asterisks*). The calcific component of the mass is better visualized with US

mass grows rapidly. Initial mineralization starts around the 2nd/3rd week. During this phase, US have been found to be superior to MR imaging and radiography to detect the initial formation of calcifications (Kramer et al. 1979; Allen and Wilson 2007) (Fig. 4). Ossification represents the main clue for the diagnosis and typically consists of highly echogenic foci with posterior acoustic shadowing located at the periphery of the lesion. The peripheral pattern of mineralization is pathognomonic for myositis ossificans given that calcification is mostly central in sarcomas as a result of necrosis. Because ossification looks hypointense in all pulse sequences, it is more difficult to detect on MR imaging at early stages. Radiography may also miss initial calcific deposits due to their blurred undefined appearance or inadequate view. Later on, myositis ossificans assumes a heterogeneous appearance with more consistent calcified shell. The mass may exhibit a hypervascular pattern both at the periphery and in the center. Central hyperemia may help distinguish this lesion from an intramuscular abscess (Koh and McNally 2007). As the maturation progresses, the lesion gradually takes the form of a bulky calcification, which is often longitudinally oriented and parallel to adjacent bone.

6 Muscle Hernia

US is an accurate means to identify muscle hernias and assess their size during dynamic scanning (Bianchi et al. 1995; Beggs 2003; Gokhale 2006). Muscle hernias most commonly occur in the lower limbs, involving the anterolateral compartment. On MR imaging, signs of muscle herniation may be subtle, often consisting of minimal fascial bulging without signal abnormalities (please see also " MRI of Muscle Injuries"). Attempts to increase the conspicuity of hernia and associated fascial defect can be made inviting the patient to repeat a known precipitating exercise prior to imaging and changing position (e.g., from plantarflexion to dorsiflexion) to check the muscle in a relaxed and contracted state (Mellado and Pérez del Palomar 1999). However, isometric contraction cannot be sustained for long time within the magnet without inducing motion artifacts. The diagnosis of muscle hernia with MR imaging remains, therefore, not straightforward, including many false negatives (Fig. 5). On the other hand, US provides a sensitive and elegant way to confirm the clinical diagnosis. US should be performed in the patient's position most adequate to reveal the lump. In general, examining the patient while

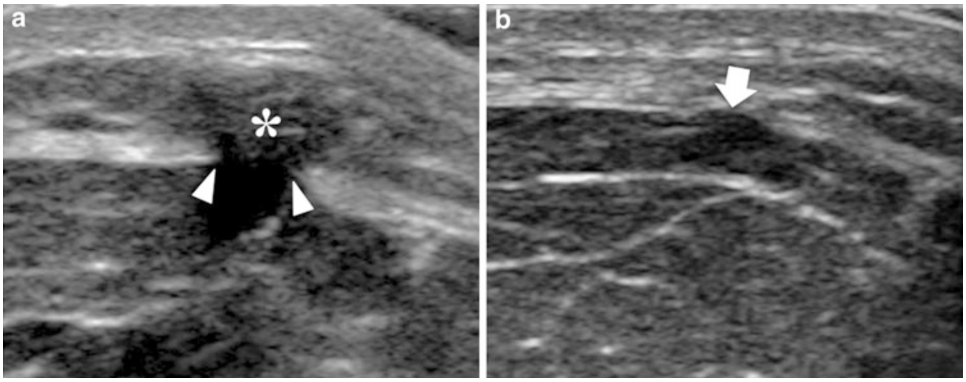

Fig. 5 Muscle hernia. **a, b** Transverse 12-5 MHz US images obtained with different degrees of probe pressure over a fascial defect (*arrowheads*) in the tibialis anterior shows a mushroom-like muscle bulge (*asterisk*) within the subcutaneous tissue. In **b** moderate pressure applied with the probe effaces the hernia (*arrow*)

squatting to increase the pressure within the anterolateral compartment of the leg, or immediately after strenuous exercise can help increase the visibility of the lump (Bates 2001). Initially, the probe is applied lightly on the skin to avoid reduction of the hernia and a false negative examination. US findings of muscle herniation include focal discontinuity of the fascia and a "mushroom-like" portion of muscle fibers outpouching focally through the defect. Because the hernia is reducible below the fascial defect in most cases, applying graded pressure with the probe over it may give real-time depiction of its intermittent extrusion and relocation (Bates 2001) (Fig. 6). It is not uncommon to demonstrate prominent vessels which traverse the fascia at the site of muscle herniation. Similar to vessels, the abnormal outgrowth of muscle tissue through fascial discontinuities can also determine entrapment of nerve bundles, such as the medial and intermediate dorsal cutaneous nerves. In these cases, patients complain about sensory disturbances over the dorsal aspect of the midfoot and forefoot.

7 Compartment Syndrome

The establishment of an acute compartment syndrome is related to an abrupt increase in pressure within a closed muscle- or fascial compartment. Edema following strenuous exercise or blunt injury may lead to increased interstitial pressure within the compartment due to the limited fascial compliance and impaired capillary perfusion up to cause damage to the neuromuscular function units, ischemia, and necrosis (Kirsten et al. 2003). Although blood flow at the capillary level is severely compromised, large arteries remain patent and there are no clinical signs of distal leg ischemia. In this setting, diagnosis and decompressive treatment must be established within a few hours to prevent irreversible damage of the affected muscles (Ulmer 2002). Nevertheless, clinical findings may be equivocal and the available options for the diagnosis (e.g., intracompartmental pressure measurement) are invasive and not always accessible and reliable, so a true gold standard is lacking (Wiemann et al. 2006). Imaging may be contributory but both US and MR imaging have inherent drawbacks in making the diagnosis. At US, initial compartment swelling and fascial bulging may not be clearly recognized. In addition, Doppler imaging is not informative because the ischemic process takes place at the capillary level (beyond the sensitivity threshold of US equipments), whereas large vessels in the compartment look normal even in cases of severe ischemia. Contrast-enhanced US is opening new perspectives as a means to check the level of microvasculature. Analysis of contrast uptake and distribution and intensity-time curve measurements can contribute to increase the

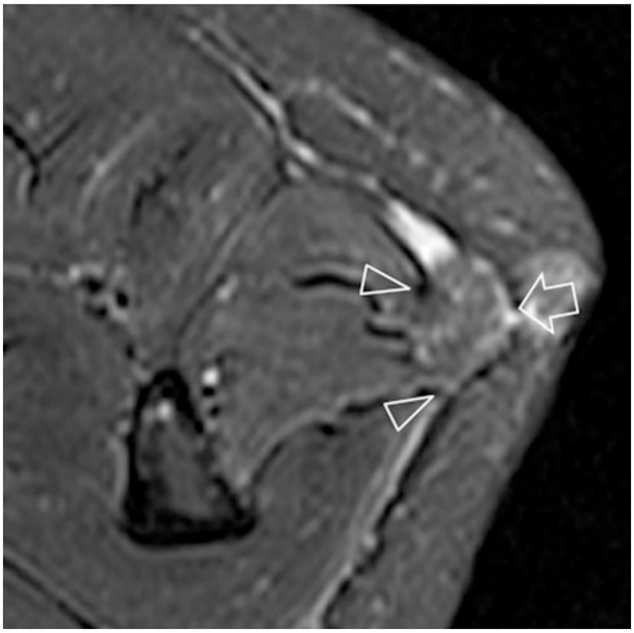

Fig. 6 Posttraumatic muscle hernia. Fat-suppressed Turbo-Spin-Echo T2-weighted MR image reveals herniation (*arrow*) of the peroneus longus muscle through a wide fascial defect (*arrowheads*). No signal intensity changes are demonstrated in the herniated and adjacent muscle

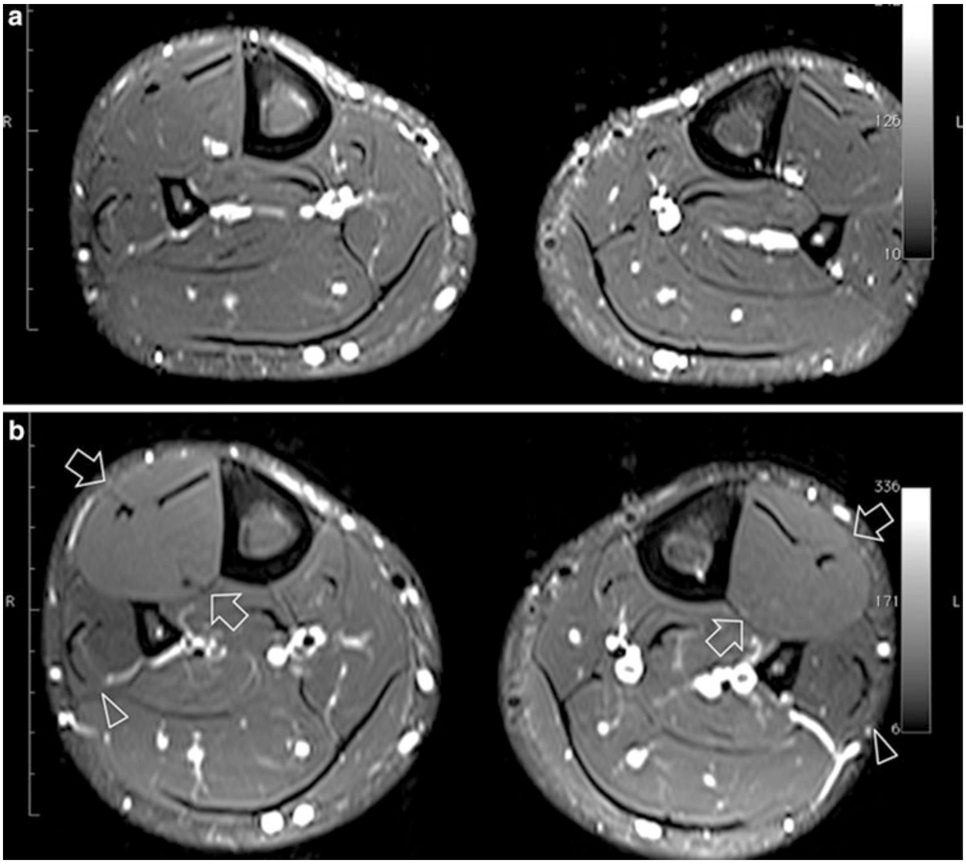

Fig. 7 Chronic exertional compartment syndrome in a 22-year-old male sportsman complaining of striking lateral leg pain when running. Transverse Turbo-Spin-Echo T2-weighted MR images of the middle third of the legs obtained **a** pre- and **b** 5 min post-exercise (5 min run). After exercise some swelling and increased T2-signal is observed in the anterior compartments of both legs, involving the tibialis anterior and extensor digitorum longus muscles (*arrows*) with loss of intramuscular vessel visualization. At the same time, a decreased signal intensity can be appreciated in the lateral compartment, involving the peroneus longus and brevis (*arrowheads*)

diagnostic confidence of US and confirm the need for immediate decompression. US detection of an abnormal echotextural appearance with blurred and less defined visualization of fibroadipose septa indicates progression of ischemia toward irreversible changes and a poor outcome. On MR imaging, signal intensity changes in the affected muscle compartment may be easily seen on T1- and T2-weighted sequences (please see also "MRI of Muscle Injuries"). Due to abnormal cell membrane permeability, the affected compartment strongly enhances after gadolinium administration (Rominger et al. 2004). Problems are related to confounding factors (e.g., atherosclerosis) that may produce misleading findings (Fleckenstein 1998; Kirsten et al. 2003). In addition, swelling and edema may not be easily distinguished from an acute compartment syndrome in a traumatic setting. Given these limitations, one should always take into account that compartment syndrome is an emergency situation and imaging must not delay surgery.

Chronic exertional compartment syndrome is a short-lived and fully reversible condition characterized by recurrent cramp-like pain triggered by physical exercise. This condition most commonly affects the lateral compartment of the leg and may worsen over years often resulting in significant limitation of sporting and daily activities. It is related to transient elevation of the intracompartmental pressure by expansion of tissue volumes related to accumulation of interstitial fluid and subsequent ischemic changes. US signs of chronic exertional compartment syndrome are subtle and include reversible compartment swelling and slight hypoechoic appearance of the affected muscles after exercise. However, most cases cannot be substantiated with this technique. MR imaging performed at rest and following exercise using fluid-sensitive sequences seems more promising in this field to disclose abnormal T2-signal related to increased permeability and blood flow associated with muscle recruitment during activity (Eskelin et al. 1998; Verleisdonk et al. 2001) (Fig. 7). Some techniques to simulate an exercise have been developed with resisted dorsiflexion directly performed in the magnet to reduce the delay from exercise to imaging and improve sensitivity (Litwiller et al. 2007).

8 Inflammatory and Infectious Disorders

Idiopathic inflammatory myopathies include a heterogeneous group of skeletal muscle disorders, including polymyositis, dermatomyositis and inclusion body myositis. Infection may also cause significant inflammatory changes in muscles. Imaging can assess the disease burden and can help monitor the status of disease activity which has

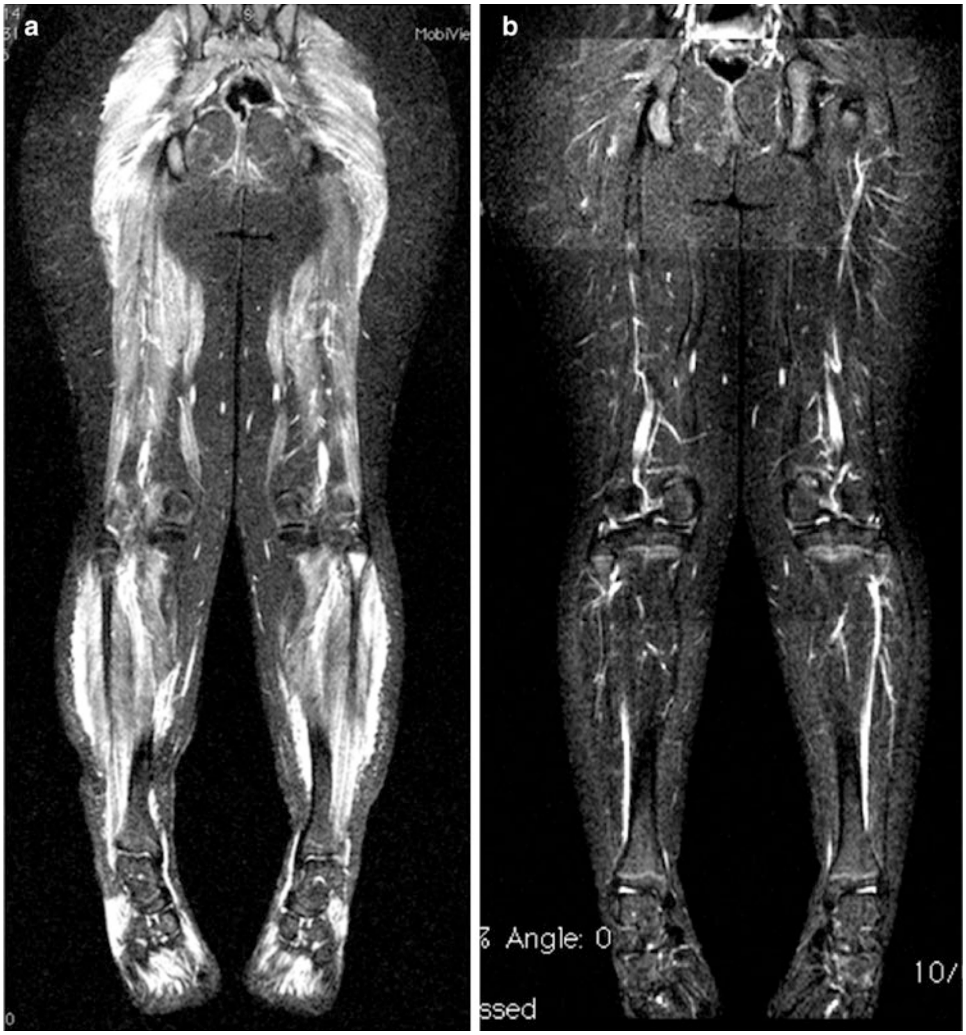

Fig. 8 Juvenile dermatomyositis in a 15-year-old female. Coronal STIR MR images of the lower limbs obtained with whole-body technique performed **a** at presentation and **b** after steroid and immunosuppressive treatment, 7 months later. Initially, the signal intensity was floridly increased in all muscle compartments of the pelvis and lower limbs as a result of diffuse edema and inflammatory changes. Complete regression of signal abnormalities was observed at follow-up after therapy

important implications on treatment decisions (Kuo and Carrino 2007) (please see also "MRI in Inflammatory Myopathies and Autoimmune-Mediated Myositis"). Autoimmune myositis is characterized by inflammatory infiltrates involving one or more skeletal muscles in one or multiple body areas. MR imaging has intrinsic advantages over US to image this class of inflammatory disorders due to its higher sensitivity to detect diffuse or focal muscle edema with fat-suppressed T2w or STIR sequences (Maillard et al. 2004; Tomasova Studynkova et al. 2007) (Fig. 8). In addition, the wider panoramicity offered by the whole-body technique enables MR imaging to detect scattered abnormalities throughout the body in a single examination (O'Connell et al. 2002) (please see also "Whole-Body MRI for Evaluation of the Entire Muscular System"). In chronic autoimmune myositis, loss in bulk and fatty infiltration of atrophic muscles can be seen on both US and MR imaging. This latter modality is, however, more accurate to grade the loss in muscle bulk and fatty replacement on T1-weighted sequences, to define those muscles with relatively preserved architecture, to detect edema-like signal in fluid-sensitive sequences as a sign of active inflammation, as well as to compare corresponding muscles side-by-side in a single scan. Newer MR imaging techniques are opening new interesting perspectives to investigate muscle pathophysiology in inflammatory myositis, including T2-mapping, BOLD imaging, DTI, and ^{31}P spectroscopy (Kuo and Carrino 2007). Although promising, the time and cost of these modalities have somewhat limited their widespread application until now. In septic myositis, MR imaging seems to be more useful than US in delineating the inflammatory process, focal abscesses, and associated extramuscular changes (e.g., fasciitis, overlying cellulitis), particularly when infection derives from systemic disease and multiple seeding is expected (Theodorou et al. 2007) (Fig. 9). In inflammatory myopathies, the use of fusion imaging with combined guidance of T2-weighted MR imaging (to locate diseased patches based on high intensity signal) and US (to execute the procedure) has potential to reduce the high incidence of false negatives or sampling errors.

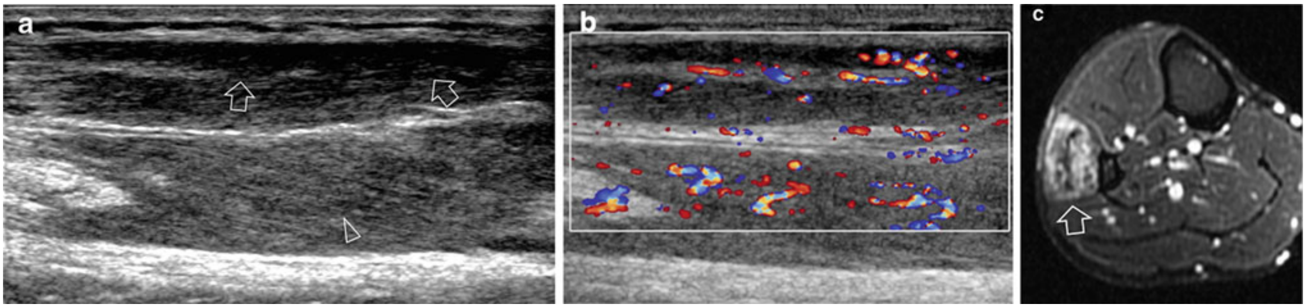

Fig. 9 Bacterial myositis from staphylococcus infection. **a** Longitudinal 12-5 MHz US image of the lateral leg reveals the peroneus longus muscle diffusely hypoechoic with loss of the fascicular echotexture (*arrowhead*). Pre-abscess changes with anechoic patches (*arrows*) are demonstrated in the superficial part of the muscle. **b** Marked intramuscular hyperemia is observed on color Doppler imaging. **c** Correlative fat-suppressed T2-weighted MR image shows edema in the affected muscle (*arrow*)

9 Muscle Tumors

The occurrence of a malignant tumor should be always kept in mind when evaluating a mass within a muscle, and even in a posttraumatic setting because a local trauma does not necessarily exclude the presence of a preexisting neoplasm (please see also "MRI in Muscle Tumors and Tumors of Fasciae and Tendon Sheaths"). With the exception of some muscle masses (i.e., vascular malformation, lipomatous tumors, intramuscular myxoma, intramuscular ganglion) showing specific US features, characterization of muscle tumors remains a major issue in the management. Although US represents a powerful and cost-effective first-line imaging modality for tumor identification, it is widely accepted that this technique plays a limited role in providing differentiation between benign and malignant types and staging soft-tissue neoplasms, being contrast-enhanced MR imaging the unquestioned gold standard in this field (Colleran et al. 2011). As technology progresses, however, US has proved to be a feasible means in specific clinical settings and especially to monitor the effects of radio- and chemotherapy in patients with high-grade sarcomas based on tumor size and blood flow measurements (Van der Woude and Vanderscheuren 1999; Adler et al. 1999). For this purpose, three-dimensional (3D) probes may help to measure tumor volumes more precisely and quantify the amount of intratumor color voxels and their intensity with greater accuracy than using 2D systems. Main limitations are related to deep-seated tumors or too large masses exceeding the field-of-view of the probe. Compared to gadolinium, ultrasonic contrast media do not pass through the interstitial spaces and can be assessed with a temporal resolution higher than theoretically possible on MR imaging. This could be an intrinsic advantage for quantification of intratumor vascular changes after therapy. Using intensity-time curves, calculation of the area under the curve has actually proved to be promising in this field but results need to be substantiated with more experience on large series to make US a reliable and effective alternative to MR imaging (Gay et al. 2012). Microbubbles have also proved to be helpful to guide the biopsy to the viable part of large heterogeneous masses, providing a reduced rate of inconclusive results related to sampling from necrotic areas (De Marchi et al. 2010; Loizides et al. 2011). With sonoelastography, hard tumors deform to a lower extent when compressed and show a low strain relative to the background, whereas soft masses tend to deform more and have a higher degree of strain (Kumm and Szabunio 2010). The ratio value increases as a function of the relative stiffness of the target lesion and tends to increase in fibrotic masses and, possibly, with malignant histotypes providing new insight into tumor characterization. Nevertheless, results are preliminary and still need validation.

Among the few histotypes presenting characteristic imaging features, US and MR imaging can complement each other for the diagnosis. Vascular malformations appear as complex ill-defined masses, characterized by a mixture of hypoanechoic (blood-filled spaces) and hyperechoic (reactive fat overgrowth) components at US (Derchi et al. 1989). Prominent vascular channels and phlebolits can be recognized (Murphey et al. 1995). In many cases, imaging is complex with US because the boundaries of the lesion are undefined, especially in large masses infiltrating more than one muscle and blending with intermuscular fatty planes. Compared to US, MR imaging offers a more complete and panoramic assessment of the mass and can better define its extension. Intramuscular lipomas include two main types: well-circumscribed and infiltrative. In the former, fatty tissue is clearly demarcated from the surrounding muscle. Because intramuscular lipomas are not compressible, US criteria for the diagnosis are essentially based on echotexture. Some lesions look nearly isoechoic with the muscle fibers. In these cases, careful scanning technique is needed not to miss even large tumors by confusing them with normal muscle tissue. In the infiltrative type, there is bland separation of muscle fibers by interspersed fat (Matsumoto

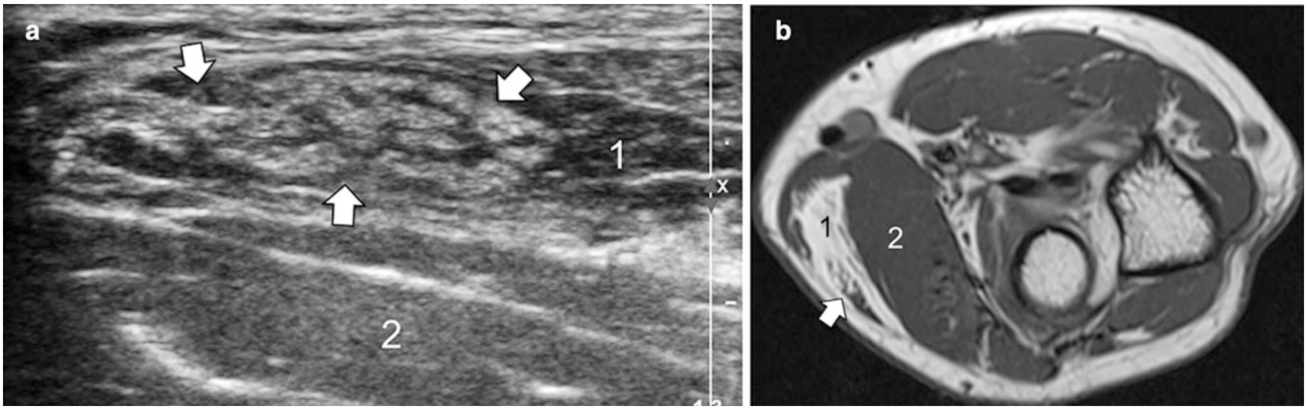

Fig. 10 Intramuscular lipoma—infiltrative type. **a** Transverse 12-5 MHz US image over a soft-tissue lump on the lateral aspect of the elbow with **b** axial T1-weighted MR imaging correlation demonstrates a heterogeneous mass within the brachioradialis muscle characterized by hypoechoic fatty background (*1*) and hyperechoic strands (*arrows*) related to intermingled muscle fibers with fat. The echotexture of lipomatous fat may be misleading as it looks (*1*) very similar to the appearance of normal muscle. Note the extensor carpi radialis longus (*2*) for comparison

et al. 1999). This produces a heterogeneous striated appearance with unclear features that may not recall a lipoma (Fig. 10). In infiltrative lipomas, T1-weighted MR imaging, possibly supplemented with fat-suppression, can provide a more confident identification of adipose tissue. Well-differentiated liposarcomas remain a challenging diagnosis with US. As a rule, detection of a lipomatous mass containing thick septa, nodular or globular foci, heterogeneous echotexture or blood flow signals needs further investigation with contrast-enhanced MR imaging and biopsy assessment (Bodner et al. 2002; Futani et al. 2003). Intramuscular myxomas exhibit "fat caps" at their poles and some perilesional edema (Bancroft et al. 2002; Murphey et al. 2002; Luna et al. 2005). MR imaging features of these masses is misleading, because they may resemble a cyst due to high intratumor water content. In these instances, US can complement MR imaging to rule out an intramuscular ganglion. Distinguishing myxomas from neurogenic tumors in an intramuscular location may be more challenging as these lesions share similar echotexture, intensity signal, and the presence of a fat rind. Desmoids (aggressive fibromatosis) are composed of arrays of fibroblasts and varying amount of dense collagen. After initial growth, they shrink with decrease in cellularity and volume of the extracellular spaces and assume the appearance of an irregularly shaped mass consisting of dense collagen tissue (Vandervenne et al. 1997). US and MR imaging may complement each other for the diagnosis. The mass may show variable appearance depending on cellularity, water content, and collagen and usually extends along the fascia and encases muscle fibers (Robbin et al. 2001; Dinauer et al. 2007). A "fascial tail" denoting linear tumor extension along the fascial plane and a "stag-horn" pattern corresponding to radiating strands of the mass interspersed through fat lobules are considered distinctive features on US and MR imaging (Robbin et al. 2001; Dinauer et al. 2007; Huang et al. 2009). In late stages, US can also demonstrate a faint fibrillar echotexture and posterior acoustic attenuation related to the bulk of dense collagen tissue and MR imaging a definite hypointensity in all pulse sequences (Bernathova et al. 2008; Dinauer et al. 2007).

References

Adler RS, Bell DS, Bamber JC, Moskovic E, Thomas JM (1999) Evaluation of soft-tissue masses using segment color Doppler velocity images; preliminary experience. Am J Roentgenol 172:781–788

Allen GM, Wilson DJ (2007) Ultrasound in sports medicine: a critical evaluation. Eur J Radiol 62:79–85

Bancroft LW, Kransdorf MJ, Menke DM, O'Connor MI, Foster WC (2002) Intramuscular myxoma: characteristic MR imaging features. Am J Roentgenol 178:1255–1259

Bates DY (2001) Dynamic ultrasound findings of bilateral anterior tibialis muscle herniation. Pediatr Radiol 31:753–755

Beggs I (2003) Sonography of muscle hernias. Am J Roentgenol 180:395–399

Bernathova M, Felfernig M, Rachbauer F, Barthi SD, Martinoli C, Zelger B, Bodner G (2008) Sonographic imaging of abdominal and extraabdominal desmoids. Ultraschall Med 29:515–519

Bianchi S, Abdelwahab IF, Mazzola CG et al (1995) Sonographic examination of muscle herniation. J Ultrasound Med 14:357–360

Blankenbaker DG, Tuite MJ (2010) Temporal changes of muscle injury. Semin Musculoskelet Radiol 14:176–193

Bodner G, Schocke MFH, Rachbauer F, Seppi K, Peer S, Fierlinger A, Sununu T, Jaschke WR (2002) Differentiation of malignant and benign musculoskeletal tumors: combined color and power Doppler US and spectral wave analysis. Radiology 223:410–416

Campbell RSD, Wood J (2002) Ultrasound of muscle. Imaging 14:229–240

Cleak MJ, Eston RG (1992) Delayed onset muscle soreness: mechanism and management. J Sports Sci 10:325–341

Colleran G, Madewell J, Foran P, Shelly M, O'Sullivan PJ (2011) Imaging of soft-tissue and osseous sarcomas of the extremities. Semin Ultrasound CT MR 32:442–455

Connell DA, Schneider-Kolsky ME, Hoving JL, Malara F, Buchbinder R, Koulouris G, Burke F, Bass C (2004) Longitudinal study comparing sonographic and MRI assessments of acute and healing hamstring injuries. Am J Roentgenol 183:975–984

De Marchi A, Brach del Prever EM, Linari A, Pozza S, Verga L, Albertini U, Forni M, Gino GC, Comandone A, Brach del Prever AM, Piana R, Faletti C (2010) Accuracy of core-needle biopsy after contrast-enhanced ultrasound in soft-tissue tumours. Eur Radiol 20:2740–2748

Derchi LE, Balconi G, de Flaviis L, Oliva A, Rosso F (1989) Sonographic appearance of hemangioma of skeletal muscle. J Ultrasound Med 8:263–267

Dierking JK, Bemben MG, Bemben DA, Anderson MA (2000) Validity of diagnostic ultrasound as a measure of delayed onset muscle soreness. J Orthop Sports Phys Ther 30:116–122

Dinauer PA, Brixey CJ, Moncur JT, Fanburg-Smith JC, Murphey MD (2007) Pathologic and MR imaging features of benign fibrous soft-tissue tumors in adults. RadioGraphics 27:173–187

Ekstrand J, Hägglund M, Waldén M (2011) Epidemiology of muscle injuries in professional football (soccer). Am J Sports Med 39:1226–1232

Ekstrand J, Healy JC, Walden M, Lee JC, English B, Hägglund M (2012) Hamstring muscle injuries in professional football: the correlation of MRI findings with return to play. Br J Sports Med 46:112–117

El-Khoury GY, Brandser EA, Kathol MH, Tearse DS, Callaghan JJ (1996) Imaging of muscle injuries. Skeletal Radiol 25:3–11

Eskelin MK, Lotjonen JM, Mantysaari MJ (1998) Chronic exertional compartment syndrome: MR imaging at 0.1 T compared with tissue pressure measurement. Radiology 206:333–337

Fleckenstein JL (1998) (Dys-)functional MR imaging of skeletal muscle: a cautionary role. Radiology 206:305–307

Futani H, Yamagiwa T, Yasojimat H, Natsuaki M, Stugaard M, Maruo S (2003) Distinction between well-differentiated liposarcoma and intramuscular lipoma by power Doppler ultrasonography. Anticancer Res 23:1713–1718

Gay F, Pierucci F, Zimmerman V, Lecocq-Teixeira S, Teixeira P, Baumann C, Blum A (2012) Contrast-enhanced ultrasonography of peripheral soft-tissue tumors: feasibility study and preliminary results. Diagn Interv Imaging 93:37–46

Gibbs NJ, Cross TM, Cameron M, Houang MT (2004) The accuracy of MRI in predicting recovery and recurrence of acute grade one hamstring muscle strains within the same season in Australian Rules football players. J Sci Med Sport 7:248–258

Gokhale S (2006) Three-dimensional sonography of muscle hernias. J Ultrasound Med 26:239–242

Huang CC, Ko SF, Yeh MC, Ng SH, Huang HY, Lee CC, Lee TY (2009) Aggressive fibromatosis of the chest wall: sonographic appearance of the fascial tail and staghorn patterns. J Ultrasound Med 28:393–396

Järvinen TAH, Järvinen TLN, Kääriäinen M, Kalimo H, Järvinen M (2005) Muscle injuries: biology and treatment. Am J Sports Med 33:745–764

Kirsten G, Elliott B, Johnstone AJ (2003) Diagnosing acute compartment syndrome. J Bone Joint Surg [Br] 85:625–632

Kneeland JB (1997) MR imaging of muscle and tendon injury. Eur J Radiol 25:199–208

Koh ES, McNally EG (2007) Ultrasound of skeletal muscle injury. Semin Musculoskelet Radiol 11:162–173

Koulouris G, Connell DA, Brukner P, Schneider-Kolsky M (2007) Magnetic resonance imaging parameters for assessing risk of recurrent hamstring injuries in elite athletes. Am J Sports Med 35:1500–1506

Kramer FL, Kurtz AB, Rubin C, Goldberg BB (1979) Ultrasound appearance of myositis ossificans. Skeletal Radiol 10:19–20

Kumm TR, Szabunio MM (2010) Elastography for the characterization of breast lesions: initial clinical experience. Cancer Control 17:156–161

Kuo GP, Carrino JA (2007) Skeletal muscle imaging and inflammatory myopathies. Curr Opin Rheumatol 19:530–535

Lee JC, Healy J (2004) Sonography of lower limb muscle injury. Am J Roentgenol 182:341–351

Litwiller DV, Amrami KK, Dahm DL, Smith J, Laskowski ER, Stuart MJ, Felmlee JP (2007) Chronic exertional compartment syndrome of the lower extremities: improved screening using a novel dual birdcage coil and in-scanner exercise protocol. Skeletal Radiol 36:1067–1075

Loizides A, Widmann G, Freuis T, Peer S, Gruber H (2011) Optimizing ultrasound-guided biopsy of musculoskeletal masses by application of an ultrasound contrast agent. Ultrashall Med 32:307–310

Luna A, Martinez S, Bossen E (2005) Magnetic resonance imaging of intramuscular myxoma with histological comparison and a review of the literature. Skeletal Radiol 34:19–28

Maillard SM, Jones R, Owens C, Pilkington C, Woo P, Wedderburn LR, Murray KJ (2004) Quantitative assessment of MRI T2 relaxation time of thigh muscles in juvenile dermatomyositis. Rheumatology 43:603–608

Matsumoto K, Hukuda S, Ishizawa M, Chano T, Okabe H (1999) MRI findings in intramuscular lipomas. Skeletal Radiol 28:145–152

Mellado JM, Pérez del Palomar L (1999) Muscle hernias of the lower leg: MRI findings. Skeletal Radiol 28:465–469

Murphey MD, Fairbairn KJ, Parman LM, Baxter KG, Parsa MB, Smith WS (1995) From the archives of the AFIP. Musculoskeletal angiomatous lesions: radiologic-pathologic correlation. RadioGraphics 15:893–917

Murphey MD, McRae GA, Fanburg-Smith JC, Temple HT, Levine AM, Aboulafia AJ (2002) Imaging of soft-tissue myxoma with emphasis on CT and MR and comparison of radiologic and pathologic findings. Radiology 225:215–224

O'Connell, MJ, Powell T, Brennan D, Lynch T, McCarthy CJ, Eustace SJ (2002) Whole-body MR imaging in the diagnosis of polymyositis. AJR Am J Roentgenol 179:967–971

Peetrons P (2002) Ultrasound of muscles. Eur Radiol 12:35–43

Robbin MR, Murphey MD, Temple HT, Kransdorf MJ, Choi JJ (2001) Imaging of musculoskeletal fibromatosis. RadioGraphics 21:585–600

Rominger MB, Lukosch CJ, Bachmann GF (2004) MR imaging of compartment syndrome of the lower leg: a case control study. Eur Radiol 14:1432–1439

Schneider-Kolsky ME, Hoving JL, Warren P, Connell DA (2006) A comparison between clinical assessment and magnetic resonance imaging of acute hamstring injuries. Am J Sports Med 34:1008–1015

Shellock FG, Fukunaga T, Mink JH, Edgerton VR (1991) Exertional muscle injury: evaluation of concentric versus eccentric actions with serial MR imaging. Radiology 179:659–664

Slavotinek JP (2010) Muscle injury: the role of imaging in prognostic assignment and monitoring of muscle repair. Semin Musculoskelet Radiol 14:194–200

Slavotinek JP, Verrall GM, Fon GT (2002) Hamstring injury in athletes: using MR imaging measurements to compare extent of muscle injury with amount of time lost from competition. Am J Roentgenol 179:1621–1628

Theodorou SJ, Theodorou DJ, Resnick D (2007) MR imaging findings of pyogenic bacterial myositis (pyomyositis) in patients with local muscle trauma: illustrative cases. Emerg Radiol 14:89–96

Tomasova Studynkova, Charvat F, Jarosova K, Vencovsky J (2007) The role of MRI in the assessment of polymyositis and dermatomyositis. Rheumatology 46:1174–1179

Ulmer T (2002) The clinical diagnosis of compartment syndrome of the lower leg: are clinical findings predictive of the disorder? J Orthop Trauma 16:572–577

Van der Wounde HJ, Vanderschueren G (1999) Ultrasound in musculoskeletal tumors with emphasis on its role in tumor follow-up. Radiol Clin N Am 37:753–766

Vandervenne JE, De Schepper AM, De Beuckeleer L, Van Marck E, Aparisi F, Bloem JL, Erkorkmaz Z, Brijs S (1997) New concepts in understanding evolution of desmoids tumors: MR imaging of 30 lesions. Eur Radiol 7:1013–1019

Verleisdonk EJ, van Gils A, van der Werken C (2001) The diagnostic value of MRI scans for the diagnosis of chronic exertional compartment syndrome of the lower leg. Skeletal Radiol 30:321–325

Wiemann J, Ueno T, Leek BT, Yost WT, Schwartz AK, Hargens AR (2006) Noninvasive measurements of intramuscular pressure using pulsed phase-locked loop ultrasound for detecting compartment syndromes—a preliminary report. J Orthop Trauma 7:458–463

Part II

Modern MRI Techniques for Assessment of the Skeletal Musculature

Whole-Body MRI for Evaluation of the Entire Muscular System

Nicolai Schramm, Sabine Weckbach, Stephen Eustace,
and Niamh M. Long

Contents

1 Key Points 55
2 Introduction 56
3 Development of WB MRI 56
4 Conventional Muscle Imaging with MRI 56
5 Why WB MRI for the Evaluation of Muscle Diseases? 57
6 MR Sequences for Muscle MRI 57
7 Normal Skeletal Muscle MR Appearances 58
8 Comprehensive Neuromuscular WB MRI Protocol 58
9 3T Versus 1.5T WB MRI 60
10 Limitations of Neuromuscular WB MRI 61
11 Possible Clinical Applications of Neuromuscular WB MRI 61
11.1 Inflammatory Myopathies 61
11.2 Degenerative Myopathies/Muscle Dystrophies 63
11.3 Imaging of Secondary Changes of Skeletal Muscles in Diseases of Peripheral Nerves 65
References 66

Abstract

Due to several technological advances, whole-body MRI (WB-MRI) is currently feasible with reasonable examination times and very good image quality. WB MRI protocols must be customized to the clinical questions they should solve. The most important MR sequences when evaluating skeletal muscle disease are as follows: T1-weighted (T1w) sequences are appropriate to depict anatomy, assess muscle atrophy, and detect fatty infiltration of muscles. Short tau inversion recovery (STIR) sequences or T2-weighted fat-saturated sequences can sensitively detect muscle edema. In this chapter, a comprehensive neuromuscular WB MRI protocol consisting of coronal T1w and STIR sequences at five body levels and additional axial T1w sequences is presented, modifications of this protocol are also discussed. In comparison to dedicated muscle MRI, WB MRI might be more useful for determination of the extent of the disease, detection of subclinical involvement, differential diagnosis, muscle biopsy planning, noninvasive follow-up examinations, and therapy monitoring. Currently, the most common application of neuromuscular WB MRI is the evaluation of inflammatory myopathies; muscle edema can be detected very sensitively. Another promising field for neuromuscular WB MRI are degenerative myopathies.

1 Key Points

- MRI has become the primary imaging modality in suspected skeletal muscle disease because of its lack of radiation, superb soft tissue contrast, and ability to cover a large field of view.

N. Schramm (✉)
Institute for Clinical Radiology,
Ludwig-Maximilians-University Hospital Munich,
Marchioninistr. 15, 81377 Munich, Germany
e-mail: nicolai.schramm@med.uni-muenchen.de

S. Weckbach
Institute of Diagnostic and Interventional Radiology,
University Hospital Heidelberg, Im Neuenheimer Feld 110,
69120 Heidelberg, Germany

S. Eustace
FFSEM, Newman Professor of Radiology,
University College Dublin,
Consultant Musculoskeletal Radiologist,
Departments of Radiology, Mater Misericordiae University
Hospital and Cappagh National, Orthopaedic Hospital,
Dublin, Ireland

N. M. Long
Department of Radiology,
Specialist Registrar in Diagnostic Radiology,
Cappagh National Orthopaedic Hospital, Dublin, Finglas, Ireland

M.-A. Weber (ed.), *Magnetic Resonance Imaging of the Skeletal Musculature*, Medical Radiology. Diagnostic Imaging,
DOI: 10.1007/174_2013_873,

© Springer-Verlag Berlin Heidelberg 2013
Published Online: 25 July 2013

- Due to several technological advances, whole-body MRI (WB MRI) is currently feasible with reasonable examination times and very good image quality.
- A comprehensive neuromuscular WB MRI protocol should include coronal and axial T1w and STIR sequences at all body levels. Contrast material is not needed in most cases.
- With T1w sequences the relevant anatomy can be visualized and symmetry of muscle groups can be assessed. T1w sequences can precisely delineate fatty infiltration, hemorrhage, and atrophy. STIR or T2w fat-saturated sequences are essential to detect muscle or subcutaneous edema sensitively.
- Neuromuscular WB MRI might be more useful than dedicated MRI for determination of the extent of the disease, detection of subclinical involvement, differential diagnosis, muscle biopsy planning, noninvasive follow-up examinations, and therapy monitoring.
- Possible clinical applications for neuromuscular WB MRI are the evaluation of degenerative and especially inflammatory myopathies.

2 Introduction

In evaluation of skeletal muscle abnormalities, MRI has multiple advantages over alternative imaging techniques and has become the primary method of investigation in suspected skeletal muscle disease—at least in adults. The soft tissue resolution of MRI is vastly superior to other forms of imaging due to MRI's inherent ability to precisely delineate fat, muscle, water, and bone (Schmidt et al. 2007; Chan and Liu 2002). For example, whole-body computed tomography (WB CT) is less sensitive to detect muscle edema. MRI also avoids the significant radiation dose exposure that WB CT, bone scintigraphy, and positron emission tomography would involve, and this is desirable in the predominantly younger patient cohort commonly affected by systemic muscle diseases (Chan and Liu 2002). In comparison to ultrasound MRI and especially whole-body MRI (WB MRI) is able to cover a larger field of view (FOV).

The increasing use of WB MRI techniques enables rapid assessment of the entire musculoskeletal system for evaluation of both focal and diffuse abnormalities (Schmidt et al. 2007). The typically described patterns of skeletal muscle abnormality include muscle edema, fatty degeneration, atrophy, (pseudo)hypertrophy, and mass lesions (May et al. 2000) (Fig. 1). These patterns are easily identified on WB MRI. Furthermore, the distribution and extent of skeletal muscle abnormalities can be quickly assessed with whole-body imaging allowing comparison between right and left sided muscle groups, which is of particular value in highlighting subtle musculoskeletal abnormalities.

This chapter will describe the development of WB MRI, discuss advantages and disadvantages of this modality, give examples for dedicated neuromuscular WB MRI protocols and show potential clinical applications of WB MRI to evaluate skeletal muscle disease.

3 Development of WB MRI

Between 1997 and 2001, the first studies about WB MRI were published (Barkhausen et al. 2001; Daldrup-Link et al. 2001; Eustace et al. 1997, 1999; Horvath et al. 1999; Johnson et al. 1997; Steinborn et al. 1999). However, these early protocols were not introduced into routine clinical care because imaging quality was reduced in comparison to dedicated examinations and examination times were too long. Furthermore, the coils had to be repeatedly rearranged and the patient had to be repositioned for several times during one examination.

Important improvements were the introduction of a rolling table platform mounted on top of the MRI table (Lauenstein et al. 2002; Zenge et al. 2005) and the implementation of parallel imaging techniques (Larkman and Nunes 2007). Parallel imaging has the advantage of a shorter acquisition time for the same spatial resolution or a higher spatial resolution within a given time in comparison to conventional techniques (Griswold et al. 2002; Sodickson and Manning 1997).

Whole-body imaging protocols employing these new MR techniques were mainly described for whole-body cancer screening and staging and for whole-body cardiovascular examinations (Steinborn et al. 1999; Schmidt et al. 2006, 2007; Kramer et al. 2005; Weckbach and Schoenberg 2009). Possible applications for musculoskeletal WB MRI beyond the evaluation of bone marrow and metastases are inflammatory arthritis and multifocal rheumatoid diseases (Weckbach 2009, 2012), or lipodystrophies (Hegele et al. 2007) (Fig. 2).

In comparison to oncology and cardiovascular applications, there are still only few publications about comprehensive WB MRI protocols for evaluation of the skeletal muscles (Schramm et al. 2008; Kesper et al. 2009; Kornblum et al. 2006; Quijano-Roy et al. 2012), even though this is a promising field for WB MRI in our opinion.

4 Conventional Muscle Imaging with MRI

Imaging in muscle disease has been and still is in many cases focused on the evaluation of particular muscle groups, especially the pelvic girdle and the thighs. Many myopathies predominantly affect the pelvic girdle and the thighs (Fischer et al. 2005). As many patients with muscular disease are

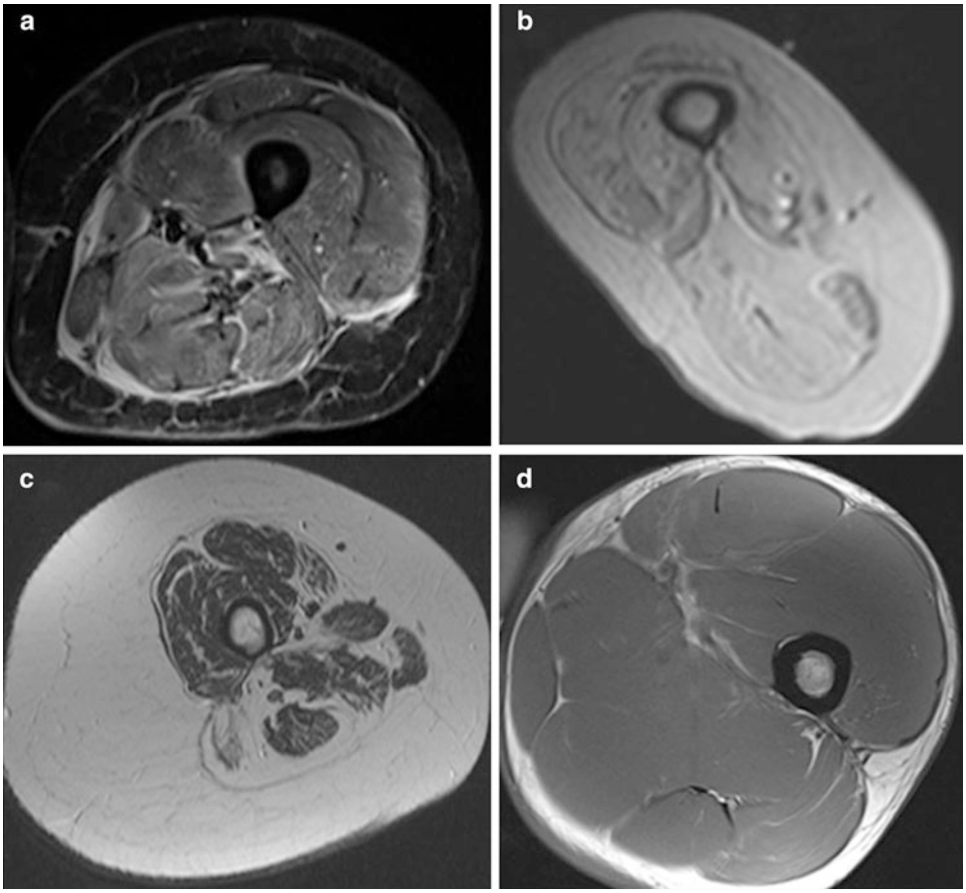

Fig. 1 Typical pathological changes in muscular tissue of the thigh shown in standard proton (1H) MRI. **a** edema like changes, **b** lipoamatous degeneration, **c** atrophy, **d** hypertrophy (images courtesy of Prof. Dr. M.-A. Weber, Heidelberg)

pediatric, short protocols sometimes only containing axial T1w sequences have been proposed (Mercuri et al. 2002).

5 Why WB MRI for the Evaluation of Muscle Diseases?

As many myopathies involve various muscle groups in different body areas, the full extent of the disease may not be detected with dedicated muscle MRI. In one of our WB MRI studies including 18 patients with different degenerative and inflammatory myopathies we found an involvement of the erector spinae muscles in 61.1 % (Schramm et al. 2008). Affection of the erector spinae muscles seems also to be common in patients with myotonic dystrophy type 1 and 2 as described by Kornblum et al. in their WB MRI study (Kornblum et al. 2006). It has been shown in WB MRI studies that involvement of other muscle groups like in the shoulder girdle or the upper arms seem to be a common finding in many myopathies, too (Schramm et al. 2008; Shelly et al. 2010).

Muscle MRI and especially WB MRI can detect subclinical involvement of muscle groups, this may be helpful for early diagnosis and differential diagnosis (Sookhoo et al. 2007). In comparison to clinical examination and dedicated muscle MRI, WB MRI could be of additional diagnostic value by depicting the extent of disease and identifying possible patterns of involvement for distinct myopathies (Olive et al. 2007; Ozsarlak et al. 2004).

The fundamentals of the diagnosis of a myopathy remain muscle biopsy with histological examination and genetic analysis. WB MRI has the potential to characterize distinct subtypes of myopathies and enable a more focused genetic testing (Fischer et al. 2005; Carlier et al. 2011). Muscle biopsy has a high rate of false-negative results (10–25 %). WB MRI can decrease this high rate by providing a WB overview of possible biopsy sites (Sookhoo et al. 2007). WB MRI a suitable modality for follow-up examinations (e.g., progress, prognosis, therapy monitoring) as it is noninvasive in contrast to electromyography or biopsy.

6 MR Sequences for Muscle MRI

T1-weighted images provide a high signal-to-noise ratio and excellent anatomic detail, while also allowing characterization of hemorrhagic lesions (e.g., hematoma, hemorrhagic neoplasm) or abnormal fat deposition (e.g., muscle

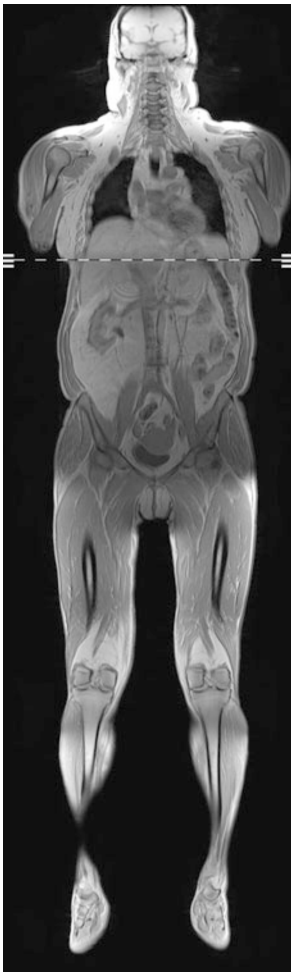

Fig. 2 Whole-body MR image of Type 2 familial partial lipodystrophy (FPLD, type Dunnigan). The coronal T1-weighted sequences (1.5T) composed of the whole-body showed rarefication of subcutaneous fat tissue of the upper and lower extremities and more fat tissue within the abdomen when compared to a control subject (images courtesy of Prof. Dr. M.-A. Weber, Heidelberg)

atrophy, lipoma) (Napier et al. 2006). Any protocol designed to highlight muscle disease must take advantage of T2 lengthening; most disease processes cause an increase in the water content of muscle resulting in prolongation of the T2 relaxation time and hence signal hyperintensity (Rybak and Torriani 2003). Fat-suppressed T2-weighted and short tau inversion recovery (STIR) fast spin echo sequences are more sensitive to the presence of muscle edema and hemorrhage than longer time to echo (TE) sequences that are not fat suppressed (May et al. 2000) (Fig. 3). Intravenous contrast material is not generally necessary in the evaluation of muscle disease as areas affected by inflammation are well demonstrated on fat-suppressed T2-weighted and STIR imaging. Occasionally, fat-suppressed T1-weighted imaging post gadolinium administration can be helpful in difficult cases (e.g., when evaluating for a cystic versus a solid mass) (Schmidt et al. 2007). In addition to producing signal abnormality, conditions affecting the musculature commonly cause changes in muscle size and shape and this is best appreciated by comparison with the contralateral, unaffected side.

7 Normal Skeletal Muscle MR Appearances

Muscle fibers form the basic functional unit of skeletal muscle. Muscle fibers are grouped into fascicles, and the fascicles are grouped into muscles. At MR imaging, skeletal muscle has an intermediate to long T1 and short T2 relaxation time and so it has signal intensity higher than water and lower than fat on T1-weighted imaging and much lower than water and fat on T2-weighted imaging (Reimers et al. 1994; Fleckenstein and Reimers 1996). Normal muscle fascicles are separated from one another by fat-containing septa, thus, normal skeletal muscle has a feathery or marbled appearance on non-fat suppressed images (Costa et al. 2012).

8 Comprehensive Neuromuscular WB MRI Protocol

The statement "one fits all" is not true for WB MRI protocols. A WB protocol should be tailored to a specific clinical question. For example, WB MRI protocols designed to evaluate cardiovascular or oncological diseases differ from each other considerably.

In this chapter, we provide an example of a comprehensive neuromuscular WB MRI protocol as it is used at the Ludwig-Maximilians-University Hospital in Munich/Germany (Schramm et al. 2008).

WB MRI is performed on a 1.5 T whole-body scanner (Magnetom Avanto, Siemens Medical Solutions, Erlangen, Germany). Multiple phased-array surface coils with up to 76 receiver coil elements and 32 receiver channels for simultaneous signal reception are used (Fig. 4). Parallel imaging techniques are utilized, and imaging is possible without patient repositioning by automated table motion (Schmidt et al. 2007). The maximum range of volume to be examined in the z-axis is 205 cm. Patients are examined from head to toe in supine position with the arms beside the body. The protocol contains T1 turbo spin echo (TSE) sequences for delineation of anatomy and to detect fatty infiltration and atrophy of skeletal muscles as well as STIR sequences for sensitive detection of muscle edema. The proposed WB protocol includes coronal T1w and STIR sequences at five body levels (head/neck, thorax/shoulders, abdomen, pelvis, thighs, lower legs) and axial T1w sequences of the upper arms, the thighs, and the lower legs. Half-Fourier acquired single-shot turbo-spin-echo (HASTE) sequences of the thorax and abdomen in axial and coronal orientation to detect organ pathologies are optional. No contrast material is administered. Sagittal sequences of the spine are dispensable for muscular WB MRI protocols.

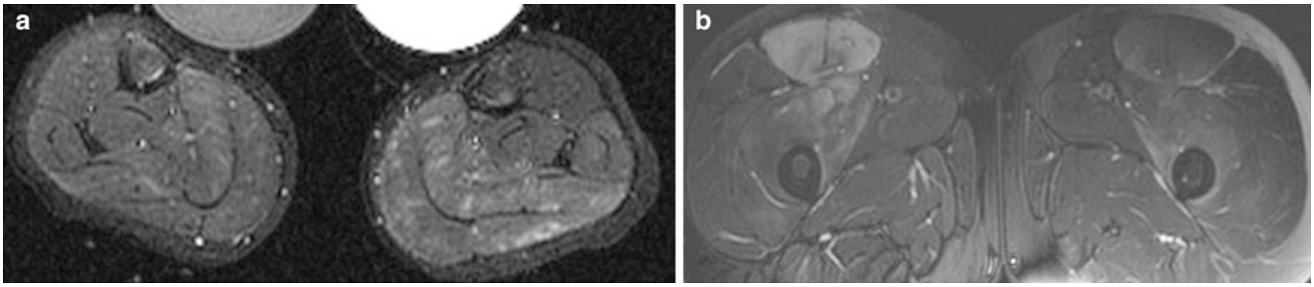

Fig. 3 **a** Axial STIR images of both lower legs in a 7-year-old boy with Duchene muscle dystrophy and edema like changes most pronounced in the left triceps surae muscle. **b** Axial fat-saturated T2-weighted MR image of both thighs in a 25-year-old rugby player with rhabdomyolysis most pronounced within the right quadriceps muscle after intensive resistance training that focuses on strengthening the quadriceps muscles. The patient presented with acute muscle tenderness (images courtesy of Prof. Dr. M.-A. Weber, Heidelberg)

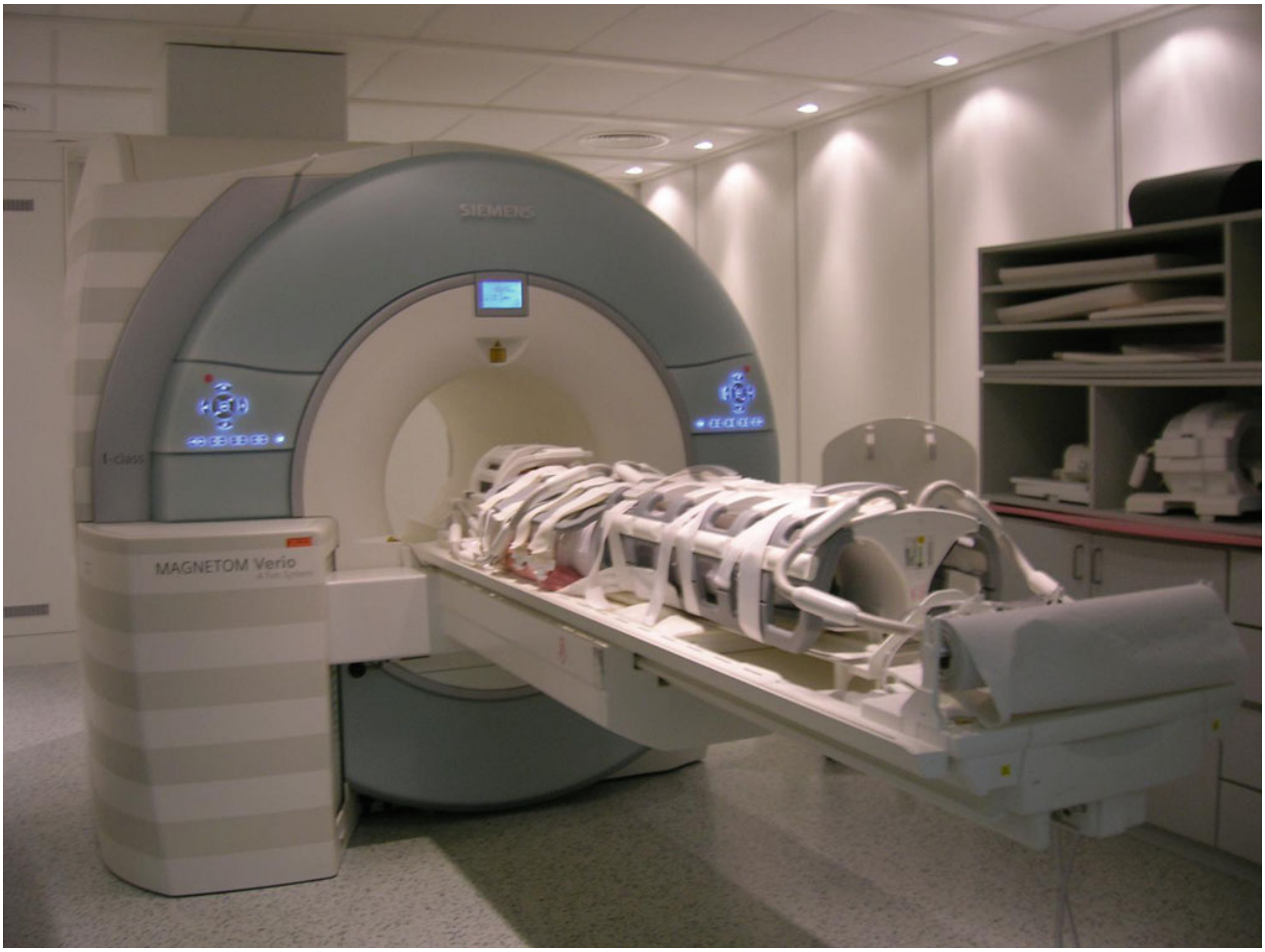

Fig. 4 For a whole-body MRI examination the entire body of the patient is covered by several coils (Magnetom Verio, Siemens Medical Solutions, Germany) (image courtesy of Prof. Dr. M.-A. Weber, Heidelberg)

Further details concerning the protocol are provided in Table 1. Relevant pathology can be demonstrated to clinicians with composed T1w and STIR whole-body images after postprocessing. Total acquisition time for this comprehensive WB MRI protocol was 41:26 min (including 1:35 min localization time). Patient preparation and coil positioning requires approximately 5–7 min.

To save time the following variant of a neuromuscular WB MRI protocol is also possible (as performed on a 3T scanner (Magnetom Verio, Siemens Medical Solutions,

Table 1 Example of a neuromuscular whole-body 1.5 Tesla MRI protocol (adapted from reference 23)

Sequence	TA (min)	Slice thickness (mm)	Slices	PAT	TR (ms)	TE (ms)	Voxel size (mm)	FOV (mm)	Matrix
T2 stir cor head/neck	01:55	5	38	3	6380	92	1.8 × 1.3 × 5	480	269 × 384
T1 cor head/neck	03:41	5	38	3	797	12	1.8 × 1.1 × 5	480	358 × 448
T2 stir cor Th + Abd mbh	02:02	5	42	3	3380	101	1.8 × 1.3 × 5	480	269 × 384
Haste tra mbh Th[a]	00:44	6	40	2	1100	45	1.2 × 1.2 × 6	380	240 × 320
Haste tra mbh Abd[a]	00:44	6	40	2	1100	45	1.2 × 1.2 × 6	380	240 × 320
T2 ha cor mbh p3 Th + Abd[a]	00:38	5	42	3	900	73	1.9 × 1.5 × 5.0	480	256 × 320
T1 cor Th + Abd + mbh	01:38	5	40	3	400	8.2	1.3 × 1.1 × 5	480	358 × 448
T1 tse cor upper arm	03:58	4	24	3	588	12	0.8 × .8 × 4.0	360	448 × 448
T1 tse tra upper arm	02:08	5	32	2	600	18	0.8 × 0.7 × 5	280	281 × 384
T2 stir cor pelvis	02:02	5	38	3	6090	84	1.8 × 1.3 × 5	480	269 × 384
T1 cor pelvis	03:41	5	38	3	797	12	1.3 × 1.1 × 5	480	358 × 448
T2 stir cor thigh	02:02	5	38	3	6090	84	1.8 × 1.3 × 5	480	260 × 384
T1 cor thigh	03:41	5	38	3	797	12	1.3 × 1.1 × 5	480	358 × 448
T1 tse tra thigh	02:51	6	34	2	637	20	1.1 × 0.9 × 6	400	240 × 448
T2 stir cor lower leg	02:45	5	38	2	5900	84	1.8 × 1.3 × 5	480	269 × 384
T1 cor lower leg	03:29	5	38	2	767	11	1.3 × 1.1 × 5	480	358 × 448
T1 tse tra lower leg	01:52	6	34	2	637	20	1.1 × 0.9 × 6	400	230 × 448

[a] optional

TA time for acquisition, *cor* coronal, *ax* axial, *TE* time to echo *TR* time to repetition, *FOV* field of view *PAT* acceleration factor
Ref. (Schramm et al. 2008)

Erlangen, Germany) in the University Hospital of Heidelberg/Germany): Routinely, the patients are examined from head to toe with coronal STIR sequences and T1 TSE sequences. Only regions that appear pathological on the coronal slices are examined with additional STIR and T1 TSE sequences in axial orientation. This approach requests a radiologist who quickly reviews the coronal sequences during the examination and tells the technologists which optional axial sequences are needed in every single case.

In 2002, O′Connell et al. published a WB MRI protocol containing only turbo-STIR sequences to evaluate patients with polymyositis (O'Connell et al. 2002). In agreement with other authors (Lenk et al. 2004) we think that a neuromuscular WB MRI protocol should include both STIR and T1w sequences to detect both muscle edema and fatty infiltration reliably. The superior anatomical resolution of T1w sequences is also useful to correlate findings in STIR imaging correctly. In some older studies, only axial slices were obtained and the body coil was utilized (Ozsarlak et al. 2004). In comparison to the approach with multiple phased-array surface coils the image quality is inferior. Coronal slices are more adequate in comparison to axial slices to determine the extent of muscle disease and necessary to create the composed whole-body images. Axial slices are often more helpful to exactly identify the affected muscle. Ideally, both orientations should be combined.

9 3T Versus 1.5T WB MRI

In 2007, Schmidt et al. published a comparative WB MRI study: 15 volunteers were examined with a WB MRI protocol at 1.5 and 3T. Image quality and frequency of artifacts were compared. Although 3T WB MRI was possible with good overall image quality at 3 T significantly more artifacts occurred. The authors concluded that 1.5T is the preferred modality for WB MRI (Schmidt et al. 2007). In accordance, two 3T muscular WB MRI studies (Kesper et al. 2009; Kornblum et al. 2006) showed subjectively inferior image quality and more artifacts in comparison to an own study at 1.5T (Schramm et al. 2008). On the other hand, scan time at 3T can be reduced at a constant image quality and further technical innovations will improve 3T WB imaging. For example, the latest scanner of one vendor (Magnetom Skyra, Siemens Medical Solutions, Erlangen, Germany) has 204 coil elements and 128 independent receiver channels. In conclusion, neuromuscular MRI at 3T is so far not clearly superior to 1.5 imaging, in contrast to other applications like neuroimaging.

10 Limitations of Neuromuscular WB MRI

Neuromuscular WB MRI has also some disadvantages and limitations: Routine imaging of the forearms is not possible as they are mostly positioned outside the maximum FOV. In large or obese patients, the shoulders and the upper arms could be located at the margin or even outside the maximum FOV, too. In cases of suspected distal myopathies an additional dedicated examination of the forearms might be useful. Of course, the proposed neuromuscular WB MRI protocol is not adequate to further evaluate cardiomyopathies. As some myopathies show cardiac involvement further cardiologic diagnostics might be necessary (Schmidt et al. 2007; Schramm et al. 2008).

11 Possible Clinical Applications of Neuromuscular WB MRI

In this chapter, we present possible clinical applications of neuromuscular WB MRI. However, not in every patient with suspected neuromuscular disease WB MRI is the modality of choice. For example, in most patients with trauma or suspicion of an abscess a dedicated MRI of the affected body region is appropriate. As soft-tissue sarcomas mostly metastasize to the lungs the combination of a high-resolution dedicated MRI (local staging, invasion of vessels and nerves) in combination with a chest CT (exclusion of lung metastases) is more adequate for staging than a WB MRI.

11.1 Inflammatory Myopathies

The idiopathic inflammatory myopathies (IIMs) are a group of chronic connective tissue diseases that are characterized by symmetrical proximal muscle weakness (see also "MRI in Inflammatory Myopathies and Autoimmune-Mediated Myositis" of this book). Although the IIMs share a common underlying pathologic process, namely an autoimmune-mediated attack on skeletal muscle, they are a heterogenous group of diseases with distinct histopathological and clinical characteristics (Dalakas and Hohlfeld 2003).

MRI is the most important imaging modality in the diagnostic work-up of IIMs because edema, fatty degeneration and atrophy can be sensitively detected (Walker 2008). The typical MRI findings early in the course of the inflammatory myopathies are bilateral and symmetric edema in pelvic and thigh musculature, in particular the vastus lateralis and vastus intermedius muscles, with the severity of muscle edema on MRI correlating with the severity of the disease. Gradual onset of muscle weakness typically progresses to involve the upper extremities, neck flexors, and pharyngeal musculature (Maillard et al. 2004; Tomasova Studynkova et al. 2007). For the clinicians detection of muscle edema in patients with IIMs is the most relevant finding. Muscle edema is thought to be an early finding in the course of muscle damage and occurs before fatty degeneration and atrophy. The correlate of musle edema is a hyerintense muscle signal in STIR or T2 sequences. However, hyperintense T2 signal in muscles is not specific for myositis and can caused by various other entities such as for instance muscle denervation, dystrophies, rhabdomyolysis (Figs. 3b, 5), and even be caused by physical strain (Weber et al. 2007). WB MRI can be useful especially for biopsy planning, differential diagnosis, and therapy monitoring. The early diagnosis of dermatomyositis and polymyositis is clinically relevant as these myopathies respond to immunosuppressive therapy in contrast to IBM

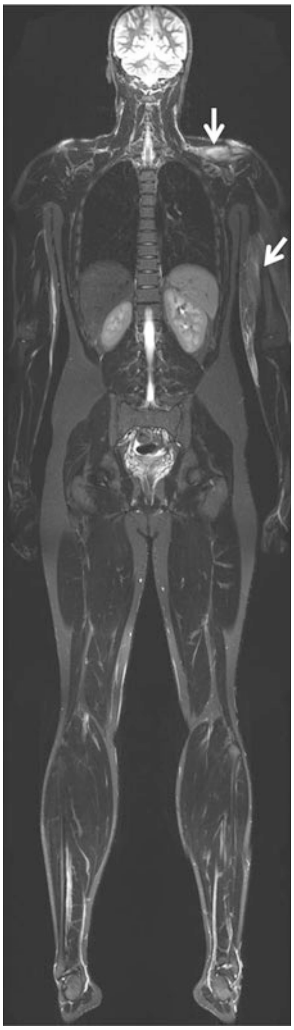

Fig. 5 Coronal STIR image of a 15-year-old male adolescent with rhabdomyolysis in the left supraspinatus and biceps brachii muscles (*arrows*) after intensive training (images courtesy of Prof. Dr. M.-A. Weber, Heidelberg)

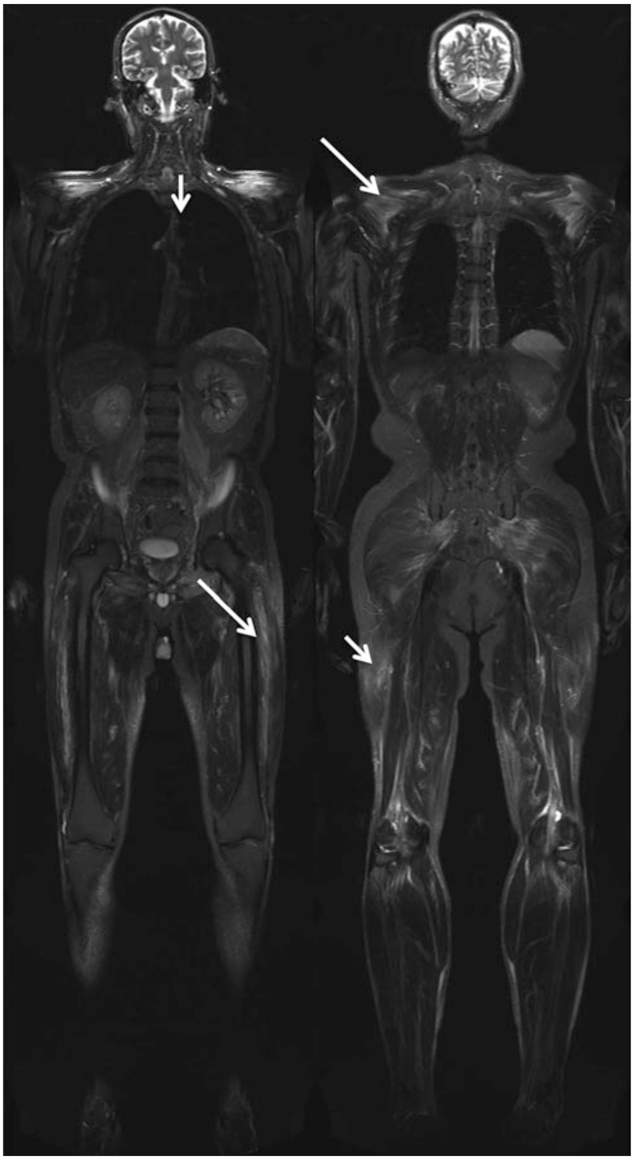

Fig. 6 Whole-body STIR MRI showing diffuse subcutaneous (*short arrows*) and muscle edema (*long arrows*) characteristic of dermatomyositis. Muscle edema is accentuated in the shoulder girdle, pelvic girdle, and the thighs (image courtesy of Prof. Dr. M.-A. Weber, Heidelberg)

(Dalakas and Hohlfeld 2003). In the following paragraphs the three most relevant entities of IIMs, namely dermatomyositis, polymyositis, and inclusion-body myositis (IBM) are introduced.

Dermatomyositis affects both the skin and skeletal muscle typically characterized by a distinctive heliotrope skin rash and slow onset, bilaterally symmetric muscle weakness that is often accompanied by myalgias. The etiology of dermatomyositis is thought to be a humorally mediated vascular injury, with perivascular inflammation and perifascicular atrophy resulting in microangiopathy and myocyte necrosis (Dalakas and Hohlfeld 2003; Bohan and Peter 1975; Curiel et al. 2009). Dermatomyositis has a bimodal pattern of distribution. The first peak occurs during childhood and is typically more severe than adult onset form. The second peak occurs during the 5th decade of life and is associated with an increased risk of malignancy. WB MRI (Figs. 6, 7) demonstrates inflammation in both muscles and subcutaneous tissues, with diffuse subcutaneous edema and patchy and diffuse muscle edema that involves both the proximal and distal extremities (Fleckenstein and Reimers 1996; Garcia 2000).

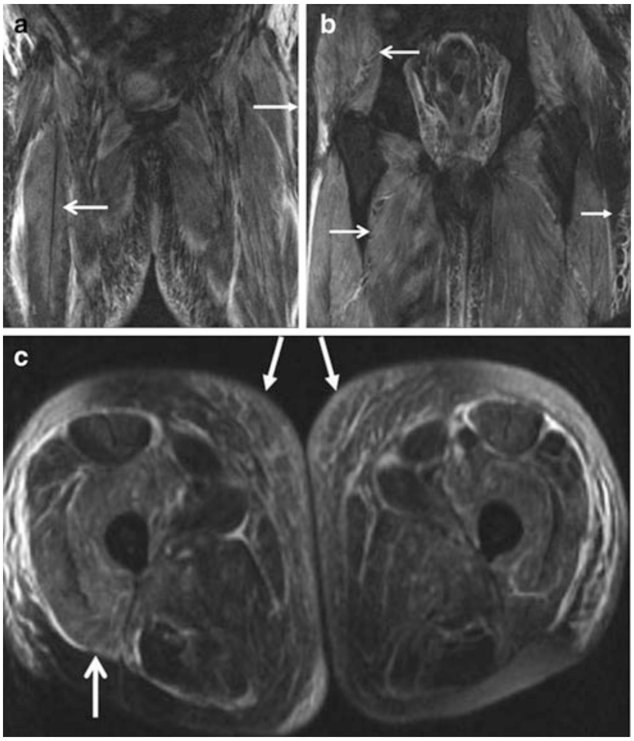

Fig. 7 Coronal (**a**, **b**) and axial (**c**) STIR images of the proximal thigh musculature demonstrating diffuse subcutaneous (*solid arrowhead*) and muscle edema (*pointed arrowhead*) typical of dermatomyositis

Polymyositis typically occurs in young adults and is characterized by symmetric muscle involvement; however, it differs from dermatomyositis by the lack of cutaneous involvement. Polymyositis appears to be caused by cell-mediated injury of myocytes by CD8 positive cytotoxic lymphocytes which, together with macrophages, surround and invade muscle fibers (Bohan and Peter 1975). WB MRI (Fig. 8) demonstrates diffuse, symmetric muscle edema centered predominantly in the shoulder and hip girdles, but also involving the neck flexors, erector spinae, and psoas muscle groups with no significant subcutaneous edema (O'Connell et al. 2002; Curiel et al. 2009; Adams et al. 1995).

In contrast to dermatomyositis and polymyositis, inclusion body myositis (IBM) tends to affect older males however can occur from the second decade of life and

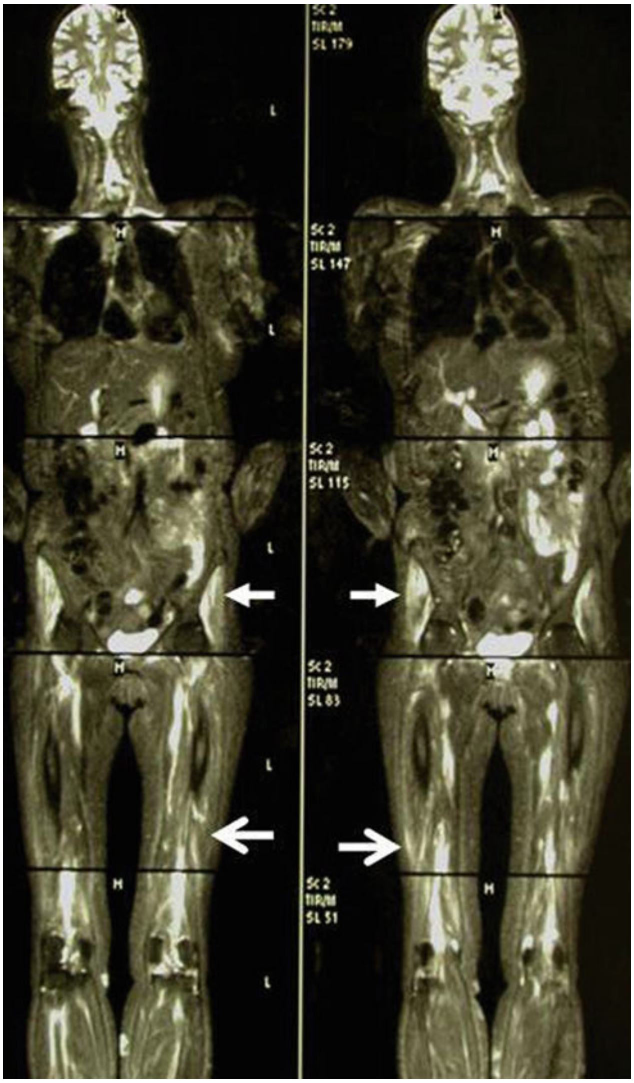

Fig. 8 Whole-body STIR MRI showing diffuse muscle edema involving the pelvic girdle muscles (*solid arrowhead*) and proximal thigh musculature (*pointed arrowhead*) typical of polymyositis. Note the characteristic lack of subcutaneous edema

begins with the involvement of distal muscles, particularly the extensors of the knee and flexors of the wrists and fingers. The pathogenesis of IBM is less clear with CD8 positive cytotoxic lymphocytes found in involved muscles as well as significant intracellular deposits of β-amyloid protein, which is also found in Alzheimer's disease, suggesting a possible neurodegenerative etiology.

Muscle weakness may be asymmetric and WB MRI demonstrates uniform, diffuse edema in involved muscle groups. In contrast to polymyositis, IBM may present with profound muscle atrophy, simultaneous fatty atrophy, and inflammatory changes or isolated involvement of the anterior compartment of the thigh (Adams et al. 1995; Askanas and Engel 2007).

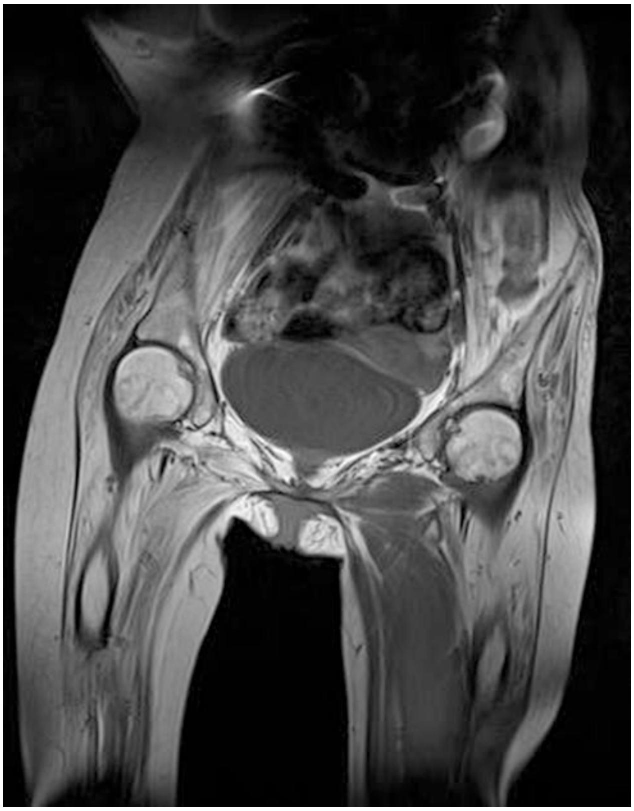

Fig. 9 Duchenne muscle dystrophy with asymmetric muscle atrophy (T1w coronal image) more pronounced on the right side (images courtesy of Prof. Dr. M.-A. Weber, Heidelberg)

11.2 Degenerative Myopathies/Muscle Dystrophies

Muscle dystrophies are a clinically and genetically heterogeneous group of primarily degenerative progressive muscle diseases that differ with respect to age of manifestation, prognosis, and progress (see also "MRI in Muscle Dystrophies and Primary Myopathies" of this book). Advancing muscle weakness and atrophy are the common symptoms of muscle dystrophies. Histologically, patients with muscle dystrophies show degeneration of muscle fibers and fibrosis. The most common entity is Duchenne dystrophy, the underlying gene defect (dystrophine gene) was identified in 1986. Because of the enormous development of molecular biology in the last decades nowadays more than 100 genetically distinct forms of inherited myopathies could be identified (Mercuri et al. 2007). These findings changed the classification of muscle dystrophies. Besides the common muscle dystrophies, type Duchenne and Becker-Kiener, multiple other dystrophies like limb girdle muscle dystrophies (LGMD) and myofibrillar muscle dystrophies (MFM) are now known. MFM are characterized by accumulation of myofibrillar proteins (Selcen and Engel 2004, 2011).

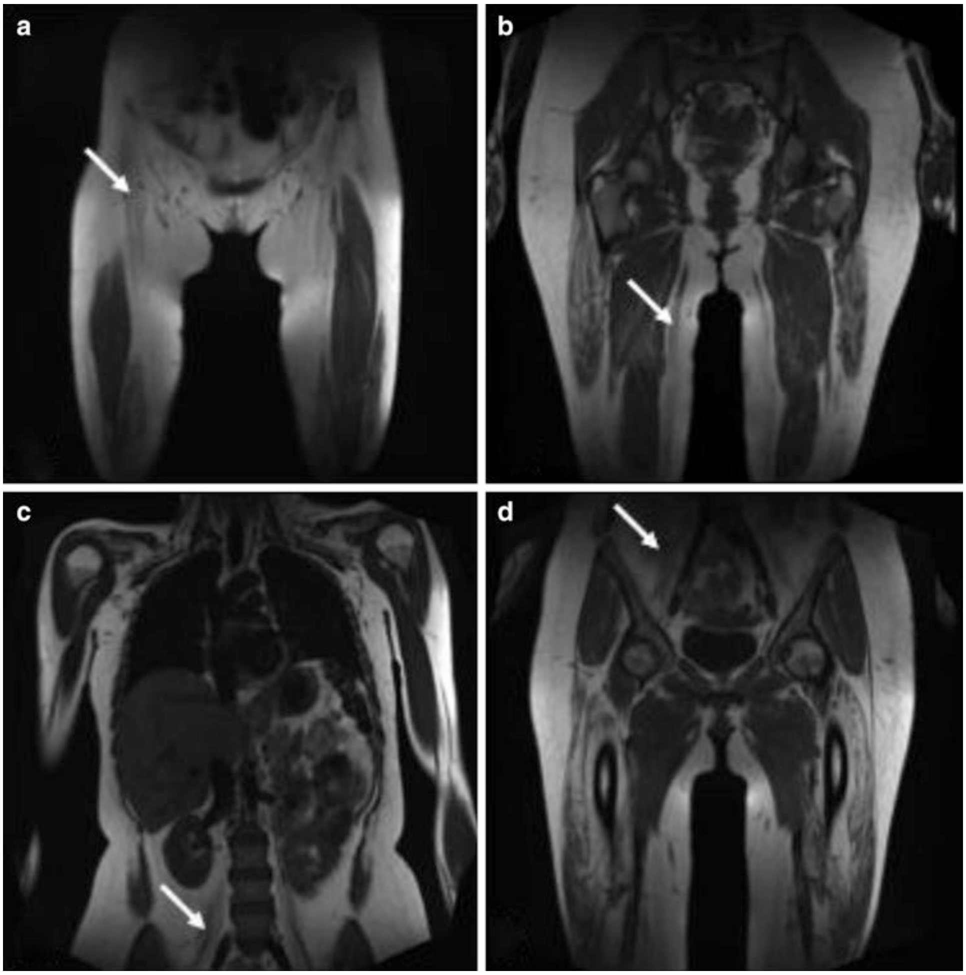

Fig. 10 Characteristic pattern of involvement in a patient with desminopathy; T1w coronal images from a WB MRI: Characteristic involvement of the sartorius (**a**), the gracilis (**b**) and the iliopsoas (**c**, **d**). Figure from reference 23

As mentioned above MR imaging in myopathies has been focused on the evaluation of the pelvic girdle and the thighs with short dedicated protocols (Mercuri et al. 2002, 2007) (Fig. 9). Still only few studies and review articles deal with the potential role of WB MRI in evaluating degenerative myopathies (Schmidt et al. 2007, 2008; Kesper et al. 2009; Kornblum et al. 2006; Carlier et al. 2011; Lenk et al. 2004). It would go beyond the scope of this book chapter to discuss the value of neuromuscular WB MRI for all different classes of degenerative myopathies. Instead we would like to present the most important results and images from a neuromuscular WB MRI pilot study from Munich University Hospital published in 2008 (Schramm et al. 2008). In this study, 18 patients with different degenerative and inflammatory myopathies were included and examined with a neuromuscular WB MRI protocol (details concerning the protocol see above). The main diagnoses were: The MFMs myotilinopathy ($n = 5$) and desminopathy ($n = 4$) and two subtypes of LGMD ($n = 4$). With the protocol characterictic involvement patterns for the MFMs could be detected: Patients with desminopathy showed frequent involvement (fatty infiltration in T1w) of the iliopsoas, the sartorius, the gracilis, and the semitendinosus, while the semimembranosus was relatively spared (Fig. 10). In contrast, myotilinopathy patients exhibited frequent involvement of the erector spinae, the rhomboid muscles, the biceps femoris, and the semimembranosus, while the semitendinosus was relatively spared (Fig. 11). The LGMD patients showed the pattern of a proximally accentuated myopathy with severe involvement of the gluteal and thigh muscles (Fig. 12). We found that involvement in muscle groups often not imaged with dedicated MR protocols seems to be quite common: e.g., erector spinae 61 %; deltoid, supraspinatus 28 %. Therefore, neuromuscular WB MRI can provide additional diagnostic information and identify distinct patterns of involvement for proximal and distal myopathies that could help to narrow the differential diagnosis even though many patterns are not specific.

Muscle edema was a frequent finding in this patient cohort with predominantly degenerative myopathies, even in cases with advanced fatty degeneration. Edema is considered to be a sign of disease activity or inflammatory components in a primarily degenerative myopathy. Recent reports (Weber et al. 2011) hypothesize that edema like

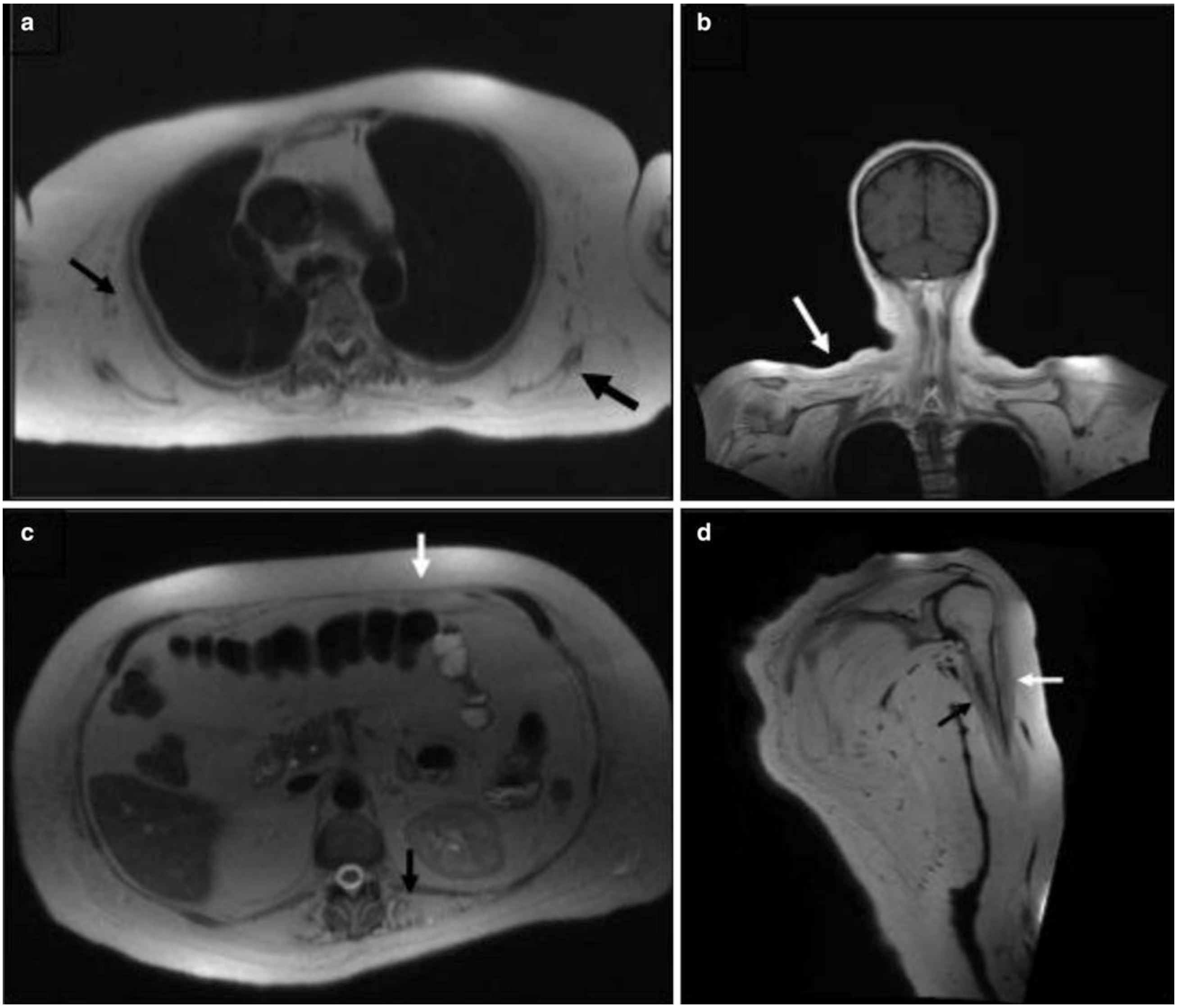

Fig. 11 WB MRI demonstrates involvement of the muscles of the shoulder, the upper arm, and the trunk in a patient with myotilinopathy. Severe fatty degeneration (T1w) of the shoulder muscles (*thick arrow*), the serratus anterior (*thin arrow*) (**a**), the trapezius (**b**), the erector spinae (*black arrow*) and the rectus abdominis (*white arrow*) (**c**), and the muscles of the upper arm (**d**). Figure from reference 23

muscular changes in Duchenne muscle dystrophy are present even before a fatty infiltration is detectable and that these edema like muscular changes may be rather osmotically driven and mainly intracellular due to elevated myoplasmic sodium (Na^+) content than inflammatory-mediated and mainly extracellular. Hence, increased muscular Na^+ concentration may be a general mechanism in muscular degeneration (see also Chapter 14 of this book). Moreover, as high T2 muscle signal is unspecific it cannot be excluded that it was exercise induced in some cases.

In conclusion, we would recommend to include STIR or fat-saturated T2-sequences to a WB MR protocol for degenerative myopathies to detect edema.

In our opinion, neuromuscular WB MRI is a valuable modality in the evaluation of degenerative myopathies: With WB MRI the extent, subclinical involvement, and distribution pattern of muscle dystrophies can be assessed. This can help to focus genetic testing, narrow the differential diagnosis, and select an appropriate biopsy site. As a noninvasive method WB MRI is a suitable method to monitor disease progress and future therapeutic trials in these patients (Schmidt et al. 2007; Schramm et al. 2008).

11.3 Imaging of Secondary Changes of Skeletal Muscles in Diseases of Peripheral Nerves

In principal, it is possible to visualize secondary changes of skeletal muscles in patients with neuropathies with WB

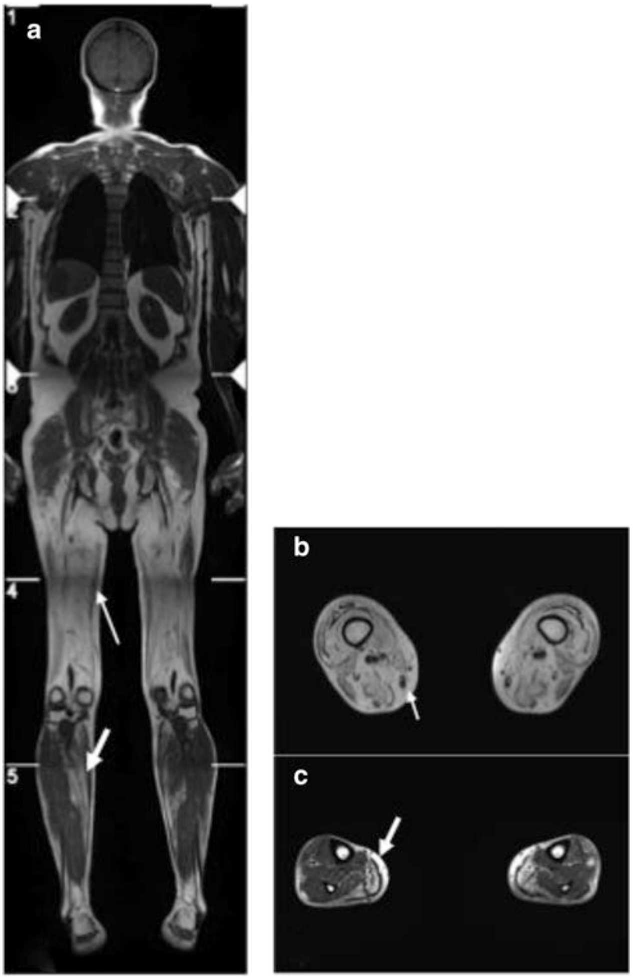

Fig. 12 Typical pattern of involvement in a patient with limb girdle muscle dystrophy (LGMD). Composed T1w image (**a**): Proximallly accentuated, symmetric, advanced fatty degeneration of the muscles of the thigh. Only the gracilis is less affected (*thin arrows*). In the lower leg only the gastrocnemii are severely affected (*thick arrows*). Corresponding transversal slices of the thighs (**b**) and the lower legs (**c**). Figure from reference 23

MRI. Chronic inflammatory demyelinating polyneuropathy (CIDP) is an acquired immune-mediated inflammatory disease of peripheral nerves that is treated with immunosuppressive therapy. Figure 13 shows the secondary muscular changes of a patient suffering from CIDP. Besides fatty degeneration of the muscles of the calves WB MRI depicts additional muscle edema as a sign of active disease. Clinically, there were no signs of active inflammation. An application of WB MRI in inflammatory neuropathies might be to visualize secondary muscle changes, assess disease activity, and noninvasively monitor therapies.

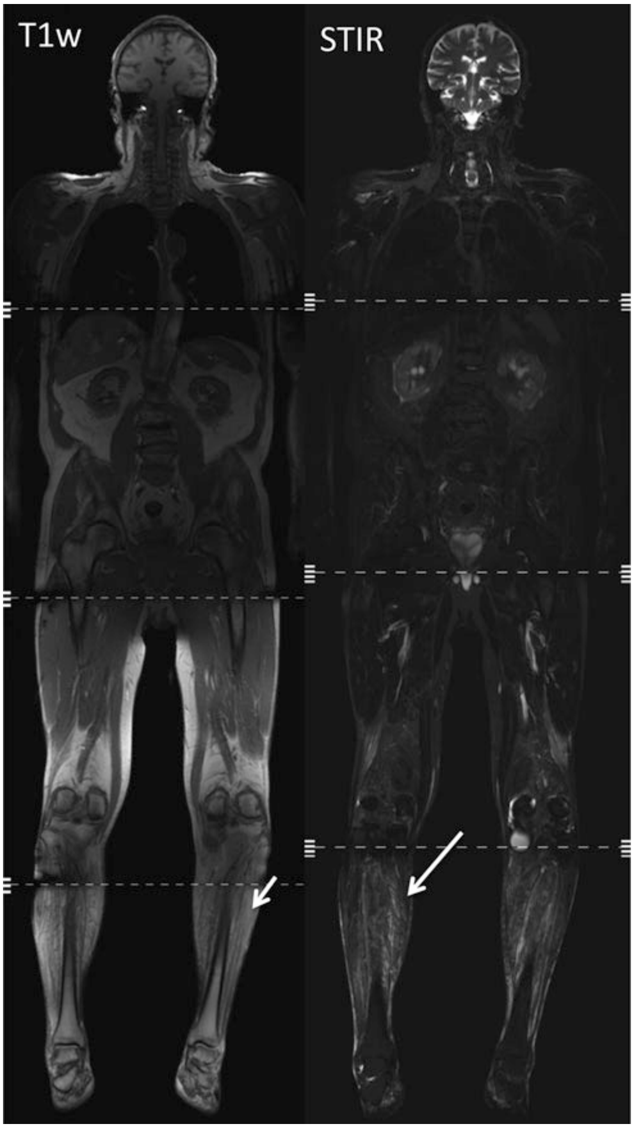

Fig. 13 Secondary muscular changes of a 75-year-old male patient suffering from chronic inflammatory demyelinating polyneuropathy (CIPD); images post immunosuppressive treatment. Besides fatty degeneration of the muscles of the calves in T1w (*short arrow*) WB MRI depicts additional muscle edema as a sign of active disease (STIR, *long arrow*). Clinically, there were no signs of active inflammation (images courtesy of Prof. Dr. M.-A. Weber, Heidelberg)

References

Adams EM, Chow CK, Premkumar A, Plotz PH (1995) The idiopathic inflammatory myopathies: spectrum of MR imaging findings. Radiographics 15(3):563–574

Askanas V, Engel WK (2007) Inclusion-body myositis, a multifactorial muscle disease associated with aging: current concepts of pathogenesis. Curr Opin Rheumatol 19(6):550–559

Barkhausen J, Quick HH, Lauenstein T et al (2001) Whole-body MR imaging in 30 seconds with real-time true FISP and a continuously rolling table platform: feasibility study. Radiology 220(1):252–256

Bohan A, Peter JB (1975) Polymyositis and dermatomyositis (first of two parts). New England J Med 292(7):344–347

Carlier RY, Laforet P, Wary C et al (2011) Whole-body muscle MRI in 20 patients suffering from late onset Pompe disease: involvement patterns. Neuromuscul Disord NMD 21(11):791–799

Chan WP, Liu GC (2002) MR imaging of primary skeletal muscle diseases in children. AJR Am J Roentgenol 179(4):989–997

Costa AF, Di Primio GA, Schweitzer ME (2012) Magnetic resonance imaging of muscle disease: a pattern-based approach. Muscle Nerve 46(4):465–481

Curiel RV, Jones R, Brindle K (2009) Magnetic resonance imaging of the idiopathic inflammatory myopathies: structural and clinical aspects. Ann N Y Acad Sci 1154:101–114

Dalakas MC, Hohlfeld R (2003) Polymyositis and dermatomyositis. Lancet 362(9388):971–982

Daldrup-Link HE, Franzius C, Link TM et al (2001) Whole-body MR imaging for detection of bone metastases in children and young adults: comparison with skeletal scintigraphy and FDG PET. AJR Am J Roentgenol 177(1):229–236

Eustace S, Tello R, DeCarvalho V et al (1997) A comparison of whole-body turboSTIR MR imaging and planar 99 mTc-methylene diphosphonate scintigraphy in the examination of patients with suspected skeletal metastases. AJR Am J Roentgenol 169(6):1655–1661

Eustace SJ, Walker R, Blake M, Yucel EK (1999) Whole-body MR imaging. practical issues, clinical applications, and future directions. Magn Reson Imaging Clin N Am 7(2):209–236

Fischer D, Walter MC, Kesper K et al (2005) Diagnostic value of muscle MRI in differentiating LGMD2I from other LGMDs. J Neurol 252(5):538–547

Fleckenstein JL, Reimers CD (1996) Inflammatory myopathies: radiologic evaluation. Radiol Clin North Am 34(2):427–439, xii

Garcia J (2000) MRI in inflammatory myopathies. Skeletal Radiol 29(8):425–438

Griswold MA, Jakob PM, Heidemann RM et al (2002) Generalized autocalibrating partially parallel acquisitions (GRAPPA). Magn Reson Med Official J Soci Magn Reson Med/Soci Magn Reson Med 47(6):1202–1210

Hegele RA, Joy TR, Al-Attar SA, Rutt BK (2007) Thematic review series: adipocyte biology. Lipodystrophies: windows on adipose biology and metabolism. J Lipid Res 48(7):1433–1444

Horvath LJ, Burtness BA, McCarthy S, Johnson KM (1999) Total-body echo-planar MR imaging in the staging of breast cancer: comparison with conventional methods–early experience. Radiology 211(1):119–128

Johnson KM, Leavitt GD, Kayser HW (1997) Total-body MR imaging in as little as 18 seconds. Radiology 202(1):262–267

Kesper K, Kornblum C, Reimann J, Lutterbey G, Schroder R, Wattjes MP (2009) Pattern of skeletal muscle involvement in primary dysferlinopathies: a whole-body 3.0-T magnetic resonance imaging study. Acta Neurol Scand 120(2):111–118

Kornblum C, Lutterbey G, Bogdanow M et al (2006) Distinct neuromuscular phenotypes in myotonic dystrophy types 1 and 2: a whole body highfield MRI study. J Neurol 253(6):753–761

Kramer H, Schoenberg SO, Nikolaou K et al (2005) Cardiovascular screening with parallel imaging techniques and a whole-body MR imager. Radiology 236(1):300–310

Larkman DJ, Nunes RG (2007) Parallel magnetic resonance imaging. Phys Med Biol 52(7):R15–R55

Lauenstein TC, Freudenberg LS, Goehde SC et al (2002) Whole-body MRI using a rolling table platform for the detection of bone metastases. Eur Radiol 12(8):2091–2099

Lenk S, Fischer S, Kotter I, Claussen CD, Schlemmer HP (2004) Possibilities of whole-body MRI for investigating musculoskeletal diseases. Der Radiologe 44(9):844–853

Maillard SM, Jones R, Owens C et al (2004) Quantitative assessment of MRI T2 relaxation time of thigh muscles in juvenile dermatomyositis. Rheumatology (Oxford) 43(5):603–608

May DA, Disler DG, Jones EA, Balkissoon AA, Manaster BJ (2000) Abnormal signal intensity in skeletal muscle at MR imaging: patterns, pearls, and pitfalls. Radiographics 20 Spec No:S295–S315

Mercuri E, Pichiecchio A, Counsell S et al (2002) A short protocol for muscle MRI in children with muscular dystrophies. Eur J Paediatric Neurol EJPN Official J Eur Paediatric Neurol Soci 6(6):305–307

Mercuri E, Pichiecchio A, Allsop J, Messina S, Pane M, Muntoni F (2007) Muscle MRI in inherited neuromuscular disorders: past, present, and future. J Magn Reson Imaging JMRI 25(2):433–440

Napier N, Shortt C, Eustace S (2006) Muscle edema: classification, mechanisms, and interpretation. Semin Musculoskeletal Radiol 10(4):258–267

O'Connell MJ, Powell T, Brennan D, Lynch T, McCarthy CJ, Eustace SJ (2002) Whole-body MR imaging in the diagnosis of polymyositis. AJR Am J Roentgenol 179(4):967–971

Olive M, Armstrong J, Miralles F et al (2007) Phenotypic patterns of desminopathy associated with three novel mutations in the desmin gene. Neuromuscul Disord NMD 17(6):443–450

Ozsarlak O, Parizel PM, De Schepper AM, De Jonghe P, Martin JJ (2004) Whole-body MR screening of muscles in the evaluation of neuromuscular diseases. Eur Radiol 14(8):1489–1493

Quijano-Roy S, Avila-Smirnow D, Carlier RY (2012) Whole body muscle MRI protocol: pattern recognition in early onset NM disorders. Neuromuscul Disord NMD 22(Suppl 2):S68–S84

Reimers CD, Schedel H, Fleckenstein JL et al (1994) Magnetic resonance imaging of skeletal muscles in idiopathic inflammatory myopathies of adults. J Neurol 241(5):306–314

Rybak LD, Torriani M (2003) Magnetic resonance imaging of sports-related muscle injuries. Top Magn Reson Imaging TMRI 14(2):209–219

Schmidt GP, Haug AR, Schoenberg SO, Reiser MF (2006) Whole-body MRI and PET-CT in the management of cancer patients. Eur Radiol 16(6):1216–1225

Schmidt GP, Reiser MF, Baur-Melnyk A (2007a) Whole-body imaging of the musculoskeletal system: the value of MR imaging. Skeletal Radiol 36(12):1109–1119

Schmidt GP, Schoenberg SO, Schmid R et al (2007b) Screening for bone metastases: whole-body MRI using a 32-channel system versus dual-modality PET-CT. Eur Radiol 17(4):939–949

Schmidt GP, Wintersperger B, Graser A, Baur-Melnyk A, Reiser MF, Schoenberg SO (2007c) High-resolution whole-body magnetic resonance imaging applications at 1.5 and 3 Tesla: a comparative study. Invest Radiol 42(6):449–459

Schramm N, Born C, Weckbach S, Reilich P, Walter MC, Reiser MF (2008) Involvement patterns in myotilinopathy and desminopathy detected by a novel neuromuscular whole-body MRI protocol. Eur Radiol 18(12):2922–2936

Selcen D, Engel AG (2004) Mutations in myotilin cause myofibrillar myopathy. Neurology 62(8):1363–1371

Selcen D, Engel AG (2011) Myofibrillar myopathies. Handb Clin Neurol 101:143–154

Shelly MJ, Bolster F, Foran P, Crosbie I, Kavanagh EC, Eustace SJ (2010) Whole-body magnetic resonance imaging in skeletal muscle disease. Semin Musculoskeletal Radiol 14(1):47–56

Sodickson DK, Manning WJ (1997) Simultaneous acquisition of spatial harmonics (SMASH): fast imaging with radiofrequency coil arrays. Magn Reson Med Official J Soci Magn Reson Med/Soci Magn Reson Med 38(4):591–603

Sookhoo S, Mackinnon I, Bushby K, Chinnery PF, Birchall D (2007) MRI for the demonstration of subclinical muscle involvement in muscular dystrophy. Clin Radiol 62(2):160–165

Steinborn MM, Heuck AF, Tiling R, Bruegel M, Gauger L, Reiser MF (1999) Whole-body bone marrow MRI in patients with metastatic disease to the skeletal system. J Comput Assist Tomogr 23(1):123–129

Tomasova Studynkova J, Charvat F, Jarosova K, Vencovsky J (2007) The role of MRI in the assessment of polymyositis and dermatomyositis. Rheumatology (Oxford) 46(7):1174–1179

Walker UA (2008) Imaging tools for the clinical assessment of idiopathic inflammatory myositis. Curr Opin Rheumatol 20(6):656–661

Weber MA, Essig M, Kauczor HU (2007) Radiological diagnostics of muscle diseases. RoFo Fortschritte auf dem Gebiete der Rontgenstrahlen und der Nuklearmedizin 179(7):712–720

Weber MA, Nagel AM, Jurkat-Rott K, Lehmann-Horn F (2011) Sodium (23Na) MRI detects elevated muscular sodium concentration in Duchenne muscular dystrophy. Neurology 77(23): 2017–2024

Weckbach S (2009) Whole-body MR imaging for patients with rheumatism. Eur J Radiol 70(3):431–441

Weckbach S (2012) Whole-body MRI for inflammatory arthritis and other multifocal rheumatoid diseases. Semin Musculoskeletal Radiol 16(5):377–388

Weckbach S, Schoenberg SO (2009) Whole body MR imaging in diabetes. Eur J Radiol 70(3):424–430

Zenge MO, Ladd ME, Vogt FM, Brauck K, Barkhausen J, Quick HH (2005) Whole-body magnetic resonance imaging featuring moving table continuous data acquisition with high-precision position feedback. Magn Reson Med Official J Soci Magn Reson Med/Soci Magn Reson Med 54(3):707–711

Diffusion-Weighted and Diffusion Tensor Imaging: Applications in Skeletal Muscles

Usha Sinha and Shantanu Sinha

Contents

1 Key Points 70

2 Introduction 70

3 Diffusion-Weighted Magnetic Resonance Imaging 71
3.1 Isotropic and Restricted Diffusion 71
3.2 Anisotropic and Restricted Diffusion 71

4 Imaging Pulse Sequences for Diffusion-Weighted Magnetic Resonance Imaging 71
4.1 Spin Echo, Echo Planar Diffusion-Weighted Imaging 72
4.2 Stimulated-Echo Planar Diffusion-Weighted Imaging 73

5 Post-processing of Diffusion-Weighted Images 74
5.1 Denoising 74
5.2 Geometric Distortions from Eddy Currents and Motion 74
5.3 Geometric Distortions from Susceptibility Artifacts 75

6 Muscle Model of Diffusion 75

7 Diffusion Tensor Indices in the Normal MSK System 76
7.1 Diffusion Tensor Imaging Under Passive and Active Muscle Contraction 77

8 Fiber Tractography 78
8.1 Fiber Pennation Angles and Fiber Lengths 81

9 Diffusion-Weighted and Diffusion Tensor Imaging in Muscle Injury 83

10 Conclusion 83

References 83

Abstract

Diffusion tensor magnetic resonance imaging (MRI) has been applied until fairly recently to the study of the brain microarchitecture. Muscle diffusion tensor imaging is still in its infancy but opens a whole new area of research in mapping microstructural organization. Diffusion arises from random motions from thermal energy; these random motions are referred to as “Brownian motion.” MRI is the only modality that allows the noninvasive determination of diffusion (which is on the order of microns) and provides an excellent probe into tissue microarchitecture. Diffusion in biological tissue can be both hindered and have a preferential direction. In the latter case, diffusion is said to be anisotropic. In this chapter, we start with a brief discussion of the technical details of diffusion tensor image acquisition and the post-processing methods. The challenges of this complex modality can be appreciated from these technical details. Diffusion is measured at the macroscopic level but reflects micro-level structural organization. Diffusion models enable one to link the microarchitecture to the observed diffusion tensor; a brief discussion of the diffusion models is presented here. The potential to infer physiological status at a microscopic level from macroscopic measurements offers exciting possibilities for understanding muscle physiology and changes with disease. In order to apply this technique to detecting changes with normal progression or disease, it is important to establish normative values as well as the reproducibility of the technique. The summary of normal ranges and reproducibility of the diffusion indices is presented and confirms that the technique can monitor changes of the order of ~ 8 %. Several studies using DTI in disease condition are also presented to provide the range of application of diffusion tensor imaging. In addition to scalar indices of diffusion, DTI also enables muscle fiber tracking. Fiber tracking is the most challenging aspect of DTI and results from several

---

U. Sinha (✉)
Department of Physics, San Diego State University,
San Diego, CA, USA
e-mail: usinha@sciences.sdsu.edu

S. Sinha
Muscle Imaging and Modeling Laboratory,
Department of Radiology, University of California,
San Diego, CA, USA

M.-A. Weber (ed.), *Magnetic Resonance Imaging of the Skeletal Musculature*, Medical Radiology. Diagnostic Imaging,
DOI: 10.1007/174_2013_932, © Springer-Verlag Berlin Heidelberg 2013
Published Online: 6 November 2013

groups are presented to demonstrate the feasibility and utility of this method in extracting fiber architectural parameters in a way that was not possible till now.

1 Key Points

1. Diffusion-weighted and diffusion tensor imaging of muscle is a novel technique that allows for probing tissue microarchitecture.
2. Image post-processing for extraction of robust diffusion indices and fiber tracking is presented in this chapter.
3. Muscle models of diffusion are also presented in this chapter which link microarchitecture to observed diffusion indices.
4. Muscle fiber tracking and extraction of fiber architecture (length, pennation angle, curvature) is feasible.
5. Applications of DWI/DTI to monitor skeletal muscle conditions are now evolving as clinically feasible tools.

2 Introduction

Diffusion tensor magnetic resonance imaging (MRI) is a relatively recent advancement which allows the in vivo study of microstructural organization (Alexander et al. 2007; Assaf and Pasternak 2008; Mukherjee and McKinstry 2006). Diffusion arises from random motions from thermal energy and is referred to as “Brownian motion” (Basser and Jones 2002; Hagmann et al. 2006). MRI is the only modality that allows the noninvasive determination of diffusion and provides an excellent probe into tissue microarchitecture. The proton is the main nucleus of interest in whole-body MRI and the main diffusion studies referred to in most studies is that of the water molecule. In contrast to a pure liquid, diffusion is hindered by the presence of macromolecules and other barriers in tissue, reducing the effective diffusion length. In addition to hindered diffusion, underlying tissue microstructure that presents regularly oriented barriers to water diffusion will selectively limit molecular excursions arising from Brownian motion in specific directions. This is termed as “anisotropic diffusion imaging.” Diffusion anisotropy has been identified in several tissues: white matter, cardiac, skeletal, and lingual muscle (Budzik et al. 2007; Gilbert and Napadow 2005; Mukherjee and McKinstry 2006; Tseng et al. 2003). By far, the maximum number of studies using diffusion tensor imaging has focused on applications in the brain (Shenton et al. 2012; Assaf and Pasternak 2008; Bennett and Rypma 2013). The relative immobility of the brain coupled with strong anisotropy of white matter fibers and the implication of white matter structural integrity in normal and disease conditions have resulted in intense research in this area.

Muscle diffusion-weighted and diffusion tensor imaging is, by contrast to brain diffusion imaging, a relatively recent development. However, many advances have been made in a short time. Muscle fiber direction determined from diffusion tensor imaging has been validated by direct anatomical examination and by optical imaging (Damon et al. 2002; Napadow et al. 2001). In vivo human DTI studies of the calf muscle have also reported the dependency on gender and age as well as the effect of injury (Galbán et al. 2004, 2005; Zaraiskaya et al. 2006). Recent studies have also identified changes in the eigenvalues and fractional anisotropy (FA) as muscle lengths change under passive and active conditions of plantar and dorsi flexion (Deux et al. 2008; Hatakenaka et al. 2008; Okamoto et al. 2010; Schwenzer et al. 2009). Models of muscle architecture have been proposed to explain observed diffusion indices in muscle compartments as well differences in age, gender and changes with flexion (Galbán et al. 2004, 2005; Karampinos et al. 2009). Model-based inferences provide an unprecedented way to link macroscopic tissue level findings (diffusion indices from MRI) to cellular level organization allowing the construction of hierarchical multiscale systems. Further, feasibility of tracking muscle fibers from in vivo diffusion tensor images of the calf and forearm has been demonstrated (Sinha et al. 2006; Lansdown et al. 2007; Froeling et al. 2012) and extended to more quantitative assessment of fiber tracks such as muscle fiber length and pennation angle (Heemskerk et al. 2009, 2010).

Imaging techniques, using both ultrasound and MRI have provided a wealth of information related to the morphology and functioning of skeletal muscle (Drace and Pelc 1994; Finni et al. 2003; Hatakenaka et al. 2008; Maganaris et al. 1998; Pappas et al. 2002; Shin et al. 2008). One potential goal for imaging is to develop subject-specific data where muscle morphological and mechanical data may be combined to develop more complete descriptions of muscle performance, intersubject variability and changes arising from onset of disease. One important issue in skeletal muscle is the orientation of muscle fibers within a muscle and the potential curvature of those fibers (Muramatsu et al. 2002). The orientation of the fibers influences the physiological cross-sectional area (PCSA) and the relationship between fiber shortening and aponeurosis shear (Azizi et al. 2008; Chi et al. 2010; Shin et al. 2008). Diffusion tensor imaging is emerging as a promising tool for in vivo mapping of fiber lengths and pennation angles from true 3D measurements and thus has the potential to advance the understanding of muscle structure and function and enable creation of accurate subject-specific muscle models.

3 Diffusion-Weighted Magnetic Resonance Imaging

Diffusion-weighted imaging refers to mapping the Brownian motion of molecules and in the case of proton imaging, the Brownian motion of water molecules. Brownian motion refers to the random molecular motion due to thermal energy of the system. This random motion called molecular diffusion was first explained by Einstein (1956). It was shown that the displacements in a liquid (e.g., water) could be modeled as a Gaussian distribution in 3D. The width of the Gaussian distribution depends on the type of molecule in the medium, the temperature, as well as the time of observation of the diffusion. The Gaussian displacement can be characterized by a single variable, the variance. In one dimension, the variance, σ^2, is given by the $2DT$ where D is referred to as the diffusion coefficient and T is the time over which the diffusion is observed. In water, the diffusion coefficient is 3.0×10^{-9} m^2/s at 37 °C (Hagmann et al. 2006).

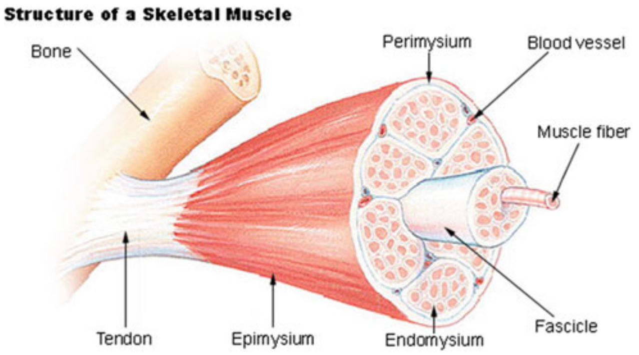

Fig. 1 This figure shows the arrangement of the muscle fibers as well as the connective tissue (endomysium, perimysium, and epimysium) surrounding the muscle fiber, bundles of muscle fiber, and the whole muscle compartment, respectively. Diffusion anisotropy can be understood in the context of the muscle fiber arrangement [Reprinted from SEER training modules, 'Structure of Skeletal Muscle'. U.S. National Institutes of Health, National Cancer Institute. 02-09-2013 (date of access), http://training.seer.cancer.gov/anatomy/muscular/structure.html]

3.1 Isotropic and Restricted Diffusion

Consider the case of diffusion if the water molecule is confined to be within objects that are impermeable. If the object dimensions are small and/or the diffusion time, T is long, the water molecule will be restricted to the object dimension. A measurement of the displacement of the water molecules in such a situation will exhibit a Gaussian distribution with a smaller variance reflecting the "restricted diffusion" arising from the water molecule in an impermeable object. The value of the diffusion coefficient will be smaller than the pure water case; restricted diffusion is exhibited by in vivo tissue such as brain gray matter, cerebrospinal fluid, and fat.

3.2 Anisotropic and Restricted Diffusion

In addition to restricted diffusion, molecules can also be in a local environment that is asymmetric (Basser and Jones 2002; Mori and Barker 1999). A microenvironment where the packing is "fiber-like" with impermeable/semi-permeable walls around the fibers will allow diffusion along the fiber length more readily than perpendicular to the fiber. This gives rise to the case of anisotropic, restricted diffusion; this diffusion type is found in the white matter in the brain as well as in muscle fibers.

3.2.1 Muscle Architecture

Skeletal muscle is a complex system with different components: muscle fibers, connective tissue, and blood and lymph vessels in addition to motor and sensor nerves. Muscle fibers are long tubular structures with diameters in the range 10–90 µm and lengths ranging from several millimeters to several centimeters. Thus the length to diameter ratio for the muscle fibers is high, ranging from 100 to 10,000. In the muscle, several fibers (few to >100 fibers) are arranged in bundles with each bundle surrounded by a layer of connective tissue. In addition, within the bundle, fibers are also surrounded by a network of connective tissue (Fig. 1). The microarchitectural arrangement of the muscle fibers provides a physiological basis for diffusion anisotropy: diffusion of water molecules is facilitated along the long muscle fibers while impeded in the perpendicular plane by the muscle fiber cell walls.

4 Imaging Pulse Sequences for Diffusion-Weighted Magnetic Resonance Imaging

The pulse sequences used to measure the diffusion tensor in muscle are similar to those implemented for the brain (Basser and Jones 2002). They are based on the spin echo, echo planar diffusion-weighted sequence. It should be noted that muscle imaging is challenged by the following characteristics of muscle: low T2 (32 ms for muscle compared to 70–80 ms for brain tissue), low FA (0.2–0.3 for muscle compared to 0.4–0.8 for white matter), and fat infiltration in the muscle (admixture of fat and muscle in a voxel). These considerations have led to sequences with a short TE and efficient fat suppression methods. Approaches to increase SNR include larger voxel sizes, increased averages, and the use of surface coils.

4.1 Spin Echo, Echo Planar Diffusion-Weighted Imaging

The basic physics behind obtaining diffusion-weighted MR images involves the use of two large balanced diffusion gradient sequences, placed around the 180° refocusing pulse (Fig. 2). The first gradient introduces a dephasing of spins that is determined by the magnitude, *G*, and duration, *δ*, of the diffusion gradient. The second gradient will completely rephase the phase introduced by the first gradient if the spins are entirely static. The large diffusion gradients and long duration, however, affect the signal from molecules undergoing motion, even on the scale of diffusion-related displacements. Since the sequence is sensitive to these small motions, it is important to acquire the image in very short times in order to freeze all physiological and other motion. This is achieved using an echo planar readout which can acquire a 2D image in ~40–100 ms (echo planar readout not shown in the figure).

The effect of the two diffusion gradient lobes (strength, duration, and diffusion time) is represented by a single term called the "*b*-factor" defined as (Basser and Jones 2002):

$$b = \gamma^2 G^2 \delta^2 \left(\Delta - {}^{\delta}\!/_{3}\right)$$

where the gradient parameters are defined in Fig. 2.

The signal intensity of a diffusion-weighted image, *S*(*b*) with respect to the baseline image (all parameters the same but without the diffusion gradient) for the general case of anisotropic diffusion is given by (Basser and Jones 2002):

$$\ln\left(\frac{S(b)}{S(b=0)}\right) = -\sum_{i=1}^{3}\sum_{j=1}^{3} b_{ij}D_{ij}$$
$$= -\left(b_{xx}D_{xx} + 2b_{xy}D_{xy} + 2b_{xz}D_{xz} + b_{yy}D_{yy} + 2b_{xz}D_{xz} + b_{zz}D_{zz}\right)$$

In order to extract the six components, D_{ij}, of the diffusion tensor, diffusion gradients have to be applied in at least six noncollinear directions. When using greater than six directions for the diffusion gradients, there is a tradeoff between number of averages and diffusion gradient directions. The diffusion tensor is diagonalized to obtain the eigenvalues (λ_1, λ_2, λ_3) and eigenvectors (v_1, v_2, v_3) of the diffusion tensor ellipsoid. The eigenvector corresponding to the largest eigenvalue has been validated to be along the fiber directions. The eigenvectors define the orientation of the anisotropic diffusion ellipsoid, while the degree of anisotropy is defined by the relative magnitude of the eigenvalues. The "mean diffusivity," MD, alternately termed as the "apparent diffusion coefficient, ADC," is the average of the three eigenvalues:

$$\mathrm{MD} = \frac{\lambda_1 + \lambda_2 + \lambda_3}{3}$$

FA is a scalar measure of this anisotropy and is derived from the eigenvalues as:

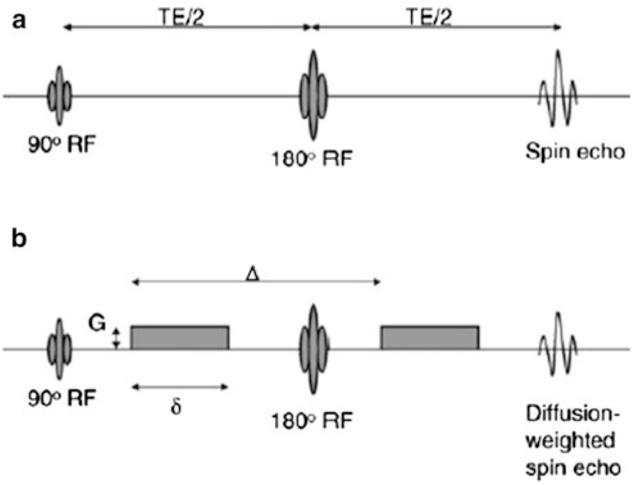

Fig. 2 Diffusion gradient sensitization with a spin echo preparation, the echo planar readout is not shown here. The *top* pulse sequence (**a**) is used for the baseline acquisition (without diffusion preparation) and the *bottom* pulse sequence (**b**) includes the diffusion gradient lobes (*G*) which can be applied along any direction

$$\mathrm{FA} = \sqrt{\frac{2}{3}}\sqrt{\left(\frac{(\lambda_1 - \lambda_{\mathrm{av}})^2 + (\lambda_2 - \lambda_{\mathrm{av}})^2 + (\lambda_3 - \lambda_{\mathrm{av}})^2}{\lambda_1^2 + \lambda_2^2 + \lambda_3^2}\right)}$$

FA values range from 0 (isotropic) to 1 (strongly anisotropic). The FA values in muscle are in the range of 0.2–0.3 which is lower than that of white matter (~0.5–0.8). Besides the mean diffusivity and the FA, several scalar measures derived from the tensor have been proposed. These include other measures of anisotropy like the shape of the diffusion: whether it is like a cigar (linear), pancake (planar), or sphere (spherical) (O'Donnell and Westin 2011).

The eigenvectors are conveniently represented in color and the following conventions are used in DTI visualization: with the *x*-projections mapped to red, *y*-projections to green, and *z*-projections to blue. The ultimate goal is to obtain the fiber tracks which represent the physiological unit of the muscle fiber bundles. Several tractography algorithms have been proposed to connect eigenvectors; the most commonly used is known as fiber assignment by continuous tracking, FACT (Mori and van Zijl 2002; O'Donnell and Westin 2011). In this algorithm, the algorithm starts from seed voxels defined by the user or by FA thresholds and follows the eigenvector direction in each voxel. Termination occurs when the FA value falls below a preset threshold or the orientation of the fiber changes by a larger angular threshold. Tract selection (using anatomical ROIs) and seed placement are highly interactive resulting in a strong operator dependence of fiber tracts. Another related approach is streamline tractography which also works by successively stepping in the direction of the principal eigenvector. Several computational methods are used to perform basic streamline tractography: Euler's method (following the eigenvector or tangent for a fixed step size) and second order or fourth order Runge–Kutta method (where the weighted average of two or four points is used for each successive step) (Basser et al. 2000). More advanced methods in tractography include probabilistic tractography that provides a measure of the probabilities of connections (Behrens et al. 2003) and tractography using advanced models for fiber crossings (Malcolm et al. 2010). Tractography is an area of active research and a recent review comparing different tractography algorithms is discussed by Lazar (2010). In muscle fiber tracking, FACT and streamline tractography methods have been used in almost all the studies reported so far. Muscle fibers do not cross and present simpler geometrical constructs compared to brain white matter fibers may be one of the reasons for the success of the simpler deterministic algorithms. However, as seen later, muscle tractography is still challenged by the lower FA values, lower SNR as well as the admixture of fat in muscle voxels.

4.1.1 Simulation Studies

Simulation studies have been performed incorporating low T2 values, % muscle fraction, DTI indices (eigenvalues, and FA) typical values for muscle in order to obtain the optimum acquisition parameters and SNR requirements to measure DTI indices with a given accuracy (Damon 2008). In the latter paper, simulations were performed with six standard diffusion gradient directions, and identified the optimum b value to be between 400 and 700 mm^2/s, and SNR of 25 for the baseline image was required to obtain an accuracy of 5 % in the DTI indices when the voxel contained only muscle tissue. The SNR requirements for eigenvector directions were more stringent: SNR $\geq$25 and $\geq$45 was required for eigenvector angular deviations of $\pm$4.5° uncertainty with muscle fractions of 1 and 0.5, respectively. When considering single voxel angular uncertainty, and SNR $\geq$60 was required for $\pm$9° uncertainty; this can have consequences for accurate fiber tracking. Froeling also performed simulation studies and determined that at least 12 gradient directions should be employed (Froeling 2012). Increasing the number of gradient directions does increase the accuracy of the eigenvector but it should be balanced by the number of averages so that the acquired diffusion-weighted images are of sufficient image quality to permit image preprocessing (for distortion corrections etc.). A more recent study also considered the effect of fat infiltration/admixture in the muscle and showed that regions must contain at least 76 % muscle tissue to reflect the diffusion properties of pure muscle accurately (Williams et al. 2013). In fat-suppressed diffusion-weighted images, high values of FA were surprisingly found in regions with high % of fat. This was attributed to the lower SNR in these regions which biased the value of the FA. This type of FA bias has been shown in earlier simulation studies focused on the brain as well (Basser and Pajevicz 2000).

It should be noted that the optimum b-value for diffusion imaging ($\sim$400 s/mm^2) is lower than that used in the brain ($\sim$1,000 s/mm^2). This allows lower TE values for the sequence which addresses the lower T2 of the muscle. Saupe et al. determined the optimum b-value at 1.5 T for muscle imaging using fiber tracking quality for evaluation; they estimated the optimum value to be 625 s/mm^2 (Saupe et al. 2009). Another important aspect is that most of the DWI/DTI sequences for the brain use a dual 180° pulse (twice refocused) to reduce the effects of eddy current. Most of the muscle DWI/DTI studies reported so far do not use the twice refocused for eddy current correction in order to keep TE at a minimum value. Further, it should be noted that the lower 'b' values used in muscle DTI do not result in large eddy current artifacts and the smaller eddy current distortions are corrected using post-processing methods.

Typical parameters and scan settings used in spin-echo echo-planar imaging (SE-EPI) based DTI acquisition for the lower leg calf muscles are listed below (Sinha et al. 2011). The acquisition included one baseline and 13 diffusion-weighted images (b factor: 500 s/mm^2) along 13 noncollinear gradient directions. Image acquisition parameters were as follows: Echo Time (TE)/Repetition Time (TR)/Field-of-View (FOV)/matrix: 48 ms/6,400 ms/24 cm/128 × 128 with parallel imaging. Images were reconstructed to a matrix size of 256 × 256; voxel resolution was 0.94 × 0.94 mm in-plane resolution (after reconstruction to a 256 × 256 matrix) with a slice thickness of 5 mm. The sensitivity encoding (SENSE) method was employed in the parallel image reconstruction and a reference scan for coil sensitivity calculation was acquired prior to each DTI acquisition; a parallel imaging reduction factor of two was used. The volume of interest was also shimmed prior to the DTI acquisition. A total of 29–30 slices were acquired contiguously, and six repeats of the acquisition were magnitude averaged for a total scan time of 9 min. A spatial spectral fat-saturation pulse was used to suppress the fat signal.

4.2 Stimulated-Echo Planar Diffusion-Weighted Imaging

The overwhelming number of muscle DTI studies have used the spin echo EPI diffusion-weighted imaging. A few studies, however, have used the stimulated echo sequence since it permits diffusion weighting at small values of TE; as explained earlier, the latter is advantageous since muscle T2 is low. In this method, three 90° pulses are applied: the first diffusion lobe is applied between the first two 90° pulses and the balancing diffusion gradient is applied after the third 90° pulse (Fig. 3). The time between the second and third 90° pulse ($\sim$the diffusion time) can be fairly long as the magnetization is stored longitudinally (Fig. 3). Thus for the same

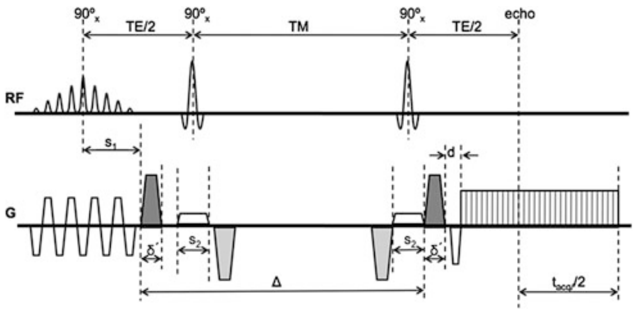

Fig. 3 Schematic of eddy-current compensated stimulated-echo prepared DW-EPU pulse sequence. Diffusion weighting gradients are in *black* and eddy current compensating gradients are in *gray* [Reprinted with permission from Karampinos et al. (2012)]

'*b*' value in SE and STE, the gradient strength and duration can be smaller since the diffusion time, delta, can be made fairly large. The TE of the STE sequence depends on the time between the first two 90° pulses: this can be made much smaller than the SE analog. However, the SNR of the STE signal is reduced by half compared to an SE signal and this affects the overall image quality. Schwenzer et al. studied the variation of muscle diffusion indices with flexion using an STE-EPI sequence (Schwenzer et al. 2009). More recently, Karampinos et al. combined eddy-current compensated diffusion-weighted stimulated-echo preparation with sensitivity encoding (SENSE, reduction factor 2.86) to obtain high SNR and to reduce the sensitivity to distortions and T(2)* blurring in high-resolution skeletal muscle single-shot DW-EPI (Karampinos et al. 2012). The rather high reduction factor of 2.86 certainly reduced distortions and fat–water mismapping artifacts, but also contributes to a loss in SNR. They were able to obtain voxel resolutions of 17 mm^3 which is of the order achievable with single-shot SE-EPI DW imaging. The TE (31 ms) is lower than that possible with SE-EPI (∼42–49 ms) but is still not low enough to compensate for the loss in signal intensity by a factor of 0.5 in a STEAM acquisition. The few studies, so far, have not convincingly demonstrated that STE diffusion preparation offers a distinct advantage over the SE diffusion preparation (note: parallel imaging has been used with both techniques to reduce the distortion/fat mismapping artifacts). A recent clinical study uses STE diffusion preparation to study Chronic Exertional Compartment Syndrome (CECS) of the Lower Leg Muscles (Sigmund et al. 2013).

5 Post-processing of Diffusion-Weighted Images

Echo planar diffusion-weighted images suffer from low signal-to-noise and from geometric distortion artifacts arising from eddy currents as well as from B0 field inhomogeneities. Several groups have adapted denoising and correction techniques originally developed for brain images to muscle DTI data.

5.1 Denoising

Froeling et al. have used a Rician linear minimum mean square error (LMMSE) noise suppression algorithm on the diffusion-weighted images and obtained visually improved images (Froeling et al. 2012; Aja-Fernandez et al. 2008). Sinha et al. evaluated log-Euclidean anisotropic filter available from the software package, MedINRIA (Sinha et al. 2011; Sinha and Sinha 2011; Arsigny et al. 2006). The latter is a tensor smoothing algorithm and is based on first transforming to the matrix logarithm L of a tensor D: $L = \log(D)$, and running computations on L. Smoothing is then performed on L to obtain $\tilde{L}$ from which the regularized tensor is obtained by taking the matrix exponential: $\tilde{D} = \exp(\tilde{L})$. The standard deviation of the lead eigenvector orientation reduced with the smoothing (average standard deviation of orientation in the original images: 3.1 ± 2.5° and in the denoised tensor images: 1.01 ± 0.6°) and this difference was also significant (paired 2-tailed, t test, $p = 0.001$). Figure 4 shows eigenvector images of the lower calf before and after denoising; the smoothing of the fiber orientation can be readily appreciated. Incorporation of noise reduction methods for muscle DTI clearly improves SNR and should be employed if fiber tractography is the end goal. A recent study reported a denoising algorithm tailored to muscle diffusion tensor data (Levin et al. 2011). A key feature of the algorithm is that it performs denoising of the lead eigenvector field simultaneously with its extraction from the noisy tensor field. This allows the vector field reconstruction to be constrained by the architectural properties of skeletal muscles. The latter algorithm shows promise and needs large-scale testing; however, it does require some a priori knowledge of fiber architecture to impose constraints on the denoising algorithm. Additional studies need to be undertaken to compare and customize the different denoising algorithms available and also to determine if the raw diffusion-weighted images or the tensor should be denoised in terms extent of noise reduction and impact on FA values.

5.2 Geometric Distortions from Eddy Currents and Motion

The diffusion-weighted images have geometric distortions from eddy currents arising from the large diffusion gradients (Sinha et al. 2011; Sinha and Sinha 2011; Heemskerk et al. 2010; Froeling et al. 2012). This distortion and motion

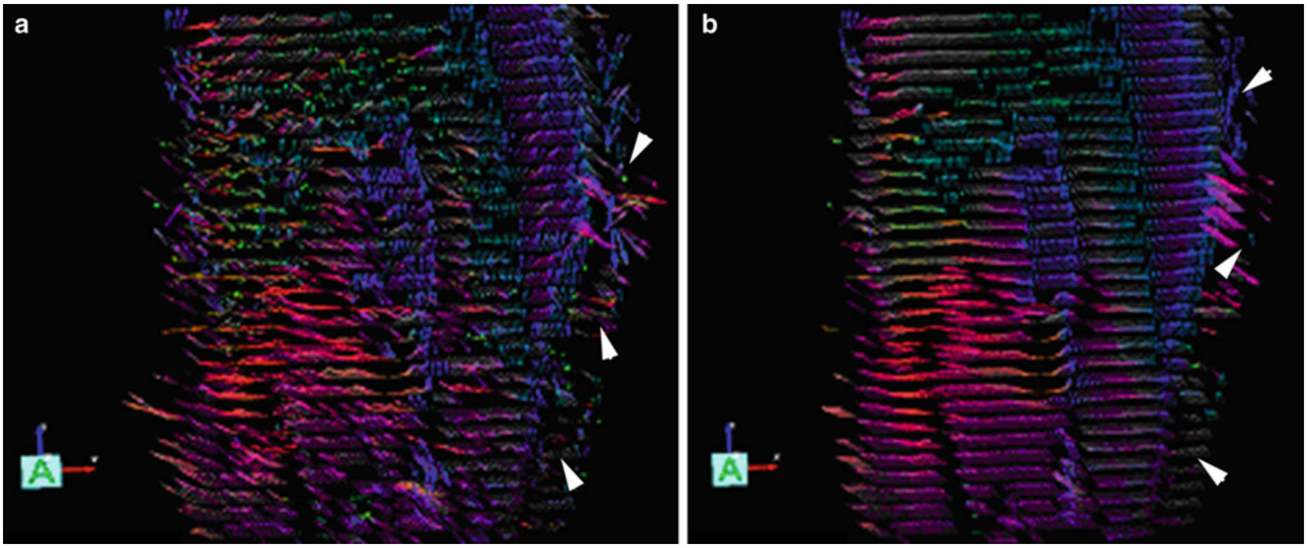

Fig. 4 The leading eigenvector is shown in both images as *arrows* with the color indicating vector direction with the following color map (*blue* superior-to-inferior direction, *red* medial to lateral direction, and *green* anterior to posterior direction). The *left image* (**a**) is unsmoothed and the *right image* (**b**) is the corresponding smoothed image. Large eigenvectors outside the muscle (indicated by *white arrowheads*) correspond to fat regions and show erroneous fractional anisotropy and eigenvector directions [Reprinted with permission from Sinha et al. (2011)]

correction is performed by an affine transform to the baseline image volume of the diffusion-weighted data. The affine transformation is used to reorient the *b*-matrix as well (Leemans and Jones 2009).

5.3 Geometric Distortions from Susceptibility Artifacts

This artifact arises from magnetic field inhomogeneities primarily due to susceptibility differences in adjacent structures. The field inhomogeneities result in a spatial mismapping with regions of signal loss and signal pile-up. The extent of distortions is the same in the baseline and in the diffusion-weighted images. Most muscle DTI studies do not correct for this artifact. However, it is important to correct for these geometric distortions in order to perform accurate fiber tractography, correlate morphological to diffusion tensor data, and to enable image-based modeling. Methods used in brain diffusion tensor imaging have been extended to muscle diffusion data. One method that has been implemented is based on acquisition of phase images which map the field inhomogeneity; these phase values can be used to directly assign voxels to the correct location (Froeling 2012; Froeling et al. 2012). This approach, however, requires an additional double echo gradient echo scan and it is not clear if it will work when parallel imaging is used. An alternate approach is to nonlinearly deform the baseline image of the diffusion-weighted dataset to a geometrically accurate structural image and apply the deformation to the diffusion tensor calculated from the uncorrected data (Sinha et al. 2011; Sinha and Sinha 2011). Figure 5 shows the axial slice of the lower leg from the baseline diffusion-weighted image as acquired and the same image after correction with a nonlinear deformation algorithm. The nonlinear deformation was applied to the diffusion tensor rather than to the diffusion-weighted images so that appropriate tensor reorientation can also be performed. The better geometrical match of the corrected data to the structural images can be readily appreciated by the better match of the contours.

6 Muscle Model of Diffusion

Tseng et al. analyzed diffusion tensor data in myocardial muscle and concluded that the eigenvectors corresponding to the leading, second, and third eigenvalues correspond to the directions along the long axis of the fibers, parallel to the myocardial sheets, and normal to the sheets (Tseng et al. 2003). This myocardial muscle model has been confirmed by histological examination as well (Scollan et al. 1998). Damon et al. were the first to confirm that the pennation angle of the lateral gastrocs fibers in a rat model estimated from DTI is close to that measured by direct anatomical inspection, DAI (Damon et al. 2002). However, the anatomical correlates of the second and third eigenvector of muscle fibers have not yet been conclusively established.

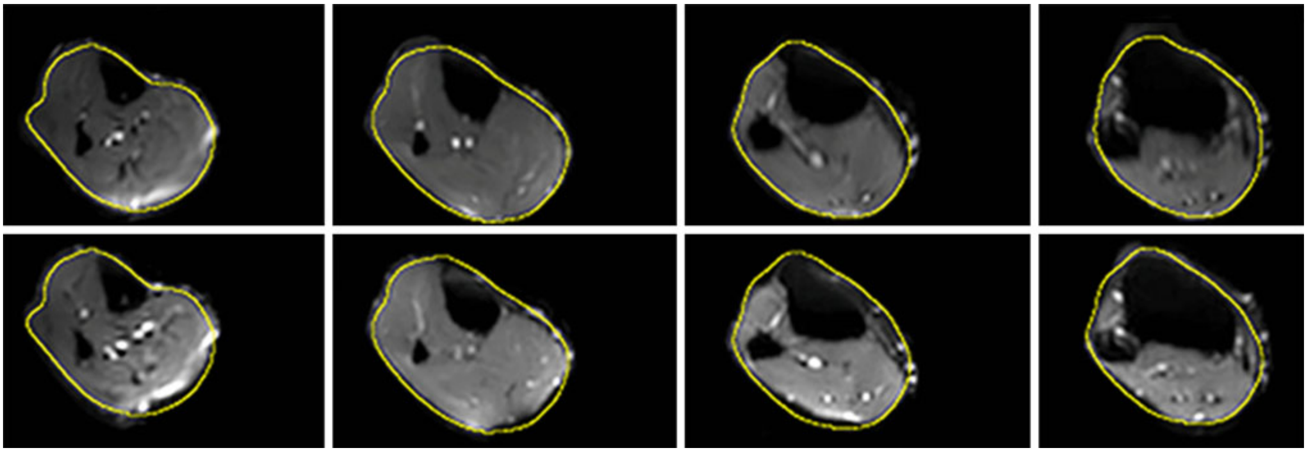

Fig. 5 *Top row* Corrected baseline images after nonlinear deformation to an image volume acquired using a gradient echo sequence with fat saturation. *Bottom row* Original baseline images of the diffusion-weighted series. The *yellow* contour superposed on both image volumes was obtained from the corresponding slice in the gradient echo image. The improvement in geometric fidelity is clearly apparent by a comparison of the contour matching for the two sets

Galbán et al. were the first to suggest a model to explain the observed diffusion tensor eigenvalues in skeletal muscle (Galbán et al. 2004). They proposed that since the lead eigenvector was along the long axis, the second and third eigenvectors are in a plane orthogonal to the long axis. The second eigenvector is hypothesized to run along the sheets of individual muscle fibers within the endomysium, the region between the fibers. The eigenvector associated with the third eigenvalue is then related to transport pathways with the muscle in this model. They verified the model prediction that PCSA is proportional to the third eigenvalue in the lower leg muscles.

An extension of this model was advanced to account for gender-based differences in DTI indices: the extended model includes the muscle fiber volume fraction in a well-defined arbitrary muscle volume (Galbán et al. 2005). The extended model predicts that a larger volume fraction of skeletal muscle in males is muscle fibers (anisotropic hindered diffusion) compared to females who have a larger fraction of endomysium (isotropic, less hindered diffusion); this was verified in their study as females had a larger ADC values while males had higher FA values (Galbán et al. 2005).

Karampinos et al. proposed an interesting diffusion tensor model which took into account the cross-sectional asymmetry of muscle fiber geometry (Karampinos et al. 2007, 2009). In their model, diffusion occurs in a space composed of the space within the muscle fiber and the extracellular space. The muscle fibers themselves were modeled as cylinders of infinite length with an elliptical cross-section with dimensions derived from histological studies of excised muscle. In the model, λ_2 and λ_3 (the second and third eigenvalues) reflect the principal diameters of the elliptical cross-sectional area of the myofibrils. Though there is no complete validation as yet for the second and third eigenvector directions, the elliptical cross-sectional model has some support since the second eigenvector has been tracked in a recent study (Gharibans et al. 2011).

It is also possible to infer the link between the eigenvalues and the fiber microarchitecture by looking at changes on flexion. Consistent changes have not been reported for plantarflexion, but most studies show that λ_3 increases. This is in line with the models relating λ_3 to muscle diameter. In the elliptical cross-sectional model, if there is isotropic deformation in the fiber cross-section, similar increases in λ_2 should be expected. However, evidence from other studies such as strain rate tensor (Englund et al. 2011; Sinha et al. 2012), show that fiber cross-sectional deformation is highly anisotropic. This suggests that if deformation is only along one direction, λ_2 should not change as much as λ_3. Experimental evidence of small changes in λ_2 with flexion comes from Hatakenaka et al. (2008) and Sinha et al. (2011). However, other studies have reported both decreases and increases in λ_2 (Deux et al. 2008). More studies using robust acquisition and post-processing techniques are required to document changes in the diffusion indices with flexion; such studies may help elucidate the diffusion model in the musculoskeletal (MSK) system.

7 Diffusion Tensor Indices in the Normal MSK System

Detailed analysis of the DTI of the forearm muscles have been reported by Froeling et al. (2012). The eigenvalues, MD, and FA were calculated for six muscles of the forearm as well as for the whole muscle volume. Typical values for the MD in the whole muscle of the forearm were $1.49 \pm 0.09 \times 10^{-9}$ m^2/s and FA values were 0.30 ± 0.02. Values reported for the MG of the lower leg are $1.32 \pm 0.06 \times 10^{-9}$ m^2/s and FA values were 0.23 ± 0.04 (Sinha and Sinha 2011). The same group also extracted the diffusion indices for the different compartments of the soleus (Sinha et al. 2011): MD and FA of posterior soleus: $1.47 \pm 0.06 \times 10^{-9}$ m^2/s and 0.20 ± 0.04; MD and FA of anterior soleus: $1.60 \pm 0.08 \times 10^{-9}$ m^2/s and 0.20 ± 0.04. Heemskerk et al. reported the values in anterior tibialis (TA) for the mean diffusivity as $1.64 \pm 0.05 \times 10^{-9}$ m^2/s and for the FA as 0.23 ± 0.04 (Heemskerk et al. 2010). Heemskerk et al. also determined the coefficient of variation (CV) for the diffusion indices, fiber orientation, and lengths. They report CV of <3 % for the eigenvalues and MD, <8 % for the FA, and the repeatability coefficients of the fiber pennation angle and length to be less than 10.2 and 50 mm, respectively. The above measurements of normal diffusion indices in skeletal muscle were performed at 3 T. A comparison of 1.5 and 3 T scanners based on two subjects scanned on 3 days to calculate the coefficient of variability (CV) showed that the values for the DTI indices as well as for the fiber orientation were in a similar range (<3 % for the eigenvalues, <8 % for the FA, and 8–12 % for the fiber orientation). Given the widespread availability of 1.5 Tesla scanners, this opens the possibilities for using DTI to monitor muscle architecture in normal and diseased states (Sinha and Sinha 2011).

The repeatability studies allow one to determine if the measurement precision is sufficient to detect changes with disease state. DTI indices are known to change in the range of 10–20 % in diseased or damaged tissue (Heemskerk et al. 2006, 2007; Qi et al. 2008). The RC of the DTI indices (eigenvalues, FA) in the lower leg muscles is reported to be less than 10 %, and thus the DTI sequences should be capable of detecting changes in muscle DTI indices with disease/damage. Changes in muscle architecture arising from changes in ankle positions or from contraction can be as small as 3–5°, so that repeatability coefficients for fiber orientations should be in this range. The average RCs of the fiber orientations in prior reported studies is ~8°, which is more than the anticipated changes in fiber orientation with ankle position or from contraction. However, it should be noted that muscle architecture changes are typically monitored without any change in patient position, so that these measurements (same session, no subject repositioning) will have a higher reproducibility than that measured on separate days with subject repositioning. This is probably the reason that fiber orientation changes of the order of 8° could be detected even when the RC value was in the same range (Sinha et al. 2011; Sinha and Sinha 2011).

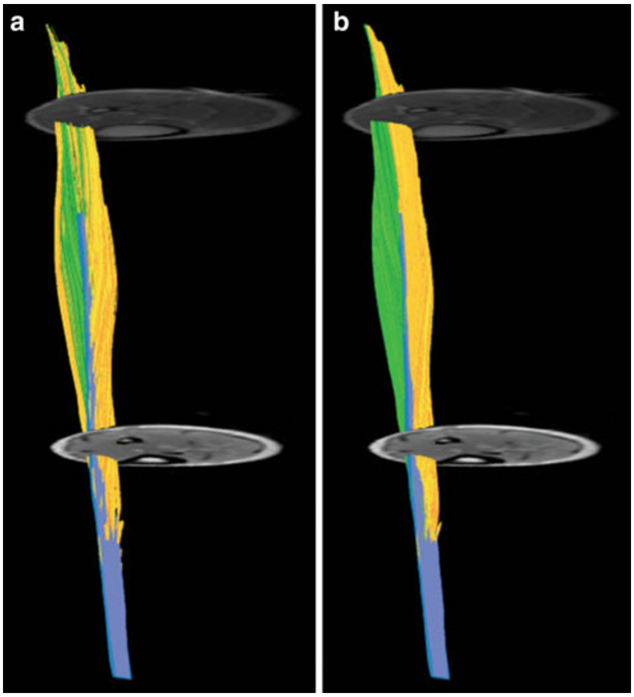

Fig. 6 Fiber trajectories for subject three before (**a**) and after (**b**) quantitative assessment. Note the *yellow* fibers in both compartments in **a**. The aponeurosis is indicated in *blue* and fibers originating from the deep aspect of the aponeurosis are indicated in shades of *yellow*, while fibers originating from the superficial aspect of the aponeurosis are indicated in shades of *green*. Color variations within the tracts exist only for contrast [Reprinted with permission from Heemskerk et al. (2009)]

7.1 Diffusion Tensor Imaging Under Passive and Active Muscle Contraction

There have been varying reports on the changes under passive and active muscle contraction. Hatakenaka reported that in the medial gastrocnemius (mGM) passive contraction resulted in a decrease in λ_1, no change in λ_2 and an increase in λ_3 which lead to a lower FA value (Hatakenaka et al. 2008). The opposite effect was seen in the TA. Duex et al. reported that in the mGM, the three eigenvalues and ADC increased while FA decreased during an active contraction from neutral to plantarflexion (Deux et al. 2008). The reverse trend was observed in the TA. Okamoto et al. also performed DTI under active contraction and found higher values for λ_1 and λ_2 as well as FA in the mGM with an opposite effect for the TA and attributed some of the changes to changes in focal temperature and perfusion (Okamoto et al. 2010). Schwenzer et al. measured orientation changes in the soleus under neutral and plantarflexed ankle positions (Schwenzer et al. 2009). For the soleus, they report increase in λ_2 and λ_3, no change in λ_1, a decrease in FA, and a small change of 4° in the fiber orientation with respect to the z-axis. Sinha et al. report much larger changes in the soleus

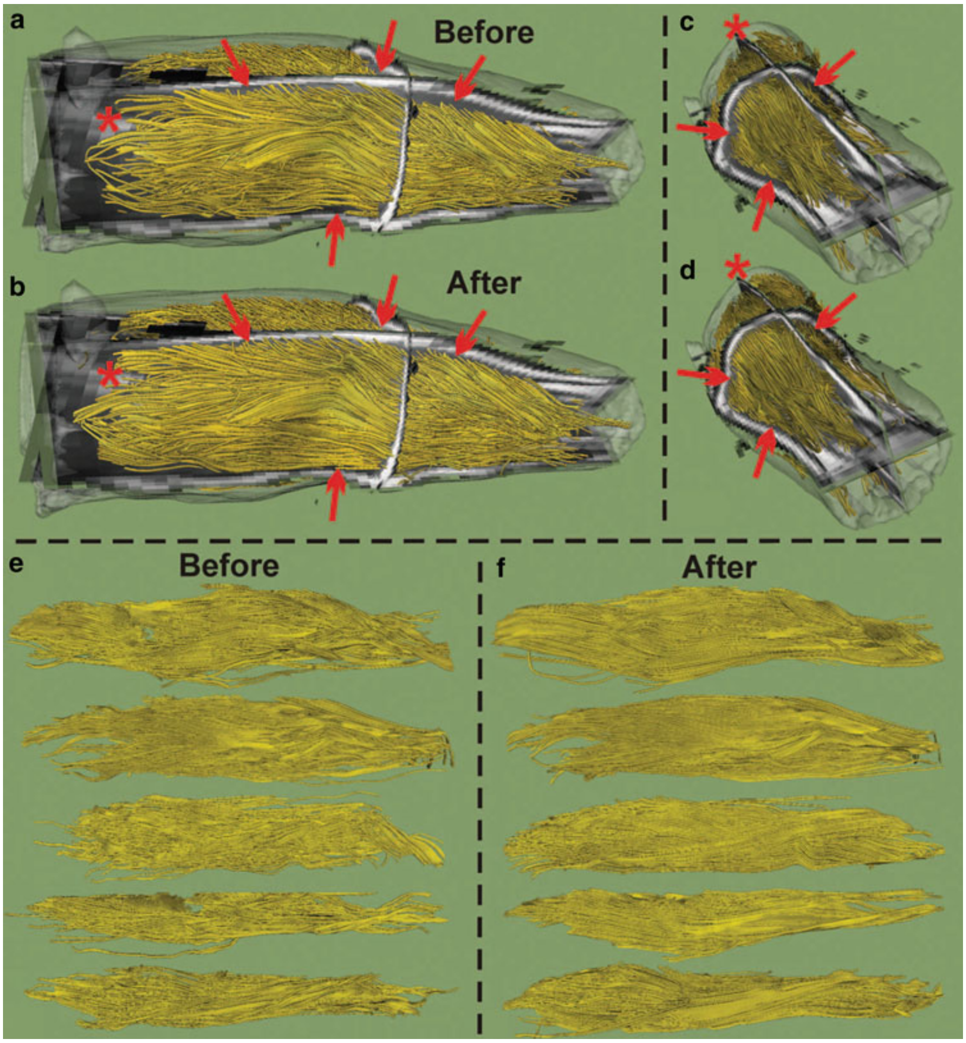

Fig. 7 Fiber tractography of the whole human forearm. Muscle fibers are shown on *top* of orthogonal cross-sections and surface renderings of the T1-weighted images. **a**, **c** Tractography before displacement and diffusion tensor shear corrections. **b**, **d** Tractography after corrections. Regions where T1-weighted data and fiber tracts were severely misregistered are indicated with *red arrows*. After postprocessing the misregistration virtually disappeared and denser fiber tracking continued toward the proximal end of the forearm as indicated by the *red asterisk*. **e**, **f** Segmented Flexor digitorum profundus of all five subjects before (**e**) and after (**f**) postprocessing [Reprinted with permission from Froeling et al. (2012)]

when the foot is in the neutral and plantarflexed states (~60° in the posterior soleus) (Sinha et al. 2011).

Hatakenaka have built on diffusive models in skeletal muscle in the literature to propose a model for contraction (Hatakenaka et al. 2008). Sarcomeres (2 μm length) are shortened on contraction, while muscle fiber cross-sectional diameter (40–120 μm), as well as that of myofibrils (3 μm), increase. Since myofibril dimensions are of the order of the observed diffusion lengths (10 μm), the diffusion in the radial direction increases due to increase in myofibril diameter; this is confirmed by observations on λ_3. Hatakenaka also suggested that sarcomere shortening may contribute to a decrease in λ_1 (Hatakenaka et al. 2008). Other models propose that λ_1 should not change with contraction as whole muscle fiber lengths are far greater than diffusion lengths, resulting in λ_1 being insensitive to muscle fiber length changes (Schwenzer et al. 2009). The increase in λ_3 seen in several studies can be attributed to an increase in muscle fiber diameter as the muscle contracts on plantarflexion. However, both experimental data and models are not consistent and more studies on flexion may help identify consistent changes in diffusion indices and may ultimately provide clues to the correct diffusion model.

8 Fiber Tractography

The ultimate aim of muscle DTI is tracking the muscle fibers to determine the microarchitecture: pennation angles, fiber lengths, and curvature. Damon et al. showed that fibers tracked in rat muscle at 4 T correlated well with direct anatomic imaging (Damon et al. 2002). Sinha et al. reported some of the earliest fiber tractography in human in vivo calf muscle (Sinha et al. 2006). They showed the feasibility of fiber tracking in several muscle compartments of the in vivo calf muscle. Lansdown et al. established an automated

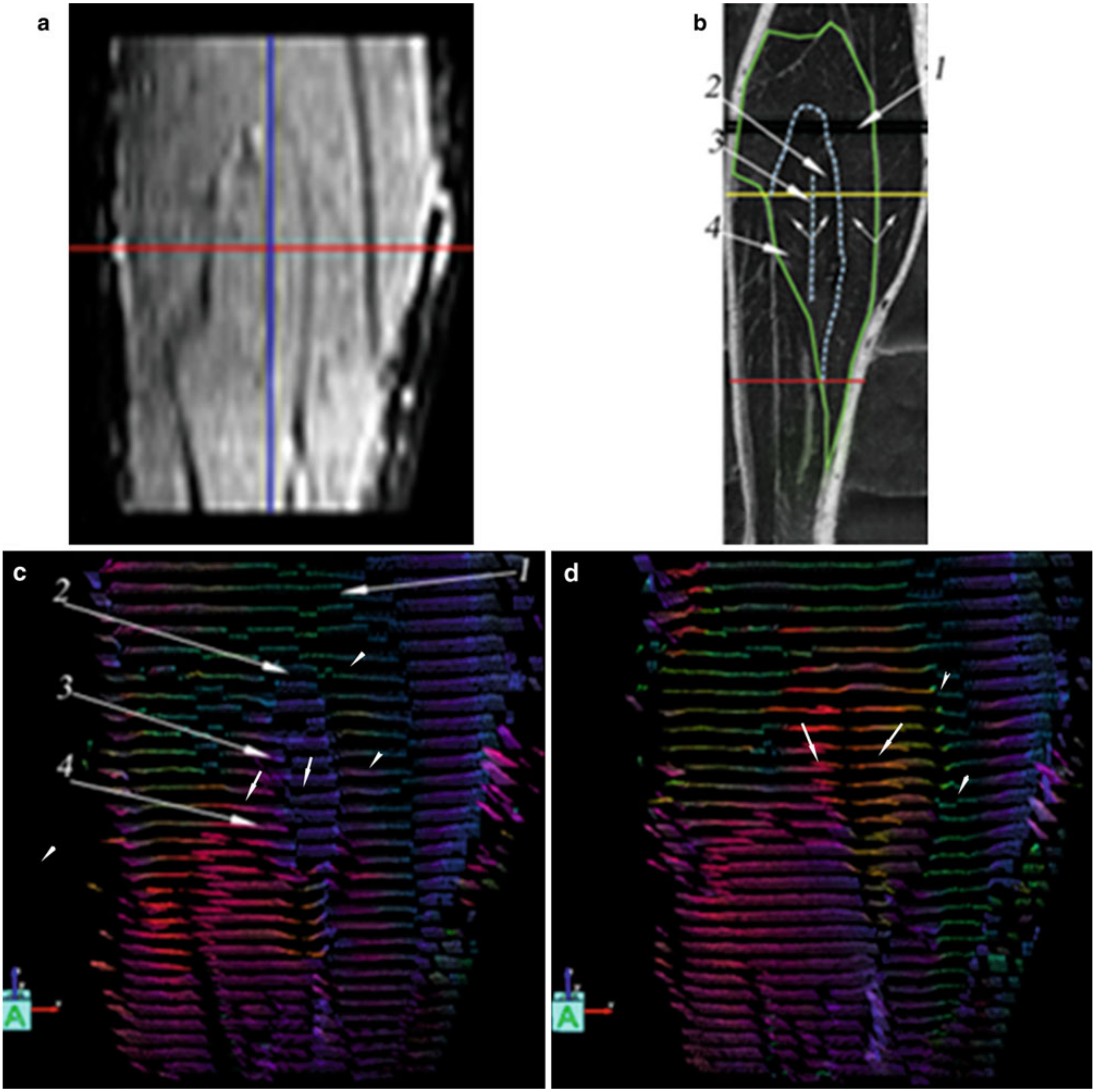

Fig. 8 Coronal view of the soleus. The coronal morphological image at rest (**a**), an image at a approximately corresponding location from the Visible Human dataset (**b**), leading eigenvector images corresponding to the coronal morphological image at rest (**c**), and in plantarflexion (**d**). In the Visible Human image (**b**), the soleus is outlined in *solid green*, the *blue dotted lines* correspond to the anterior soleus. The compartments identified in the visible human are posterior soleus (*arrow 1*), the medial anterior soleus (*arrow 2*), the median septum (*arrow 3*), and the lateral anterior soleus (*arrow 4*). These compartments are also identified on the eigenvector image at rest (**c**) with the same arrow labels as in **b**. On plantar flexion there are large fiber orientation changes in both compartments of the anterior soleus and in the posterior soleus visualized as a change of colors in **d**. *Short arrowheads* (*solid* for posterior soleus and *unfilled* for anterior soleus indicate the respective regions in the rest and plantarflexed state)

method for fiber tracking; in their approach, seed points were not manually placed (as in most other fiber tracking studies) but were automatically generated from the aponeurosis surface for the muscle of interest (Lansdown et al. 2007). They determined pennation angles automatically from seed points close to the aponeurosis of origin for the deep and superficial compartment of the TA. They report that the pennation angle decreased from 16.3° (SD: 6.9) to 11.4° (SD: 5.0) along the muscle's superior-to-inferior direction. The mean value of the pennation angle was greater in the

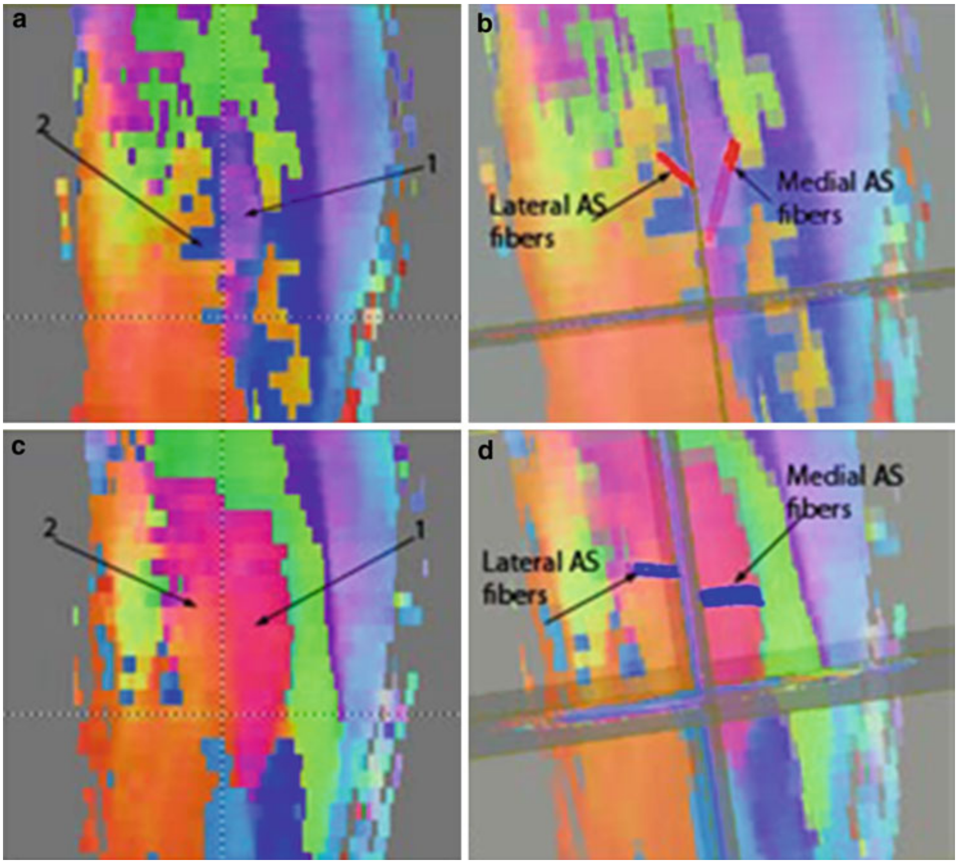

Fig. 9 Coronal color map of the lead eigenvector at neutral (**a**) and at plantar flexion (**b**) with *arrows* showing the anterior soleus medial and lateral subcompartments (*arrows 1* and *2*, respectively) separated by the median septum. A *vertical dotted line* is placed at the location of the median septum. Fibers (in *red* for neutral and in *blue* for plantarflexed ankle positions) tracked from seed points located in the lateral and medial subcompartments of the anterior soleus in the neutral (**c**) and in the plantarflexed positions (**d**). Fiber colors are assigned by the user so as to maximize the contrast with the underlying eigenvector images

deep than in the superficial compartment. In an extension of this work, Heemskerk et al. used quantitative criteria to assess fiber tracking in the deep and superficial compartments of the TA (Heemskerk et al. 2009). Quantitative criteria for fiber tracking included the presence and similarity of fibers to neighboring tracts, length of fibers including only those that terminated close (within two voxels) to the muscle border (Fig. 6). They also evaluated SNR requirements and optimized the fiber tracking parameters including termination criteria of FA ($0.15 < \mathrm{FA} < 0.75$) and curvature (<45°). They conclude that SNR levels of 106 and 147 in the superficial and deep compartments were sufficient for generating fibers that covered 89.4 ± 9.6 % and 75.0 ± 15.2 % of the aponeurosis area in the superficial and deep compartments, respectively. A more recent paper by the same group deals with the reproducibility of fiber tracts in the TA (Heemskerk et al. 2010). They determined that while the repeatability of the diffusion indices (MD, FA, eigenvalues) is very good, the repeatability of the architectural measurements (pennation angle and fiber length) is acceptable. This emphasizes the fact that fiber tracking is challenging and extraction of quantitative architectural parameters should be approached with a robust acquisition scheme (high SNR, good fat suppression, low distortions) and rigorous post-processing algorithms.

The importance of optimized image acquisition and post-processing to reduce noise, correct for eddy current, and susceptibility-induced distortions has also been emphasized by Froeling et al. (2012). The latter study showed that significant improvements in forearm fiber tracking as well as in diffusion indices resulted from the post-processing corrections. They employed several post-processing steps including signal-to-noise improvement by a Rician noise suppression algorithm, image registration to correct for motion and eddy currents, and correction of susceptibility-induced deformations using magnetic field inhomogeneity maps. Fibers were generated using a custom built tool, the DTITool program (http://bmia.bmt.tue.nl/software/dtitool) from 1 to 5 seeding ROIs per muscle (van Aart et al. 2011). The angular change per integration step was limited to <5° per step, which restricts fiber curvature rather severely. Figure 7 shows the marked improvements in fiber tractography with the implementation of the post-processing tools.

Sinha et al. reported on the complex architecture within the soleus; this study also identified the potential for DTI studies to map fibers under rest and plantarflexion conditions (Sinha et al. 2011). It should be noted that compared to the TA and the muscles of the forearm, the soleus architecture is much more complex and presents additional challenges in fiber tracking. The soleus has posterior and anterior

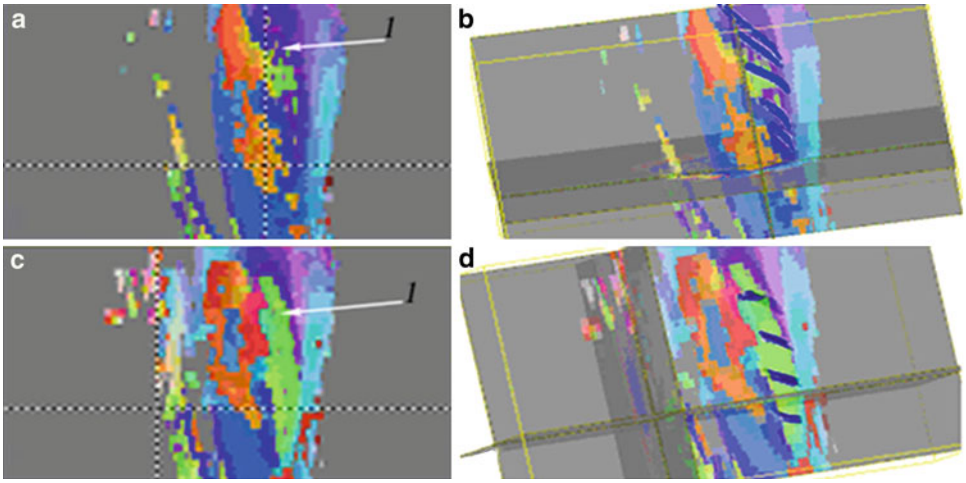

Fig. 10 Sagittal color map at rest (**a**) and at plantar flexion (**c**) with *arrow* showing the posterior soleus. The color maps show that the posterior soleus has a stronger anterior–posterior orientation at plantarflexion. Fibers (in *blue*) tracked from seed points located along the length of the posterior soleus run anterosuperior to posteroinferior in both rest (**b**) and plantarflexion (**d**); in the *latter* the fibers are shorter with larger pennation angles (**d**)

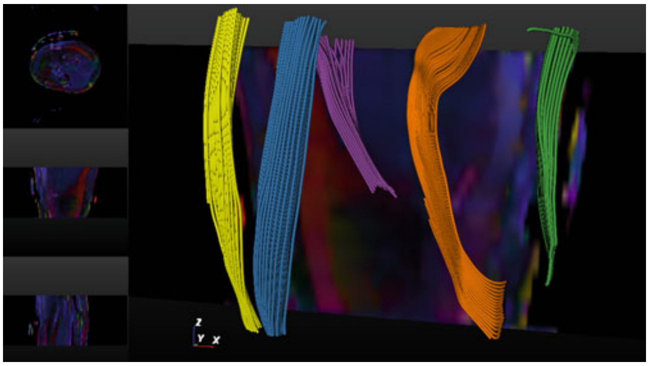

Fig. 11 Fibers tracked from seed points in each muscle compartment using DTITool. Fibers in each compartment are shown in different color to facilitate visualization. Fibers are overlaid on the color FA map to provide an anatomical reference. Fibers are colored as follows: *yellow* (superficial anterior tibialis), *blue* (deep anterior tibialis), *purple* (lateral gastrocnemius), *brown* (soleus), *green* (medial gastrocnemius)

compartments; 3D cadaveric analysis had shown that the anterior soleus is bipennate with the fiber bundles joining the median septum and the anterior aponeurosis (Agur et al. 2003). Figure 8 shows lead eigenvector DTI images from the soleus under rest and plantarflexion states. A qualitative comparison to the 3D cadaveric analysis by Agur et al. identifies three muscle compartments: posterior, anterior, and marginal soleus (Agur et al. 2003). The eigenvector directions and compartments from the DTI data (Fig. 8) agreed with the fiber directions inferred earlier using the Visible Human dataset by Hodgson et al. (Hodgson et al. 2006). In the latter paper, fibers were identified indirectly from the direction of the fascicles and can thus be only considered as rough indicators of fiber direction. Agur et al. identify the posterior soleus fiber bundles as attaching to the posterior surface of the anterior aponeurosis and to the anterior surface of the posterior aponeurosis. The fiber bundles are directed from anterosuperior to posteroinferior. This direction is confirmed in the eigenvector images (Fig. 8). Agur et al. also identify the anterior soleus as bipennate where the fiber bundles join the median septum and the anterior aponeurosis (Agur et al. 2003). The median septum is a tapering vertical sheet of aponeurosis with fiber bundles attaching to the medial and lateral surfaces and directed superomedially and superolaterally. The bipennate structure, the median septum as well as the superomedial and superolateral directions of the anterior soleus are confirmed by the eigenvector visualization (Fig. 8) and the fiber tracts (Fig. 9). Fiber tracking in the compartments in the posterior soleus under rest and plantarflexion are shown in Fig. 10. In both the anterior and posterior soleus, fiber orientation changes are such that fibers oriented primarily along the proximal–distal (superior–inferior) directions in the neutral position change to either a medial–lateral (anterior soleus) or an anteroposterior (posterior soleus) direction. As the aponeurosis runs approximately parallel to the proximal–distal direction, the directional change seen in both the posterior and anterior soleus translates to larger pennation angles.

Figure 11 shows fiber tracks generated in all the lower calf muscles using DTITool. The diffusion tensor was smoothed using a log anisotropic diffusion filter prior to tracking and post processing included eddy current and motion correction algorithms. This figure shows that with optimized image acquisition and post-processing methods, robust delineation of fibers is possible.

8.1 Fiber Pennation Angles and Fiber Lengths

The report by Heemskerk et al. is a comprehensive evaluation of fiber lengths and pennation angles (Heemskerk et al. 2009). They divided the aponeurosis surface of the deep and superficial compartments of the TA into 15 segments and reported the average values of the fiber lengths and pennation angles in each segment. Fiber lengths ranged

Table 1 Reproducibility of medial gastrocnemius fiber architecture at 1.5 T

	Fiber length (mm)		X (°)		Y (°)		Z (°)	
	N	PF	N	PF	N	PF	N	PF
Mean	44.56	29.86	79.88	71.78	99.88	98.40	16.13	26.33
STD	3.71	5.26	2.24	5.94	3.69	4.80	3.58	5.68
CV-av	6.34	10.35	2.80	8.20	3.94	4.78	22.59	16.57
RC-av	7.68	8.83	6.19	16.27	10.92	12.98	10.18	12.69

Reprinted with permission from Sinha and Sinha (2011)

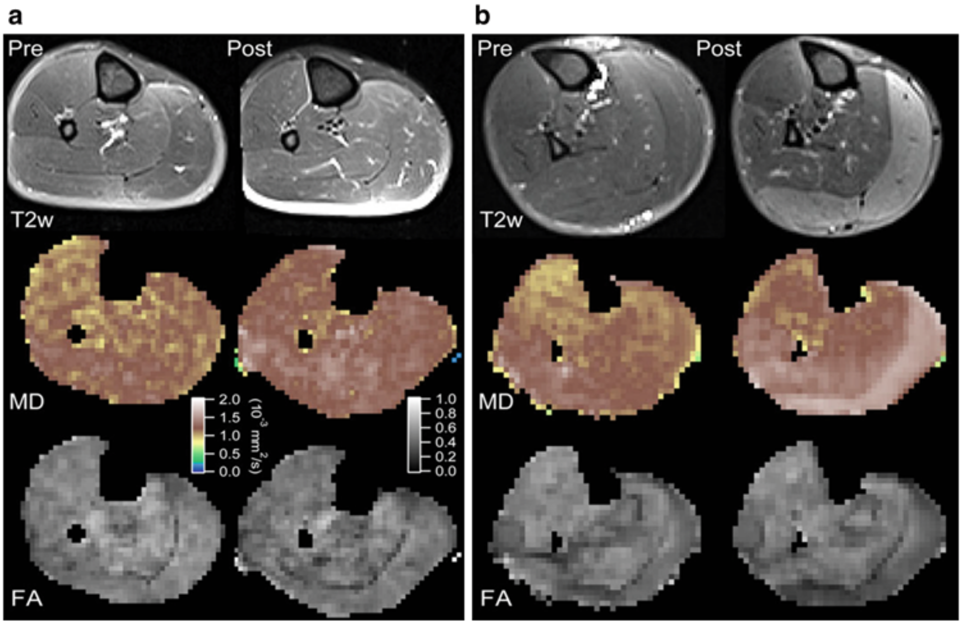

Fig. 12 T2-weighted MRI and DTI in a healthy volunteer (**a**) and a CECS patient (**b**). Right calf muscle before (pre) and after (post) treadmill exercise [Reprinted with permission from Sigmund et al. (2013)]

from 60 to 120 mm in the superficial compartment with longer fiber occurring more distally and the pennation angle (18–20°) peaked in the mid-portion along the length of the TA. Similar patterns were seen for the deep compartment of the TA with the exception of the pennation angle which had the lowest value in the mid-section of the muscle.

Sinha et al. report a preliminary estimate of fiber lengths (averaged over three subjects) in the neutral and plantarflexed positions for the soleus: posterior soleus: 21.8 ± 2.7 mm (neutral) and 17.7 ± 3.1 mm (plantarflexed); anterior medial soleus: 19.31 ± 3.4 mm (neutral) and 20.04 ± 2.9 mm (plantarflexed); anterior lateral soleus: 10.69 ± 2.6 mm (neutral) and 14.47 ± 2.8 mm (plantarflexed). As anticipated, the posterior soleus fibers decrease in length on contraction. However, the changes in the anterior soleus are contradictory as the fiber length increases on contraction. This can be explained by the fact the anterior soleus cross-section increases (at the location where the fibers were tracked) in the plantarflexed ankle position (Fig. 8). The soleus fiber lengths in the neutral and plantarflexed positions from this study are lower than that reported by Martin et al. using ultrasound measurements (Martin et al. 2001). One reason advanced by the authors for lower fiber lengths is that a very low threshold was set for angular changes of successive fiber orientations to prevent fibers being tracked across the different muscle subcompartments. This low threshold may have prevented fibers from tracking across voxels with even moderate changes in curvature, leading to shorter fiber lengths.

Sinha et al. have also reported on fiber architecture for the mGM, MG in the neutral and plantarflexed state (Sinha and Sinha 2011). They found fiber tracking to be most robust from seed points positioned (on coronal images) 45–55 mm from the most distal aspect of the MG and just adjacent to the aponeurosis of insertion in a coronal view. Seed voxel selection influenced fiber lengths more than the fiber orientation since many seed voxels lead to early termination of correctly oriented fibers. This was true especially for the most distal regions of the MG. The mean fiber length and fiber orientation of the tracked fibers in the MG

(Table 1) compare well with the ultrasound measurements on MG fiber length and pennation angles in the relaxed and contracted state (Muramatsu et al. 2002). The latter study reported the fiber length in the relaxed/contracted state as 43.6 ± 8.6 mm/27.7 ± 5.6 mm which is comparable to the values in Table 1.

9 Diffusion-Weighted and Diffusion Tensor Imaging in Muscle Injury

DWI and DTI have been used to monitor muscle injury in animal models and humans. Bley et al. have a recent review on diffusion-weighted imaging applied to MSK trauma, tumors, and inflammation (Bley et al. 2009). Line scan diffusion imaging of denervated rat muscle showed the potential of early detection of peripheral nerve injury before changes can be detected on T2 weighted MRI or electromyography (Yamabe et al. 2007). Heemskerk et al. have monitored dynamic changes in T2 and DTI indices after femoral artery ligation (Heemskerk et al. 2007). ADC increased immediately after ischemia was induced and then recovered to baseline values as muscle regeneration occurred. DTI was also performed on healthy and dystrophic skeletal muscle after lengthening contractions on mouse models at 7 T. The latter study found greater increases in ADC and decreases in FA in dystrophic than normal muscle which reflected the larger loss in torque in the dystrophic muscle (McMillan et al. 2011). Esposito et al. recently reported that multiparametric MRI can be used to monitor inflammatory and structural muscle changes in mice models (7 T); increases in T2 and FA were observed in response to inflammatory infiltration and muscle regeneration in the transient response of the tissue to acute injury and in age-related sarcopenia (Esposito et al. 2013).

ADC and FA have been shown to increase after lengthening contractions in human skeletal muscle (Nakai et al. 2008). Zaraiskaya et al. were one of the first to report on DTI evaluation of human muscle injury. They reported an increase in ADC and marked decrease in FA in the soleus and gastrocnemius muscles after calf muscle injury (Zaraiskaya et al. 2006). A recent report showed that DT-MRI (ADC and FA) can detect changes in muscle structure after eccentric exercise; DTI changes correlated with histological indices obtained by muscle biopsy (Cermak et al. 2012). The utility of DWI in monitoring inflammatory myopathies has also been reported (Qi et al. 2008). Sigmund et al. recently reported DTI measurements in CECS of the Lower Leg Muscles; they found that all diffusivities significantly increased ($P < 0.0001$) and FA decreased ($P = 0.0014$) with exercise (Fig. 12). In normal the increase in MD was significantly less than that in subjects with CECS (Sigmund et al. 2013).

10 Conclusion

Diffusion-weighted and diffusion tensor imaging of the muscle are emerging as potential tools to characterize muscle structure and relate to functional status. The methodology to extract diffusion indices is now well established and has been shown to have sufficient reproducibility to track changes that occur with disease states. There have been relatively few applications of this powerful method in the clinical setting. However, the technology is mature enough for application to monitor conditions such as sarcopenia, compartmental syndrome, myopathies, and disuse atrophy.

While diffusion indices can be extracted rather reliably, fiber tracking is a more challenging task. In order to establish fiber architecture from diffusion tensor imaging on a clinical footing, more large-scale studies on reproducibility of these parameters needs to be established. This will include further technical improvements in acquisition and in postprocessing. However, many of the tools are already available and a focused effort at establishing the guidelines for tractography may enable clinical studies using this method. In summary, DWI and DTI of muscle open a range of possibilities for assessing muscle structure and its changes with normal aging and in disease conditions.

References

Agur AM, Ng-Thow-Hing V, Ball KA, Fiume E, McKee NH (2003) Documentation and three-dimensional modeling of human soleus muscle architecture. Clin Anat 16:285–293. doi:10.1002/ca.10112

Aja-Fernandez S, Niethammer M, Kubicki M, Shenton ME, Westin CF (2008) Restoration of DWI data using a Rician LMMSE estimator. IEEE Trans Med Imaging 27:1389–1403. doi:10.1109/TMI.2008.920609

Alexander AL, Lee JE, Lazar M, Field AS (2007) Diffusion tensor imaging of the brain. Neurotherapeutics 4:316–329. doi:10.1016/j.nurt.2007.05.011

Arsigny V, Fillard P, Pennec X, Ayache N (2006) Log-euclidean metrics for fast and simple calculus on diffusion tensors. Magn Reson Med 56:411–421. doi:10.1002/mrm.20965

Assaf Y, Pasternak O (2008) Diffusion tensor imaging (DTI)-based white matter mapping in brain research: a review. J Mol Neurosci 34:51–61. doi:10.1007/s12031-007-0029-0

Azizi E, Brainerd EL, Roberts TJ (2008) Variable gearing in pennate muscles. Proc Natl Acad Sci U S A 105:1745–1750. doi:10.1073/pnas.0709212105

Basser PJ, Jones DK (2002) Diffusion-tensor MRI: theory, experimental design and data analysis—a technical review. NMR Biomed 15:456–467

Basser PJ, Pajevicz S (2000) Statistical artifacts in diffusion tensor MRI (DT-MRI) caused by background noise. Magn Reson Med 44:41–50. doi:10.1002/1522-2594(200007)44:1<41::AID-MRM8>3.0.CO;2-O

Basser PJ, Pajevic S, Pierpaoli C, Duda J, Aldroubi A (2000) In vivo fiber tractography using DT-MRI data. Magn Reson Med 44:625–632

Behrens TEJ, Woolrich MW, Jenkinson M et al (2003) Characterization and propagation of uncertainty in diffusion weighted MR imaging. Magn Reson Med 50:1077–1088. doi:10.1002/mrm.10609

Bennett IJ, Rypma B (2013) Advances in functional neuroanatomy: a review of combined DTI and FMRI studies in healthy younger and older adults. Neurosci Biobehav Rev 37:1201–1210. doi:10.1016/j.neubiorev.2013.04.008

Bley TA, Wieben O, Uhl M (2009) Diffusion-weighted MR imaging in musculoskeletal radiology: applications in trauma, tumors, and inflammation. Magn Reson Imaging Clin N Am 17:263–275. doi:10.1016/j.mric.2009.01.005

Budzik JF, Le Thuc V, Demondion X, Morel M, Chechin D, Cotten A (2007) In vivo MR tractography of thigh muscles using diffusion imaging: initial results. Eur Radiol 17:3079–3085. doi:10.1007/s00330-007-0713-z

Cermak NM, Noseworthy MD, Bourgeois JM, Tarnopolsky MA, Gibala MJ (2012) Diffusion tensor MRI to assess skeletal muscle disruption following eccentric exercise. Muscle Nerve 46:42–50. doi:10.1002/mus.23276

Chi SW, Hodgson J, Chen JS, Reggie Edgerton V, Shin DD, Roiz RA, Sinha S (2010) Finite element modeling reveals complex strain mechanics in the aponeuroses of contracting skeletal muscle. J Biomech 43:1243–1250. doi:10.1016/j.jbiomech.2010.01.005

Damon BM (2008) Effects of image noise in muscle diffusion tensor (DT)-MRI assessed using numerical simulations. Magn Reson Med 60:934–944. doi:10.1002/mrm.21707

Damon BM, Ding Z, Anderson AW, Freyer AS, Gore JC (2002) Validation of diffusion tensor MRI-based muscle fiber tracking. Magn Reson Med 48:97–104. doi:10.1002/mrm.10198

Deux JF, Malzy P, Paragios N et al (2008) Assessment of calf muscle contraction by diffusion tensor imaging. Eur Radiol 18:2303–2310. doi:10.1007/s00330-008-1012-z

Drace JE, Pelc NJ (1994) Tracking the motion of skeletal muscle with velocity encoded MR imaging. J Magn Reson Imaging 4:773–778 PMID: 7865936

Einstein A (1956) Investigations on the theory of the Brownian movement. Dover, New York

Englund EK, Elder CP, Xu Q, Ding Z, Damon BM (2011) Combined diffusion and strain tensor MRI reveals a heterogeneous, planar pattern of strain development during isometric muscle contraction. Am J Physiol Regul Integr Comp Physiol 300:R1079–R1090. doi:10.1152/ajpregu.00474.2010

Esposito A, Campana L, Palmisano A, De Cobelli F, Canu T, Santarella F, Colantoni C, Monno A, Vezzoli M, Pezzetti G, Manfredi AA, Rovere-Querini P, Maschio AD (2013) Magnetic resonance imaging at 7 T reveals common events in age-related sarcopenia and in the homeostatic response to muscle sterile injury. PLoS ONE 8:e59308. doi:10.1371/journal.pone.0059308

Finni T, Hodgson JA, Lai AM, Edgerton VR, Sinha S (2003) Nonuniform strain of human soleus aponeurosis-tendon complex during submaximal voluntary contractions in vivo. J Appl Physiol 95:829–837. PMID: 12716873

Froeling M (2012) DTI of human skeletal muscle: from simulation to clinical implementation. PhD thesis, Department of Biomedical Engineering, Technische Universiteit Eindhoven

Froeling M, Nederveen AJ, Heijtel DF, Lataster A, Bos C, Nicolay K, Maas M, Drost MR, Strijkers GJ (2012) Diffusion-tensor MRI reveals the complex muscle architecture of the human forearm. J Magn Reson Imaging 36:237–248. doi:10.1002/jmri.23608

Galbán CJ, Maderwald S, Uffmann K, de Greiff A, Ladd ME (2004) Diffusion sensitivity to muscle architecture: a magnetic resonance diffusion tensor imaging study of the human calf. Eur J Appl Physiol 93:253–262. doi:10.1007/s00421-004-1186-2

Galbán CJ, Maderwald S, Uffmann K, Ladd ME (2005) A diffusion tensor imaging analysis of gender differences in water diffusivity within human skeletal muscle. NMR Biomed 18:489–498. doi:10.1002/nbm.975

Gharibans AA, Johnson CL, Chen DD, Georgiadis JG (2011) Reconstruction of 3D fabric structure and fiber nets in skeletal muscle via in vivo DTI. International society for magnetic resonance in medicine, Montreal, May 2011, p 1154

Gilbert RJ, Napadow VJ (2005) Three-dimensional muscular architecture of the human tongue determined in vivo with diffusion tensor magnetic resonance imaging. Dysphagia 20:1–7. doi:10.1007/s00455-003-0505-9

Hagmann P, Jonasson L, Maeder P, Thiran JP, Wedeen VJ, Meuli R (2006) Understanding diffusion MR imaging techniques: from scalar diffusion-weighted imaging to diffusion tensor imaging and beyond. Radiographics 26(Suppl 1):S205–S223. doi:10.1148/rg.26si065510

Hatakenaka M, Yabuuchi H, Matsuo Y et al (2008) Effect of passive muscle length change on apparent diffusion coefficient: detection with clinical MR imaging. Magn Reson Med Sci 7:59–63. pii:JST.JSTAGE/mrms/7.59

Heemskerk A, Drost M, van Bochove G et al (2006) DTI-based assessment of ischemia-reperfusion in mouse skeletal muscle. Magn Reson Med 56:272–281. doi:10.1002/mrm.20953

Heemskerk A, Strijkers G, Drost M, van Bochove G, van Nicolay K (2007) Skeletal muscle degeneration and regeneration after femoral artery ligation in mice: monitoring with diffusion MR imaging. Radiology 243:413–421. doi:10.1148/radiol.2432060491

Heemskerk AM, Sinha TK, Wilson KJ, Ding Z, Damon BM (2009) Quantitative assessment of DTI-based muscle fiber tracking and optimal tracking parameters. Magn Reson Med 61:467–472. doi:10.1002/mrm.21819

Heemskerk AM, Sinha TK, Wilson KJ, Ding Z, Damon BM (2010) Repeatability of DTI-based skeletal muscle fiber tracking. NMR Biomed 23:294–303. doi:10.1002/nbm.1463

Hodgson JA, Finni T, Lai AM, Edgerton VR, Sinha S (2006) Influence of structure on the tissue dynamics of the human soleus muscle observed in MRI studies during isometric contractions. J Morphol 267:584–601. doi:10.1002/jmor.10421

Karampinos DC, King KF, Sutton BP, Georgiadis JG (2007) In vivo study of cross-sectional skeletal muscle fiber asymmetry with diffusion-weighted MRI. Conf Proc IEEE Eng Med Biol Soc 2007:327–330. doi:10.1109/IEMBS.2007.4352290

Karampinos DC, King KF, Sutton BP, Georgiadis JG (2009) Myofiber ellipticity as an explanation for transverse asymmetry of skeletal muscle diffusion MRI in vivo signal. Ann Biomed Eng 37:2532–2546. doi:10.1007/s10439-009-9783-1

Karampinos DC, Banerjee S, King KF, Link TM, Majumdar S (2012) Considerations in high-resolution skeletal muscle diffusion tensor imaging using single-shot echo planar imaging with stimulated-echo preparation and sensitivity encoding. NMR Biomed 25:766–778. doi:10.1002/nbm.1791

Lansdown DA, Ding Z, Wadington M, Hornberger JL, Damon BM (2007) Quantitative diffusion tensor MRI-based fiber tracking of human skeletal muscle. J Appl Physiol 103:673–681. doi:10.1152/japplphysiol.00290.2007

Lazar M (2010) Mapping brain anatomical connectivity using white matter tractography. NMR Biomed 23:821–835. doi:10.1002/nbm.1579

Leemans A, Jones DK (2009) The B-matrix must be rotated when correcting for subject motion in DTI data. Magn Reson Med 61:1336–1349. doi:10.1002/mrm.21890

Levin DI, Gilles B, Mädler B, Pai DK (2011) Extracting skeletal muscle fiber fields from noisy diffusion tensor data. Med Image Anal 15:340–353. doi:10.1016/j.media.2011.01.005

Maganaris CN, Baltzopoulos V, Sargeant AJ (1998) In vivo measurements of the triceps surae complex architecture in man: implications for muscle function. J Physiol 512:603–614. PMID: 9763648

Malcolm JG, Shenton ME, Rathi Y (2010) Filtered multi-tensor tractography. IEEE Trans Med Imaging 29:1664–1675. doi:10.1109/TMI.2010.2048121

Martin DC, Medri MK, Chow RS, Oxorn V, Leekam RN, Agur AM, McKee NH (2001) Comparing human skeletal muscle architectural parameters of cadavers with in vivo ultrasonographic measurements. J Anat 199:429–434. PMID: 11693303

McMillan AB, Shi D, Pratt SJ, Lovering RM (2011) Diffusion tensor MRI to assess damage in healthy and dystrophic skeletal muscle after lengthening contractions. J Biomed Biotechnol 2011:970726. doi:10.1155/2011/970726

Mori S, Barker PB (1999) Diffusion magnetic resonance imaging: its principle and applications. Anat Rec 257:102–109. doi:10.1002/(SICI)1097-0185(19990615)257:3<102::AID-AR7>3.0.CO;2-6

Mori S, van Zijl PC (2002) Fiber tracking: principles and strategies—a technical review. NMR Biomed 15:468–480. doi:10.1002/nbm.781

Mori S, Crain BJ, Chacko VP et al (1999) Three-dimensional tracking of axonal projections in the brain by magnetic resonance imaging. Ann Neurol 45:265–269 PMID: 9989633

Mukherjee P, McKinstry RC (2006) Diffusion tensor imaging and tractography of human brain development. Neuroimaging Clin N Am 16:19–43. doi:10.1016/j.nic.2005.11.004

Muramatsu T, Muraoka T, Kawakami Y, Shibayama A, Fukunaga T (2002) In vivo determination of fascicle curvature in contracting human skeletal muscles. J Appl Physiol 92:129–134. PMID: 11744651

Nakai R, Azuma T, Sudo M, Urayama S, Takizawa O, Tsutsumi S (2008) MRI analysis of structural changes in skeletal muscles and surrounding tissues following long-term walking exercise with training equipment. J Appl Physiol 105:958–963. doi:10.1152/japplphysiol.01204.2007

Napadow VJ, Chen Q, Mai V, So PT, Gilbert RJ (2001) Quantitative analysis of three-dimensional resolved fiber architecture in heterogeneous skeletal muscle tissue using NMR and optical imaging methods. Biophys J 80:2968–2975. doi:10.1016/S0006-3495(01)76262-5

O'Donnell LJ, Westin CF (2011) An introduction to diffusion tensor image analysis. Neurosurg Clin N Am 22:185–196. doi:10.1016/j.nec.2010.12.004

Okamoto Y, Kunimatsu A, Kono T, Nasu K, Sonobe J, Minami M (2010) Changes in MR diffusion properties during active muscle contraction in the calf. Magn Reson Med Sci 9:1–8. pii:JST.JSTAGE/mrms/9.1

Qi J, Olsen NJ, Price RR, Winston JA, Park JH (2008) Diffusion weighted imaging of the inflammatory myopathies: polymyositis and dermatomyositis. J Magn Reson Imaging 27:212–217. doi:10.1002/jmri.21209

Pappas GP, Asakawa DS, Delp SL, Zajac FE, Drace JE (2002) Nonuniform shortening in the biceps brachii during elbow flexion. J Appl Physiol 92:238123–238129. doi: 10.1152/japplphysiol.00843.2001

Saupe N, White LM, Stainsby J, Tomlinson G, Sussman MS (2009) Diffusion tensor imaging and fiber tractography of skeletal muscle: optimization of B value for imaging at 1.5 T. Am J Roentgenol 192:W282–W290. doi:10.2214/AJR.08.1340

Schwenzer NF, Steidle G, Martirosian P, Schraml C, Springer F, Claussen CD, Schick F (2009) Diffusion tensor imaging of the human calf muscle: distinct changes in fractional anisotropy and mean diffusion due to passive muscle shortening and stretching. NMR Biomed 22:1047–1053. doi:10.1002/nbm.1409

Scollan DF, Holmes A, Winslow R, Forder J (1998) Histological validation of myocardial microstructure obtained from diffusion tensor imaging. Am J Physiol 275:H2308–H2318 PMID: 9843833

Shenton ME, Hamoda HM, Schneiderman JS, Bouix S, Pasternak O, Rathi Y, Vu MA, Purohit MP, Helmer K, Koerte I, Lin AP, Westin CF, Kikinis R, Kubicki M, Stern RA, Zafonte R (2012) A review of magnetic resonance imaging and diffusion tensor imaging findings in mild traumatic brain injury. Brain Imaging Behav 6:137–192. doi:10.1007/s11682-012-9156-5

Shin D, Finni T, Ahn S, Hodgson JA, Lee HD, Edgerton VR, Sinha S (2008) Effect of chronic unloading and rehabilitation on human achilles tendon properties: a velocity-encoded phase-contrast MRI study. J Appl Physiol 105:1179–1186. doi:10.1152/japplphysiol.90699.2008

Sigmund EE, Sui D, Ukpebor O, Baete S, Fieremans E, Babb JS, Mechlin M, Liu K, Kwon J, McGorty K, Hodnett PA, Bencardino J (2013) Stimulated echo diffusion tensor imaging and SPAIR T(2)-weighted imaging in chronic exertional compartment syndrome of the lower leg muscles. J Magn Reson Imaging. doi:10.1002/jmri.24060

Sinha S, Sinha U (2011) Reproducibility analysis of diffusion tensor indices and fiber architecture of human calf muscles in vivo at 1.5 tesla in neutral and plantarflexed ankle positions at rest. J Magn Reson Imaging 34:107–119. doi:10.1002/jmri.22596

Sinha S, Sinha U, Edgerton VR (2006) In vivo diffusion tensor imaging of the human calf muscle. J Magn Reson Imaging 24:182–190. doi:10.1002/jmri.20593

Sinha U, Sinha S, Hodgson JA, Edgerton RV (2011) Human soleus muscle architecture at different ankle joint angles from magnetic resonance diffusion tensor imaging. J Appl Physiol 110:807–819. doi:10.1152/japplphysiol.00923.2010

Sinha U, Moghadassi A, Sinha S (2012) Strain rate mapping of the lower leg muscles during plantarflexion excursion using MR velocity mapping. Int Soc Magn Res Med, Melbourne, Australia. May 2012

Tseng WY, Wedeen VJ, Reese TG, Smith RN, Halpern EF (2003) Diffusion tensor MRI of myocardial fibers and sheets: correspondence with visible cut-face texture. J Magn Reson Imaging 17:31–42. doi:10.1002/jmri.10223

van Aart E, Sepasian N, Jalba A, Vilanova A (2011) CUDA-accelerated geodesic ray-tracing for fiber tracking. Int J Biomed Imaging 2011:698908. doi:10.1155/2011/698908

Williams SE, Heemskerk AM, Welch EB, Li K, Damon BM, Park JH (2013) Quantitative effects of inclusion of fat on muscle diffusion tensor MRI measurements. J Magn Reson Imaging. doi:10.1002/jmri.24045

Yamabe E, Nakamura T, Oshio K, Kikuchi Y, Toyama Y, Ikegami H (2007) Line scan diffusion spectrum of the denervated rat skeletal muscle. J Magn Reson Imaging 26:1585–1589. doi:10.1002/jmri.21184

Zaraiskaya T, Kumbhare D, Noseworthy MD (2006) Diffusion tensor imaging in evaluation of human skeletal muscle injury. J Magn Reson Imaging 24:402–408. doi:10.1002/jmri.20651

Assessment of Skeletal Muscle Microperfusion Using MRI

Sasan Partovi, Bjoern Jacobi, Yaron Gordon, Lisa Zipp, Anja-Carina Schulte, Sasan Karimi, Rolf Huegli, and Deniz Bilecen

Contents

1 **Keypoints** 88

2 **Part 1 Skeletal Muscle BOLD MRI** 88
2.1 General Principles of BOLD MRI 88
2.2 Clinical Applications of BOLD MRI 94

3 **Part 2 Arterial Spin Labeling MRI** 96
3.1 General Principles of ASL 96
3.2 Technical Principles 98
3.3 Clinical Applications of ASL 100

4 **Part 3 Dynamic Contrast Enhanced (DCE)-MRI** 101
4.1 General Principles of Dynamic Contrast Enhanced (DCE)-MRI 101
4.2 Dynamic Susceptibility MRI 105
4.3 Investigations of the Musculoskeletal System with DCE-MRI Techniques 107

5 **Conclusion** 109

References 109

Abstract

Blood oxygenation level-dependent (BOLD) MRI, arterial spin labeling (ASL) and dynamic contrast enhancement (DCE) are current magnetic resonance imaging (MRI) techniques allowing the non-invasive functional assessment of peripheral microvasculature in healthy and diseased individuals. The functional imaging of skeletal muscle microvasculature helps to understand muscular and vascular physiology and alterations of microcirculation under certain pathological conditions such as peripheral arterial occlusive disease, diabetes mellitus, chronic compartment syndrome and rheumatic disorders. BOLD MRI uses blood as an endogenous contrast agent provided by the different magnetic properties of oxy- and deoxyhemoglobin. The BOLD contrast in skeletal muscle tissue primarily arises from the microcirculation yielding a very sensitive tool for alterations of the physiological oxygen supply and demand. However, the complex nature of the BOLD contrast's origin also entails a variety of variables complicating the interpretation of BOLD signal changes. ASL's ability to directly measure muscle perfusion may prove to be a powerful tool for the evaluation of disease progression and the evaluation of therapies aimed at improving muscle perfusion. As is the case with BOLD MRI, this holds particularly true for patients who are unable to receive contrast agents, a collective which is often afflicted with vascular impairments. Dynamic contrast enhanced MRI may contribute considerably to objectively evaluate many musculoskeletal diseases through its ability to measure multiple microvascular properties. The potential of these three MRI methods to non-invasively assess disease severity and the efficacy of new therapeutic strategies, such as stem cell and gene therapy, renders them as very appealing future research targets.

S. Partovi · L. Zipp · A.-C. Schulte · R. Huegli · D. Bilecen (✉)
Department of Radiology and Nuclear Medicine,
University Hospital Bruderholz, Bottmingen, Switzerland
e-mail: deniz.bilecen@unibas.ch

S. Partovi
Department of Radiology,
University Hospitals Case Medical Center,
Case Western Reserve University,
Cleveland, OH, USA

B. Jacobi
Third Department of Medicine-Hematology,
Oncology, Pneumology, University Medical Center of Johannes
Gutenberg-University, Mainz, Germany

Y. Gordon
Department of Diagnostic and Interventional Radiology,
University Hospital Heidelberg, Heidelberg, Germany

L. Zipp
Department of Pediatrics,
Rainbow Babies and Chidren's Hospital,
Cleveland, OH, USA

S. Karimi
Department of Neuroradiology,
Memorial Sloan-Kettering Cancer Center,
New York, NY, USA

M.-A. Weber (ed.), *Magnetic Resonance Imaging of the Skeletal Musculature*, Medical Radiology. Diagnostic Imaging,
DOI: 10.1007/174_2013_911, © Springer-Verlag Berlin Heidelberg 2013

Published Online: 20 September 2013

1 Keypoints

1. BOLD MRI of skeletal muscle tissue relies on the intravascular ratio between deoxy- and oxyhemoglobin primarily in small muscle vessels. This ratio is dependent on the microcirculatory function, small vessel perfusion, blood volume, oxygen consumption, and hemoglobin content. It is measured as $T2^*$ signal in gradient echo MR sequences.
2. The muscle BOLD MRI signal is influenced by a variety of factors, among them are age, weight, physical activity, examined muscle fiber type, and the intake of vasoactive drugs.
3. Muscle BOLD MRI requires special paradigms for provoking an adequate signal which can be analyzed quantitatively. Three paradigms are currently used in the clinical arena: Arterial occlusion to provoke ischemia and reactive hyperemia, muscle exercise, and oxygen inhalation.
4. Muscle BOLD MRI shows significant differences in the $T2^*$ time course and key parameters between healthy volunteers and patients with peripheral arterial occlusive disease, chronic compartment syndrome, diabetes mellitus, or rheumatic disease, such as systemic sclerosis and granulomatosis with polyangiitis (also known as Wegener's granulomatosis).
5. ASL utilizes the selective excitement (tagging) of inflowing blood spins into a tissue of interest. Without the use of contrast agents and applying specially designed radiofrequency pulses, the inflowing tagged spins induce a measurable change in the apparent tissue $T1$, which is directly used to calculate local perfusion.
6. DCE-MRI investigates the tissues intensity response to an intravenously injected bolus of contrast agent over a period of time. By applying compartmental models to the data obtained, microvascular properties, such as fractional volumes of plasma and blood, vessel permeability and perfusion can be obtained.

2 Part 1 Skeletal Muscle BOLD MRI

2.1 General Principles of BOLD MRI

2.1.1 The BOLD Effect in Muscle Tissue

The oxygenation level of intravascular hemoglobin can be used for the assessment of muscular microcirculation (i.e., arterioles, capillaries, and venules) in magnetic resonance imaging (MRI) because of its influence on the static magnetic field (Jacobi et al. 2012). This method is called blood oxygenation level-dependent (BOLD) MRI and is derived from functional MRI of the human brain where it has been applied since the early 1990s (Ogawa et al. 1990a).

The BOLD signal is based on the principle that the hemoglobin iron ion without a coordinated oxygen molecule has unpaired electrons in its atomic shell which render deoxyhemoglobin paramagnetic. That means that deoxyhemoglobin leads to changes of the magnetic susceptibility of water protons in the vessel surrounding, whereas diamagnetic oxyhemoglobin does not (Thulborn et al. 1982; Ogawa et al. 1990b). The result is a dropout of $T2/T2^*$ weighted MR signal with an increasing ratio between intravascular deoxy- and oxyhemoglobin. Initially, this effect has been used to map functional active brain regions (Bandettini et al. 1992; Ogawa et al. 1992). In these regions, neuronal activation is accompanied by a paradoxically larger increase of local microperfusion than of neuronal oxygen consumption, an observation first made in 1986 (Fox and Raichle 1986). This coupling of neuronal activity and microperfusion results in an increase of the ratio between capillary and venous oxy- and deoxyhemoglobin, resulting in a decrease of paramagnetic species and hence a positive BOLD signal. The understanding of the main functional origin of the BOLD effect has led to a broad application of BOLD studies in functional brain imaging (Fig. 1) (Partovi et al. 2012a, e). But owing to the diverse physical and physiological factors influencing the BOLD signal in the brain, this field is still under investigation (Logothetis and Wandell 2004).

Similar to neuronal tissue, skeletal muscles offer pronounced alterations of microvascular blood flow depending on the degree of resistance vessel vasodilatation (Boushel et al. 2000). During muscular activity, local arteriolar smooth muscle contraction is mainly reduced via local mediators such as pCO_2, H^+/lactate, K^+, adenosine, NO, and recently discovered myokines such as IL-6, IL-8, and IL-15 (Sarelius and Pohl 2010; Pedersen et al. 2007). The first attempts to use these large functional variations of muscular perfusion in BOLD MR imaging were performed in the late 1990s.

In one study, an arterial occlusion paradigm (see *Paradigms and related time courses*) was applied to show that the $T2^*$ signal in a gradient echo sequence decreases during ischemia and shows a fast surge to a pronounced peak approximately 30 s after reactive hyperemia (Toussaint et al. 1996). Both effects were mainly attributed to the susceptibility effect of deoxyhemoglobin on protons in the vessel surrounding already known from BOLD studies of the human brain. This hypothesis was strengthened by the finding that mean $\Delta R2$ correlated well with perfusion as measured indirectly by MR plethysmography during reactive hyperemia. Another study from this early muscle BOLD era further supported the fact that hemoglobin oxygenation is mainly responsible for the $T2^*$ signal since the desaturation of muscle myoglobin—as measured with MR spectroscopy—started later and slower when compared

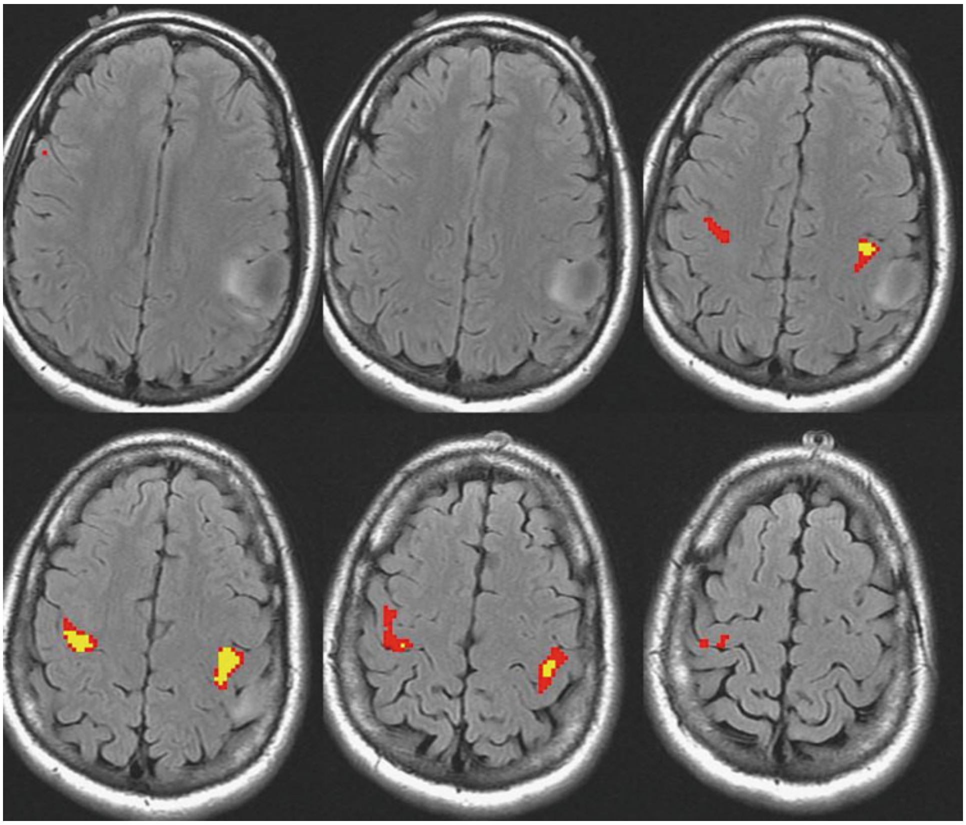

Fig. 1 BOLD MRI of the brain showing activation in motor gyrus as response to a finger tapping task. BOLD imaging in this patient with a low grade glioma was performed preoperatively for surgical planning

with the $T2^*$ signal dropout during ischemia (Lebon et al. 1998a). Given the strong functional relationship between neuronal activity and BOLD signal changes in the human brain, it is quite interesting that first comparable studies, investigating the physiological relationship between muscle contraction and $T2^*$ signal changes, were not undertaken until the beginning of the early 2000s. In a first report, specific transient $T2^*$ signal boosts were discovered in the calf after short 3 s lasting isometric muscle tension exercises with the gastrocnemius or soleus muscles (see *Paradigms and related time courses*) (Hennig et al. 2000). Interestingly, those muscular hemodynamic responses bared similar inherent time constants when compared with neuronal tissue, indicating a possible common coupling mechanism between oxygen demand and blood supply in both tissues. Another study using a comparable exercise paradigm with short muscle contractions demonstrated a good temporal correlation between stimulation induced BOLD signal surges and hemoglobin saturation as measured by near infrared spectrometry (NIRS) (Meyer et al. 2004). This correlation could even be clarified in a recent work by Towse et al. showing that hemoglobin oxygenation plays a major role in muscle BOLD signal changes, depending primarily on perfusion and blood volume (Towse et al. 2011). They proposed that—at least with regard to exercise paradigms—muscle activity induces an increase of blood volume in the local microcirculation that, depending on hemoglobin's oxygenation status, lead to a positive (in case of an increase of the oxy- to deoxyhemoglobin ratio) or negative (in case of a decrease of the oxy- to deoxyhemoglobin ratio) BOLD response.

These major determinants of the BOLD effect in skeletal muscle, i.e., hemoglobin oxygenation, perfusion, and blood volume, have also been found to play a pivotal role with regard to arterial occlusion paradigms. The increase of muscle perfusion—as measured by arterial spin labeling (ASL)—has been shown to be strongly associated with BOLD signal peaking (Duteil et al. 2006). This effect was closely dependent from the venous filling state, with extensive venous filling producing a larger BOLD response. The muscular BOLD response has also been compared with standard clinical diagnostic tools for the assessment of tissue perfusion (i.e., laser Doppler flowmetry, LDF) and oxygenation (i.e., transcutaneous oxygen pressure measurement, $TcPO_2$) (Ledermann et al. 2006a). Although LDF and $TcPO_2$ measurements are limited to superficial skin layers and do not measure perfusion or oxygenation changes in the muscle tissue, the BOLD signal in the calf muscles was closely correlated with blood flow and oxygenati on during ischemia and reactive hyperemia.

In the case that perfusion and volume dependent hemoglobin oxygenation changes are the main source of the

BOLD effect in skeletal muscle, one would expect that primarily intravascular relaxation effects are responsible for the measured $T2^*$ changes in muscle tissue. According to experimental data and numerical simulations from the last decade this is indeed the case (Meyer et al. 2004; Sanchez et al. 2010). Sanchez et al. were able to eliminate $T2^*$ changes induced by arterial occlusion using an inversion-recovery sequence to null the arterial signal, showing that a significant extravascular contribution to the bulk muscle BOLD contrast could be ruled out (Sanchez et al. 2010).

Taken together, the current evidence of skeletal muscle BOLD MRI supports a model, in which alterations of muscle perfusion lead to blood volume changes that—depending on the oxygenation status of hemoglobin—increase or decrease the $T2^*$ signal. Of course, further work will need to be done to fully understand the mechanisms yielding a BOLD response in muscle tissue. It has to be taken into account that the qualitative and especially the quantitative influence of each physiological parameter on the BOLD signal might change under different experimental conditions and imaging paradigms. However, as the skeletal muscle tissue represents the "end organ" of the peripheral vasculature, BOLD MRI is a promising and evolving imaging method for the functional evaluation of vascular diseases, such as peripheral arterial occlusive disease (PAOD), diabetes mellitus, compartment syndrome, and the majority of rheumatic diseases (Partovi et al. 2012b).

2.1.2 Technical Fundamentals of BOLD MRI

BOLD MRI of skeletal muscles is usually performed in whole body MRI scanners with magnetic field strengths ranging between 1.5 and 4 T. Consecutively, it is possible to analyze every muscle within the body, but—with regard to accessibility for cuff compression and typical clinical questions—usually arm or leg muscles are imaged. Regardless of the paradigm used, it is crucial to place the individual on the MR examiner couch for 10–15 min prior to the beginning of the examination to prevent extensive filling of venous vessels that will impact the results (Duteil et al. 2006).

As oxygenation changes appear in a short time frame, BOLD imaging needs high-speed acquisition methods. These are generally based on echo-planar imaging (EPI) (Howseman and Bowtell 1999). BOLD signal alterations of conventional single-shot EPI are sensitive to changes in $T2^*$ and $T2$—reflecting oxygenation—and initial BOLD signal intensity (S_0). S_0 is influenced by several confounding parameters such as blood inflow, changes in $T1$, and baseline drifts (Speck and Hennig 1998; Schulte et al. 2001). With Multi-echo gradient-echo EPI sequences it is possible to isolate oxygenation-related changes ($T2^*$) from these other effects (Ledermann et al. 2006b; Schulte et al. 2008). With each excitation, images at different effective echo times usually ranging between 7 and 80 ms are acquired (Jacobi et al. 2012; Ledermann et al. 2006b; Kos et al. 2009). Acquisition parameters have to be adjusted to the short $T2^*$ (<20 ms) in skeletal muscle.

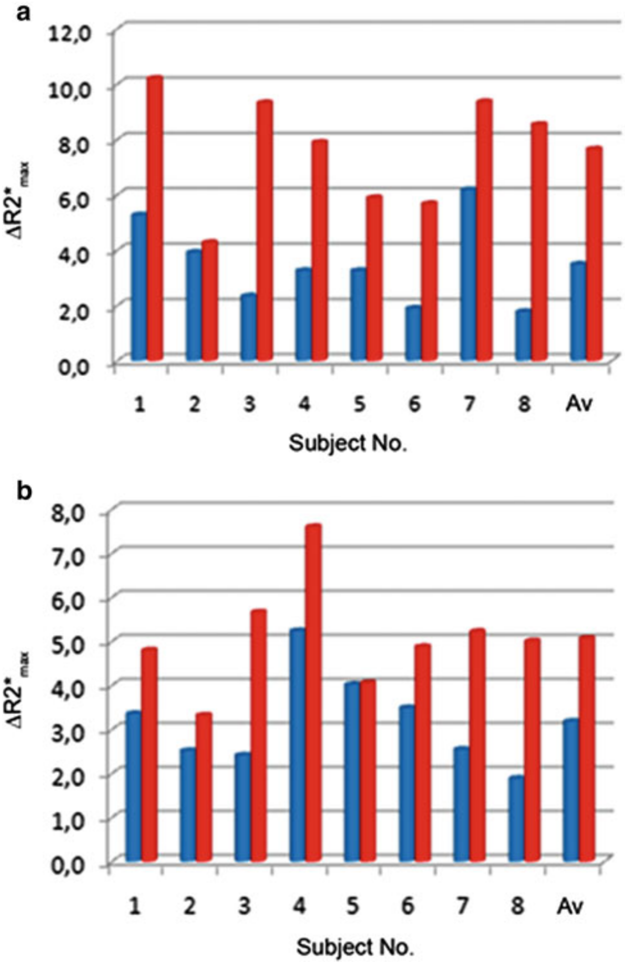

Fig. 2 $\Delta R2^*$max values at 1.5 T (*blue*) and 3.0 T (*red*) BOLD MRI of soleus **a** and gastrocnemius **b** muscle in each of the eight examined volunteers. From Partovi et al. (2012c). This material is reproduced with permission of John Wiley and Sons, Inc

Several studies have shown that the magnetic field strength has a significant impact on the extent of $R2^*$ changes in skeletal muscle in both, arterial occlusion and exercise paradigms (Meyer et al. 2004; Lebon et al. 1998b; Partovi et al. 2012c). Partovi et al. directly analyzed the relation between $\Delta R2^*$ and the magnetic field (B_0) strength using 1.5 and 3.0 T whole body scanners (Partovi et al. 2012c). This study showed a nearly proportional relationship between B_0 and $\Delta R2^*$, being in good concordance with previous studies evaluating this relationship in the human brain (Fig. 2) (Turner 1997; Gati et al. 1997; Van der Zwaag et al. 2009).

Spin echo sequences ($T2$) may also be applicable for BOLD imaging but offer a bad temporal resolution.

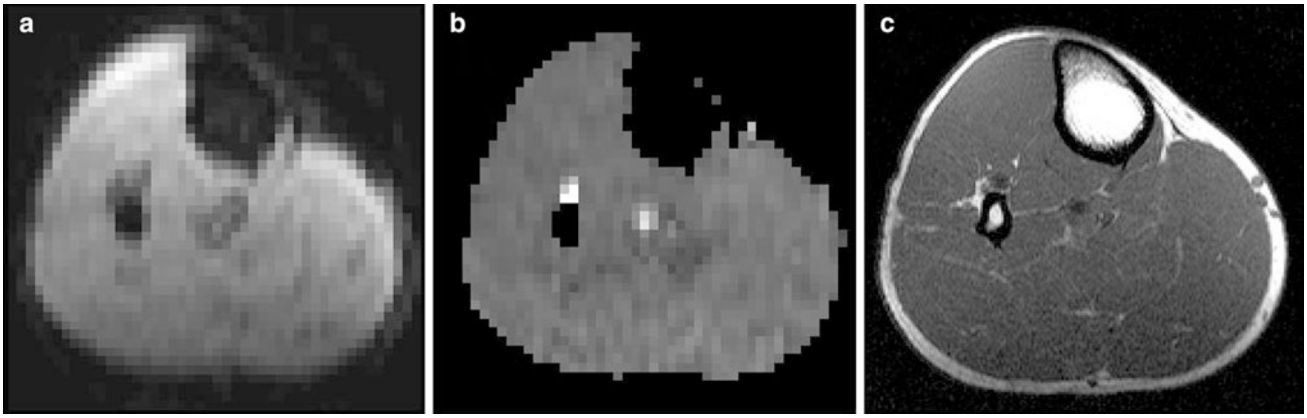

Fig. 3 Echo-planar-imaging (**a**), $T2^*$ map (**b**) and T1 anatomical reference image (**c**) of a healthy 34-year-old volunteer showing the upper region of the left calf. Anatomical reference is used to map ROIs in the $T2^*$ maps and to exclude visible vessels which could influence the BOLD signal

Additionally, gradient echo sequences emphasize local magnetic field distortions induced by paramagnetic species such as deoxyhemoglobin. To facilitate and improve the placement of the ROIs on $T2$* maps calculated from the EPI data, $T1$-weighted images of the same layers should also be obtained. With regard to the placement of regions of interest (ROI) for extracting the $T2^*$ dataset, this enables avoidance of visible vessels from the BOLD measurement to minimize inflow artifacts (Fig. 3).

2.1.3 Paradigms and Related Time Courses

BOLD imaging of skeletal muscles is based on the principle of temporal changes in the ratio between oxy- and deoxyhemoglobin inside skeletal muscle microvessels, that lead to an endogenous contrast in $T2/T2^*$ MR sequences. To provoke measurable BOLD signal alterations in skeletal muscles, different imaging paradigms have been developed. The most often applied paradigms are arterial occlusion (= cuff compression), muscle exercise, and oxygen inhalation.

Arterial occlusion is probably the most often applied imaging paradigm in skeletal muscle BOLD MRI. This may be due to its early implementation at the beginning of the evaluation of BOLD MRI in skeletal muscle tissue and several advantages when compared with other BOLD muscle MRI settings (Toussaint et al. 1996; Lebon et al. 1998a). Arterial occlusion contains a simple experimental setup, in which a standard air cuff is wrapped around the mid-thigh or upper arm of the examined extremity (Fig. 4). If the device consists of ferromagnetic parts, a safe distance from the magnet should be achieved by using an extended tube. Fast (automated) inflation of the air cuff to an occlusion pressure at least 50 mmHg above the individual systolic blood pressure is needed to induce complete ischemia and, on the other hand, minimize the discomfort of patients with vascular disease and reduce their risk of exacerbating critical limb ischemia. Medial calcific sclerosis (Mönckeberg's arthrosclerosis) should be considered if higher cuff pressures are needed to achieve full ischemic conditions, especially in patients with diabetes. MR measurements are usually started during resting state (reflecting baseline), ischemia and during reactive hyperemia after cuff deflation till reaching baseline level. The most important advantage of this paradigm for skeletal muscle BOLD MRI is the induction of profound oxygenation changes and a consecutively excellent BOLD contrast. Furthermore, this paradigm is independent from patient compliance, it can be standardized in the clinical setting and motion artifacts—as known from BOLD imaging of the brain or exercise paradigms in muscle tissue—are reduced to a minimum. The BOLD signal time courses extracted from studies with arterial occlusion paradigms typically show a faster initial $T2^*$ signal decay at the beginning of ischemia followed by a slower decrease to a minimum ischemic value (MIV, $T2^*_{\mathrm{min}}$) (Fig. 5). After cuff deflation, a fast surge of the

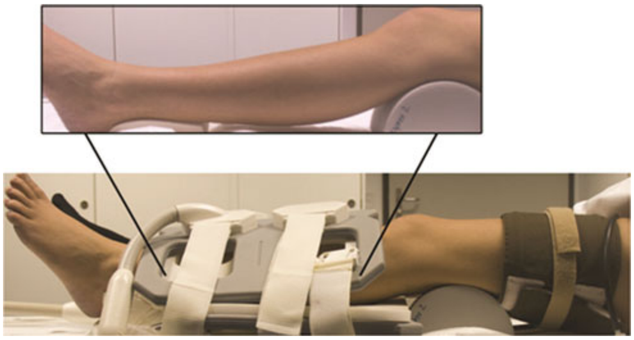

Fig. 4 Experimental setup of an arterial occlusion paradigm including two flexible array coils and sphygmomanometer wrapped around the thigh of the investigated leg. The cuff was additionally fixed with a velcro strap. The lower leg was supported at knee and foot level (insert) to prevent compression of the calf muscles. From Jacobi et al. (2012). This material is reproduced with permission of John Wiley and Sons, Inc

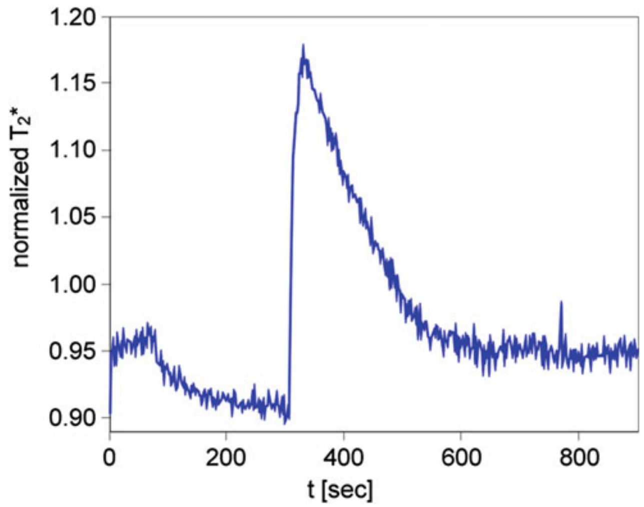

Fig. 5 Typical BOLD $T2^*$ time course extracted from a 30-year-old male healthy volunteer during an arterial occlusion paradigm showing the typical signal decrease during a 3 min lasting ischemia period and a $T2^*$ surge after cuff deflation with subsequent hyperemia peaking after approximately 40 s (TTP)

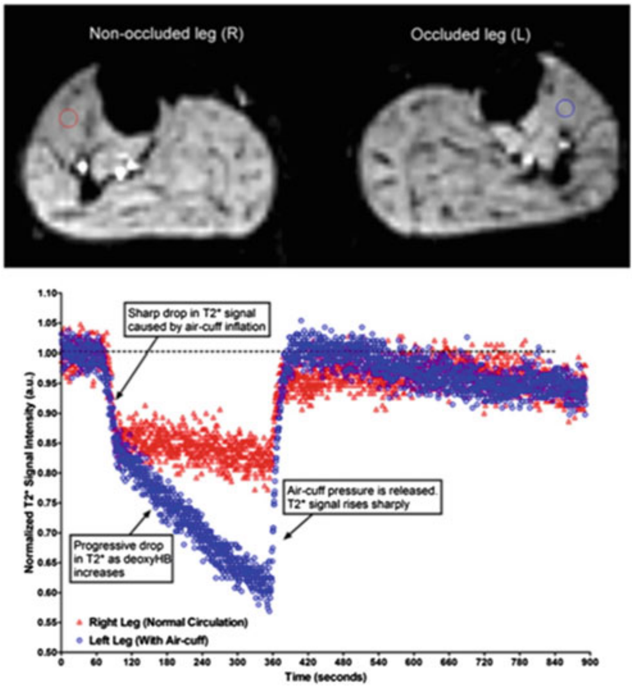
Non-occluded leg (R)
Occluded leg (L)
Sharp drop in T2* signal caused by air-cuff inflation
Air-cuff pressure is released. T2* signal rises sharply
Progressive drop in T2* as deoxyHB increases
Right Leg (Normal Circulation)
Left Leg (With Air-cuff)
Normalized T2* Signal Intensity (a.u.)
1.10
1.05
1.00
0.95
0.90
0.85
0.80
0.75
0.70
0.65
0.60
0.55
0.50
0
60
120
180
240
300
360
420
480
540
600
660
720
780
840
900
Time (seconds)

Fig. 6 $T2^*$ dynamic images (*upper panel*) acquired from both legs of a healthy female volunteer with corresponding ROIs (left leg: *blue;* right leg: *red*). Ischemia was only induced at the left leg. An aberrant fast initial $T2^*$ signal drop could be detected in the left tibialis anterior muscle. The similar pattern was also detected in the non-occluded right leg. From Yeung et al. (2012). This material is reproduced with permission of John Wiley and Sons, Inc

BOLD signal is observed with peak values (HPV, $T2^*_{\text{max}}$) after approximately 30–60 s (Time to peak, TTP) and a subsequent decrease to a steady state value around baseline. A recent study performed with a lower limb phantom and healthy volunteers revealed that compressed oxygen from an air cuff can induce magnetic susceptibility changes leading to a fast decline of the $T2^*$ signal (Yeung et al. 2012). This $T2^*$ signal dropout proofed to be pressure-dependent and could also be localized in the contralateral leg of the examined volunteers, where the blood flow was not interrupted (Fig. 6). These interesting results call for a critical reevaluation of the described fast initial signal dropouts during the ischemia phase of arterial occlusion studies. Furthermore it has to be evaluated, if cuff position can be optimized or special inflation gases without effects on magnetic susceptibility, such as nitrogen, need to be used in this setting in the future.

Muscle exercise paradigms have also been applied in a variety of muscle BOLD studies. They take advantage of the physiological coupling between muscle contraction and local perfusion. It has been shown that brief isometric contractions of only 1 s are sufficient to evoke measurable BOLD responses (Hennig et al. 2000; Meyer et al. 2004). The peaking of such responses follows approximately 8 s after each contraction induced motion artifact and the baseline value is reached again after 10–15 s (Meyer et al. 2004). Those BOLD responses have been proven to be dependent on the muscle contraction intensity (Wigmore et al. 2004). Although being the most “physiological” of the usually applied paradigms in skeletal muscle BOLD imaging, voluntary muscle contractions are largely dependent on patient compliance. Thus, standardization in the clinical setting seems to be challenging. Motion artifacts are a further drawback and require the use of specific fixation devices.

Oxygen inhalation has been used to provoke a BOLD signal increase of skeletal muscle (O_2-enhanced MRI) (Noseworthy et al. 1999, 2003). Prior to MR imaging, the individual breathes 100 % oxygen for several minutes to increase the amount of dissolved O_2 of the blood. As arterial hemoglobin is nearly completely saturated with oxygen under normal conditions, it has been proposed that the BOLD response of muscle tissue in oxygen inhalation paradigms is primarily increased via an oxygen uptake by venous deoxyhemoglobin (Noseworthy et al. 2003). However, O_2 itself is paramagnetic and leads to changes of $T1$, $T2$, and $T2^*$. Studies using this paradigm should thus be analyzed with care regarding true BOLD effects that depend on hemoglobin oxygenation (Partovi et al. 2012b).

2.1.4 Important Parameters Influencing Muscle BOLD Signal

Different parameters have been shown to have a certain influence on the $T2/T2^*$ signal of skeletal muscles. The most prominent role among those factors play age, weight, physical activity, examined muscle fiber type, intake of

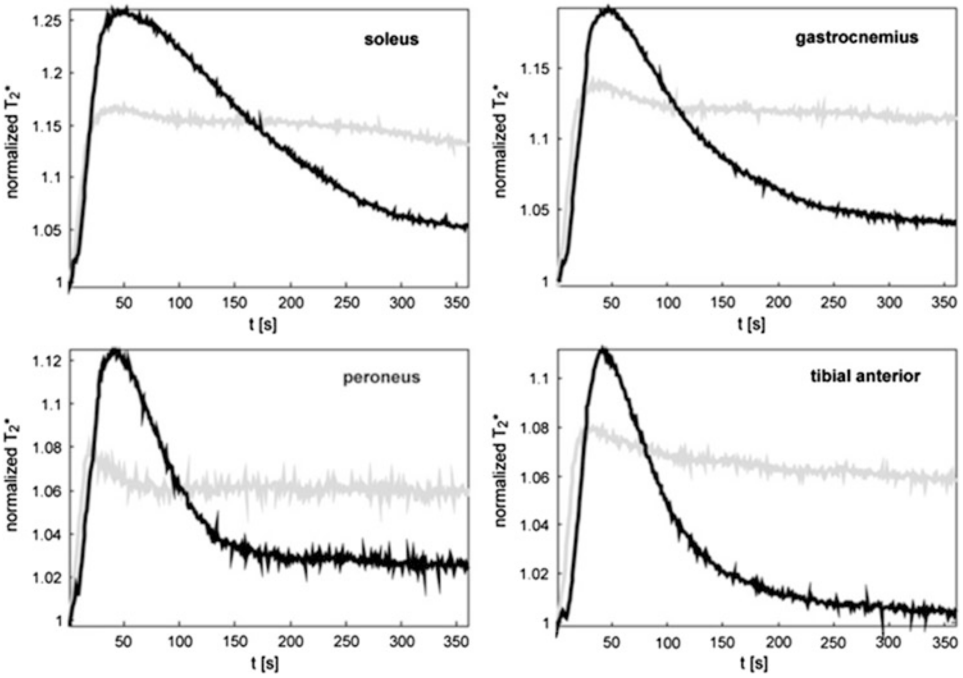

Fig. 7 Mean BOLD responses of four investigated calf muscles during 360 s of reactive hyperemia in elderly healthy subjects (*gray lines*) and young healthy subjects (*black lines*). Note, the significantly lower $T2^*$ hyperemia peak value ($P = 0.005$) and significantly elevated $T2^*$ end value ($P < 0.001$) in the elderly group compared with the younger individuals. From Schulte et al. (2008). This material is reproduced with permission of Radiological Society of North America (RSNA)

vasoactive drugs, and Hb-content, some of which will be further discussed in this section. Regardless of performing skeletal muscle BOLD studies in a preclinical or clinical setting it is crucial to take these parameters into account since they may possibly confound the results.

Aging leads to specific structural and functional impairments of skeletal muscle vasculature that result in an increased vascular rigidity and decreased perfusion reserve (Muller-Delp 2006; Proctor et al. 2003). Those alterations might explain the BOLD $T2^*_{\max}$ and TTP reduction found in elderly volunteers (mean age 64.0 years ± 6.4, $n = 11$) after cuff induced reactive hyperemia when compared with younger subjects (mean age 30.3 years ± 6.5, $n = 17$) (Schulte et al. 2008). However, due to the missing correlation with methods enabling to investigate the relationship to blood volume, perfusion, or oxygenation, the authors could only speculate with regard to the noticeable elevated end value after 350 s of hyperemia in the older study collective (Fig. 7). During cuff induced ischemia, a significant reduction of $T2^*_{\min}$ and delay of the $T2^*$ decrease (Time to reach half ischemic minimum, THIM) has been described in the elderly (Kos et al. 2009). Interestingly, this ischemia BOLD pattern does not match the alterations found in patients with peripheral arterial occlusive disease (PAOD, see *Clinical applications*), indicating that further mechanisms beside atherosclerosis play a role in vascular aging.

Increased body weight is associated with vascular dysfunction and decreased vasodilatation reserve (Gu and Xu 2013). For this reason, it is not surprising that the BOLD response of skeletal muscle tissue is also compromised in obese patients when compared with lean people. However, this effect could only be detected at a level of significance in one of the examined muscles (extensor digitorum longus), at maximum voluntary contractions and a short TE of 6 ms, primarily reflecting blood volume changes (Sanchez et al. 2011).

Slow-twitch oxidative muscles (i.e., soleus, tibialis anterior) show a higher capillary density and myoglobin content than fast-twitch glycolytic muscles (i.e., gastrocnemius, extensor digitorum longus) (Noseworthy et al. 2003; Zierath and Hawley 2004). Consecutively, the largest BOLD responses are usually detected in slow-twitch muscles, whereas smaller changes are typically found in fast-twitch muscles (Ledermann et al. 2006b; Noseworthy et al. 2003; Donahue et al. 1998). Regarding the high oxygen sensitivity of BOLD MRI and the interindividual variation of absolute $T2^*$ values, the selection of the optimal muscle type to investigate is crucial to obtain significant results when assessing patient and control collectives.

With regard to the activity level, individuals reporting to participate in aerobic sports greater than 30 min per day for at least 5 days a week bear an up to threefold larger BOLD signal increase when compared with sedentary individuals reporting no regular physical activity (Towse et al. 2005, 2011). The relation of constant physical activity to the oxygenation status of skeletal muscle microcirculation may obviously be explained by vascular adaptations such as increased capillary density, collateral blood flow, and exercise-provoked vasodilation (Green et al. 2011, 2012). Thus, it will be helpful to control for the physical activity level in muscle BOLD studies, for example by using an adapted questionnaire. Furthermore, even brief exercising over several minutes prior to BOLD imaging induces a remarkable $T2^*$ increase in the exercised muscles and thus has to be avoided in clinical settings (Bulte et al. 2006).

Especially in (pre)clinical muscle BOLD studies with patient collectives suffering from vascular diseases, the intake of vasoactive drugs might be a problem which has to be taken into account. As the BOLD response has been shown to be primarily dependent on perfusion induced blood volume and oxygenation changes, drugs affecting the vasodilatation capacity will influence the measured BOLD signal changes. Indeed it has been demonstrated that drugs inducing vasodilatation significantly increased oxygen- and ischemia-induced BOLD responses, whereas vasoconstrictors significantly reduced $\Delta T2^*$ (Bulte et al. 2006; Utz et al. 2005).

2.2 Clinical Applications of BOLD MRI

2.2.1 Peripheral Arterial Occlusive Disease

The morphological correlate of peripheral arterial occlusive disease (PAOD) is stenoses and occlusions in peripheral arteries leading to impaired blood supply to the end organs, such as the muscular system and the skin. Symptoms ranging from claudication to gangrene are the sequela of these morphological changes. Stenoses on the arterial level can be detected non-invasively with magnetic resonance angiography (Prince 1998; Rofsky and Adelman 2000) or color-encoded doppler ultrasonography (Leng et al. 1991). In a couple of studies muscle BOLD MRI proved to be useful for non-invasive assessment of PAOD. In one of the earlier studies BOLD MRI during the hyperemic phase using the arterial occlusion paradigm has been investigated in PAOD patients versus an age-matched healthy volunteer group. Despite inducing ischemia by cuff compression followed by hyperemia after pressure release, the paradigm was well tolerated with minor discomfort in the patient group. In comparison to the healthy volunteers the BOLD time course in PAOD patients showed a decreased $T2^*_{max}$ and a delayed TTP (Fig. 8) (Ledermann et al. 2006b). The lower $T2^*_{max}$ might be caused by a slower flow of blood through the muscle microvasculature resulting in efficient deoxygenation of hemoglobin and by a rarefaction of capillaries in the calf muscle as a result of the disease as it was found in previous studies (Hickey et al. 1992; Dawson and Hudlicka 1990). The delayed TTP might be based on impaired flow of oxygenated blood into the microcirculatory system of the calf muscle (Lebon et al. 1998a). Besides a relationship between TTP and the ankle brachial pressure index could be demonstrated; with some exceptions a lower ankle brachial pressure index was associated with a higher TTP (Ledermann et al. 2006b). Muscle BOLD MRI investigations during the ischemic phase in PAOD patients have been published as well. A significant altered $T2^*$ time course in comparison to an age-matched healthy volunteer group was found (Potthast et al. 2009). The $T2^*_{min}$ was lower in the PAOD group versus the non-PAOD group (Fig. 9).

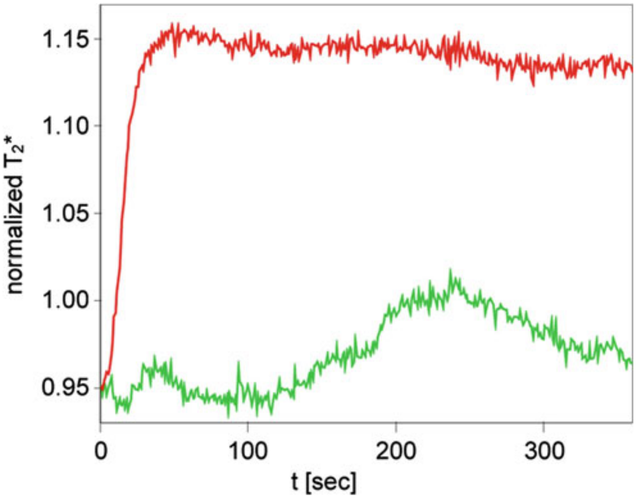

Fig. 8 BOLD $T2^*$ signal changes of a male PAOD patient (stage IIA) during reactive hyperemia is shown in *green*. For comparison, a normal $T2^*$ time course of a healthy 67-year-old female volunteer is shown in *red*. Pay attention to the profoundly decreased $T2^*$ recovery during reactive hyperemia with no obvious peak in the patient with PAOD

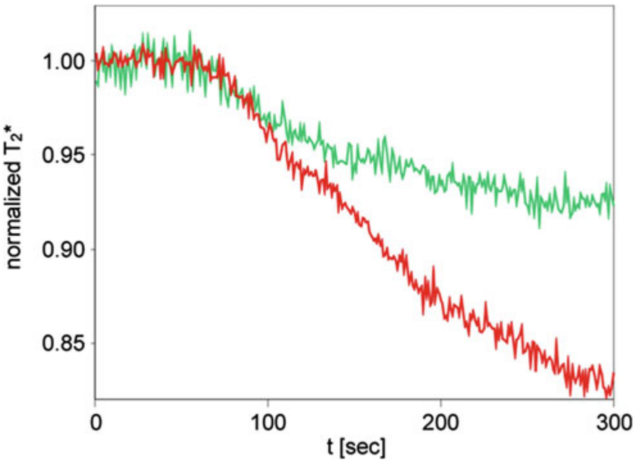

Fig. 9 $T2^*$ time course of a 36-year-old female PAOD patient (stage IIa, *green line*) with a marked reduction of $T2^*$ decline during ischemia. In *red*, a normal $T2^*$ time course of a healthy 52-year-old male is shown with a substantially lower MIV at the end of ischemia

The BOLD sequence as part of a multiparametric MR imaging protocol is highly interesting for therapy response evaluation. A study monitored PAOD patients longitudinally 1 day before and 6 weeks after percutaneous transluminal angioplasty (PTA) performing muscle BOLD MRI. The arterial occlusion paradigm was well tolerated in this

PAOD patient population as well, proving the feasibility of the innovative technique (Huegli et al. 2009). The cuff compression paradigm is advantageous for clinical use as it does not require compliance and its standardization is easier than an exercise based approach (Berglund and Eklund 1981). It can be safely applied in PAOD patients with intermittent claudication. However, those with higher grade of the disease (critical limb ischemia or necrosis) were not enrolled in previously published studies because of a theoretical risk of exacerbation when ischemia is provoked in the early phase of the paradigm (Huegli et al. 2009). After PTA $T2^*_{\max}$ increased, whereas TTP and EV decreased but these changes in BOLD key parameters did not reach statistical significance. However, they demonstrated a trend resulting in reversal of the BOLD response towards a normal healthy course. Post PTA $T2^*_{\max}$ increase can be explained by improved blood supply and TTP decrease might be based on a more effective and faster flow through the re-opened superficial femoral arteries. Another reason for the higher $T2^*_{\max}$ is an improved vasodilatation reserve after percutaneous intervention. The decreased EV found in this study might be explained by a fast washout of oxygenated blood from the musculature.

A recently published study analyzed the reproducibility of imaging techniques for the assessment of the macro- and microcirculatory network in a PAOD patient collective in comparison to a healthy volunteer group. The evaluation of the microcirculation included dynamic BOLD imaging during the hyperemic phase performing the arterial occlusion paradigm. For BOLD imaging reproducibility was not demonstrated. In detail the key parameter relative $T2^*_{\max}$ revealed poor reproducibility, whereas TTP showed moderate reproducibility (Versluis et al. 2011). Further studies with a standardized paradigm and imaging parameters are warranted to improve the reliability of the BOLD response. A potential alternative to muscle BOLD MRI for assessment of PAOD is contrast-enhanced ultrasound. A recently published study on healthy volunteers used an arterial occlusion paradigm for muscle perfusion quantification performing contrast-enhanced ultrasound. The arterial occlusion paradigm can be applied in patient populations, such as in subjects with PAOD for the evaluation of skeletal muscle microperfusion (Krix et al. 2011). Another study also showed that contrast-enhanced ultrasound is able to diagnose PAOD by detecting skeletal muscle microperfusion and arterial perfusion reserve alterations (Amarteifio et al. 2011).

2.2.2 Rheumatic Disorders

The skeletal muscle tissue is the functional end organ of the peripheral vascular system. In patients with rheumatic disorders BOLD MRI has the potential to contribute to non-invasive evaluation of the clinically relevant microcirculatory system disorders. Furthermore, in those patients with symptoms of the musculoskeletal system muscle BOLD MRI may even elucidate the cause as subclinical microcirculatory alterations.

In a recently published case study a female patient with a history of granulomatosis with polyangiitis (also known as Wegener's granulomatosis) presented with bilateral severe myalgia (Jacobi et al 2013). The patient had no signs of atherosclerotic disease and no associated risk factor for macrovascular compromise. Morphological MR with $T2$ weighted images did not reveal any signs of inflammation explaining the symptoms of the patient. However, BOLD MRI could demonstrate pronounced impairment of calf muscle microcirculation. In comparison to the BOLD signal time course of a matched healthy volunteer substantial differences in key parameters were shown: The $T2^*_{\min}$ was decreased and the declining slope during ischemia was increased in the patient. The lower MIV might be explained by small vessel vasculitis leading to a larger amount of oxygen consumption.

Investigations of the BOLD response in systemic sclerosis (SSc) patients generated interesting results. SSc is a disease with microangiopathy leading to insufficiency in a variety of tissues (Gabrielli et al. 2009). Up to one-third of patients have symptoms in the musculoskeletal system (Walker et al. 2007). In a study the microvasculature of SSc patients was analyzed performing BOLD imaging of the calf muscle with the arterial occlusion paradigm. Impaired muscle microcirculation was demonstrated by altered BOLD time courses in the patients compared to a healthy volunteer control group (Partovi et al. 2012d). Key parameters were significantly different with lower $T2^*_{\max}$, $T2^*_{\min}$, declining slope values and a prolonged TTP. Lower $T2^*_{\min}$ might be based on rarefaction of capillary or occlusion of the microcirculatory system. The hyperemia parameter differences might be the result of structural (capillary loss or obliteration) or functional (vasoconstrictor effect or decreased vasodilatation reserve) vasculopathy. BOLD response alterations have been found to be more pronounced in the gastrocnemius than the soleus muscle in this study. A further study with SSc patients tried to elucidate the origin of altered muscle BOLD MR time courses by means of correlation with transcutaneous oxygen pressure (TcPO2) measurements. TcPO2 is a technique utilizing the modified Clark electrodes and reflecting the tissue oxygenation status (Bunt and Holloway 1996; Slagsvold et al. 1992). A comparison with healthy volunteers was included in the analysis as well. Very strong cross correlations between both imaging techniques in the patient and healthy volunteer group were demonstrated for a time lag of approximately 40 s (Partovi et al 2013). This proves BOLD MRI as a valuable tool for the assessment of patients with SSc as it reveals oxygen deficits in this patient population.

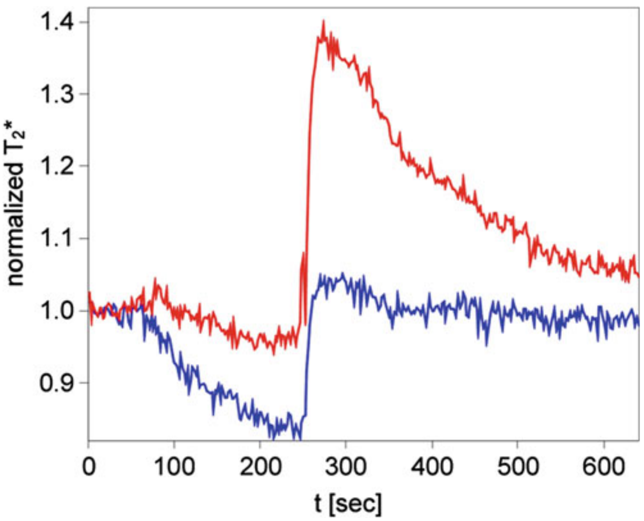

Fig. 10 BOLD time courses of a 53-year-old male SSc patient (*blue*) and a 26-year-old healthy female volunteer (*red*) showing a clear reduction of $T2^*_{\min}$ and $T2^*_{\max}$ in this rheumatic disorder

The origin of the $T2^*$ signal of BOLD MRI can be explained at least partially by tissue oxygenation alterations. When comparing the signal course of both modalities, the $T2^*$ decrease was more pronounced than the decrease of the TcPO2 signal during ischemia. From a pathophysiological standpoint this lower signal might be caused by the adaption of the microcirculatory system to chronic hypoxia leading to a pronounced capillary oxygen consumption. $T2^*_{\max}$ and the TcPO2 signal were lower in the patient population versus healthy volunteers which is based on either structural or functional vasculopathy as discussed above. In the future vasoactive drugs might help to further clarify whether the structural or the functional component contributed to the BOLD response or if both components impact the signal to a certain degree (Bulte et al. 2006). Furthermore muscle BOLD MRI correlations in SSc patients with laser Doppler flowmetry are of interest (Fagrell 1986; Ranft et al. 1986) (Fig. 10).

2.2.3 Diabetes Mellitus

It is well known from a clinical perspective that the microvasculature is impaired in patients with diabetes mellitus type I and type II (Picchi et al. 2010; Marcovecchio and Chiarelli 2011). Muscle BOLD MRI was assessed in patient with diabetes mellitus type I and II versus healthy controls conducting maximal isometric ankle dorsiflexion for 1 s (muscle exercise) as paradigm. The authors of this study also evaluated the distal macrovasculature with phase contract MR angiography. No significant differences in the BOLD response between patients and healthy controls could be found. There was also no different in the findings from phase contract MR angiography. This study could confirm the impact of age on the BOLD signal time course (Slade et al. 2011). Combining BOLD with a technique to assess macrovasculature is a promising approach towards functional musculoskeletal imaging.

For assessing the microvasculature of the skeletal muscle in patients with diabetes mellitus contrast-enhanced ultrasound could be an interesting imaging modality. Contrast-enhanced ultrasound in patients with diabetes mellitus type II performing the arterial occlusion paradigm revealed impaired skeletal muscle microperfusion in comparison to healthy volunteers (Amarteifio et al 2013).

2.2.4 Compartment Syndrome

For certain applications it was suggested to integrate muscle BOLD MRI and other advanced MR techniques in one imaging protocol. For instance BOLD MRI can be combined with diffusion tensor imaging which enables depiction of muscle tears. In the same publication BOLD MRI was demonstrated to be feasible for the detection of vascular insufficiency in compartment syndrome (Noseworthy et al. 2010).

3 Part 2 Arterial Spin Labeling MRI

3.1 General Principles of ASL

3.1.1 Origin of the ASL Signal

The principal underlying ASL is the selective visualization of fresh inflowing blood into a tissue of interest which can be imaged with this technique. This is achieved by magnetically labeling (or “tagging”) of inflowing arterial blood water proximal of the tissue of interest, generally through inversion or saturation of the longitudinal magnetization using specifically designed radiofrequency (RF) pulses (Detre et al. 1992).

The water molecules, acting as an endogenous contrast agents and carrying the labeled magnetization, travel through the vascular tree to a particular tissue where they are extracted from the microvascular bed and join the larger pool of tissue water distal of the tagging location. Once arriving in the tissue, after a duration termed arterial transit time, the tagged spins induce a measurable change in the apparent tissue $T1$ signal and in the tissue magnetization, which it is detected by a conventional MR sequence. To produce a control image, the experiment is then repeated without the labeling procedure. Consecutively, the image signals are subtracted in pairs to yield a difference of signal, which enables detection of tagged blood that was delivered to the imaging slice (Fig. 11). This signal directly reflects quantitative local perfusion which is calculated using modifications in the original Bloch equations.

However, the tagging sequence produces additional static signals in the tissue to be imaged (a process termed

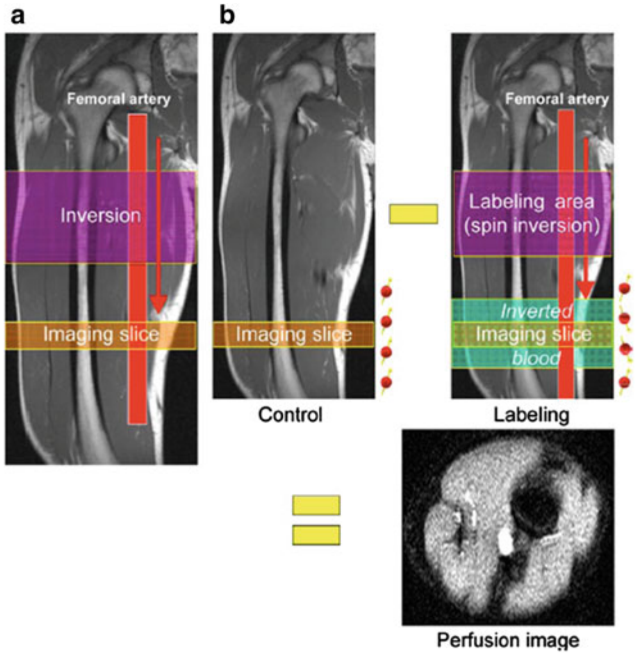

Fig. 11 Principle of ASL MR perfusion imaging. **a** In ASL MRI, blood serves as intrinsic contrast agent. For this, blood is magnetically labeled by an inversion pulse outside the imaging slice and then flows, depending on the blood flow, into the imaging slice. **b** The difference between the MR image with and the MR image without labeled blood yields an image with signal only from inflowing blood, whereas background signal is suppressed. This image is the perfusion weighted ASL image. From Weber et al. (2007). This material is reproduced with permission of Springer

magnetization transfer), and therefore the control sequence must produce an identical signal without labeling the inflowing blood. Provided that the off-resonance and magnetization transfer effects of the tagged and control pulses are equal, the ASL signal is simply proportional to the difference in longitudinal magnetization in the tissue due to the blood that entered the voxel during the defined time interval. The goal of all the ASL techniques is to produce a tagged image and a non-tagged control image in which the static tissue signals are the same.

The essential problem in quantifying the ASL signal is to estimate how much the magnetization of the tagged spins has decayed by the time of measurement, so that the measured ASL signal can be appropriately scaled to represent a quantity of blood delivered to the voxel (Buxton et al. 1998).

For each ASL method, a detailed model of the process combining kinetics and relaxation is needed in order to extract a quantitative measurement of perfusion. Although all of these models rely on the same theoretical background one should take into account that each ASL technique uses different types of parameter values. These parameters include: the degree of arterial spin inversion, transit time from the labeling slice to the imaging slice, $T1$ of blood and tissue, equilibrium magnetization of arterial blood, clearance of magnetization by venous flow, blood-tissue partition coefficient for water, duration of the labeling pulse, and the amount of blood water extracted by the tissue. These parameters are subsequently used in equations describing perfusion which are derived from the modified Bloch equation.

It should be considered that the ASL calculation of perfusion is not derived from dynamic datasets and does not require deconvolution processing. The ASL signal is directly and linearly proportional to perfusion.

3.1.2 Advantages and Disadvantages of ASL

The main advantage of ASL lies in its complete non-invasive assessment of perfusion and microcirculation. This permits serial measurements without the need for administration of contrast agents. ASL is quantitative in absolute terms and evaluates the actual tissue microperfusion as opposed to blood flow to an organ. The information derived from BOLD imaging can be acquired partially when applying the ASL technique (Duteil et al. 2006; Carlier et al. 2006). Additionally, ASL exhibits relatively high spatial and high temporal resolution. Finally, ASL may be used to conduct non-invasive MR angiography (Katoh et al. 2008; Rehwald et al. 2004; Wheaton and Miyazaki 2012).

The greatest disadvantage of ASL is the intrinsic low signal-to-noise ratio (SNR). The difference in signal between the two images is approximately 1 %, thus multiple images are acquired (consisting of repeats of tag minus control image) which are then averaged. This process is time consuming and makes low perfusion states (such as muscle perfusion at rest) more difficult to quantify, although not impossible.

Since its first demonstration by Detre et al. (1992) and Kwong et al. (1992), ASL has been applied extensively to studies of the brain (Detre et al. 1999; Chalela et al. 2000; Alsop et al. 2000), the heart (Troalen et al. 2013; Kober et al. 2004; Zhang et al. 2005) as well as other organs (such as the kidneys and lungs) (Robson et al 2012; Mai and Berr 1999) including the skeletal muscle (see section below and Fig. 12).

3.1.3 Sources of Error and Artifacts Associated with ASL

Motion Artifacts: Due to the lengthy acquisitions to achieve adequate SNR, as well as the fact that ASL perfusion imaging involves the subtraction of two images with an intensity almost 100 times larger than the difference between them, ASL scans are susceptible to motion artifacts. Recent technical advances offer several solutions to the problem (Norris and Schwarzbauer 1999; Wong et al. 2006; Frouin et al. 2006; Garcia et al. 2005; Ye et al. 2000; Blamire and Styles 2000; Duyn et al. 2001).

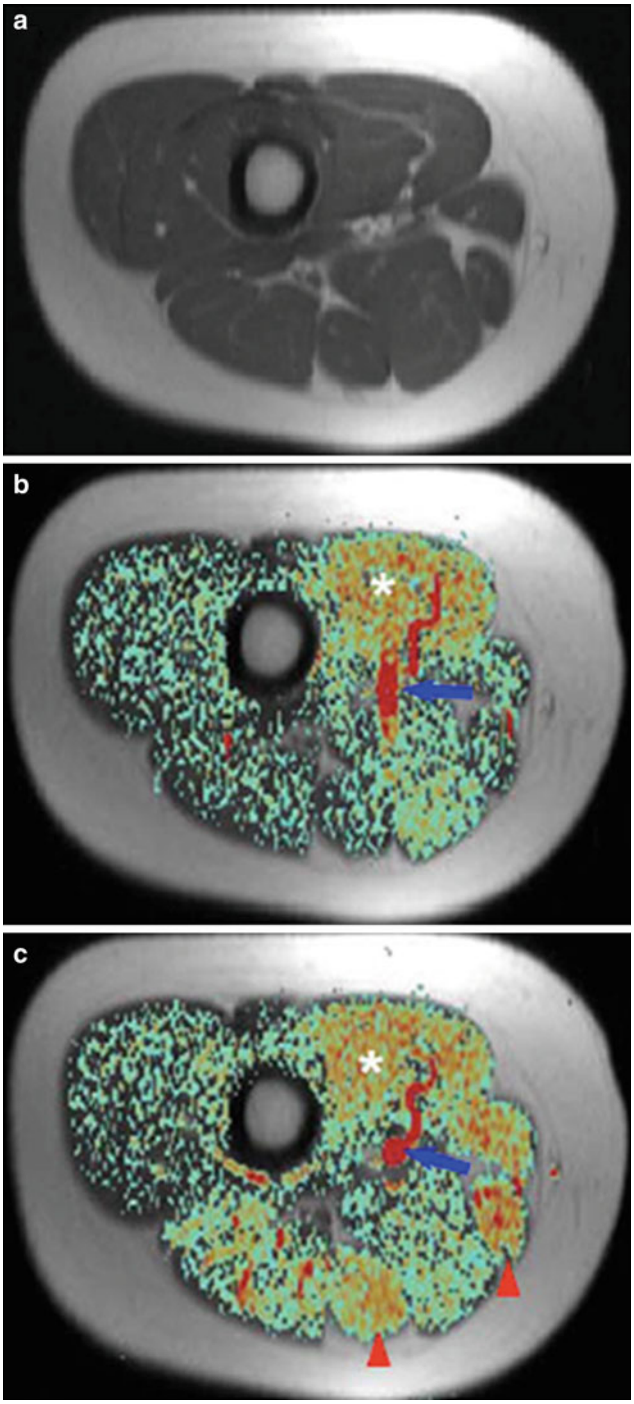

Fig. 12 Anatomic $T1$-weighted image (**a**) and color-coded perfusion weighted ASL image (**b**) of the right mid-thigh of a 24-year-old woman at rest on a 1.5-T whole body scanner (PICORE tagging scheme, 10-mm slice thickness, $TR = 3{,}500$ ms, $TE = 30$ ms, inflow time $TI = 600$ ms, 256–128 matrix, 25 averages, acquisition time $TA = 3$ min). After knee flexion exercise against a 3-kg weight for 5 min significant hyper-perfusion in all thigh-flexor muscles can be observed (*arrowheads*), while the adductor muscles (*asterisk*) already have elevated perfusion at rest-resulting from a preceding exercise test (**c**). The *blue arrow* indicates the femoral vessels, which have the highest signal on ASL images. As expected, no perfusion signal appears in bones and subcutaneous fat tissue. From Weber et al. (2007). This material is reproduced with permission of Springer

Magnetization Transfer (Discussed Above): Magnetization transfer effects can be a significant source of error in ASL measurements. They can be particularly problematic in skeletal muscle, where magnetization transfer rates are relatively high (Niemi et al. 1992) and can change significantly and rapidly during exercise (Mattila et al. 1993; Zhu et al. 1992).

Post Labeling Transit Time Delay: The exact duration of the transit time is challenging to determine as it is not uniform across a slice or between slices. The artifact results from intravascular labeling that has not yet reached capillaries and tissue by the time the image the acquisition is carried out. As a consequence perfusion might be underestimated.

Alsop and Detre reduced the sensitivity of the continuous ASL techniques to transit time heterogeneity by inserting a postlabeling delay (PLD) (Alsop and Detre 1996). However, this approach still requires a good estimation of the transit time since the optimal delay time equals the transit time. This makes the approach difficult to implement in skeletal muscle where arterial flow velocities can be expected to change considerably between rest and exercise (Wu et al. 2008).

Contribution of Labeled Water in Large Vessels: Intravascular tagged blood flowing through the slice creates large focal intensities, which are unrelated to tissue perfusion. In practice, the signal from large arteries is typically destroyed in the course of the echo-planar imaging acquisition without the need of additional bipolar gradients (Buxton et al. 1998). To further reduce this artifact another possibility is to carefully exclude voxels containing vessels or lipids (which cause large focal intensities as well).

Incomplete Inversion of the Arterial Blood (Labeling Efficiency): In the skeletal muscle blood flow velocity can range from very low to very high levels, potentially resulting in different labeling efficiencies.

Venous Outflow Effect: An implicit assumption in most existing quantitative perfusion models is that the tagged blood does not leave the tissue prior to data acquisition. In situations involving high flow rate this might not hold true. It is particularly important to consider this in investigations in the skeletal muscle, where fast flow rates are encountered as well as conditions associated with low hematocrit levels such as anemia (Wu et al. 2008). Insufficient consideration of these artifacts will result in perfusion estimation errors.

3.2 Technical Principles

According to the tagging scheme, ASL can be divided into four categories: continuous ASL (CASL), pulsed ASL (PASL), pseudo-continuous ASL (pCASL), and alternative labeling schemes.

3.2.1 Continuous ASL

With CASL techniques, the blood is continuously labeled. A spatially localized RF field, positioned through the feeding arteries of the tissue of interest, inverts the longitudinal magnetization of the protons in the blood as they flow through a thin slice. This technique uses long RF pulses. The original scheme proposed only allows quantification of perfusion in a single slice (Detre et al. 1992). This problem was overcome when a new CASL techniques was developed in order to quantify regional cerebral blood flow in multiple slices with a single coil (Alsop and Detre 1998; Talagala et al. 1998).

3.2.2 Pulsed ASL

As opposed to labeling blood as it flows through a plane, PASL relies on the instantaneous labeling of a thick slice (large blood volume) with a short RF pulse (~10–20 ms). PASL sequences are based on a scheme originally referred to as flow-sensitive alternating inversion recovery (FAIR) sequences (Kwong et al. 1995; Kim 1995; Schwarzbauer et al. 1996). In FAIR, an inversion-recovery sequence is performed twice—a labeled one with slice-selective inversion and a control one with nonselective inversion. Following each inversion imaging is performed. The inversion-recovery image with the slice-selective inversion pulse is then subtracted from the image with the nonselective inversion pulse (Fig. 13).

3.2.3 Pseudo-Continuous ASL Techniques

pCASL is a novel labeling scheme that combines the advantages of PASL and CASL (Silva and Kim 1999). The advantages of pCASL include an increase of 50 % in SNR as compared to PASL and a higher tagging efficiency than CASL (Wu et al. 2007). pCASL measurement sequences are available on MR systems of all three major vendors.

3.2.4 PASL versus CASL

Whereas pCASL and PASL can be implemented with standard MR-systems, CASL requires a dedicated coil with a capacity for generating continuous RF pulses (Wu et al. 2011). PASL is performed with shorter repetition times and thus leads to superior temporal resolution (Wong et al. 1998). PASL is also less sensitive to variations in the assumed or measured values of the tissue parameters. BOLD data can be acquired simultaneously with PASL. PASL exhibits lower influence of magnetization transfer (Boss et al. 2006) and inversion efficiency is higher and thus essentially flow-velocity independent.

For PASL, the inherent SNR is lower than that of CASL. However, when tagging efficiency and coil configuration are considered, the SNR is comparable between PASL and CASL and is highest with pCASL (Wu et al. 2011). In addition, CASL techniques are less susceptible to motion interferences (Wong et al. 1998; Frank et al. 1999; Richardson et al. 2001).

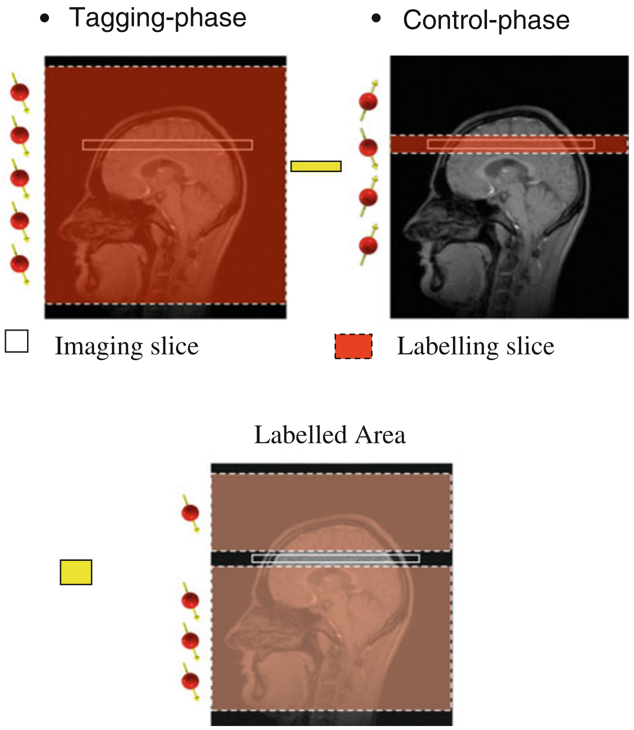

Fig. 13 Principal of FAIR (flow-sensitive alternating inversion recovery). During the tagging phase all the spins in the tagging slice are inverted. Following this, only the spins in the imaging slice are inverted (*white box*). The difference between the intensity of the imaging slice at both these times delivers the signal, which is used to calculate the blood flow. From Weber et al. (2004). This material is reproduced with permission of Springer

3.2.5 Skeletal Muscle ASL

The first ASL measurements of muscle perfusion date back to 1996 (Toussaint et al. 1996). The authors used a CASL-NMR model originally developed by Detre et al. (1992). for the brain, to measure perfusion in the calf muscle of human volunteers during rest, ischemia, and reactive hyperemia. The authors correlated the results successfully with NMR plethysmography and were able to observe significantly different perfusion rates in the various muscle groups.

Flow-Driven Arterial Water Stimulation with Elimination of Tissue Signal

FAWSETS was the first ASL sequence introduced to specifically quantify muscle perfusion (Marro 1997; Marro et al. 2005a). FAWSETS, a CASL technique, differs from other CASL techniques in that the label consists of flow-driven adiabatic excitation rather than saturation or inversion of the arterial water. The technique offers several advantages: It eliminates the need to compensate for magnetization transfer and also for arterial transit time effects. Furthermore, it provides an improvement in time resolution in the range of factor 2. Alas, FAWSETS can only eliminate arterial transit times in a single slice. FAWSTES was conducted in several studies to investigate perfusion in the hind limb of rats (Marro et al. 2005a, b), combining FAWSTES with ^{31}P MR spectroscopy (though not simultaneously) in order to investigate local perfusion and metabolic demand.

Another manuscript presented a further CASL sequence designed to specifically quantify muscle perfusion (Frank et al. 1999) using a standard 1.5-*T* clinical imaging system fitted with a local gradient self-designed knee coil. The authors applied a modified version of continuous ASL to demonstrate spatially and temporally resolved perfusion images of exercising human skeletal muscle (Alsop and Detre 1996). They were able to demonstrate the spatial heterogeneity of perfusion values within the various muscle groups of the lower leg and perfusion sensitivity to muscle workload. In this manuscript a method for eliminating the most serious sources of error in the measurement of muscle perfusion with ASL was demonstrated as well (Alsop and Detre 1996). This technique was combined later with ^{31}P chemical shift (CSI) imaging to compare metabolic demand and perfusion response to exercise (Richardson et al. 2001).

Saturation Inversion Recovery

The first PASL sequence for the purpose of specifically quantifying muscle perfusion was SATIR (Raynaud et al. 2001). SATIR offers the following advantages: The calculation of perfusion using SATIR is independent of possible $T2$ variations, which are known to increase in exercising muscles, and of $T2^*$ making it insensitive to the BOLD effect. SATIR is highly temporal efficient, displaying a high perfusion contrast per unit of time. The new sequence was utilized to conduct multiple experiments in various setups, combining multiple interleaved additional measurements (termed multiparametric functional-NMR) to study muscle physiology both at rest and at activity (Duteil et al. 2004, 2006; Gerontol et al. 2009; Baligand et al. 2011; Bertoldi et al. 2006; Ménard et al. 2010).

3.2.6 Comparison of ASL and BOLD MRI for Muscle Perfusion

Superiority of ASL

1. BOLD contrast is of a multifactorial nature. While ASL provides a direct absolute measurement of perfusion changes, $T2^*$ weighted BOLD MRI measures the local increases in oxygenation. This should be taken into account when interpreting BOLD information.
2. The vascular network architecture in skeletal muscle, with a preferential alignment along fibers, may induce an angular dependence of BOLD relative to the Bo field.
3. ASL is less susceptible to artifacts arising from large draining veins.
4. The exercising muscle induces an intrinsic $T2$ increase which can be a confounding effect in BOLD signal interpretation.
5. BOLD response tends to plateau at high perfusion rates (Duteil et al. 2006).
6. ASL perfusion contrast is based on longitudinal magnetization, and as such it is insensitive to bulk susceptibility effects which may impact BOLD studies (Detre and Alsop 1999).
7. In conditions where angiogenesis is stimulated, associated changes in tissue vascular fractional volume could affect BOLD response to a greater extent than vasodilation itself, thus obscuring the evaluation of the skeletal muscle vasodilatory capacity (Carlier et al. 2006).

Superiority of BOLD

1. The major advantage that BOLD has over ASL is that while a typical BOLD signal is 2 % of the raw image intensity, a typical baseline ALS signal (control-tag) is only 1 % of the raw image intensity. Although the change in ASL signal can be relatively high, this still represents only 1 % of the raw image intensity. Signal averaging can compensate for this drawback of ASL but requires an increase in scan time which limits spatial and/or temporal resolution (Lebon et al. 1998c).
2. ASL temporal resolution is limited by the need to obtain two images (tag and control). Additionally, because of the time required to allow for tagged blood to flow into the imaging slice, even multislice ASL is limited in its maximum rate of image acquisition relative to BOLD.
3. ASL requires a large number of additional measurements or assumptions, which can result in the generation of subsequent significant errors.
4. BOLD signal can be increased using high magnetic field strengths (Partovi et al. 2012c). Higher magnetic field strengths are gaining an increasing interest in the clinical arena of musculoskeletal imaging.
5. Spin echo BOLD imaging has the advantage of minimizing large vessel contributions. Moreover, it can be extracted from the same series of ASL spin echo images, which are acquired for perfusion quantification.
6. ASL suffers from a greater sensitivity to movement in comparison to BOLD MRI.

3.3 Clinical Applications of ASL

3.3.1 Recent Human ASL Studies

ASL measurements for examining perfusion in multiple human extremities was first recently performed performed

(Wu et al. 2008). This study applied an ischemic-hyperemic paradigm and a CASL scheme to study the flow heterogeneity between a variety of muscle groups (Wu et al. 2008). Another study used a clinical 3.0T scanner and standard coils in combination with the pulsed ASL technique FAIR-TrueFISP, to investigate perfusion response in the forearm musculature of healthy volunteers (Boss et al. 2006). While employing an intense exercise paradigm, good delineation could be achieved between active muscles and musculature not involved in the exercise technique. Using the same technique, it was feasible to assess perfusion changes in the relatively small Masseter muscle after sustained clenching (Schraml et al. 2011).

3.3.2 ASL in Peripheral Arterial Occlusive Disease

The first attempt to employ a continuous version of ASL to measure calf muscle perfusion in subjects with PAOD was realized using an ischemic-hyperemic paradigm to examine calf microvascular flow in 40 subjects with varying degrees of PAOD and 17 age-matched PAOD-free subjects. The authors applied a CASL scheme on a 3T scanner demonstrating that CASL flow measurements correlate with disease state as measured by ankle brachial pressure index and that those measurements exhibited preserved microvascular flow reserve in the presence of early to intermediate vascular disease (Wu et al. 2009).

A PASL method was used in another study to measure calf muscle perfusion in subjects with PAOD. The data of this study was acquired on a 3T scanner with a peak exercise paradigm to measure flow in 15 healthy volunteers and 15 age-matched patients with PAOD. In this study the Q2TIPS [QUIPSS (Quantitative Imaging of Perfusion Using a Single Subtraction) II with thin-slice TI1 periodic saturation] sequence was implemented. Q2TIPS minimizes errors caused by variable transit delay and deletes the intravascular signal (Pollak et al. 2012). In this study a higher peak exercise calf perfusion was found in healthy volunteers in comparison to PAOD patients, thus differentiating healthy from PAOD patients. Moreover, in the healthy subjects, the anterior tibialis and gastrocnemius revealed to be the calf muscles with the highest perfusion rate. In contrast for the PAOD group the calf muscle with the highest perfusion was the anterior tibialis muscle. The within subject correlation coefficient between repeated studies was 0.87 and the interobserver reproducibility was 0.96 indicating both reliability and reproducibility (Luh et al. 1999).

In conclusion ASL may prove useful for the evaluation of disease progression in PAOD. Those patients unable to receive contrast agents may profit from perfusion imaging with ASL. Clinical trials in a large patient collective are warranted to further elucidate the application of ASL in PAOD.

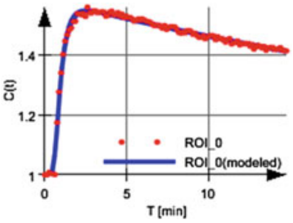

Fig. 14 Typical time-intensity curve derived from a subcutaneous tumor. The initial upslope describes the wash in phase and the subsequent downslope the washout phase. In DCE-MRI quantitative analysis the whole curve is used to calculate single values of different microvascular parameters

4 Part 3 Dynamic Contrast Enhanced (DCE)-MRI

4.1 General Principles of Dynamic Contrast Enhanced (DCE)-MRI

4.1.1 Origin of the DCE-MRI Signal and Technical Principles

Dynamic contrast enhancement (DCE) is the temporal study of the tissues response to an intravenously injected bolus of contrast agent (CA). This technique is conducted through acquisition of baseline native images, followed by a series of images acquired over time after administration of the CA.

A paramagnetic CA is present into the vascular system of a subject over a short period of time. The CA disperses and as it enters a tissue, it changes the MR signal intensity of the tissue to a degree that is associated with its local concentration. The induced signal intensity variation of the tissue is monitored over time through a serial acquisition of images every few seconds. This signal is used to plot a so-called time-intensity curve (TIC, Fig. 14) for the tissue which reflects the tissue's response to the arrival of the CA. Through the analysis of this curve, certain physiological properties that are related to the microvascular blood flow can be derived, such as vessel permeability, vessel surface area product and tissue volume fractions.

In a typical DCE-MRI imaging session, a region of interest (ROI) is selected and MR images are collected. Each image acquired corresponds to one time point, and each pixel in each set of images generates its own time course of intensity values. Images of the resultant changes in signal intensity can then be analyzed to derive parametric maps of specific microvascular biomarkers (Fig. 15). These parameters generally reflect the two-compartment pharmacokinetics exhibited by contrast agents, comprising of intravascular and extravascular components.

A paramagnetic particle will induce changes in the MRI-signal of a tissue, through which it passes due to two different physical–chemical properties:

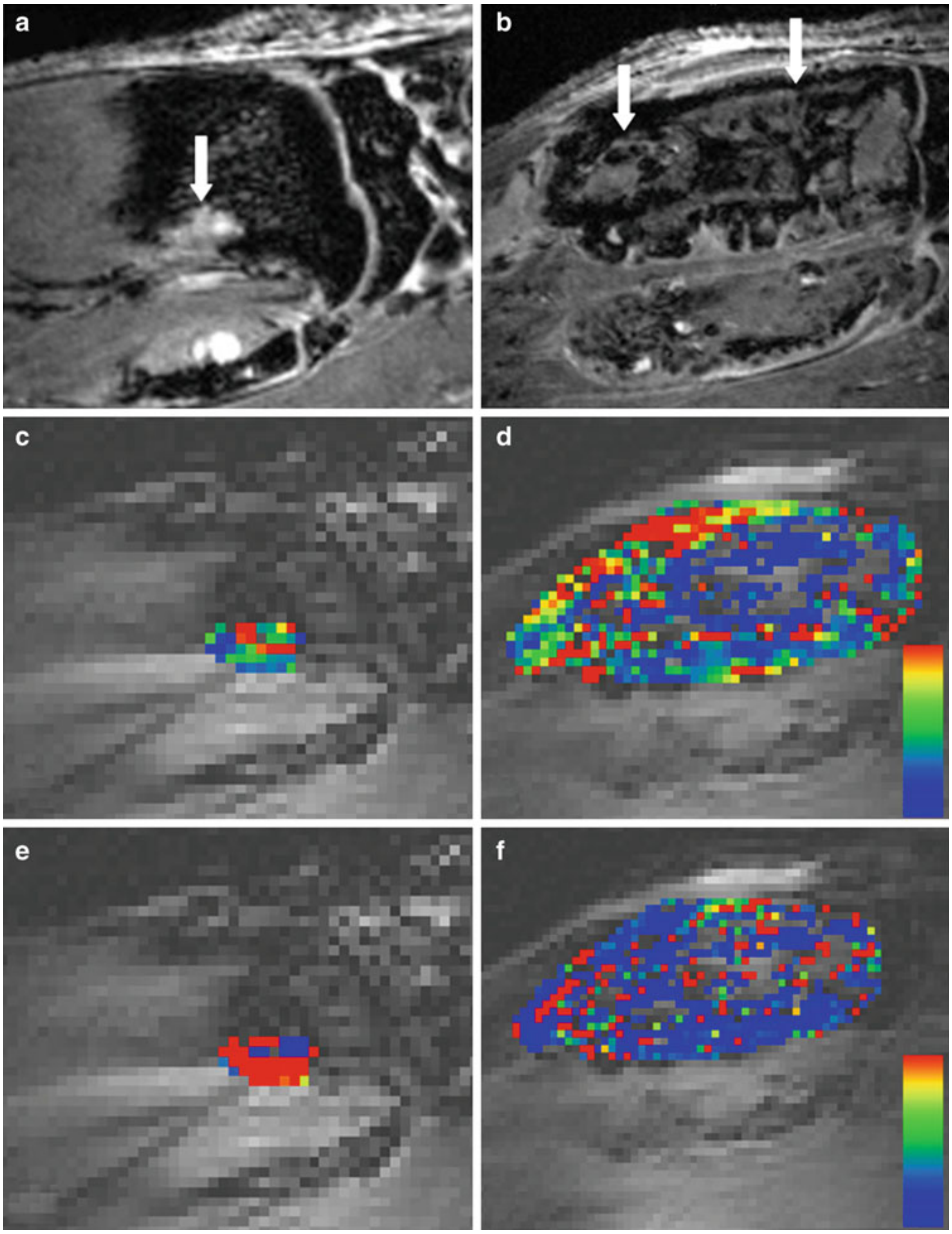

Fig. 15 Comparison of treated experimental breast cancer bone metastases-bearing rats at day 30 after tumor cell injection; $T1$-weighted MRI after contrast agent application (**a**), DCEMRI-derived color-coded maps for amplitude A (**c**), and exchange rate constant k_{ep} (**e**) with sham-treated rats; $T1$-weighted MRI after contrast agent application (**b**), DCEMRI-derived color-coded maps for amplitude A (**d**), and exchange rate constant k_{ep} (**f**). *Arrows point* to soft tissue parts of bone metastases. DCEMRI color code; *red color* indicates higher values and *blue color* depicts lower values for amplitude A (**d**) and exchange rate constant k_{ep} (*f*)

1. Reduction of tissue relaxation times $T1$ and $T2$ through diffusible CA (relaxation effect). This effect is used to generate positive enhanced $T1$ weighted images and the technique is called DCE-MRI or $T1$-W DCE or Dynamic Relaxivity MRI.
2. Transient formation of magnetic field heterogeneities during the passage of a paramagnetic CA through the capillaries (susceptibility effect). This effect is used to produce negative enhanced $T2$ or $T2^*$ weighted images. Studies assessing this effect are commonly referred to *dynamic susceptibility contrast* (DSC) MRI or $T2$-W DCE (Themen 1997).

4.1.2 Data Acquisition Using DCE-MRI

For data acquisition using DCE-MRI three steps are required:

(1) Recording a map of the native $T1$ values ($T1_0$ map) before contrast administration, as the calculation of the CA concentrations also requires knowledge of the initial $T1$ value of the tissues prior to CA arrival (Yankeelov and Gore 2009).

(2) Acquisition of heavily $T1$-weighted images before and after CA introduction. Quick acquisition of heavily $T1$-weighted images is commonly carried out by spoiled gradient echo sequences (synonym: fast low angle

shot = FLASH). Using a saturation-recovery-turbo FLASH sequence enables estimation of precontrast $T1$ relaxation times derived from the dynamic image series (Brix et al. 2004).

(3) The arterial input function (AIF) is a method to estimate the concentration of the CA in the blood plasma of a feeding vessel as a function of time.

Acquiring the AIF is essential for nearly all quantitative analysis methods. A perquisite of pharmacokinetic models is the arrival of the CA at the tissue in the form of an ultra-narrow, well-defined bolus (i.e., impulse input of tracer) (Themen 1997). This ideal bolus will flood the tissue and create a response, a concentration time curve within the tissue, which is termed the residue (or residual) response. It is this curve that can be used to extract quantitative information regarding intrinsic tissue properties. However, in reality the concentration time course of the CA in a vessel entering the tissue (the AIF) differs substantially from the ideal form and hence the residual function cannot be measured directly (Fig. 16). Alternatively concentration times curves of both the tissue and a feeding artery (AIF) can be measured whereupon these two curves can be used to reconstruct the residual function and quantification can performed accurately. The mathematical process of deriving information in order to reconstruct an underlying unknown original function (in our case the residual function) which has been altered by a second function (the AIF) to consequently produce a third function (tissue concentration time course) is termed deconvolution.

In practice the form of the CA bolus is affected by individual parameters, such as CA dose, injection technique, cardiovascular status, and other physiological variables. These variations can be minimized by the deconvolution of data from each voxel using the AIF. The analysis relies on the measurement of a surrogate AIF from a major feeding artery which equals only an approximation of the true AIF.

The number of measurements required for data acquisition is dependent on the quantification method one wishes to apply. For simple semiquantitative analysis of signal intensity curves, method 2 will suffice. For additional CA concentration values method 1 must also be included. For quantitative pharmacokinetic analysis all three methods should take place.

4.1.3 DCE Analysis Procedure

Shortly after a bolus of paramagnetic contrast agent is intravenously administered it enters the tissue. The enhancement pattern of the tissue depends on a wide variety of factors, including but not limited to vascularity, capillary permeability, perfused capillary surface area, volume and composition of extracellular fluid, renal clearance and tissue perfusion. The analysis of the contrast enhancement pattern can be performed using a variety of techniques, such as simple semiquantitative methods, analysis of curve morphology and quantitative methods. Simple semiquantitative values can be derived from the tissue time-intensity curve alone. More complex pharmacokinetic based analyses require the identification of the AIF.

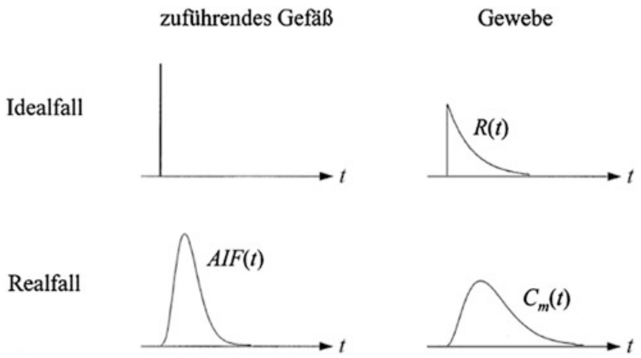

Fig. 16 Should a CA arrive at the tissue as an ideal, ultra-narrow flooding bolus, the tissue response is the sought after residual function. In reality the form of the bolus in the feeding artery (the AIF) differs substantially from the ideal form. The measured signal in the tissue is not the residual function but a widely spread time-concentration curve. From Themen (1997). This material is reproduced with permission of Springer

4.1.4 Semiquantitative Analysis

The signal intensity curve alone is very helpful for simple semiquantative analysis.

Model-free parameter extractions have several advantages as they are (1) robust, (2) obviate the need for an AIF measurement, (3) some of them, such as area under-curve (AUC) are independent of injection protocols (Galbraith et al. 2002), (4) easy to calculate, and (5) do not have any rigorous requirements in terms of data acquisition (Jaspers et al. 2010). Regrettably semiquantitative parameters do not necessarily have any obvious physiological correlates, since they represent a mix of microcirculatory and tissue properties. The degree to which each of these physiological parameters contributes is challenging to determine. Another limitation is the fact that most of the signal intensity based methods are influenced by the type of acquisition protocol applied. They depend on factors such as sequence parameters, hardware settings, scan duration, amount of administered CA (Lavini et al. 2007), CA properties, injection protocol and so on. These varations will occur even if identical sequences are used since the baseline signal for any given tissue, using a particular sequence, will differ by the choice of imager. In summary the comparison of semiquantitative studies are difficult and should be made with caution due to the aforementioned variations.

Having said this, semiquantitative parameters reflect physiological mechanisms and qualitative signal based analysis is very useful, especially where measurement of relative changes in an individual or group of patients is required.

Commonly used metrics for this measurement technique include:

1. *Initial area under the curve (iAUC)*: computes the area under tissue concentration time curve up to a stipulated time that includes a major portion of tissue response.
2. *Maximum (relative) enhancement* (in %): maximum signal difference (MSD)/signal baseline (SB).
3. *Time to maximum signal intensity* (in sec.): time between the arterial peak enhancement and SI_{max}.
4. *Time to peak enhancement* (in sec.): time between the arterial peak enhancement and the end of the steepest portion of enhancement.
5. *Rate of peak enhancement*: [(SIend − SIprior/(SI-base × T)] × 100 (in %/min).
6. *Rate of enhancement*: [(SImax – Slbase)/(SIbsae × Tmax)] × 100 (in %/min).

The slope of the time-intensity curve can also be normalized by dividing it with the arterial TIC slope. This parameter is termed perfusion index (PI) by some authors and has been used both in studies of skeletal muscle and the myocardium (Isbell et al. 2007; Jiji et al. 2013; Panting et al. 2002).

7. *T90* (in sec.): Measurement of the time taken for the tissue to attain 90 % of its subsequent maximal enhancement.
8. *Maximum rate of change of enhancement* (maximal intensity change per time interval ratio)(in %/min).

The last two parameters are designed to minimize the variation which occurs between patients as a result of variations in contrast dose, injection, scanning techniques, and scanner type (Jackson 2004).

Semiquantitative analysis can also be applied performing *first-pass methods*. These methods are easily implemented in clinical settings with relatively low scanning time. It is assumed that the dynamic enhancement pattern observed early during the first pass (the slope) will represent above all, the kinetics of the contrast agent within the blood vessels. The method has been applied in several studies of cervical cancer (Mayr et al. 1996, 2000) and other variations of the method have been applied extensively in studies of the heart (Panting et al. 2002; Pack and DiBella 2010; Saeed 2001) and the skeletal muscle (see section Investigations of the musculoskeletal system with DCE-MRI techniques).

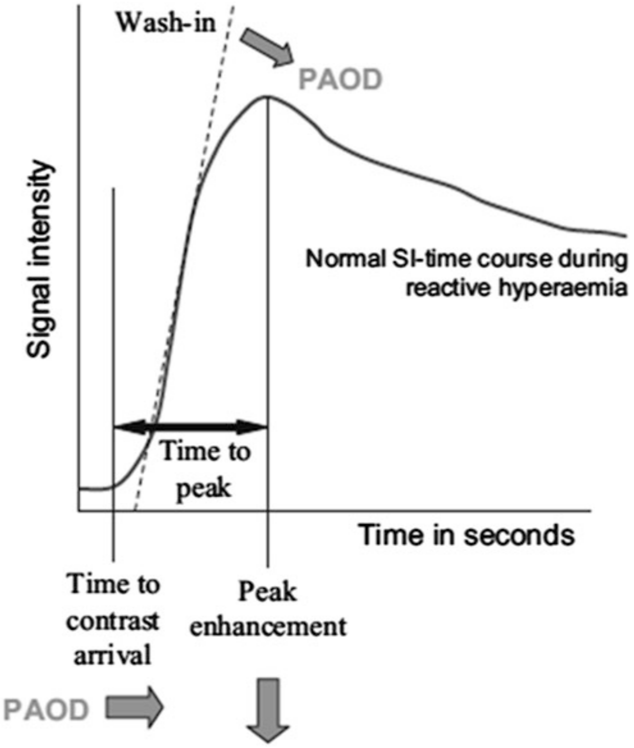

Fig. 17 Diagram of a signal intensity curve of DCE-MRI, representing the contrast agent dependent signal intensity over time. Characteristic curve segments are the linear upslope (wash-in) reaching a maximum intensity, i.e., peak enhancement. Subsequently, there is a washout of contrast medium. The time to peak describes the time from onset of bolus appearance (time to contrast arrival) to peak contrast enhancement. The perfusion reserve of patients can be assessed by measuring the reactive hyperemia after occluding the arterial inflow by suprasystolic cuff compression or after symptom-limited treadmill exercise in comparison with age-matched controls. In case of peripheral arterial occlusive disease (PAOD), there is a delay in contrast arrival time, a less steep upslope, and a lower peak enhancement (*arrows*). From Weber et al. (2007). This material is reproduced with permission of Springer

4.1.5 Morphologic Analysis

This approach primarily considers the shape of the uptake and washout of the TIC and has been named “curve-ology” (Yankeelov and Gore 2009). Distinctive curve patterns are defined and attempts are made to assign them to physiological or pathological findings (Van Rijswijk et al. 2001). For instance in the skeletal muscle, a rapid signal intensity increase followed by a narrow peak and a washout phase is evident for an adequate vascular reserve. In contrary, should the signal intensity curve shows a shallow increment, a delayed peak and only a weak or absent washout after exercise, this might be a hint toward a limited vascular reserve (Leppek et al. 2004) (Fig. 17). The method has been successfully applied to rheumatoid arthritis (Van de Sande et al. 2012; Van der Leij et al. 2009), breast imaging (Rieber et al. 2002) and a variety of musculoskeletal lesions (Lavini et al. 2007).

4.1.6 DCE Quantitative Analysis

One of the appealing features of DCE-MRI is its capability to calculate absolute measures directly related to the physiological and pathophysiological properties of the microvascular environment and the surrounding tissue. This is usually performed by means of model-based pharmacokinetic analysis. The purpose of a model is to describe the underlying physiological phenomenon in mathematical terms in order to enable the estimation of specific tissue parameters from a measured signal. Tracer kinetic models describe tracer transport processes within the tissue. The model should adequately describe the aspects relevant for the investigation. To this end the result of a quantitative analysis is model dependent.

The fundamental physiological parameters describing the CA movement across the vascular endothelium include: vessel wall permeability, vessel surface area, intravascular and extracellular extravascular volume fractions, blood flow (i.e., perfusion) and ratios of the CA concentrations across the endothelium.

With model-based quantitative analysis three relevant microscopic parameters for the characterization of the microcirculation are acquired: CA exchange rates between the capillaries and the interstitial tissue (the so-called capillary permeability), regional blood volumes, and regional blood flow.

To enable quantitative analysis the following steps are performed:

a. Measurement of baseline $T1$ before gadolinium injection (this enables transformation of the signal intensity-time curve into a time-concentration curve).
b. Measurement of signal intensity changes before and after CA application in the tissue.
c. Conversion of signal intensity data to CA concentrations: The conversion of signal intensity curves into time-concentration curves is carried out by means of an appropriate signal-model since in MRI there is no direct correlation between CA concentration and measured signal intensity changes.
d. Computed time-concentration curves (TCC) are analyzed by tracer kinetic modeling using curve-fitting techniques, either on a region of interest or, less commonly, on a pixel-by-pixel basis.

4.1.7 Curve Fitting

The bulk of quantitative analyses techniques rely on curve-fitting methods to produce estimates of parametric values. Each model is an equation containing multiple numbers of free fitting (adjustable) parameters. These are the physiological parameters which are extracted in order to ascertain receipt of significant information about the tissue. By varying the parameters' values in those equations using mathematical algorithms (for example nonlinear least squares fit), a parameter combination that best fits the observed TCC is sought. Pharmacokinetic analysis and interpretation of dynamic data are complex and computationally demanding. It is complicated by the availability of a plethora of analysis algorithms and by the fact that some calculated parameters may represent different biological phenomena depending on the model applied. Model derived pharmacokinetic parameters have the advantage of being more directly related to physiological events in the tissues and are potentially independent of the type of scanner, scanning technique, or individual patient variations. Longitudinal studies as well as accurate comparison between results are very well doable.

4.2 Dynamic Susceptibility MRI

In conventional MRI local magnetic heterogeneities arise on the boundaries between structures that differ in their magnetic susceptibility leading to signal reduction on $T2^*$ weighted gradient echo sequences (Themen 1997) (Fig. 18). The same effect occurs when a paramagnetic CA resides in the intravascular space of a tissue. Thus, this effect can only be utilized in tissues where specific vascular barriers prevent a fast passage of the CA into the interstitial space such as brain, retina, and testes. Alternatively, the use of intravascular (blood pool) contrast agents, which leave the vessels at a much slower rate, are warranted.

In DSC a CA bolus is quickly injected intravenously and the resulting transient $T2^*$ reductions are monitored during the first passage of the CA through the capillary bed. The rapid loss of MR signal on $T2^*$ weighted images is measured and then used to calculate the change in concentration of CA for each individual voxel. The conversion of time-intensity curves into time-concentration curves is utilized to calculate estimates of local blood volume and flow. The transient signal reduction is proportional to local blood volume and flow (Fig. 19).

4.2.1 Data Acquisition Using DSC MRI

The typical imaging technique for DSC is single or multi-shot echo-planar imaging (EPI).

Either spin echo or gradient echo sequences can be employed. Spin echo sequences minimize the signal contribution from large vessels, gradient echo sequences maximize $T2^*$ weighting (Essig et al. 2002).

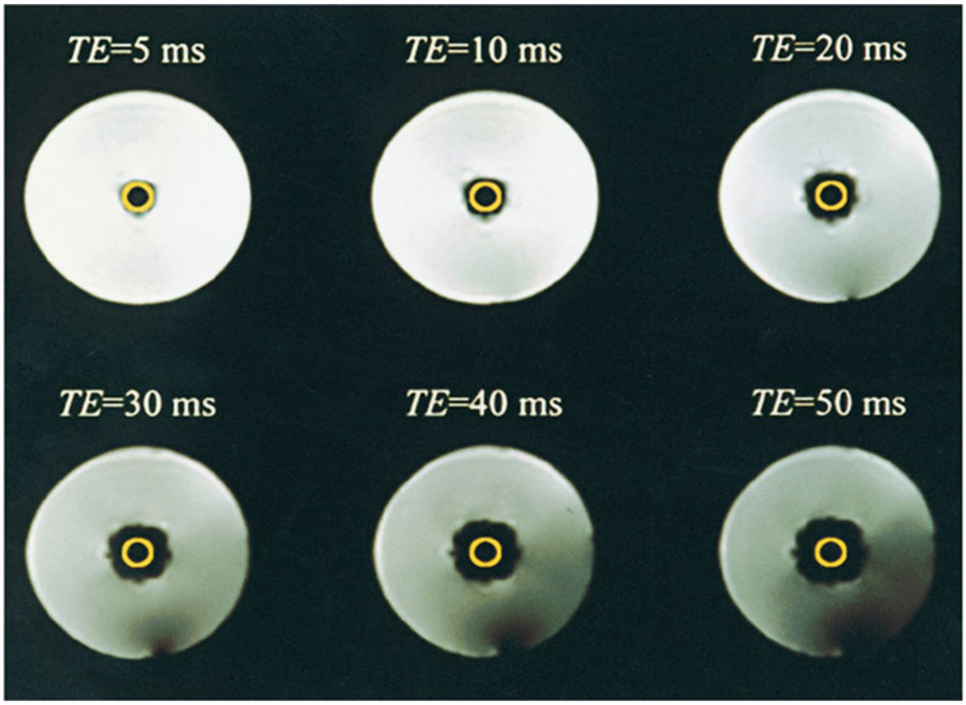

Fig. 18 $T2^*$-W images of a tube filled with a Gd-DTPA solution within a water phantom. The signal reduction effect increases as the echo times are prolonged (i.e., the stronger the $T2^*$-W). From Themen (1997). This material is reproduced with permission of Springer

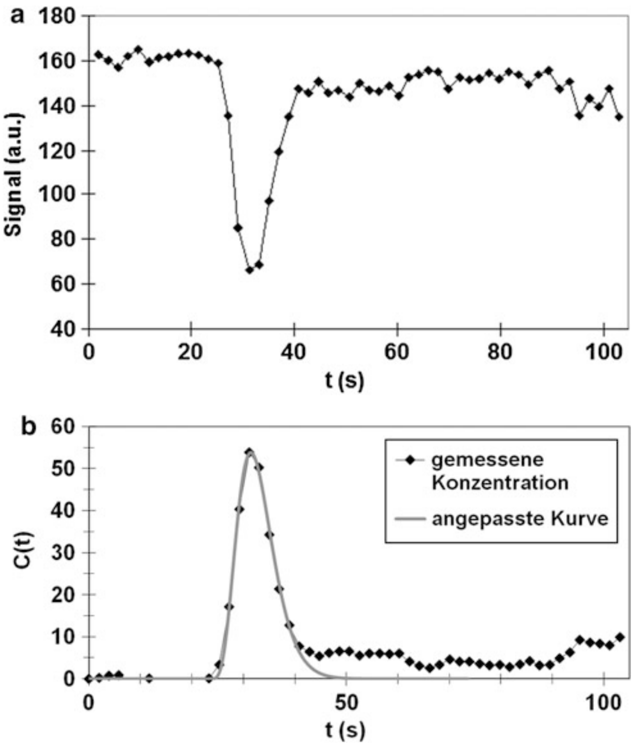

Fig. 19 Conversion of a signal time-intensity curve (**a**) into a time-concentration curve (**b**). The signal time-intensity curve (**a**) depicts the signal loss during the passage of a CA through a tissue, which is registered with a $T2^*$-weighted GE-EPI sequence. The relative blood volume is proportional to area under the time-concentration curve (**b**). From Weber et al. (2005). This material is reproduced with permission of Springer

4.2.2 DSC Quantification Approaches

The main objectives of DSC MRI are the measurement of:

(a) *Regional blood volume* (rBV): volume (ml) of blood perfused vessel in a voxel divided by the tissue mass in the voxel (g).
(b) *Mean transit time* (MTT): average transit time of a tracer particle through the capillary bed.
(c) *Regional blood flow* (rBF): i.e., perfusion (milliliters per minute).

Analysis of DSC MRI data works with the assumption that the contrast agent remains within the vascular space throughout the examination acting as an intravascular CA (blood pool). As mentioned earlier this assumption is only valid for very few tissues and naturally not for tumors. Therefore, the application of DCS was initially limited to studies of normal brain although modifications of the technique have subsequently allowed its use in other tissues.

The standard approach for estimating absolute blood flow from the obtained data includes four steps:

1. The time-concentration data from an individual voxel are deconvolved with an arterial input function (AIF), derived from a major vessel (O'Connor et al 2011).
2. The area under the contrast concentration curve is used for an analytical calculation to estimate the blood volume (BV) within the pixel.
3. The mean transit time (MTT) is then estimated using some form of a standardized relationship between the surface and the height of the time-concentration curve.
4. Blood flow is calculated using the central volume theorem: $rBF = rBV/MTT$ ($\mathrm{ml \cdot min^{-1} \cdot g^{-1}}$).

Challenges exist, which makes the estimation of absolute flow complex (O'Connor et al 2011). Quantitative measurements are complicated by the following factors: Contrast leakage and subsequent tissue enhancement, contrast recirculation, bolus dispersion and accurate estimation of rBV and MTT.

The most prevailing clinical applications of DSC are stroke (Wang et al. 2012; MacDonald et al. 2011), cerebrovascular insufficiency (Crane et al. 2012; Calviere et al. 2012) and brain tumors (Aronen et al. 1993, 1994), though it has been used on occasion to measure muscle perfusion in animal experiments (Rissanen et al. 2005; Goyault et al. 2012).

4.2.3 DCE and DSC MRI Combination Approaches

Dual-echo DSC MRI can be used to simultaneously extract reliable DCE-MRI kinetic parameters (related to extravasation) in addition to conventional blood volume and blood flow metrics. The feasibility of separately measuring $T1$- and $T2^*$-weighted induced signal changes using dual-echo pulse sequences was conducted in studies of brain tumors (Kuperman et al 1996; Vonken et al. 2000; Barbier et al. 1999). When combined with a precontrast $T1$ map the dual-echo DSC MRI technique enables reliable determination of K^{trans} and v_{e}. These parameters showed a high degree of correlation with the DSC MRI-derived measurements (Quarles et al. 2012) (Table 1).

4.3 Investigations of the Musculoskeletal System with DCE-MRI Techniques

4.3.1 Human Studies

Early DCE-MRI studies of the muscle focused on assessing the potential of the technique for distinguishing between malignant and benign conditions using semiquantitative slope values. Though significant differences were found between benign compared to malignant tissues and the method exhibited fair sensitivity, a significant overlap persisted between malignant neoplasms and several highly vascularized benign lesions (Verstraete et al. 1994; Konez et al 1997; Van der Woude et al. 1998). A variety of musculoskeletal (MSK) pathological conditions have been investigated with the previously described semiquantitative curve shape analysis method (Lavini et al. 2007). Although the shape maps obtained revealed a significant heterogeneity of TIC patterns within the lesions, the method was not able to differentiate malignant from benign. In patients suffering from medial tibial pain the sensitivity of DCE-MRIs to depict periosteal edema was compared to other MRI sequences such as proton density, $T2$ weighted and post-contrast $T1$ weighted images (Mattila et al. 1999). The gradually enhancing periostitis was best demonstrated by DCE-MRI in comparison to the other techniques.

Similar to other functional MRI methods, DCE uses the hyperemia and exercise paradigms to investigate muscle perfusion. The majority of perfusion experiments using the technique were directly performed on patients with PAOD (discussed in the section below). DCE measurements of the calf of four healthy young adults performing a plantar flexion exercise paradigm at different workloads were compared with blood flow in the popliteal artery by ultrasonography. The collected MRI parameters enabled to visually separate the muscles into an exercising and non-exercising group. However, the increase in SI measured by MRI was much smaller compared to the increase in blood flow values acquired from ultrasonography and the correlation between the two measurements was limited (Nygren et al. 2000).

A further investigation applied a postarterial occlusion paradigm leading to reactive hyperemia for assessing the first pass perfusion in the calf muscle of 20 healthy volunteers. Applying the general Tofts model (Tofts et al. 1999) for quantification, the data was then compared to corresponding measurements from segmental volume plethysmography. Results showed highly significant changes in calf muscle signal dynamics in the hyperemic leg versus those in the contralateral resting leg, both when applying semiquantitative and deconvolution (quantitative) analysis. Furthermore, flow extraction fraction products within the non-compressed leg were in agreement with published resting perfusion values (Lutz et al. 2004).

In 2005 a new method was described to quantitatively measure skeletal muscle first pass blood flow during post-ischemic reactive hyperemia without the requirement of deconvolution. This method uses the quick release of an occlusive thigh cuff to deliver a step-input of CA that was injected after cuff inflation. The simple input function required only the optimization of Larsson's model (Larsson et al. 1994) to extract K^{trans} (or $K_i = E{\cdot}F$) and v_e. The authors compared the DCE protocol to blood flow studies with the same volunteers, using phase-contrast velocimetry (PCV) obtained from the popliteal artery. The results for the distribution volume (v_e) were in good agreement with values reported in the literature and correlated significantly with the blood flow studies with the same volunteers, though the PCV yielded significantly lower flow values. DCE blood flow values were significantly different in the observed muscle groups and correlated well with the known distribution of different muscle fibers (Thompson et al. 2005).

4.3.2 Animal Studies

Similar to human studies the majority of animal experiments examining muscle microperfusion deal with PAOD.

Table 1

Symbol	Name	Definition	Units
K^{trans}	Transfer constant (or coefficient)	Volume transfer constant between blood plasma and EES	min^{-1}
k_{ep}	Rate constant[a]	Rate constant between EES and blood plasma (backflux exchange rate)	min^{-1}
v_e	Volume of extravascular extracellular space (EES)	Volume of extravascular extracellular space per unit volume of tissue	None (values either $0 < v_e < 1$ or as %)

[a] $K_{ep} = K^{trans} / v_e$

Table 2

Quantity	Definition	Unit
C_a	Tracer concentration in arterial whole blood	mM = 1 mmol/L
C_e	Tracer concentration in EES	mM
C_p	Tracer concentration in arterial blood plasma	mM
C_t	Tracer concentration in tissue	mM
C_v	Tracer concentration in venous whole blood	mM
CL_d	Distribution clearance	$ml\ min^{-1}$
E	Initial extraction ratio (fractional reduction in capillary blood concentration of a CA as it passes through tissue)	None (%)
Hct	Hematocrit	None
F	Perfusion (or flow) of whole blood per unit mass of tissue	$ml\ g^{-1}\ min^{-1}$
P	Total permeability of capillary wall	$cm\ min^{-1}$
PS	Permeability surface area product per unit mass of tissue	$ml\ min^{-1}\ g^{-1}$
S	Surface area per unit mass of tissue	$cm^2\ g^{-1}$
V_b	Total whole blood volume[a]	ml
V_e	Total EES volume[a]	ml
V_p	Total blood plasma volume[a]	ml
V_t	Total tissue volume[a]	ml
v_b	Whole blood volume per unit volume of tissue[a]	None (%)
v_p	Blood plasma volume per unit volume of tissue	None (%)
λ	Tissue blood partition coefficient	$ml\ g^{-1}$
ρ	Density of tissue	$g\ ml^{-1}$

[a] $V_b = v_b V_t$; $V_e = v_e Vt$; $V_p = v_p V_t = (1 - \mathrm{Hct}) V_b$
C = concentrations (mM)
V = total volumes (ml)
v = fractional volumes (%)
$_{e,\ a,\ p,\ t,\ v}$ = extravascular extracellular space, arterial blood, plasma, tissue, venous respectively [for example: k_{ep} stands for—constant (k) extravascular extracellular space ($_e$) to plasma ($_p$)]

Mainly utilizing the well-established arterial ligation model (Jaspers et al. 2010; Rissanen et al. 2005; Luo et al. 2002; De Lussanet et al. 2007; Ziv et al. 2004) several experiments have successfully quantified muscle perfusion in small animals using both DCE-MRI (Luo et al. 2002; De Lussanet et al. 2007; Ziv et al. 2004; Loerakker et al. 2011; Faranesh et al. 2006; Cheng 2007) and DSC MRI (Rissanen et al. 2005; Goyault et al. 2012) administering a variety CAs [including blood pool agents (Jaspers et al. 2010; Ziv et al. 2004; Faranesh et al. 2006; Cheng 2007) and Superparamagnetic Iron Oxide Particles (Rissanen et al. 2005)].

4.3.3 Peripheral Arterial Occlusive Disease

Blood flow to the lower leg muscles were quantified at rest and after individually adjusted plantar flexion muscular exercise in five subjects: A female patient with PAOD (Fontaine IIb) before and after PTA, a male patient with coronary heart disease without clinical signs of a PAOD, a healthy volunteer and two professional athletes. The semi-quantitative analysis showed distinctive exercise induced changes of the upslope, wash-in, peak and washout of the SI-curves in the different muscles of the calf in all subjects. The magnitude of the changes induced also seemed to be dependent on the individual fitness of the subjects. Notably, the PAOD patient demonstrated a steeper SI-curve post-exercise after PTA (Leppek et al. 2004).

A sequence was presented enabling simultaneous acquisition of the arterial input function and tissue perfusion images. The technique utilized a saturation recovery GRE sequence for the estimation of the AIF, interleaved with an inversion-recovery GRE sequence for the measurement of tissue perfusion. Though the study did not employ model based analysis, a normalized perfusion index (PI) was defined as the slope of the time-intensity curve in muscle divided by the arterial TIC slope. First pass imaging was applied to the measurement of the PI in 11 patients with mild to moderate symptomatic PAOD and 22 normal subjects directly after peak exercise. In the PAOD group the ankle-brachial index (ABI) failed to correlate with PI. Neither the ABI nor the PI correlated with the workloads achieved (PAOD patients approx. 450 J, normal subjects approx. 1,100 J). Interestingly, peak-exercise measurements were able to distinguish PAOD patients from normal subjects (Isbell et al. 2007).

New methods were applied to determine the utility and reproducibility of rest, exercise, and perfusion reserve (PR = ratio of exercise to rest blood flow) measured by DCE-MRI. Tissue perfusion and arterial input both at rest and peak exercise in the calves of PAOD patients with claudication and age-matched controls were investigated. Though highly reproducible, rest perfusion parameters were too variable and too low in the muscle to distinguish between controls and PAOD patients. This held also true for the PR which was reproducible but highly variable as well. The exercise parameters could distinguish between patients and healthy volunteers (Jiji et al. 2013).

Recently, the ability of DCE to reproducibly asses the functional peripheral vascular status was tested. In this study the first pass step-input method was used (Thompson et al. 2005) extracting the influx constant K_i ($K^{\mathrm{trans}} = E{\cdot}F{\cdot}_p$ $(1 - Hct)$ and K_i is defined as $E{\cdot}F$). Besides, the area under the curve up to 90 s after CA arrival was calculated. Inter-scan and inter-reader reproducibility were determined as well. The reproducibility of DCE-MRI to measure microvascular function was poor in patients due to large inter-scanvariations (Versluis et al. 2011). In a similar study Gadofosveset, a blood pool CA (Blood pool agents are a CA group, also referred to as intravascular CA, which in contrast to conventional contrast agents leave the intravascular space at a much slower rate) was used. The pharmacokinetic parameters v_{p} and k were significantly lower for all muscle groups in PAOD patients as compared to healthy control subjects (Versluis et al. 2012) (Table 2).

DCE-MRI has been applied for studying plaque neovascularization in animals and patients with atherosclerosis (Kerwin et al. 2003; Calcagno et al. 2008). Plaque angiogenesis is an attractive target to identify asymptomatic yet high-risk atherosclerotic lesions.

5 Conclusion

Muscle BOLD MRI has proven to be a very sensitive tool to detect microvascular pathologies in a variety of different disease settings. Despite its multifactorial origin in skeletal muscle tissue, the BOLD contrast primarily depends on perfusion related changes of muscle tissue oxygenation. However, current muscle BOLD studies often suffer from the uncertainty of uncontrolled parameters influencing the $T2^*$ signal. ASL allows a direct measurement of microvascular perfusion and—as BOLD MRI—is independent of the administration of contrast agents but suffers from a bad signal to noise ratio and the need of additional parameter measurements or assumptions what may compromise the resulting datasets. With DCE, microvascular properties, such as fractional volumes of plasma and blood, vessel permeability and perfusion can be obtained. If these MR techniques are to find their way into the clinics, standardization, further validation, and reproducibility experiments must precede.

References

Alsop DC, Detre JA (1996) Reduced transit-time sensitivity in noninvasive magnetic resonance imaging of human cerebral blood flow. J Cereb Blood Flow Metab 16:1236–1249

Alsop DC, Detre JA (1998) Multisection cerebral blood flow MR imaging with continuous arterial spin labeling. Radiology 208:410–416

Alsop DC, Detre JA, Grossman M (2000) Assessment of cerebral blood flow in Alzheimer's disease by spin-labeled magnetic resonance imaging. Ann Neurol 47:93–100

Amarteifio E et al (2011) Dynamic contrast-enhanced ultrasound for assessment of skeletal muscle microcirculation in peripheral arterial disease. Invest Radiol 46:504–508

Amarteifio E et al (2013) Assessment of skeletal muscle microcirculation in type 2 diabetes mellitus using dynamic contrast-enhanced ultrasound: a pilot study. Diab Vasc Dis Res. doi:10.1177/1479164113484165 (Epub ahead of print)

Aronen HJ, Cohen MS, Belliveau JW, Fordham JA, Rosen BR (1993) Ultrafast imaging of brain tumors. Top Magn Reson Imaging 5:14–24

Aronen HJ et al (1994) Cerebral blood volume maps of gliomas: comparison with tumor grade and histologic findings. Radiology 191:41–51

Baligand C et al (2011) Measuring perfusion and bioenergetics simultaneously in mouse skeletal muscle: a multiparametric functional-NMR approach. NMR Biomed 24:281–290

Bandettini PA, Wong EC, Hinks RS, Tikofsky RS, Hyde JS (1992) Time course EPI of human brain function during task activation. Magn Reson Med 25:390–397

Barbier EL et al (1999) A model of the dual effect of gadopentetate dimeglumine on dynamic brain MR images. J Magn Reson Imaging 10:242–253

Berglund B, Eklund B (1981) Reproducibility of treadmill exercise in patients with intermittent claudication. Clin Physiol (Oxford England) 1:253–256

Bertoldi D et al (2006) New insight into abnormal muscle vasodilatory responses in aged hypertensive rats by in vivo nuclear magnetic resonance imaging of perfusion. J Vasc Res 43:149–156

Blamire AM, Styles P (2000) Spin echo entrapped perfusion image (SEEPAGE). A nonsubtraction method for direct imaging of perfusion. Magn Reson Med 43:701–704

Boss A, Martirosian P, Claussen CD, Schick F (2006) Quantitative ASL muscle perfusion imaging using a FAIR-TrueFISP technique at 3.0 T. NMR Biomed 19:125–132

Boushel R et al (2000) Blood flow and oxygenation in peritendinous tissue and calf muscle during dynamic exercise in humans. J Physiol 524(Pt 1):305–313

Brix G et al (2004) Microcirculation and microvasculature in breast tumors: pharmacokinetic analysis of dynamic MR image series. Magn Reson Med 52:420–429

Bulte DP, Alfonsi J, Bells S, Noseworthy MD (2006) Vasomodulation of skeletal muscle BOLD signal. J Magn Reson Imaging 24:886–890

Bunt TJ, Holloway GA (1996) TcPO2 as an accurate predictor of therapy in limb salvage. Ann Vasc Surg 10:224–227

Buxton RB et al (1998) A general kinetic model for quantitative perfusion imaging with arterial spin labeling. Magn Reson Med 40:383–396

Calcagno C et al (2008) Detection of neovessels in atherosclerotic plaques of rabbits using dynamic contrast enhanced MRI and 18F-FDG PET. Arterioscler Thromb Vasc Biol 28:1311–1317

Calviere L et al (2012) Executive dysfunction in adults with moyamoya disease is associated with increased diffusion in frontal white matter. J Neurol Neurosurg Psychiatry 83:591–593

Carlier PG, Bertoldi D, Baligand C, Wary C, Fromes Y (2006) Muscle blood flow and oxygenation measured by NMR imaging and spectroscopy. NMR Biomed 19:954–967

Chalela JA et al (2000) Magnetic resonance perfusion imaging in acute ischemic stroke using continuous arterial spin labeling. Stroke 31:680–687

Cheng H-LM (2007) T1 measurement of flowing blood and arterial input function determination for quantitative 3D T1-weighted DCE-MRI. J Magn Reson Imaging 25:1073–1078

Crane DE et al (2012) Evaluating quantitative approaches to dynamic susceptibility contrast MRI among carotid endarterectomy patients. J Magn Reson Imaging 37:936–943

Dawson JM, Hudlicka O (1990) Changes in the microcirculation in slow and fast skeletal muscles with long term limitations of blood supply. Cardiovasc Res 24:390–395

De Lussanet QG et al (2007) Dynamic contrast-enhanced MRI of muscle perfusion combined with MR angiography of collateral artery growth in a femoral artery ligation model. NMR Biomed 20:717–725

Detre JA, Alsop DC (1999) Perfusion fMRI with arterial spin labeling. In: Bandettini PA, Moonen C (eds) Functional MRI. Springer, Berlin pp 47–62

Detre JA, Leigh JS, Williams DS, Koretsky AP (1992) Perfusion imaging. Magn Reson Med 23:37–45

Detre JA et al (1999) Noninvasive magnetic resonance imaging evaluation of cerebral blood flow with acetazolamide challenge in patients with cerebrovascular stenosis. J Magn Reson Imaging 10:870–875

Donahue KM, Van Kylen J, Guven S, Luh WM, El-Bershawi A, Bandettini PA, Hyde JS, Kissebah AH, Cox RW (1998) Simultaneous gradient-echo/spin-echo EPI of graded ischemia in human skeletal muscle. J Magn Reson Imaging 8:1106–1113

Duteil S et al (2004) Metabolic and vascular support for the role of myoglobin in humans: a multiparametric NMR study. Am J Physiol Regul Integr Comp Physiol 287:R1441–R1449

Duteil S et al (2006) Influence of vascular filling and perfusion on BOLD contrast during reactive hyperemia in human skeletal muscle. Magn Reson Med 55:450–454

Duyn JH, Tan CX, van Gelderen P, Yongbi MN (2001) High-sensitivity single-shot perfusion-weighted fMRI. Magn Reson Med 46:88–94

Essig M et al (2002) Dynamic susceptibility contrast-enhanced echo-planar imaging of cerebral gliomas. Effect of contrast medium extravasation. Acta Radiol 43:354–359

Fagrell B (1986) Microcirculatory methods for the clinical assessment of hypertension, hypotension, and ischemia. Ann Biomed Eng 14:163–173

Faranesh AZ, Kraitchman DL, McVeigh ER (2006) Measurement of kinetic parameters in skeletal muscle by magnetic resonance imaging with an intravascular agent. Magn Reson Med 55:1114–1123

Fox PT, Raichle ME (1986) Focal physiological uncoupling of cerebral blood flow and oxidative metabolism during somatosensory stimulation in human subjects. Proc Natl Acad Sci USA 83:1140–1144

Frank LR, Wong EC, Haseler LJ, Buxton RB (1999) Dynamic imaging of perfusion in human skeletal muscle during exercise with arterial spin labeling. Magn Reson Med 42:258–267

Frouin F et al (2006) An automated image-processing strategy to analyze dynamic arterial spin labeling perfusion studies. Application to human skeletal muscle under stress. Magn Reson Imaging 24:941–951

Gabrielli A, Avvedimento EV, Krieg T (2009) Mechanisms of disease. Scleroderma. N Engl J Med 19:1989–2003

Galbraith SM et al (2002) Reproducibility of dynamic contrast-enhanced MRI in human muscle and tumours: comparison of quantitative and semi-quantitative analysis. NMR Biomed 15:132–142

Garcia DM, Duhamel G, Alsop DC (2005) Efficiency of inversion pulses for background suppressed arterial spin labeling. Magn Reson Med 54:366–372

Gati JS, Menon RS, Ugurbil K, Rutt BK (1997) Experimental determination of the BOLD field strength dependence in vessels and tissue. Magn Reson Med 38:296–302

Gerontol J et al (2009) Multiparametric NMR-based assessment of skeletal muscle perfusion and metabolism during exercise in elderly persons : preliminary findings. J Gerontol A Biol Sci Med Sci 64:968–974

Goyault G et al (2012) Diffusion-weighted MRI, dynamic susceptibility contrast MRI and ultrasound perfusion quantification of denervated muscle in rabbits. Skeletal Radiol 41:33–40

Green DJ, Spence A, Halliwill JR, Cable NT, Thijssen DHJ (2011) Exercise and vascular adaptation in asymptomatic humans. Exp Physiol 96:57–70

Green HJ et al (2012) Can increases in capillarization explain the early adaptations in metabolic regulation in human muscle to short-term training? Can J Physiol Pharmacol 90:557–566

Gu P, Xu A (2013) Interplay between adipose tissue and blood vessels in obesity and vascular dysfunction. Rev Endoc Metab Disord. doi: 10.1007/s11154-012-9230-8

Hennig J, Schreiber A, Scheffler K (2000) Time resolved observation of BOLD effect in muscle during isometric exercise. Proc Int Soc Magn Reson Med 8:122

Hickey NC, Hudlicka O, Simms MH (1992) Claudication induces systemic capillary endothelial swelling. Eur J Vasc Surg 6:36–40

Howseman AM, Bowtell RW (1999) Functional magnetic resonance imaging: imaging techniques and contrast mechanisms. Philos Trans R Soc Lond B Biol Sci 354:1179–1194

Huegli RW et al (2009) Effects of percutaneous transluminal angioplasty on muscle BOLD-MRI in patients with peripheral arterial occlusive disease: preliminary results. Eur Radiol 19:509–515

Isbell DC et al (2007) Calf muscle perfusion at peak exercise in peripheral arterial disease: measurement by first-pass contrast-enhanced magnetic resonance imaging. J Magn Reson Imaging 25:1013–1020

Jackson A (2004) Analysis of dynamic contrast enhanced MRI. Br J Radiol 77:S154–S166

Jacobi B et al (2012) Skeletal muscle BOLD MRI: from underlying physiological concepts to its usefulness in clinical conditions. J Magn Reson Imaging 35:1253–1265

Jacobi B et al (2013) Alterations of skeletal muscle microcirculation detected by blood oxygenation level-dependent MRI in a patient with granulomatosis with polyangiitis. Rheumatology (Oxford, England) 52, 579–581

Jaspers K et al (2010) Optimized pharmacokinetic modeling for the detection of perfusion differences in skeletal muscle with DCE-MRI: effect of contrast agent size. Med Phys 37:5746

Jiji RS et al (2013) Reproducibility of rest and exercise stress contrast-enhanced calf perfusion magnetic resonance imaging in peripheral arterial disease. J Cardiovasc Magn Reson 15:14

Katoh M, Spuentrup E, Barmet C, Stuber M (2008) Local re-inversion coronary MR angiography: arterial spin-labeling without the need for subtraction. J Magn Reson Imaging 27:913–917

Kerwin W et al (2003) Quantitative magnetic resonance imaging analysis of neovasculature volume in carotid atherosclerotic plaque. Circulation 107:851–856

Kim SG (1995) Quantification of relative cerebral blood flow change by flow-sensitive alternating inversion recovery (FAIR) technique: application to functional mapping. Magn Reson Med 34:293–301

Konez O et al (1997) Gradient-echo perfusion imaging of musculoskeletal abnormalities with contrast-enhanced two-dimensional fat-saturation FLASH. J Magn Reson Imaging 7:895–902

Kober F et al (2004) High-resolution myocardial perfusion mapping in small animals in vivo by spin-labeling gradient-echo imaging. Magn Reson Med 51:62–67

Kos S et al (2009) Simultaneous dynamic blood oxygen level-dependent magnetic resonance imaging of foot and calf muscles: aging effects at ischemia and postocclusive hyperemia in healthy volunteers. Invest Radiol 44:741–747

Krix M et al (2011) Comparison of transient arterial occlusion and muscle exercise provocation for assessment of perfusion reserve in skeletal muscle with real-time contrast-enhanced ultrasound. Eur J Radiol 78:419–424

Kuperman VY et al (1996) Differentiating between T1 and $T2^*$ changes caused by gadopentetate dimeglumine in the kidney by using a double-echo dynamic MR imaging sequence. J Magn Reson Imaging 6:764–768

Kwong KK et al (1992) Dynamic magnetic resonance imaging of human brain activity during primary sensory stimulation. Proc Natl Acad Sci USA 89:5675–5679

Kwong KK et al (1995) MR perfusion studies with T1-weighted echo planar imaging. Magn Reson Med 34:878–887

Larsson HB, Stubgaard M, Søndergaard L, Henriksen O (1994) In vivo quantification of the unidirectional influx constant for Gd-DTPA diffusion across the myocardial capillaries with MR imaging. J Magn Reson Imaging 4:433–440

Lavini C et al (2007) Pixel-by-pixel analysis of DCE MRI curve patterns and an illustration of its application to the imaging of the musculoskeletal system. Magn Reson Imaging 25:604–612

Lebon V, Carlier PG, Brillault-Salvat C, Leroy-Willig A (1998a) Simultaneous measurement of perfusion and oxygenation changes using a multiple gradient-echo sequence: application to human muscle study. Magn Reson Imaging 16:721–729

Lebon V, Bloch G, Leroy-Willig A, Carlier PG, Brillault-Salvat C (1998b) Evidence of muscle BOLD effect revealed by simultaneous interleaved gradient-echo NMRI and myoglobin NMRS during leg ischemia. Magn Reson Med 40:551–558

Lebon VPG, Brillault-Salvat C, Bloch G, Leroy-Willig AC (1998c) Anisotropy of the BOLD effect in the skeletal muscle. In: Proceedings ISMRM Sydney 1424

Ledermann HP et al (2006a) Calf muscles imaged at BOLD MR: correlation with TcPO2 and flowmetry measurements during ischemia and reactive hyperemia–initial experience. Radiology 241:477–484

Ledermann HP et al (2006b) Blood oxygenation level-dependent magnetic resonance imaging of the skeletal muscle in patients with peripheral arterial occlusive disease. Circulation 113:2929–2935

Leng GC, Fowkes FG, Allan PL, Ruckley CV (1991) Doppler colour flow imaging in peripheral arterial disease. Br J Hosp Med 45:200, 202, 204–207

Leppek R et al (2004) MR-Imaging of lower leg muscle perfusion. Herz 29:32–46

Loerakker S et al (2011) Ischemia-reperfusion injury in rat skeletal muscle assessed with T2-weighted and dynamic contrast-enhanced MRI. Magn Reson Med 66:528–537

Logothetis NK, Wandell BA (2004) Interpreting the BOLD signal. Annu Rev Physiol 66:735–769

Luh WM, Wong EC, Bandettini PA, Hyde JS (1999) QUIPSS II with thin-slice TI1 periodic saturation: a method for improving accuracy of quantitative perfusion imaging using pulsed arterial spin labeling. Magn Reson Med 41:1246–1254

Luo Y et al (2002) Evaluation of tissue perfusion in a rat model of hind-limb muscle ischemia using dynamic contrast-enhanced magnetic resonance imaging. J Magn Reson Imaging 16:277–283

Lutz AM et al (2004) Assessment of skeletal muscle perfusion by contrast medium first-pass magnetic resonance imaging: technical feasibility and preliminary experience in healthy volunteers. J Magn Reson Imaging 20:111–121

MacDonald ME, Smith MR, Frayne R (2011) Deconvolution with simple extrapolation for improved cerebral blood flow measurement in dynamic susceptibility contrast magnetic resonance imaging during acute ischemic stroke. Magn Reson Imaging 29:620–629

Mai VM, Berr SS (1999) MR perfusion imaging of pulmonary parenchyma using pulsed arterial spin labeling techniques: FAIRER and FAIR. J Magn Reson Imaging 9:483–487

Marcovecchio ML, Chiarelli F (2011) Microvascular disease in children and adolescents with type 1 diabetes and obesity. Pediatr Nephrol (Berlin, Germany) 26:365–375

Marro K (1997) FAWSETS: flow-driven arterial water stimulation with elimination of tissue signal. J Magn Reson (San Diego, CA: 1997) 124:240–244

Marro KI, Hyyti OM, Vincent MA, Kushmerick MJ (2005a) Validation and advantages of FAWSETS perfusion measurements in skeletal muscle. NMR Biomed 18:226–234

Marro KI, Hyyti OM, Kushmerick MJ (2005b) FAWSETS perfusion measurements in exercising skeletal muscle. NMR Biomed 18:322–330

Mattila KT, Komu ME, Koskinen SK, Niemi PT (1993) Exercise-induced changes in magnetization transfer contrast of muscles. Acta Radiol (Stockholm, Sweden: 1987) 34:559–562

Mattila KT, Komu ME, Dahlström S, Koskinen SK, Heikkilä J (1999) Medial tibial pain: a dynamic contrast-enhanced MRI study. Magn Reson Imaging 17:947–954

Mayr NA et al (1996) Tumor perfusion studies using fast magnetic resonance imaging technique in advanced cervical cancer: a new noninvasive predictive assay. Int J Radiat Oncol Biol Phys 36:623–633

Mayr NA et al (2000) Pixel analysis of MR perfusion imaging in predicting radiation therapy outcome in cervical cancer. J Magn Reson Imaging 12:1027–1033

Ménard JC, Giacomini E, Baligand C, Fromes Y, Carlier PG (2010) Non-invasive and quantitative evaluation of peripheral vascular resistances in rats by combined NMR measurements of perfusion and blood pressure using ASL and dynamic angiography. NMR Biomed 23:188–195

Meyer RA et al (2004) BOLD MRI mapping of transient hyperemia in skeletal muscle after single contractions. NMR Biomed 17:392–398

Muller-Delp JM (2006) Aging-induced adaptations of microvascular reactivity. Microcirculation 13:301–314

Niemi PT, Komu ME, Koskinen SK (1992) Tissue specificity of low-field-strength magnetization transfer contrast imaging. J Magn Reson Imaging 2:197–201

Norris DG, Schwarzbauer C (1999) Velocity selective radiofrequency pulse trains. J Magn Reson (San Diego, CA: 1997) 137:231–236

Noseworthy MD, Kim JK, Stainsby JA, Stanisz GJ, Wright GA (1999) Tracking oxygen effects on MR signal in blood and skeletal muscle during hyperoxia exposure. J Magn Reson Imaging 9:814–820

Noseworthy MD, Bulte DP, Alfonsi J (2003) BOLD magnetic resonance imaging of skeletal muscle. Semin Musculoskelet Radiol 7:307–315

Noseworthy MD, Davis AD, Elzibak AH (2010) Advanced MR imaging techniques for skeletal muscle evaluation. Semin Musculoskelet Radiol 14:257–268

Nygren AT, Greitz D, Kaijser L (2000) Skeletal muscle perfusion during exercise using Gd-DTPA bolus detection. J Cardiovasc Magn Reson 2:263–270

O'Connor JPB et al (2011) Dynamic contrast-enhanced imaging techniques: CT and MRI. Br J Radiol 84:S112–S120

Ogawa S, Lee TM, Nayak AS, Glynn P (1990a) Oxygenation-sensitive contrast in magnetic resonance image of rodent brain at high magnetic fields. Magn Reson Med 14:68–78

Ogawa S, Lee TM, Kay AR, Tank DW (1990b) Brain magnetic resonance imaging with contrast dependent on blood oxygenation. Proc Natl Acad Sci USA 87:9868–9872

Ogawa S et al (1992) Intrinsic signal changes accompanying sensory stimulation: functional brain mapping with magnetic resonance imaging. Proc Natl Acad Sci USA 89:5951–5955

Pack NA, DiBella EVR (2010) Comparison of myocardial perfusion estimates from dynamic contrast-enhanced magnetic resonance imaging with four quantitative analysis methods. Magn Reson Med 64:125–137

Panting JR et al (2002) Abnormal subendocardial perfusion in cardiac syndrome X detected by cardiovascular magnetic resonance imaging. N Engl J Med 346:1948–1953

Partovi S et al (2012a) Effects of covert and overt paradigms in clinical language fMRI. Acad Radiol 19:518–525

Partovi S et al (2012b) Clinical implications of skeletal muscle blood-oxygenation-level-dependent (BOLD) MRI. Magma New York NY. doi:10.1007/s10334-012-0306-y

Partovi S et al (2012c) Blood oxygenation level-dependent (BOLD) MRI of human skeletal muscle at 1.5 and 3 T. J Magn Reson Imaging 35:1227–1232

Partovi S et al (2012d) Impaired skeletal muscle microcirculation in systemic sclerosis. Arthritis Res Ther 14:R209

Partovi S et al (2012e) Clinical standardized fMRI reveals altered language lateralization in brain tumor patients. Am J Neuroradiol 1–7. doi:10.3174/ajnr.A3137

Partovi S et al (2013) Correlation of muscle BOLD MRI with transcutaneous oxygen pressure for assessing microcirculation in patients with systemic sclerosis. J Magn Reson Imaging. doi: 10.1002/jmri.24046. (Epub ahead of print)

Pedersen BK, Akerstrom TC, Nielsen AR, Fischer CP (2007) Role of myokines in exercise and metabolism. J Appl Physiol 103:1093–1098

Picchi A et al (2010) Coronary microvascular dysfunction in diabetes mellitus: a review. World J Cardiol 2:377–390

Pollak AW et al (2012) Arterial spin labeling MR imaging reproducibly measures peak-exercise calf muscle perfusion: a study in patients with peripheral arterial disease and healthy volunteers. JACC Cardiovasc Imaging 5:1224–1230

Potthast S, Schulte A, Kos S, Aschwanden M, Bilecen D (2009) Blood oxygenation level-dependent MRI of the skeletal muscle during ischemia in patients with peripheral arterial occlusive disease. Rofo 181:1157–1161

Prince MR (1998) Peripheral vascular MR angiography: the time has come. Radiology 206:592–593

Proctor DN, Koch DW, Newcomer SC, Le KU, Leuenberger UA (2003) Impaired leg vasodilation during dynamic exercise in healthy older women. J Appl Physiol 95:1963–1970

Quarles CC, Gore JC, Xu L, Yankeelov TE (2012) Comparison of dual-echo DSC-MRI- and DCE-MRI-derived contrast agent kinetic parameters. Magn Reson Imaging 30:944–953

Ranft J, Heidrich H, Peters A, Trampisch H (1986) Laser-Doppler examinations in persons with healthy vasculature and in patients with peripheral arterial occlusive disease. Angiology 37:818–827

Raynaud JS et al (2001) Determination of skeletal muscle perfusion using arterial spin labeling NMRI: validation by comparison with venous occlusion plethysmography. Magn Reson Med 46:305–311

Rehwald WG, Chen E-L, Kim RJ, Judd RM (2004) Noninvasive cineangiography by magnetic resonance global coherent free precession. Nat Med 10:545–549

Richardson RS, Haseler LJ, Nygren AT, Bluml S, Frank LR (2001) Local perfusion and metabolic demand during exercise: a noninvasive MRI method of assessment. J Appl Physiol (Bethesda, MD: 1985) 91:1845–1853

Rieber A et al (2002) Breast MRI for monitoring response of primary breast cancer to neo-adjuvant chemotherapy. Eur Radiol 12:1711–1719

Rissanen TT et al (2005) Blood flow remodels growing vasculature during vascular endothelial growth factor gene therapy and determines between capillary arterialization and sprouting angiogenesis. Circulation 112:3937–3946

Robson PM et al (2012) Imaging of renal masses: correlation with Histopathologic. 265:799–808

Rofsky NM, Adelman MA (2000) MR angiography in the evaluation of atherosclerotic peripheral vascular disease. Radiology 214:325–338

Saeed M (2001) New concepts in characterization of ischemically injured myocardium by MRI. Exp Biol Med (Maywood, NJ) 226:367–376

Sanchez OA, Copenhaver EA, Elder CP, Damon BM (2010) Absence of a significant extravascular contribution to the skeletal muscle BOLD effect at 3 T. Magn Reson Med 64:527–535

Sanchez OA et al (2011) Postmaximal contraction blood volume responses are blunted in obese and type 2 diabetic subjects in a muscle-specific manner. Am J Physiol 301:H418–H427

Sarelius I, Pohl U (2010) Control of muscle blood flow during exercise: local factors and integrative mechanisms. Acta Physiol (Oxf) 199:349–365

Schraml C, Schwenzer NF, Martirosian P, Claussen CD, Schick F (2011) Temporal course of perfusion in human masseter muscle during isometric contraction assessed by arterial spin labeling at 3T. Magma (New York, NY) 24:201–209

Schulte AC, Speck O, Oesterle C, Hennig J (2001) Separation and quantification of perfusion and BOLD effects by simultaneous acquisition of functional I(0)- and T2(*)-parameter maps. Magn Reson Med 45:811–816

Schulte AC, Aschwanden M, Bilecen D (2008) Calf muscles at blood oxygen level-dependent MR imaging: aging effects at postocclusive reactive hyperemia. Radiology 247:482–489

Schwarzbauer C, Morrissey SP, Haase A (1996) Quantitative magnetic resonance imaging of perfusion using magnetic labeling of water proton spins within the detection slice. Magn Reson Med 35:540–546

Silva AC, Kim SG (1999) Pseudo-continuous arterial spin labeling technique for measuring CBF dynamics with high temporal resolution. Magn Reson Med 42:425–429

Slade JM, Towse TF, Gossain VV, Meyer RA (2011) Peripheral microvascular response to muscle contraction is unaltered by early diabetes but decreases with age. J Appl Physiol (Bethesda, MD: 1985) 111, 1361–1371

Slagsvold C-E, Stranden E, Rosen L, Kroese AJ (1992) The role of blood perfusion and tissue oxygenation in the postischemic transcutaneous pO2 response. Angiology 43:155–162

Speck O, Hennig J (1998) Functional imaging by I0- and T2*-parameter mapping using multi-image EPI. Magn Reson Med 40:243–248

Talagala SL, Barbier EL, Williams DS, Silva AC, Koretsky AP (1998) Multi-slice perfusion MRI using continuous arterial water labeling: controling for MT effects with simultaneous proximal and distal RF irradiation. In: Proceedings of the 6th annual meeting of ISMRM 381. http://cds.ismrm.org/ismrm-1998/PDF2/p0381.pdf

Themen F (1997) Methodische Ansätze zur quantitativen Beurteilung der Mikrozirkulation im Gewebe mit der dynamischen. Radiologe 37: 470–480

Thompson RB et al (2005) Measurement of skeletal muscle perfusion during postischemic reactive hyperemia using contrast-enhanced MRI with a step-input function. Magn Reson Med 54:289–298

Thulborn KR, Waterton JC, Matthews PM, Radda GK (1982) Oxygenation dependence of the transverse relaxation time of water protons in whole blood at high field. Biochim Biophys Acta 714:265–270

Tofts PS et al (1999) Estimating kinetic parameters from dynamic contrast-enhanced T(1)-weighted MRI of a diffusable tracer: standardized quantities and symbols. J Magn Reson Imaging 10:223–232

Toussaint JF et al (1996) Perfusion changes in human skeletal muscle during reactive hyperemia measured by echo-planar imaging. Magn Reson Med 35:62–69

Towse TF, Slade JM, Meyer RA (2005) Effect of physical activity on MRI-measured blood oxygen level-dependent transients in skeletal muscle after brief contractions. J Appl Physiol 99:715–722

Towse TF, Slade JM, Ambrose JA, Delano MC, Meyer RA (2011) Quantitative analysis of the post-contractile blood-oxygenation-level-dependent (BOLD) effect in skeletal muscle. J Appl Physiol 111:27–39

Troalen T, Capron T, Cozzone PJ, Bernard M, Kober F (2013) Cine-ASL: a steady-pulsed arterial spin labeling method for myocardial perfusion mapping in mice. Part I. Experimental study. Magn Reson Med. doi:10.1002/mrm.24565

Turner R (1997) Signal sources in bold contrast fMRI. Adv Exp Med Biol 413:19–25

Utz W et al (2005) Blood oxygen level-dependent MRI of tissue oxygenation: relation to endothelium-dependent and endothelium-independent blood flow changes. Arterioscler Thromb Vasc Biol 25:1408–1413

Van der Leij C, van de Sande MGH, Lavini C, Tak PP, Maas M (2009) Rheumatoid synovial inflammation: pixel-by-pixel dynamic contrast-enhanced MR imaging time-intensity curve shape analysis – a feasibility study. Radiology 253:234–240

Van der Woude HJ et al (1998) Musculoskeletal tumors: does fast dynamic contrast-enhanced subtraction MR imaging contribute to the characterization? Radiology 208:821–828

Van der Zwaag W et al (2009) fMRI at 1.5, 3 and 7 T: characterising BOLD signal changes. Neuroimage 47:1425–1434

Van Rijswijk CS, Hogendoorn PC, Taminiau AH, Bloem JL (2001) Synovial sarcoma: dynamic contrast-enhanced MR imaging features. Skeletal Radiol 30:25–30

Versluis B et al (2011) Magnetic resonance imaging in peripheral arterial disease: reproducibility of the assessment of morphological and functional vascular status. Invest Radiol 46:11–24

Versluis B et al (2012) Dynamic contrast-enhanced MRI assessment of hyperemic fractional microvascular blood plasma volume in peripheral arterial disease: initial findings. PLoS ONE 7:e37756

Verstraete KL et al (1994) Benign and malignant musculoskeletal lesions: dynamic contrast-enhanced MR imaging–parametric "first-pass" images depict tissue vascularization and perfusion. Radiology 192:835–843

Vonken EP, van Osch MJ, Bakker CJ, Viergever MA (2000) Simultaneous quantitative cerebral perfusion and Gd-DTPA extravasation measurement with dual-echo dynamic susceptibility contrast MRI. Magn Reson Med 43:820–827

Walker UA et al (2007) Clinical risk assessment of organ manifestations in systemic sclerosis: a report from the EULAR Scleroderma trials and research group database. Ann Rheum Dis 66:754–763

Van de Sande MGH et al (2012) Characteristics of synovial inflammation in early arthritis analysed by pixel-by-pixel time-intensity curve shape analysis. Rheumatology (Oxford, England) 51:1240–1245

Wang DJJ et al (2012) The value of arterial spin-labeled perfusion imaging in acute ischemic stroke: comparison with dynamic susceptibility contrast-enhanced MRI. Stroke 43:1018–1024

Weber M-A, Kroll A, Günther M (2004) Noninvasive measurement of relative cerebral blood flow using arterial spin labeling techniques: physical basics and clinical applications. Radiologe 44:164–173

Weber MA, Risse F, Giesel FL, Schad LR, Kauczor HU, Essig M (2005) Measurement of perfusion using the first-pass dynamic susceptibility-weight ed contrast-enhanced (DSC) MRI in neuro-oncology. Physical basics and clinical applications. Radiologe 45:618–632

Weber MA, Krix M, Delorme S (2007) Quantitative evaluation of muscle perfusion with CEUS and with MR. Eur Radiol 17:2663–2674

Wheaton AJ, Miyazaki M (2012) Non-contrast enhanced MR angiography: physical principles. J Magn Reson Imaging 36:286–304

Wigmore DM, Damon BM, Pober DM, Kent-Braun JA (2004) MRI measures of perfusion-related changes in human skeletal muscle during progressive contractions. J Appl Physiol (Bethesda, MD: 1985) 97:2385–2394

Wong EC, Buxton RB, Frank LR (1998) A theoretical and experimental comparison of continuous and pulsed arterial spin labeling techniques for quantitative perfusion imaging. Magn Reson Med 40:348–355

Wong EC et al (2006) Velocity-selective arterial spin labeling. Magn Reson Med 55:1334–1341

Wu W-C, Fernández-Seara M, Detre JA, Wehrli FW, Wang J (2007) A theoretical and experimental investigation of the tagging efficiency of pseudocontinuous arterial spin labeling. Magn Reson Med 58:1020–1027

Wu W-C, Wang J, Detre JA, Ratcliffe SJ, Floyd TF (2008) Transit delay and flow quantification in muscle with continuous arterial spin labeling perfusion-MRI. J Magn Reson Imaging 28:445–452

Wu W-C et al (2009) Skeletal muscle microvascular flow in progressive peripheral artery disease: assessment with continuous arterial spin-labeling perfusion magnetic resonance imaging. J Am Coll Cardiol 53:2372–2377

Wu W, Lawrence KSS, Licht DJ, Wang DJJ (2011) Quantification issues in arterial spin labeling perfusion. 21:65–73

Yankeelov TE, Gore JC (2009) Dynamic contrast enhanced magnetic resonance imaging in oncology: theory, data acquisition, analysis, and examples. Curr Med Imaging Rev 3:91–107

Ye FQ, Frank JA, Weinberger DR, McLaughlin AC (2000) Noise reduction in 3D perfusion imaging by attenuating the static signal in arterial spin tagging (ASSIST). Magn Reson Med 44:92–100

Yeung DKW, Griffith JF, Li AFW, Ma HT, Yuan J (2012) Air pressure-induced susceptibility changes in vascular reactivity studies using BOLD MRI. J Magn Reson Imaging. doi: 10.1002/jmri.23926

Zhang H et al (2005) Accurate myocardial T1 measurements: toward quantification of myocardial blood flow with arterial spin labeling. Magn Reson Med 53:1135–1142

Zhu XP, Zhao S, Isherwood I (1992) Magnetization transfer contrast (MTC) imaging of skeletal muscle at 0.26 Tesla–changes in signal intensity following exercise. Br J Radiol 65:39–43

Zierath JR, Hawley JA (2004) Skeletal muscle fiber type: influence on contractile and metabolic properties. PLoS Biol 2:e348

Ziv K et al (2004) Longitudinal MRI tracking of the angiogenic response to hind limb ischemic injury in the mouse. Magn Reson Med 51:304–311

Skeletal Muscle MR Imaging Beyond Protons: With a Focus on Sodium MRI in Musculoskeletal Applications

Armin M. Nagel, Marc-André Weber, Arijitt Borthakur,
and Ravinder Reddy

Contents

1 **Key points** 115

2 **Introduction** 116

3 **Physical and Technical Aspects of Non-proton MRI** 116
3.1 Sensitivity and Signal to Noise Ratio (SNR) 116
3.2 Radiofrequency Coils 118
3.3 Pulse Sequences: Why Short Echo Times and Anisotropic Spatial Resolution? 118
3.4 Pulse Sequences: Separation Between Different Sodium Compartments 119

4 **Applications of ^{23}Na MRI in Muscular Channelopathies and Muscle Dystrophies** 121

5 **Musculoskeletal Applications Beyond Muscle Tissue: Sodium MRI as a Biomarker of Cartilage Degeneration** 124

6 **Outlook: Imaging of More Exotic X-Nuclei (^{35}Cl, ^{39}K, and ^{17}O)** 127
6.1 ^{35}Cl MRI 127
6.2 ^{39}K MRI 127
6.3 ^{17}O MRI 128

References 131

A. M. Nagel (✉)
Medical Physics in Radiology,
German Cancer Research Center (DKFZ),
Heidelberg, Germany
e-mail: a.nagel@Dkfz-Heidelberg.de

M.-A. Weber
Diagnostic and Interventional Radiology,
University Hospital Heidelberg,
Heidelberg, Germany

A. Borthakur · R. Reddy
Center for Magnetic Resonance and Optical Imaging,
Department of Radiology,
University of Pennsylvania School of Medicine,
Philadelphia, PA, USA

Abstract

Proton MRI is the mainstay of muscle MR imaging, however with the advent of dedicated coil and sequence technology, also non-proton MRI is now possible using high-field MRI units. This chapter includes a discussion of the principles and challenges of non-proton muscle imaging with focus on the use of sodium MRI. Dedicated sequences and the benefit of higher field strength will be discussed and clinical applications within the musculoskeletal system, such as sodium MRI in muscular diseases and cartilage/joint abnormalities will be reviewed. Moreover, other nuclei that are prone to MR imaging, such as chlorine, potassium, and oxygen will also be addressed.

1 Key points

- The increasing availability of ultrahigh field MRI systems ($B_0 \geq 3$ T) enables MR imaging beyond protons (e.g., ^{23}Na, ^{35}Cl, ^{39}K, ^{17}O) in clinically feasible measurement time and acceptable spatial resolution.
- Since sodium nucleus transverse relaxation time of muscle tissue is very short ($T_{2f}^{*} \approx 1$ ms), it requires ultrashort echo time sequences of less than 0.5 ms for imaging. As the T_1 of sodium nucleus within the muscle tissue is short, rapid averaging can be used to improve the signal to noise ratio (SNR) of sodium MRI.
- Changes of the intracellular sodium content can be visualized using *Inversion Recovery* sodium MRI.
- Sodium MRI can depict changes of muscular sodium concentration in sodium muscle channelopathies and other rare muscle channelopathies and dystrophies, such as hypokalemic periodic paralysis and Duchenne muscle dystrophy.
- Besides applications in the skeletal muscle, sodium MRI is beneficial in other musculoskeletal application. In early stages of osteoarthritis (OA), proteoglycans (PG) of

M.-A. Weber (ed.), *Magnetic Resonance Imaging of the Skeletal Musculature*, Medical Radiology. Diagnostic Imaging,
DOI: 10.1007/174_2013_923, © Springer-Verlag Berlin Heidelberg 2013

Published Online: 10 October 2013

cartilage are degraded. Glycosaminoglycans (GAG) side chains of PG contain fixed negative charge density (FCD) in the form of sulfate and carboxylic groups, which are counter balanced by Na^+ ions. Sodium MRI can be used to quantify [Na] and hence [GAG] with high specificity and sodium MRI has been shown to measure GAG depletion in ex vivo OA cartilage, in animal models of OA as well as in human OA subjects.

2 Introduction

This chapter describes techniques for skeletal muscle magnetic resonance imaging (MRI) beyond protons (^1H) and their applications. In principle all nuclei that possess a nuclear magnetic spin moment can be detected by MRI or MR spectroscopy. Imaging of these nuclei is often called X-nuclei MRI or non-proton-MRI. In this context "X" stands for any nucleus except for ^1H. Besides ^1H, sodium (^{23}Na) is the nucleus that is best suited for in vivo imaging, due to its physical properties and its high natural abundance. Sodium ions (Na^+) play an important role in many cellular physiological processes. In healthy tissue the extracellular concentration of Na^+ is approximately ten-fold higher than the intracellular concentration ($[Na^+]_i = 10$–15 mmol/L, $[Na^+]_e \approx 145$ mmol/L) (Robinson and Flashner 1979). The enzyme Na^+-K^+-ATPase ("sodium/potassium pump") helps to maintain this gradient by pumping Na^+ out of the cell and potassium (K^+) into the cell with a ratio of 3:2. Thus, the Na^+-K^+-ATPase is an electrogenic pump that contributes to maintain the membrane potentials of cells. For K^+, the concentration gradient is reversed. The intracellular concentration is much higher than the extracellular concentration ($[K^+]_i \approx 145$ mmol/L, $[K^+]_e = 2.5$–3.5 mmol/L) (Robinson and Flashner 1979). The described Na^+-K^+ regulation plays an important role in skeletal muscle contractility (Clausen 2003). Besides the described active transport of Na^+ and K^+ ions, there are ion channels that are gating the flow of ions across the cell membrane. Thus, nowadays, ^{23}Na MRI is often used as a valuable tool in clinical research—also beyond muscular applications (Madelin and Regatte 2013). In this chapter different applications of ^{23}Na MRI within the musculoskeletal system (e.g., imaging of healthy muscle using different field strength, its use in imaging various skeletal muscle diseases, such as channelopathies (see also "MRI in Inflammatory Myopathies and Autoimmune-Mediated Myositis") and Duchenne muscle dystrophy, as well as ^{23}Na MRI as biomarker of cartilage degeneration) are exemplarily described.

Phosphorous (^{31}P) also exhibits high MR sensitivity and is involved in cellular metabolic processes. As ^{31}P exists in different chemical compounds (e.g., ATP, ADP, Phosphocreatine) it is usually investigated by MR spectroscopy and spectroscopic imaging, which is thoroughly described in "MR Spectroscopy and Spectroscopic Imaging for Evaluation of Skeletal Muscle Metabolism: Basics and Applications in Metabolic Diseases." In this chapter it is also discussed, that—compared to ^1H MRI—different soft- (e.g., pulse sequences) and hardware (e.g., appropriate radiofrequency (RF) coils and broad band amplifier) are required. Besides ^{23}Na and ^{31}P, there are also other MR accessible nuclei that are involved in cellular physiology and whose applicability for clinical research is currently under investigation (e.g., ^{35}Cl, ^{39}K, ^{17}O). In future, imaging of these nuclei might enable the visualization of further (patho-)physiological processes in vivo.

3 Physical and Technical Aspects of Non-proton MRI

In this section, physical properties of non-proton nuclei with relevance to the MRI experiment are discussed. To be accessible via MRI, an atomic nucleus requires a magnetic spin moment that aligns in a strong external magnetic and can be used for signal excitation and detection. All nuclei with an odd number of protons or neutrons possess such a spin. On the other hand, nuclei with an even number of protons and neutrons exhibit no nuclear spin, and, thus, cannot be used for MRI. Among these are highly abundant nuclei such as oxygen (^{16}O) and carbon (^{12}C). For conventional MRI it is a lucky coincidence that ^1H—which is the nucleus with the highest in vivo concentration—has also the highest MR sensitivity among all nuclei, except for tritium (^3H), which has no relevance for MRI due to its negligible natural abundance ($\sim 10^{-15}$ %).

3.1 Sensitivity and Signal to Noise Ratio (SNR)

MRI is a technique with an intrinsically low sensitivity, e.g., approximately only one of 1 million nuclei contributes to the signal. Thus, SNR is usually crucial in MRI. The SNR—which is an important measure for image quality—is defined as the signal intensity divided by the image noise. The MR signal is proportional to voltage induced in a nearby receive coil (c.f. Eq. 1). This signal is proportional to the concentration c of spins (i.e., the concentration of the measured atom multiplied by its natural abundance). In non-proton MRI the concentration is approximately four orders of magnitude smaller than the concentration of ^1H, which leads to a corresponding signal loss. Furthermore, the spin I and the gyromagnetic ratio (γ)—which is proportional to the resonance frequency—affect the signal (c.f. Table 1).

Table 1 Isotopes that can be used for MRI or MR spectroscopy

Isotope	Natural abundance (%)	Spin	MR frequency (MHz/7 T)	Relative signal (same concentration of element)	Relative SNR* (same concentration of element)
^{1}H	99.99	1/2	300	100	100
^{7}Li	92.41	3/2	117	27.1	69.8
^{13}C	1.07	1/2	75	0.017	0.0677
^{17}O	**0.038**	**5/2**	**41**	**0.0011**	**0.00815**
^{19}F	100	1/2	282	83.3	88.5
^{23}Na	**100**	**3/2**	**79**	**9.25**	**35.0**
^{31}P	100	1/2	121	6.63	16.4
^{35}Cl	**75.78**	**3/2**	**29**	**0.356**	**3.64**
^{37}Cl	24.22	3/2	24	0.0657	0.806
^{39}K	**93.26**	**3/2**	**14**	**0.0473**	**1.02**

Their Larmor frequencies are given for a magnetic field strength of 7 T. The relative MR signal is normalized to the signal for ^{1}H MRI. For the calculation of the relative SNR it is assumed that image noise increases linearly with frequency. Note, relative signal and SNR do not account for variations of the in vivo concentration. The lower in vivo concentrations of the non-proton nuclei leads to a further reduction of the signal and SNR: Values for natural abundances are taken from Ref. Harris et al. (2002)

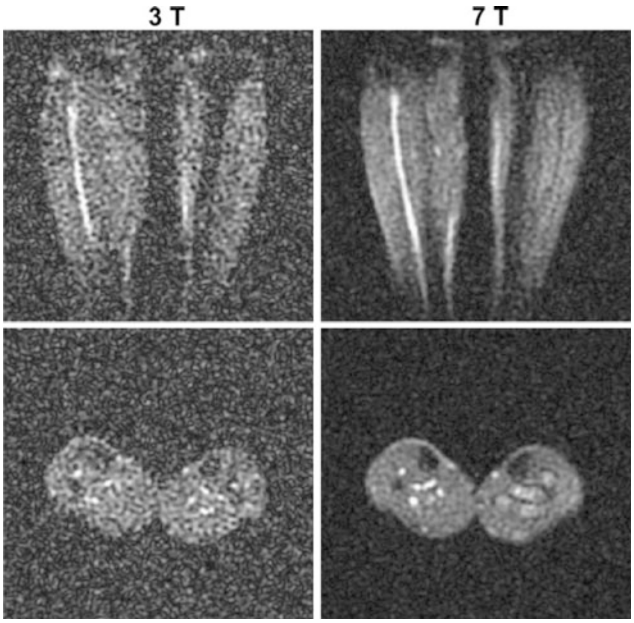

Fig. 1 Transversal and coronal slices of 3D ^{23}Na MR datasets of the human calf muscles. Images were acquired at a magnetic field strength of 3 and 7 T with similar parameters and coil design, to demonstrate the increase of SNR with magnetic field strength. The SNR increases approximately linearly with field strength. Reproduced by permission of Springer from: Amarteifio et al. (2011). ©European Society of Radiology 2011

Since image noise increases also with frequency, the SNR increases only quadratically with the gyromagnetic ratio (c.f. Eq. 2), if a linear relationship between frequency and image noise is assumed. This is the case for sample dominated losses (i.e., main cause for image noise is inductive losses in the investigated sample) (Hoult and Lauterbur 1979). For small samples (e.g., small animal imaging), electronic losses—which increase only with the square root of the frequency—can dominate image noise.

$$\text{signal} \propto c \cdot I \cdot (I+1) \cdot \gamma^{3} \tag{1}$$

$$\text{SNR} \propto c \cdot I \cdot (I+1) \cdot \gamma^{2} \tag{2}$$

Using known in vivo concentrations and the physical properties as shown in Table 1, the relative in vivo SNR for non-proton MRI can be estimated. Besides the above mentioned aspects, also the relaxation times (Eq. 3), the performance, and geometry of the used receive coil and the magnetic field strength contribute to the final image SNR.

$$\text{SNR} \propto \sqrt{T_2^{*}/T_1} \tag{3}$$

The SNR can be increased by the use of higher magnetic field strength. For imaging of small samples (e.g., small animal imaging), a slightly higher increase with magnetic field strength compared to imaging of humans is expected (c.f. Eqs. 4a, b). To further increase SNR, measurement time (T_{AQ}), and voxel dimensions (Δx) can be increased (c.f. Eq. 5).

$$\text{SNR}_{\text{small objects}} \propto B_0^{7/4} \tag{4a}$$

$$\text{SNR}_{\text{large objects}} \propto B_0 \tag{4b}$$

$$\text{SNR} \propto \Delta x^{3} \cdot \sqrt{T_{AQ}} \tag{5}$$

The magnetic spin moment of most X-nuclei is higher than for ^{1}H (c.f. Table 1). Nuclei with spin ≥ 1 (e.g., ^{23}Na, ^{35}Cl, ^{39}K, ^{17}O) exhibit an electrical quadrupole-moment. In

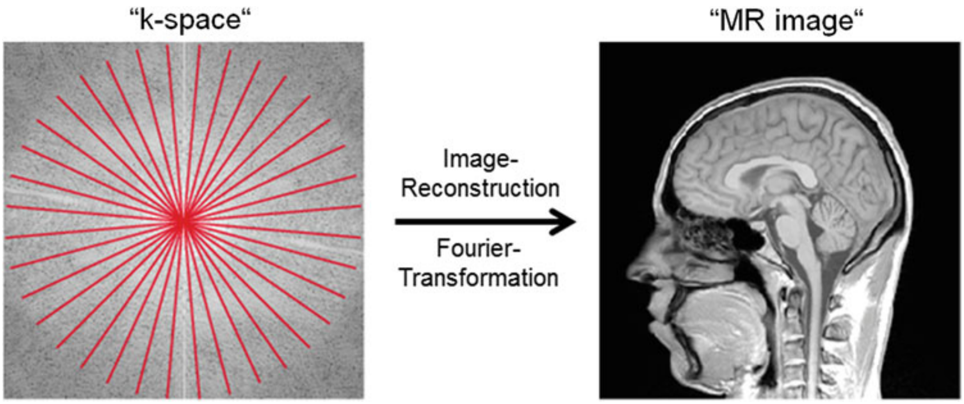

Fig. 2 2D visualization of radial (c.f. *red lines*) k-space sampling. Data acquisition starts directly in the center of k-space enabling ultra-short echo times (TE < 0.5 ms). After gridding the acquired k-space data to a Cartesian grid, a Fast Fourier Transformation (FFT) generates the MR image

contrast, spin ½ nuclei (e.g., ^{1}H, ^{31}P) exhibit only a magnetic dipole-moment. The electrical quadrupole-moment leads to a much stronger interaction of the nucleus with its surrounding and, thus, this leads to much shorter relaxation times. As a spin-3/2 nucleus with a non-zero quadrupolar moment, sodium nuclei (^{23}Na) exhibit bi-exponential relaxation in tissues, i.e., fast and slow components of T_2 and T_2^* (van der Maarel 1989; Woessner and Bansal 1998). Constantinides et al. (2000) reported for the transverse relaxation time a fast component of $T_{2f}^* = 0.46 \pm 0.21$ ms and a slow component of $T_{2s}^* = 12.3 \pm 1.9$ ms for skeletal muscle tissue (measured at a magnetic field strength of 1.5 T). The inherently short T_2 of sodium makes the images blurry due to a broader point spread function. On the other side, the short T_1 of sodium ($\sim$30 ms in tissues) can be used to mitigate some signal loss by rapid signal averaging. However, high-field scanners (7 T and above) with pulse sequences that enable short echo time imaging and dedicated radiofrequency (RF) coil hardware are desirable for X-Nuclei MRI to achieve sufficient SNR and spatial resolution (Fig. 1).

3.2 Radiofrequency Coils

Since all nuclei exhibit different Larmor frequencies, imaging of each nucleus requires dedicated hardware, such as a broad band amplifier and appropriate transmit and receive radiofrequency (RF) coils. Double-tuned RF coils are often used. Normally, they are tuned to the desired non-proton frequency and to the ^{1}H frequency. The latter enables co-registered acquisition of morphological images and non-proton data. Additionally, shimming of the magnetic field homogeneity can be performed with the routine provided by the scanner manufacturer. However, the double-resonance complicates coil design and leads to a trade-off compared to signal-tuned coils (Mispelter et al. 2006). Since the RF coils are usually optimized for the low SNR non-proton nucleus, SNR, and diagnostic quality of the conventional ^{1}H MRI data can be reduced compared to conventional, single resonant ^{1}H RF coils.

3.3 Pulse Sequences: Why Short Echo Times and Anisotropic Spatial Resolution?

Usually, imaging techniques provided by the manufacturer of the scanner are optimized for ^{1}H MRI. However, most non-proton nuclei exhibit much shorter transverse relaxation times than ^{1}H, which makes the application of specially tailored acquisition techniques favorable. A recent review on this topic can be found in (Konstandin and Nagel 2013). Signal acquisition in MRI requires sampling of the so called "k-space" (Fig. 2). After filling k-space, a Fast Fourier Transform (FFT) is applied to calculate the image. Most acquisition techniques applied for routine clinical imaging, sample k-space on a Cartesian grid. This leads to relatively long echo times (TE). TE is defined as the period of time between signal excitation and the acquisition of the center of k-space that defines image contrast (this is the location of the maximum signal intensity). Even if a fast switching of the readout gradients is applied, echo times are normally larger than a few milliseconds. Since transverse ^{23}Na relaxation times of tissue are in the same range or shorter, this leads to T_2^* weighting and signal loss. This can be partially overcome by the application of an asymmetric readout. Asymmetric sampling can be performed due to the Hermitian character of k-space, which leads to the fact that sampling one half of k-space is theoretically sufficient to provide all required data for image reconstruction. However, ultra-short echo times (TE < 0.5 ms) that are required for spin-density weighted ^{23}Na MRI (Boada et al. 1994) can still not be achieved.

To achieve these short echo times, k-space can be sampled by projection imaging (Fig. 2), which was basically the first technique used for MRI (Lauterbur 1973). In projection imaging, k-space is sampled on center-out radial lines.

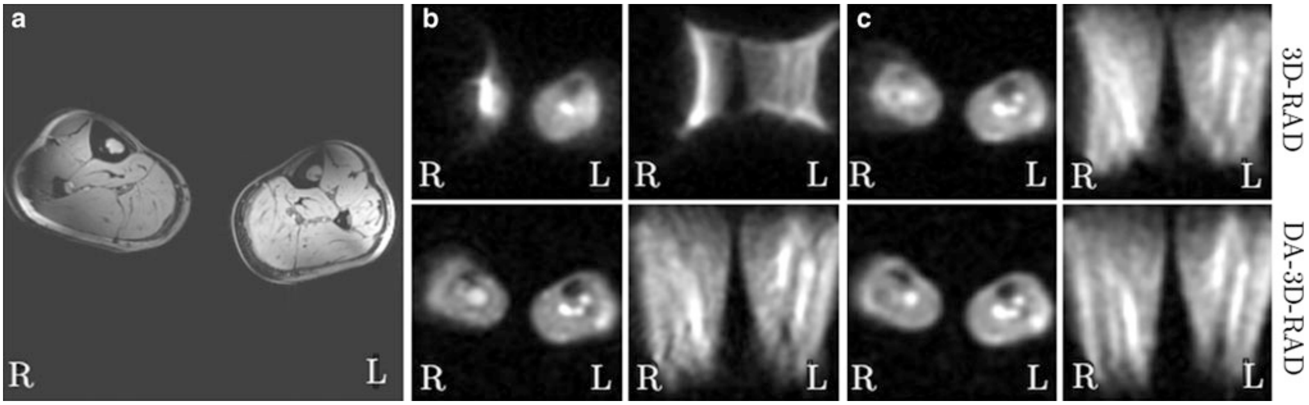

Fig. 3 Images of the calf muscles from a healthy volunteer ($B_0 = 7$ T). This is a worst-case scenario, where a bad B_0-homogeneity in the area of the right lower leg leads to severe image artifacts in ^{23}Na MRI. **a** ^{1}H MRI yields acceptable image quality, except for chemical shift artifacts and signal variations due to B_1-inhomogeneities. **b**, **c** Conventional radial imaging (DA-3D-RAD) leads to severe distortions and signal extinctions. A shorter readout duration (T_{RO}) leads to improved image quality (**c**). The density-adapted (DA) readout scheme further improves image quality. **a** ^{1}H, T_1-FLASH. **b** ^{23}Na ($T_{RO} = 20$ ms). **c** ^{23}Na ($T_{RO} = 5$ ms). Figure reproduced from Nagel (2009)

Signal acquisition can be started directly after the excitation pulse is turned off. Only a very short delay ($\tau \approx 50$ µs) between signal excitation and reception is required due to technical reasons of the scanner hardware. This enables ultra-short echo times (TE < 0.5 ms) and the acquisition of "spin-density weighted" ^{23}Na images, that are a prerequisite for concentration measurements. A drawback of conventional projection reconstruction techniques is that the sampling density is not homogenous throughout k-space, i.e., the center is sampled more densely than the outer part (c.f. Fig. 2). This leads to decreased SNR and can be the cause of image artifacts. Therefore, density-adapted projection reconstruction (DA-3DPR) (Nagel et al. 2009) or twisted projection imaging (TPI) (Boada et al. 1997; Lu et al. 2010) techniques are applied. These techniques lead to a more homogenous distribution of the sampling density. This is achieved be slowing down the sampling velocity in the outer part of k-space (i.e., reducing the amplitude of the readout gradient; DA-3DPR) or by sampling k-space in a spiral manner (TPI). The homogenous distribution of the sampling density leads to a decrease in image noise and thus to an increase in SNR. Additionally, k-space positions are sampled ahead of time compared to conventional projection imaging. This leads to the fact that less signal has decayed at a certain k-space position, which results in less image blurring. In the presence of inhomogeneities of the main magnetic field (B_0), the DA-3DPR sequence is also less susceptible to image artifacts, when compared with conventional projection imaging. This is exemplarily demonstrated at images of the calf muscles (Fig. 3). In the area of the right lower leg, a bad homogeneity (or off-resonance) of the B_0-field was present, most likely due to insufficient shimming of the main magnetic field. Whereas ^{1}H MRI showed acceptable image quality, ^{23}Na images acquired with the conventional 3DPR sequence exhibit severe distortions and signal excitations in the area of the right lower leg. These artifacts increase with increasing readout duration. The DA-3DPR sequence shows much better image quality.

The described projection imaging techniques sample k-space isotropically and, thus, lead to isotropic spatial resolution. To avoid partial volume effects, sequences that enable anisotropic spatial resolution are applied. This enables higher in-plane resolutions, if larger slice thicknesses can be applied. For elongated structures, such as skeletal muscle, this is usually possible without loss of information. A simple approach is 2D projection imaging (Bergin et al. 1991). However, 2D techniques require slice selective excitation pulses that usually lead to longer echo times than for 3D imaging. 3D techniques with anisotropic spatial resolution—based on cones (Staroswiecki et al. 2010), TPI (Watts et al. 2011), and density-adapted projection (Nagel et al. 2012)—were recently developed. By increasing the slice thickness, higher in-plane resolutions can be achieved at similar SNR (Fig. 4).

3.4 Pulse Sequences: Separation Between Different Sodium Compartments

A selective measurement of different sodium compartments (e.g., intra- and extracellular sodium) is of great interest, since it could provide valuable physiological information. *Paramagnetic shift reagents* (SR), such as the anionic complexes of $D_y(PPP_i)_2^{7-}$ (Gupta et al. 1984), $D_y(TTHA)^{3-}$ (Balschi et al. 1990) and $Tm(DOTP)_5^{-1}$ (Bansal et al. 1993), that do not cross the cell membrane can selectively shift the resonance line of extracellular Na^+. Thus, SR allow for a

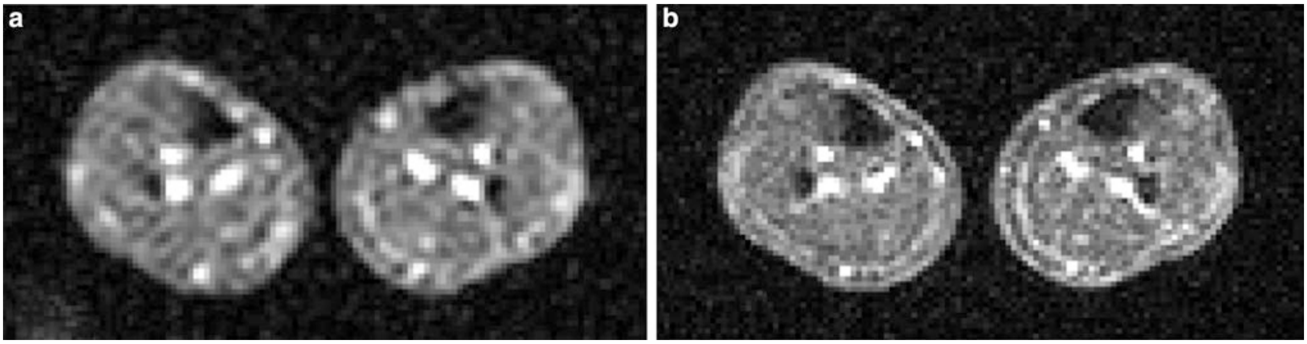

Fig. 4 ^{23}Na MR image of the human calf muscle. For both acquisitions (**a**, **b**) the same measurement times were used (13 min 54 s). **a** Isotropic nominal spatial resolution (5.1 mm)^3. **b** The anisotropic sequence enables higher in-plane resolution (3.3 × 3.3 mm^3) at similar SNR (slice thickness: 12.7 mm). Figure adapted from Nagel et al. 2012

clear separation between intra- and extracellular Na$^+$. Naritomi et al. (1987) obtained the first in vivo spectra of mouse brain and Balschi et al. (1990) studied normal and ischemic rat muscle using D$_y$(TTHA)$^{3-}$. Chemical shift imaging (CSI) can be conducted to measure the local distribution of the SR. However, the major drawback of SR is their putative toxicity that hinders its application in humans.

Relaxation weighted approaches can be used to separate different Na$^+$ pools, non-invasively. *Inversion Recovery* (IR) imaging can be employed to suppress signal from a Na$^+$ compartment with a distinct T_1 relaxation time, if an appropriate inversion time (TI) is used (Fig. 5, Eq. 6). Kline et al. (2000) employed IR imaging to monitor the response to chemotherapy of mouse tumors. Drug administration resulted in an increased IR signal intensity, which is suggestive of an increased intracellular Na$^+$ concentration. In human brain, IR imaging was employed to suppress signal Na$^+$ signal from cerebrospinal fluid (CSF) (Stobbe and Beaulieu 2005) and to suppress edema and CSF in brain tumor patients (Nagel et al. 2011a). Examinations of patients with a muscular channelopathy, where an increase of the intracellular Na$^+$ content can be easily triggered with high reproducibility, demonstrate that IR imaging can provide a weighting toward intracellular sodium (Nagel et al. 2011b) (c.f. Sect. 4).

$$\mathrm{TI} = \ln\left(\frac{2}{1 + \mathrm{e}^{-\mathrm{TR}/\mathrm{T1}}}\right) \cdot T_1 \tag{6}$$

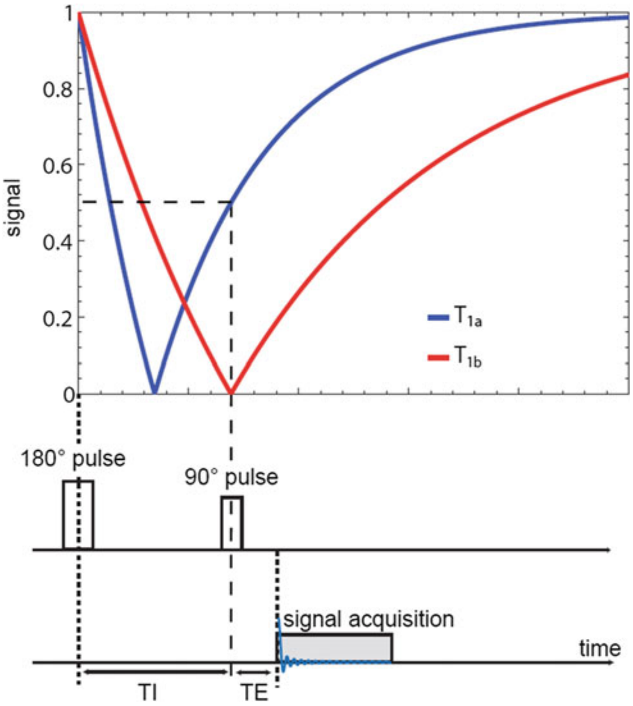

Fig. 5 Sequence diagram of an IR pulse sequence. The signal intensities are plotted for two different types of tissue with longitudinal relaxation times T_{1a} and T_{1b}. The inversion time TI is chosen to suppress signal from sodium ions with relaxation time T_{1b}. IR imaging reduces also the signal intensity of the tissue with relaxation time T_{1a}

If the mobility of the sodium ions is restricted (e.g., in the intracellular space) the transverse relaxation becomes bi-exponential. This bi-exponential relaxation behavior can be detected using double or triple-quantum filters (Pekar and Renshaw 1969; Jaccard et al. 1986), which is an additional approach to separate different sodium pools. Disadvantages of double or triple-quantum filtered ^{23}Na MRI are a high sensitivity to B_0- and B_1-inhomogeneities and low SNR. Higher SNR can be achieved with bi-exponential weighted ^{23}Na MRI (Benkhedah et al. 2012). In isotropic environments a bi-exponential weighted image contains mainly triple-quantum coherences, but an up to three fold higher SNR is achieved compared to conventional TQF brain imaging. However, up to now this type of sequence has not been applied to muscular ^{23}Na MRI.

To conclude, MRI of fast relaxing nuclei, such as sodium (^{23}Na) requires specially tailored hardware (RF coils and broad band amplifier). High magnetic field strengths ($B_0 \geq 3$ T) and specially adapted pulse sequences are a prerequisite to achieve good image quality. Similar to conventional ^{1}H MRI, different image contrasts such as spin density weighted or inversion recovery imaging can be employed.

4 Applications of ^{23}Na MRI in Muscular Channelopathies and Muscle Dystrophies

In healthy cells the intracellular Na$^+$ content is about a factor of 10 lower than the extracellular concentration. This concentration gradient is mandatory for the functioning of cells. The energy-consuming Na$^+$-K$^+$-ATPase contributes to this concentration gradient and helps to maintain the membrane potential of cells. While pumping three sodium ions out of the cell it carries only two potassium ions into the cell. Thus, in total it removes charge from the intracellular space. A breakdown of the Na$^+$-K$^+$-ATPase or an increased open probability of mutated cellular ion channels [e.g., in muscular channelopathies (Lehmann-Horn and Jurkat-Rott 1999)], can lead to an increase of the intracellular Na$^+$ concentration and to a depolarization of the cells (Fig. 6). Since ^{23}Na MRI is currently a research tool and not a widespread clinical tool, only a few muscular disease processes have been studied using ^{23}Na MRI. Constantinides et al. (2000) reported an up to 70 % increase of the sodium signal intensity in an affected muscle group of a patient with myotonic dystrophy. In diabetes, a decreased Na$^+$/K$^+$-ATPase activity is expected (Clausen 2003). Chang et al. (2010) measured pre- and post-exercise sodium signal intensities in healthy muscle tissue of healthy volunteers and patients with diabetes. Exercise leads to increased sodium signal intensity. Their results indicate that the subsequent signal intensity recovery is more slowly in diabetics than in healthy subjects. A possible explanation might be a reduced activity of the Na$^+$-K$^+$-ATPase. Many studies have been performed on patients with muscular channelopathies where increased ^{23}Na signal intensities were detected (Amarteifio et al. 2012; Jurkat-Rott et al. 2009; Weber et al. 2006a, b) (see also "MRI in Muscle Channelopathies" for more details). In this section we exemplarily demonstrate the application of different ^{23}Na MRI techniques for the examination of patients with Paramyotonia Congenita (PC). PC is an example of a rare muscular channelopathy, where an increased intracellular Na$^+$ concentration and cell depolarization can be easily and reproducibly provoked. A trigger mechanism is exposure to cold, which causes a long-lasting depolarizing Na$^+$ inward current and muscle weakness (Lehmann-Horn and Jurkat-Rott 1999). At an early stage, this does not lead to morphological changes that can be visualized by conventional imaging techniques. ^{23}Na MRI can visualize this increase of the intracellular Na$^+$ content. Different ^{23}Na MRI techniques were tested. Conventional ^{1}H MRI to visualize possible fatty infiltration of the muscles or muscular edema was performed for comparison. Between the first and the second measurement a provocation of one lower leg was performed. The provocation consists of cooling for 25 min (Fig. 6c) followed by a short exercise (2 min). The exercise was performed directly after cooling. The subjects had to dorsiflect their feet against resistance and stand on their tiptoes. The provoked muscle of the PC patients showed a pronounced decrease of muscle strength and an increase of the ^{23}Na MRI signal, whereas ^{1}H MRI showed no pathological findings (Fig. 7b). The signal increase was most pronounced for ^{23}Na IR imaging. No significant changes were visible for the muscle tissue of healthy subjects (Fig. 7a). These results indicate, that the ^{23}Na IR sequence provides a strong weighting toward intracellular sodium and that the ^{23}Na IR sequence enables a better visualization of intracellular sodium content changes than the ^{23}Na T_1 or ^{23}Na TSC sequences (Nagel et al. 2011b).

Besides muscular channelopathies, recent studies have shown a role of sodium MRI also for muscle dystrophies, such as Duchenne muscular dystrophy (Weber et al. 2011, 2012). In a recent study on eight patients with Duchenne muscular dystrophy (mean age, 9.5 ± 5.4 years) and eight volunteers (mean age, 9.5 ± 3.2 years), the presence and persistence of muscular edema and the myoplasmic sodium (Na$^+$) concentration was assessed using 3-T proton (^{1}H) and ^{23}Na density-adapted 3D-radial MR sequences. Seven Duchenne patients were re-examined about 7 months later without change of therapy. The muscle edema was quantified on STIR images with background noise as reference and fatty degeneration on T_1-weighted images using subcutaneous fat as reference. Na$^+$ was quantified by a muscular tissue Na$^+$ concentration (TSC) sequence employing a reference containing 51.3 mmol/L Na$^+$ with 5 % agarose. With an IR sequence, mainly the myoplasmic Na$^+$ was determined. In this study, the normalized muscular ^{23}Na IR signal intensity was higher in Duchenne patients than in volunteers (Fig. 8) and persisted at second measurement. When compared to volunteers (25.6 ± 2.0 mmol/L), TSC was markedly increased in DMD (38.0 ± 5.9 mmol/L, $p < 0.001$) and remained constant ($n = 7$, 1st: 37.9 ± 6.4 mmol/L, 2nd: 37.0 ± 4.0 mmol/L, $p = 0.49$). Muscular edema ($p < 0.001$) and fat content ($p = 0.003$) were also elevated in Duchenne patients when compared with healthy volunteers. This could also be confirmed during follow-up ($n = 7$, $p = 0.91$, $p = 0.12$). The authors concluded upon their initial data that ^{23}Na MRI detects a muscular Na$^+$ overload in Duchenne muscular dystrophy. This permanent myoplasmic Na$^+$ overload in all Duchenne patients may be osmotically relevant and may play a role in the development of the muscle edema, which was present and persisted in all studied Duchenne patients. This muscle

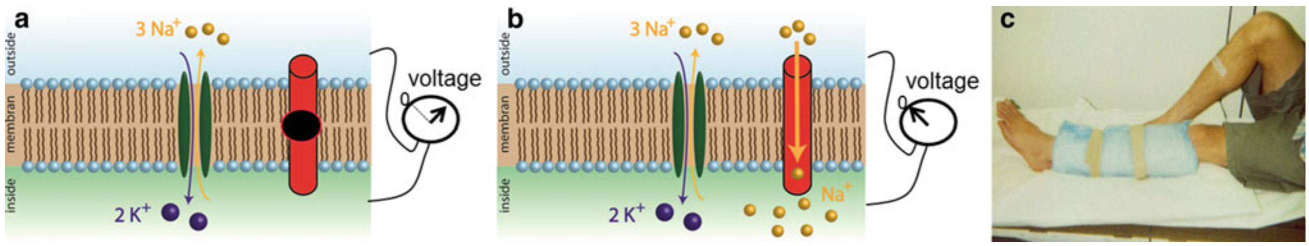
a
3 Na+
outside
membran
inside
2 K+
voltage
b
3 Na+
outside
membran
inside
2 K+
Na+
voltage
c

Fig. 6 The Na$^+$-K$^+$-ATPase helps to maintain the membrane potential (**a**). In muscular sodium channelopathies, a mutated sodium channel (**b**) can have an increased open-probability, which leads to an inflow of Na$^+$ into the cell and to a breakdown of the membrane potential. **c** In patients with paramyotonia congenita (PC)—a rare muscular sodium channelopathy—this increase can be triggered with exposure to cold

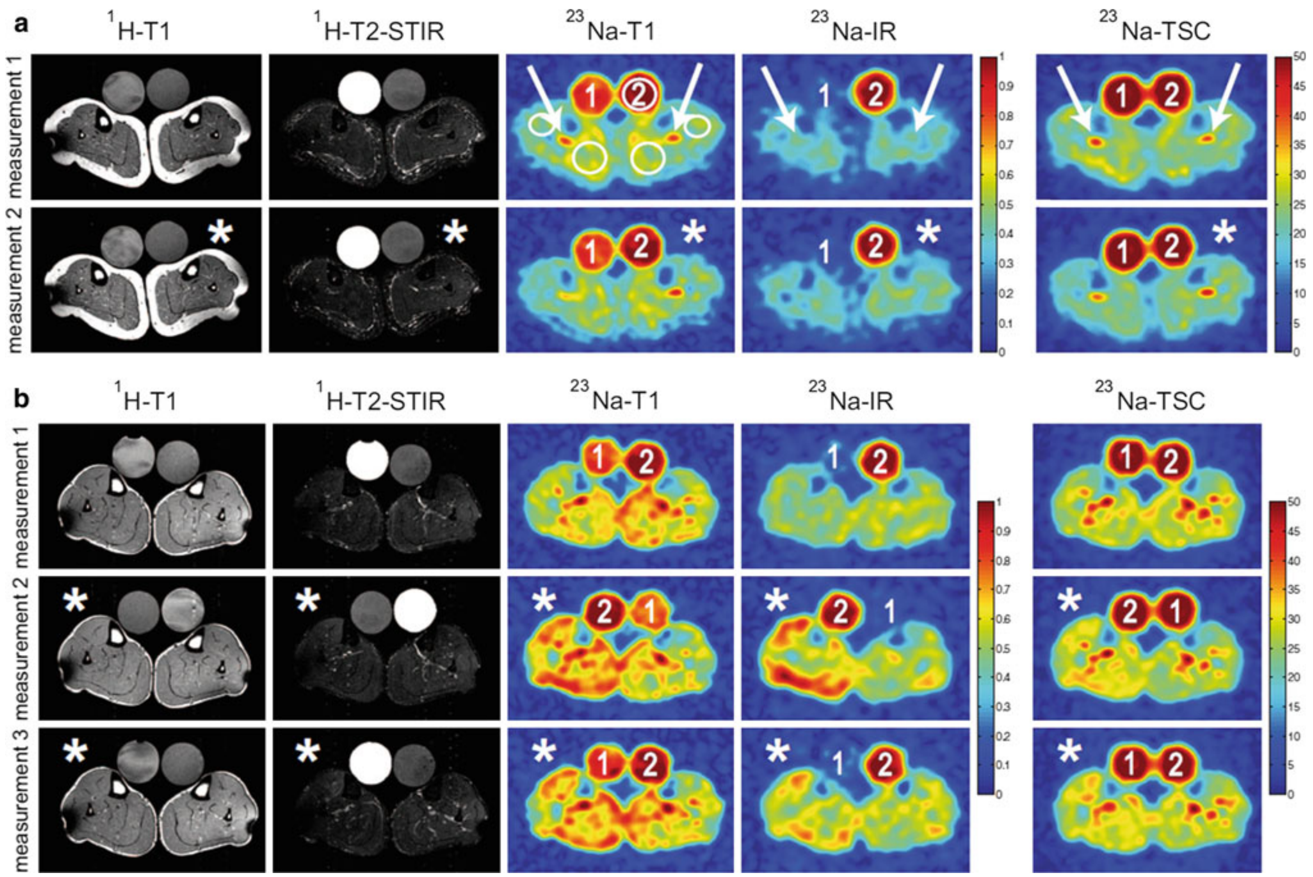
a
1H-T1
1H-T2-STIR
23Na-T1
23Na-IR
23Na-TSC
measurement 1
measurement 2
1
2
*
0
0.1
0.2
0.3
0.4
0.5
0.6
0.7
0.8
0.9
1
0
5
10
15
20
25
30
35
40
45
50
b
1H-T1
1H-T2-STIR
23Na-T1
23Na-IR
23Na-TSC
measurement 1
measurement 2
measurement 3

Fig. 7 **a** Transversal ^{1}H MR and ^{23}Na MR images of the lower legs of a healthy subject before (measurement 1) and after provocation of the left lower leg muscle (*, measurement 2). Signal intensities of ^{23}Na T$_1$ and ^{23}Na IR imaging were normalized to reference tube 2 (51.3 mmol/L NaCl and 5 % agarose gel). The ^{23}Na TSC signal intensities are given in mmol/L. Note that reference tube one (pure 51.3 mmol/L saline solution) shows no signal intensity in ^{23}Na IR imaging. The positions of the ROIs are shown, exemplarily. The signal emanating from intravascular sodium ions is suppressed in ^{23}Na IR imaging (*arrows*). In ^{23}Na T$_1$ imaging reference tube one shows also reduced signal intensity compared with reference tube 2 (5 % agarose gel). Fat and bone exhibits lower signal intensities compared with muscle tissue in all three ^{23}Na MRI sequences. After provocation (*) no distinct signal change is visible for all sequences. **b** ^{1}H MR and ^{23}Na MR images of a PC patient. ^{1}H MRI revealed no pathologic signal changes before and after provocation. The cooled leg (*) showed a distinct muscular ^{23}Na signal increase in ^{23}Na T$_1$ and ^{23}Na IR imaging, as well as a slight increase in the total Na$^+$-concentration (^{23}Na TSC), when compared with measurement 1 and the non-provoked leg. Slight ^{23}Na signal increases are still visible in measurement 3 (110 min after provocation). The increase is most pronounced in ^{23}Na IR imaging. Images and figure caption reproduced from: Nagel et al. 2011b. Reproduced by permission of Lippincott Williams & Wilkins. Copyright © Lippincott Williams & Wilkins

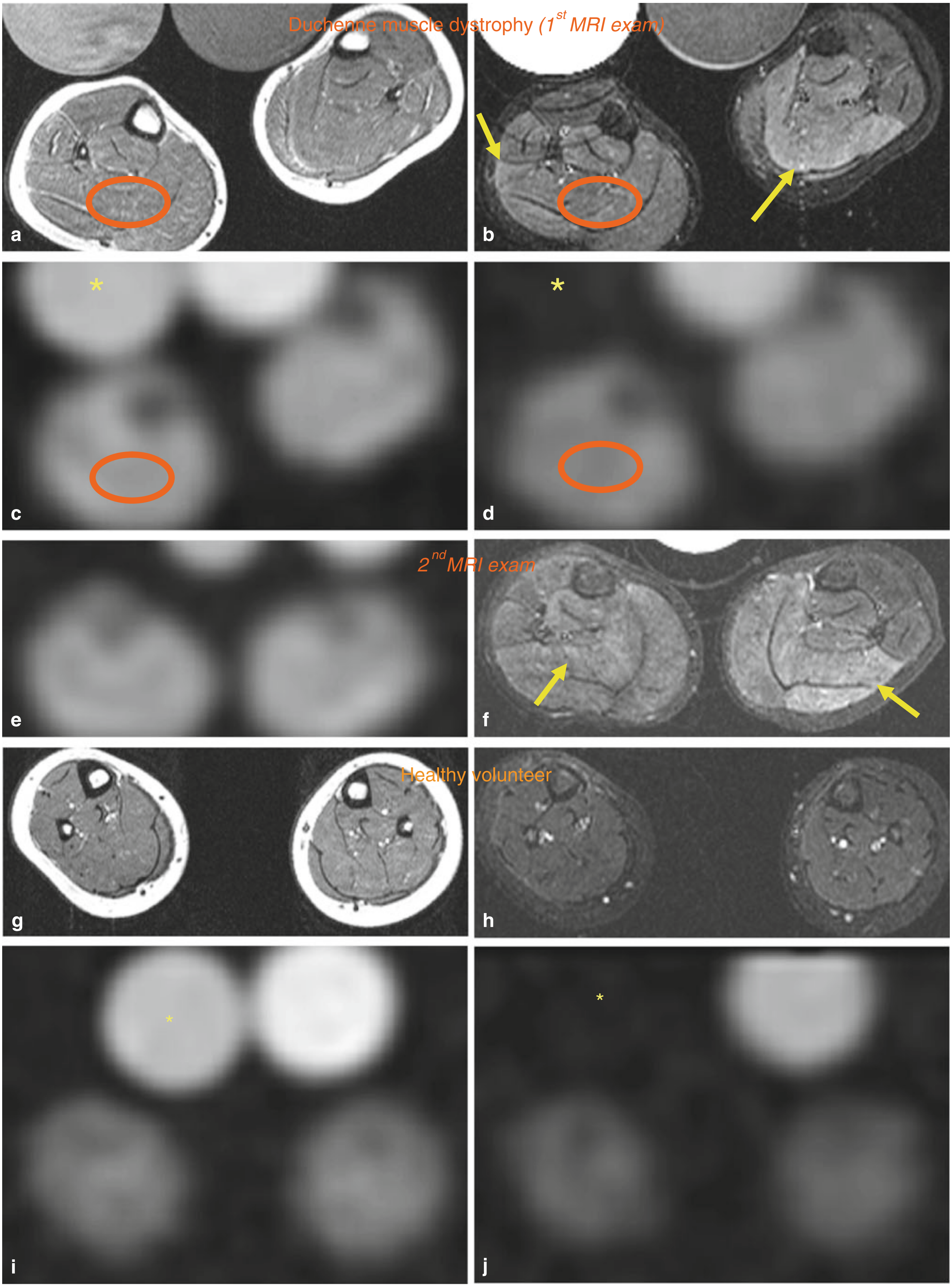
Duchenne muscle dystrophy (1st MRI exam)
a
b
*
c
*
d
2nd MRI exam
e
f
Healthy volunteer
g
h
*
i
*
j

◀ **Fig. 8** Edema-like changes and increased muscular sodium are constantly present in Duchenne muscular dystrophy. MRI of both calves of a 5-year-old Duchenne boy without glucocorticoid medication (deleted exons 45–50; **a–f**) and a 5-year-old healthy volunteer (**g–j**); **a, g** T1-weighted, **b, f, h** STIR, **c, e, i** ^{23}Na TSC images, **d, j** ^{23}Na T_1 IR images. There is no fatty degeneration of the triceps surae muscles both in the Duchenne boy (**a**) and the age-matched healthy volunteer (**g**). However, muscular edema most pronounced in both soleus muscles (*arrows* in **b, f**) are visible, both at first (**b**) and follow-up MR images (**f**) compared to normal findings in the volunteer (**h**). ^{23}Na IR (**d**) and TSC ^{23}Na MRI (**c**) reveal elevated signal in both soleus muscles (muscular Na$^+$ concentration in mmol/L of 39.32) compared to the volunteer (muscular Na$^+$ concentration in mmol/L of 25.26; **i, j** without changes at follow-up (**e**). The tibial bones present with low ^{23}Na signal. With the ^{23}Na IR sequence, the ^{23}Na signal emitted from vasogenic edema and vessels was sufficiently suppressed. Note that the signal of the reference tube containing free 51.3 mmol/L Na$^+$ solution (asterisks in **c, d, i, j**) is suppressed in the ^{23}Na IR sequence (**d, j**), while the contralateral reference tube filled with 51.3 mM Na$^+$ in 5 % agarose gel is well visible. Exemplary, the ROI positioning on the right soleus muscles on the ^{23}Na MR and ^{1}H MR images is given in **a–d**. Adapted by permission of Springer from: Weber et al. (2012). Copyright © by AAN Enterprises

edema may contribute to the progressive muscle degeneration and may be part of a general mechanism in muscular degeneration, because a muscular Na$^+$ overload was also reported in the chronic form of hypokalemic periodic paralysis (Jurkat-Rott et al. 2009) (see also "MRI in Muscle Channelopathies" for more details).

5 Musculoskeletal Applications Beyond Muscle Tissue: Sodium MRI as a Biomarker of Cartilage Degeneration

Osteoarthritis (OA) affects over 50 million Americans (Felson et al. 1995a, b) and has a significant negative impact on the quality of life of elderly individuals. At present, treatment for OA has largely been directed toward symptomatic relief and has included both pharmacologic and non-pharmacologic therapies (Zhang et al. 2008). Although there is no cure for this debilitating disease, an early detection and appropriate therapeutic intervention may have the potential to stop disease progression at the initial stages of the disease (Zhang et al. 2008). While OA progression is multi-factorial and slow progressing disease, the earliest changes in the cartilage due to OA results in a partial breakdown in the proteoglycan (PG) matrix with a decrease in total content of glycosaminoglycans (GAG) and loss of collagen from the extracellular matrix. GAG loss also implicated in degenerative disk disease (DDD) of the intervertebral disk (IVD). It is widely accepted that DDD contributes directly to axial low back pain (LBP), which is the second most frequent reason for a physician visit, and permanently disables more than 5 million Americans with annual costs of $100 billion in the US (Felson et al. 1995a, b). Conventional MRI based on T_1 and T_2 contrasts permits the direct visualization of cartilage morphology at high resolution and can detect morphologic changes with high levels of accuracy. However, it has not proven either sensitive or specific for changes in cartilage biochemistry and physiology, such as the detection of early [GAG] changes (Saadat et al. 2008). While proton imaging based methods such as delayed Gadolinium enhanced MRI of cartilage (dGEMRIC) using T_1 relaxation mapping have been shown to be useful for measuring GAG, dGEMRIC involves exogenous contrast agent. Although $T_{1\rho}$ is a promising technique, it is sensitive to both PG and collagen changes and thus is not completely specific to GAG (Burstein et al. 2001). Several studies have demonstrated that sodium MRI can be used to directly map [GAG] in cartilage and IVDs in vivo (Reddy et al. 1998; Borthakur et al. 2000; Shapiro et al. 2000, 2002; Wheaton et al. 2004; Wang et al. 2009, 2010). Most of these techniques have been developed to specifically detect the GAG component of cartilage and disks, which is the more important element due to the small contribution of collagen degradation during the initiating steps of OA and DDD (Dijkgraaf et al. 1995). Here, we briefly describe the rationale, validation studies on phantoms and animal models, and in vivo human studies of sodium MRI as a biomarker for quantifying early degenerative changes in cartilage and IVD. Potential advantages and challenges associated with this method in quantifying changes in GAG content in vivo are discussed.

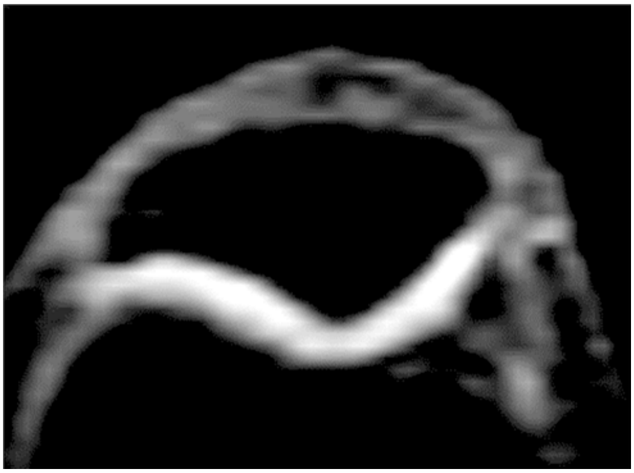

Fig. 9 Axial slice of sodium image of a healthy human knee obtained at 4T GE MRI scanner. High sodium content in articular cartilage is reflected in the high signal compared to surrounding tissues (Reddy et al. 1998)

In cartilage, the fixed negative charge density (FCD) on GAG side-chains attracts Na^+ ions (Maroudas et al. 1969). Under normal concentrations in cartilage ($\sim$300 mM) sodium produces an osmotic gradient that results in a swelling pressure in cartilage (Maroudas 1976, 1979). Based on the fact that Donnan equilibrium holds for cartilage equilibrated in very dilute solutions, Maroudas et al. (1969) have shown that FCD of cartilage is correlated to the GAG content of cartilage. Since the FCD is counter balanced by the Na^+ ions, loss of PG (hence GAG and FCD) due to cartilage degeneration results in the loss of sodium ions from the tissue. The loss of the negatively charged PG lowers the FCD in the tissue, thereby releasing positively charged sodium ions. Using ideal Donnan equilibrium conditions FCD can be related to tissue sodium concentration according to the following equation (Lesperance et al. 1992):

$$\mathrm{FCD(mM)} = \frac{\left[\mathrm{Na}^{+}_{\mathrm{fluid}}\right]^{2}}{\left[\mathrm{Na}^{+}_{\mathrm{tissue}}\right]} - \left[\mathrm{Na}^{+}_{\mathrm{tissue}}\right] \tag{7}$$

where $\left[\mathrm{Na}^{+}_{\mathrm{fluid}}\right]$ is the sodium concentration in the synovial fluid and $\left[\mathrm{Na}^{+}_{\mathrm{tissue}}\right]$ is the sodium concentration in the tissue. $\left[\mathrm{Na}^{+}_{\mathrm{fluid}}\right]$ is typically in the range of 140–150 mM, while in phosphate-buffered saline (PBS) it is 154 mM. Depending on the age and location in the tissue, healthy human cartilage FCD ranges from −50 to −250 mM (Lesperance et al. 1992). FCD from [GAG] can be calculated by the following equation by assuming 2 mol of negative charge per mole of chondroitin sulfate (one from sulfate and one from carboxylate) and a molecular weight of chondroitin sulfate of 502.5 g/mol (Lesperance et al. 1992):

$$\mathrm{FCD(mM)} = -2 \times \frac{[\mathrm{GAG}]\left(\mathrm{mg}/\mathrm{L}\right)}{502.5\left(\mathrm{mg}/\mathrm{mM}\right)} \tag{8}$$

The loss of the PG during the early onset of OA lowers FCD on the GAG, thereby reducing [Na] and osmotic pressure in the tissue. Thus the changes in GAG in cartilage can be quantified by computing the [Na] derived from sodium MRI and thereby providing the rationale for sodium MRI as a biomarker for cartilage pathology.

Sodium MRI inherently will have lower SNR due to lower [Na] as well as lower gyromagnetic ratio (γ) of ^{23}Na nuclei that requires fourfold stronger gradients in order to obtain sodium images of equal resolution to that of conventional proton MRI. Recently sub-millisecond echo time sodium imaging of cartilage has been demonstrated (Nielles-Vallespin et al. 2007). Despite its lower signal and resolution, sodium MRI offers high specificity toward [GAG] and enables the quantitation of GAG-specific changes during the course of the degeneration (Reddy et al. 1998; Shapiro et al. 2000, 2002; Wheaton et al. 2004, 2005; Wang et al. 2010; Insko et al. 1997, 1999). While the in vivo sodium MRI of knee was performed at 3 and 4 T, the SNR and spatial resolution were not optimal (Shapiro et al. 2002; Wheaton et al. 2004) requiring high-field scanners (7 T and above) with short-echo pulse sequences and sodium RF coil hardware. Low resolution sodium MRI was acquired from human knee in vivo (Granot 1988) at 1.5 T. Reddy et al. (1998) at 4 T, for the first time, demonstrated the feasibility of acquiring a high-resolution (voxel size of 6.25 μL) 3D data set of sodium images of the knee of healthy human volunteers with excellent SNR (16:1) at 4 T (Fig. 9).

Sodium concentration was measured from human cartilage specimens obtained from knee replacement surgery. Clear differences in sodium concentrations in healthy and osteoarthritic specimens were noted (Fig. 10).

Comparison of axial sodium in vivo MR images of healthy and symptomatic human subjects is shown in Fig. 11.

Borthakur et al. (2002) demonstrated the feasibility of quantifying sodium in the human wrist joint in vivo on a 4 T whole-body scanner. Employing a fast gradient echo sequence, a 3D data set of 16 slices with 16 averages was obtained in 22 min. The image resolution was 0.06 cm × 0.25 cm × 0.4 cm. In these studies, it was found that in healthy human wrist average sodium concentration ranged from 115 to 150 mM in non-cartilaginous regions and from 200 to 210 mM in cartilaginous regions. Moreover, sodium image data was used to generate FCD maps. The average FCD of cytokine treated cartilage was 49 % lower than that of saline-treated patellae reflecting a loss of PG content. These results were supported by histologic and immunochemical findings, most notably a reduction in staining for PG and an increase in matrix metalloproteinases in the synovial fluid. Using a 7 T whole body human scanner and a new MRI pulse sequence developed by Nielles-Vallespin et al. (2007) that could achieve sub-millisecond echo times for time-efficient and high SNR sodium imaging, an ultra-short echo time (TE = 200 μs) was obtained to generate 3D sodium MRI data using a birdcage coil in a clinically acceptable image acquisition time of under 15 min. Superior SNR ($\sim$25) of the images is evident even with a high resolution of 1.5 mm^3 isotropic voxels. This sequence was also used to quantify sodium concentration in vivo on healthy normal and OA subjects, in which the mean sodium concentration of healthy subjects ranged from 240 mM/L to 280 mM/L with $\sim$10 % variation in each group. However, OA patients showed significantly lower [Na] by 30–60 % based on disease severity (Fig. 12).

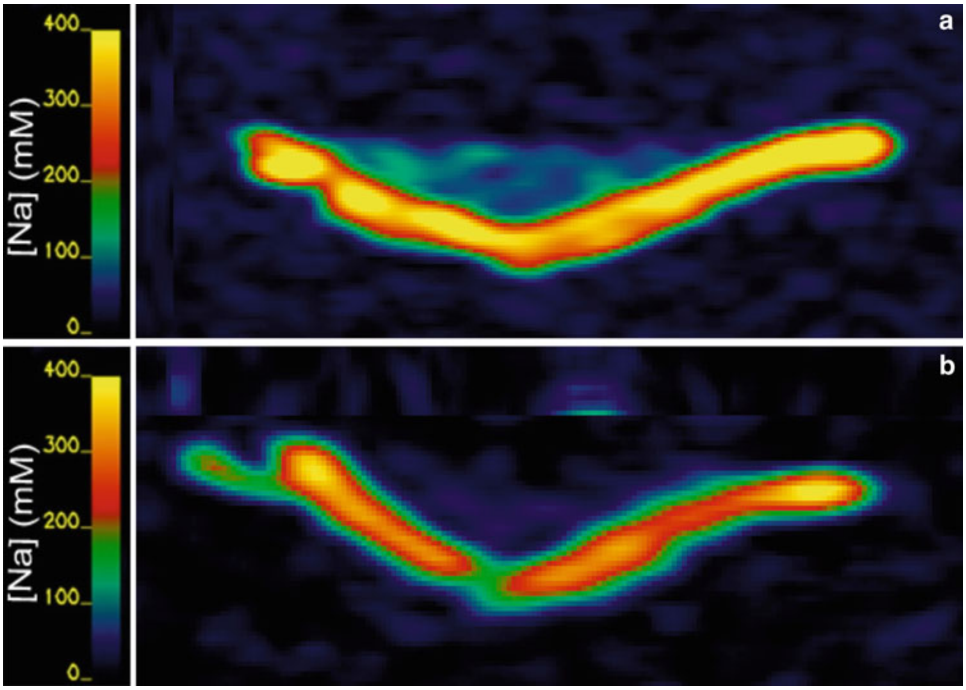

Fig. 10 Sodium images of human patellar cartilage specimens obtained following knee replacement surgery. The image in **a** is from healthy appearing cartilage while the one in **b** is from osteoarthritic specimen. Bar scale shows [Na] in mM

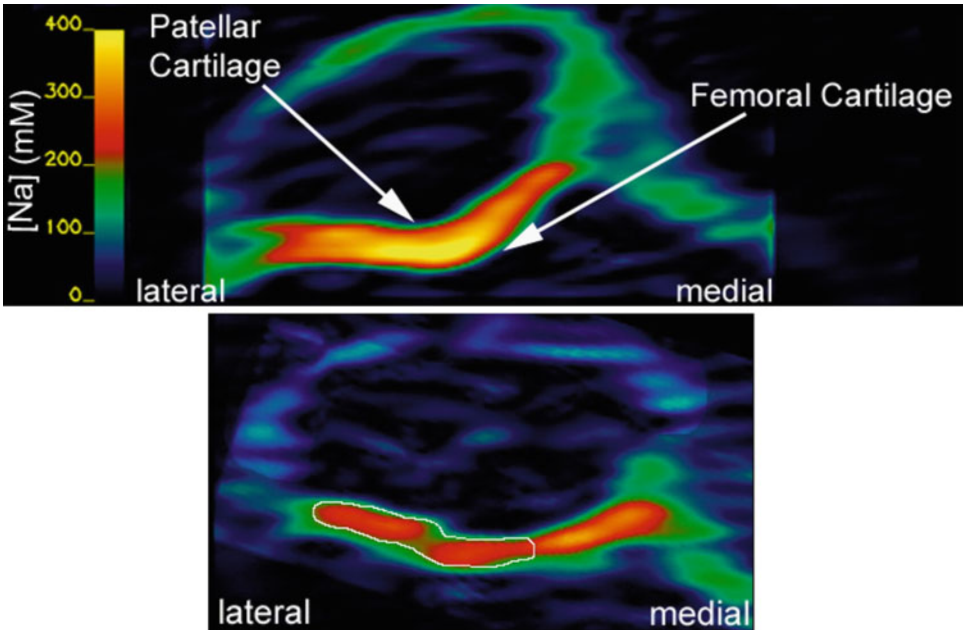

Fig. 11 Sodium axial images from human knee in vivo. Bar scale shows the [Na] in mM. Image on the top is from a healthy volunteer. Fairly uniform and high sodium content can be seen. The image on the *bottom* is from a symptomatic osteoarthritic subject. Low [Na] and heterogeneous distribution reflect the loss of GAG in this subject (Wheaton et al. 2004). Adapted from: Wheaton et al. (2004). Figure reproduced by permission of the Radiological Society of North America (RSNA)

Schmitt et al. (2011) and Krusche-Mandl et al. (2012) compared GAG content measurement by sodium MRI with that obtained from proton-based chemical exchange saturation transfer (gagCEST) imaging method, where the MR signal is sampled symmetrically around the water peak by frequency-selective saturation pulses. They found a strong correlation between sodium and gagCEST in cartilage (Fig. 13).

Furthermore, imaging of the human IVD in vivo noticed differences in the sodium MRI between an asymptomatic subject and a subject with lower back pain (Fig. 14). The lower Na concentration in both L3–L4 and L4–L5 IVDs in

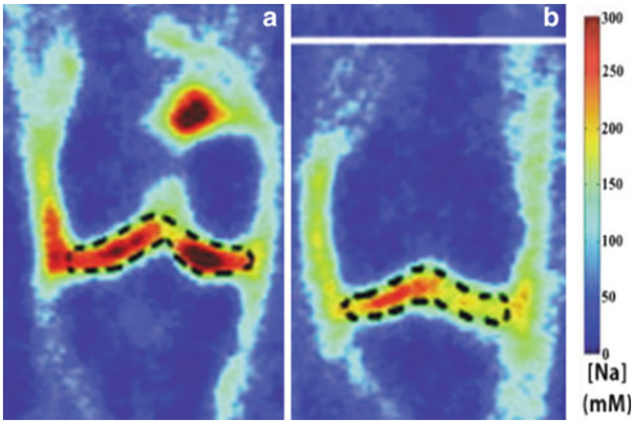

Fig. 12 Representative [Na] maps of a healthy volunteer (**a**) and an OA patient (**b**). These concentration maps were calculated from sodium MRI using the method of Shapiro et al. (2000) and show a significant decrease in [Na] in the OA patient's femoral cartilage (Wang et al. 2009). The *color bar scale* on the right indicates total sodium concentration ([Na]) in millimolar. Adapted from: Wang et al. (2009). © 2009 Wiley-Liss, Inc

the back pain patient indicated a loss of PG, perhaps an early sign of disk disease.

In summary, sodium MRI despite its inherently lower sensitivity compared to conventional MRI is highly specific to GAG content in cartilage and disk tissues and has shown promise in evaluating OA in humans. But in order for sodium MRI to be translated to clinical practice, multicenter studies will need to be performed to standardize protocols and determine grading schemes. Also, despite the high specificity to cartilage physiology and biochemistry, the method has several challenges in studying human OA. First, the resolution of this method is limited by its inherently broad point spread function due to very short T_2 component of sodium signal. Because of this limitation, in addition to sodium map, an anatomic image also invariably required to assess the true spatial variation of sodium signal, which increases the total scan time. The second point that has to be considered is that the contribution from sodium signal from synovial fluid, which although has lower sodium concentration than cartilage often has longer T_2 and may confound the quantitation of sodium and hence GAG content of cartilage, although it may be mitigated to some extent by employing short TR. Finally, given the inherently low SNR of the method, it requires ultrahigh field scanners to obtain quality sodium images with adequate SNR for quantifying pathological changes. However, this may not be an issue in the near future, as the ultrahigh field whole body human scanners such as 7 T, are rapidly proliferating around the globe.

6 Outlook: Imaging of More Exotic X-Nuclei (^{35}Cl, ^{39}K, and ^{17}O)

Besides ^{23}Na, there are many other MR accessible nuclei that are involved in physiological cellular processes (Fig. 15). However—except for ^{31}P—their MR sensitivities are much lower compared to the sensitivity of ^{23}Na (c.f. Table 1).

6.1 ^{35}Cl MRI

Chlorine (Cl^-) is the most abundant anion in the human organism and is involved in many physiological processes. In skeletal muscle tissue, Cl^- is passively distributed in response to the resting membrane potential. This results from very high Cl^- conductance, making up ~80 % of the total membrane conductance at rest (Lehmann-Horn and Jurkat-Rott 1999). Thus, the resting membrane potential of muscle cells can be approximated by the *Nernst* equation for Cl^-, which requires only intra- and extracellular Cl^- concentrations. The resting membrane potential is reduced in various muscular diseases (e.g., periodic paralysis). Cl^- MRI can determine the total tissue Cl^- concentration and thus can help to calculate the required intracellular concentration. The extracellular concentration is easily accessible by blood chemistry. Data for the intracellular volume fraction are available in literature (Donahue et al. 1995; Sykova and Nicholson 2008) and can be estimated from the tissue sodium concentration (e.g., as obtained by ^{23}Na MRI (Thulborn et al. 1999)), as well. Chlorine has two naturally occurring, MR sensitive isotopes, ^{35}Cl and ^{37}Cl, with natural abundances of 75.78 and 24.22 %, respectively (Harris et al. 2002) (c.f. Table 1). The feasibility of ^{35}Cl MRI in humans has recently been demonstrated (Nagel et al. 2012, 2013). In future, ^{35}Cl MRI might enable non-invasive electrophysiological measurements in vivo, such as determination of the resting membrane potential of muscle cells.

6.2 ^{39}K MRI

Intra- and extracellular K^+ concentrations largely affect the excitability and membrane potential of cells (Hodgkin and Huxley 1952). Therefore, a determination of the muscular K^+ content is highly desirable. Naturally occurring potassium is composed of three MR sensitive isotopes (^{39}K, ^{40}K, ^{41}K). Among these isotopes, ^{39}K has the highest natural abundance (93.26 %) (Harris et al. 2002). The expected relative SNR of ^{39}K MRI (c.f. Table 1) is more than a factor

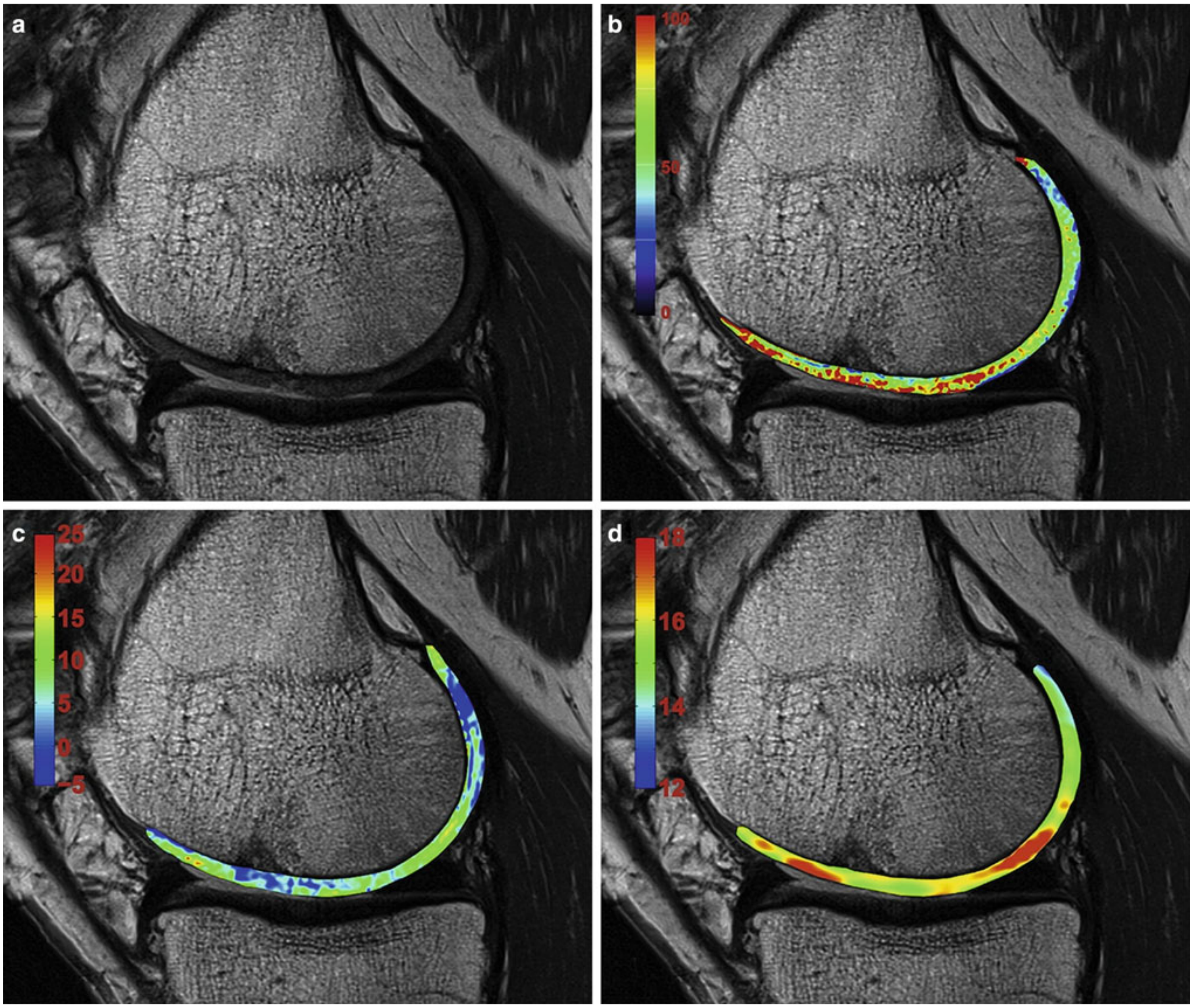

Fig. 13 Sagittal knee images from a 49-year-old patient with a secondary cartilage defect **a** 9.4 years after ACT at the MFC. Color maps are overlaid to visualize **b** T_2 map, **c** gagCEST, and **d** Sodium MRI (Krusche-Mandl et al. 2012). *Color bars* represent T_2 relaxation times in [ms], higher values = more water, disturbed collagen architecture. Whereas MTR_{asym} gagCEST values summed over offsets from 0 to 1.3 ppm and sodium signal to noise ratio values, lower values indicate lower PG content. Both gagCEST and sodium MRI show a correlated decrease signal from cartilage adjacent to the defect compared to surrounding native tissue. Reproduced by permission of Elsevier Ltd from: Krusche-Mandl et al. (2012). ©2012 Osteoarthritis Research Society International

of 30 lower compared to the SNR of ^{23}Na MRI. However, the feasibility of ^{39}K MRI of human brain and muscle in vivo has recently been demonstrated on a 7 T whole-body MRI system (Umathum et al. 2013).

6.3 ^{17}O MRI

Oxygen uptake and metabolism is a key parameter in nearly any living subject. In healthy skeletal muscle tissue, the amount of high-energy phosphates, the oxidative-phosphorylation potential, and the perfusion-related O_2-availability are crucial for proper muscle function. Disturbances in the kinetics of energy metabolism, such as oxidative phosphorylation during recovery from exercise, may limit the contracting ability of the muscles (Argov et al. 2000). Furthermore, changes in myocellular high-energy phosphate metabolism are encountered in diseases leading to muscular degeneration (Argov et al. 2000). Intracellular pH, as well as the MR signal intensity ratios P_i/PCr (inorganic phosphate

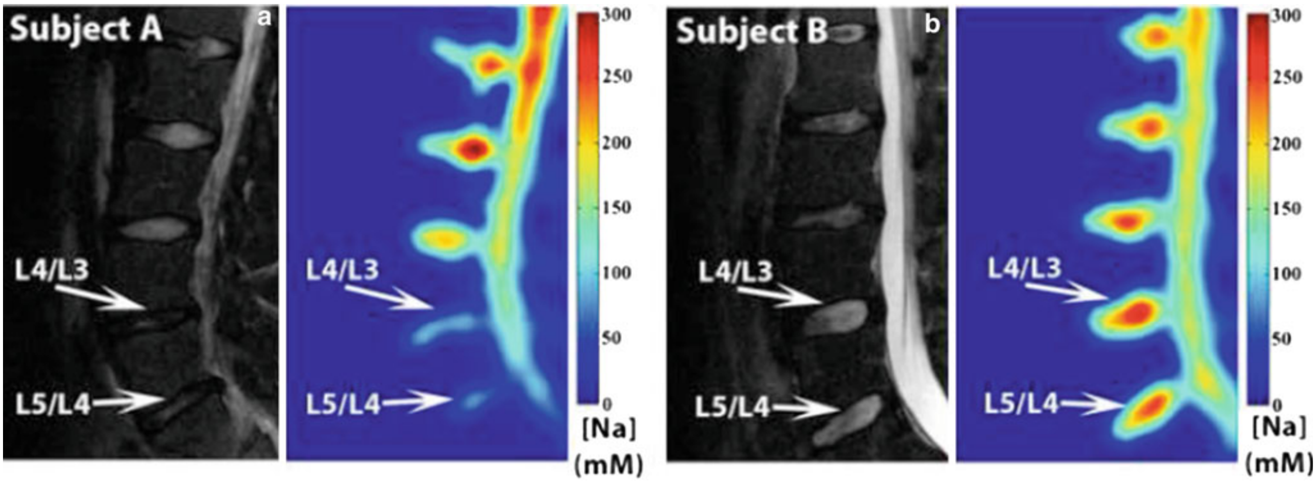
Subject A
a
L4/L3
L5/L4
300
250
200
150
100
50
0
[Na]
(mM)
Subject B
b
L4/L3
L5/L4
300
250
200
150
100
50
0
[Na]
(mM)

Fig. 14 Representative proton T_2 MRI (*gray scale*) and corresponding [Na] maps (*color*) obtained in vivo on an 22-year-old male with lower lumbar trauma that resulted in chronic lower back and a 26-year-old healthy male (Wang et al. 2010). The *color bar scale* on the *right* of each *panel* indicates total sodium concentration ([Na]) in millimolar. Reproduced from: Wang et al. (2010). Copyright © Lippincott Williams & Wilkins

Fig. 15 ^{1}H, ^{23}Na, ^{39}K, and ^{35}Cl MRI of the healthy thigh muscle of a female volunteer. Each X-nuclei MR image was acquired in an acquisition time of 10 min. Nominal spatial resolutions of 3.8 × 3.8 × 10 mm^3 (^{23}Na MRI), 8 × 8 × 16 mm^3 (^{39}K MRI) and 12 × 12 × 24 mm^3 (^{35}Cl MRI) were achieved. Images courtesy of: Dres. Reiner Umathum, Manual B. Rösler, Armin M. Nagel; German Cancer Research Center (DKFZ), Heidelberg, Germany

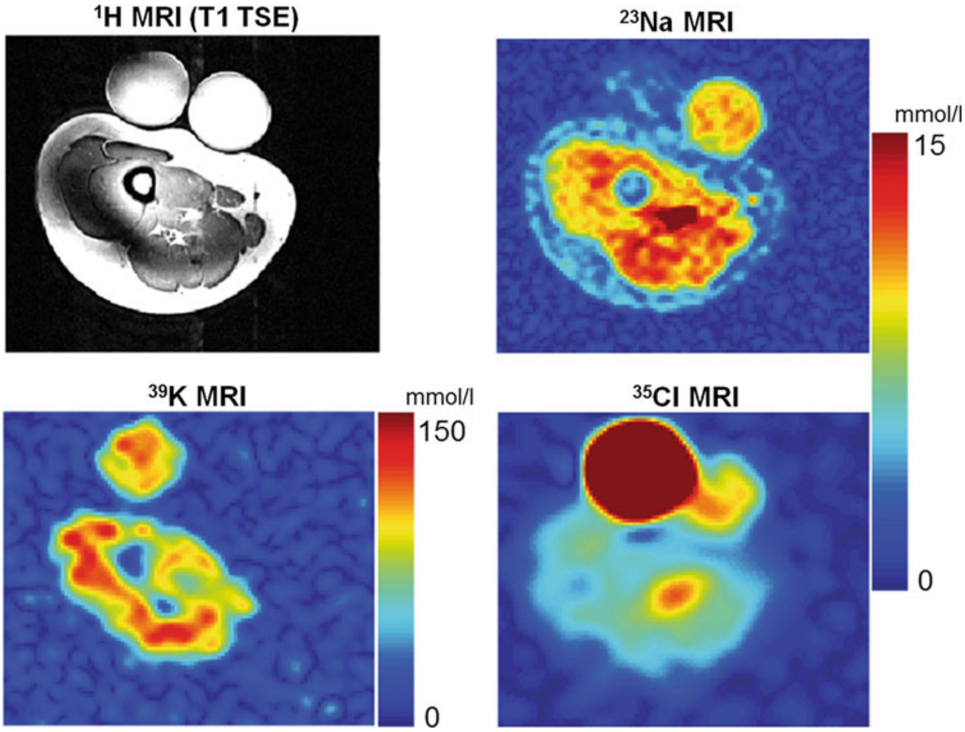
¹H MRI (T1 TSE)
²³Na MRI
mmol/l
15
0
³⁹K MRI
mmol/l
150
0
³⁵Cl MRI

(P_i) to phosphocreatine (PCr)), and PDE/PCr (phosphodiester (PDE) to PCr), have been reported to increase depending on the stage and severity of the muscle degeneration (see also Chapter "MR Spectroscopy and Spectroscopic Imaging for Evaluation of Skeletal Muscle Metabolism: Basics and Applications in Metabolic Diseases"). Also, there are two principal ways to categorize muscle fibers: the type of myosin (fast or slow) present, and the degree of oxidative

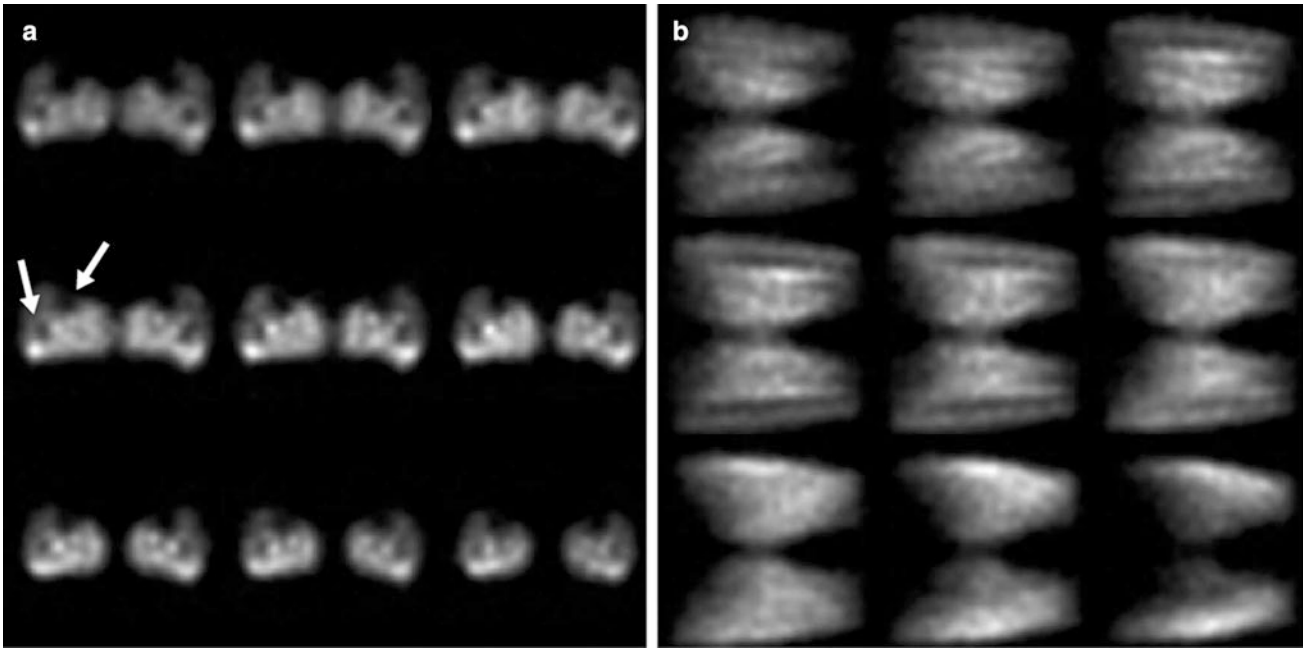

Fig. 16 In vivo natural abundance ^{17}O MRI of a healthy subject. Transversal (**a**) and coronal (**b**) slices of both lower legs. In an acquisition time of 10 min a nominal spatial resolution of $(6.2\ mm)^3$ was achieved ($B_0 = 7$ T). Tibia and fibula can be resolved (c.f. white arrows). Images courtesy of: Stefan H. Hoffmann, DKFZ Heidelberg, Germany (Hoffmann 2011)

phosphorylation that the fiber undergoes. Type I fibers appear red due to the presence of the oxygen binding protein myoglobin. These fibers are suited for endurance (for instance endurance athletes such as long-distance runners) and are slow to fatigue because they use oxidative metabolism to generate ATP. Type II fibers are white due to the absence of myoglobin and a reliance on glycolytic enzymes. These fibers are efficient for short bursts of speed and power (for instance in sprinters) and use both oxidative metabolism and anaerobic metabolism depending on the particular sub-type, but these fibers are quicker to fatigue. The oxygen consumption rate is also important in tumor tissue, for instance regarding the tumor's aggressiveness and its treatment resistance (Miles and Williams 2008).

In nature, three stable isotopes of oxygen (^{16}O, ^{17}O, and ^{18}O) exist. Among these nuclei, only ^{17}O—the isotope with the lowest natural abundance (0.038 %) (Harris et al. 2002)—exhibits a nuclear magnetic spin moment and can be detected by MRI. ^{17}O MRI enables the determination of the in vivo oxygen consumption. Inhalation of highly enriched ^{17}O gas is used to quantify the cerebral metabolic rate of oxygen consumption ($CMRO_2$) which has recently been shown in the human brain (Atkinson and Thulborn 2010). However, due to the high costs of enriched oxygen gas, an efficient MR compatible gas delivery system with a closed rebreathing circuit is desirable (Hoffmann et al. 2011; Baumgardner et al. 2008). The gold standard to quantify the oxygen consumption rate is ^{15}O positron emission tomography (PET). Nuutila et al. (2000) determined the rates of oxygen consumption, blood flow, and glucose uptake of skeletal muscle using $^{15}O_2$, $H_2^{15}O$, and ^{18}F Fluorodeoxyglucose. However, ^{15}O PET studies have only rarely been performed in muscle due to several reasons. First of all the short ^{15}O half-life of about 2 min requires an on-site cyclotron for isotope production. Additionally, due to the complex quantification process of the oxygen consumption rate by ^{15}O PET, different measurements with various tracers (e.g., $^{15}O_2$ and $H_2^{15}O$) are required. ^{17}O MRI on the other hand, enables quantification of the oxygen consumption rate without ionizing radiation and only one dynamic inhalation study, since the inhaled $^{17}O_2$ remains invisible in the MR images until it is metabolized to $H_2^{17}O$ water (Zhu et al. 2005). MR relaxation times of ^{17}O in skeletal muscle ($T_1 = 4.0 \pm 0.2$ ms; $T_2 = 2.4 \pm 0.1$ ms) are approximately 30 % shorter than those in the human brain (Hoffmann 2011). Therefore efficient pulse sequences with ultra-short echo times (Nagel et al. 2009) are required for in vivo ^{17}O MRI of skeletal muscle tissue (Fig. 16). In future, ^{17}O MRI might also be combined with a dynamic inhalation study of enriched $^{17}O_2$ gas to determine the muscular oxygen consumption rate.

Acknowledgments Especially the implementation of X-nuclei MR imaging profits much from an interdisciplinary team working on this subject together. Thus we thank several physicists, radiologists, physiologists, orthopedic surgeons and neurologists with whom we worked for several years together on X-nuclei MRI. Explicitly, we would thank the following collaborators: Reiner Umathum, Manuela

B. Roesler, Stefan H. Hoffmann, and Wolfhard Semmler, all Medical Physics in Radiology, German Cancer Research Center (DKFZ), Heidelberg/Germany; Frank Lehmann-Horn and Karin Jurkat-Rott, Neurophysiology, Ulm University, Ulm/Germany. Work on Sects. 1–4 and 6 was funded in part by the Helmholtz Alliance ICEMED - Imaging and Curing Environmental Metabolic Diseases, through the Initiative and Networking Fund of the Helmholtz Association. Moreover, we acknowledge that Sect. 5 was performed at a NIH-NIBIB supported Biomedical Technology Research Center (P41 EB015893).

References

Amarteifio E, Nagel AM, Kauczor HU, Weber MA (2011) Functional imaging in muscular diseases. Insights Imaging 2(5):609–619. doi:10.1007/s13244-011-0111-6

Amarteifio E, Nagel AM, Weber MA, Jurkat-Rott K, Lehmann-Horn F (2012) Hyperkalemic periodic paralysis and permanent weakness: 3-T MR imaging depicts intracellular 23Na overload-initial results. Radiology 264(1):154–163. doi:10.1148/radiol.12110980

Argov Z, Lofberg M, Arnold DL (2000) Insights into muscle diseases gained by phosphorus magnetic resonance spectroscopy. Muscle Nerve 23(9):1316–1334

Atkinson IC, Thulborn KR (2010) Feasibility of mapping the tissue mass corrected bioscale of cerebral metabolic rate of oxygen consumption using 17-oxygen and 23-sodium MR imaging in a human brain at 9.4 T. Neuroimage 51(2):723-733. doi:10.1016/j.neuroimage.2010.02.056

Balschi JA, Bittl JA, Springer CS Jr, Ingwall JS (1990) 31P and 23Na NMR spectroscopy of normal and ischemic rat skeletal muscle. Use of a shift reagent in vivo. NMR Biomed 3(2):47–58

Bansal N, Germann MJ, Seshan V, Shires GT 3rd, Malloy CR, Sherry AD (1993) Thulium 1,4,7,10-tetraazacyclododecane-1,4,7,10-tetrakis(methylene phosphonate) as a 23Na shift reagent for the in vivo rat liver. Biochemistry 32(21):5638–5643

Baumgardner JE, Mellon EA, Tailor DR, Mallikarjunarao K, Borthakur A, Reddy R (2008) Mechanical ventilator for delivery of (1)(7)O(2) in brief pulses. Open Biomed Eng J 2:57–63. doi:10.2174/1874120700802010057

Benkhedah N, Bachert P, Semmler W, Nagel AM (2012) Three-dimensional biexponential weighted (23) Na imaging of the human brain with higher SNR and shorter acquisition time. Magn Reson Med. doi:10.1002/mrm.24516

Bergin CJ, Pauly JM, Macovski A (1991) Lung parenchyma: projection reconstruction MR imaging. Radiology 179(3):777–781

Boada FE, Christensen JD, Huang-Hellinger FR, Reese TG, Thulborn KR (1994) Quantitative in vivo tissue sodium concentration maps: the effects of biexponential relaxation. Magn Reson Med 32(2): 219–223

Boada FE, Gillen JS, Shen GX, Chang SY, Thulborn KR (1997) Fast three dimensional sodium imaging. Magn Reson Med 37(5): 706–715

Borthakur A, Shapiro E, Beers J, Kudchodkar S, Kneeland J, Reddy R (2000) Sensitivity of MRI to proteoglycan depletion in cartilage: comparison of sodium and proton MRI. Osteoarthr Cartil 8(4):288–293. doi:S1063-4584(99)90303-5 [pii] 10.1053/joca.1999.0303

Borthakur A, Shapiro E, Akella S, Gougoutas A, Kneeland J, Reddy R (2002) Quantifying sodium in the human wrist in vivo by using MR imaging. Radiology 224(2):598–602

Burstein D, Velyvis J, Scott KT, Stock KW, Kim YJ, Jaramillo D, Boutin RD, Gray ML (2001) Protocol issues for delayed Gd(DTPA)2—enhanced MRI (dGEMRIC) for clinical evaluation of articular cartilage. Magn Reson Med 45(1):36–41

Chang G, Wang L, Schweitzer ME, Regatte RR (2010) 3D 23Na MRI of human skeletal muscle at 7 Tesla: initial experience. Eur Radiol 20(8):2039–2046. doi:10.1007/s00330-010-1761-3

Clausen T (2003) Na + -K + pump regulation and skeletal muscle contractility. Physiol Rev 83(4):1269–1324. doi:10.1152/physrev.00011.2003

Constantinides CD, Gillen JS, Boada FE, Pomper MG, Bottomley PA (2000) Human skeletal muscle: sodium MR imaging and quantification-potential applications in exercise and disease. Radiology 216(2):559–568

Dijkgraaf LC, de Bont LG, Boering G, Liem RS (1995) The structure, biochemistry, and metabolism of osteoarthritic cartilage: a review of the literature. J Oral Maxillofac Surg 53(10):1182–1192. doi:0278-2391(95)90632-0 [pii]

Donahue KM, Weisskoff RM, Parmelee DJ, Callahan RJ, Wilkinson RA, Mandeville JB, Rosen BR (1995) Dynamic Gd-DTPA enhanced MRI measurement of tissue cell volume fraction. Magn Reson Med 34(3):423–432

Felson D, Zhang Y, Hannan M, Kannel W, Kiel D (1995a) Alcohol intake and bone mineral density in elderly men and women. The Framingham Study. Am J Epidemiol 142(5):485–492

Felson D, Zhang Y, Hannan M, Naimark A, Weissman B, Aliabadi P, Levy D (1995b) The incidence and natural history of knee osteoarthritis in the elderly. The Framingham Osteoarthritis Study. Arthritis Rheum 38(10):1500–1505

Granot J (1988) Sodium imaging of human body organs and extremities in vivo. Radiology 167:547–550

Gupta RK, Gupta P, Moore RD (1984) NMR studies of intracellular metal ions in intact cells and tissues. Annu Rev Biophys Bioeng 13:221–246. doi:10.1146/annurev.bb.13.060184.001253

Harris RK, Becker ED, Cabral de Menezes SM, Goodfellow R, Granger P (2002) NMR nomenclature: nuclear spin properties and conventions for chemical shifts. IUPAC Recommendations 2001. International Union of Pure and Applied Chemistry. Physical Chemistry Division. Commission on Molecular Structure and Spectroscopy. Magn Reson Chem 40(7):489–505. doi:10.1002/mrc.1042

Hodgkin AL, Huxley AF (1952) A quantitative description of membrane current and its application to conduction and excitation in nerve. J Physiol 117(4):500–544

Hoffmann SH (2011) Localized quantification of the cerebral metabolic rate of oxygen consumption (CMRO2) with 17O magnetic resonance tomograghy. Dissertation, Universität Heidelberg, Heidelberg

Hoffmann SH, Begovatz P, Nagel AM, Umathum R, Schommer K, Bachert P, Bock M (2011) A measurement setup for direct 17O MRI at 7 T. Magn Reson Med 66(4):1109–1115. doi:10.1002/mrm.22871

Hoult DI, Lauterbur PC (1979) The sensitivity of the zeugmatographic experiment involving human samples. J Magn Reson 34(2):425–433. doi:10.1016/0022-2364(79)90019-2

Insko EK, Reddy R, Leigh JS (1997) High resolution, short echo time sodium imaging of articular cartilage. J Magn Reson Imaging 7(6):1056–1059

Insko EK, Kaufman JH, Leigh JS, Reddy R (1999) Sodium NMR evaluation of articular cartilage degradation. Magn Reson Med 41:30–34

Jaccard G, Wimperis S, Bodenhausen G (1986) Multiplequantum NMR spectroscopy of $S = 3/2$ spins in isotropic phase: a new probe for multiexponential relaxation. J Chem Phys 85:6282. doi:10.1063/1.451458

Jurkat-Rott K, Weber MA, Fauler M, Guo XH, Holzherr BD, Paczulla A, Nordsborg N, Joechle W, Lehmann-Horn F (2009) K+-dependent paradoxical membrane depolarization and Na+ overload, major and reversible contributors to weakness by ion channel leaks. Proc Natl Acad Sci U S A 106(10):4036–4041. doi:0811277106 [pii] 10.1073/pnas.0811277106

Kline RP, Wu EX, Petrylak DP, Szabolcs M, Alderson PO, Weisfeldt ML, Cannon P, Katz J (2000) Rapid in vivo monitoring of chemotherapeutic response using weighted sodium magnetic resonance imaging. Clin Cancer Res 6(6):2146–2156

Konstandin S, Nagel AM (2013) Measurement techniques for magnetic resonance imaging of fast relaxing nuclei. Magn Reson Mater Phy. doi:10.1007/s10334-013-0394-3

Krusche-Mandl I, Schmitt B, Zak L, Apprich S, Aldrian S, Juras V, Friedrich KM, Marlovits S, Weber M, Trattnig S (2012) Long-term results 8 years after autologous osteochondral transplantation: 7 T gagCEST and sodium magnetic resonance imaging with morphological and clinical correlation. Osteoarthr Cartil/OARS, Osteoarthr Res Soc 20(5):357–363. doi:10.1016/j.joca.2012.01.020

Lauterbur PC (1973) Image formation by induced local interactions: examples employing nuclear magnetic resonance. Nature 242(5394): 190–191

Lehmann-Horn F, Jurkat-Rott K (1999) Voltage-gated ion channels and hereditary disease. Physiol Rev 79(4):1317–1372

Lesperance LM, Gray ML, Burstein D (1992) Determination of fixed charge-density in cartilage using nuclear-magnetic-resonance. J Orthop Res 10(1):1–13

Lu A, Atkinson IC, Claiborne TC, Damen FC, Thulborn KR (2010) Quantitative sodium imaging with a flexible twisted projection pulse sequence. Magn Reson Med 63(6):1583–1593. doi:10.1002/mrm.22381

Madelin G, Regatte RR (2013) Biomedical applications of sodium MRI in vivo. J Magn Reson Imaging (Epub ahead of print). doi:10.1002/jmri.24168

Maroudas AI (1976) Balance between swelling pressure and collagen tension in normal and degenerate cartilage. Nature 260(5554):808–809

Maroudas A (1979) Physicochemical properties of articular cartilage. In: Freeman MAR (ed) Adult articular cartilage, 2nd edn. Pitman Medical, Kent, pp 215–290

Maroudas A, Muir H, Wingham J (1969) The correlation of fixed negative charge with glycosaminoglycan content of human articular cartilage. Biochim Biophys Acta 177(3):492–500

Miles KA, Williams RE (2008) Warburg revisited: imaging tumour blood flow and metabolism. Cancer Imaging 8:81–86. doi:10.1102/1470-7330.2008.0011

Mispelter J, Lupu M, Briguet A (2006) NMR probeheads for biophysical and biomedical experiments: theoretical principles and practical guidelines. Imperial College Press, London

Nagel AM (2009) Sodium magnetic resonance imaging: development of a 3D radial acquisition technique with optimized k-space sampling density and high SNR-efficiency. Dissertation, Universität Heidelberg, Heidelberg

Nagel AM, Meise FM, Weber MA, Jurkat-Rott K, Lehmann-Horn F, Bock M, Semmler W, Umathum R (2012) Chlorine (35Cl) Magnetic resonance imaging of the human brain and muscle. In: Proceedings of the The International Society for Magnetic Resonance in Medicine, 2012, p 1699

Nagel AM, Laun FB, Weber MA, Matthies C, Semmler W, Schad LR (2009) Sodium MRI using a density-adapted 3D radial acquisition technique. Magn Reson Med 62(6):1565–1573. doi:10.1002/mrm.22157

Nagel AM, Bock M, Hartmann C, Gerigk L, Neumann JO, Weber MA, Bendszus M, Radbruch A, Wick W, Schlemmer HP, Semmler W, Biller A (2011a) The potential of relaxation-weighted sodium magnetic resonance imaging as demonstrated on brain tumors. Invest Radiol 46(9):539–547. doi:10.1097/RLI.0b013e31821ae918

Nagel AM, Amarteifio E, Lehmann-Horn F, Jurkat-Rott K, Semmler W, Schad LR, Weber MA (2011b) 3 Tesla sodium inversion recovery magnetic resonance imaging allows for improved visualization of intracellular sodium content changes in muscular channelopathies. Invest Radiol 46(12):759–766. doi:10.1097/RLI.0b013e31822836f6

Nagel AM, Weber MA, Wolf MB, Semmler W (2012) 3D density-adapted projection reconstruction 23Na-MRI with anisotropic resolution and field-of-view. In: Proceedings of the International Society for Magnetic Resonance in Medicine, 2012, p 2282

Nagel AM, Weber MA, Lehmann-Horn F, Jurkat-Rott K, Radbruch A, Umathum R, Semmler W (2013) Cl- Alterations do not correspond to disease-related Na+ changes. In: Proceedings of the International Society for Magnetic Resonance in Medicine, 2013, p 116

Naritomi H, Kanashiro M, Sasaki M, Kuribayashi Y, Sawada T (1987) In vivo measurements of intra- and extracellular Na+ and water in the brain and muscle by nuclear magnetic resonance spectroscopy with shift reagent. Biophys J 52(4):611–616. doi:10.1016/S0006-3495(87)83251-4

Nielles-Vallespin S, Weber M, Bock M, Bongers A, Speier P, Combs S, Wöhrle J, Lehmann-Horn F, Essig M, Schad L (2007) 3D radial projection technique with ultrashort echo times for sodium MRI: clinical applications in human brain and skeletal muscle. Magn Reson Med 57(1):74–81

Nuutila P, Peltoniemi P, Oikonen V, Larmola K, Kemppainen J, Takala T, Sipila H, Oksanen A, Ruotsalainen U, Bolli GB, Yki-Jarvinen H (2000) Enhanced stimulation of glucose uptake by insulin increases exercise-stimulated glucose uptake in skeletal muscle in humans: studies using [15O]O2, [15O]H2O, [18F]fluoro-deoxy-glucose, and positron emission tomography. Diabetes 49(7): 1084–1091

Pekar J, Renshaw PF (1969) Leigh JS (1987) Selective detection of intracellular sodium by coherence-transfer NMR. J Magn Reson 72(1):159–161

Reddy R, Insko EK, Noyszewski EA, Dandora R, Kneeland JB, Leigh JS (1998) Sodium MRI of human articular cartilage in vivo. Magn Reson Med 39(5):697–701

Robinson JD, Flashner MS (1979) The (Na + + K +)-activated ATPase. Enzymatic and transport properties. Biochim Biophys Acta 549(2):145–176

Saadat E, Jobke B, Chu B, Lu Y, Cheng J, Li X, Ries MD, Majumdar S, Link TM (2008) Diagnostic performance of in vivo 3-T MRI for articular cartilage abnormalities in human osteoarthritic knees using histology as standard of reference. Eur Radiol 18(10):2292–2302. doi:10.1007/s00330-008-0989-7

Schmitt B, Zbýn S, Stelzeneder D, Jellus V, Paul D, Lauer L, Bachert P, Trattnig S (2011) Cartilage quality assessment by using glycosaminoglycan chemical exchange saturation transfer and (23)Na MR imaging at 7 T. Radiology 260 (1):257–264. doi:radiol.11101841 [pii] 10.1148/radiol.11101841

Shapiro E, Borthakur A, Dandora R, Kriss A, Leigh J, Reddy R (2000) Sodium visibility and quantitation in intact bovine articular cartilage using high field (23)Na MRI and MRS. J Magn Reson 142(1):24–31. doi:S1090-7807(99)91932-8 [pii] 10.1006/jmre.1999.1932

Shapiro E, Borthakur A, Gougoutas A, Reddy R (2002) 23Na MRI accurately measures fixed charge density in articular cartilage. Magn Reson Med 47(2):284–291. doi:10.1002/mrm.10054 [pii]

Staroswiecki E, Bangerter NK, Gurney PT, Grafendorfer T, Gold GE, Hargreaves BA (2010) In vivo sodium imaging of human patellar cartilage with a 3D cones sequence at 3 T and 7 T. J Magn Reson Imaging 32(2):446–451. doi:10.1002/jmri.22191

Stobbe R, Beaulieu C (2005) In vivo sodium magnetic resonance imaging of the human brain using soft inversion recovery fluid attenuation. Magn Reson Med 54(5):1305–1310

Sykova E, Nicholson C (2008) Diffusion in brain extracellular space. Physiol Rev 88(4):1277–1340. doi:10.1152/physrev.00027.2007

Thulborn KR, Gindin TS, Davis D, Erb P (1999) Comprehensive MR imaging protocol for stroke management: tissue sodium concentration as a measure of tissue viability in nonhuman primate studies and in clinical studies. Radiology 213(1):156–166

Umathum R, Roesler MB, Nagel AM (2013) In Vivo Potassium (39 K) magnetic resonance imaging of human muscle and brain. Radiology. doi:10.1148/radiol.13130757

van der Maarel JRC (1989) Relaxation of spin 3/2 in a non-zero average electric field gradient. Chem Phys Lett 155:288–296

Wang L, Wu Y, Chang G, Oesingmann N, Schweitzer ME, Jerschow A, Regatte RR (2009) Rapid isotropic 3D-sodium MRI of the knee joint in vivo at 7T. J Magn Reson Imaging 30(3):606–614. doi: 10.1002/jmri.21881

Wang C, McArdle E, Fenty M, Witschey W, Elliott M, Sochor M, Reddy R, Borthakur A (2010) Validation of sodium magnetic resonance imaging of intervertebral disc. Spine 35(5):505–510. doi:10.1097/BRS.0b013e3181b32d3b

Watts A, Stobbe RW, Beaulieu C (2011) Signal-to-noise optimization for sodium MRI of the human knee at 4.7 Tesla using steady state. Magn Reson Med 66(3):697–705. doi:10.1002/mrm.22838

Weber MA, Nielles-Vallespin S, Essig M, Jurkat-Rott K, Kauczor HU, Lehmann-Horn F (2006a) Muscle Na+ channelopathies: MRI detects intracellular 23Na accumulation during episodic weakness. Neurology 67(7):1151–1158. doi:01.wnl.0000233841.75824.0f [pii] 10.1212/01.wnl.0000233841.75824.0f

Weber MA, Nielles-Vallespin S, Huttner HB, Wohrle JC, Jurkat-Rott K, Lehmann-Horn F, Schad LR, Kauczor HU, Essig M, Meinck HM (2006b) Evaluation of patients with paramyotonia at 23Na MR imaging during cold-induced weakness. Radiology 240(2): 489–500

Weber MA, Nagel AM, Jurkat-Rott K, Lehmann-Horn F (2011) Sodium (23Na) MRI detects elevated muscular sodium concentration in Duchenne muscular dystrophy. Neurology 77(23):2017–2024. doi: 10.1212/WNL.0b013e31823b9c78

Weber MA, Nagel AM, Wolf MB, Jurkat-Rott K, Kauczor HU, Semmler W, Lehmann-Horn F (2012) Permanent muscular sodium overload and persistent muscle edema in Duchenne muscular dystrophy: a possible contributor of progressive muscle degeneration. J Neurol 259(11):2385–2392. doi:10.1007/s00415-012-6512-8

Wheaton A, Borthakur A, Shapiro E, Regatte R, Akella S, Kneeland J, Reddy R (2004) Proteoglycan loss in human knee cartilage: quantitation with sodium MR imaging—feasibility study. Radiology 231(3):900–905. doi:231/3/900 [pii] 10.1148/radiol.2313030521

Wheaton A, Dodge G, Borthakur A, Kneeland J, Schumacher H, Reddy R (2005) Detection of changes in articular cartilage proteoglycan by T(1rho) magnetic resonance imaging. J Orthop Res 23(1):102–108. doi:S0736-0266(04)00155-X [pii] 10.1016/j.orthres.2004.06.015

Woessner DE, Bansal N (1998) Temporal characteristics of NMR signals from spin 3/2 nuclei of incompletely disordered systems. J Magn Reson 133:21–35

Zhang W, Moskowitz RW, Nuki G, Abramson S, Altman RD, Arden N, Bierma-Zeinstra S, Brandt KD, Croft P, Doherty M, Dougados M, Hochberg M, Hunter DJ, Kwoh K, Lohmander LS, Tugwell P (2008) OARSI recommendations for the management of hip and knee osteoarthritis, Part II: OARSI evidence-based, expert consensus guidelines. Osteoarthritis Cartilage 16(2):137–162. doi:S1063-4584(07)00397-4 [pii] 10.1016/j.joca.2007.12.013

Zhu XH, Zhang N, Zhang Y, Zhang X, Ugurbil K, Chen W (2005) In vivo 17O NMR approaches for brain study at high field. NMR Biomed 18(2):83–103. doi:10.1002/nbm.930

MR Spectroscopy and Spectroscopic Imaging for Evaluation of Skeletal Muscle Metabolism: Basics and Applications in Metabolic Diseases

Chris Boesch

Contents

1 **Introduction** 136

2 **Basics of MR Spectroscopy in the Musculoskeletal System** 137
2.1 Definitions 137
2.2 Observable Nuclei 138
2.3 Observable Metabolites, Biomarkers 139
2.4 Magnetic Resonance Spectroscopy/Magnetic Resonance Spectroscopic Imaging Acquisition Techniques 142
2.5 Ergometer and Muscular Energy Metabolism 143

3 **Magnetic Resonance Spectroscopy Studies of the Metabolism in Diseases of the Human Skeletal Muscle** 143
3.1 General Reviews 144
3.2 Insulin Resistance, Glucose Transport, and Ectopic Lipids 144
3.3 Glycogen Storage Diseases 146
3.4 Mitochondrial Myopathies 147
3.5 Muscular Dystrophies 149
3.6 Inflammatory Myopathies 150
3.7 Other Diseases and Conditions Affecting the Musculoskeletal Metabolism 151

4 **Conclusions and Outlook** 154

References 155

C. Boesch (✉)
AMSM (DKF and DIPR), University and Inselspital Bern,
Pavilion 52A Inselspital, P.O.Box 353010 Bern, Switzerland
e-mail: chris.boesch@insel.ch

Abstract

Magnetic resonance spectroscopy (MRS) and spectroscopic imaging (MRSI) provide metabolic information on the musculoskeletal system, thus helping to understand the biochemical and pathophysiological nature of numerous diseases. In particular, MRS has been used to study the energy metabolism of muscular tissue since the very beginning of magnetic resonance examinations in humans when small-bore magnets for studies of the limbs became available. Even more than in other organs, the observation of non-proton-nuclei was important in muscle tissue. Spatial localization was less demanding in these studies, however, high temporal resolution was necessary to follow metabolism during exercise and recovery. The observation of high-energy phosphates during and after the application of workload gives insight into oxidative phosphorylation, a process that takes place in the mitochondria and characterizes impaired mitochondrial function. New applications in insulin-resistant patients followed the development of volume-selective ^{1}H-MRS in whole-body magnets. Nowadays, multinuclear MRS and MRSI of the musculoskeletal system provide several windows to vital biochemical pathways noninvasively. It is shown how MRS and MRSI have been used in numerous diseases to characterize an involvement of the muscular metabolism.

Abbreviations

^{1}H	1-Hydrogen, protons
^{13}C	13-Carbon
^{19}F	19-Fluor
^{23}Na	23-Sodium
^{31}P	31-Phosphorus
ADP	Adenosinediphosphate
AOD	Arterial occlusive disease
ATP	Adenosinetriphosphate

M.-A. Weber (ed.), *Magnetic Resonance Imaging of the Skeletal Musculature*, Medical Radiology. Diagnostic Imaging,
DOI: 10.1007/174_2013_847, © Springer-Verlag Berlin Heidelberg 2013

Published Online: 29 May 2013

BMD	Becker muscle dystrophies
CPEO	Chronic progressive external ophthalmoplegia
CPOD	Chronic obstructive pulmonary disease
CSI	Chemical shift imaging
DMD	Duchenne muscle dystrophies
DNA	Deoxyribonucleic acid
EMCL	Extramyocellular lipids
FSHD	Facioscapulohumeral muscular dystrophy
G6P	Glucose-6-phosphate
GHD	Growth hormone deficiency
GPCh	Glycerophosphocholine
GPEt	Glycerophosphoethanolamine
IMCL	Intramyocellular lipids
ISIS	Image-selected in vivo spectroscopy
KSS	Kearns-Sayre syndrome
LGMD	Limb girdle muscular dystrophy
LHON	Leber's hereditary optic neuropathy
MELAS	Mitochondrial encephalopathy, lactic acidosis and stroke-like episodes
MERRF	Myoclonus epilepsy with ragged red fibers
MH	Malignant hyperthermia
MIDD	Maternally inherited diabetes and deafness
MRI	Magnetic resonance imaging
MRS	Magnetic resonance spectroscopy
MRSI	Magnetic resonance spectroscopic imaging
NADH	Nicotinamide adenine dinucleotide
NARP	Neuropathy, ataxia, and retinitis pigmentosa
NIDDM	Non-insulin-dependent-diabetes-mellitus
NIRS	Near infrared spectroscopy
OPMD	Oculopharyngeal muscular dystrophy
PAD	Peripheral arterial disease
PCh	Phosphocholine
PCr	Phosphocreatine
PDE	Phosphodiester
PEt	Phosphoethanolamine
PFK	Phosphofructokinase
pH	Concentration of hydrogen
Pi	Inorganic phosphate
PME	Phosphomonoester
PRESS	Point resolved spectroscopy
QMAX	Apparent maximum rate of oxidative ATP synthesis
SNR	Signal-to-noise ratio
STEAM	Stimulated echo acquisition mode
TCA	Tricarboxylic acid cycle
TE	Echo time
TMA	Trimethyl ammonium containing metabolites
TR	Repetition time
tRNA	Transfer ribonucleic acid
VEGF	Vascular endothelial growth factor
VO_2max	Maximal oxygen uptake

Key Points

1. MRS is particularly well suited to study metabolic consequences of systemic, non-focal diseases on the musculoskeletal system.
2. Publications on ^{31}P-MRS still represent the major part of MRS in metabolic diseases of the musculoskeletal system.
3. ^{31}P-MRS can provide extremely valuable information on muscular metabolism, in particular on the oxidative phosphorylation.
4. ^{1}H-MRS is increasingly used in whole-body scanners to study insulin resistance and the effect on skeletal muscle.
5. The combination of multinuclear MRS, i.e., the observation of muscular metabolism with more than one nucleus, gives insight into biochemical pathways which is unsurpassed by any other noninvasive method.

1 Introduction

This chapter describes applications of Magnetic Resonance Spectroscopy (MRS) and MRS imaging (MRSI) to study metabolism in diseases of the human musculoskeletal system. Focusing on the muscular metabolism in human diseases has several consequences: (i) only studies on human patients are included and there are no animal models; (ii) focal lesions such as tumors or cysts are not included; and (iii) influences of systemic diseases on the metabolism of skeletal muscle are also considered, even if the major target of a disease is another organ, e.g., the heart in chronic heart failure.

In is well established that traditional radiology, including Magnetic Resonance Imaging (MRI), is excellent at the diagnoses of focal lesions in individual patients. It might be an oversimplification to claim that the strength of MRS is more the elucidation of systemic diseases in cohorts of patients, but nonetheless this statement points toward an important difference between MRI and MRS. It does not negate examples of MRS-based individual diagnoses in focal diseases, e.g., in the evaluation of the aggressiveness of a tumor, but emphasizes that the value of a clinical method is not limited to the diagnostic power in an individual patient but also includes possible contributions to our understanding of diseases. Unlike most radiological applications, where the individual patients have a direct advantage of the examination, MRS can help patients as a group through the contribution to clinical textbook knowledge. For e.g., when MRS proves a metabolic involvement of the musculoskeletal system in a specific disease, treatment can be adapted and improved, thus helping eventually also an individual patient. This chapter shows in numerous examples how MRS can contribute to this field of research.

Table 1 List of nuclei with common applications in human MR scanners

Nucleus	Spin	Frequency at 3 Tesla (MHz)	Inherent sensitivity (relative to ^{1}**H**)	Natural abundance (%)	Typical concentration (Mol)	Relative overall sensitivity	Edge length of cube with comparable signal
^{1}Hydrogen in water	1/2	127.74	1.000	99.99	10^2 in water	1 (reference)	0.1 cm (reference)
^{1}Hydrogen in metabolites	1/2	127.74	1.000	99.99	from 10^{-3} to 10^{-2} in metabolites	from 10^{-5} to 10^{-4}	3 cm
^{12}Carbon	0	N/A	0.000	98.89	from 10^{-2} to 10^{-1} in metabolites	0	N/A
^{13}Carbon	1/2	32.12	0.016	1.11	from 10^{-2} to 10^{-1} in metabolites	from 10^{-8} to 10^{-7}	35 cm
^{19}Fluor	1/2	120.20	0.833	100	$<10^{-3}$ in metabolites	$<10^{-5}$	10 cm
^{23}Sodium	3/2	33.79	0.093	100	from 10^{-2} to 10^{-1}	from 10^{-5} to 10^{-4}	3 cm
^{31}Phosphor	1/2	51.71	0.066	100	from 10^{-3} to 10^{-2}	from 10^{-6} to 10^{-5}	7 cm

The presented numbers can only give an impression of the order of magnitudes since concentrations of metabolites in human tissue and the number of nuclei in a specific metabolite varies tremendously. In particular, the edge length of a cube with the same signal yield per time is just an illustration since nuclei with low sensitivity such as ^{13} C are acquired much longer and with much less SNR than a comparable MRI of the water signal, thus allowing a reduction of the necessary volume. The relative overall sensitivity includes influences of the inherent sensitivity, natural abundance, and typical concentrations in human tissue

The chapter starts with a brief description of the basics, in particular emphasizing the special conditions of musculoskeletal MRS in comparison with MRS of other organs. For a more comprehensive explanation of MRS in general, the interested reader is referred to reviews on the basics of MRS (Boesch 1999, 2007; Boesch et al. 2006; Machann et al. 2008; Chang et al. 2010; Glunde and Bhujwalla 2011; Subhawong et al. 2012; Pola et al. 2012). In a second and major part, MRS applications on the metabolism in diseased skeletal muscle are reviewed.

2 Basics of MR Spectroscopy in the Musculoskeletal System

This section provides a brief introduction to the methodology of MRS and MRSI, mainly to support the understanding of the technical expressions used in the next section of this chapter.

2.1 Definitions

The major methodological difference between MRI and MRS is the fact that an additional dimension is added when the chemical shift in a spectrum is resolved. While MRI experiences the chemical shift mainly as an artifact which is responsible for fat and water to be slightly shifted relative to each another, MRS is resolving this dimension and is using its biochemical information.

Figure 1 shows a synthetic spectrum and the related terminology. The frequency differences that separate the individual lines are extremely small compared to gradient-generated frequency ranges in MRI. This has several consequences, all making the acquisition of MR spectra challenging: the applied magnetic field must be extremely homogeneous, which is achieved with careful shimming far beyond the requirements for MRI. In addition, resolving small frequency differences requires long acquisition windows in MRS to detect low-frequency components. A further challenge for MRS results from the fact that MRI can encode one spatial dimension during the acquisition ("read") period while most MRS and MRSI techniques need the acquisition window to resolve the spectral dimension. Only echoplanar MRSI techniques use the time between two sampling points during acquisition for a spatial encoding. Together with the fact that metabolites have much lower concentrations than water and fat, which generate the signal in typical MRI examinations, the acquisition of the additional spectral dimension results in inherently

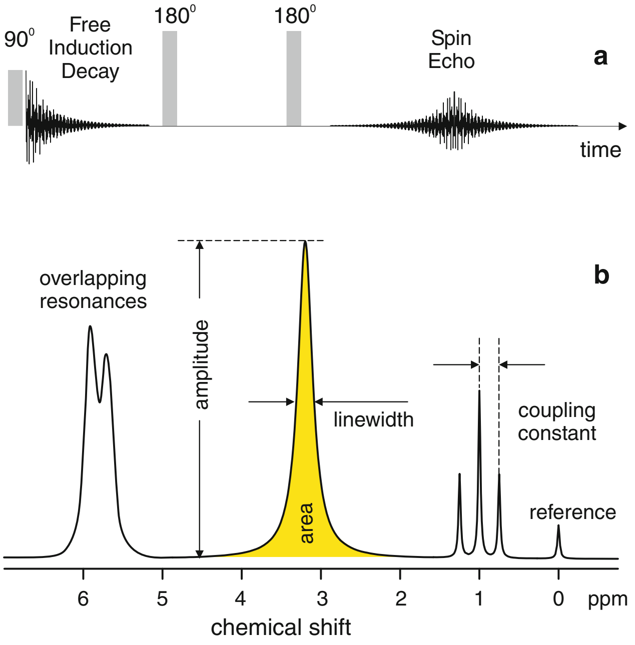

Fig. 1 **a** The two common acquisition sequences free induction decay and spin echo together with, **b** a synthetic spectrum with definitions of the major parts. If the spectrum has been acquired under relaxed conditions and without loss by the transversal relaxation time, the position on the frequency axis (ppm) represents the chemical identity and the area under the curve the concentration of a metabolite. Since inhomogeneity broadens the signal at the costs of the amplitude, the area has to be used for a calculation of metabolite concentrations. Overlapping resonances represent a major challenge for spectral quantitation, in particular in crowded ^{1}H-MR spectra

longer acquisition times for MRS and MRSI compared to MRI. Since concentrations of the observed metabolites are proportional to the area of the resonance lines only if the spectrum has been obtained without influence of the relaxation times, spectra are acquired with long repetition times (TR) and short-echo times (TE), or corrections are necessary. Unlike MRI, where T_1- and T_2-weighting is used to generate contrast in the images, MRS/MRSI "proton-density" (or more general the "nuclei-density") weighted spectra are desired.

2.2 Observable Nuclei

While ^{1}H-MRS particularly in the brain became the major spectroscopy application on clinical scanners, MRS in the musculoskeletal system began with the observation of ^{31}P-nuclei (Hoult et al. 1974; Ross et al. 1981; Chance et al. 1981, 1982, 1986; Radda et al. 1982; Meyer et al. 1982; Haselgrove et al. 1982; Edwards et al. 1982; Eleff et al. 1984; Taylor et al. 1986; Miller et al. 1988). As it can be seen in the following section, the majority of the published papers still use ^{31}P-MRS in muscle even if ^{1}H-MRS became much more popular in the last decade, as will be seen in the third section of this chapter.

Table 1 shows the characteristics of different nuclei which are used in clinical MRS. However, the next section will be essentially limited to ^{1}H, ^{13}C, and ^{31}P which represent the huge majority of the clinical MRS applications on muscular metabolism. Applications with ^{23}Na are mainly used in an imaging mode, i.e., without resolution of the chemical shift dimension and will thus be discussed in other chapters.

The inherent sensitivity of a nucleus depends on the resonance frequency since this governs the induced voltage in the detection coil of the scanner. This fact explains why ^{1}H with the highest resonance frequency of all nuclei (except ^{3}H-tritium, which is irrelevant in that context) has the highest inherent sensitivity. ^{31}P, and in particular ^{13}C, have a lower resonance frequency and suffer thus from less signal yield. A second disadvantage is the much lower concentration of metabolites compared to water or fat, which are the sources of the MRI-signal. Even worse, ^{13}C nuclei represent only 1 % of all carbon nuclei which are made of 99 % MR-invisible ^{12}C nuclei. While this is a serious challenge for spectroscopy of natural abundance carbon, it can be turned into an advantage when ^{13}C-labeled substances are infused. Newly infused ^{13}C-enriched-metabolites and its products show up in the spectrum with a much higher signal-to-noise ratio (SNR) than the pre-existing carbons and can thus be followed along the metabolic steps of the infused substance.

Table 1 also lists volumes that would be necessary to obtain an equal SNR in the spectra as an MR image. This list is for illustration only since MRS compensates the lower inherent signal yield by longer acquisition times and lower SNR than MR images. However, even if longer acquisition times and lower SNR are taken into account, there are still gross differences between the resolution of MR images of water and typical MR spectra of metabolites. For field strengths of 3 T, as a rule of thumb, ^{1}H-MRS can observe metabolites above 1 mMol in a volume of a few cm^{3} within a few minutes' acquisition time. In turn, ^{31}P-MRS of muscle tissue can observe metabolites above 10 mMol in a volume of about 100 ml with a temporal resolution of a few seconds. If no temporal resolution is necessary, a ^{31}P-MR spectrum can observe metabolites in the mMol range in a few minutes from about a volume of 100 ml. ^{13}C-MR spectroscopy of unlabeled metabolites (typically glycogen) can be applied to metabolites in the 10–100 mMol in a volume of 100 ml or more and within 10–20 min. All these

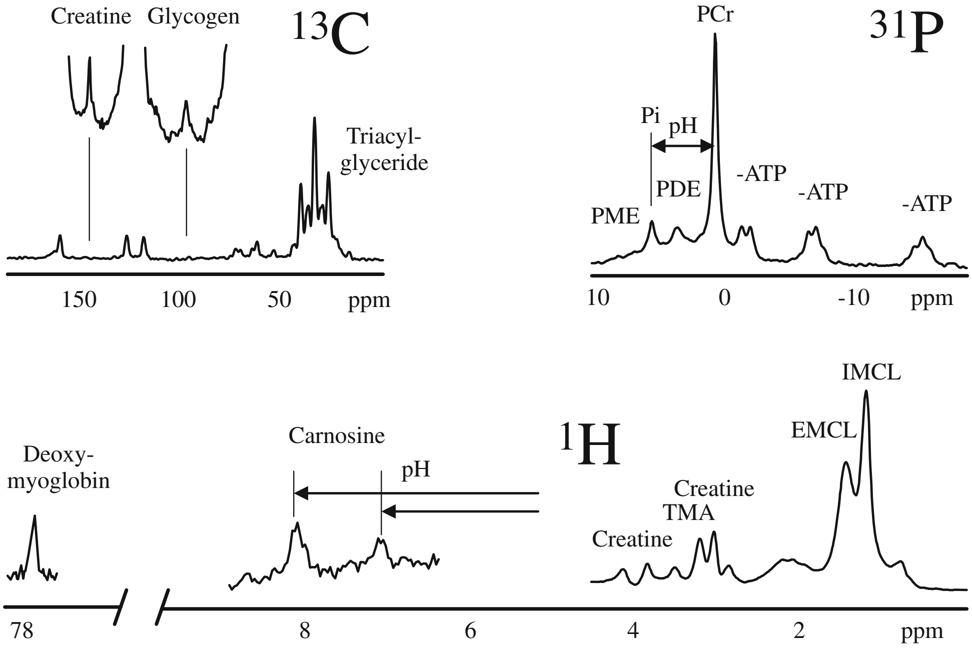

Fig. 2 The observable metabolites in ^{1}H-, ^{13}C-, and ^{31}P-MR spectra of the skeletal muscle

numbers can be modified because total acquisition time, required metabolite concentration, and acceptable SNR can be balanced in different ways. Nonetheless, these numbers show that MRS is always fighting against low SNR, in particular non-proton-nuclei. Since the SNR increases with field strength, MRS benefits from current installation of numerous 3 T scanners in the clinics and up to 9.4 T systems in research institutions.

2.3 Observable Metabolites, Biomarkers

Figure 2 illustrates the observable metabolites in ^{1}H-, ^{13}C-, and ^{31}P-MR spectra of the skeletal muscle. It also emphasizes that multinuclear MRS can follow metabolism via the observation of very different substances and that a limitation to ^{1}H-MRS—as it happens in many clinical scanners—restricts the number of observable metabolites significantly.

^{31}P-MRS in muscular tissue is particularly helpful for an evaluation of the energy metabolism since phosphocreatine (PCr) and adenosine-triphosphate (visible are three resonances of α-, β-, and γ-ATP) represent vital high-energy molecules of the cell. Since inorganic phosphate (Pi) exists in a protonated and unprotonated form with different resonance frequencies and fast exchange, the averaged position of the Pi peak titrates with the concentration of protons between the two forms

$$H_2PO_4^- \leftrightarrow HPO_4^{2-} + H^+ \qquad (1)$$

and can thus be used to measure the intramyocellular pH (Moon and Richards 1973; Hoult et al. 1974; Flaherty et al. 1982; Seo et al. 1983; Taylor et al. 1983; Kemp et al. 1993a):

$$\mathrm{pH} = 6.75 + \log(\delta - 3.27)/(5.69 - \delta) \qquad (2)$$

δ representing the ppm difference between PCr and Pi. The noninvasive observation of proton concentration, i.e., the pH, buffering, and proton efflux during exercise and recovery is a unique tool within ^{31}P-MRS that plays an important role in clinical studies of muscular diseases. PCr, ATP, and Pi take part in the reversible creatine kinase reaction:

$$\mathrm{PCr} + \mathrm{Mg\ ADP} + \mathrm{H}^+ \leftrightarrow \mathrm{Mg\ ATP} + \mathrm{Cr} \qquad (3)$$

thus allowing the muscle to maintain constant ATP levels with the synthesis of ATP from adenosine-diphosphate (ADP) and PCr. ADP is a key metabolic control which is not directly visible in the ^{31}P-MR spectrum, yet can be calculated from (Arnold et al. 1984; Chance et al. 1985) the equation:

$$[\mathrm{ADP}] = [\mathrm{Cr}]\,[\mathrm{ATP}]\,/\,K_{eq}[\mathrm{PCr}]\,[\mathrm{H}^+] \qquad (4)$$

with K_{eq} using known values, metabolite concentration from the spectrum, and [H$^+$] from the pH as determined by Eq. (2). During exercise, ATP is used and PCr provides

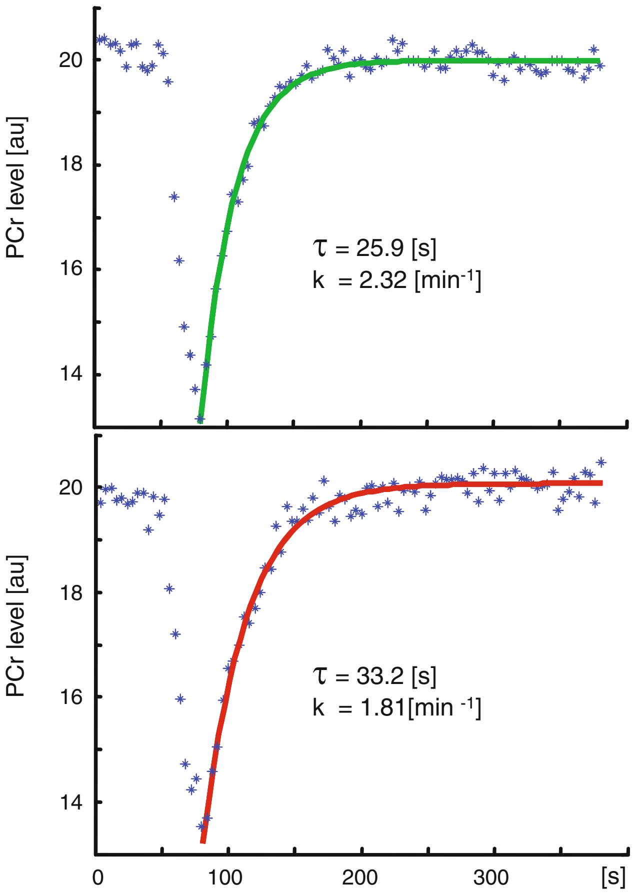

Fig. 3 The ^{31}P-MRS recovery curve of PCr following exercise in an athlete (recovery time $\tau = 25.9$ s) and a sedentary subject ($\tau = 33.2$ s). The time constants *k* of the exponential curves (athlete 2.32 and 1.81 min^{-1} for the sedentary subject, respectively) are given for comparison with Fig. 4. The comparison illustrates how the oxidative phosphorylation in the athletic muscle provides the necessary energy faster than the untrained muscle (courtesy of Andreas Boss)

high-energy phosphate groups to maintain ATP at a constant level. This leads to a reduction of PCr and an increase of Pi which can be observed in the ^{31}P-MR spectrum (Fig. 3). During the recovery period after exercise, ATP and thus PCr are resynthesized by oxidative phosphorylation which takes place in the mitochondria (Dawson et al. 1977; Chance et al. 1982; Radda et al. 1982; Eleff et al. 1984), given that the blood supply provides the necessary oxygen (Harris et al. 1975; Taylor et al. 1983; Quistorff et al. 1993). Therefore, the recovery of PCr is a direct measure of the mitochondrial oxidative phosphorylation (Fig. 4), a fact used in numerous papers to test mitochondrial activity as can be seen in the section on muscular diseases.

An additional peak in the ^{31}P-MR spectrum results from phosphomonoesters (PME), which include sugar phosphates such as glucose-6-phosphate (G6P), as well as membrane precursors like phosphocholine (PCh) and phosphoethanolamine (PEt). Phosphodiesters (PDE), like glycerophosphocholine (GPCh) and glycerophosphoethanolamine (GPEt), are attributed to break down products from membrane lipids. Since membrane-turnover is increased in tumors, PME and PDE signals are often abnormal in tumorous tissue (Negendank 1992).

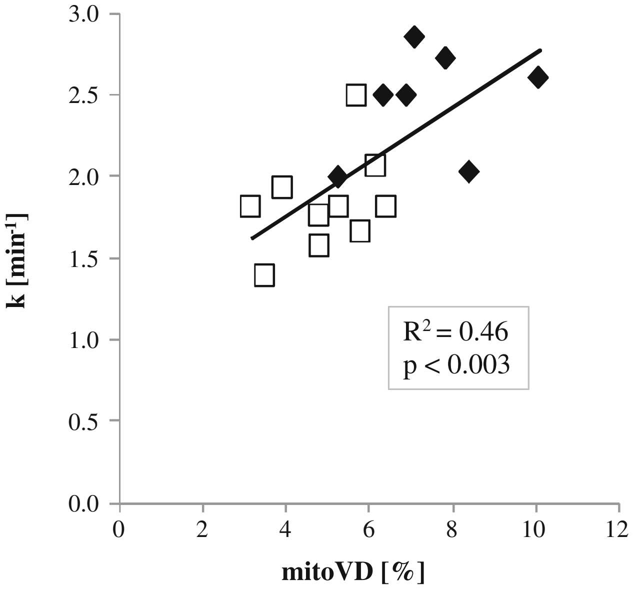

Fig. 4 The rate constant *k* of PCr recovery versus mitochondrial volume density (mitoVD). *Black diamonds* represent athletes while the open squares stand for sedentary subjects. The correlation of mitochondrial density as determined in a biopsy with the noninvasively measured reaction constant *k* is clearly visible. It can also be seen that athletes have both more mitochondrial volume density and faster recovery, i.e., elevated oxidative phosphorylation (reproduced with permission (Boss et al. 2013))

^{31}P-MR magnetization transfer experiments can be used to follow creatine kinase and ATP synthase reactions (Forsen and Hoffman 1963; Befroy et al. 2012). An irradiation of the γ-ATP resonance leads to a saturation of phosphate groups that are in exchange with PCr and Pi. Since the saturated spins do not produce a signal at the "new" position in the spectrum, and since unsaturated spins are exchanged to the γ-ATP position where they are saturated, the kinetics of these reactions can be determined.

The ^{13}C-MR spectrum is dominated by lipid signals which can pose baseline problems in obese subjects when the focus is on smaller signals from less abundant metabolites. In skeletal muscle, ^{13}C-MRS is mainly used to follow the glycogen-C$_1$ signal, sometimes in connection with the creatine peak as an internal concentration reference (Rotman et al. 2000) (Fig. 5). Since large molecules are usually not visible in MR spectra due to very short T_2 values of "solid-like" material, it was somewhat surprising and fortunate for MRS that glycogen is 100 % visible thanks to sufficient internal mobility (Gruetter et al. 1991).

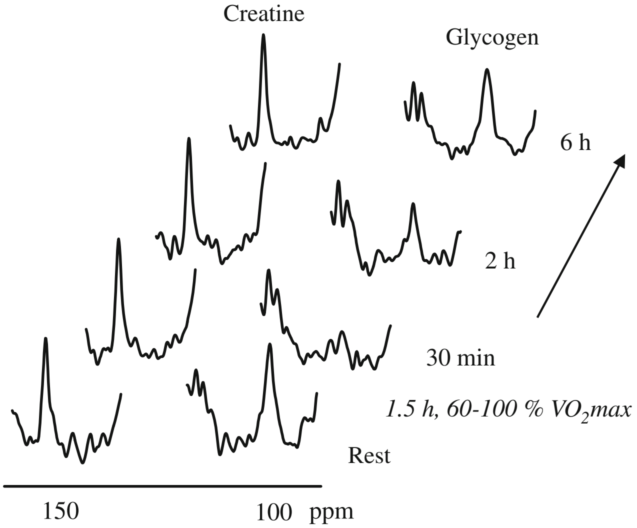

Fig. 5 The usage and replenishment of glycogen in human skeletal muscle observed by natural abundance ^{13}C-MRS. The resonance of creatine is used for relative quantitation (reproduced with permission (Rotman et al. 2000))

Meanwhile, glycogen synthesis and glycogenolysis are major targets in exercise physiology (Fig. 5), studies on insulin resistance (Shulman et al. 1990), and in glycogenoses (Vorgerd et al. 2002a). While the application of ^{13}C-enriched infusions in humans can yield very specific metabolic information, only very few research groups worldwide conquer the technical and financial challenges. Unlike mass spectroscopy and other analytical methods which are using stable isotopes in breathing air or urine, ^{13}C-MR spectroscopy needs large quantities of labeled substances to see a measurable effect, resulting in substantial costs per experiment. One specifically attractive target of ^{13}C-enriched infusions is the tricarboxylic acid cycle (TCA cycle, Krebs cycle, or citric acid cycle). Several labeled substrates can be infused and followed by ^{13}C-MRS, including acetate, pyruvate, lactate, or glucose. Infusion of ^{13}C-acetate leads to an increase of the glutamate signal in the ^{13}C-MR spectrum which is in rapid equilibrium with α-keto-glutarate, an intermediate product in the TCA cycle and thus an indicator for TCA cycle activity. Since the TCA cycle takes place in the mitochondria, a measurement allows some conclusions on the mitochondrial activity, which is discussed in many diseases and also in the aging process. Recently, MRI and MRS of hyperpolarized ^{13}C-substrates have been suggested (Kurhanewicz et al. 2011) and reached the level of clinical investigations in selected research sites. The usage of hyperpolarized ^{13}C-substrates might change ^{13}C-MRS in general since more scanners will be equipped with the necessary hardware and software to acquire non-proton-nuclei. While many publications deal with cardiac applications of hyperpolarized ^{13}C, examples in the musculoskeletal system have already been reported in animals (Kohler et al. 2007; MacKenzie et al. 2011; Larson and Gold 2011).

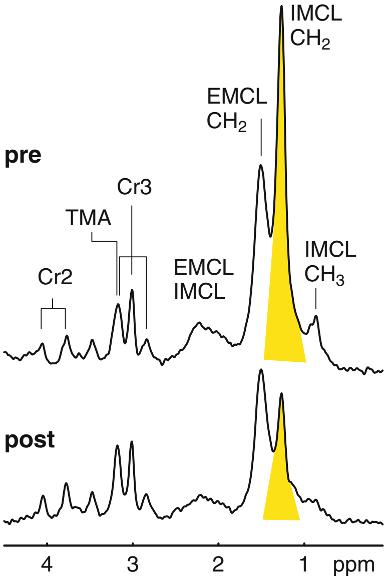

Fig. 6 The depletion of intramyocellular lipids (IMCL) during exercise, best visible at the reduction of the CH_2 signal at 1.28 ppm. Abbreviations: extramyocellular lipids (EMCL), creatine groups (Cr_2 and Cr_3), trimethyl ammonium containing groups (TMA)

The potential of ^{1}H-MR spectroscopy of skeletal muscle was underestimated for quite a long time since the large lipid resonances were hiding most of the interesting metabolite signals. The detection of deoxymyoglobin was an early exception since the resonance is shifted to the far left at 78 ppm (Wang et al. 1990; Mancini et al. 1994; Brillault-Salvat et al. 1997; Mole et al. 1999; Kreis et al. 2001). The use of gradient-based volume localization in combination with very careful placement of the voxel allowed for an acquisition of ^{1}H-MRS of skeletal muscle without too large signals from lipids (Boesch and Kreis 2001; Boesch et al. 2006; Boesch 2007). It was found that the highly ordered skeletal muscle led to very specific and unexpected MR-effects and that the spectra were orientation-dependent due to dipolar coupling effects (Boesch and Kreis 2001). The observation of two separate lipid signals by Schick et al. (1993), and subsequently the characterization of the two signals as intra- (IMCL) and extramyocellular lipids (EMCL) (Boesch et al. 1997), prepared the ground for a much more widespread application of ^{1}H-MRS of skeletal muscle (Boesch et al. 2006) with a depletion experiment illustrated in Fig. 6. Several groups demonstrated the relation of IMCL and insulin resistance (Machann et al. 1998; Perseghin et al. 1999; Cline et al. 1999; Jacob et al. 1999; Krssak et al. 1999; Decombaz et al. 2001) which led to a series of MRS studies in diabetology which are described in the next section. Since many metabolites contain ^{1}H and the chemical shift range of the ^{1}H-MR spectra is relatively small, ^{1}H-MR spectra are crowded but highly informative. Many resonances have been assigned and have already been used for physiological or pathophysiological studies, such as acetylcarnitine, total creatine (tCr), carnosine, trimethyl ammonium (TMA) containing metabolites, and amide protons. Others like taurine are visible but partially hidden such that a reliable determination of concentrations is difficult. Lactate is also hidden underneath lipid peaks, yet can be measured with the help of editing sequences (Pan et al. 1991). While higher magnetic field strengths will be beneficial for the SNR in non-proton spectra, it will be equally beneficial for ^{1}H-MR spectra due to the better resolution of the overlapping resonances.

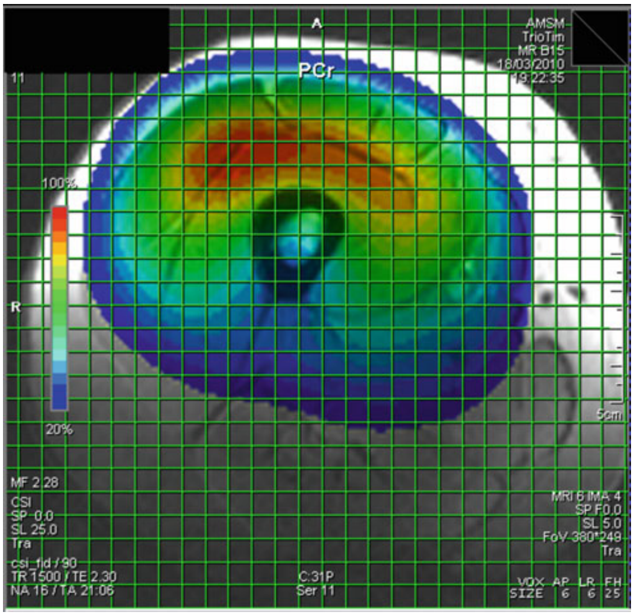

Fig. 7 A CSI data set in the thigh. This display of the CSI data set shows the spatial variation of the signal intensity of a single metabolite, in this example PCr. The spatial variation of the signal strength is mainly a result of the varying pulse angle in a pulse-and-acquire sequence with a transmit/receive surface coil and much less the distribution of the metabolite concentration. In healthy resting muscles, the PCr concentration can be assumed to be constant, however, examples of spatial variations due to pathology are shown below

2.4 Magnetic Resonance Spectroscopy/Magnetic Resonance Spectroscopic Imaging Acquisition Techniques

While other organs are almost exclusively observed with the help of gradient-based localization techniques, a large number of ^{13}C- and ^{31}P-MRS studies are using transmit/receive surface coils in combination with pulse-and-acquire acquisition. This has several advantages including a higher SNR, no signal loss due to transversal relaxation, very fast acquisition, and minimal artifacts due to gradient imperfection. The acquisition of metabolites with very short transversal relaxation times, such as deoxymyoglobin and glycogen, makes pulse-and-acquire techniques essential. Any echo formation would reduce dramatically the already very small signal of these metabolites. The size of the selected volume of a transmit/receive surface coil is large and close to the receiver which guarantees maximal SNR that cannot be equaled by cube-like selected volumes in gradient-based techniques. Artifacts from gradient imperfections have been reduced dramatically with the advent of shielded gradients in the 1990s. However, when MRS of muscle had been introduced, long before shielded gradients were developed, these artifacts had been a crucial issue, in particular in small-bore MR systems for limbs which were used successfully for more than a decade. Since the chemical shift dispersion of ^{31}P- and in particular of ^{13}C-MR spectra is much larger than for ^{1}H-MR spectra, the chemical shift displacement becomes intolerable with common strengths of the gradients. This problem does not occur with transmit/receive surface coils where the volume selection is defined by the position of the coil. On the other hand, the selected volume of a transmit/receive surface coil is extremely complex and absolute quantitation of metabolites is very challenging since the pulse angle of a transmit/receive surface coil is highly variable in space (Fig. 7). One practical reason for the usage of transmit/receive surface coils is also the fact that no clinical MR system is equipped with a body coil that is tuned to ^{13}C- or ^{31}P-frequencies and allows for a homogeneous irradiation.

Gradient-based localization schemes of single voxel such as ISIS, STEAM, or PRESS are widely used in other organs. In the musculoskeletal system, they are increasingly important, in particular for ^{1}H-MRS or when the target is the spatial distribution of a metabolite. Nevertheless, gradient-based localization of non-proton-nuclei is still less widely used in the muscle than pulse-and-acquire techniques. The chemical shift displacement of ^{13}C- and ^{31}P-MR spectra is such that strictly spoken only single resonances can be observed at the correct spatial localization with gradients. ISIS has the advantage of minimal signal loss due to the transversal relaxation; therefore, it is the method of choice for ^{31}P-MRS where short T_2 values reduce the signal in echo-based sequences too much. STEAM or PRESS sequences are crucial for the observation of ^{1}H-metabolites where the signal loss due to the delayed echo formation is not a big issue, even if short-echo-times are preferred to avoid large TE-correction terms. Long TE are sometimes used to clean the spectrum and to increase the separation of overlapping resonances. However, only gradient-based localization and careful positioning of the voxel provide a sufficient suppression of lipid signals from outside the voxel. Relaxation times of ^{1}H-metabolites are well suited for echo-based techniques, in particular if short-echo sequences are used.

Chemical shift imaging or MRSI is illustrated in Fig. 7. While this technique is popular in other organs, only a few ^{1}H- and ^{31}P-MRSI applications are using it in skeletal muscle (Kan et al. 2010; Vermathen et al. 2012), to mainly document spatial variations of the metabolites. As long as all three spatial dimensions are CSI-encoded, there occurs no chemical shift displacement due to the large chemical shift dispersion in non-proton-nuclei. However, an encoding in all three spatial dimensions results in very long acquisition times since every phase step has to be made in all three spatial directions. As soon as one dimension is selected with a slice gradient, chemical shift displacement has to be considered. Echoplanar spectroscopy sequences can help in that respect and are promising (Wilhelm and Bachert 2001), but have not yet been widely used in human skeletal muscle.

2.5 Ergometer and Muscular Energy Metabolism

Exercise and recovery is a crucial element of MRS of skeletal muscle. Unlike cardiac tests, where the working muscle can be outside of the magnet, the working skeletal muscle has to be in the homogeneous center of the magnet and the acquisition has to go on during exercise. This explains why many ergometers constructed to support MRI of the heart during workload are not suited for MRS of skeletal muscle.

In general, examinations during workload are much more critical than recovery from exercise. Many practical challenges occur when power output should be measured in the technically hostile MR environment with static magnetic field, switching gradients, and strong radio frequency-pulses. Measurements outside of the magnet are technically easier, however, are limited since the power loss along the power transmission remains largely unknown but can be substantial.

A measurement of the PCr decrease as a function of power output suffers also from several physiological problems, such as recruitment of specific parts of muscles or evasive movements of the subjects (Akima et al. 2002). This might result in an involvement of musculatures around the hip joint with subsequently reduced workload for the observed musculature. A problem often underestimated is the blood flow in the exercising limb since ischemia can severely affect PCr recovery, which is an oxidative process. Therefore, any peripheral vascular disease or even an unintentionally limited blood flow, e.g., in the arteria poplitea due to the supporting structures for the exercise, can falsify the examination. Concentric workload describes a pushing of the contracting muscle against a load while eccentric workload is a deceleration of an applied force by the expanding muscle, e.g., while walking down a hill. Since blood flow can be limited by the permanently contracted muscles in the combination of concentric and eccentric workload—e.g., by a permanent weight lifting—concentric workload only would be preferable. In addition, eccentric workload represents a different physiological phenomenon than concentric workload and requires a specific interpretation since much larger loads can be handled.

PCr recovery has the advantage that it does not depend on the preceding power output as long as some precautions are respected. Nonetheless some problems remain, e.g., that the subject adheres to the protocol, stops immediately when recovery should start, and does not contract the muscle during the recovery phase. When values after exercise are compared to measurements before exercise, it is important that the sensitive volume has not shifted by heavy workload and extensive motion. In patients, it might be difficult to measure the appropriate workload prior to the ^{31}P-MR examination, since repeated measurements are not tolerated by patients who experience muscle pain with exercise. As long as pH drop is less than pH 6.75, the recovery curve can be fitted to an exponential curve (Forbes et al. 2009) (Fig. 3).

Application of electrically induced contractions (Vandertohmmen et al. 2003) can be more reproducible than voluntary exercise, however, if they are supramaximal and thus independent of other factors, they are rather painful and not tolerated by patients. Therefore, an appropriate design of the ergometer and a precise monitoring of the voluntary workload are mandatory.

3 Magnetic Resonance Spectroscopy Studies of the Metabolism in Diseases of the Human Skeletal Muscle

MRS-methodology in studies of the metabolism of skeletal muscle can be roughly differentiated in four major categories: observation of oxidative phosphorylation by ^{31}P-MRS, lipid metabolism as observed by ^{1}H-MRS, carbohydrate metabolism observed by ^{13}C-MRS, and some combinations of the above-mentioned categories.

While the first magnets for humans were still too small for whole-body examinations, it was however possible to study arms and legs in the small-bore/high-field magnets at rest or during exercise, which led to seminal papers in the field (Ross et al. 1981; Chance et al. 1982; Radda et al. 1982; Edwards et al. 1982; Newman et al. 1982; Eleff et al. 1984; Arnold et al. 1985; Wilson et al. 1985; Lewis et al. 1985).

In these early days, physiologists recognized the value of ^{31}P-MRS for studies of the oxidative phosphorylation of muscle tissue, which remained one of the major applications throughout the next decades as can be seen in the following sections. Since most clinical whole-body magnets were not equipped for non-proton-nuclei, the euphoria for ^{31}P-MRS did not really spill over from physiology laboratories to radiological departments. On the other hand, the availability of artifact-free gradients in clinical whole-body systems fostered the application of ^{1}H-MRS in all organs, including the musculoskeletal system. During all these years ^{13}C-MRS remained an instrument for a few expert groups, however, this might change in future with the dissemination of hyperpolarized techniques in clinical whole-body magnets and the installation of MR systems with higher magnetic field strength.

3.1 General Reviews

The characterization of focal lesions such as the increase of choline in tumors will not be discussed in this chapter. Instead, the focus lies on metabolic musculoskeletal diseases or metabolic involvement of skeletal muscle in generalized diseases. MR spectroscopy of focal, mostly tumorous lesions in the musculoskeletal system is described in numerous publications, including some comprehensive review articles (Fayad et al. 2007, 2012; Glunde and Bhujwalla 2011; Wang et al. 2011; Glunde et al. 2011; Beloueche-Babari et al. 2011; Costa et al. 2011; Subhawong et al. 2012).

A first overview of metabolic studies of musculoskeletal diseases was published in Lancet as early as 1982 (Edwards et al. 1982) and has already shown the potential of the then called "topical nuclear magnetic resonance." The effect of training was then described in an overview on metabolic versus non-metabolic myopathies (Taivassalo et al. 1999). In the following years, many reviews were published, describing the value of MRS for investigations of the musculoskeletal system (Argov and Bank 1991; Argov 1998; Taylor 2000; Argov et al. 2000; Vorgerd and Zange 2002; Miller 2002; Leroy-Willig et al. 2003; Parry and Matthews 2003; Mattei et al. 2004; Tarnopolsky and Raha 2005; Guis et al. 2005; Petersen and Shulman 2006; Boesch 2007; Savage et al. 2007; Weber et al. 2007; Kuo and Carrino 2007; Phielix and Mensink 2008; Wells et al. 2008; Schocke et al. 2008; Walker 2008; Lindquist 2008; Pedersen et al. 2009; Kent-Braun 2009; Lang et al. 2010; Phielix et al. 2011; Befroy and Shulman 2011; Befroy et al. 2012; Finanger et al. 2012; Tarnopolsky 2012).

3.2 Insulin Resistance, Glucose Transport, and Ectopic Lipids

The incidence of insulin resistance and the so-called metabolic syndrome is dramatically increasing, almost independent of the industrialization level of the countries that collect these statistical numbers. In particular in the older population, 40 % and more is affected by this crucial disorder. Since insulin resistance is a major risk factor for the development of cardiovascular diseases, it represents an enormous challenge for health care systems and dramatically reduces the quality of life for the individual patient.

Multinuclear MRS has served for more than a decade in the elucidation of insulin resistance and is currently increasingly used to better understand this major threat. One can distinguish three major fields where MRS has been and is currently used in the research on insulin resistance:

(a) The understanding of glucose transport and glycogen synthesis in the skeletal muscle tissue.
(b) Relation of insulin resistance and ectopic lipids, in particular IMCL.
(c) Relation of insulin resistance and impaired mitochondrial activity, including the effect of aging.

Using ^{13}C-MR spectroscopy, the Yale group has shown in a first step that muscle glycogen synthesis is the major non-oxidative approach for our body to lower high glucose concentrations in the plasma and that muscle glycogen synthesis is reduced in non-insulin-dependent-diabetes-mellitus (NIDDM) patients compared to healthy persons (Shulman et al. 1990). In a very elegant application of multinuclear MRS, the same group used ^{31}P-MR spectroscopy to follow G6P during a hyperglycemic-hyperinsulinemic clamp (Rothman et al. 1992). Since G6P was lower in diabetic subjects compared to healthy controls, and since this could be restored by increased insulin concentrations in NIDDM subjects, it has been concluded that a defect in muscle glucose transport or phosphorylation leads to a reduced muscle glycogen synthesis in NIDDM patients. Figure 8 illustrates the respective biochemical pathways which allowed this conclusion. In order to distinguish a primary from an acquired defect that leads to this reduced glucose transport/phosphorylation, normoglycemic offspring of parents with overt diabetes mellitus were studied by a combination of ^{31}P- and ^{13}C-MRS (Rothman et al. 1995). These offspring showed reduced rate of muscle glycogen synthesis and muscle G6P concentrations, analogous to the NIDDM patients in the earlier study (Rothman et al. 1992) where the findings were explained by an impaired muscle glucose transport/hexokinase activity. The authors concluded that insulin-resistant offspring of parents with NIDDM have impaired muscle glucose transport/hexokinase activity even before the onset of overt hyperglycemia, subsequently leading to a reduced muscle glycogen synthesis (Rothman et al. 1995). Therefore, it was concluded that this might be the primary factor in the pathogenesis of NIDDM. In a follow-up study, the effect of 6 weeks' exercise training on normoglycemic offspring of NIDDM parents was studied (Perseghin et al. 1996). While the concentrations of G6P and glycogen synthesis rate were lower in the offspring group as compared to controls without family history of NIDDM before the training period, it was restored to normal levels after 6 weeks of exercise training. It is remarkable that not only the offspring group increased glucose transport/phosphorylation with training but also the healthy control group, yet to a lesser extent than the offspring group. Obesity is often associated with reduced insulin sensitivity and a major risk factor for the development of NIDDM. Using again the combination of ^{13}C- and ^{31}P-MRS, the authors could show decreased muscle glucose transport and/or phosphorylation activity in a cohort of obese women (Petersen et al. 1998). It was concluded that insulin resistance in obesity can be mostly attributed to an impairment of reduced glucose transport and/or phosphorylation activity that leads to a limited ability of the body to reduce blood glucose concentrations by a synthesis of muscle glycogen. While the studies mentioned so far were conducted by clamp techniques with closely controlled insulin and glucose blood levels, a ^{13}C-MRS study was designed to evaluate the day-to-day pathophysiology of impaired glucose metabolism in NIDDM (Carey et al. 2003). After the consumption of sequential mixed meals, the postprandial glycogen levels were significantly lower in the gastrocnemius muscle of the diabetic patients compared to healthy controls, showing the inability of insulin-resistant persons to reduce blood glucose levels by an efficient uptake of glucose into the muscle cell and subsequent synthesis of muscular glycogen.

The possibility to separate the ^{1}H-MR signals from intra- (IMCL) and extra- (EMCL) myocellular lipids (see Fig. 6 and additional references in overview (Boesch et al. 2006)) led to an intense application of this technique in physiology and pathophysiology, in particular after several groups reported a negative correlation of insulin sensitivity and IMCL levels (Machann et al. 1998; Perseghin et al. 1999; Cline et al. 1999; Jacob et al. 1999; Krssak et al. 1999). For several years, contradicting results were found, depending on the cohorts who had been studied (insulin-resistant patients vs healthy persons and sedentary subjects vs trained athletes). The studies with cohorts of athletes showed a positive correlation of insulin sensitivity and IMCL levels (Decombaz et al. 2001), which was apparently contradicting the observation in NIDDM patients. This so-called "athlete paradox" was then solved in a comprehensive study by the Tübingen group who showed a complex, "u-shaped" relation of VO_2max (as a measure of exercise capacity), IMCL levels, and insulin sensitivity (Thamer et al. 2003). While lower insulin sensitivity in subjects with low VO_2max was related to high IMCL levels, athletes with high VO_2max showed both high IMCL levels and high insulin sensitivity. This observation made it questionable that high IMCL levels in insulin-resistant subjects per se would be a cause for insulin resistance. On the contrary, it became more probable that high IMCL levels on their part were a consequence of insulin resistance. Newer concepts make now the accumulation of other lipid metabolites, such as diacylglycerol or fatty acyl CoAs, responsible for insulin resistance. However, this mechanism is not yet fully understood. It was also recognized that resting IMCL levels were affected by many factors, such as short-term exercise and diet. Since exercise was able to reduce IMCL levels significantly, exercise protocols were applied, however, with the disadvantage that insulin resistant and often obese patients were not able to show the same exercise performance. A low-level exercise diet regime was proposed, which should enable also patient groups with reduced exercise capacity to reduce IMCL levels effectively (Ith et al. 2010). In a study of obese children and adolescents it was found that intramyocellular and intra-abdominal lipid accumulation was linked to the development of peripheral insulin resistance (Weiss et al. 2003). A study on insulin-resistant offspring of diabetes type 2 parents showed increased IMCL levels (Petersen et al. 2004). Effects of insulin-sensitizing drugs were evaluated in multiple studies (Teranishi et al. 2007; Bajaj et al. 2010). Pioglitazone and metformin studies showed effects on the IMCL concentrations as observed by ^{1}H-MRS, which might be secondary to changes of serum factors such as adiponectin (Teranishi et al. 2007). Pioglitazone was also found in another ^{1}H-MRS study to reduce IMCL levels (Bajaj et al. 2010). Interethnic differences in the fat depot of muscle, liver, and abdomen were found in a study comparing Hispanics and African Americans with Caucasians (Liska et al. 2007). In contrast, no difference was found between African Americans and Caucasians for the infusion of intralipids with comparable increase of IMCL and reduction of insulin sensitivity (Lee et al. 2013).

It has been speculated that impaired mitochondrial function could explain the reduced ability of the diabetic muscles to metabolize glucose and fat. A study applied ^{31}P-MRS in the heart and skeletal muscle and measured recovery of PCr in the skeletal muscle after exercise to get information on the mitochondrial functions (Scheuermann-Freestone et al. 2003). The authors concluded that diabetes type 2 patients have impaired myocardial and skeletal muscle energy metabolism despite apparently normal cardiac function. In a study with healthy elderly subjects it was found that they were significantly less insulin-sensitive than body-mass-matched young controls (Petersen et al. 2003). The IMCL levels were increased and mitochondrial oxidative and phosphorylation activity was reduced as measured by ^{13}C-MRS with labeled [2-^{13}C] acetate infusion and ^{31}P-MRS saturation transfer, respectively. The authors concluded that elderly subjects show a decline in mitochondrial function which in turn is responsible for the higher incidence of insulin resistance in the elderly. In a study with overweight and normal-weight children, no difference in the oxidative phosphorylation was found between the two groups as measured by PCr recovery after exercise (Fleischman et al. 2009). Furthermore, oxidative phosphorylation was dependent on the insulin sensitivity of all the participants of the study, supporting the hypothesis of a relation between metabolic function and insulin sensitivity. However, this hypothesis of mitochondrial function as a cause of insulin resistance has been challenged by another study which found elevated IMCL levels in m.vastus lateralis of insulin-resistant patients as compared to healthy controls, but no differences in the oxidative phosphorylation as measured by ^{31}P-MRS and PCr recovery after exercise (De Feyter et al. 2008). A subsequent study of the same authors with a one-year exercise training of the diabetes type 2 patients came to the conclusion that mitochondrial dysfunction was apparent only in inactive longstanding T2DM patients (van Tienen et al. 2012). This would support the hypothesis that mitochondrial function and insulin resistance are not related. In addition, exercise training could positively influence mitochondrial activity in diabetes type 2 patients. Because of the enormous impact of insulin resistance on our health care system and individual patients, in particular the elderly, further studies—including ones which apply MR spectroscopy—are necessary.

3.3 Glycogen Storage Diseases

Glycogenoses (Vorgerd et al. 2002a) in general, and McArdle's disease in particular (glycogenosis type V), have been in the interest of MRS since the very beginning, on the one hand because it was one of the first observations (Ross et al. 1981) of the value of ^{31}P-MRS, and on the other hand because the pH development during exercise is pathognomonic in McArdle's disease. For a systematic review of glycogenoses, clinical reviews are available (Vorgerd and Zange 2002; Vorgerd et al. 2002a). In the following, glycogenoses are listed not systematically but according to the role that MR spectroscopy has played in the past.

McArdle's disease (glycogenosis type V) is an autosomal recessive inherited defect of the muscle glycogen phosphorylase which leads to a reduced ability to use glycogen reserves when energy is needed. In a seminal paper, Ross et al. (1981) have shown the potential of ^{31}P-MRS to follow the pH development during exercise which—in contrast to healthy subjects—becomes alkaline in McArdle patients. In addition, PCr depletion and Pi increase during exercise is much more pronounced in these patients. Figure 8 illustrates that a reduced breakdown of glycogen is responsible for the fact that glycogen reserves cannot be used during exercise in the same amount as in healthy subjects (Argov et al. 1987). In turn, it has been shown that glucose infusion leads to an improvement in the clinical symptoms and the PCr reduction (Lewis et al. 1985), since glucose gets available via glucose transport to the cell instead of the impaired glycogenolysis. In a family with multiple consanguinities and parents with overt McArdle's disease, ^{31}P-MRS has shown the pathognomonic pH-behavior in a so far totally asymptomatic 5-year-old boy (Gruetter et al. 1990). In a comparison of ^{31}P-MRS data and T2-MRI-measurements, McArdle patients neither showed a pH drop nor changes of T2 as seen in healthy controls (deKerviler et al. 1991). Using ^{13}C-MR spectroscopy, it was possible to directly observe the glycogen reserves in skeletal muscle and thus to distinguish McArdle patients with increased glycogen levels from healthy controls (Jehenson et al. 1991). Figure 8 also shows this potential of observing the metabolism in vivo at different places of the biochemical pathways using MRS of different nuclei. In a patient suffering from glycogenosis type VI (liver glycogen phosphorylase deficiency), where muscle is not involved, normal glycogen levels were found in skeletal muscle, yet increased glycogen levels were observed in liver, thus allowing a differentiation from McArdle glycogenosis where skeletal muscle is affected (Labrune et al. 1992). Different phases of the exercise-related changes in ^{31}P-MR signals in McArdle patients were reported in more detail, such as the transient Pi disappearance at the onset of recovery (Bendahan et al. 1992a), the failure to show cytosolic acidification and PME accumulation (Siciliano et al. 1995), the indirectly observed ADP (Argov et al. 1996), or functional compartmentation with a small number of muscle fibers that reach metabolic depletion earlier than the majority (Zange et al. 2003). ^{31}P-MR spectroscopy was also used to follow and quantify effects of treatment on McArdle patients, such as infusion of amino acids which did not change working capacity (Jensen et al. 1990), medication with Ramipril (an angiotensin-converting enzyme inhibitor) and Gentamycin which both showed no effect on ^{31}P-MRS parameters (Schroers et al. 2006; Martinuzzi et al. 2008), and creatine therapy which resulted in a certain improvement of skeletal function (Vorgerd et al. 2000), however, at the cost of neurologic adverse effects at higher dosage of creatine (Vorgerd et al. 2002b). The model of cellular acid–base balance was found to describe cellular pH changes during both exercise and recovery in McArdle's disease adequately (Kemp

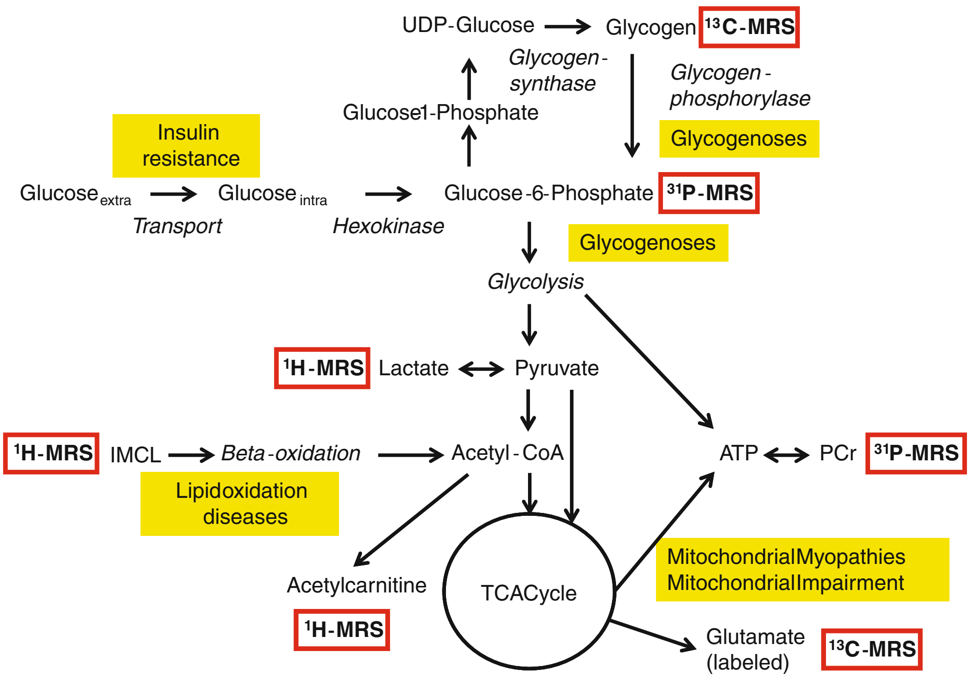
UDP-Glucose
Glycogen
^{13}C-MRS
Glycogen-synthase
Glycogen-phosphorylase
Glucose1-Phosphate
Glycogenoses
Insulin resistance
Glucose extra
Glucose intra
Transport
Hexokinase
Glucose-6-Phosphate
^{31}P-MRS
Glycogenoses
Glycolysis
^{1}H-MRS
Lactate
Pyruvate
^{1}H-MRS
IMCL
Beta-oxidation
Acetyl-CoA
ATP
PCr
^{31}P-MRS
Lipidoxidation diseases
MitochondrialMyopathies
MitochondrialImpairment
Acetylcarnitine
TCACycle
^{1}H-MRS
Glutamate (labeled)
^{13}C-MRS

Fig. 8 Simplified biochemical pathways and the respective metabolites that can be observed with multinuclear MRS. Examples of impaired metabolism in skeletal muscle as discussed in the text are shown in *yellow boxes*

et al. 2009). A comparison of ^{31}P-MRS results and muscle sympathetic nerve activity in a group of McArdle and two other glycogenoses' patients (Vissing et al. 1998) led to the conclusion that muscle acidosis is not necessary to generate sympathetic activation in exercise.

While glycogenolysis is impaired in McArdle's disease, and thus the glycolysis path is inhibited (pathways illustrated in Fig. 8), phosphofructokinase (PFK) deficiency (Glykogenose type VII, Tarui-disease) leads to a block in a next step of glycolysis. The resulting trapping of phosphorylated sugar compounds should be observable by ^{31}P-MRS. In a seminal paper, Britton Chance's group has shown the increased sugar phosphates and was able to enlighten the control mechanisms of mitochondrial activity which they assigned to ADP (Chance et al. 1982). The behavior of the sugar phosphate peak was evaluated in an early study in various glycogenoses (Duboc et al. 1987), including PFK, and it was shown that sugar phosphates can be used to differentiate glycogenoses, being high in PKF deficiency (type VII) and phosphoglycerate kinase (type IX) deficiency, while it was undetectable in lacking debrancher enzyme (type III) and McArdle (type V). Using ^{31}P-MRS, it could be shown that lactate infusion increases oxidative phosphorylation in PFK patients (Bertocci et al. 1993) by a bypass of the PFK step. A case report of a late-onset PFK deficiency led the authors of the ^{31}P-MR study to conclude that progressive polysaccharide accumulation was the source of the clinical signs and less an acute shortage of energy supply in the muscle fibers (Massa et al. 1996). Another group observed the known accumulation of PME during exercise and came to the conclusion that continuing episodes of muscle fiber destruction were responsible for the late-onset muscle weakness (Sivakumar et al. 1996). A comparison of an asymptotic heterozygous PFK patient with homozygous patients (Grehl et al. 1998) closed with the assumption that the turnover of the TCA cycle was reduced in homozygous PFK patients.

Other glycogenoses with involvement of the skeletal muscle were evaluated by various MRS techniques. A patient suffering from debrancher enzyme deficiency (M. Cori-Forbes, glycogenosis type IIIA) showed increased glycogen levels as shown by ^{13}C-MRS (Beckmann et al. 1990; Wary et al. 2010) and elevated pH and accumulation of PME as shown by multiparametric MRI/MRS (Wary et al. 2010). Phosphoglycerate mutase deficiency (glycogenosis type X) patients showed accumulation of PME only on fast "glycolytic" exercise at ^{31}P-MRS (Vita et al. 1994). Glycogen/creatine as observed by undecoupled ^{13}C-MRS was significantly higher in a group of acid maltase deficiency (glycogenosis type II, Pompe's disease) patients compared to healthy volunteers, with glycogen concentrations above the normal 95 % confidence limits in 7 of the 11 patients (Wary et al. 2003).

3.4 Mitochondrial Myopathies

Mitochondrial myopathies belong to the metabolic myopathies and describe a very heterogeneous group of defects in biochemical pathways that take place in the mitochondria (Tarnopolsky and Raha 2005; DiMauro 2006). Since oxidative phosphorylation, i.e., defects in the mitochondrial respiratory chain, can be observed noninvasively by ^{31}P-MR spectroscopy, it is logical that many ^{31}P-MRS publications deal with the heterogeneous group of mitochondrial diseases mainly to increase the understanding of mitochondrial processes and less for individual diagnoses.

In recent years, mitochondrial disorders were grouped along the mutations in mitochondrial DNA and tRNA (DiMauro 2006), however, a description of MRS examinations along these categories would go far beyond the scope of this article. In addition, some of the mitochondrial mutations (e.g. A3243G) can be responsible for a spectrum of diverging clinical syndromes ranging from MELAS (mitochondrial encephalopathy, lactic acidosis, and stroke-like episodes) to MIDD (maternally inherited diabetes and deafness). Therefore, the grouping is organized along the historical sequence and the impact for the applications of MR spectroscopy.

In their seminal papers on the MRS examination of two patients with NADH-CoQ reductase deficiency, the Oxford group introduced ^{31}P-MRS for studies of myopathies and in particular the concept of PCr recovery after exercise (Gadian et al. 1981; Radda et al. 1982). This defect in the electron transport chain of the mitochondria led to an abnormal recovery of PCr and pH after exercise of the forearm, thus allowing an assessment of the relative importance of oxidative and glycolytic regeneration of high-energy phosphates. A 15-year-old girl with deficiency of NADH-CoQ reductase activity showed reduced PCr and increased Pi, and ADP levels in muscle showed analogous ^{31}P-MRS values also in the brain (Hayes et al. 1985). In a group of 12 various mitochondrial myopathy patients, 11 patients showed an abnormality in the ^{31}P-MR spectra at rest (Arnold et al. 1985). In order to estimate the apparent maximum rate of oxidative ATP synthesis (QMAX) in various pathologies, including a group of 20 mitochondrial myopathy patients, Kemp et al. (1993b) used the hyperbolic relationship between cytosolic [ADP] and the rate of PCr resynthesis after exercise. It could be shown that QMAX was reduced and [ADP] increased in the group of mitochondrial myopathies. In a girl suffering from NARP (Neuropathy, ataxia, and retinitis pigmentosa), increased resting inorganic phosphate and lower PCr concentrations could be demonstrated (Lodi et al. 1994). Three members of a family affected with Leber's hereditary optic neuropathy (LHON) showed an altered mitochondrial energy metabolism in muscle and a mutation of 11778 mtDNA (Cortelli et al. 1991). This observation in LHON patients was supported by another ^{31}P-MRS study where six of nine patients with the mutation showed a low rate of post-exercise PCr recovery (Barbiroli et al. 1995). Normal findings at ^{31}P-MRS were observed in carriers with low percentage of mutated mtDNA. A ^{31}P-MRS study in 10 LHON patients revealed a reduced maximal mitochondrial ATP production after exercise depending on the exact type of mutation (Lodi et al. 1997b). In a study with 14 patients suffering from defects of mitochondrial respiratory chain enzymes, a series of indices derived from the PCr recovery curve matched in 10 of 14 cases with conventional test scores while no obvious correlation existed between pH parameters and clinics (Kuhl et al. 1994). In a comparison of 22 well-defined mitochondrial myopathy patients with 24 patients with unclear exercise tolerance, 17/24 unassigned also showed ADP recovery at ^{31}P-MRS examinations (Argov et al. 1997). The authors concluded that many patients suffering from exercise intolerance of undetermined origin may have impaired muscular oxidative metabolism that could be proven by ^{31}P-MRS examinations.

In addition to these studies, which essentially confirmed clinical findings, a series of ^{31}P-MRS publications gave additional information beyond the clinical symptoms. While only three out of eight MERRF patients (myoclonus epilepsy with ragged red fibers) had myopathic symptoms, ^{31}P-MRS showed significantly increased relative intracellular inorganic phosphate concentrations (Matthews et al. 1991). A case report on two brothers with A3243G mutations showed that even very low levels of mutations can already affect mitochondrial ATP production considerably (reduction to 21 % with 85 % mutation level vs. 35 % in the less affected brother with 6 % mutations only) (Chinnery et al. 2000). A report that is particularly interesting in view of the discussion of a mitochondrial involvement in insulin resistance has been published by van Elederen et al. (van Elderen et al. 2009). In a group of 11 patients with MIDD (with an A3243G mutation), 6 patients presented with and 5 presented without diabetes mellitus. The MIDD patients showed a prolonged recovery of PCr, however, no association was found with the presence of diabetes mellitus. While these studies show the potential of ^{31}P-MRS to provide additional information on mitochondrial myopathies, a critical review on the sensitivity of ^{31}P-MRS tests was published by Jeppesen et al. (Jeppesen et al. 2007) who found an almost 100 % specificity of some ^{31}P-MRS variables for the detection of mitochondrial myopathies, however, with a low sensitivity between 0 and 63 %.

Since ^{31}P-MRS provides quantitative data on oxidative phosphorylation, it is attractive to use this method to follow treatment effects in mitochondrial myopathy patients in addition to an observation of the clinical signs. The treatment with coenzyme Q has been studied several times with the help of ^{31}P-MRS, however, the findings are not yet conclusive both for the ^{31}P-MRS findings and for the clinical symptoms. Therapy with coenzyme Q10 plus vitamins K3 and C, riboflavin, thiamine, and niacin was evaluated by Matthews et al. (1993) who found no significant improvement in clinical symptoms or in ^{31}P-MRS measures of oxidative metabolism. Treatment of eight patients suffering from various mitochondrial myopathies with coenzyme Q led the authors to conclude that a single responder showed a beneficial effect but would not represent the whole group (Gold et al. 1996). The authors suggested monitoring treatment with objective metabolic tests to identify responders for long-term treatment. In contrast, Bendahan et al. found positive treatment effects with coenzyme Q in two patients with electron transport chain defects (Bendahan et al. 1992b). Bicycle ergometer tests and ^{31}P-MRS showed significant improvement, in particular an increase in the PCr/Pi ratio at rest and faster kinetics of recovery for pH, PCr, and PCr/Pi ratio following exercise. A study with patients suffering from different mitochondrial cytopathies showed a beneficial effect of 6-month treatment with coenzyme Q10, such that the mitochondrial muscular function, which was reduced to levels of 29 %, improved to levels of 56 % from the control group (Barbiroli et al. 1997).

A series of other treatments were tested using ^{31}P-MRS with differing outcomes. Fifteen patients suffering from progressive external ophthalmoplegia (CPEO) or Kearns-Sayre syndrome (KSS) obtained creatine over a period of 6 weeks (Kornblum et al. 2005). Neither clinical symptoms nor ^{31}P-MRS findings were changed with the treatment. In particular, there was no improvement of post-exercise PCr recovery. A positive treatment effect has been reported for the application of menadione and ascorbate in patients with defects in complex III of the electron transport chain (Eleff et al. 1984). While PCr/Pi recovery from exercise was 2.5 % of normal at baseline, treatment improved it to within 56 % of the recovery rate of controls. MELAS patients treated with riboflavin and nicotinamide for 18 months showed positive effects of treatment on PCr/ATP recovery rates and on Pi/PCr (Penn et al. 1992). Methylprednisolone treatment of a family of five generations with mitochondrial myopathy and a documented respiratory chain enzyme defect resulted in a significant improvement of resting ^{31}P-MRS findings (Heiman-Patterson et al. 1997). The acute application of oxygen did not change ^{31}P-MR spectra at rest in six patients with CPEO and MELAS. Nevertheless, it improved maximal ATP synthesis rate by 33 % in the patients while it changed it by only 5 % in healthy controls (Trenell et al. 2007). Two reports agree on the positive effect of exercise on patients with mitochondrial myopathies (Taivassalo et al. 1998; Trenell et al. 2006a). Aerobic exercise for 8 weeks improved ADP recovery by more than 60 % in ten patients with mitochondrial myopathies (Taivassalo et al. 1998) while 12 weeks of exercise training improved mitochondrial function in 10 CPEO and MELAS patients (Trenell et al. 2006a).

3.5 Muscular Dystrophies

Muscular dystrophies are a group of—generally inherited—muscular diseases that are characterized by muscle weakness and progressive destruction of the muscle tissue.

The most prominent muscle dystrophies are Morbus Duchenne (DMD) and Becker (BMD)—both have been widely studied with the help of ^{31}P-MRS following the very first, seminal publication on six patients suffering from Duchenne muscular dystrophy (Newman et al. 1982). PCr/ATP and PCr/Pi were reduced in these patients, obviously based on reduced PCr concentrations, while a signal in the PDE region showed up and the intracellular pH in the patients was abnormally alkaline. ^{1}H-MR spectra of the Duchenne patients showed a much higher lipid peak in the affected muscles than controls. In a ^{1}H-MRS study of eight DMD boys and eight healthy controls, ratios of TMA/water, tCr/water, and TMA/tCr were significantly lower in patients than in volunteers (Hsieh et al. 2009). In addition, fatty infiltration of the muscles has been documented in all patients. Muscle function scores and TMA/tCr were negatively correlated in the patients. A randomized, placebo-controlled ^{31}P-MRS study of creatine treatment in 33 DMD patients (18 creatine, 15 placebo) showed increased PCr/Pi levels in the verum group (Banerjee et al. 2010). While parents reported subjective improvement in the treatment group, no change in the functional state was observed. A combination of ^{1}H- and ^{31}P-MRS in nine boys with DMD and eight healthy age- and BMI-matched boys revealed higher fat fractions, higher pH values in the anterior compartments, and lower PCr/Pi in the posterior compartments (Torriani et al. 2012). The author concluded that lower leg muscles of boys with DMD show a distinct involvement pattern and that a noninvasive evaluation might help to demonstrate the severity of muscle involvement. Female DMD/BMD carriers were investigated in a ^{31}P-MRS study which showed a reduced rate of post-exercise recovery of PCr/Pi ratio in all carriers (Barbiroli et al. 1992). A detailed analysis of the ^{31}P-MRS signals during the evolution of exercise in the skeletal muscle of 14 Becker muscular dystrophy patients showed a distinct behavior of the pH (Lodi et al. 1999b). The authors interpreted the findings as reduced glucose availability in dystrophin-deficient muscles. During incremental workload, nine mildly affected BMD patients showed deregulation of resting pH and a slightly increased PDE signal which might indicate intramuscular membrane breakdown at ^{31}P-MRS examinations (Tosetti et al. 2011).

Other muscular dystrophies that have been investigated with the help of multinuclear MRS are Myotonic

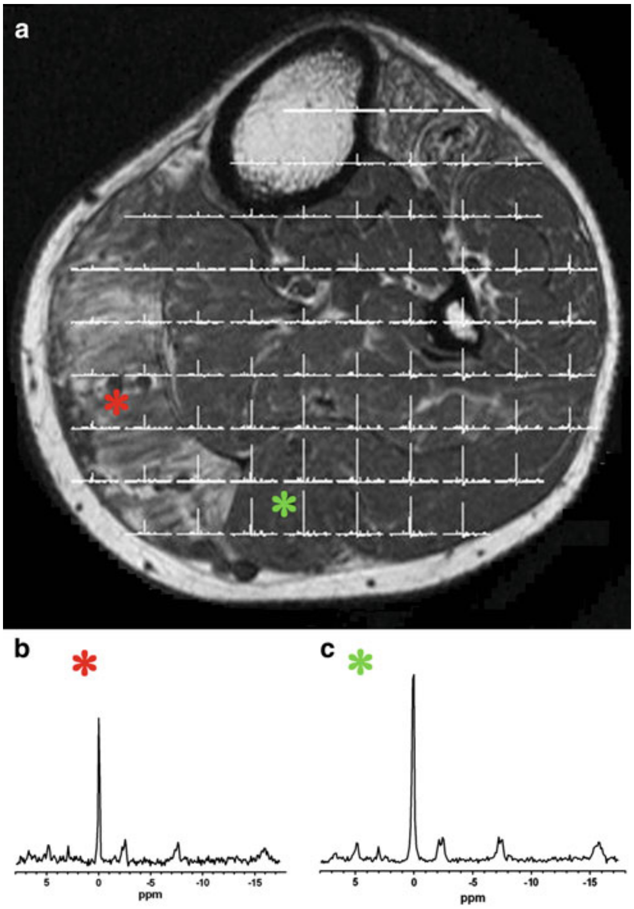

Fig. 9 **a** A $T1$-weighted MR image and a ^{31}P-MRSI data set with two spectra (**b**, **c**) from a patient with FSHD. Metabolites are only altered in regions with fatty infiltration. Spectrum (**b**) from the affected m.gastrocnemius medialis (*red star*) shows a smaller SNR due to lower metabolite concentrations and a reduced PCR/ATP ratio while spectrum (Cr) from the unaffected m. gastrocnemius lateralis (*green star*) shows metabolite levels as in healthy subjects (not shown). This example also illustrates a different way to display CSI data set compared to Fig. 7 where one specific metabolite is color-coded. Spectra (**b**, **c**) are scaled to the γ-ATP resonance (adapted with permission (Kan et al. 2010))

Dystrophy, Oculopharyngeal Muscular Dystrophy (OPMD), Limb Girdle Muscular Dystrophy (LGMD), and Facioscapulohumeral Muscular Dystrophy (FSHD). In 15 patients suffering from myotonic dystrophy intracellular pH was normal, but there were significant elevations in the concentration ratios of Pi/ATP, PME/ATP, PDE/ATP, and—in more affected patients—a reduced PCr/ATP ratio (Taylor et al. 1993). During exercise, there was less muscle acidification in patients with myotonic dystrophy while the PCr recovery was normal after workload with high levels of [ATP]. The authors concluded that oxidative capacity was normal in myotonic dystrophy patients. A ^{23}Na-MRS study of seven myotonic dystrophy patients at various stages of the disease and 11 healthy volunteers showed an increased total sodium content and fast transverse relaxation time, which was correlated with the severity of the disease (Kushnir et al. 1997). The authors concluded that ^{23}Na-MRS enables the quantitation of myotonic dystrophy progression. A ^{31}P-MRS followed the beneficial effect of 12 weeks exercise therapy in a patient with myotonic dystrophy (Trenell et al. 2006b). At rest, muscle PDE and pH were elevated while the recovery halftime of PCr was prolonged. After 12 weeks of aerobic exercise therapy, PCr/Pi and PCr recovery halftime improved while resting pH and PDE remained unchanged. In five siblings suffering from autosomal dominant OPMD pH was elevated and PCr was reduced at rest as compared to controls (Zochodne et al. 1992). Exercise-induced reduction of PCR and acidosis was more pronounced than in controls except in one patient who showed normal ^{31}P-MRS values at rest and during exercise. The authors concluded that OPMD is a more widespread disorder of striated muscle than clinically appreciated. Seven patients with LGMD showed normal ^{31}P metabolite concentrations at rest but the cytosolic pH was increased. Muscle oxidative metabolism was normal in LGMD patients (Lodi et al. 1997a). A ^{31}P-MRSI study of nine FSHD patients showed that metabolic changes, i.e., impaired metabolite levels and pH, were only present in muscle groups with fatty infiltration (Kan et al. 2010) (Fig. 9).

3.6 Inflammatory Myopathies

Dermatomyositis and polymyositis are the most prominent inflammatory myopathies and studies are sometimes performed in combined groups of both patient categories.

An MRI/^{31}P-MRS study of four patients with dermatomyositis and five controls showed ATP and PCr levels 30 % below controls and increased Pi levels at rest and during exercise (Park et al. 1990). T_1 and T_2 values determined by MRI and ^{31}P-MRS metabolite data correlated with symptoms and clinical tests. Amyopathic variants of dermatomyositis patients present with the typical rash but without severe muscle weakness, while myopathic dermatomyositis includes erythematous rash and severe, proximal muscle weakness (Park et al. 1995). Nine patients with amyopathic and 11 patients with myopathic dermatomyositis were compared with 11 healthy subjects, using ^{31}P-MRS. While amyopathic patients showed no muscle inflammation and normal MRS data at rest, the MRS data revealed significant differences between amyopathic DM patients and control subjects during exercise. Myopathic patients showed differences from healthy controls already at rest. The authors concluded that ^{31}P-MRS is able to unmask the hidden defect in amyopathic patients during exercise. The development of an artificial network analysis showed usefulness in a longitudinal study on 10 amyopathic and 17 myopathic patients (Park et al. 1998a). Juvenile dermatomyositis was evaluated in 13 patients and revealed significant metabolic abnormalities in the thigh muscles of 10 severely affected patients during rest, exercise, and recovery (Park et al. 2000). At rest ATP and PCr levels were 35–40 % below the values in controls and Pi/PCr levels were increased together with ADP levels. The three patients with normal MRS findings had either improved under prednisone treatment or had an amyopathic variant of juvenile dermatomyositis, respectively. Short-term alterations of ^{31}P-metabolites were specifically addressed in a study with 10 dermatomyositis patients and 18 healthy controls (Pfleiderer et al. 2004).

Combined groups of dermatomyositis and polymyositis patients showed increased ratios of Pi to PCr during exercise (Newman and Kurland 1992). A study including nine dermatomyositis and five polymyositis patients together with 18 age-matched controls revealed impaired ^{31}P-MRS values in both groups; however, there was no correlation between the MRS-detectable abnormalities and the degree of inflammation or MRI-determined fatty infiltration of the muscle (Cea et al. 2002). From the observation of a reduced proton efflux, the authors concluded that the impaired muscle function is secondary to an impaired blood supply. Treatment effects with creatine plus exercise during 6 months were followed in combined groups of 37 dermatomyositis or polymyositis patients (Chung et al. 2007). A test for muscle function showed significantly improved performance with both creatine and placebo while PCr/ATP increased significantly in the creatine group only. Using ^{31}P-MRS and near infrared spectroscopy (NIRS), 12 polymyositis patients were evaluated before and after steroid therapy and compared with 12 healthy controls (Okuma et al. 2007). Before steroid therapy, polymyositis patients had markedly lower intracellular pH during exercise and experienced a significantly slower recovery than normal individuals. Following steroid therapy, the pH drop during exercise was less dramatic and the recovery time after exercise was shortened. In a study with seven patients with sporadic inclusion body myositis, 8 normal controls and 20 mitochondrial myopathies, six of seven myositis patients showed elevated Pi values while PCr recovery time after exercise was not increased—in contrast to the mitochondrial myopathy patients in the comparison (Argov et al. 1998). The authors concluded that mitochondrial oxidative capacity is not impaired in inclusion body myositis. While not strictly an inflammatory myositis, macrophagic myofascitis has been studied in nine patients using ^{31}P-MRS (Guis et al. 2004). It was found that no differences in the MRS indices for oxidative energy metabolism exist between these patients and controls and that thus the observed clinical symptoms cannot be explained by an underlying anomaly of muscle energy metabolism.

3.7 Other Diseases and Conditions Affecting the Musculoskeletal Metabolism

Due to the large number of publications that deal with muscle metabolism as a consequence of other diseases and conditions, a detailed discussion of each and every publication is not possible. In turn, this chapter illustrates the diversity of the field. To get a certain order for the many different applications, publications are summarized in sometimes rather arbitrary groups.

Malignant hyperthermia (MH) is a rare, yet serious disease that occurs during the application of certain drugs, in particular volatile anesthesia agents, in genetically predisposed subjects. A classical diagnosis in relatives of patients who suffered an MH episode is an application of caffeine and halothane on muscle biopsy samples. Numerous publications documented an abnormal energy metabolism in skeletal muscle of subjects who are susceptible to MH (Kozak-Reiss et al. 1986; Olgin et al. 1991, 1988; Payen et al. 1993; Bendahan et al. 1998, 2001; Guis et al. 2001). Thus, the authors of an initial case report concluded that MH is in fact a latent myopathy (Kozak-Reiss et al. 1986). While some publications observed abnormal resting ^{31}P-MR spectra (Olgin et al. 1991, 1988; Payen et al. 1993), others found normal values at rest (Kozak-Reiss 1989; Bendahan et al. 1998, 2001). During exercise, a large drop in PCr and a pronounced decrease of pH was found (Bendahan et al. 1998). A study with a cohort of 42 patients, 27 MH-susceptible and 15 MH-negative, showed a sensitivity of 99 % and a specificity of 95 % (Olgin et al. 1991). These numbers were confirmed by a study in 14 MH-susceptible and 22 MH-negative subjects, where a sensitivity of 93 % and a specificity of 95 % was found.

Peripheral arterial disease (PAD) or arterial occlusive disease (AOD) are not myopathies in the strict sense, nonetheless, insufficient blood supply affects the metabolism of skeletal muscle, which can be objectively documented by MR spectroscopy (Schocke et al. 2008). All clinical studies with PAD patients observed slower PCr recovery after exercise in the affected leg (Zatina et al. 1986; Kemp et al. 1995, 2002; Greiner et al. 2006; Schocke et al. 2006; Esterhammer et al. 2008). A few publications analyzed the ^{31}P-MR spectra during exercise in more detail, in particular calculated ADP recovery (Kemp et al. 1995, 2002). A few publications followed treatment by MR spectroscopy (Taylor et al. 1996; Schunk et al. 1998; Baumgartner et al. 2005). One study with nine PAD patients found no group effects after 3 months of treatment with propionyl-L-carnitine; however, the study could distinguish responders from non-responders and found a correlation of ^{31}P-MRS indices with clinical outcome (maximum walking distance) in responders (Taylor et al. 1996). Thirty-one

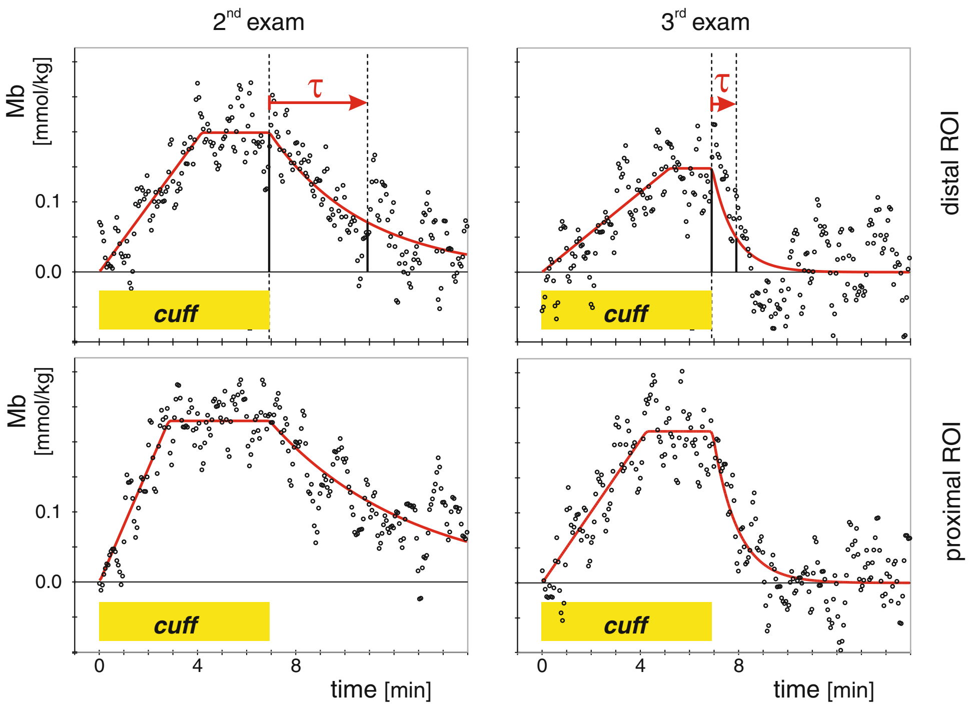

Fig. 10 The effect of ischemia and reperfusion on the ^{1}H-MR signal of deoxymyoglobin. Two surface coil positions detect the signal from deoxymyoglobin in the distal and proximal leg. The recovery after ischemia significantly improved at the third exam after intramuscular vascular endothelial growth factor gene therapy (adapted with permission (Baumgartner et al. 2005))

patients with AOD underwent different surgical treatments (percutaneous transluminal angioplasty, stents, vascular operations) and were followed by ^{31}P-MRS (Schunk et al. 1998). Exercise-induced metabolic changes of the quadriceps muscle (Pi, pH) were significantly improved after therapy. The authors concluded that a markedly increased recovery rate of Pi/PCr is a consequence of an improved oxidative metabolism of muscle cells because of increased tissue perfusion. While the publications above all used ^{31}P-MRS to follow muscle energy metabolism, it is possible to use ^{1}H-MR spectroscopy of deoxymyoglobin to investigate the oxidative status of the leg directly (Baumgartner et al. 2005). Treatment of five patients with critical limb ischemia with intramuscular vascular endothelial growth factor (pVEGF)-C gene therapy was followed by ^{1}H-MRS and MR-angiography. MR spectroscopy was reproducible and showed a significant correlation with disease extent (Fig. 10).

While the postulated decrease of mitochondrial activity with age has been described in the section on insulin resistance, a few additional MRS studies on changes in elderly subjects (70+ years) are summarized here. Since ^{31}P-MRS can probe the oxidative capacity of skeletal muscle, it is not surprising that it has been used by various groups to document changes of the aging muscle. The recovery rate of PCr after exercise was found to be slower and the drop in PCr during exercise was more pronounced in elderly subjects (McCully et al. 1991, 1993; Chilibeck et al. 1998; Horska et al. 2000; Conley et al. 2000; Kent-Braun et al. 2002). One study found 50 % lower oxidative capacity in elderly subjects which was accompanied with a reduction in mitochondrial content with age as seen in biopsy samples (Conley et al. 2000). Somewhat diverging results were reported for the pseudo-first-order reaction rate k(PCr → ATP) where one study found comparable values for young and elderly subjects (Horska et al. 2000), while another study found an approximately 40 % reduction in this constant (Petersen et al. 2003). The latter study supported this finding with a ^{13}C-MRS examination of infused [2-^{13}C] acetate to measure TCA cycle flux. In contrast to the studies cited above, a multiparameter MRS approach did not find markedly slower PCr recovery rates in elderly people (Wray et al. 2009a). A comparison of preferred walking speed and oxidative capacity as determined by ^{31}P-MRS revealed a correlation of these parameters and the authors conclude that preferred walking speed could be determined by mitochondrial efficiency (Coen et al. 2013). Treatment with an oral antioxidant cocktail (vitamins C and E and alpha-lipoic acid) showed improved oxidative capacity in a group of older subjects, yet not in a group of younger people (Wray et al. 2009b).

Failures of organs other than the musculoskeletal system, e.g., chronic heart failure, hypertension, pulmonary diseases, or renal insufficiency can affect the metabolism of skeletal muscle. ^{31}P-MRS values from chronic heart failure patients showed significantly slower PCr recovery and greater acidosis with exercise (Wilson et al. 1985; Massie et al. 1987a, b, 1988; Duboc et al. 1991). At rest, only minor (Massie et al. 1987b) or no abnormalities were observed (Wilson et al. 1985; Duboc et al. 1991). Parallel measurements of peripheral blood flow showed that changes in the ^{31}P-MRS values could not be explained by reduced blood flow only (Massie et al. 1987a, 1988), therefore, it is concluded that chronic heart failure leads to metabolic abnormalities such as increased glycolytic metabolism (Massie et al. 1988). Treatment of these patients with exercise training led to improved ^{31}P-MRS findings (Minotti et al. 1990; Adamopoulos et al. 1993) while low-frequency electrical stimulation led to higher exercise capacity and muscle volumes without significant changes in the ^{31}P-MRS values (Maillefert et al. 1998). Patients presenting with essential hypertension showed higher [ADP] concentrations at the end of exercise, while PCr and ADP recovery rates were normal (Dudley et al. 1990). Patients suffering from chronic obstructive pulmonary disease (CPOD) or respiratory failure experienced greater and faster PCr depletion and intracellular acidosis during exercise (Thompson et al. 1993; Kutsuzawa et al. 1995; Levy et al. 1997). Patients with renal insufficiency showed a reduction in the high Pi levels during dialysis (Cardoso et al. 1988; Thompson et al. 1994) while resting ATP levels were unaffected. Eight patients obtaining intraperitoneal amino acid administration over a period of 6 months revealed improved oxidative phosphorylation in the ^{31}P-MRS examinations (de Bisschop et al. 1997). An influence of chronic heart failure on muscular metabolism was evaluated by ^{1}H-MRS of deoxymyoglobin (Mancini et al. 1994).

There is a very heterogeneous group of publications which evaluates involvement of skeletal muscle in central and peripheral nervous system defects. In most cases, ^{31}P-MRS is used to assess the metabolic status of skeletal muscle and only few papers are using ^{1}H-MRS. Since some studies with muscular biopsy material suggested mitochondrial defects in the electron transport chain of Parkinson patients, ^{31}P-MRS was used to follow muscular metabolism, however, with conflicting results. While one study did not find an abnormality of muscle energetics (Taylor et al. 1994), another found significant differences in the Pi/PCr ratio between patients and healthy controls (Penn et al. 1995). Multiple sclerosis, another disease of the central nervous system where skeletal muscle was evaluated, showed significantly slower PCr recovery after exercise in patients (Kent-Braun et al. 1994). Friedreich ataxia is an autosomal recessive spinocerebellar ataxia with a defect protein in the mitochondria and increased intracellular iron. Therefore, it was appealing to study mitochondrial ATP production in the skeletal muscle to test the effect of this disease in mitochondria outside of the central nervous system (Lodi et al. 1999a, 2001). Mitochondrial ATP production was below normal and related to the number of GAA repeats, the genetic defect that is responsible for the disease (Lodi et al. 1999a). Antioxidant treatment with coenzyme Q10 and vitamin E led to a considerable increase in muscular mitochondrial ATP production, pointing toward the oxidative stress by the accumulated iron that may play a role in Friedreich ataxia (Lodi et al. 2001). Since impaired mitochondrial energy production in the motoneurons may play a role in the pathogenesis of amyotrophic lateral sclerosis, a study evaluated an effect on the metabolism in the skeletal muscle yet without finding evidence for such an involvement (Grehl et al. 2007). Groups of patients with various neuromuscular pathologies were studied by ^{1}H-MRS and combinations of ^{31}P- and ^{1}H-MRS imaging of the skeletal muscle (Schröder et al. 2006; Hsieh et al. 2007). An effect of denervation on the metabolism of skeletal muscle cells was found by ^{31}P-MRS (Frostick et al. 1992). Post poliomyelitis patients showed decreased energy metabolism in skeletal muscle (Mizuno et al. 1997; Ljungberg et al. 2003; Sharma et al. 2007) which could be improved by long-term treatment with coenzyme Q10 (Mizuno et al. 1997). Myasthenia gravis is an autoimmune disease which affects the neuromuscular junction and thus the skeletal muscle. Effects of this disease on the muscular metabolism were not found in mildly affected patients, however, could be proven in severely affected patients (Ko et al. 2008) where a thymectomy improved the muscular energy metabolism.

It is not surprising that the muscular metabolism, in particular the mitochondrial energy production, is of interest in endocrine syndromes and thus has been studied with the help of ^{31}P-MR spectroscopy. Thyroid disorders can affect the energy metabolism of skeletal muscle and hypothyroid patients have been studied in a series of publications (Taylor et al. 1992; Kaminsky et al. 1992; Hagspiel et al. 1992; Reeves 1996; Erkintalo et al. 1998; Khushu et al. 2010). Reduced PCr levels at rest and slower PCr recovery after exercise were found consistently. In addition, treatment with thyroid hormone improved the energy metabolism in muscle. It is concluded that hypothyroid muscle needs more energy for the same output than healthy muscle (Erkintalo et al. 1998). A comparison of hypo- and hyperthyroid patients at rest showed a reduced PCr/Pi and increased PDE/ATP and Pi/ATP ratios in hypothyroid patients while hyperthyroid patients show opposite findings for all three ^{31}P-MRS values (Khushu et al. 2010). Since growth hormone affects the lipid metabolism, several studies used ^{1}H-MRS of intramyocellular lipids (IMCL) to characterize growth hormone deficiency, treatment, and excess growth hormone in acromegaly (Trepp et al. 2008; Madsen et al. 2012; Sato et al. 2012). An exercise study in growth hormone deficient (GHD) patients showed a higher usage of IMCL by the patients group compared to healthy controls (Trepp et al. 2008). Resting IMCL levels were found to be higher in GHD patients who were correlated with indices for insulin resistance (Sato et al. 2012). IMCL levels were also studied in a comparison of two treatment schemes for acromegaly patients suffering from excess growth hormone (Madsen et al. 2012). Treatment with a somatostatin analog only or in combination with a growth hormone antagonist showed stronger reduction of IMCL levels for the combined therapy. Multinuclear MR spectroscopy (^{1}H-MRS and ^{13}C-MRS) were used to evaluate substrate selection during normoglycemic and hyperglycemic exercise in diabetes type 1 patients (Jenni et al. 2008). During euglycemia, substrate oxidation in type 1 diabetic patients was similar to healthy individuals. With increased blood glucose levels, carbohydrate oxidation dominated without sparing intramyocellular glycogen.

Toxic substances, including certain medication (Guis et al. 2012), or other causes for muscle damage can influence muscle energy metabolism and thus were evaluated with ^{31}P-MRS. Treatment with bryostatin showed an increased PDE/ATP ratio at rest (Hickman et al. 1995), probably a result of increased membrane degradation following the application of a cytotoxic agent. Bryostatin and BW12C79 showed significant effects on PCr breakdown during exercise or slower PCr recovery (Philip et al. 1993; Hickman et al. 1995; Thompson et al. 1996) while the selective mitochondrial toxin MKT077 showed effects only in one patient after a longer application (Propper et al. 1999). HIV patients with AZT-treatment experienced a significantly slower PCr recovery rate, which can be due to the fact that the clinically occurring myopathy during treatment with AZT is a result of the reduced mitochondrial DNA synthesis and subsequently, the reduced oxidative phosphorylation (Weissman et al. 1992). Treatment with statins (3-hydroxymethylglutaryl-coenzyme A reductase inhibitors) is indicated for the reduction of high cholesterin levels and led in some patients to myalgia. ^{31}P-MRS at rest and during exercise showed no anomaly (Guis et al. 2006). However, based on a slowed pH recovery, the authors suggest that statins might unmask a latent pathology in susceptible subjects. In contrast to the latter study, PCr recovery was found to be significantly slower in ten patients with hypercholesterolemia before and after a 4-week regimen of statin therapy (Wu et al. 2011). Strenuous exercise can lead to muscle damage and has been evaluated with the result that Pi was elevated at rest and during exercise for the next days (McCully et al. 1988; Davies et al. 2011). A combined ^{31}P-/^{13}C-MRS investigated the effect of smoking on the carbohydrate metabolism in skeletal muscle, revealing a reduced glycogen synthesis and G6P levels during the insulin-dependent phase, indicating reduced glucose transport or hexokinase activity (Price et al. 2003) similar to insulin-resistant subjects (Rothman et al. 1995).

On the one hand, it is difficult to provide a systematic description of MRS studies in complex systemic syndromes. On the other hand, some disorders with unclear pathophysiology, e.g., chronic fatigue syndrome or fibromyalgia, have been quite prominent in MRS research, such that a summary is desirable. Others, like cancer-related cachexia, hypohydration, or chronic malnutrition, have a clearer origin yet withstand a systematic classification. Results of ^{31}P-MRS studies on the muscular energy metabolism are contradictory—while some find no difference to healthy controls (Kent-Braun et al. 1993; McCully et al. 2003), others find defects in the oxidative metabolism (Wong et al. 1992; McCully et al. 1996; Lane et al. 1998). A certain agreement exists that subgroups of the patients reveal objective findings at ^{31}P-MRS (Barnes et al. 1993; Lane et al. 1998) and concluded that the chronic fatigue syndrome is a heterogeneous disorder and that subgroups might be distinguished by ^{31}P-MRS. An abnormality in the pH-handling by skeletal muscle with a reduced proton efflux visible in ^{31}P-MRS has been suggested (Hollingsworth et al. 2010; Jones et al. 2010). A similar controversy can be found in studies on fibromyalgia where some results show no differences to healthy subjects under the specific conditions of the study (de Blecourt et al. 1991; Simms et al. 1994) while others report significantly lower PCr and ATP levels, as well as reduced PCr/Pi ratios at rest (Park et al. 1998b). Using ^{31}P-MRS, specific abnormalities in the muscular metabolism were found in diseases like the Marfan syndrome (Crilley et al. 2007), cystic fibrosis (Wells et al. 2011), or a case of adenylosuccinate lyase deficiency (Salerno et al. 1997). In a lipid storage disease with subclinical myopathy, ^{1}H-MRS showed a severe accumulation of triglycerides in skeletal muscle (Akman et al. 2010). Cancer-related cachexia leads to a loss of muscle tissue, however, without changes in the muscular energy metabolism (Weber et al. 2009). Moderate hypohydration induced in healthy volunteers showed similar muscular energetic as in the eu-hydrated state (Montain et al. 1998), while in contrast chronic malnutrition shows a maintenance of ATP levels at the cost of PCr (Gupta et al. 1994).

4 Conclusions and Outlook

As one can clearly see from the previous section, publications on ^{31}P-MRS still represent the major part of MRS in metabolic diseases of the musculoskeletal system. Other nuclei are increasingly researched, in particular in studies of insulin resistance, but the observation of oxidative metabolism using ^{31}P-MRS remains attractive.

From the clinical point of view, ^{31}P-MRS can provide extremely valuable information on muscular metabolism. However, since numerous diseases affect oxidative phosphorylation in one way or another, it can rarely be used to help with a diagnosis as stand-alone method. In contrast, knowing the disease in a patient, ^{31}P-MRS can document an involvement of the skeletal muscle objectively and quantitatively.

^{13}C-MRS in particular suffers from the fact that most scanners have no broadband equipment for the detection of non-proton nuclei. The advent of MRI using hyperpolarized ^{13}C might change this in the future and ^{13}C-MRS may benefit from an increasing number of broadband scanners in radiology departments. One attractive application of hyperpolarized ^{13}C-MRS has been published recently for inflammatory arthritis (MacKenzie et al. 2011; Larson and Gold 2011).

^{1}H-MRS is increasingly used in whole-body scanners to study insulin resistance and the effect on skeletal muscle. Physiologists, diabetologists, endocrinologists, pharmacologists, and other groups are often highly interested in the potential of ^{1}H-MRS of skeletal muscle, however, have no access to a scanner. It would therefore be desirable that in the future research-oriented radiologists cooperated with these groups and provided them the necessary know-how on MRS.

The combination of multinuclear MRS, i.e., the observation of muscular metabolism with more than one nucleus, gives insight into biochemical pathways which is unsurpassed by any other noninvasive method. Figure 8 illustrates how multinuclear MRS gives insight into many key positions of biochemical pathways in the human body. Other noninvasive methods can provide very specific information on metabolites that are much less concentrated than the typical MRS "suspects"; however, these methods often lack the spatial information if the samples are drawn from blood plasma, breathing air, or urine. Multinuclear MRS has a low spatial resolution, however, it can assign metabolite levels and reaction constants to a specific organ. The downside of these studies is the time required to acquire the data. While volunteers in clinical studies are willing to stay in the magnet for quite a long time, hospital administrations are usually not satisfied if that happens in the daily diagnostic routine.

In the future, MRS hopefully will benefit from several factors: (i) popular MRI applications require improved scanners with stronger gradients, stronger field strength, better SNR, etc., and MRS will benefit from these general improvements as it had in the past from shielded gradients developed for echo planar sequences, (ii) increasing distribution of broadband scanners for the observation of non-proton-nuclei, (iii) increasing collaboration of research-oriented radiologists with bedside clinicians resulting in a broader interest for functional and metabolic information. However, even if there are some very positive developments in favor of MRS, it will remain methodologically demanding and it will require special knowledge beyond anatomy.

References

Adamopoulos S, Coats AJ, Brunotte F, Arnolda L, Meyer T, Thompson CH, Dunn JF, Stratton J, Kemp GJ, Radda GK, Rajagopalan B (1993) Physical training improves skeletal muscle metabolism in patients with chronic heart failure. J Am Coll Cardiol 21:1101–1106

Akima H, Foley JM, Prior BM, Dudley GA, Meyer RA (2002) Vastus lateralis fatigue alters recruitment of musculus quadriceps femoris in humans. J Appl Physiol 92:679–684

Akman HO, Davidzon G, Tanji K, Macdermott EJ, Larsen L, Davidson MM, Haller RG, Szczepaniak LS, Lehman TJ, Hirano M, DiMauro S (2010) Neutral lipid storage disease with subclinical myopathy due to a retrotransposal insertion in the PNPLA2 gene. Neuromuscul Disord 20:397–402

Argov Z (1998) Functional evaluation techniques in mitochondrial disorders. Eur Neurol 39:65–71

Argov Z, Bank WJ (1991) Phosphorus magnetic resonance spectroscopy (31P MRS) in neuromuscular disorders. Ann Neurol 30:90–97

Argov Z, Bank WJ, Maris J, Peterson P, Chance B (1987) Bioenergetic heterogeneity of human mitochondrial myopathies: phosphorus magnetic resonance spectroscopy study. Neurology 37:257–262

Argov Z, De Stefano N, Arnold DL (1996) ADP recovery after a brief ischemic exercise in normal and diseased human muscle—a 31P MRS study. NMR Biomed 9:165–172

Argov Z, De SN, Taivassalo T, Chen J, Karpati G, Arnold DL (1997) Abnormal oxidative metabolism in exercise intolerance of undetermined origin. Neuromuscul Disord 7:99–104

Argov Z, Taivassalo T, De SN, Genge A, Karpati G, Arnold DL (1998) Intracellular phosphates in inclusion body myositis—a 31P magnetic resonance spectroscopy study. Muscle Nerve 21:1523–1525

Argov Z, Lofberg M, Arnold DL (2000) Insights into muscle diseases gained by phosphorus magnetic resonance spectroscopy. Muscle Nerve 23:1316–1334

Arnold DL, Matthews PM, Radda GK (1984) Metabolic recovery after exercise and the assessment of mitochondrial function in vivo in human skeletal muscle by means of 31P NMR. Magn Reson Med 1:307–315

Arnold DL, Taylor DJ, Radda GK (1985) Investigation of human mitochondrial myopathies by phosphorus magnetic resonance spectroscopy. Ann Neurol 18:189–196

Bajaj M, Baig R, Suraamornkul S, Hardies LJ, Coletta DK, Cline GW, Monroy A, Koul S, Sriwijitkamol A, Musi N, Shulman GI, DeFronzo RA (2010) Effects of pioglitazone on intramyocellular fat metabolism in patients with type 2 diabetes mellitus. J Clin Endocrinol Metab 95:1916–1923

Banerjee B, Sharma U, Balasubramanian K, Kalaivani M, Kalra V, Jagannathan NR (2010) Effect of creatine monohydrate in improving cellular energetics and muscle strength in ambulatory Duchenne muscular dystrophy patients: a randomized, placebo-controlled 31P MRS study. Magn Reson Imaging 28:698–707

Barbiroli B, Funicello R, Ferlini A, Montagna P, Zaniol P (1992) Muscle energy metabolism in female DMD/BMD carriers: a 31P-MR spectroscopy study. Muscle Nerve 15:344–348

Barbiroli B, Montagna P, Cortelli P, Iotti S, Lodi R, Barboni P, Monari L, Lugaresi E, Frassineti C, Zaniol P (1995) Defective brain and muscle energy metabolism shown by in vivo 31P magnetic resonance spectroscopy in nonaffected carriers of 11778 mtDNA mutation. Neurology 45:1364–1369

Barbiroli B, Frassineti C, Martinelli P, Iotti S, Lodi R, Cortelli P, Montagna P (1997) Coenzyme Q10 improves mitochondrial respiration in patients with mitochondrial cytopathies. An in vivo study on brain and skeletal muscle by phosphorous magnetic resonance spectroscopy. Cell Mol Biol 43:741–749

Barnes PR, Taylor DJ, Kemp GJ, Radda GK (1993) Skeletal muscle bioenergetics in the chronic fatigue syndrome. J Neurol Neurosurg Psychiatry 56:679–683

Baumgartner I, Thoeny HC, Kummer O, Roefke C, Skjelsvik C, Boesch C, Kreis R (2005) Leg ischemia: assessment with MR angiography and spectroscopy. Radiology 234:833–841

Beckmann N, Seelig J, Wick H (1990) Analysis of glycogen storage disease by in vivo 13C NMR: comparison of normal volunteers with a patient. Magn Reson Med 16:150–160

Befroy DE, Shulman GI (2011) Magnetic resonance spectroscopy studies of human metabolism. Diabetes 60:1361–1369

Befroy DE, Rothman DL, Petersen KF, Shulman GI (2012) 31P-magnetization transfer magnetic resonance spectroscopy measurements of in vivo metabolism. Diabetes 61:2669–2678

Beloueche-Babari M, Workman P, Leach MO (2011) Exploiting tumor metabolism for non-invasive imaging of the therapeutic activity of molecularly targeted anticancer agents. Cell Cycle 10:2883–2893

Bendahan D, Confort-Gouny S, Kozak-Ribbens G, Cozzone PJ (1992a) 31-P NMR characterization of the metabolic anomalies associated with the lack of glycogen phosphorylase activity in human forearm muscle. Biochem Biophys Res Commun 185:16–21

Bendahan D, Desnuelle C, Vanuxem D, Confort-Gouny S, Figarella-Branger D, Pellissier JF, Kozak-Ribbens G, Pouget J, Serratrice G, Cozzone PJ (1992b) 31P NMR spectroscopy and ergometer exercise test as evidence for muscle oxidative performance improvement with coenzyme Q in mitochondrial myopathies. Neurology 42:1203–1208

Bendahan D, Kozak-Ribbens G, Rodet L, Confort-Gouny S, Cozzone PJ (1998) 31Phosphorus magnetic resonance spectroscopy characterization of muscular metabolic anomalies in patients with malignant hyperthermia: application to diagnosis. Anesthesiology 88:96–107

Bendahan D, Kozak-Ribbens G, Confort-Gouny S, Ghattas B, Figarella-Branger D, Aubert M, Cozzone PJ (2001) A noninvasive investigation of muscle energetics supports similarities between exertional heat stroke and malignant hyperthermia. Anesth Analg 93:683–689

Bertocci LA, Haller RG, Lewis SF (1993) Muscle metabolism during lactate infusion in human phosphofructokinase deficiency. J Appl Physiol 74:1342–1347

Boesch C (1999) Molecular aspects of magnetic resonance imaging and spectroscopy. Mol Aspects Med 20:185–318

Boesch C (2007) Musculoskeletal spectroscopy. J Magn Reson Imaging 25:321–338

Boesch C, Kreis R (2001) Dipolar coupling and ordering effects observed in magnetic resonance spectra of skeletal muscle. NMR Biomed 14:140–148

Boesch C, Slotboom H, Hoppeler H, Kreis R (1997) In vivo determination of intra-myocellular lipids in human muscle by means of localized 1H-MR-spectroscopy. Magn Reson Med 37:484–493

Boesch C, Machann J, Vermathen P, Schick F (2006) Role of proton MR for the study of muscle lipid metabolism. NMR Biomed 19:968–988

Boss A, Broskey NT, Kreis R, Amati F, Boesch C (2013) In vivo oxidative capacity vs. mitochondrial volume density in skeletal muscle of age-matched, elderly athletes and sedentary subjects—A matter of function and content. Proc Intl Soc Magn Reson Med 21:362

Brillault-Salvat C, Giacomini E, Wary C, Peynsaert J, Jouvensal L, Bloch G, Carlier PG (1997) An interleaved heteronuclear NMRI-NMRS approach to non-invasive investigation of exercising human skeletal muscle. Cell Mol Biol 43:751–762

Cardoso M, Shoubridge E, Arnold D, Leveille M, Prud'Homme M, St-Louis G, Vinay P (1988) NMR monitoring of the energy status of skeletal muscle during hemodialysis using acetate. Clin Invest Med 11:292–296

Carey PE, Halliday J, Snaar JE, Morris PG, Taylor R (2003) Direct assessment of muscle glycogen storage after mixed meals in normal and type 2 diabetic subjects. Am J Physiol 284:E688–E694

Cea G, Bendahan D, Manners D, Hilton-Jones D, Lodi R, Styles P, Taylor DJ (2002) Reduced oxidative phosphorylation and proton efflux suggest reduced capillary blood supply in skeletal muscle of patients with dermatomyositis and polymyositis: a quantitative 31P-magnetic resonance spectroscopy and MRI study. Brain 125:1635–1645

Chance B, Eleff S, Leigh JS, Sokolow D, Sapega A (1981) Mitochondrial regulation of phophocreatine/inorganic phosphate ratios in exercising human muscle: a gated 31P NMR study. Proc Natl Acad Sci USA 78:6714–6718

Chance B, Eleff S, Bank W, Leigh JS, Warnell R (1982) 31P NMR studies of control of mitochondrial function in phosphofructokinase-deficient human skeletal muscle. Proc Natl Acad Sci USA 79:7714–7718

Chance B, Leigh JS, Clark BJ, Maris J, Kent J, Nioka S, Smith D (1985) Control of oxidative meatbolism and oxygen delivery in human skeletal muscle: a steady-state analysis of the work/energy cost transfer function. Proc Natl Acad Sci USA 82:8384–8388

Chance B, Leigh JS, Kent J, McCully K, Nioka S, Clark BJ, Maris JM, Graham T (1986) Multiple controls of oxidative metabolism in living tissues as studied by phosphorus magnetic resonance. Proc Natl Acad Sci USA 83:9458–9462

Chang G, Wang L, Cardenas-Blanco A, Schweitzer ME, Recht MP, Regatte RR (2010) Biochemical and physiological MR imaging of skeletal muscle at 7 Tesla and above. Semin Musculoskelet Radiol 14:269–278

Chilibeck PD, McCreary CR, Marsh GD, Paterson DH, Noble EG, Taylor AW, Thompson RT (1998) Evaluation of muscle oxidative potential by 31P-MRS during incremental exercise in old and young humans. Eur J Appl Physiol 78:460–465

Chinnery PF, Taylor DJ, Brown DT, Manners D, Styles P, Lodi R (2000) Very low levels of the mtDNA A3243G mutation associated with mitochondrial dysfunction in vivo. Ann Neurol 47:381–384

Chung YL, Alexanderson H, Pipitone N, Morrison C, Dastmalchi M, Stahl-Hallengren C, Richards S, Thomas EL, Hamilton G, Bell JD, Lundberg IE, Scott DL (2007) Creatine supplements in patients with idiopathic inflammatory myopathies who are clinically weak after conventional pharmacologic treatment: six-month, double-blind, randomized, placebo-controlled trial. Arthritis Rheum 57:694–702

Cline GW, Petersen KF, Krssak M, Shen J, Hundal RS, Trajanoski Z, Inzucchi S, Dresner A, Rothman DL, Shulman GI (1999) Impaired glucose transport as a cause of decreased insulin-stimulated muscle glycogen synthesis in type 2 diabetes. N Engl J Med 341:240–246

Coen PM, Jubrias SA, Distefano G, Amati F, Mackey DC, Glynn NW, Manini TM, Wohlgemuth SE, Leeuwenburgh C, Cummings SR, Newman AB, Ferrucci L, Toledo FG, Shankland E, Conley KE, Goodpaster BH (2013) Skeletal muscle mitochondrial energetics are associated with maximal aerobic capacity and walking speed in older adults. J Gerontol A Biol Sci Med Sci 68:447–455

Conley KE, Jubrias SA, Esselman PC (2000) Oxidative capacity and ageing in human muscle. J Physiol 526:203–210

Cortelli P, Montagna P, Avoni P, Sangiorgi S, Bresolin N, Moggio M, Zaniol P, Mantovani V, Barboni P, Barbiroli B (1991) Leber's hereditary optic neuropathy: genetic, biochemical, and phosphorus magnetic resonance spectroscopy study in an Italian family. Neurology 41:1211–1215

Costa FM, Canella C, Gasparetto E (2011) Advanced magnetic resonance imaging techniques in the evaluation of musculoskeletal tumors. Radiol Clin North Am 49:1325–1358

Crilley JG, Bendahan D, Boehm EA, Styles P, Rajagopalan B, Wordsworth P, Clarke K (2007) Investigation of muscle bioenergetics in the Marfan syndrome indicates reduced metabolic efficiency. J Cardiovasc Magn Reson 9:709–717

Davies RC, Eston RG, Fulford J, Rowlands AV, Jones AM (2011) Muscle damage alters the metabolic response to dynamic exercise in humans: a 31P-MRS study. J Appl Physiol 111:782–790

Dawson MJ, Gadian DG, Wilkie DR (1977) Contraction and recovery of living muscles studied by 31-P nuclear magnetic resonance. J Physiol 267:703–735

de Bisschop E, Allein S, Van der Niepen P, Verbeelen D, Luypaert R, Osteaux M, Malaisse W (1997) Effect of amino acid administration on uremic muscle metabolism: a 31P-spectroscopy study. Kidney Int 51:1182–1187

de Blecourt AC, Wolf RF, van Rijswijk MH, Kamman RL, Knipping AA, Mooyaart EL (1991) In vivo 31P magnetic resonance spectroscopy (MRS) of tender points in patients with primary fibromyalgia syndrome. Rheumatol Int 11:51–54

De Feyter HM, van den Broek NM, Praet SF, Nicolay K, van Loon LJ, Prompers JJ (2008) Early or advanced stage type 2 diabetes is not accompanied by in vivo skeletal muscle mitochondrial dysfunction. Eur J Endocrinol 158:643–653

Decombaz J, Schmitt B, Ith M, Decarli B, Diem P, Kreis R, Hoppeler H, Boesch C (2001) Post-exercise fat intake repletes intramyocellular lipids, but no faster in trained than in sedentary subjects. Am J Physiol 281:R760–R769

deKerviler E, Leroy-Willig A, Jehenson P, Duboc D, Eymard B, Syrota A (1991) Exercise-induced muscle modifications: study of healthy subjects and patients with metabolic myopathies with MR imaging and 31-P spectroscopy. Radiology 181:259–264

DiMauro S (2006) Mitochondrial myopathies. Curr Opin Rheumatol 18:636–641

Duboc D, Jehenson P, Tran DS, Marsac C, Syrota A, Fardeau M (1987) Phosphorus NMR spectroscopy study of muscular enzyme deficiencies involving glycogenolysis and glycolysis. Neurology 37:663–671

Duboc D, Jehenson P, Tamby JF, Payen JF, Syrota A, Guerin F (1991) Abnormalities of the skeletal muscle in hypertrophic cardiomyopathy. Spectroscopy using phosphorus-31 nuclear magnetic resonance. Arch Mal Coeur Vaiss 84:185–188

Dudley CR, Taylor DJ, Ng LL, Kemp GJ, Ratcliffe PJ, Radda GK, Ledingham JG (1990) Evidence for abnormal Na+/H+ antiport activity detected by phosphorus nuclear magnetic resonance spectroscopy in exercising skeletal muscle of patients with essential hypertension. Clin Sci 79:491–497

Edwards RH, Wilkie DR, Dawson MJ, Gordon RE, Shaw D (1982) Clinical use of nuclear magnetic resonance in the investigation of myopathy. Lancet 1:725–731

Eleff S, Kennaway NG, Buist NRM, Darley-Usmar VM, Bank WJ, Chance B (1984) 31P NMR study of improvement in oxidative phosphorylation by vitamins K3 and C in a patient with a defect in electron transport at complex III in skeletal muscle. Proc Natl Acad Sci USA 81:3529–3533

Erkintalo M, Bendahan D, Mattei JP, Fabreguettes C, Vague P, Cozzone PJ (1998) Reduced metabolic efficiency of skeletal muscle energetics in hyperthyroid patients evidenced quantitatively by in vivo phosphorus-31 magnetic resonance spectroscopy. Metabolism 47:769–776

Esterhammer R, Schocke M, Gorny O, Posch L, Messner H, Jaschke W, Fraedrich G, Greiner A (2008) Phosphocreatine kinetics in the calf muscle of patients with bilateral symptomatic peripheral arterial disease during exhaustive incremental exercise. Mol Imaging Biol 10:30–39

Fayad LM, Barker PB, Bluemke DA (2007) Molecular characterization of musculoskeletal tumors by proton MR spectroscopy. Semin Musculoskelet Radiol 11:240–245

Fayad LM, Jacobs MA, Wang X, Carrino JA, Bluemke DA (2012) Musculoskeletal tumors: how to use anatomic, functional, and metabolic MR techniques. Radiology 265:340–356

Finanger EL, Russman B, Forbes SC, Rooney WD, Walter GA, Vandenborne K (2012) Use of skeletal muscle MRI in diagnosis and monitoring disease progression in Duchenne muscular dystrophy. Phys Med Rehabil Clin N Am 23:1–10, ix

Flaherty JT, Weisfeldt ML, Bulkley BH, Gardner TJ, Gott VL, Jacobus WE (1982) Mechanisms of ischemic myocardial cell damage assessed by phosphorus-31 nuclear magnetic resonance. Circulation 65:561–570

Fleischman A, Kron M, Systrom DM, Hrovat M, Grinspoon SK (2009) Mitochondrial function and insulin resistance in overweight and normal-weight children. J Clin Endocrinol Metab 94:4923–4930

Forbes SC, Paganini AT, Slade JM, Towse TF, Meyer RA (2009) Phosphocreatine recovery kinetics following low- and high-intensity exercise in human triceps surae and rat posterior hindlimb muscles. Am J Physiol 296:R161–R170

Forsen S, Hoffman RA (1963) Study of moderately rapid chemical exchange reactions by means of nuclear magnetic double resonance. J Chem Phys 39:2892–2901

Frostick SP, Taylor DJ, Dolecki MJ, Radda GK (1992) Human muscle cell denervation: the results of a 31-phosphorus magnetic resonance spectroscopy study. J Hand Surg Br 17:33–45

Gadian D, Ross B, Bore P, Radda G, Hockaday J, Taylor D (1981) Examination of a myopathy by phosphorus nuclear magnetic resonance. Lancet 2:774–775

Glunde K, Bhujwalla ZM (2011) Metabolic tumor imaging using magnetic resonance spectroscopy. Semin Oncol 38:26–41

Glunde K, Bhujwalla ZM, Ronen SM (2011) Choline metabolism in malignant transformation. Nat Rev Cancer 11:835–848

Gold R, Seibel P, Reinelt G, Schindler R, Landwehr P, Beck A, Reichmann H (1996) Phosphorus magnetic resonance spectroscopy in the evaluation of mitochondrial myopathies: results of a 6-month therapy study with coenzyme Q. Eur Neurol 36:191–196

Grehl T, Muller K, Vorgerd M, Tegenthoff M, Malin JP, Zange J (1998) Impaired aerobic glycolysis in muscle phosphofructokinase deficiency results in biphasic post-exercise phosphocreatine recovery in 31P magnetic resonance spectroscopy. Neuromuscul Disord 8:480–488

Grehl T, Fischer S, Muller K, Malin JP, Zange J (2007) A prospective study to evaluate the impact of 31P-MRS to determinate mitochondrial dysfunction in skeletal muscle of ALS patients. Amyotroph Lateral Scler 8:4–8

Greiner A, Esterhammer R, Messner H, Biebl M, Muhlthaler H, Fraedrich G, Jaschke WR, Schocke MF (2006) High-energy phosphate metabolism during incremental calf exercise in patients with unilaterally symptomatic peripheral arterial disease measured by phosphor 31 magnetic resonance spectroscopy. J Vasc Surg 43:978–986

Gruetter R, Kaelin P, Boesch C, Martin E, Werner B (1990) Non-invasive P-31 magnetic resonance spectroscopy revealed McArdle disease in an asymptomatic child. Eur J Pediatr 149:483–486

Gruetter R, Prolla TA, Shulman RG (1991) 13C NMR visibility of rabbit muscle glycogen in vivo. Magn Reson Med 20:327–332

Guis S, Jouglard J, Kozak-Ribbens G, Figarella-Branger D, Vanuxem D, Pellissier JF, Cozzone PJ (2001) Malignant hyperthermia susceptibility revealed by myalgia and rhabdomyolysis during fluoroquinolone treatment. J Rheumatol 28:1405–1406

Guis S, Mattei JP, Pellissier JF, Nicoli F, Figarella-Branger D, Le Fur Y, Kaplanski G, Pelletier J, Harle JR, Cozzone PJ, Bendahan D (2004) MRI and 31PMR spectroscopy investigations of muscle function disclose no abnormality in macrophagic myofasciitis. J Rheumatol 31:2313–2314

Guis S, Mattei JP, Cozzone PJ, Bendahan D (2005) Pathophysiology and clinical presentations of rhabdomyolysis. Joint Bone Spine 72:382–391

Guis S, Figarella-Branger D, Mattei JP, Nicoli F, Le Fur Y, Kozak-Ribbens G, Pellissier JF, Cozzone PJ, Amabile N, Bendahan D (2006) In vivo and in vitro characterization of skeletal muscle metabolism in patients with statin-induced adverse effects. Arthritis Rheum 55:551–557

Guis S, Mattei JP, Bendahan D (2012) Toxic myopathies. Joint Bone Spine. doi:10.1016/j.jbspin.2012.10.008

Gupta RK, Mittal RD, Agarwal KN, Agarwal DK (1994) Muscular sufficiency, serum protein, enzymes and bioenergetic studies (31-phosphorus magnetic resonance spectroscopy) in chronic malnutrition. Acta Paediatr 83:327–331

Hagspiel KD, von Weymarn C, McKinnon G, Haldemann R, Marincek B, von Schulthess GK (1992) Effect of hypothyroidism on phosphorus metabolism in muscle and liver: in vivo P-31 MR spectroscopy study. J Magn Reson Imaging 2:527–532

Harris RC, Hultman E, Kaijser L, Nordesjo LO (1975) The effect of circulatory occlusion on isometric exercise capacity and energy metabolism of the quadriceps muscle in man. Scand J Clin Lab Invest 35:87–95

Haselgrove JC, Subramanian VH, Leigh JS, Gyulai L, Chance B (1982) In vivo one-dimensional imaging of phosphorus metabolites by phosphorus-31 nuclear magnetic resonance. Science 220:1170

Hayes DJ, Hilton-Jones D, Arnold DL, Galloway G, Styles P, Duncan J, Radda GK (1985) A mitochondrial encephalomyopathy. A combined 31P magnetic resonance and biochemical investigation. J Neurol Sci 71:105–118

Heiman-Patterson TD, Argov Z, Chavin JM, Kalman B, Alder H, DiMauro S, Bank W, Tahmoush AJ (1997) Biochemical and genetic studies in a family with mitochondrial myopathy. Muscle Nerve 20:1219–1224

Hickman PF, Kemp GJ, Thompson CH, Salisbury AJ, Wade K, Harris AL, Radda GK (1995) Bryostatin 1, a novel antineoplastic agent and protein kinase C activator, induces human myalgia and muscle metabolic defects: a 31P magnetic resonance spectroscopic study. Br J Cancer 72:998–1003

Hollingsworth KG, Jones DE, Taylor R, Blamire AM, Newton JL (2010) Impaired cardiovascular response to standing in chronic fatigue syndrome. Eur J Clin Invest 40:608–615

Horska A, Fishbein KW, Fleg JL, Spencer RG (2000) The relationship between creatine kinase kinetics and exercise intensity in human forearm is unchanged by age. Am J Physiol 279:E333–E339

Hoult DI, Busby SJW, Gadian DG, Radda GK, Richards RE, Seeley PJ (1974) Observation of tissue metabolites using 31P nuclear magnetic resonance. Nature 252:285–287

Hsieh TJ, Wang CK, Chuang HY, Jong YJ, Li CW, Liu GC (2007) In vivo proton magnetic resonance spectroscopy assessment for muscle metabolism in neuromuscular diseases. J Pediatr 151:319–321

Hsieh TJ, Jaw TS, Chuang HY, Jong YJ, Liu GC, Li CW (2009) Muscle metabolism in Duchenne muscular dystrophy assessed by in vivo proton magnetic resonance spectroscopy. J Comput Assist Tomogr 33:150–154

Ith M, Huber PM, Egger A, Schmid JP, Kreis R, Christ E, Boesch C (2010) Standardized protocol for a depletion of intramyocellular lipids (IMCL). NMR Biomed 23:532–538

Jacob S, Machann J, Rett K, Brechtel K, Volk A, Renn W, Maerker E, Matthaei S, Schick F, Claussen CD, Haring HU (1999) Association of increased intramyocellular lipid content with insulin resistance in lean nondiabetic offspring of type 2 diabetic subjects. Diabetes 48:1113–1119

Jehenson P, Duboc D, Bloch G, Fardeau M, Syrota A (1991) Diagnosis of muscular glycogenosis by in vivo natural abundance 13C NMR spectroscopy. Neuromuscul Disord 1:99–101

Jenni S, Oetliker C, Allemann S, Ith M, Tappy L, Wuerth S, Egger A, Boesch C, Schneiter PH, Diem P, Christ E, Stettler C (2008) Fuel metabolism during exercise in euglycaemia and hyperglycaemia in patients with type 1 diabetes mellitus—a prospective single-blinded randomised crossover trial. Diabetologia 51:1457–1465

Jensen KE, Jakobsen J, Thomsen C, Henriksen O (1990) Improved energy kinetics following high protein diet in McArdle's syndrome. A 31P magnetic resonance spectroscopy study. Acta Neurol Scand 81:499–503

Jeppesen TD, Quistorff B, Wibrand F, Vissing J (2007) 31P-MRS of skeletal muscle is not a sensitive diagnostic test for mitochondrial myopathy. J Neurol 254:29–37

Jones DE, Hollingsworth KG, Taylor R, Blamire AM, Newton JL (2010) Abnormalities in pH handling by peripheral muscle and potential regulation by the autonomic nervous system in chronic fatigue syndrome. J Intern Med 267:394–401

Kaminsky P, Robin-Lherbier B, Brunotte F, Escanye JM, Walker P, Klein M, Robert J, Duc M (1992) Energetic metabolism in hypothyroid skeletal muscle, as studied by phosphorus magnetic resonance spectroscopy. J Clin Endocrinol Metab 74:124–129

Kan HE, Klomp DW, Wohlgemuth M, van Loosbroek-Wagemans I, van Engelen BG, Padberg GW, Heerschap A (2010) Only fat infiltrated muscles in resting lower leg of FSHD patients show disturbed energy metabolism. NMR Biomed 23:563–568

Kemp GJ, Taylor DJ, Styles P, Radda GK (1993a) The production, buffering and efflux of protons in human skeletal muscle during exercise and recovery. NMR Biomed 6:73–83

Kemp GJ, Taylor DJ, Thompson CH, Hands LJ, Rajagopalan B, Styles P, Radda GK (1993b) Quantitative analysis by 31P magnetic resonance spectroscopy of abnormal mitochondrial oxidation in skeletal muscle during recovery from exercise. NMR Biomed 6:302–310

Kemp GJ, Hands LJ, Ramaswami G, Taylor DJ, Nicolaides A, Amato A, Radda GK (1995) Calf muscle mitochondrial and glycogenolytic ATP synthesis in patients with claudication due to peripheral vascular disease analysed using 31P magnetic resonance spectroscopy. Clin Sci 89:581–590

Kemp GJ, Roberts N, Bimson WE, Bakran A, Frostick SP (2002) Muscle oxygenation and ATP turnover when blood flow is impaired by vascular disease. Mol Biol Rep 29:187–191

Kemp GJ, Tonon C, Malucelli E, Testa C, Liava A, Manners D, Trevisi E, Martinuzzi A, Barbiroli B, Lodi R (2009) Cytosolic pH buffering during exercise and recovery in skeletal muscle of patients with McArdle's disease. Eur J Appl Physiol 105:687–694

Kent-Braun JA (2009) Skeletal muscle fatigue in old age: whose advantage? Exerc Sport Sci Rev 37:3–9

Kent-Braun JA, Sharma KR, Weiner MW, Massie B, Miller RG (1993) Central basis of muscle fatigue in chronic fatigue syndrome. Neurology 43:125–131

Kent-Braun JA, Sharma KR, Miller RG, Weiner MW (1994) Postexercise phosphocreatine resynthesis is slowed in multiple sclerosis. Muscle Nerve 17:835–841

Kent-Braun JA, Ng AV, Doyle JW, Towse TF (2002) Human skeletal muscle responses vary with age and gender during fatigue due to incremental isometric exercise. J Appl Physiol 93:1813–1823

Khushu S, Rana P, Sekhri T, Sripathy G, Tripathi RP (2010) Bioenergetic impairment in human calf muscle in thyroid disorders: a 31P MRS study. Magn Reson Imaging 28:683–689

Ko SF, Huang CC, Hsieh MJ, Ng SH, Lee CC, Lee CC, Lin TK, Chen MC, Lee L (2008) 31P MR spectroscopic assessment of muscle in patients with myasthenia gravis before and after thymectomy: initial experience. Radiology 247:162–169

Kohler SJ, Yen Y, Wolber J, Chen AP, Albers MJ, Bok R, Zhang V, Tropp J, Nelson S, Vigneron DB, Kurhanewicz J, Hurd RE (2007) In vivo 13 carbon metabolic imaging at 3T with hyperpolarized 13C-1-pyruvate. Magn Reson Med 58:65–69

Kornblum C, Schroder R, Muller K, Vorgerd M, Eggers J, Bogdanow M, Papassotiropoulos A, Fabian K, Klockgether T, Zange J (2005) Creatine has no beneficial effect on skeletal muscle energy metabolism in patients with single mitochondrial DNA deletions: a placebo-controlled, double-blind 31P-MRS crossover study. Eur J Neurol 12:300–309

Kozak-Reiss G (1989) New research on muscular function: NMR spectroscopy. Application to malignant hyperthermia. Ann Fr Anesth Reanim 8:400–405

Kozak-Reiss G, Gascard JP, Redouane-Benichou K (1986) Detection of peranesthetic malignant hyperthermia by muscle contracture tests and NMR spectroscopy. Ann Fr Anesth Reanim 5:584–589

Kreis R, Brügger K, Skjelsvik C, Zwicky S, Ith M, Jung B, Baumgartner I, Boesch C (2001) Quantitative 1H magnetic resonance spectroscopy of myoglobin de- and re-oxygenation in skeletal muscle: reproducibility and effects of localization and disease. Magn Reson Med 46:240–248

Krssak M, Petersen KF, Dresner A, DiPietro L, Vogel SM, Rothman DL, Shulman GI, Roden M (1999) Intramyocellular lipid concentrations are correlated with insulin sensitivity in humans: a 1H NMR spectroscopy study. Diabetologia 42:113–116

Kuhl CK, Layer G, Traeber F, Zierz S, Block W, Reiser M (1994) Mitochondrial encephalomyopathy: correlation of P-31 exercise MR spectroscopy with clinical findings. Radiology 192:223–230

Kuo GP, Carrino JA (2007) Skeletal muscle imaging and inflammatory myopathies. Curr Opin Rheumatol 19:530–535

Kurhanewicz J, Vigneron DB, Brindle K, Chekmenev EY, Comment A, Cunningham CH, Deberardinis RJ, Green GG, Leach MO, Rajan SS, Rizi RR, Ross BD, Warren WS, Malloy CR (2011) Analysis of cancer metabolism by imaging hyperpolarized nuclei: prospects for translation to clinical research. Neoplasia 13:81–97

Kushnir T, Knubovets T, Itzchak Y, Eliav U, Sadeh M, Rapoport L, Kott E, Navon G (1997) In vivo 23Na NMR studies of myotonic dystrophy. Magn Reson Med 37:192–196

Kutsuzawa T, Shioya S, Kurita D, Haida M, Ohta Y, Yamabayashi H (1995) Muscle energy metabolism and nutritional status in patients with chronic obstructive pulmonary disease. A 31P magnetic resonance study. Am J Respir Crit Care Med 152:647–652

Labrune P, Jehenson P, Syrota A, Odievre M (1992) In vivo 13C-NMR evaluation of glycogen content in a patient with glycogen storage disease. J Inherit Metab Dis 15:723–726

Lane RJ, Barrett MC, Taylor DJ, Kemp GJ, Lodi R (1998) Heterogeneity in chronic fatigue syndrome: evidence from magnetic resonance spectroscopy of muscle. Neuromuscul Disord 8:204–209

Lang T, Streeper T, Cawthon P, Baldwin K, Taaffe DR, Harris TB (2010) Sarcopenia: etiology, clinical consequences, intervention, and assessment. Osteoporos Int 21:543–559

Larson PE, Gold GE (2011) Science to practice: can inflammatory arthritis be monitored by using MR imaging with injected hyperpolarized 13C-pyruvate? Radiology 259:309–310

Lee S, Boesch C, Kuk JL, Arslanian S (2013) Effects of an overnight intravenous lipid infusion on intramyocellular lipid content and insulin sensitivity in African-American versus Caucasian adolescents. Metabolism 62:417–423

Leroy-Willig A, Fromes Y, Paturneau-Jouas M, Carlier P (2003) Assessing gene and cell therapies applied in striated skeletal and cardiac muscle: is there a role for nuclear magnetic resonance? Neuromuscul Disord 13:397–407

Levy P, Wuyam B, Pepin JL, Reutenauer H, Payen JF (1997) Skeletal muscle abnormalities in chronic obstructive lung disease with respiratory insufficiency. Value of P31 magnetic resonance spectroscopy. Rev Mal Respir 14:183–191

Lewis SF, Haller RG, Cook JD, Nunnally RL (1985) Muscle fatigue in McArdle's disease studied by 31P-NMR: effect of glucose infusion. J Appl Physiol 59:1991–1994

Lindquist D (2008) What can 31P MR spectroscopy tell us about muscle disease? Radiology 247:1–2

Liska D, Dufour S, Zern TL, Taksali S, Cali AM, Dziura J, Shulman GI, Pierpont BM, Caprio S (2007) Interethnic differences in muscle, liver and abdominal fat partitioning in obese adolescents. PLoS One 2:e569

Ljungberg M, Sunnerhagen KS, Vikhoff-Baaz B, Starck G, Forssell-Aronsson E, Hedberg M, Ekholm S, Grimby G (2003) 31P MRS evaluation of fatigue in anterior tibial muscle in postpoliomyelitis patients and healthy volunteers. Clin Physiol Funct Imaging 23:190–198

Lodi R, Montagna P, Iotti S, Zaniol P, Barboni P, Puddu P, Barbiroli B (1994) Brain and muscle energy metabolism studied in vivo by 31P-magnetic resonance spectroscopy in NARP syndrome. J Neurol Neurosurg Psychiatry 57:1492–1496

Lodi R, Muntoni F, Taylor J, Kumar S, Sewry CA, Blamire A, Styles P, Taylor DJ (1997a) Correlative MR imaging and 31P-MR spectroscopy study in sarcoglycan deficient limb girdle muscular dystrophy. Neuromuscul Disord 7:505–511

Lodi R, Taylor DJ, Tabrizi SJ, Kumar S, Sweeney M, Wood NW, Styles P, Radda GK, Schapira AH (1997b) In vivo skeletal muscle mitochondrial function in Leber's hereditary optic neuropathy assessed by 31P magnetic resonance spectroscopy. Ann Neurol 42:573–579

Lodi R, Cooper JM, Bradley JL, Manners D, Styles P, Taylor DJ, Schapira AH (1999a) Deficit of in vivo mitochondrial ATP production in patients with Friedreich ataxia. Proc Natl Acad Sci USA 96:11492–11495

Lodi R, Kemp GJ, Muntoni F, Thompson CH, Rae C, Taylor J, Styles P, Taylor DJ (1999b) Reduced cytosolic acidification during exercise suggests defective glycolytic activity in skeletal muscle of patients with Becker muscular dystrophy. An in vivo 31P magnetic resonance spectroscopy study. Brain 122:121–130

Lodi R, Hart PE, Rajagopalan B, Taylor DJ, Crilley JG, Bradley JL, Blamire AM, Manners D, Styles P, Schapira AH, Cooper JM (2001) Antioxidant treatment improves in vivo cardiac and skeletal muscle bioenergetics in patients with Friedreich's ataxia. Ann Neurol 49:590–596

Machann J, Schick F, Jacob S, Lutz O, Häring HU, Claussen CD (1998) MR-spectroscopic determination of extra- and intramyocellular lipids in human calf muscle and correlation with insulin sensitivity. Magn Reson Mater Phy 6-Suppl1: 220

Machann J, Stefan N, Schick F (2008) (1)H MR spectroscopy of skeletal muscle, liver and bone marrow. Eur J Radiol 67:275–284

MacKenzie JD, Yen YF, Mayer D, Tropp JS, Hurd RE, Spielman DM (2011) Detection of inflammatory arthritis by using hyperpolarized 13C-pyruvate with MR imaging and spectroscopy. Radiology 259:414–420

Madsen M, Krusenstjerna-Hafstrom T, Moller L, Christensen B, Vendelbo MH, Pedersen SB, Frystyk J, Jessen N, Hansen TK, Stodkilde-Jorgensen H, Flyvbjerg A, Jorgensen JO (2012) Fat content in liver and skeletal muscle changes in a reciprocal manner in patients with acromegaly during combination therapy with a somatostatin analog and a GH receptor antagonist: a randomized clinical trial. J Clin Endocrinol Metab 97:1227–1235

Maillefert JF, Eicher JC, Walker P, Dulieu V, Rouhier-Marcer I, Branly F, Cohen M, Brunotte F, Wolf JE, Casillas JM, Didier JP (1998) Effects of low-frequency electrical stimulation of quadriceps and calf muscles in patients with chronic heart failure. J Cardiopulm Rehabil 18:277–282

Mancini DM, Wilson JR, Bolinger L, Li H, Kendrick K, Chance B, Leigh JS (1994) In vivo magnetic resonance spectroscopy measurement of deoxymyoglobin during exercise in patients with heart failure. Demonstration of abnormal muscle metabolism despite adequate oxygenation. Circulation 90:500–508

Martinuzzi A, Liava A, Trevisi E, Frare M, Tonon C, Malucelli E, Manners D, Kemp GJ, Testa C, Barbiroli B, Lodi R (2008) Randomized, placebo-controlled, double-blind pilot trial of ramipril in McArdle's disease. Muscle Nerve 37:350–357

Massa R, Lodi R, Barbiroli B, Servidei S, Sancesario G, Manfredi G, Zaniol P, Bernardi G (1996) Partial block of glycolysis in late-onset phosphofructokinase deficiency myopathy. Acta Neuropathol 91:322–329

Massie B, Conway M, Yonge R, Frostick S, Ledingham J, Sleight P, Radda G, Rajagopalan B (1987a) Skeletal muscle metabolism in patients with congestive heart failure: relation to clinical severity and blood flow. Circulation 76:1009–1019

Massie BM, Conway M, Yonge R, Frostick S, Sleight P, Ledingham J, Radda G, Rajagopalan B (1987b) 31P nuclear magnetic resonance evidence of abnormal skeletal muscle metabolism in patients with congestive heart failure. Am J Cardiol 60:309–315

Massie BM, Conway M, Rajagopalan B, Yonge R, Frostick S, Ledingham J, Sleight P, Radda G (1988) Skeletal muscle metabolism during exercise under ischemic conditions in congestive heart failure. Evidence for abnormalities unrelated to blood flow. Circulation 78:320–326

Mattei JP, Bendahan D, Cozzone P (2004) P-31 magnetic resonance spectroscopy. A tool for diagnostic purposes and pathophysiological insights in muscle diseases. Reumatismo 56:9–14

Matthews PM, Berkovic SF, Shoubridge EA, Andermann F, Karpati G, Carpenter S, Arnold DL (1991) In vivo magnetic resonance spectroscopy of brain and muscle in a type of mitochondrial encephalomyopathy (MERRF). Ann Neurol 29:435–438

Matthews PM, Ford B, Dandurand RJ, Eidelman DH, O'Connor D, Sherwin A, Karpati G, Andermann F, Arnold DL (1993) Coenzyme Q10 with multiple vitamins is generally ineffective in treatment of mitochondrial disease. Neurology 43:884–890

McCully KK, Argov Z, Boden BP, Brown RL, Bank WJ, Chance B (1988) Detection of muscle injury in humans with 31-P magnetic resonance spectroscopy. Muscle Nerve 11:212–216

McCully KK, Forciea MA, Hack LM, Donlon E, Wheatley RW, Oatis CA, Goldberg T, Chance B (1991) Muscle metabolism in older subjects using 31P magnetic resonance spectroscopy. Can J Physiol Pharmacol 69:576–580

McCully KK, Fielding RA, Evans WJ, Leigh JS Jr, Posner JD (1993) Relationships between in vivo and in vitro measurements of metabolism in young and old human calf muscles. J Appl Physiol 75:813–819

McCully KK, Natelson BH, Iotti S, Sisto S, Leigh JS Jr (1996) Reduced oxidative muscle metabolism in chronic fatigue syndrome. Muscle Nerve 19:621–625

McCully KK, Smith S, Rajaei S, Leigh JS, Natelson BH (2003) Blood flow and muscle metabolism in chronic fatigue syndrome. Clin Sci 104:641–647

Meyer RA, Kushmerick MJ, Brown TR (1982) Application of 31P-NMR spectroscopy to the study of striated muscle metabolism. Am J Physiol 242:C1–C11

Miller RG (2002) Role of fatigue in limiting physical activities in humans with neuromuscular diseases. Am J Phys Med Rehabil 81:S99–S107

Miller RG, Boska MD, Moussavi RS, Carson PJ, Weiner MW (1988) 31P nuclear magnetic resonance studies of high energy phosphates and pH in human muscle fatigue. Comparison of aerobic and anaerobic exercise. J Clin Invest 81:1190–1196

Minotti JR, Johnson EC, Hudson TL, Zuroske G, Murata G, Fukushima E, Cagle TG, Chick TW, Massie BM, Icenogle MV (1990) Skeletal muscle response to exercise training in congestive heart failure. J Clin Invest 86:751–758

Mizuno M, Quistorff B, Theorell H, Theorell M, Chance B (1997) Effects of oral supplementation of coenzyme Q10 on 31P-NMR detected skeletal muscle energy metabolism in middle-aged post-polio subjects and normal volunteers. Mol Aspects Med 18:S291–S298

Mole PA, Chung Y, Tran TK, Sailasuta N, Hurd R, Jue T (1999) Myoglobin desaturation with exercise intensity in human gastrocnemius muscle. Am J Physiol 277:R173–R180

Montain SJ, Smith SA, Mattot RP, Zientara GP, Jolesz FA, Sawka MN (1998) Hypohydration effects on skeletal muscle performance and metabolism: a 31P-MRS study. J Appl Physiol 84:1889–1894

Moon RB, Richards JH (1973) Determination of intracellular pH by 31P magnetic resonance. J Biol Chem 248:7276–7278

Negendank W (1992) Studies of human tumors by MRS: a review. NMR Biomed 5:303–324

Newman ED, Kurland RJ (1992) P-31 magnetic resonance spectroscopy in polymyositis and dermatomyositis. Altered energy utilization during exercise. Arthritis Rheum 35:199–203

Newman RJ, Bore PJ, Chan L, Gadian DG, Styles P, Taylor D, Radda GK (1982) Nuclear magnetic resonance studies of forearm muscle in Duchenne dystrophy. Br Med J 284:1072–1074

Okuma H, Kurita D, Ohnuki T, Haida M, Shinohara Y (2007) Muscle metabolism in patients with polymyositis simultaneously evaluated by using 31P-magnetic resonance spectroscopy and near-infrared spectroscopy. Int J Clin Pract 61:684–689

Olgin J, Argov Z, Rosemberg H, Tuchler M, Chance B (1988) Non-invasive evaluation of malignant hyperthermia susceptiblity with phosphorus nuclear magnetic resonance spectroscopy. Anesthesiology 68:507–513

Olgin J, Rosenberg H, Allen G, Seestedt R, Chance B (1991) A blinded comparison of noninvasive, in vivo phosphorus nuclear magnetic resonance spectroscopy and the in vitro halothane/caffeine contracture test in the evaluation of malignant hyperthermia susceptibility. Anesth Analg 72:36–47

Pan JW, Hamm JR, Hetherington HP, Rothman DL, Shulman RG (1991) Correlation of lactate and pH in human skeletal muscle after exercise by 1H NMR. Magn Reson Med 20:57–65

Park JH, Vansant JP, Kumar NG, Gibbs SJ, Curvin MS, Price RR, Partain CL, James AE (1990) Dermatomyositis: correlative MR imaging and P-31 MR spectroscopy for quantitative characterization of inflammatory disease. Radiology 177:473–479

Park JH, Olsen NJ, King L, Vital T, Buse R, Kari S, Hernanz-Schulman M, Price RR (1995) Use of magnetic resonance imaging and P-31 magnetic resonance spectroscopy to detect and quantify muscle dysfunction in the amyopathic and myopathic variants of dermatomyositis. Arthritis Rheum 38:68–77

Park JH, Kari S, King LE Jr, Olsen NJ (1998a) Analysis of 31P MR spectroscopy data using artificial neural networks for longitudinal evaluation of muscle diseases: dermatomyositis. NMR Biomed 11:245–256

Park JH, Phothimat P, Oates CT, Hernanz-Schulman M, Olsen NJ (1998b) Use of P-31 magnetic resonance spectroscopy to detect metabolic abnormalities in muscles of patients with fibromyalgia. Arthritis Rheum 41:406–413

Park JH, Niermann KJ, Ryder NM, Nelson AE, Das A, Lawton AR, Hernanz-Schulman M, Olsen NJ (2000) Muscle abnormalities in juvenile dermatomyositis patients: P-31 magnetic resonance spectroscopy studies. Arthritis Rheum 43:2359–2367

Parry A, Matthews PM (2003) Roles for imaging in understanding the pathophysiology, clinical evaluation, and management of patients with mitochondrial disease. J Neuroimaging 13:293–302

Payen JF, Bosson JL, Bourdon L, Jacquot C, Le Bas JF, Stieglitz P, Benabid AL (1993) Improved noninvasive diagnostic testing for malignant hyperthermia susceptibility from a combination of metabolites determined in vivo with 31P-magnetic resonance spectroscopy. Anesthesiology 78:848–855

Pedersen BL, Baekgaard N, Quistorff B (2009) Muscle mitochondrial function in patients with type 2 diabetes mellitus and peripheral arterial disease: implications in vascular surgery. Eur J Vasc Endovasc Surg 38:356–364

Penn AM, Lee JW, Thuillier P, Wagner M, Maclure KM, Menard MR, Hall LD, Kennaway NG (1992) MELAS syndrome with mitochondrial tRNA(Leu)(UUR) mutation: correlation of clinical state, nerve conduction, and muscle 31P magnetic resonance spectroscopy during treatment with nicotinamide and riboflavin. Neurology 42:2147–2152

Penn AM, Roberts T, Hodder J, Allen PS, Zhu G, Martin WR (1995) Generalized mitochondrial dysfunction in Parkinson's disease detected by magnetic resonance spectroscopy of muscle. Neurology 45:2097–2099

Perseghin G, Price TB, Petersen KF, Roden M, Cline GW, Gerow K, Rothman DL, Shulman GI (1996) Increased glucose transport-phosphorylation and muscle glycogen synthesis after exercise training in insulin-resistant subjects. N Engl J Med 335:1357–1362

Perseghin G, Scifo P, De Cobelli F, Pagliato E, Battezzati A, Arcelloni C, Vanzulli A, Testolin G, Pozza G, Del Maschio A, Luzi L (1999) Intramyocellular triglyceride content is a determinant of in vivo insulin resistance in humans: a 1H–13C nuclear magnetic resonance spectroscopy assessment in offspring of type 2 diabetic parents. Diabetes 48:1600–1606

Petersen KF, Shulman GI (2006) New insights into the pathogenesis of insulin resistance in humans using magnetic resonance spectroscopy. Obesity 14(Suppl 1):34S–40S

Petersen KF, Hendler R, Price T, Perseghin G, Rothman DL, Held N, Amatruda JM, Shulman GI (1998) 13C/31P NMR studies on the mechanism of insulin resistance in obesity. Diabetes 47:381–386

Petersen KF, Befroy D, Dufour S, Dziura J, Ariyan C, Rothman DL, DiPietro L, Cline GW, Shulman GI (2003) Mitochondrial dysfunction in the elderly: possible role in insulin resistance. Science 300:1140–1142

Petersen KF, Dufour S, Befroy D, Garcia R, Shulman GI (2004) Impaired mitochondrial activity in the insulin-resistant offspring of patients with type 2 diabetes. N Engl J Med 350:664–671

Pfleiderer B, Lange J, Loske KD, Sunderkotter C (2004) Metabolic disturbances during short exercises in dermatomyositis revealed by real-time functional 31P magnetic resonance spectroscopy. Rheumatology 43:696–703

Phielix E, Mensink M (2008) Type 2 diabetes mellitus and skeletal muscle metabolic function. Physiol Behav 94:252–258

Phielix E, Szendroedi J, Roden M (2011) Mitochondrial function and insulin resistance during aging—a mini-review. Gerontology 57:387–396

Philip PA, Thompson CH, Carmichael J, Rea D, Mitchell K, Taylor DJ, Stuart NS, Dennis I, Rajagopalan B, Ganesan T (1993) A phase I study of the left-shifting agent BW12C79 plus mitomycin C and the effect on the skeletal muscle metabolism using 31P magnetic resonance spectroscopy. Cancer Res 53:5649–5653

Pola A, Sadananthan SA, Yaligar J, Nagarajan V, Han W, Kuchel PW, Velan SS (2012) Skeletal muscle lipid metabolism studied by advanced magnetic resonance spectroscopy. Prog NMR Spectroscopy 65:66–76

Price TB, Krishnan-Sarin S, Rothman DL (2003) Smoking impairs muscle recovery from exercise. Am J Physiol 285:E116–E122

Propper DJ, Braybrooke JP, Taylor DJ, Lodi R, Styles P, Cramer JA, Collins WC, Levitt NC, Talbot DC, Ganesan TS, Harris AL (1999) Phase I trial of the selective mitochondrial toxin MKT077 in chemo-resistant solid tumours. Ann Oncol 10:923–927

Quistorff B, Johansen L, Sahlin K (1993) Absence of phosphocreatine resynthesis in human calf muscle during ischaemic recovery. Biochem J 291:681–686

Radda GK, Bore PJ, Gadian DG, Ross BD, Styles P, Taylor DJ, Morgan-Hughes J (1982) 31P NMR examination of two patients with NADH-CoQ reductase deficiency. Nature 295:608–609

Reeves RR (1996) Effects of thyroid hormone treatment on 31P-NMR spectroscopy of muscle and on nerve conduction studies in a patient with long-standing severe hypothyroidism. J Am Osteopath Assoc 96:424–428

Ross BD, Radda GK, Gadian DG, Rocker G, Esiri M, Falconer-Smith J (1981) Examination of a case of suspected McArdle's syndrome by 31P nuclear magnetic resonance. N Engl J Med 304:1338–1342

Rothman DL, Shulman RG, Shulman GI (1992) 31P nuclear magnetic resonance measurements of muscle glucose-6-phosphate: evidence for reduced insulin-dependent muscle glucose transport or phosphorylation activity in non-insulin-dependent diabetes mellitus. J Clin Invest 89:1069–1075

Rothman DL, Magnusson I, Cline G, Gerard D, Kahn CR, Shulman RG, Shulman GI (1995) Decreased muscle glucose transport/phosphorylation is an early defect in the pathogenesis of non-insulin-dependent diabetes mellitus. Proc Natl Acad Sci USA 92:983–987

Rotman S, Slotboom J, Kreis R, Boesch C, Jequier E (2000) Muscle glycogen recovery after exercise measured by 13C-MRS in humans: effect of nutritional solutions. Magn Reson Mater Phys 11:114–121

Salerno C, Iotti S, Lodi R, Crifo C, Barbiroli B (1997) Failure of muscle energy metabolism in a patient with adenylosuccinate lyase deficiency. An in vivo study by phosphorus NMR spectroscopy. Biochim Biophys Acta 1360:271–276

Sato T, Katabami T, Furukawa K, Narimatsu H, Hashimoto T, Nakajima Y, Ohta A, Sasaoka T, Tanaka Y (2012) Intracellular lipid content of liver and skeletal muscle in patients with adult growth hormone deficiency without diabetes mellitus. Obes Res Clin Pract 6:e321–e329

Savage DB, Petersen KF, Shulman GI (2007) Disordered lipid metabolism and the pathogenesis of insulin resistance. Physiol Rev 87:507–520

Scheuermann-Freestone M, Madsen PL, Manners D, Blamire AM, Buckingham RE, Styles P, Radda GK, Neubauer S, Clarke K (2003) Abnormal cardiac and skeletal muscle energy metabolism in patients with type 2 diabetes. Circulation 107:3040–3046

Schick F, Eismann B, Jung WI, Bongers H, Bunse M, Lutz O (1993) Comparison of localized proton NMR signals of skeletal muscle and fat tissue in vivo: two lipid compartments in muscle tissue. Magn Reson Med 29:158–167

Schocke MF, Esterhammer R, Ostermann S, Santner W, Gorny O, Fraedrich G, Jaschke WR, Greiner A (2006) High-energy phosphate metabolism during calf ergometry in patients with isolated aorto-iliac artery stenoses. Invest Radiol 41:874–882

Schocke M, Esterhammer R, Greiner A (2008) High-energy phosphate metabolism in the exercising muscle of patients with peripheral arterial disease. Vasa 37:199–210

Schröder L, Weber MA, Ulrich M, Regula JU (2006) Metabolic imaging of atrophic muscle tissue using appropriate markers in 1H and 31P NMR spectroscopy. Neuroradiology 48:809–816

Schroers A, Kley RA, Stachon A, Horvath R, Lochmuller H, Zange J, Vorgerd M (2006) Gentamicin treatment in McArdle disease: failure to correct myophosphorylase deficiency. Neurology 66:285–286

Schunk K, Romaneehsen B, Rieker O, Duber C, Kersjes W, Schadmand-Fischer S, Schmiedt W, Thelen M (1998) Dynamic phosphorus-31 magnetic resonance spectroscopy in arterial occlusive disease: effects of vascular therapy on spectroscopic results. Invest Radiol 33:329–335

Seo Y, Murakami M, Watari H, Imai Y, Yoshizaki K, Nishikawa H, Moromoto T (1983) Intracellular pH determination by a 31P-NMR technique. The second dissociation constant of phosphoric acid in a biological system. J Biochem 94:729–734

Sharma U, Kumar V, Wadhwa S, Jagannathan NR (2007) In vivo (31)P MRS study of skeletal muscle metabolism in patients with postpolio residual paralysis. Magn Reson Imaging 25:244–249

Shulman GI, Rothman DL, Jue T, Stein P, DeFronzo RA, Shulman RG (1990) Quantitation of muscle glycogen synthesis in normal subjects and subjects with non-insulin-dependent diabetes by 13C nuclear magnetic resonance spectroscopy. N Engl J Med 322:223–228

Siciliano G, Rossi B, Martini A, Angelini C, Martinuzzi A, Lodi R, Zaniol P, Barbiroli B, Muratorio A (1995) Myophosphorylase deficiency affects muscle mitochondrial respiration as shown by 31P-MR spectroscopy in a case with associated multifocal encephalopathy. J Neurol Sci 128:84–91

Simms RW, Roy SH, Hrovat M, Anderson JJ, Skrinar G, LePoole SR, Zerbini CA, de Luca C, Jolesz F (1994) Lack of association between fibromyalgia syndrome and abnormalities in muscle energy metabolism. Arthritis Rheum 37:794–800

Sivakumar K, Vasconcelos O, Goldfarb L, Dalakas MC (1996) Late-onset muscle weakness in partial phosphofructokinase deficiency: a unique myopathy with vacuoles, abnormal mitochondria, and absence of the common exon 5/intron 5 junction point mutation. Neurology 46:1337–1342

Subhawong TK, Wang X, Durand DJ, Jacobs MA, Carrino JA, Machado AJ, Fayad LM (2012) Proton MR spectroscopy in metabolic assessment of musculoskeletal lesions. AJR Am J Roentgenol 198:162–172

Taivassalo T, De Stefano N, Argov Z, Matthews PM, Chen J, Genge A, Karpati G, Arnold DL (1998) Effects of aerobic training in patients with mitochondrial myopathies. Neurology 50:1055–1060

Taivassalo T, De SN, Chen J, Karpati G, Arnold DL, Argov Z (1999) Short-term aerobic training response in chronic myopathies. Muscle Nerve 22:1239–1243

Tarnopolsky M (2012) Exercise testing in metabolic myopathies. Phys Med Rehabil Clin N Am 23:173–86, xii

Tarnopolsky MA, Raha S (2005) Mitochondrial myopathies: diagnosis, exercise intolerance, and treatment options. Med Sci Sports Exerc 37:2086–2093

Taylor DJ (2000) Clinical utility of muscle MR spectroscopy. Semin Musculoskelet Radiol 4:481–502

Taylor DJ, Bore PJ, Styles P, Gadian DG, Radda GK (1983) Bioenergetics of intact human muscle: a 31P nuclear magnetic resonance study. Mol Biol Med 1:77–94

Taylor DJ, Styles P, Matthews PM, Arnold DA, Gadian DG, Bore P, Radda GK (1986) Energetics of human muscels: exercise-induced ATP depletion. Magn Reson Med 3:44–54

Taylor DJ, Rajagopalan B, Radda GK (1992) Cellular energetics in hypothyroid muscle. Eur J Clin Invest 22:358–365

Taylor DJ, Kemp GJ, Woods CG, Edwards JH, Radda GK (1993) Skeletal muscle bioenergetics in myotonic dystrophy. J Neurol Sci 116:193–200

Taylor DJ, Krige D, Barnes PR, Kemp GJ, Carroll MT, Mann VM, Cooper JM, Marsden CD, Schapira AH (1994) A 31P magnetic resonance spectroscopy study of mitochondrial function in skeletal muscle of patients with Parkinson's disease. J Neurol Sci 125:77–81

Taylor DJ, Amato A, Hands LJ, Kemp GJ, Ramaswami G, Nicolaides A, Radda GK (1996) Changes in energy metabolism of calf muscle in patients with intermittent claudication assessed by 31P magnetic resonance spectroscopy: a phase II open study. Vasc Med 1:241–245

Teranishi T, Ohara T, Maeda K, Zenibayashi M, Kouyama K, Hirota Y, Kawamitsu H, Fujii M, Sugimura K, Kasuga M (2007) Effects of pioglitazone and metformin on intracellular lipid content in liver and skeletal muscle of individuals with type 2 diabetes mellitus. Metabolism 56:1418–1424

Thamer C, Machann J, Bachmann O, Haap M, Dahl D, Wietek B, Tschritter O, Niess A, Brechtel K, Fritsche A, Claussen C, Jacob S, Schick F, Haring HU, Stumvoll M (2003) Intramyocellular lipids: anthropometric determinants and relationships with maximal aerobic capacity and insulin sensitivity. J Clin Endocrinol Metab 88:1785–1791

Thompson CH, Davies RJ, Kemp GJ, Taylor DJ, Radda GK, Rajagopalan B (1993) Skeletal muscle metabolism during exercise and recovery in patients with respiratory failure. Thorax 48:486–490

Thompson CH, Kemp GJ, Barnes PR, Rajagopalan B, Styles P, Taylor DJ, Radda GK (1994) Uraemic muscle metabolism at rest and during exercise. Nephrol Dial Transplant 9:1600–1605

Thompson CH, Macaulay VM, O'Byrne KJ, Kemp GJ, Wilner SM, Talbot DC, Harris AL, Radda GK (1996) Modulation of bryostatin 1 muscle toxicity by nifedipine: effects on muscle metabolism and oxygen supply. Br J Cancer 73:1161–1165

Torriani M, Townsend E, Thomas BJ, Bredella MA, Ghomi RH, Tseng BS (2012) Lower leg muscle involvement in Duchenne muscular dystrophy: an MR imaging and spectroscopy study. Skeletal Radiol 41:437–445

Tosetti M, Linsalata S, Battini R, Volpi L, Cini C, Presciutti O, Muntoni F, Cioni G, Siciliano G (2011) Muscle metabolic alterations assessed by 31-phosphorus magnetic resonance spectroscopy in mild Becker muscular dystrophy. Muscle Nerve 44:816–819

Trenell MI, Sue CM, Kemp GJ, Sachinwalla T, Thompson CH (2006a) Aerobic exercise and muscle metabolism in patients with mitochondrial myopathy. Muscle Nerve 33:524–531

Trenell MI, Thompson CH, Sue CM (2006b) Exercise and myotonic dystrophy: a 31P magnetic resonance spectroscopy and magnetic resonance imaging case study. Ann Neurol 59:871–872

Trenell MI, Sue CM, Thompson CH, Kemp GJ (2007) Supplemental oxygen and muscle metabolism in mitochondrial myopathy patients. Eur J Appl Physiol 99:541–547

Trepp R, Fluck M, Stettler C, Boesch C, Ith M, Kreis R, Hoppeler H, Howald H, Schmid JP, Diem P, Christ ER (2008) Effect of growth hormone (GH) on human skeletal muscle lipid metabolism in GH-deficiency. Am J Physiol 294:E1127–E1134

van Elderen SG, Doornbos J, van Essen EH, Lemkes HH, Maassen JA, Smit JW, De Roos A (2009) Phosphorus-31 magnetic resonance spectroscopy of skeletal muscle in maternally inherited diabetes and deafness A3243G mitochondrial mutation carriers. J Magn Reson Imaging 29:127–131 van Tienen FH, Praet SF, De Feyter HM, van den Broek NM, Lindsey PJ, Schoonderwoerd KG, de Coo I, Nicolay K, Prompers JJ, Smeets HJ, van Loon LJ (2012) Physical activity is the key determinant of skeletal muscle mitochondrial function in type 2 diabetes. J Clin Endocrinol Metab 97:3261–3269

Vanderthommen M, Duteil S, Wary C, Raynaud JS, Leroy-Willig A, Crielaard JM, Carlier PG (2003) A comparison of voluntary and electrically induced contractions by interleaved 1H- and 31P-NMRS in humans. J Appl Physiol 94:1012–1024

Vermathen P, Saillen P, Boss A, Zehnder M, Boesch C (2012) Skeletal muscle 1H MRSI before and after prolonged exercise I. muscle specific depletion of intramyocellular lipids. Magn Reson Med 68:1357–1367

Vissing J, Vissing SF, MacLean DA, Saltin B, Quistorff B, Haller RG (1998) Sympathetic activation in exercise is not dependent on muscle acidosis. Direct evidence from studies in metabolic myopathies. J Clin Invest 101:1654–1660

Vita G, Toscano A, Bresolin N, Meola G, Fortunato F, Baradello A, Barbiroli B, Frassineti C, Zaniol P, Messina C (1994) Muscle phosphoglycerate mutase (PGAM) deficiency in the first Caucasian patient: biochemistry, muscle culture and 31P-MR spectroscopy. J Neurol 241:289–294

Vorgerd M, Zange J (2002) Carbohydrate oxidation disorders of skeletal muscle. Curr Opin Clin Nutr Metab Care 5:611–617

Vorgerd M, Grehl T, Jager M, Muller K, Freitag G, Patzold T, Bruns N, Fabian K, Tegenthoff M, Mortier W, Luttmann A, Zange J, Malin JP (2000) Creatine therapy in myophosphorylase deficiency (McArdle disease): a placebo-controlled crossover trial. Arch Neurol 57:956–963

Vorgerd M, Kilimann MW, Zange J, Malin JP (2002a) Muskelglykogenosen. Dtsch Ärzteblatt 99:A2328–A2340

Vorgerd M, Zange J, Kley R, Grehl T, Husing A, Jager M, Muller K, Schroder R, Mortier W, Fabian K, Malin JP, Luttmann A (2002b) Effect of high-dose creatine therapy on symptoms of exercise intolerance in McArdle disease: double-blind, placebo-controlled crossover study. Arch Neurol 59:97–101

Walker UA (2008) Imaging tools for the clinical assessment of idiopathic inflammatory myositis. Curr Opin Rheumatol 20:656–661

Wang Z, Noyszewski EA, Leigh JS (1990) In vivo MRS measurement of deoxymyoglobin in human forearms. Magn Reson Med 14:562–567

Wang X, Jacobs MA, Fayad L (2011) Therapeutic response in musculoskeletal soft tissue sarcomas: evaluation by MRI. NMR Biomed 24:750–763

Wary C, Laforet P, Eymard B, Fardeau M, Leroy-Willig A, Bassez G, Leroy JP, Caillaud C, Poenaru L, Carlier PG (2003) Evaluation of muscle glycogen content by 13C NMR spectroscopy in adult-onset acid maltase deficiency. Neuromuscul Disord 13:545–553

Wary C, Nadaj-Pakleza A, Laforet P, Claeys KG, Carlier R, Monnet A, Fleury S, Baligand C, Eymard B, Labrune P, Carlier PG (2010) Investigating glycogenosis type III patients with multi-parametric functional NMR imaging and spectroscopy. Neuromuscul Disord 20:548–558

Weber MA, Essig M, Kauczor HU (2007) Radiological diagnostics of muscle diseases. Fortschr Röntgenstr 179:712–720

Weber MA, Krakowski-Roosen H, Schroder L, Kinscherf R, Krix M, Kopp-Schneider A, Essig M, Bachert P, Kauczor HU, Hildebrandt W (2009) Morphology, metabolism, microcirculation, and strength of skeletal muscles in cancer-related cachexia. Acta Oncol 48:116–124

Weiss R, Dufour S, Taksali SE, Tamborlane WV, Petersen KF, Bonadonna RC, Boselli L, Barbetta G, Allen K, Rife F, Savoye M, Dziura J, Sherwin R, Shulman GI, Caprio S (2003) Prediabetes in obese youth: a syndrome of impaired glucose tolerance, severe insulin resistance, and altered myocellular and abdominal fat partitioning. Lancet 362:951–957

Weissman JD, Constantinitis I, Hudgins P, Wallace DC (1992) 31P magnetic resonance spectroscopy suggests impaired mitochondrial function in AZT-treated HIV-infected patients. Neurology 42:619–623

Wells GD, Noseworthy MD, Hamilton J, Tarnopolski M, Tein I (2008) Skeletal muscle metabolic dysfunction in obesity and metabolic syndrome. Can J Neurol Sci 35:31–40

Wells GD, Wilkes DL, Schneiderman JE, Rayner T, Elmi M, Selvadurai H, Dell SD, Noseworthy MD, Ratjen F, Tein I, Coates AL (2011) Skeletal muscle metabolism in cystic fibrosis and primary ciliary dyskinesia. Pediatr Res 69:40–45

Wilhelm T, Bachert P (2001) In vivo 31P echo-planar spectroscopic imaging of human calf muscle. J Magn Reson 149:126–130

Wilson JR, Fink L, Maris J, Ferraro N, Power-Vanwart J, Eleff S, Chance B (1985) Evaluation of energy metabolism in skeletal muscle of patients with heart failure with gated phosphorus-31 nuclear magnetic resonance. Circulation 71:57–62

Wong R, Lopaschuk G, Zhu G, Walker D, Catellier D, Burton D, Teo K, Collins-Nakai R, Montague T (1992) Skeletal muscle metabolism in the chronic fatigue syndrome. In vivo assessment by 31P nuclear magnetic resonance spectroscopy. Chest 102: 1716–1722

Wray DW, Nishiyama SK, Monnet A, Wary C, Duteil S, Carlier PG, Richardson RS (2009a) Multiparametric NMR-based assessment of skeletal muscle perfusion and metabolism during exercise in elderly persons: preliminary findings. J Gerontol A Biol Sci Med Sci 64:968–974

Wray DW, Nishiyama SK, Monnet A, Wary C, Duteil SS, Carlier PG, Richardson RS (2009b) Antioxidants and aging: NMR-based evidence of improved skeletal muscle perfusion and energetics. Am J Physiol 297:H1870–H1875

Wu JS, Buettner C, Smithline H, Ngo LH, Greenman RL (2011) Evaluation of skeletal muscle during calf exercise by 31-phosphorus magnetic resonance spectroscopy in patients on statin medications. Muscle Nerve 43:76–81

Zange J, Grehl T, Disselhorst-Klug C, Rau G, Muller K, Schroder R, Tegenthoff M, Malin JP, Vorgerd M (2003) Breakdown of adenine nucleotide pool in fatiguing skeletal muscle in McArdle's disease: a noninvasive 31P-MRS and EMG study. Muscle Nerve 27:728–736

Zatina MA, Berkowitz HD, Gross GM, Maris JM, Chance B (1986) 31P nuclear magnetic resonance spectroscopy: noninvasive biochemical analysis of the ischemic extremity. J Vasc Surg 3:411–420

Zochodne DW, Koopman WJ, Witt NJ, Thompson T, Driedger AA, Gravelle D, Bolton CF (1992) Forearm P-31 nuclear magnetic resonance spectroscopy studies in oculopharyngeal muscular dystrophy. Can J Neurol Sci 19:174–179

Dynamic MR Imaging of the Skeletal Musculature: From Static Measures to a Dynamic Assessment of the Muscular (Loco-) Motion

Shantanu Sinha and Usha Sinha

Contents

1 Key Points 166

2 Introduction 166

3 Magnetic Resonance Imaging 167
3.1 Velocity Encoded-Phase Contrast MR (VE-PC MR) Imaging 167
3.2 Displacement Imaging (Spin Tag Imaging) 167
3.3 Displacement Imaging (DENSE Imaging) 168

4 Strain and Strain Rate Mapping 168
4.1 Two-Dimensional Strain Rate Mapping 171

5 MR Compatible Device for MR Measurements 173

6 Velocity Encoded-Phase Contrast (VE-PC) MR Musculoskeletal Imaging 173
6.1 Soleus 175
6.2 Medial Gastrocs 177

7 Functional Imaging of Muscle: Altered and Diseased Conditions 179
7.1 Achilles Tendon Rupture 179
7.2 Chronic Unloading 180

8 2D and 3D Strain and Strain Rate Measurements in Skeletal Muscles 181

9 Conclusions 182

References 182

Abstract

The muscle–tendon is a complex structure and involves the complex interplay of passive and active elements, fiber architecture that ultimately determines the force transmission and muscle mechanics. The ability to noninvasively image the muscle–tendon complex during contractions provides an unprecedented tool to study the normal physiology and its changes under different conditions (e.g., in normal aging, sarcopenia, limb disuse and muscle atrophy, and muscle diseases such as dystrophy). We describe the development of sophisticated MR imaging sequences that can directly map muscle motion (velocity), or muscle tissue displacement. A brief overview of imaging sequences, post processing is provided as a background to the technology. The derivation of 1D, 2D and 3D strain, and strain rate maps is outlined underlying the ability to extract the complete 3D strain tensor from appropriate MR datasets. The MR-compatible device to enable different muscle motion is described in detail; this piece is critical for the successful implementation of functional muscle dynamics using MRI. Velocity and strain distributions in the normal lower leg muscles, in the forearm are presented. These studies highlight the heterogeneous strain distributions and the link to connective tissue distribution in the muscles as well as to the geometry of the fibers (fiber length, pennation angle, and curvature differences along the length the muscle aponeurosis). These studies have also identified inter- and intra-fascicular heterogeneities in strain and in novel indices such as the architectural gear ratio. Tendon dynamics can also be mapped using the velocity-encoded data and force-dependent length changes, stiffness, and the transition point from linear to nonlinear behavior of the force-length (F-L) curve in human Achilles tendon are discussed. The applications of these elegant MR techniques to altered muscle conditions are presented; however the number of studies is limited. The application of MR dynamic muscle

---

S. Sinha (✉)
Department of Radiology, University of California,
San Diego, CA 92130, USA
e-mail: shsinha@mail.ucsd.edu

U. Sinha
Department of Physics, San Diego State University,
San Diego, CA, USA

M.-A. Weber (ed.), *Magnetic Resonance Imaging of the Skeletal Musculature*, Medical Radiology. Diagnostic Imaging,
DOI: 10.1007/174_2013_927, © Springer-Verlag Berlin Heidelberg 2013

Published Online: 24 October 2013

imaging with the velocity encoded-phase contrast imaging to subjects with Achilles tendon rupture and chronic unloading under controlled conditions are presented. In both applications, the utility of the technique in identifying muscle functional and structural changes indicate that this is a valuable tool awaiting widespread clinical implementation. This chapter concludes with technical developments in this area of MR imaging where 2D and 3D strain tensor mappings are outlined. These developments offer exciting possibilities to explore muscle structure and functional relationships. Coupled with diffusion tensor imaging to extract muscle fiber architecture, dynamic 3D muscle imaging will enable the detailed understanding of muscle physiology in normal and altered conditions.

1 Key Points

1. Functional Magnetic Resonance Imaging of skeletal muscle is presented in this chapter.
2. Velocity, displacement, strain, strain rate muscle imaging has become possible.
3. A MR compatible device for muscle motion imaging is described.
4. Velocity and strain maps in lower leg muscles (soleus, medial gastrocnemius), Achilles tendon, forearm (biceps brachii), and the quadriceps femorii are now possible to obtain.
5. Velocity and strain maps in subjects with Achilles tendon rupture and under chronic unloading are introduced under controlled conditions.
6. Recent developments in 2D and 3D strain tensor imaging and their potential to correlate with muscle fiber directions from diffusion tensor imaging are presented in this chapter.

2 Introduction

To understand the muscle–tendon mechanics during locomotion, it is necessary to know the detailed architecture of the muscle and its dynamics during contractions. Action of a muscle is functionally coupled with its adjacent structures, creating a complex interaction between passive and active tissues. Importantly, the force from the active muscle is transmitted longitudinally to tendons and laterally to the neighboring agonist and even antagonist muscles (15). In humans, studies on the relative movement between muscles and strain in the aponeurosis between the muscles may provide information on the force transmission (2, 8, 9, 13). Dynamic magnetic resonance (MR) imaging techniques have made it possible to characterize in vivo motion and shortening of skeletal muscle tissue during joint movement. For example, cine phase-contrast (cine-PC) magnetic resonance images taken of the long head of the biceps brachii showed nonuniform shortening along some muscle fascicles during low-load elbow flexion (Pappas et al. 2002).

Although many of the cellular properties of muscle fiber and sarcomere are well understood, the relationship between muscle geometry and function of the whole muscle (and muscle–tendon complex) requires much more elucidation. Most of our understanding has come from in vitro and in situ muscle preparations. Furthermore, relatively little attention has been given to the physiology of aponeurosis and tendon during active muscle. With an improved geometric muscle model, we would be allowed to gain insight into better understandings of the effects of architectural properties on muscle function and also, better predictions of force-length and force-velocity relationships. Therefore, effects of aging (Narici et al. 2004), training (Aagaard et al. 2001; Kawakami et al. 1993) and clinical intervention (chronic unloading) (Abe et al. 2001; Akima et al. 2000; Kawakami et al. 2000; Narici and Cerretelli 1998), surgical operations (e.g. tendon rupture reconstruction, tenotomy and aponeurotomy) (Jaspers et al. 1999, 2002; Lieber 1993) on muscle function can be more accurately predicted.

Within the last decade, advances in noninvasive technology have begun to allow muscle physiologists to gain greater insight into these strain events of in vivo human muscle contraction. Fukunaga et al. 1997; Narici et al. 1996), have used ultrasound techniques to visualize changes in fascicle lengths in human muscle during contractions. Fukunaga (1997) found that “the compliance of the muscle-tendon unit causes internal shortening of fascicles even during isometric contractions.” More recently, Fukunaga found that the difference in muscle–tendon complex length between eccentric and concentric action in the human vastus lateralis muscle in vivo is due to the series elastic component (SEC). “The SEC is stretched during eccentric phase, and recoiled during concentric phase.” Also by using ultrasound, Narici et al. (1996) analyzed changes in the architecture of the human medial gastrocnemius muscle during an in vivo isometric contraction and passive change in joint angle. They found that the fiber length decreased from 57.0 to 34.0 mm when the ankle moved from 90 to 150°, and decreased from 50.8 to 32.9 mm during an isometric contraction. They also found changes in the pennation angles of the muscle fibers in both situations.

A detailed understanding of these strain events within muscular complexes can provide new insight into the etiology of a variety of musculoskeletal strain injuries, both chronic and acute (Garrett 1996; Noonan 1994; Kibler 1990). Dynamic MR imaging allows velocity or displacement mapping and allows strain mapping in 3D. The data from these experimental studies can be used to create accurate subject specific mathematical models of selected muscle–tendon complexes. These studies have led to a clearer understanding of the normal strain events in human muscle–tendon complexes as a function of force and can potentially greatly improve our ability to identify the critical elements of motor output and the control mechanisms related to these output properties.

3 Magnetic Resonance Imaging

3.1 Velocity Encoded-Phase Contrast MR (VE-PC MR) Imaging

Phase contrast MR techniques use bipolar gradients to sensitize signal intensity to motion (velocity). Two sequences with reversed polarities of the bipolar gradients are acquired in succession and a complex subtraction of the images yields phase images where the phase at each voxel is a direct measure of the velocity (scaled by the magnitude of the velocity encoding magnetic field gradients). Gradient sensitization can be performed along all three directions, allowing measurement of the velocity vector (Drace and Pelc 1994a, b, c, d). While the ability to directly encode velocity is a very attractive feature, significant errors in quantification are introduced by phase variations arising from sources such as magnetic field inhomogeneities and eddy currents.

3.1.1 Phase Correction

The phase contrast images directly provide measurement of the velocity but prior to extraction of the velocity data, corrections have to be made to remove other contributions to phase (shading artifacts). Three schemes for phase correction were evaluated using a phantom with a known motion pattern (Sinha et al. 2004). They determined that the most reliable method for phase shading correction was to subtract an average of the dynamic images from each individual frame in the dynamic phases. This method, selected on the basis of preliminary studies, is based on the assumption that the average velocity in the tissue during one cycle of motion is zero (Finni et al. 2003a).

3.1.2 Advantages of Velocity Encoded-Phase Contrast MRI for Tendomuscular Dynamics

Most of the early in vivo muscle length changes have been measured using sonomicrometry in animal models where the transmitting and receiving crystals are sutured to the origin and insertion of the muscle fascicle (Biewener et al. 1998; Griffiths 1991; Roberts et al. 1997). In human studies, noninvasive ultrasonography has been widely used to measure fascicle length changes during isometric (Ito et al. 1998) and dynamic exercises (Finni et al. 2001; Fukunaga et al. 2001).

Velocity encoded-phase contrast (VE-PC) MRI is a definitive method of quantifying flow noninvasively and in vivo. It has been widely used in angiography and cardiovascular flow quantification, in determining blood flow patterns and myocardial motion. While uniform flow can be imaged ungated, a pulsatile flow requires gating typically to the electrocardiogram (ECG) trace. Repetitive skeletal muscle motion (Drace and Pelc 1994b), bone movement (Brossmann et al. 1993), and tendon strain (Drace and Pelc 1994a; Finni et al. 2003b; Sheehan et al. 1999; Sheehan and Drace 2000) can be imaged with innovative strategies, substituting the R-wave of ECG by an electronic spike to which repetitive motion of a part of the body is synchronized for gating purposes. MRI can also be used to detect the orientation of muscle fascicles (Scott et al. 1993). All of these studies can be done in vivo, noninvasively, and combined with all the strengths of MRI, including excellent soft tissue contrast, nonionizing radiation, oblique plane prescription, and velocity encoding orthogonal to these planes. Similar to ultrasonography, phase contrast MRI also has limited time resolution, but the visualized area can be much greater ($\sim$30 cm), allowing observation of tissue movement in large areas simultaneously with excellent spatial resolution. This is important for understanding the complex interactions between muscle and tendon tissues, interaction between muscle groups and the joint effect of muscle architecture, and function in vivo.

The ultrasonographic method requires that the probe be oriented strictly perpendicular to the muscle fascicle plane in order to visualize the fascicles. In many muscles, particularly during dynamic exercises, detection of the fascicles becomes difficult due to 3D rotation rather than movement in 2D plane. The method of PC MRI particularly with 3D velocity encoding overcomes this difficulty. The authors' group has firmly established this technique as a viable clinical tool for assessment of muscle function.

3.2 Displacement Imaging (Spin Tag Imaging)

MR also offers the capability to map tissue displacements so that strain can be calculated directly from the data. In Spin Tag imaging, the radiofrequency pulses invert spatially separated thin bands of protons in the imaging plane. Subsequent dynamic imaging allows visualization of the tag motion as distortion of the tagged lines in subsequent temporal phases (Zerhouni et al. 1988; Axel and Dougherty 1989; Niitsu et al. 1992; Pipe et al. 1991). While spin tag imaging permits direct visualization of tissue motion, it suffers from fading of the tag lines due to T1 relaxation and requires complex postprocessing to derive the displacement at each pixel (Sinha et al.

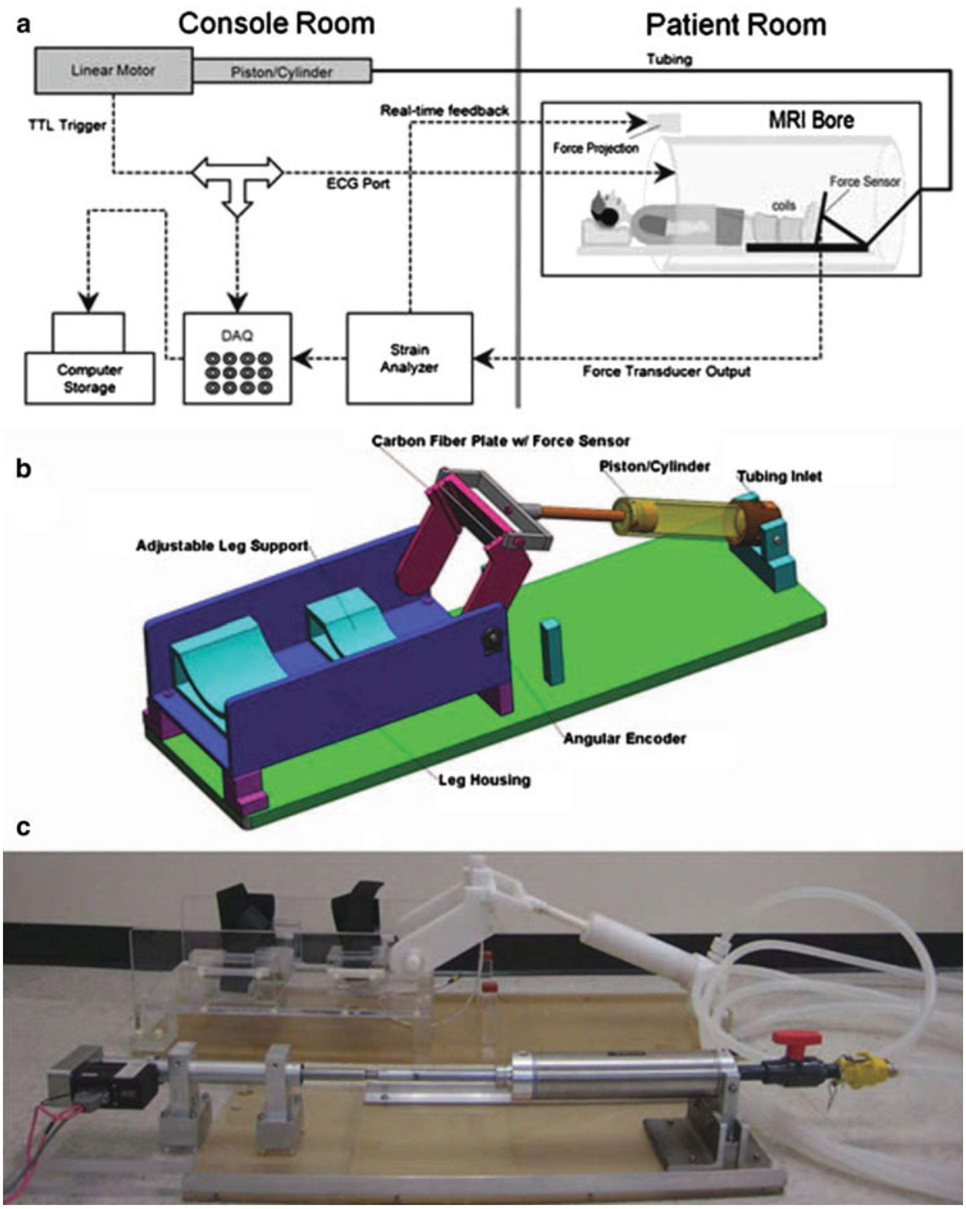
a
Console Room
Patient Room
Linear Motor
Piston/Cylinder
Tubing
TTL Trigger
Real-time feedback
MRI Bore
Force Projection
ECG Port
Force Sensor
coils
Computer Storage
DAQ
Strain Analyzer
Force Transducer Output
b
Carbon Fiber Plate w/ Force Sensor
Piston/Cylinder
Tubing Inlet
Adjustable Leg Support
Angular Encoder
Leg Housing
c

Fig. 1 **a** Schematic diagram of the experimental setup. The experimental components are interconnected via coaxial cables. Work output of the motor was transmitted to the foot pedal via hydraulic fluid (water) in high-pressure tubing. The tube passed from the *console room* to the MRI scanning room through a waveguide in the wall. Force data from the foot pedal was projected onto the *white* front surface of the magnet through a projector for realtime feedback to the subject. An electronic trigger signal was transmitted directly from the motor to the ECG port of the scanner at a preselected point of each contraction cycle for gated image acquisition. **b** Schematic of the foot pedal apparatus: assembly of all CAD parts. Different components are annotated. **c** Photo of the actual foot-pedal device. The motor is shown in the *lower left* connected to the stainless steel piston-cylinder, hydraulic tubing coiled on the right, connected to the white, nonmetallic *piston-cylinder* which goes inside the magnet bore. The piston can be seen connected to the foot pedal in the upper middle part of the picture. (Reprinted with permission from Sinha et al. 2012*)*

2004; Kinugasa et al. 2008). Spin tag imaging has been used to derive 3D strain tensors (Englund et al. 2011). Comparison of spin tag and phase contrast imaging for muscle motion mapping is presented later.

3.3 Displacement Imaging (DENSE Imaging)

MR imaging using displacement encoding with stimulated echoes (DENSE) has been used in a few studies to map 2D strain fields (Zhong et al. 2008). In this technique, the sequence encodes tissue displacement into the phase of the stimulated echo, relative to an initial displacement encoding time. A sequence of phase reconstructed images is obtained using cine DENSE MRI to achieve the required spatial resolution to extract tissue displacements.

4 Strain and Strain Rate Mapping

Strain describes how the tissue is deformed with respect to a reference state and requires 3D tissue tracking. Strain rate (SR) describes the rate of regional deformation (deformation or strain per unit time) and does not require 3D tracking, or a reference state since strain rate is an instantaneous measure of kinematic properties.

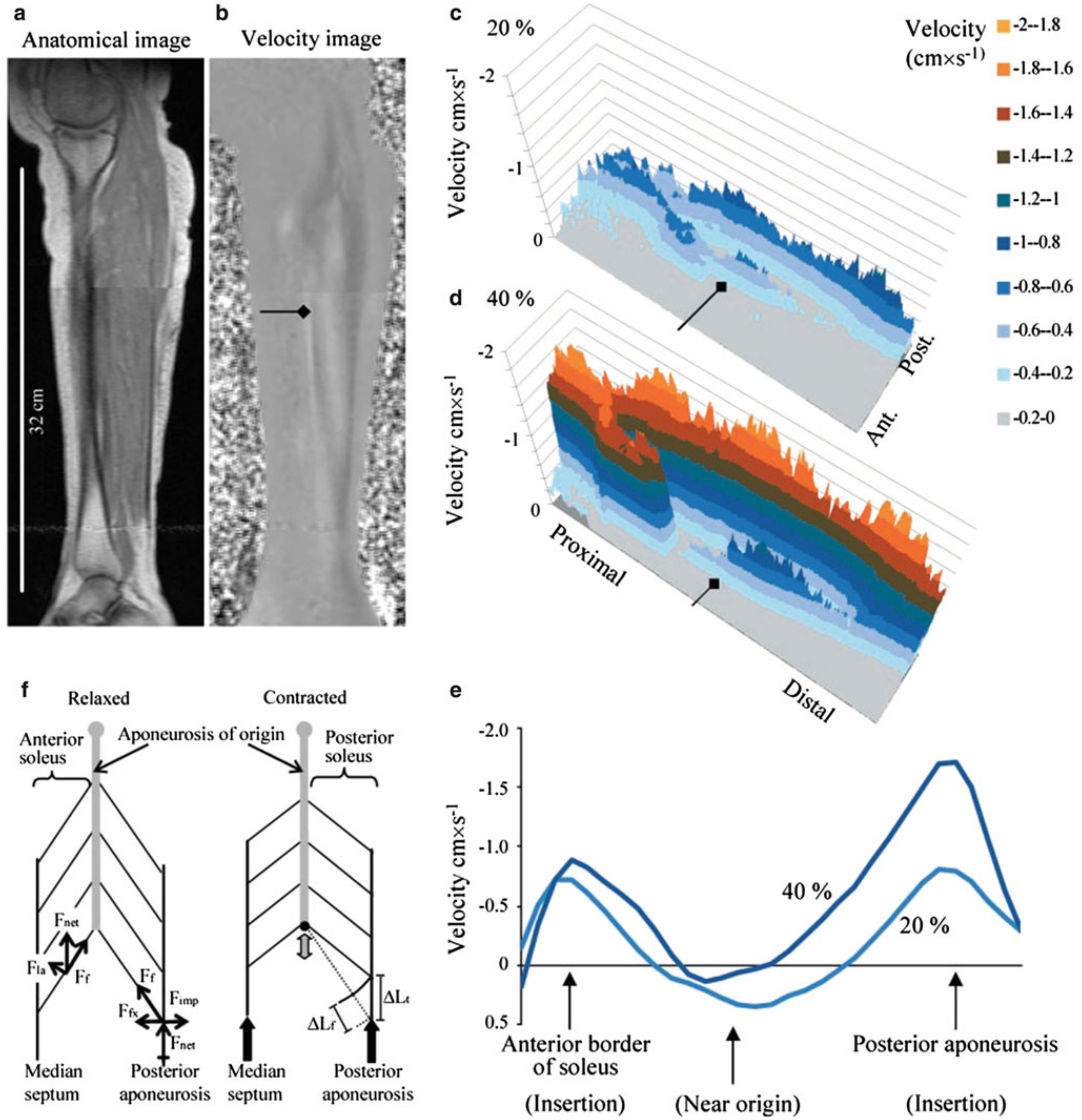
a
Anatomical image
32 cm
b
Velocity image
c
20 %
Velocity cm×s⁻¹
-2
-1
0
Velocity (cm×s⁻¹)
-2--1.8
-1.8--1.6
-1.6--1.4
-1.4--1.2
-1.2--1
-1--0.8
-0.8--0.6
-0.6--0.4
-0.4--0.2
-0.2-0
Post.
Ant.
d
40 %
Proximal
Distal
f
Relaxed
Contracted
Anterior soleus
Aponeurosis of origin
Posterior soleus
Fnet
Fla
Ff
Fimp
Ffx
ΔLt
ΔLf
Median septum
Posterior aponeurosis
e
-2.0
-1.5
-1.0
-0.5
0
0.5
40 %
20 %
Anterior border of soleus
(Insertion)
(Near origin)
Posterior aponeurosis
(Insertion)

Fig. 2 Cine phase-contrast MR images provide both anatomy (**a**) and velocity (**b**) image sequences. These sagittal images (and data in **c**–**e**) were taken from the beginning of the contraction during early force rise. In **b**, the *dark* and *light gray shades* represent high velocities in the proximal and distal direction, respectively. Contour velocity maps of the soleus during 20 (**c**) and 40 % (**d**) MVC further illustrate the velocity distributions and their dependence on load. The negative velocities represent movement proximally. Positive velocities are not shown in these plots for clarity. **e** velocity distribution across the soleus muscle taken from midmuscle at the level of the diamond arrows shown in **b**–**d**. The midmuscle moves distally, whereas the anterior and posterior edges of the muscle move proximally. **f** a simple model of part of the soleus muscle in relaxed and contracted conditions illustrating the relative movement of the aponeuroses (*thick arrows*) and consequent rotation of the muscle fibers. Rotation of the fibers while the interaponeuroses distance is kept constant results in a smaller change in fiber length (ΔL_f) than in tendon length (ΔL_t). Force vectors placed on the anterior soleus (relaxed scheme) illustrate the idea that longitudinally (F_f) and laterally (F_{la}) transmitted forces relative to the fiber orientation produce a net force (F_{net}) in the proximal direction to produce proximal tissue movements that supplement fiber length changes in shortening contractions. Force vectors placed on the posterior soleus show that the intramuscular pressure (F_{imp}) counteracts the fiber force component (F_{fx}) that would move the aponeuroses closer together. (Reprinted with permission from Finni et al. 2003b)

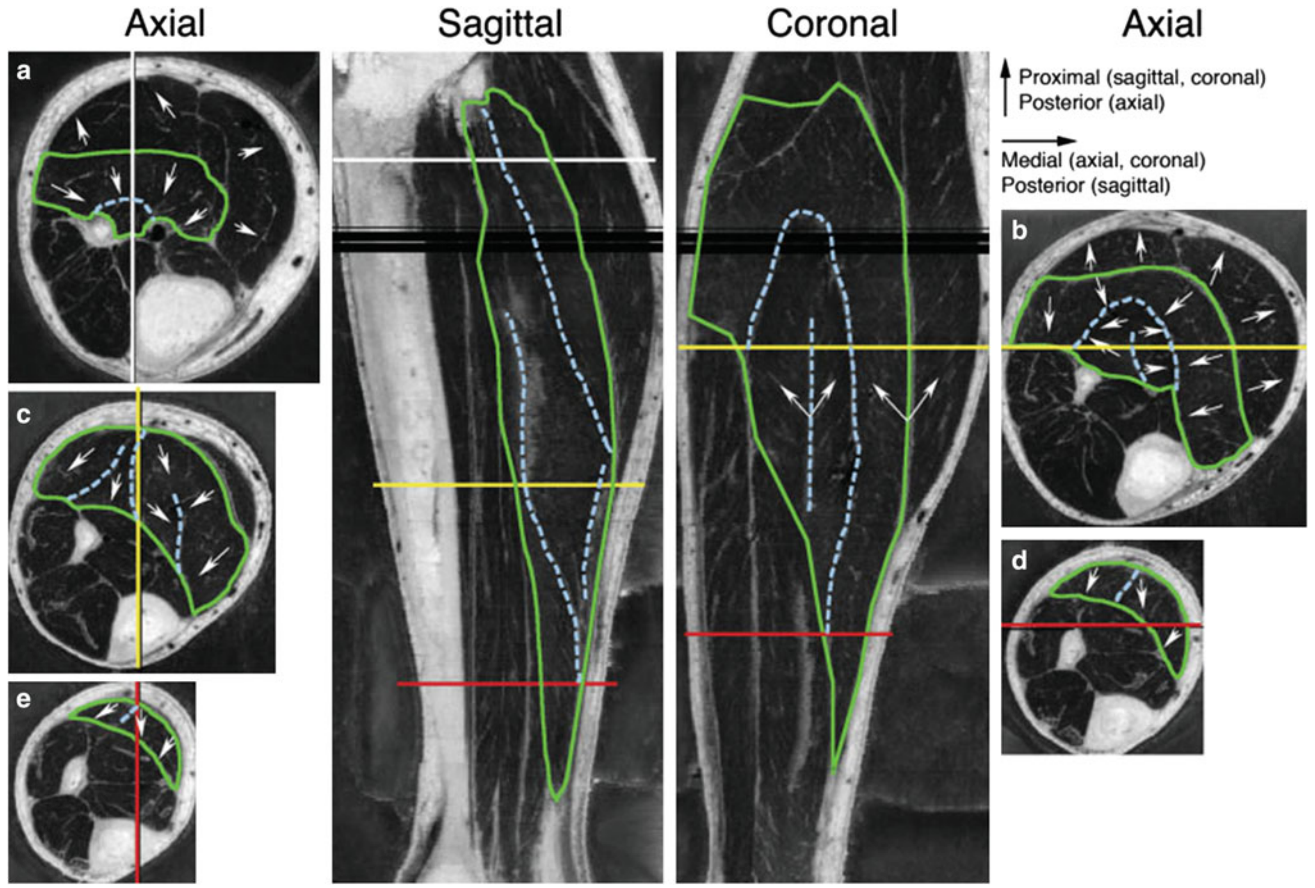

Fig. 3 *Axial* and computer reconstructed *sagittal* and *coronal* images from the Visible Human Dataset. The levels of the three *axial* images on the *left* (*Axial* **a, c, e**) are shown in the sagittal image using color-coded lines. The orientation of the *sagittal* image is shown by *vertical lines* in the *axial* images. Similarly, the orientations of the *coronal* and *axial* images on the *right* (*Axial* **b, d**) are color coded. The *green lines* outline the soleus muscle and the *dashed light blue lines* identify the major intramuscular connective tissue structures. In the proximal leg, the *dashed light blue lines* distinguish the anterior compartment of the soleus muscle (*Axial* **a, b**). The *arrows* show the orientation of the bands of white tissue that probably correspond to fascicle orientation. The *arrowheads* indicate the more proximal end of the fascicles. Note that the fascicles may not be oriented along the plane of the *coronal* or *sagittal* sections. The dark bands across the *sagittal* and *coronal* images indicate missing data. (Reprinted with permission from Hodgson et al. 2006)

1D strain is calculated with respect to a reference length (e.g., a baseline length, L_0). The strain,ε, in one dimension is defined as:

$$\varepsilon_{1D} = L - L_0/L_0$$

where L is the length in the ‘deformed’ state. Strain is dimensionless and represents the fractional or percentage change in dimension.

It is also possible to define the instantaneous strain defined by:

$$\varepsilon_{1D}(t) = L(t) - L_0(t)/L_0(t)$$

It should be noted that there are two types of strain defined based on the reference length. If the reference length is the initial length, the strain is called Lagrangian strain. On the other hand, if the reference length (e.g., in the instantaneous strain) is a previous time point (rather than a static reference at the initial time point), it is then termed as the natural or engineering strain.

1D strain rate, ε_{SR}, is defined as:

$$\varepsilon_{SR} = \frac{\Delta\varepsilon}{\Delta t} = \frac{\left(\Delta L/_{L_0}\right)}{\Delta t} = \frac{\left(\Delta L/_{\Delta t}\right)}{L_0} = \frac{\Delta v}{L_0}$$

where Δv is the velocity gradient and ε_{SR} has the units of $\sec^{-1}$. Strain rate has the same direction as the strain (negative strain during shortening and positive strain during elongation). Velocity encoded-phase contrast MRI provides a direct measure of velocity and this strain rates can be directly measured from them.

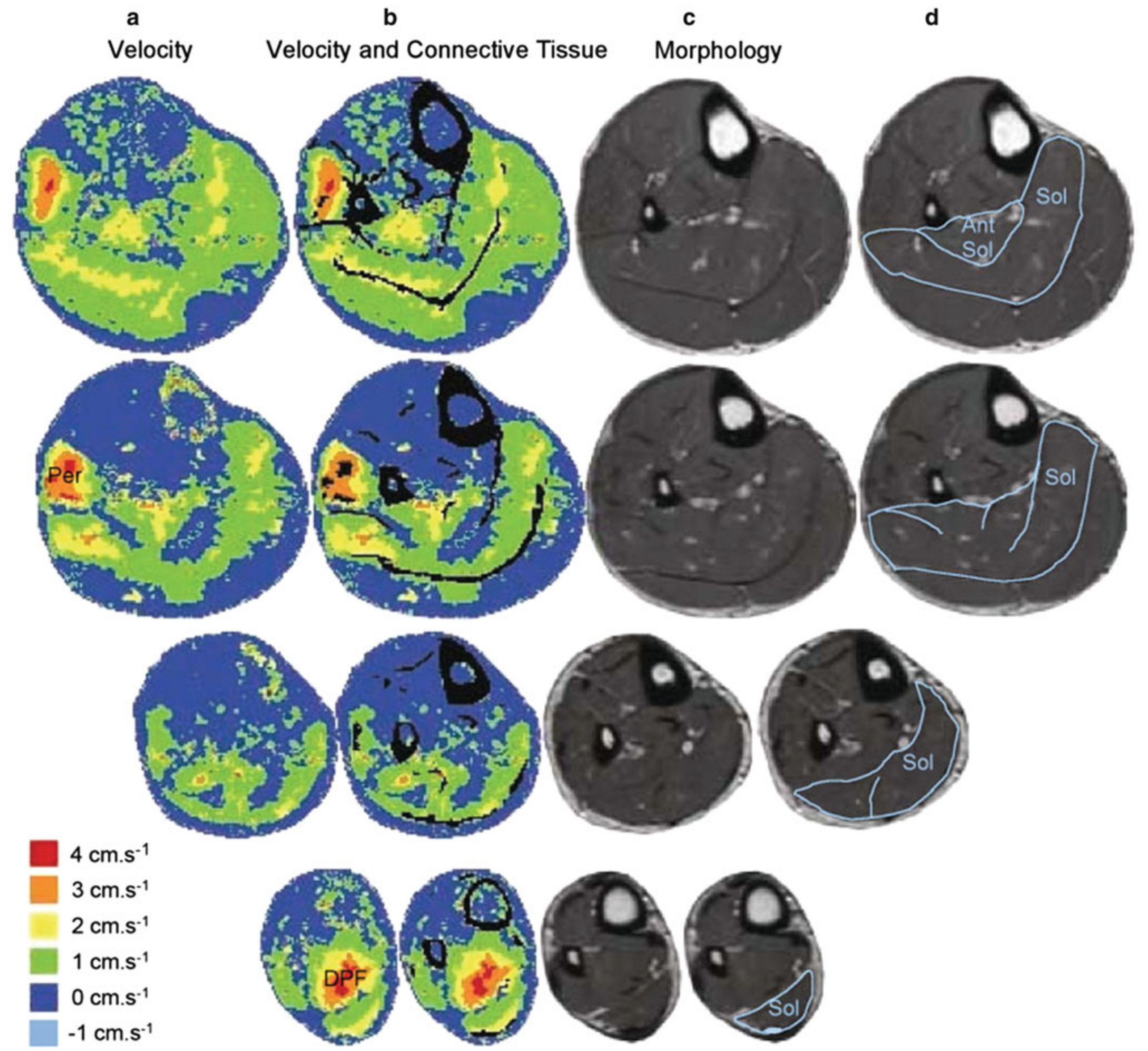

Fig. 4 Axial images to show the relationship between the leg structures and the velocities recorded during isometric contractions. Each row illustrates data from different levels of the calf musculature. **a** Velocities in the superior–inferior direction during early force development. Speckled areas in the cortical bone and tendon are noise due to low signal levels from these tissues. **b** Cortical bone and connective tissue are shown in black and superimposed on the velocity images. Note the correspondence between the distribution of velocities and connective tissues within several muscles. **c** The morphological images used to identify bone and connective tissue. **d** The morphological images with the soleus muscle and its major connective tissue components identified. Note that the regions near the soleus aponeurosis of insertion (posterior aponeurosis and median septum) had faster velocities than regions close to the aponeurosis of origin (anterior aponeurosis). Note also that this subject activated the deep plantarflexors (DPF) and peroneus muscle (Per), shown by the higher velocities in the area to the left of the fibula. (Reprinted with permission from Hodgson et al. 2006)

4.1 Two-Dimensional Strain Rate Mapping

The 2D spatial gradient of the velocity vector, L is first calculated as:

$$L = \begin{bmatrix} \frac{\partial u}{\partial x} \frac{\partial u}{\partial y} ; & \frac{\partial v}{\partial x} \frac{\partial v}{\partial y} \end{bmatrix}$$

where u and v are the x and y components of the velocity vector. Next, the symmetric part of the strain rate tensor is calculated from: $\varepsilon_{2D} = 0.5(L + L^T)$. The 2×2 strain rate tensor, ε_{2D}, is then diagonalized to obtain the eigenvalues and eigenvectors. The positive and negative values at each voxel representing the local expansion and contraction, respectively, are usually stored as separate images.

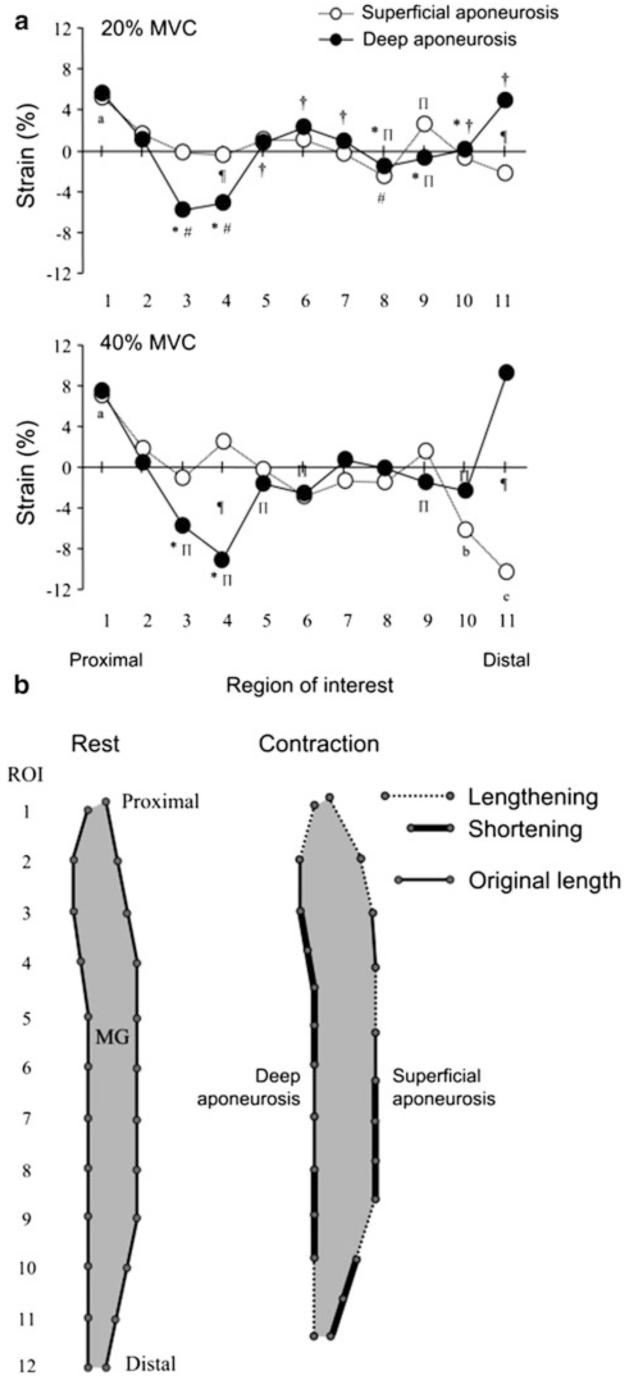

Fig. 5 (*Left column*) Strain distribution along the superficial and deep aponeuroses. **a** average strain distribution along the superficial and deep aponeuroses during 20 (*top*) and 40 % (*bottom*) MVC from eight subjects. Positive and negative strain indicate lengthening and shortening, respectively. Values are means. *$P < 0.05$ versus ROI 1; ≠$P < 0.05$ versus ROI 2; †$P < 0.05$ versus ROI 3; _$P < 0.05$ versus ROI 11; a$P < 0.05$ versus from ROI 3 to ROIs 8, 10, and 11; b$P < 0.05$ versus ROIs 2, 4, and 10; c$P < 0.05$ versus ROIs 2–9; ¶$P < 0.05$, 20 versus 40 % MVC. **b** model of strain distribution along the proximal–distal axis of both aponeuroses. This model resulted from the strain during 40 % MVC. *Dashed lines* indicate location of aponeurosis lengthening, and thick *solid lines* indicate location of aponeurosis shortening. Thin solid lines are the original length of the aponeurosis, i.e., where strain is undetectable. (Reprinted with permission from Kinugasa et al. 2008)

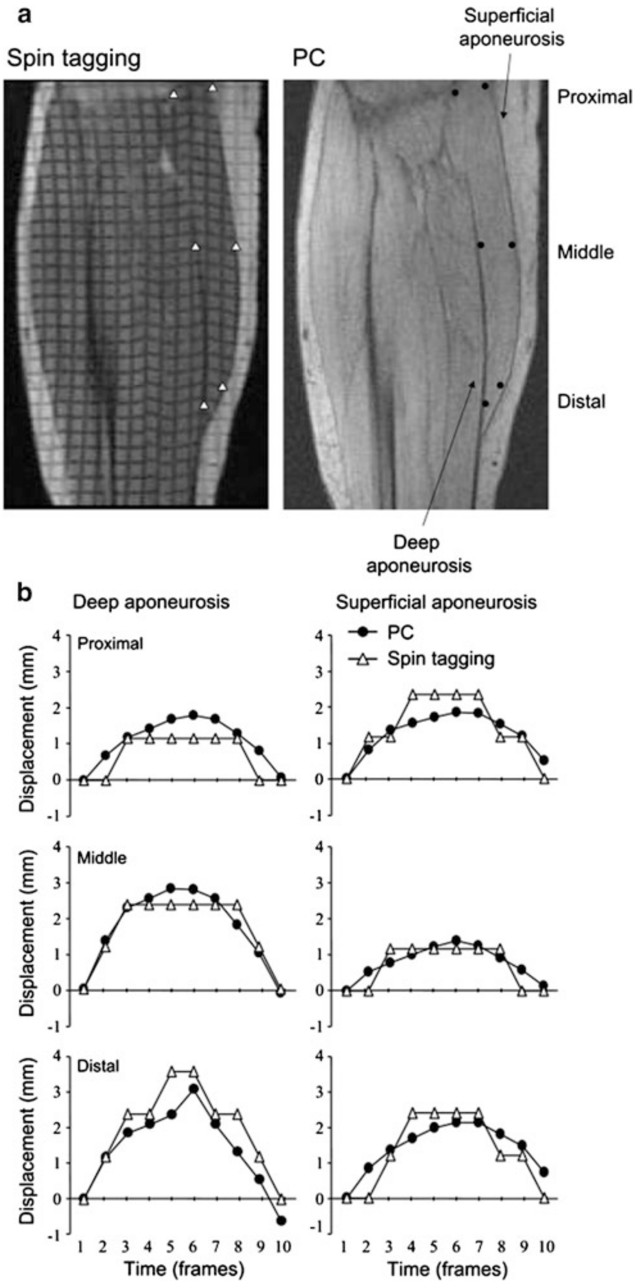
a
Spin tagging
PC
Superficial aponeurosis
Proximal
Middle
Distal
Deep aponeurosis
b
Deep aponeurosis
Superficial aponeurosis
Proximal
PC
Spin tagging
Middle
Distal
Displacement (mm)
Time (frames)

Fig. 6 (*Right column*) Validation of displacement as determined from PC MRI by comparison with spin-tag experiment. **a** representative oblique–sagittal spin tagging and PC images during phase 6, which correspond to the peak torque. ROIs are prescribed graphically along both the superficial and deep aponeuroses. **b** displacement at three different points along the superficial and deep aponeuroses during the first 10 phases is compared between the PC and spin-tagged data. The single-pixel resolution of the spin-tag data results in steps in the displacement curves, whereas the subpixel resolution of the PC imaging provides smoother curves. The displacement measurements show good correlation (r = 0.89 for superficial aponeurosis and r = 0.89 for deep aponeurosis). (Reprinted with permission from Kinugasa et al. 2008)

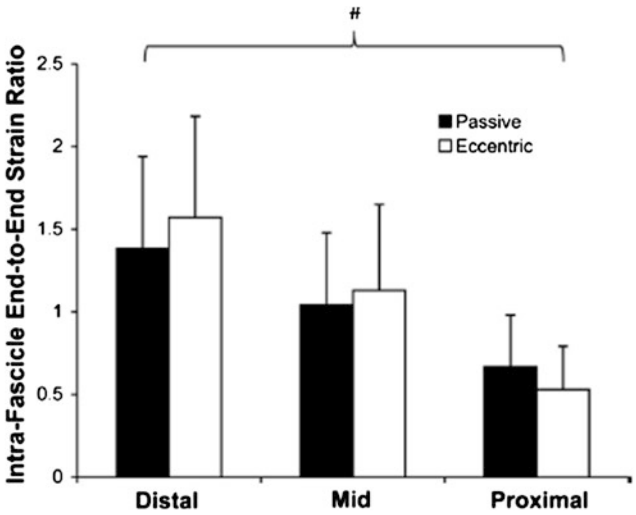

Fig. 7 *Left* Intrafascicular end-to-end strain ratio for all subjects showing significant regional differences but no difference between the passive and eccentric mode. Values are mean ± SD; n = 12 (*distal*), 30 (*mid*), and 12 (*proximal*). (Reprinted with permission from Shin et al. 2009)

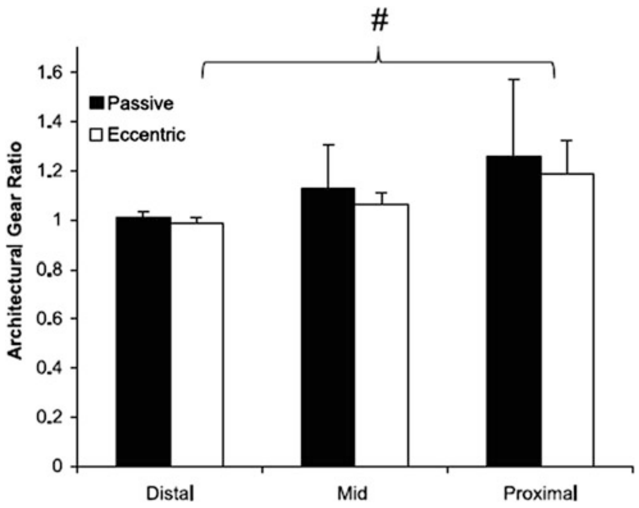

Fig. 8 *Right* Architectural gear ratio as a function of muscle region and mode of contraction. Summary data from all subjects are shown. $\neq P < 0.05$, significant differences between all regions. Values are mean ± SD; n = 12 (*distal*), 30 (*mid*), and 12 (*proximal*). (Reprinted with permission from Shin et al. 2009)

The same procedure is applied to map 2D strains except that the 2D velocity vector (u, v) in the above equation will be replaced with the 2D deformation vector (where the deformation vector is estimated for a given voxel with respect to a reference position). The extension to 3D will involve the velocity vector and deformation vector in 3D and the spatial derivatives will have t estimated in all three (x, y, and z) directions.

5 MR Compatible Device for MR Measurements

Dynamic MRI studies of the musculoskeletal (MSK) system require MR compatible devices to enable the acquisition of displacement/velocity sensitive images under different contraction conditions. Sinha et al. report the design and development of an MR-compatible, computer-controlled, foot-pedal device capable of operating inside the bore of an MR scanner at both 1.5 and 3 Tesla (Sinha et al. 2012). This device enabled dynamic acquisitions to map the changes in strain and shape during passive and neutral conditions and at different activation levels, load, and ankle joint angle under dynamic conditions of plantarflexion or dorsiflexion use. Figure 1 shows the schematic of the setup including the positioning of the foot pedal and subject in the scanner. The foot was secured with a Velcro strap and subjects could exert force against the foot-pedal plate during plantarflexion (concentric contraction) or dorsiflexion (eccentric contraction), or exert no force at all for passive movement. Provision for isometric contraction was also made with the foot pedal anchored at a neutral 90°. A Fabry–Perot optical strain gauge bonded to the foot pedal and the force proportional output voltage was projected in real-time to provide feedback and modulate the contraction from the subject. The output is also used to generate a trigger pulse for gating the acquisition during isometric contractions.

A modification of this device for dynamic images of the thigh has also been reported (Sinha et al. 2013). Zhong et al. have reported an MR compatible device to perform a full range of elbow flexion–extension in order to map displacements and strains in the biceps brachii muscle (Zhong et al. 2008). Image acquisition was gated to the onset of elbow flexion using a photodiode circuit.

6 Velocity Encoded-Phase Contrast (VE-PC) MR Musculoskeletal Imaging

The first study of musculoskeletal imaging using velocity encoded-phase contrast imaging was reported by Drace and Pelc (Drace and Pelc 1994a, b, c, d). In the latter study, they successfully tracked the in vivo motion of the human forearm muscles during finger extension and flexion, and the muscles of the anterior and posterior compartment of the lower extremity with varying levels of resistance for ankle dorsi- and plantarflexion. They also measured the strain of the myotendinous junction and tendon using an in situ model and motion phantom apparatus. The motion phantom apparatus consisted of a pair of rotating disks in the axial plane, and on one disk the belly of a gastrocnemius muscle was sutured and on the other disk, the distal end of the

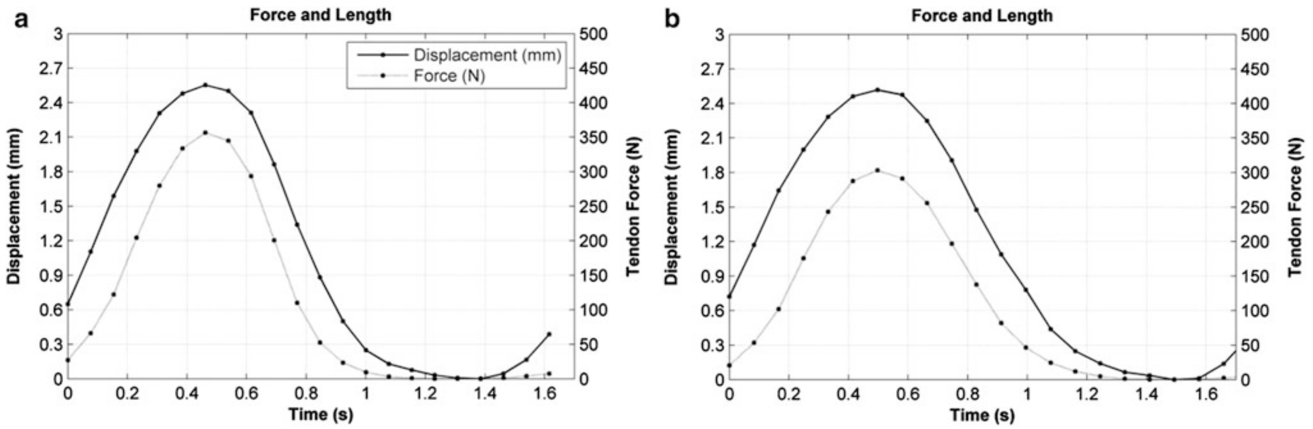

Fig. 9 Typical tendon displacement and force profiles during an isometric contraction–relaxation cycle. Two trials (denoted by **a**, **b**) were collected within a same day. (Reprinted with permission from Shin et al. 2008)

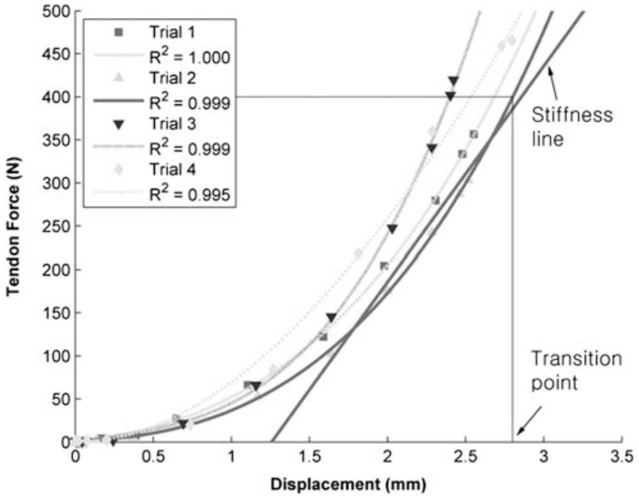

Fig. 10 Force-Length (F-L) relationships after least-squares fitting of the cubic polynomial to each trial set. A sample line is shown from which the stiffness and transition point were calculated. Coefficient correlation values are also shown to assess the quality of the fit. (Reprinted with permission from Shin et al. 2008)

tendon of the gastrocnemius muscle was sutured. A grid was inked onto the tendon, muscle, and muscle–tendon junction and motion was videotaped with specific grid points on the tendon, muscle, and muscle–tendon junction being digitized. The changes in position of these grid points allowed calculation of strain. These strain values from video images were compared to those derived from the velocity-encoded cine phase MRI technique. The MRI technique involved measuring the velocities of the same ROI's and then performing successive iterations of movement of the ROI (by multiplying the velocity over the time delay of the phase to get the next position of the same region of interest). The tendon and myotendionous junction strain as determined from the MR imaging experiments was plotted as a function of the strain determined from the video with a correlation coefficient being 0.992 for the myotendinous junction and 0.987 for the tendon (Drace and Pelc 1994b).

Lingamneni et al. measured the motion of a rotating phantom and averaged the trajectories using the MRI-measured velocity data both forward and backward in time from the starting point (Lingamneni et al. 1995). The motion of the phantom was tracked using custom-built algorithms through a complete rotation to an accuracy of two pixels. They also explored the forward and backward integration techniques to measure true trajectories of another rotating phantom. By using the MRI-measured velocity data of points on the phantom, they found that the measured (integrated) and true trajectories agreed to within 3.3 %. The velocity encoded-phase contrast MRI technique has also been used to study the motion of skeletal structures such as the patella (Sheehan et al. 1999; Shellock et al. 1999).

Based on cine phase contrast imaging studies, Pappas et al. reported nonuniform shortening along some muscle fascicles during low load elbow flexion (Pappas et al. 2002). In this study, they calculated displacements of square ROIs from the velocity measurements and 1D strain was determined by calculating the length change between the ROIs placed along the muscle fascicles. These results were later confirmed by finite element model predictions that nonuniform strains can arise from complex features of muscle architecture (Blemker et al. 2005).

A number of studies based on MRI for either velocity or displacement mapping of the lower extremity muscle have been reported. These studies show that the MRI is a promising tool for exploring the architectural features as well as muscle function under different types of muscle activation. Many subtle aspects of the velocity and strain distribution in different muscles can be determined which in turn, allows a deeper understanding of muscle physiology and the potential modifications to these patterns under altered conditions or disease states.

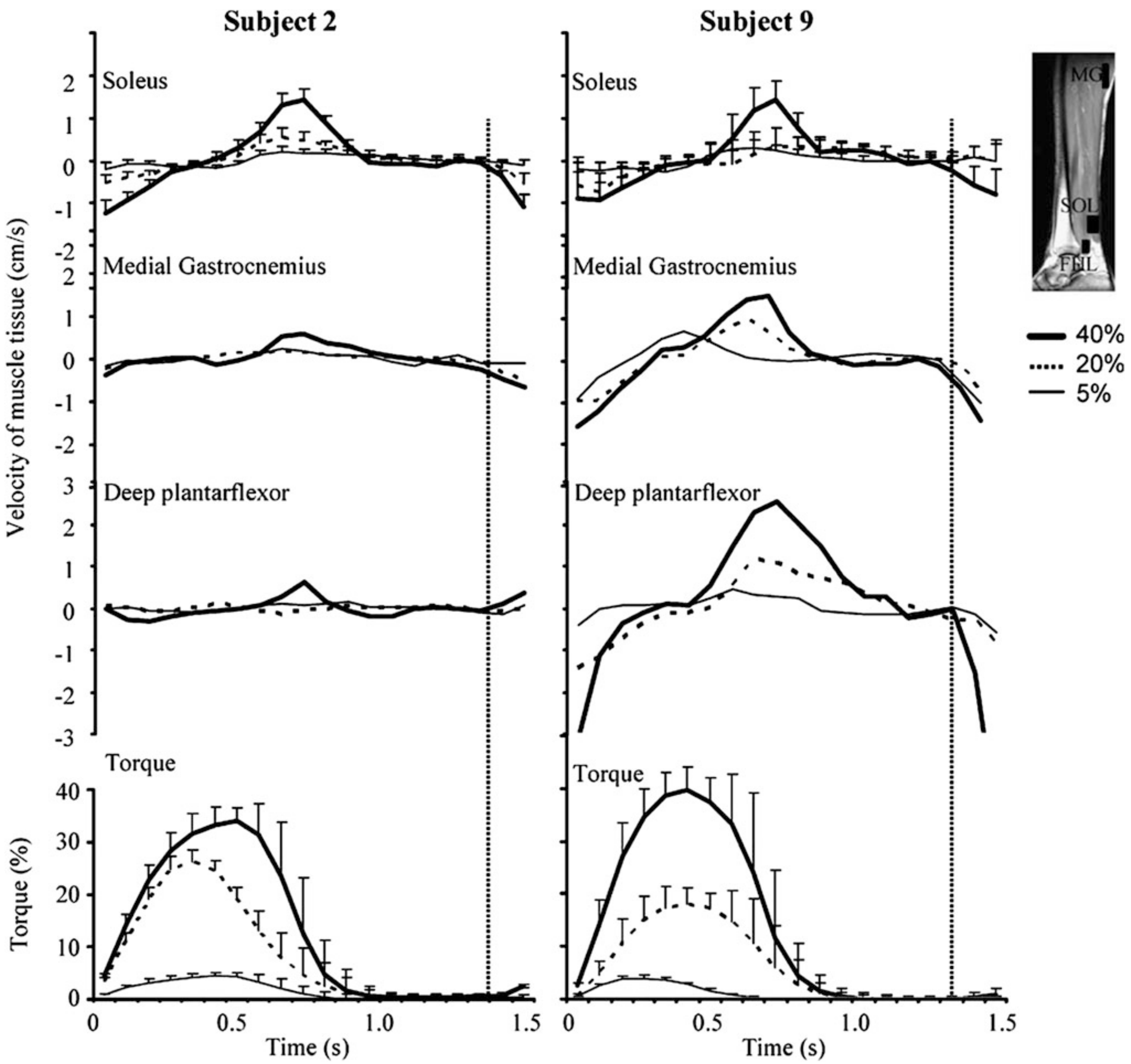

Fig. 11 Velocity and torque patterns during contraction cycles at 40, 20, and 5 % torque levels from two different subjects. The contraction cycle begins (*dashed vertical lines*) when the muscles starts to move in the proximal direction (*negative velocity*). The peak negative velocities are reached in the early torque development phase. Zero velocity occurs near the peak torque. After peak torque the muscles have a positive velocity and return to the relaxed position. Each curve is an average velocity from the region of interests (*black rectangles*) shown in a sagittal image (*right*) in the distal soleus, medial gastrocnemius, and flexor hallucis longus (FHL). The error bars in the soleus muscle represent the standard deviation of pixel velocities in the specified area. The standard deviations of MG and FHL were of similar magnitude and were left out for clarity. The error bars in the torque curves represent the standard deviation during the ~70 contractions performed during each scanning series. Examples are shown from a control subject (≠ 2) and a patient (≠ 9). (Reprinted with permission from Finni et al. 2006)

6.1 Soleus

Finni et al. reported the first comprehensive study of the distribution of strain along the soleus aponeurosis tendon during isometric contractions at 20 and 40 % MVC (Finni et al. 2003a). Displacement and strain in the apparent Achilles tendon and in the aponeurosis were calculated from cine phase-contrast MRI; the apparent Achilles tendon lengthened 2.8 and 4.7 % in 20 and 40 % maximal voluntary contraction, respectively. Nonuniformity in aponeurosis strain was reported with the midregion of the aponeurosis, below the gastrocnemius insertion, lengthening by 1.2 and

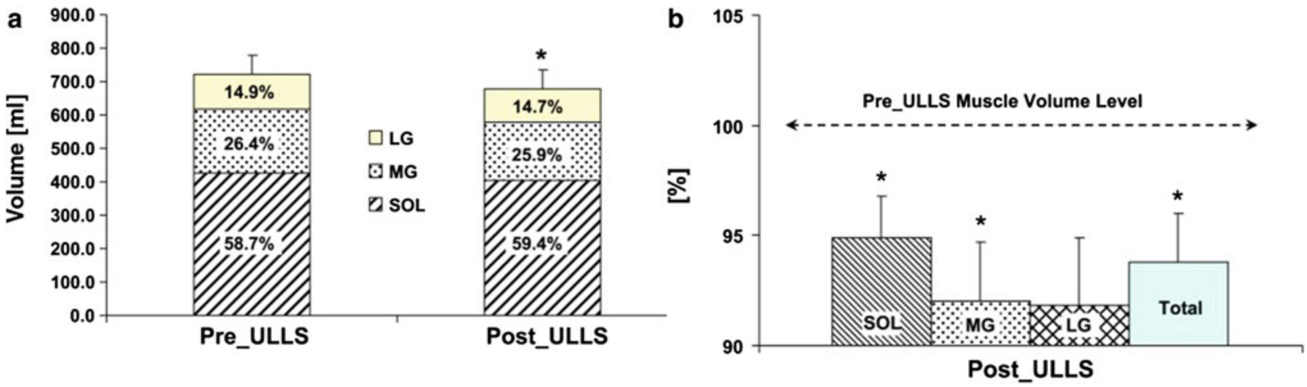

Fig. 12 **a** (*Left*) the total volume of the triceps surae decreased significantly following the ULLS, but the relative volume of each muscle, presented inside the bars, to the total volume remained constant following the ULLS. **b** (*Right*) for each muscle, the Sol and the MG showed a decrease in volume following the ULLS. *R* right; *L* left; *I* inferior; *S* superior. *Outlier value for that particular variable. (Reprinted with permission from Lee et al. 2006)

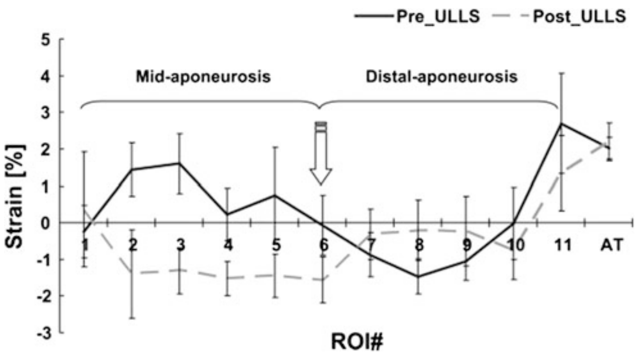

Fig. 13 Strain distribution along the length of posterior aponeurosis of the Sol and the Achilles tendon (AT) before (*Pre-ULLS: thick solid line*) and immediately after (*Post-ULLS: dashed line*) the 4-week ULLS. Positive strain indicates lengthening. The strain distribution was obtained at the moment the torque level reached the peak during 20 % MVCpre submaximal contraction. Each data point presented is mean ± 1 SE across all subjects. The ROI number 1 corresponds to the MG insertion region and number 11 to the most distal point of the Sol. The arrow on ROI number 6 represents the emerging region of anterior protrusion of the Sol aponeurosis, and it was used as a reference for dividing the aponeurosis into two regions: mid- and distal aponeurosis. (Reprinted with permission from Lee et al. 2006)

2.2 %, while the distal aponeurosis shortened by 2.1 and 2.5 %, respectively. Finni et al. postulated that the nonuniformity in aponeurosis strain within an individual was due to the presence of active and passive motor units along the length of the muscle, causing variable force along the measurement site. Force transmission along intrasoleus connective tissue was also considered as a significant source of nonuniform strain in the aponeurosis. A closely related paper by the same group confirmed the strong relationship between the complex 3D structure of the muscle–tendon system of the human soleus and the intramuscular distribution of tissue velocities during in vivo isometric contractions (Finni et al. 2003b). The proximal region of the muscle is unipennate, whereas the midregion has a radially bipennate hemicylindrical structure, and the distal region is quadripennate. Tissue velocity mapping showed that the highest velocity regions overlay the aponeuroses connected to the Achilles tendon (Fig. 2). These are located on the anterior and posterior surfaces of the muscle. The lowest velocities overlay the aponeuroses connected to the origin of the muscle and are generally located intramuscularly. The heterogeneity in the dynamics is attributed by the authors to a combination of an uneven spatial distribution of the motor units that are recruited and the physical structures within the muscle. The heterogeneity parallels the 3D of the muscle–tendon unit, suggesting that further detailed studies of muscle structure are essential for a better understanding of muscle function.

In order to further understand the correlation of structure to function, the same group explored the structure/function of the soleus muscle in another study. Hodgson et al. provide a detailed comprehensive analysis of the soleus muscle structure and the correlation to function (Hodgson et al. 2006). High resolution images of the soleus muscle from the Visible Human Dataset (available from the National Library of Medicine), magnetic resonance images (MRI), and cadaver studies revealed a complex 3D connective tissue structure populated with pennate muscle fibers. Tracking of these structures through multiple images revealed a regular organization that paralleled the expected orientation of muscle fibers. Figure 3 shows the images reconstructed from the Visible Human dataset and the directions of the muscle fibers inferred from the direction of the intramuscular connective tissue.

An important contribution of the paper by Hodgson et al. is the attempt to link the inhomogeneity of the velocity distribution patterns in the soleus to the muscle structure including to the connective tissue components. One striking feature was the high velocities observed near the posterior aponeurosis

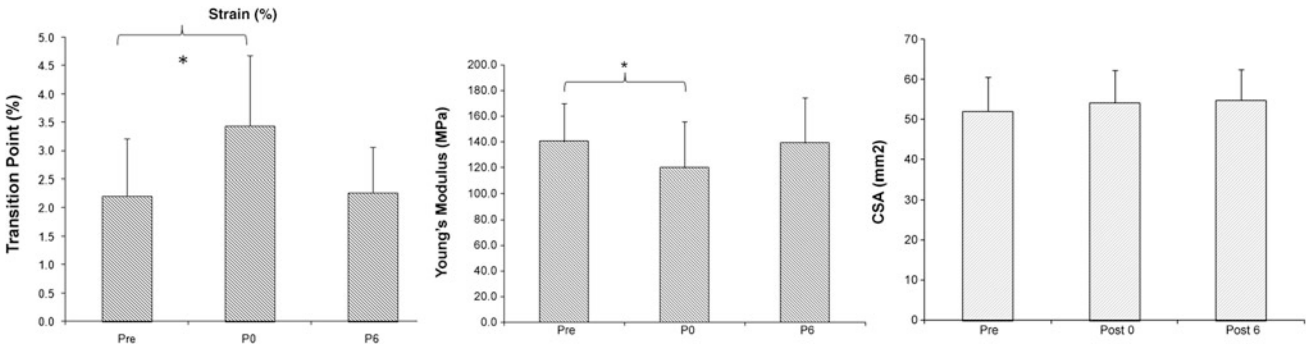

Fig. 14 Average tendon transition point at Pre, P0, and P6. $*P < 0.05$, Pre versus P0. Achilles tendon Young's modulus at Pre, P0, and P6. Values are mean ± SD. Repeated measures ANOVA with Fisher's (least significant difference) pairwise comparison showed 17.1 % reduction in the modulus after unilateral lower limb suspension: $*P < 0.05$. Tendon cross-sectional area (CSA) at Pre, P0, and P6. Tendon CSA was not changed over the duration of the study. Values are mean ± SD. (Reprinted from Shin et al. 2008)

and median septum and the low, or even reverse, velocities near the anterior aponeurosis (Fig. 4). The maximum velocities were observed in regions overlying the aponeuroses connected to the Achilles tendon. This was the case for both the posterior soleus aponeurosis and the median septum, which was also connected to the Achilles tendon. Thus, the pattern of intramuscular movement during a muscle contraction corresponded to muscle fibers shortening and rotating as the interdigitating aponeuroses of origin and insertion slid longitudinally relative to each other. Hodgson et al. also inferred that the distribution of the connective tissue (more concentration of noncontractile material in the central regions of the muscle) should result in the appropriate curvature of muscle fibers (Hodgson et al. 2006).

6.2 Medial Gastrocs

Kinugasa et al. also reported an anomalous behavior of the MG (medial gastrocnemius) superficial and deep aponeurosis during isometric plantarflexion at 20 and 40 % of MVC. Positive strain (lengthening) occurred in both ends of the deep aponeurosis and in the proximal region of the superficial aponeurosis (Kinugasa et al. 2008). In contrast, negative strain (shortening) was observed in the middle region of the deep aponeurosis and in the distal region of the superficial aponeurosis. Consistent with this shortening of the deep aponeurosis length along the proximal–distal axis was expansion of the aponeuroses in the medial–lateral and anterior–posterior directions in the cross-sectional plane. It is concluded that at low to moderate force levels of isometric contraction, regional differences in strain occur along the proximal–distal axis of both aponeuroses, and some regions of both aponeuroses shorten (Fig. 5). This paper also evaluated the spin tag and phase contrast imaging methods and confirmed that the two methods provide comparable accuracy of displacement measures (Fig. 6).

In a continuing series of experiments, Kinugasa et al. further explored the symmetry of muscle fiber deformation (Kinugasa et al. 2012). Constant volume considerations of the deforming muscle predicts that if the fibers lengthen, then the cross-sectional area should decrease. In-plane area measurements along segments of the MG and determination of fiber length changes from phase contrast MRI data allowed deduction of the through-plane deformation. Kinugasa et al. established the asymmetry in fascicle cross-section deformation for both passive and active muscle fibers with a ~22 % in-plane and ~6 % through-plane fascicle thickness change. They postulate that the fiber deformations have functional relevance, not only because they affect the force production of the muscle itself, but also because they affect the characteristics of adjacent muscles by deflecting their line of pull.

Shin et al. showed that PC-MRI allows extraction of parameters beyond velocity, displacement, and strain; these additional parameters enable further characterization of muscle performance and highlight muscle heterogeneity (Shin et al. 2009). The latter paper reports on the intramuscular fascicle-aponeuroses dynamics of the human medial gastrocnemius during plantarflexion and dorsiflexion of the foot. They determined intrafascicular strain defined as the ratio of strain in the fascicle segment at the insertion to strain at its origin. This ratio was nonuniform along the proximo-distal axis of the muscle, increasing from the proximal to distal direction (Fig. 7).

The distribution of strain correlated with the muscle regions that are likely to encounter high stress concentrations. Another parameter extracted in this study was the architectural gear ratio, which is defined as the mechanical amplification ratio of fascicle length displacement to that of the tendon/aponeuroses in a pennate muscle. This also exhibited significant regional differences with the highest ratios in the proximal regions accompanied by a higher initial pennation angle and a larger change in the pennation

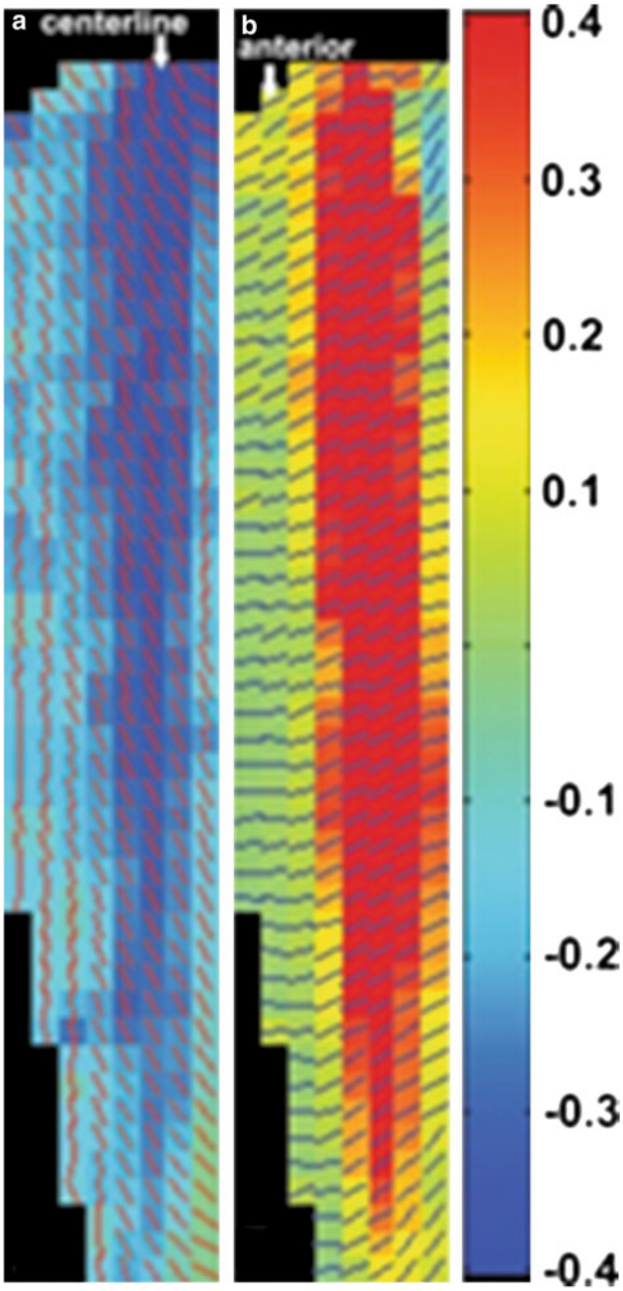

Fig. 15 Example of the first principal strain *E1* (**a**) and the second principal strain *E2* (**b**) with the bars indicating the direction of strain vectors. Negative strain values represent local tissue element shortening during elbow flexion; and positive strain values represent local tissue element stretching. The centerline and the anterior fascicles can be easily identified in the strain maps. (Reprinted with permission from Zhong et al. 2008)

angle (Fig. 8). The intrafascicular strain patterns seen experimentally also matched some finite element models that predicted high stress and strain patterns at both ends of the muscle where it thins to become the tendon (Jenkyn et al. 2002; Yucesoy et al. 2002).

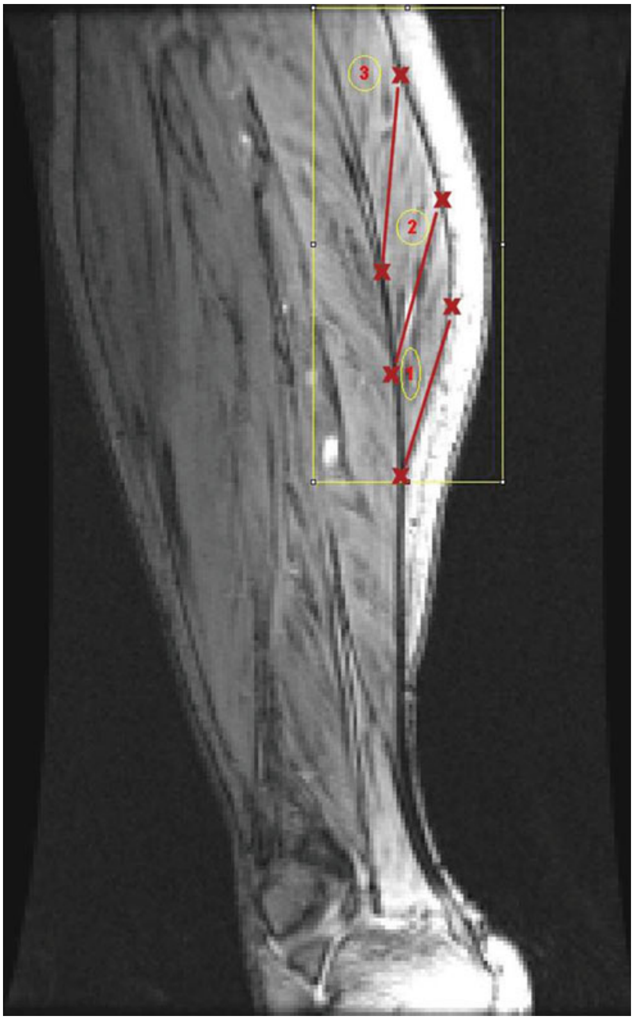

Fig. 16 Magnitude image from the dynamic phase contrast images acquired on one of the subjects. The rectangular box centered on the medial gastrocnemius is zoomed for the positive and negative eigenvector images. The location of three ROIs (labeled 1–3) placed along the gastrocnemius and used in the analysis is also shown

Quadriceps femoris Compared to the lower extremity calf muscle, fewer studies have focused on the quadriceps femoris. Finni et al. examined the relationships between morphology and muscle–tendon dynamics of the quadriceps femoris muscle of 11 men using velocity encoded-phase contrast magnetic resonance imaging (Finni et al. 2008). The average displacement in the proximal and distal halves of the rectus femoris and vastus intermedius aponeuroses was different ($P = 0.049$), reflecting shortening (1.6 %), but the tensile strain along the length of the aponeuroses was uniform. This is in contrast to their findings of nonuniform strain in the soleus aponeurosis during isometric contractions of 20–40 % MVC (Finni et al. 2003a, b). They hypothesized that the different result in the QF may arise because of different muscle, type of contraction, and a

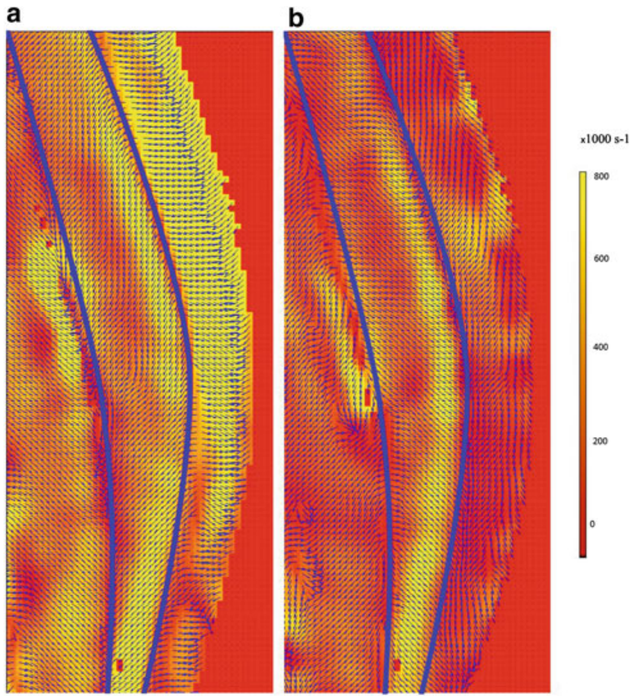

Fig. 17 The rectangular box in Fig. 16 is zoomed and shown for the positive eigenvalue images in the relaxation phase (**a**) and in the contraction phase (**b**). The outline of the medial gastrocnemius in blue was manually contoured for ease of visualization. Area to the right of the gastrocnemius is fat tissue. The pixel color is assigned according to the magnitude of the eigenvalue and ranges from 0 (*red*) to 0.8 (*yellow*) s^{-1}. In the relaxation phase (**a**), the positive strain rate direction is approximately along the fiber direction, and is approximately perpendicular to the muscle fiber in the contraction phase (**b**)

smaller load used in their study compared to the calf muscle study.

Achilles tendon dynamics The previous sections establish PC velocity-encoded MRI as a powerful tool for muscle functional studies. The extension to studying tendon dynamics with phase contrast MRI was first reported Shin et al. (Shin et al. 2008). They estimated force-dependent length changes, stiffness, and the transition point from linear to nonlinear behavior of the force-length (F-L) curve in human Achilles tendon and established inter- and intra-exam variability of these measurements. Achilles tendon force and calcaneus-movement-adjusted displacement were measured during a submaximal isometric plantarflexion in four healthy subjects with four repeated trials for each subject (Fig. 9). The measured force-length (F-L) relationship was least-squares fitted to a cubic polynomial (Fig. 9). F-L curves have been characterized as consisting of an initial "toe-region" and, at higher values of displacement as a "linear region" with a "transition point" between these two regions (Proske and Morgan 1987). Tendon stiffness (N/mm) was calculated as the slope of the linear region (Fig. 10). The elastic modulus was also estimated by multiplying the tendon stiffness by the ratio of each subject's initial tendon length to tendon CSA. The tendon displacement after subtraction of calcaneus movement was 2.87 ± 0.20, 3.38 ± 0.07, 2.76 ± 0.05, and 2.91 ± 0.06 mm. In this study, the transition point was identified at a force level of 400 N. The quantification of changes in the toe region provides different information from the typically reported stiffness values. For example, due to some form of clinical intervention the stiffness in a high force region may remain the same while the toe region elongates. The toe region is associated with the presence of structural crimps, and sinusoidal shapes of collagen fibers within the tendon (Proske and Morgan 1987; Benjamin and Ralphs 1997). Thus, as the changes in transition point and stiffness arise from two independent phenomena, they provide valuable information on tendon adaptation. This technique holds promise for investigating tendon structural changes with aging, after an injury, disease, and with altered loading.

7 Functional Imaging of Muscle: Altered and Diseased Conditions

Few studies have reported on changes in muscle strain patterns using magnetic resonance imaging in altered MSK conditions or disease states. Ultrasound studies of the MSK system underline the potential of imaging in characterizing changes; these will in turn allow a better understanding of the pathophysiology of disease. In contrast to ultrasound, MRI can provide better soft tissue contrast, direct velocity or displacement imaging of muscle tissue, and offers 3D and large fields of view imaging capabilities. The full potential of functional MRI as a clinical tool is yet to be established. However, the following studies on patients with Achilles tendon rupture and on subjects with controlled chronic uploading highlight the potential of MRI in altered/diseased MSK conditions.

7.1 Achilles Tendon Rupture

Finni et al. explored muscle synergism during isometric plantarflexion in Achilles tendon rupture patients and in normal subjects (Finni et al. 2006). They estimated the relative contribution of the triceps surae (TS) and the deep plantarflexor muscles to the plantarflexion torque based on muscle velocities during an isometric contraction in normal and Achilles tendon rupture (ATR) subjects. They report marked individual differences in the use of the different muscles during plantarflexion task in control subjects. Soleus to flexor hallucis longus displacement ratio during contraction varied from 0.4 to 9.6 while the moment arm ratio between Achilles tendon and flexor hallucis longus tendons was 1.9 (± 0.2). In Achilles tendon rupture patients

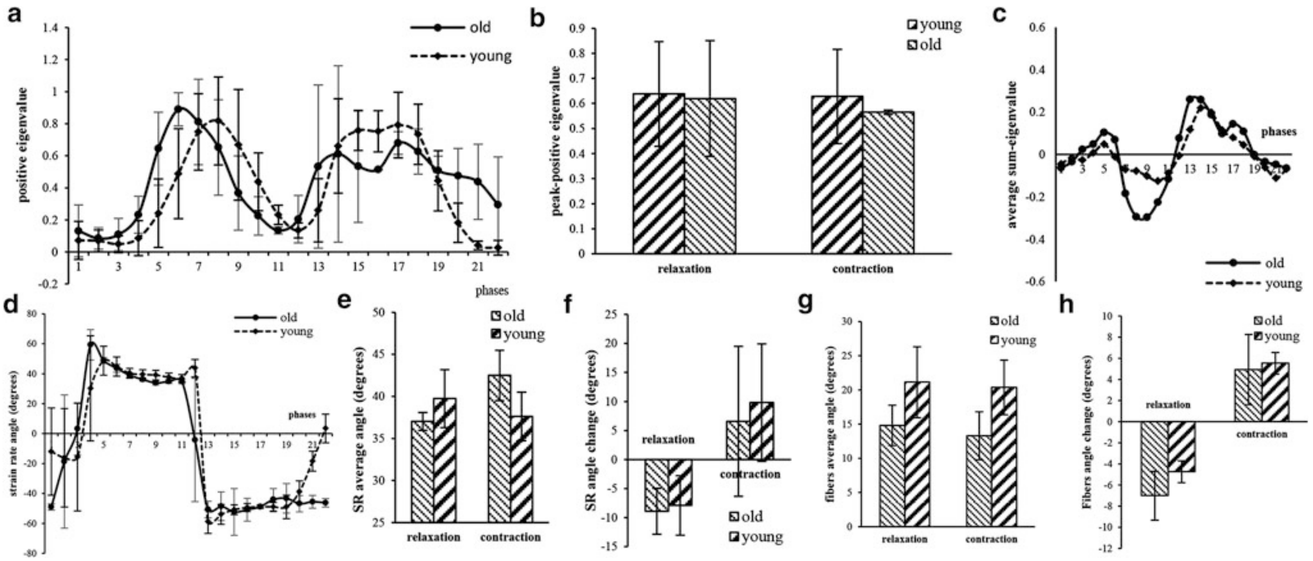

Fig. 18 Positive strain rate eigenvalue versus the plantarflexion (PF) cycle **a** peak +eigenvalue in expansion and contraction phases **b** out-of-plane eigenvalue versus the PF cycle **c** +ve SR angle wrt y-axis versus phases **d** average extension and contraction SR angle **e** change in SR angle in extension and contraction **f** average extension and contraction fiber angle **g** change in fiber angle in extension and contraction **h**

the relative contribution of flexor hallucis longus was very high both in their injured and uninjured leg. This coordinative strategy remained throughout rehabilitation. Figure 11 highlights the differences in velocity distributions in the TS and in the deep plantarflexor muscles between a control and an ATR subject. The study suggests that early recovery of plantarflexion torque after Achilles tendon rupture may be due to compensation by flexor hallucis longus as well as to normalization of the triceps surae muscle function. Further, individual differences in coordinative strategies in addition to moment arms and muscle–tendon properties also influence the calculation of forces produced by individual muscles.

7.2 Chronic Unloading

The effects of chronic unloading on skeletal muscle have been widely studied given its clinical importance in an increasingly aging population, in patients with significant length of bed rest or limb disuse due to injury and in the rarer occurrence of astronauts exposed to microgravity. Several alterations at the cellular level have been associated with chronic uploading and include myofibril protein loss (Steffen and Musacchia 1986), muscle fiber size reduction (Riley et al. 2000; Widrick et al. 1999), altered neuronal recruitment pattern, and fiber type conversion (Edgerton and Roy 1996). These cellular changes translate to macroscopically observable degradation of muscle structure and function, which include a marked decline in muscle volume (Lee et al. 2006), a reduced load production capability (Lee et al. 2006; Greenleaf et al. 1989), and an increased fatigability (Caiozzo et al. 1994), all of which underscore the importance of rehabilitative strategies for restoration of muscle function. Ultrasound studies have been reported on in vivo gastrocnemius tendinous structures following chronic unloading (Reeves et al. 2005); the latter study demonstrated that the stiffness of the gastrocnemius tendinous structure decreased from 124 to 52 N/mm (58 % decrease) following a 90-day bed rest along with 28 % decrease in maximum voluntary isometric force, with, however, no change in the tendon cross-sectional area (CSA). Lee et al. reported on the changes in the structural and mechanical properties of the whole aponeurosis and tendon in human skeletal muscle in vivo following chronic uploading using phase contrast velocity-encoded imaging (Lee et al. 2006). They mapped the Achilles tendon strain and changes in its force–displacement relationship concomitant with chronic unloading and subsequent recuperation. The study included eight healthy volunteers who underwent 4 weeks of unilateral lower limb suspension (ULLS) to induce chronic unloading (Lee et al. 2006). Following ULLS, volumes of the soleus and the medial gastrocnemius and the maximum isometric ankle plantar flexion (maximum voluntary contraction) decreased by 5.5 ± 1.9, 7.5 ± 2.7, and 48.1 ± 6.1 %, respectively (Fig. 12). The strain of the aponeurosis along the length of the muscle before the ULLS was 0.3 ± 0.3 %, in different locations of the aponeurosis. Following ULLS, the mean strain was 6.4 ± 0.3 % (Fig. 13). Lee et al. identified that the strain distribution of the midregion of the aponeurosis was significantly influenced by the ULLS, whereas the more distal component showed no consistent changes. Further, the Achilles tendon strain was not affected by the ULLS. Lee et al. hypothesized that the changes in strain distribution may affect the functional properties of the TS and may increase the probability of strain injuries due to the unusual strain patterns.

Shin et al. extended this chronic unloading model to monitor changes in the Achilles tendon stress–strain relationship by measuring its elastic modulus and transition point, thus providing a new and independent insight with regard to the mechanical properties of the tendon (Shin et al. 2008). In the latter study, five healthy volunteers underwent unilateral lower limb suspension (4 weeks) followed by weekly physiotherapy (6 weeks of physical rehabilitation). After chronic unloading, triceps surae muscle strength decreased to 53.2 ± 15.6 % (mean ± SD) of the presuspension level ($P < 0.05$). Young's modulus, estimated from the slope of the tendon stress–strain relationship, decreased by 17.1 %, while the tendon transition point, reflecting the "toe region," increased by 55.7 % (Fig. 14). Muscle strength, tendon stiffness, and transition point recovered to presuspension levels by the end of 6 weeks of rehabilitation. Tendon cross-sectional area determined from anatomic axial magnetic resonance images remained unchanged, suggesting that the altered tendon elastic modulus and transition point were largely due to material deterioration.

An extension of the Shin et al.'s paper looked in greater detail at the correlation between morphological and elastic (Young's modulus) changes of the Achilles tendon and distal aponeurosis in response to chronic ULLS (Kinugasa et al. 2010). As in the previous study, there was 46.7 % decrease in maximum plantar flexion torque. The total volumes of entire tendinous tissue increased significantly by 6.4 % (11.9 versus 12.7 ml) after ULLS. In contrast, Young's modulus decreased significantly by 10.4 % (211.7 versus 189.6 MPa) for the Achilles tendon and 29.0 % for the distal aponeurosis (158.8 versus 113.0 MPa) following ULLS. There was no significant correlation between relative change in volume and Young's modulus with 4 weeks of ULLS. The lack of significant correlation suggests that factors other than morphological changes are responsible for the reduced Young's modulus.

8 2D and 3D Strain and Strain Rate Measurements in Skeletal Muscles

The MR-based studies outlined in the previous sections calculate the 1D strain. However, given the 3D nature of the MR acquisition, it is possible to derive 2D and even the 3D strain or strain rate tensors. This provides an exciting area of research where strain directions can be correlated to muscle fiber directions. Strain tensors can be calculated directly from spin tag displacement imaging or from velocity images of the VE-PC MRI acquisitions. Alternately, strain rate tensors can be calculated from VE-PC MRI data; this approach is convenient as there is no requirement of a reference frame. Zhong et al. first reported 2D Lagrangian displacements and strains in the arm muscle during elbow flexion (Zhong et al. 2008). They showed that the directions of the first and second principal strains varied throughout the muscle and that the direction is not necessarily aligned with the fascicle direction (Fig. 15).

Englund et al. mapped the 3D strain and diffusion tensor in one region of interest each in the superficial and deep compartments of the anterior tibialis (Englund et al. 2011). The strain was estimated by measuring the displacement of tag lines between the maximum-contracted and relaxed states. Their study revealed a planar strain pattern with the principal shortening direction deviated from the muscle fiber directions in the deep and superficial anterior tibialis compartments by 24 and 40°, respectively (Englund et al. 2011). They postulated that the reason for the noncollinearity of the eigenvectors of the strain tensor and the diffusion tensor was related to the heterogeneity in fiber length and pennation angles. The heterogeneity referred here is the fact that fiber lengths are shorter and pennation angles are larger in the proximal regions than in the distal regions. The role of architectural heterogeneity in causing the strain tensor to be noncollinear to the fiber direction has been explored in models of muscle structure/function (Blemker 2005).

More, recently the authors have explored 2D strain rate (SR) and 3D strain rate (SR) mapping using VE-PC MRI in the lower calf muscles. A preliminary study was undertaken to map the 2D strain rate (SR) tensor in the medial gastrocnemius from a series of velocity-encoded images acquired during plantarflexion (PF) excursion under passive conditions and to investigate age-related changes (Sinha et al. 2013). Figure 16 is the magnitude image with ROIs and Fig. 17 shows a zoomed region of the positive strain rate tensor during contraction and relaxation.

The absolute peak values of the strain rate ranges from 0.5 to 0.8 s^{-1} and are higher in the expansion phase (by a factor ranging from 0.9 to 0.6) than the corresponding value for the contraction phase (Fig. 18a, b). The out-of-plane component was derived from the sum of the two eigenvalues; as muscle is incompressible, the sum of the two eigenvalues should be close to zero if the strain rate is completely in-plane. The sum of the eigenvalues is thus referred to as the out-of-plane component of the SR tensor (Fig. 18c); in all 3 ROIs, the out-of-plane values are smaller than the first two eigenvalues by factors ranging from 1/8 to

3/8. For all the regions, young subjects had a smaller out-of-plane component than the older subjects. Figure 18d is a plot of the average angle of the SR +ve eigenvector makes (wrt y-axis) as a function of the plantarflexion phase. Positive angle values are seen during the relaxation cycle of the plantarflexion in a direction approximately along the muscle fiber direction. Negative angle values occur during the contraction cycle of the plantarflexion when the direction of the +ve SR eigenvector is orthogonal to the muscle fiber direction. The large jumps in angle are when the SR directions change abruptly when the cycle alternates between muscle extension and contraction.

Figures 18e, f, g, h refer to the average angles and change in angle of the SR and fiber directions. The out-of plane SR component is smaller for the younger subjects than the older subjects ($p < 0.05$). It has been postulated that the asymmetry in deformation in the fiber cross-section may arise from the orientation of the curvature of fibers in the 3D muscle structure or through the incorporation of tensile materials oriented along the through-plane axis of the fiber to limit expansion in that direction (Kinugasa et al. 2012). The current study shows that the asymmetric deformation reduces with age and may potentially throw light on reduction in muscle function with age. Another important finding is that the SR orientation (25–30°) is significantly different from the fiber orientation (15–20°) ($p < 0.01$) for both young and old subjects (SR rotated more toward the distal end of muscle than the fiber). The angle between the SR and fiber direction may be an index of architectural integrity and tracking it may potentially enable objectification of disease conditions such as muscular dystrophy where architectural disruption decreases lateral force transmission (Englund et al. 2011).

9 Conclusions

Functional magnetic resonance imaging based on phase contrast velocity-encoded sequences has been established as a viable technique for mapping velocity and strain patterns in the extremity muscles. A series of publications have mapped the muscle motion patterns in the lower extremity in normal subjects and have highlighted the link between structure and function. This elegant technique has also been applied, in a limited way, to study altered muscle conditions. Clearly, the technique is mature to support larger scale clinical studies and has the potential to be a strong tool in the armamentarium of MR techniques to diagnose, monitor, and manage MSK disease conditions. More recent developments in 2D and 3D strain and strain rate tensor imaging combined with muscle diffusion tensor imaging may offer greater insights into muscle physiology including the role of lateral force transmission; the latter may be a critical factor that is affected in muscle dystrophy.

References

Aagaard P, Andersen JL, Dyhre-Poulsen P, Leffers AM, Wagner A, Magnusson SP, Halkjaer-Kristensen J, Simonsen EB (2001) A mechanism for increased contractile strength of human pennate muscle in response to strength training: changes in muscle architecture. J Physiol 534:613–623. PMID-11454977

Akima H, Kawakami Y, Kubo K, Sekiguchi C, Ohshima H, Miyamoto A, Fukunaga T (2000) Effect of short-duration spaceflight on thigh and leg muscle volume. Med Sci Sports Exerc 32:1743–1747. PMID-11039647

Abe T, Fukashiro S, Harada Y, Kawamoto K (2001) Relationship between sprint performance and muscle fascicle length in female sprinters. J Physiol Anthropol Appl Human Sci 20:141–147. PMID-11385937

Axel L, Dougherty L (1989) Heart wall motion: improved method of spatial modulation of magnetization for MR imaging. Radiology 171:841–845

Benjamin M, Ralphs JR (1997) Tendons and ligaments—an overview. Histol Histopathol 12:1135–1144. doi:10.1016/j.ejcb.2006.06.002

Biewener AA, Corning WR, Tobalske BW (1998) In vivo pectoralis muscle force-length behavior during level flight in pigeons (Columba livia) J Exp Biol 201(Pt 24):3293–3307 PMID-9817827

Blemker SS, Pinsky PM, Delp SL (2005) A 3D model of muscle reveals the causes of nonuniform strains in the biceps brachii. J Biomech 38:657–665. doi:10.1016/j.jbiomech.2004.04.009

Brossmann J, Muhle C, Schroder C, Melchert UH, Bull CC, Spielmann RP, Heller M (1993) Patellar tracking patterns during active and passive knee extension: evaluation with motion-triggered cine MR imaging. Radiology 187:205–212. PMID-8451415

Caiozzo VJ, Baker MJ, Herrick RE, Tao M, Baldwin KM (1994) Effect of spaceflight on skeletal muscle: mechanical properties and myosin isoform content of a slow muscle. J Appl Physiol 76:1764–1773

Drace JE, Pelc NJ (1994a) Measurement of skeletal muscle motion in vivo with phase-contrast MR imaging. J Magn Reson Imaging 4:157–163

Drace JE, Pelc NJ (1994b) Skeletal muscle contraction: analysis with use of velocity distributions from phase-contrast MR imaging. Radiology 193:423–429

Drace JE, Pelc NJ (1994c) Tracking the motion of skeletal muscle with velocity-encoded MR imaging. J Magn Reson Imaging 4:773–778

Drace JE, Pelc NJ (1994d) Elastic deformation in tendons and myotendinous tissue: measurement by phase-contrast MR imaging. Radiology 191:835–839

Englund EK, Elder CP, Xu Q, Ding Z, Damon BM (2011) Combined diffusion and strain tensor MRI reveals a heterogeneous, planar pattern of strain development during isometric muscle contraction. Am J Physiol Regul Integr Comp Physiol 300:R1079–R1090. doi:10.1152/ajpregu.0 0474.2010

Edgerton VR, Roy RR (1996) Neuromuscular adaptations to actual and simulated spaceflight. In: Handbook of physiology, environmental phsyiology. Am Physiol Soc Bethesda, MD p 721–763

Finni T, Hodgson JA, Lai AM, Edgerton VR, Sinha S (2003a) Nonuniform strain of human soleus aponeurosis-tendon complex during submaximal voluntary contractions in vivo. J Appl Physiol 95:829–837. doi:10.1152/japplphysiol.0 0775.2002

Finni T, Hodgson JA, Lai AM, Edgerton VR, Sinha S (2003b) Mapping of movement in the isometrically contracting human soleus muscle reveals details of its structural and functional complexity. J Appl Physiol 95:2128–2133. doi:10.1152/japplphysiol.0 0596.2003

Finni T, Hodgson JA, Lai AM, Edgerton VR, Sinha S (2006) Muscle synergism during isometric plantarflexion in achilles tendon rupture patients and in normal subjects revealed by velocity-encoded cine phase-contrast MRI. 21:67–74, Clin Biomech (Bristol, Avon). doi:10.1016/j.clinbiomech.2005.08.007

Finni T, Havu M, Sinha S, Usenius JP, Cheng S (2008) Mechanical behavior of the quadriceps femoris muscle tendon unit during low-load contractions. J Appl Physiol 104:1320–1328. doi: 10.1152/japplphysiol.0 1069.2007

Fukunaga T, Ichinose Y, Ito M, Kawakami Y, Fukashiro S (1997) Determination of fascicle length and pennation in a contracting human muscle in vivo. J Appl Physiol 82:354–358. PMID-9029238

Fukunaga T, Kubo K, Kawakami Y, Fukashiro S, Kanehisa H, Maganaris CN (2001) In vivo behaviour of human muscle tendon during walking. Proc Biol Sci 268:229–233. doi:10.1098/rspb.2000.1361

Garrett WE Jr (1996) Muscle strain injuries. Am J Sports Med 24(Suppl):S2S88. PMID: 8947416

Greenleaf JE, Bulbulian R, Bernauer EM, Haskell WL, Moore T (1989) Exercise-training protocols for astronauts in microgravity. J Appl Physiol 67:2191–2204

Griffiths RI (1991) Shortening of muscle fibres during stretch of the active cat medial gastrocnemius muscle: the role of tendon compliance J Physiol 436:219–236. PMID-2061831

Hodgson JA, Finni T, Lai AM, Edgerton VR, Sinha S (2006) Influence of structure on the tissue dynamics of the human soleus muscle observed in MRI studies during isometric contractions. J Morphol 267:584–601. doi:10.1002/jmor.10421

Jenkyn TR, Koopman B, Huijing P, Lieber RL, Kaufman KR (2002) Finite element model of intramuscular pressure during isometric contraction of skeletal muscle. Phys Med Biol 47:4043–4061

Jaspers RT, Brunner R, Pel JJ, Huijing, PA (1999) Acute effects of intramuscular aponeurotomy on rat gastrocnemius medialis: force transmission, muscle force and sarcomere length. J Biomech 32:71–79. PMID-10050953

Jaspers RT, Brunner R, Baan GC, Huijing PA (2002) Acute effects of intramuscular aponeurotomy and tenotomy on multitendoned rat EDL: indications for local adaptation of intramuscular connective tissue. Anat Rec 266:123–135. PMID-11788946

Kawakami Y, Abe T, Fukunaga T (1993) Muscle-fiber pennation angles are greater in hypertrophied than in normal muscles. J Appl Physiol 74:2740–2744. PMID-8365975

Kawakami Y, Muraoka Y, Kubo K, Suzuki Y, Fukunaga T (2000) Changes in muscle size and architecture following 20 days of bed rest. J Gravit Physiol 7:53–59. PMID-12124185

Kibler WB (1990) Clinical aspects of muscle injury. Med Sci Sports Exerc 22:450–452. PMID-2402204

Kinugasa R, Shin D, Yamauchi J, Mishra C, Hodgson JA, Edgerton VR, Sinha S (2008) Phase-contrast MRI reveals mechanical behavior of superficial and deep aponeuroses in human medial gastrocnemius during isometric contraction. J Appl Physiol 105:1312–1320. doi:10.1152/japplphysiol.9 0440.2008

Kinugasa R, Hodgson JA, Edgerton VR, Shin DD, Sinha S (2010) Reduction in tendon elasticity from unloading is unrelated to its hypertrophy. J Appl Physiol 109:870–877. doi:10.1152/japplphysiol.0 0384.2010

Kinugasa R, Hodgson JA, Edgerton VR, Sinha S (2012) Asymmetric deformation of contracting human gastrocnemius muscle. J Appl Physiol 112:463–470. doi:10.1152/japplphysiol.0 0666.2011

Lee HD, Finni T, Hodgson JA, Lai AM, Edgerton VR, Sinha S (2006) Soleus aponeurosis strain distribution following chronic unloading in humans: an in vivo MR phase-contrast study. J Appl Physiol 100:2004–2011. doi:10.1152/japplphysiol.0 1085.2005

Lingamneni A, Hardy PA, Powell KA, Pelc NJ, White RD (1995) Validation of cine phase-contrast MR imaging for motion analysis. J Magn Reson Imaging 5:331–338. PMID-7633111

Lieber RL (1993) Skeletal muscle architecture: implications for muscle function and surgical tendon transfer. J Hand Ther 6:105–113. PMID-8343877

Narici MV, Binzoni T, Hiltbrand E, Fasel J, Terrier F, Cerretelli P (1996) In vivo human gastrocnemius architecture with changing joint angle at rest and during graded isometric contraction. J Physiol 496(Pt 1):287–297. PMID-8910216

Narici M, Cerretelli P (1998) Changes in human muscle architecture in disuse-atrophy evaluated by ultrasound imaging. J Gravit Physiol 5:P73-P74. PMID-11542371

Narici MV, Reeves ND, Morse CI, Maganaris CN (2004) Muscular adaptations to resistance exercise in the elderly. J Musculoskelet Neuronal Interact 4:161–164. PMID-15615118

Niitsu M, Campeau NG, Holsinger BA, Riederer SJ, Ehman RL (1992) Tracking motion with tagged rapid gradient-echo magnetization-prepared MR imaging. J Magn Reson Imaging 2:155–163. PMID-1562766

Noonan TJ, Best TM, Seaber AV, Garrett WE Jr (1994) Identification of a threshold for skeletal muscle injury. Am J Sports Med 22:257–261. PMID-8198196

Pappas GP, Asakawa DS, Delp SL, Zajac FE, Drace JE (2002) Nonuniform shortening in the biceps brachii during elbow flexion. J Appl Physiol 92:2381–2389. doi:10.1152/japplphysiol.0 0843.2001

Pipe JG, Boes JL, Chenevert TL (1991) Method for measuring three-dimensional motion with tagged MR-imaging. Radiology 181:591–595. PMID-1924810

Proske U, Morgan DL (1987) Tendon stiffness: methods of measurement and significance for the control of movement. A rev J Biomech 20:75–82. PMID-3558432

Reeves ND, Maganaris CN, Ferretti G, Narici MV (2005) Influence of 90 day simulated microgravity on human tendon mechanical properties and the effect of resistive countermeasures. J Appl Physiol 98:2278–2286. doi:10.1152/japplphysiol.0 1266.2004

Riley DA, Bain JL, Thompson JL, Fitts RH, Widrick JJ, Trappe SW, Trappe TA, Costill DL (2000) Decreased thin filament density and length in human atrophic soleus muscle fibers after spaceflight. J Appl Physiol 88:567–572. PMID-10658024

Roberts TJ, Marsh RL, Weyand PG, Taylor CR (1997) Muscular force in running turkeys: the economy of minimizing work. Science 275:1113–1115. PMID-9027309

Sheehan FT, Zajac FE, Drace JE (1999) In vivo tracking of the human patella using cine phase contrast magnetic resonance imaging. J Biomech Eng. 121:650–656. PMID-10633267

Sheehan FT, Drace JE (2000) Human patellar tendon strain. A noninvasive, in vivo study. Clin Orthop Relat Res 370:201–207. PMID-10660714

Shellock FG, Stone KR, Crues JV (1999) Development and clinical application of kinematic MRI of the patellofemoral joint using an extremity MR system. Med Sci Sports Exerc. 31:788–791. PMID-10378904

Shin DD, Hodgson JA, Edgerton VR, Sinha S (2009) In vivo intramuscular fascicle-aponeuroses dynamics of the human medial gastrocnemius during plantarflexion and dorsiflexion of the foot. J Appl Physiol 107:1276–1284. doi:10.1152/japplphysiol.9 1598.2008

Shin D, Finni T, Ahn S, Hodgson JA, Lee HD, Edgerton VR, Sinha S (2008) In vivo estimation and repeatability of force-length relationship and stiffness of the human achilles tendon using phase contrast MRI. J Magn Reson Imaging 28:1039–1045. doi: 10.1002/jmri.21533

Sinha S, Hodgson JA, Finni T, Lai AM, Grinstead J, Edgerton VR (2004) Muscle kinematics during isometric contraction: development of phase contrast and spin tag techniques to study healthy and atrophied muscles. J Magn Reson Imaging 20:1008–1019. doi: 10.1002/jmri.20210

Sinha S, Shin DD, Hodgson JA, Kinugasa R, Edgerton VR (2012) Computer-controlled, MR-compatible foot-pedal device to study dynamics of the muscle tendon complex under isometric, concentric, and eccentric contractions. J Magn Reson Imaging 36:498–504. doi:10.1002/jmri.23617

Sinha S, Moghadassi A, Malis V, Sinha U (2013) Dynamic functional imaging of quadriceps and hamstring muscles under isometric and active extension-flexion contraction. In: Proceedings of the international society mgnetic resonance medicine, 21:3481, Salt Lake, Utah, April 20–26

Steffen JM, Musacchia XJ (1986) Spaceflight effects on adult rat muscle protein, nucleic acids, and amino acids. Am J Physiol Regul Integr Comp Physiol 251:R1059–R1063. PMID-2431627

Widrick JJ, Knuth ST, Norenberg KM, Romatowski JG, Bain JL, Riley DA, Karhanek M, Trappe SW, Trappe TA, Costill DL, Fitts RH (1999) Effect of a 17 day spaceflight on contractile properties of human soleus muscle fibres. J Physiol 516:915–930. PMID-2431627

Yucesoy CA, Koopman BH, Huijing PA, Grootenboer HJ (2002) Three-dimensional finite element modeling of skeletal muscle using a two domain approach: linked fiber-matrix mesh model. J Biomech 35:1253–1262. pii:S0021929002000696

Zhong X, Epstein FH, Spottiswoode BS, Helm PA, Blemker SS (2008) Imaging two-dimensional displacements and strains in skeletal muscle during joint motion by cine DENSE MR. J Biomech 41(3):532–540. doi:10.1016/j.jbiomech.2007.10.026

Zerhouni E, Parish D, Rogers W, Yang A, Shapiro E (1988) Human heart: tagging with MR imaging—a method for noninvasive assessment of myocardial motion. Radiology 169:59–63

Part III

MRI in the Diagnostic Work-up of the Skeletal Musculature

MRI of Muscle Injuries

Simon Dimmick, Christoph Rehnitz, Marc-André Weber, and James M. Linklater

Contents

1 Anatomy of Muscle 188
1.1 Structure of Skeletal Muscle 188
1.2 Tendons 189
1.3 Aponeuroses 189
1.4 Muscle–Tendon junction 189

2 Patterns of Traumatic Injury 189
2.1 Introduction 189
2.2 Acute Tensile Overload 189
2.3 Muscle Contusion 191
2.4 Delayed Onset Muscle Soreness 191
2.5 Pressure Overload (Compartment Syndrome) 191
2.6 Muscle Hernia 191

3 Muscle Healing 191

4 Complications of Muscle Injury 192
4.1 Introduction 192
4.2 Myositis Ossificans/Heterotopic Ossification 192
4.3 Calcific Myonecrosis 192

5 Imaging Modalities and Technique 192
5.1 Introduction 192
5.2 Magnetic Resonance Imaging 193
5.3 Ultrasound 201

6 Specific Muscle Injuries 206
6.1 Side Strain 207
6.2 Rectus Abdominis Strain 208
6.3 Flexor Pronator Musculature 209
6.4 Hamstring Injuries 209
6.5 Calf Muscle Complex 212
6.6 Rectus Femoris Tears 213

References 216

Abstract

MRI is the "gold standard" for the assessment of muscle injuries. This chapter includes a discussion of the structure of muscle and the muscle–tendon junction, the use of MRI and ultrasound for the assessment of muscle injury and the current grading systems for both modalities. Muscle injuries include: muscle strain/tear, muscle contusion, delayed onset muscle soreness, compartment syndrome and muscle hernias. Complications of muscle injuries include: myositis ossificans and calcific myonecrosis. Sports specific injuries to rectus abdominis, the flexor-pronator muscle group, hamstrings (acute and recurrent injuries) and rectus femoris and side strain have also been addressed.

Key points:

1. MRI is the "gold standard" for investigation of muscle injuries using fluid sensitive sequences.
2. The widely used grading system for muscle injuries (Grade 1 strain, Grade 2 partial tear and Grade 3 complete tear) is inadequate in so far as it fails to address the issue of concomitant injury to the intramuscular component of the tendon. Recent studies have demonstrated that injury to the intramuscular component of the tendon has prognostic significance.
3. Measures of the longitudinal lengths as well as percentage and volume of muscle injury in MRI have some predictive value with respect to time to return to sports activities.
4. The MRI appearance of a muscle contusion may be similar to a muscle strain/tear.
5. On MRI, recently exercised muscle demonstrates increased signal intensity on fluid-sensitive sequences secondary to an increase in intracellular water which normally resolves within minutes of cessation of activity. However, mild post exercise oedema can persist for some time and can mimic a low grade muscle strain injury.

S. Dimmick · J. M. Linklater (✉)
Castlereagh Imaging, 60 Pacific Highway,
St Leonards, NSW 2065, Australia
e-mail: JamesLinklater@casimaging.com

C. Rehnitz · M.-A. Weber
Department of Diagnostic and Interventional Radiology,
University Hospital Heidelberg, Im Neuenheimer Feld 110,
69120 Heidelberg, Germany

M.-A. Weber (ed.), *Magnetic Resonance Imaging of the Skeletal Musculature*, Medical Radiology. Diagnostic Imaging,
DOI: 10.1007/174_2013_878,

© Springer-Verlag Berlin Heidelberg 2013
Published Online: 22 October 2013

Table 1 Categories of muscles based on the orientation of muscle fibres

Shape and architecture	Subcategory	Example
Fibres parallel to the line of pull	Strap-like	Sartorius
	Tendinous intersections at intervals	Rectus abdominis
Fusiform muscle—close to parallel in the belly. Converge on a tendon either proximally, distally or both		Biceps femoris
Fibres oblique to the line of pull	Triangular	Adductor longus
	Unipennate	Flexor pollicis longus
	Bipennate	Rectus femoris
	Multipennate	Deltoid
	Spiral or twisted arrangement	Sternal fibres of pectoralis major, latissimus dorsi
	Passes obliquely from superficial to deep aponeuroses (“unipennate” type)	Soleus
	Spiral around a bone	Supinator
	Two or more planes of fibres arranged in differing directions	Sternocleidomastoid

6. Muscle injuries are not specific to certain sports, but some biomechanics are typical and therefore some injury patterns occur more often in particular sports and will be presented in this book chapter. The reporting radiologist should know these mechanisms to best plan the MRI scans and interpret the MRI findings.

1 Anatomy of Muscle

1.1 Structure of Skeletal Muscle

Skeletal muscle consists of parallel bundles of long, multinucleate fibres and is capable of powerful contractions due to the regular organisation of its contractile proteins (please see also “Correlation of skeletal muscle anatomical to MRI and US findings”). Skeletal muscle may be classified according to its general shape and predominant orientation of fibres (Table 1) (Standring 2005). Skeletal muscles consist of a variable number of anatomically discrete fascicles. Each fascicle is composed of multiple muscle fibres (myofibres). Muscle fibres are long, cylindrical structures that range in size from 10 to 100 μm for different muscles. Each muscle fibre consists of thousands of myofibrils. Sarcomeres are the functional subunit of myofibrils and are joined end-to-end and contain two types of protein filaments: a thick filament (consisting of myosin) and a thin filament (consisting of actin, troponin and tropomyosin).

When a muscle fibre is viewed microscopically, transversely orientated bands or striations are identified due to differences in refractive indexes of the various parts of the sarcomere. Z-lines constitute the boundaries of the sarcomere. The A-band consists of thick filaments with interdigitation and a degree of overlap of the thin filaments at each end. The I-band consists of two adjacent sarcomeres where the thin filaments do not overlap the thick filaments (Standring 2005).

Nuclei of the muscle fibre are located at the periphery, under the plasma membrane or sarcolemma and are most numerous in the region of the neuromuscular junction. Also located adjacent to the nuclei and to a lesser extent, adjacent to the myofibrils, are Golgi apparatus, ribosomes and mitochondria.

The endomysium is a delicate network of connective tissue, which surrounds muscle fibres. It contains capillaries and bundles of small nerve fibres and is the site of metabolic exchange between muscle and blood.

The perimysium covers groups of muscle fibres to form parallel bundles called fasciculi. The perimysium is the inward extension of the epimysium, which is a collagenous sheath that invests entire muscle groups. All three sheaths (endomysium, perimysium and epimysium) coalesce at sites of attachment to tendons, aponeuroses and fasciae, thereby creating the ability to resist shear stresses (Standring 2005).

Muscle fibres are functionally divided into two groups—type I (also known as slow-twitch fibres) and type II (also known as fast-twitch fibres). Type II fibres are further subdivided into types IIa, IIx and IIc. The human body consists of 50 % type I, 25 % type IIa, 23–24 % type IIx and 1–2 % type IIc fibres (Exeter and Connell 2010).

Type I fibres have a longer time to reach peak tension (110 ms), compared with type II fibres (50 ms). Type II fibres are larger, contain a faster form of ATPase and have a more developed sarcoplasmic reticulum, ensuring more effective calcium delivery. Different fibre types also contain a variety of different ATP generation mechanisms for muscle contraction—type I fibres are slow oxidative, type

IIa are fast oxidative/glycolytic, type IIx are fast glycolytic (Exeter and Connell 2010).

Neural innervation also differs between fibre types. The type of motor neuron that innervates a specific group of muscle fibres determines the muscle fibre type. Each motor unit (varying number of muscle fibres) innervates only one fibre type (Standring 2005).

Specific muscles and muscle groups throughout the body are therefore able to perform certain functions depending on the type of muscle fibres they contain. Type I fibres are activated during low intensity exercise or endurance events and produce less force than type II fibres. Type II fibres are recruited during short duration, high intensity activities. Aerobic, anaerobic or resistance training is capable of changing fibre types (Standring 2005).

1.2 Tendons

Tendons facilitate the transmission of forces generated by muscle contraction on to bone, facilitating movement and maintenance of posture. Tendons are present at the insertion of most muscles. Many muscles also have a tendinous origin. Tendons are round or oval in cross-section and consist of fascicles of type I collagen, orientated parallel to the long axis of the tendon. Small vessels and nerves course within loose connective tissue between fascicles.

Tendons attach to bone, both at the periosteum and through fasciculi that continue deep into the cortex of the bone. A plate of fibrocartilage at the site of bony attachment serves to cushion and reinforce the site of attachment (Standring 2005). Tendons vary in length in different muscles and may have an intramuscular component or component at the muscle surface, resulting in a relatively elongated muscle tendon junction.

The elasticity of tendons allows them to be elongated by up to 6 % without damage. Recovery of the elastic recoil of tendons may also make movement more efficient (Standring 2005).

1.3 Aponeuroses

Aponeuroses are flattened tendons (Benjamin et al. 2008) which may be separate structures emerging from a muscle belly (e.g. tendons of latissimus dorsi and pectoralis major) or fibrous sheet on the surface or within a muscle (e.g. soleus). Strain within the tendon of soleus differs in the aponeurotic portion when compared with the remainder of the tendon (Finni et al. 2003). This is associated with the pattern of force transmission via intramuscular connective tissue. Non-homogeneous strains may occur within the aponeurosis of soleus, which may be secondary to a compartmentalised recruitment of muscle fibres for a submaximal contraction (Finni et al. 2003).

1.4 Muscle–Tendon junction

The muscle–tendon junction (musculotendinous or myotendinous junction) is the weakest link in the muscle tendon unit (Palmer et al. 1999). At the muscle–tendon junction, tendon fibrils insert into deep recesses between finger-like processes of skeletal muscle cells, which are covered by a thick layer of basement membrane (Jozsa and Kannus 1997). The tendon fibrils attach to the basement membrane of the skeletal muscle cells.

Interdigitation between the tendon fibrils and myocytes increases the contact area between myocytes and extracellular collagen fibres and results in the ability to dissipate enormous tensile forces during muscle contraction (Palmer et al. 1999). Unfortunately, when compared with the adjacent muscle, tendon and osseous insertion, the muscle–tendon junction has poorer viscoelastic properties and a reduced capacity for energy absorption (Palmer et al. 1999). As a consequence, in adults, the most common site of muscle strain or tear is at the muscle–tendon junction.

2 Patterns of Traumatic Injury

2.1 Introduction

Muscle injuries are one of the most common injuries sustained while playing sport and constitute between 10 and 55 % of all sporting injuries (Beiner and Jokl 2001; Best and Hunter 2000; Garrett 1996; Huard et al. 2002; Järvinen et al. 2005). Muscle injury results from a variety of mechanisms including muscle strain/tear, epimyseal fascial injury, delayed onset muscle soreness (DOMS), muscle contusion, muscle herniation and lacerations (Kijowski 2011; Kneeland 1997). Avulsions of the origin or insertion of muscles and tendinopathy is beyond the scope of this chapter.

Mimics of muscle injury on magnetic resonance imaging include—subacute denervation, muscle infarction, inflammatory myositis, normal immediate post exercise muscle oedema and deep venous thrombosis (Farber and Buckwalter 2002).

2.2 Acute Tensile Overload

Muscle strain is the most common muscle injury sustained by both the general and sporting populations (Blankenbaker and Tuite 2010; Linklater et al. 2010; Shelly et al. 2009; Slavotinek 2010). Muscle strains occur when the muscle is subjected to an excessive tensile force, which leads to overstretching and rupture of myofbrils (Kijowski 2011). Most commonly, muscle strains occur during eccentric contraction. During an eccentric muscle contraction, muscle fibres are forced to lengthen, creating greater tensile forces than can be created during concentric contraction, when muscle fibres shorten. Injuries predominantly occur at the musculotendinous junction and may involve the intramuscular tendon.

The majority of muscle injuries are diagnosed clinically (Kijowski 2011). There is a spectrum in the clinical presentation of muscle strain injury, which may range from a severe tearing sensation to a mild tightening sensation. Historically, the most commonly used grading system was devised by O'Donoghue (1962) on the basis of the clinical impression of the extent of injury. Grade 1 injury (strain) consists of a minor degree of microscopic tearing with no macroscopic muscle fibre discontinuity. Grade 2 injury (partial tear) is defined as an incomplete disruption of muscle fibres. Clinically, grade 1 and grade 2 injuries can be difficult to distinguish—both grades result in loss of function and in some studies have shown no significant difference in time to return to sport (Blankenbaker and Tuite 2010). Grade 3 injury (complete tear) is a complete rupture of the muscle. This grading system fails to take into account the presence or absence of concomitant tendon injury and if present, the extent of tendon injury. There is scope for development of a new classification system which more precisely characterises the extent of muscle and tendon injury, hopefully providing a higher level of prognostic significance with respect to time to return to sport and risk of recurrent tear (Linklater et al. 2010).

There are specific characteristics of a muscle that makes it more susceptible to injury. Long, fusiform muscles that extend across two joints and have a propensity for eccentric contraction are more susceptible to injury. Examples of these muscles include biceps brachii, rectus femoris, long head of biceps femoris, semitendinosus and semimembranosus (hamstrings) and the medial head of gastrocnemius. A predominance of type II fibres may also predispose to injury.

Other factors which may predispose to muscle tears include: past muscle strain injury, low muscle strength, muscle fatigue, age, lack of warm-up, muscle temperature and poor flexibility (Garrett 1996; Mair et al. 1996; Orchard 2001).

The long head of biceps femoris, semimembranosus, and semitendinosus muscles consist of a proximal and distal "free" tendon and relatively extensive tendon–muscle interface which may be intramuscular (central tendon) or at the muscle surface, such that the proximal and distal tendons overlap or almost overlap. The central tendon is similar in configuration to the central rachis of a feather, with radiating myofibrils arising from it, exemplified by the proximal tendon of long head biceps femoris (Comin et al. 2013). As stated previously, the most common site of muscle strain/tear occurs adjacent to the muscle–tendon junction, which may be located at the central aspect of the muscle or eccentrically at the muscle surface (Blankenbaker and Tuite 2010; Noonan and Garrett 1992) (Fig. 1). A study by Weishaupt (2001) demonstrated that 33 % of hamstring tears occur at the proximal muscle–tendon junction, 53 % at the intramuscular muscle–tendon junction and 13 % at the distal muscle–tendon junction (Weishaupt et al. 2001). These findings therefore indicate that the most common site of muscle–tendon junction injury is within its intramuscular portion.

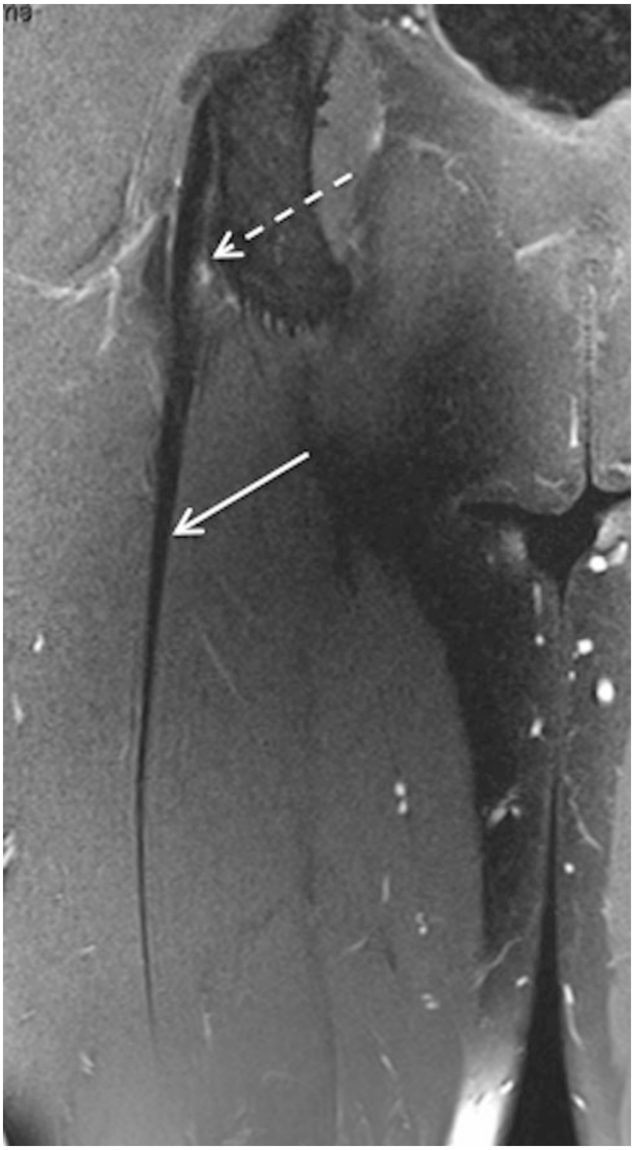

Fig. 1 Coronal proton density weighted MR image with fat saturation demonstrates the normal intramuscular component of the proximal tendon of the long head biceps femoris (*long arrow*). Note the presence of hamstring origin tendinopathy and non-acute, non-retracted deep surface partial thickness tear (*short arrow*)

In a study by (Comin et al. 2013), central tendon disruption occurred exclusively in biceps femoris injury (12 of 45 cases). There were no central tendon disruptions of the semimembranosus or semitendinosus. In this same study, recovery times for injuries to the biceps femoris were significantly greater if there was central tendon disruption (Comin et al. 2013).

The investing fascia of a muscle can be described as a fascial ectoskeleton, providing an additional anchor point for muscle fascicles in addition to the proximal and distal tendons. Peripheral/epimyseal muscle injuries adjacent to the investing fascia/epimysium are less common than muscle–tendon junction injuries (Kijowski 2011). When they occur, they are thought to relate to differences in elasticity between epimysium and the adjacent muscle fibres (Blankenbaker and Tuite 2010). This is similar in pathogenesis to injuries at the muscle–tendon junction (Koulouris and Connell 2005). Peripheral/epimyseal injury has been described in the quadriceps and hamstring muscles, caused by an eccentric contraction (Connell et al. 2004; Cross et al. 2004). Differential contraction in two adjacent muscles may lead to injury involving both muscles.

2.3 Muscle Contusion

Muscle contusions constitute 2 % of muscle injuries, most commonly involving the quadriceps muscle group. They occur when a muscle sustains a sudden blunt force/direct blow, causing compression of the deep portion of the muscle against the underlying bone (Järvinen et al. 2005). As a result, there is disruption of capillaries and muscle fibres and an intramuscular haematoma which forms between muscle fibres, without muscle fibre disruption in most cases. Occasionally direct blunt trauma may result in muscle fibre discontinuity, for example in surfboard injuries to the biceps brachii muscle.

Contusional injuries are typically deep within the muscle belly, often involve more than one muscle and tend to be less symptomatic and have a shorter clinical course compared to muscle strain injuries. Clinically there are three severity grades described: mild, moderate and severe, depending on the remaining range of motion (Jackson and Feagin 1973). The loss of range of motion does not necessarily correlate with the extent of the haematoma on imaging and does not always correlate with loss of function (Megliola et al. 2006).

2.4 Delayed Onset Muscle Soreness

DOMS is an indirect muscle injury with reversible structural damage to the muscle at a cellular level resulting in an acute inflammatory response and an increase in intracellular fluid (Armstrong 1984; Cleak and Eston 1992). DOMS is associated with eccentric muscle contraction and is directly related to the intensity and duration of physical activity (Cleak and Eston 1992). Acute grade 1 muscle strain may be differentiated from DOMS clinically. Grade 1 strains have an acute onset of pain and dysfunction. Symptoms associated with DOMS typically commence at 1–2 days after the causative activity, is greatest at 24–48 h and gradually resolves over the next 48–72 h (Armstrong 1984; Cleak and Eston 1992).

2.5 Pressure Overload (Compartment Syndrome)

A compartment syndrome is elevation of pressure within a confined anatomic space resulting in a reduction in blood flow that threatens the viability and function of the tissues within the compartment (Stedman 2000). Compartment syndromes may present as a complication of an acute muscle injury. The most common causes include: fracture, blunt or penetrating trauma, burns, intramuscular haemorrhage and less likely, secondary to muscle tear. Patients commonly present with pain, which is disproportionate to the injury, exacerbation of pain when the affected muscle group is passively stretched. Neurological symptoms may also be present (Arciero et al. 1984; Davies 1979; Pearl 1981). Acute compartment syndrome is a surgical emergency requiring exploration and fasciotomy. In contrast, chronic exertional compartment syndrome involves exercise related pain which resolves with rest.

2.6 Muscle Hernia

Muscle hernias are an uncommon complication of muscle/compartmental injury and represents herniation of muscle through a small fascial defect which may relate to prior penetrating injury or develop at a site of penetration of the investing fascia by a nerve (e.g. superficial peroneal nerve as it penetrates the investing fascia of the lateral compartment in the leg).

3 Muscle Healing

Skeletal muscle healing occurs in a predictable sequence, regardless of the underlying cause of the injury (Hurme et al. 1991; Kalimo et al. 1997). The ruptured myofibres contract and the gap fills with blood products. An inflammatory response develops, with neutrophils and macrophages infiltrating the site of injury.

Release of proteases results in localised myofibre breakdown and necrosis. Macrophages then remove cell debris and secrete growth factors. The basement membrane remains intact, which subsequently acts as a scaffold that facilitates anatomically aligned reconstitution of the myofibrils.

Growth factors activate the regenerative stem cells of the muscle (called satellite or progenitor cells) which form myoblasts. Myoblasts differentiate into mononucleate myoblasts, then fuse to form multinucleated myotubes and finally undergo maturation to become myofibres (Hurme et al. 1991).

The ends of the repaired myofibres do not reattach to each other. Each ruptured myofibre attaches to, and is separated by interposed scar tissue produced by myofibroblasts (Hurme et al. 1991; Kalimo et al. 1997). A remodelling phase occurs, which is a period of maturation of the regenerated myofibres, retraction and reorganisation of the scar tissue and revascularisation with ingrowth of capillaries into the reparative tissue (Järvinen et al. 2005).

When there is a significant sized muscle tear, in the long term, there may be focal muscle fatty atrophy at the margins of the scar tissue and an overall reduction in muscle volume (Kääriäinen et al. 1998; Silder et al. 2008).

The single most important determinant of subsequent muscle function and risk of reinjury is the quality of scar formation and remodelling (Clanton and Coupe 1998; Stauber 1989). Scar formation may inhibit innervation of regenerating muscle tissue and reduce muscle contractility and range of motion (Quintero et al. 2009). The developing scar is the weakest point for recurrent tears up to 12 days post injury. After this time, re-tears occur in the adjacent myofibrils at the margins of the scar (Järvinen et al. 2000).

4 Complications of Muscle Injury

4.1 Introduction

Complications of acute muscle injury include—haematoma, acute compartment syndrome, myositis ossificans and calcific myonecrosis (Counsel and Breidahl 2010).

4.2 Myositis Ossificans/Heterotopic Ossification

Myositis ossificans is extensively presented in "MRI of muscle tumours" and thus here only briefly discussed in the direct context of muscle injuries.

As a complication of muscle injuries, heterotopic ossification occurs as myositis ossificans circumscripta. Following a muscle tear or a direct contusion and sometimes without a remembered trauma, a haematoma is initially present. This haematoma typically undergoes a maturation process exhibiting characteristic clinical, radiological and histological features.

4.3 Calcific Myonecrosis

Calcific myonecrosis presents as an expanding calcific mass that develops within a muscle post trauma. Most reported cases have occurred in the anterior and lateral compartments of the lower leg, with only single cases reported in the foot and forearm (Holobinko et al. 2003; Larson et al. 2004).

This entity most commonly occurs due to compartment syndrome post fracture of the tibia or femur and more rarely after neurovascular injury (Early et al. 1994; Milisano and Hunter 1992; Renwick et al. 1994; Viau et al. 1993). The reported interval from injury to presentation ranges from 10 to 64 years (average, 36 years) (Wang and Chen 2001).

The pathogenesis of calcific myonecrosis is unknown. An entire single muscle is replaced with central liquefaction and peripheral calcification.

The radiographic findings demonstrate a fusiform mass, which involves the entire muscle, with linear, peripherally oriented, plaque-like amorphous calcification. Differential diagnoses on radiographs include tumoral calcinosis, calcific tendonitis, calcific bursitis, synovial osteochondromatosis, synovial sarcoma, chondrosarcoma, osteosarcoma, and myositis ossificans (Olsen and Chew 2006).

On MRI, the mass is diffusely T2 hyperintense/fluid signal, while other areas of the lesion demonstrate heterogeneous, intermediate signal (Muramatsu et al. 2009; Ryu et al. 1996).

5 Imaging Modalities and Technique

5.1 Introduction

The role of imaging in acute muscle injuries includes establishing the site and extent of injury and providing some prognostic guidance regarding return to sport. In general the threshold for imaging is substantially lower in the elite athlete, when compared to the recreational athlete. In the recreational athlete, depending on the clinical context, there may still be a role for imaging to exclude an injury requiring surgery such as a hamstring origin avulsion (Colosimo et al. 2005; Cross et al. 2004; Folsom and Larson 2008; Slavotinek et al. 2002). In the elite athlete there may be a role for imaging in monitoring healing of a muscle injury.

Both MRI and ultrasound (US) may be utilised for the diagnosis of muscle injury (please see also "Imaging the skeletal muscle – when to use MRI and when to use ultrasound"). In Europe, US is often used as the first-line

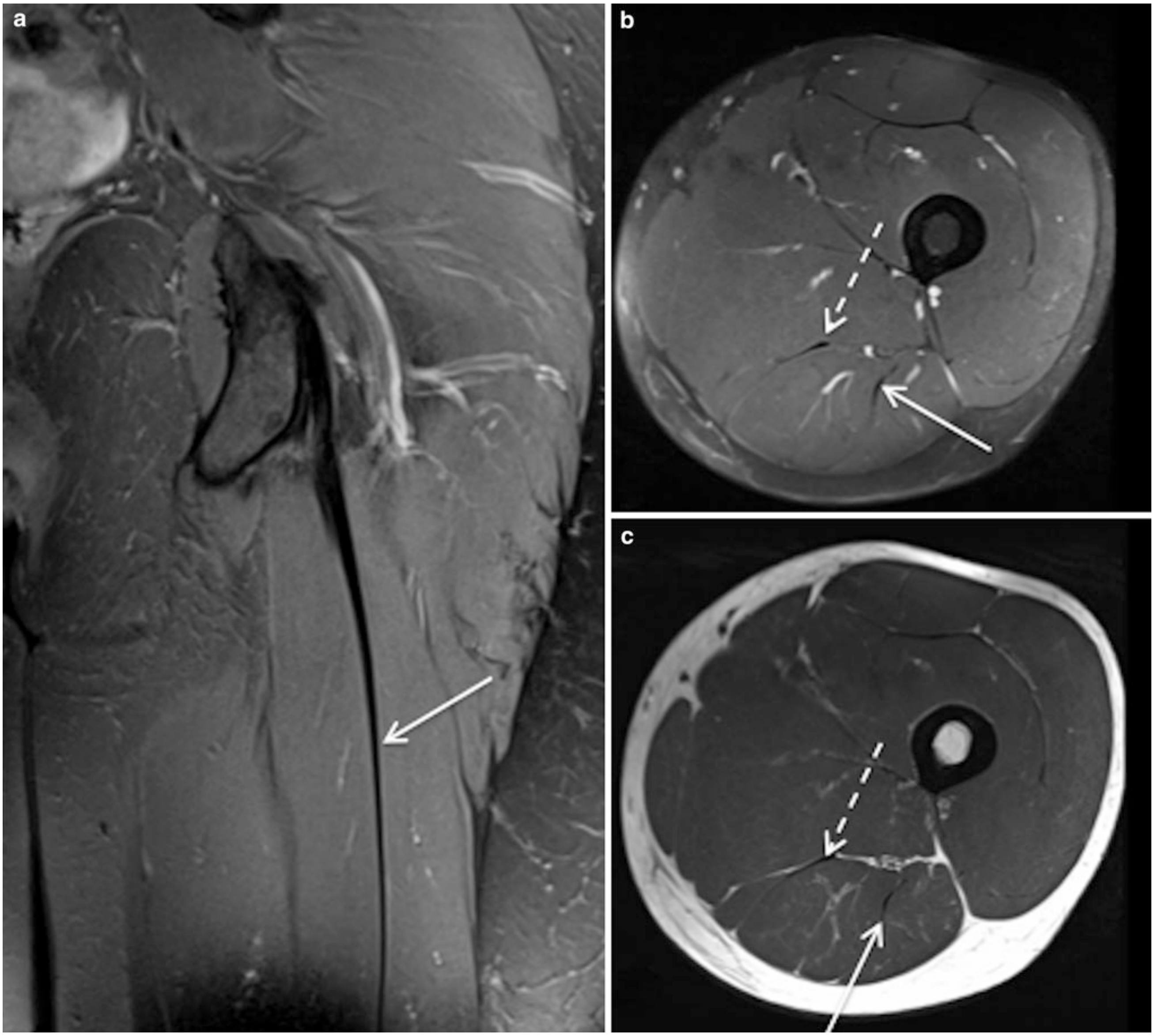

Fig. 2 Coronal proton density weighted MR image with fat saturation (**a**) and axial proton density weighted MR images, with and without fat saturation (**b** and **c** respectively) demonstrates the normal proximal tendon of long head biceps femoris (*arrows*) and semimembranosus (*dashed arrows*)

imaging modality. Ekstrand et al. (2012) have investigated which imaging methods are used to investigate hamstring injuries in 23 European professional soccer teams and revealed the following distribution: 58 % were examined by MRI, 29 % by US only and 40 % by both MRI and US. Interestingly, 13 % were managed clinically without the use of imaging. In North America and Australia, MRI is more commonly utilised in the first line assessment of acute muscle injury. The accuracy of MRI is superior to US, particularly with deep muscle injuries (Guillodo et al. 2011).

5.2 Magnetic Resonance Imaging

5.2.1 Introduction and Pulse Sequences

MRI is the “gold standard” for investigation of muscle injuries (Hayashi et al. 2012). Fluid sensitive sequences (Short Tau Inversion recovery (STIR), Dixon or frequency selective fat suppressed Proton Density (PD) or T2 sequences) are most efficacious in rendering conspicuous the intramuscular oedema associated with acute muscle injury, in demonstrating muscle fibre discontinuity and tendon injury. Fluid sensitive sequences are often combined

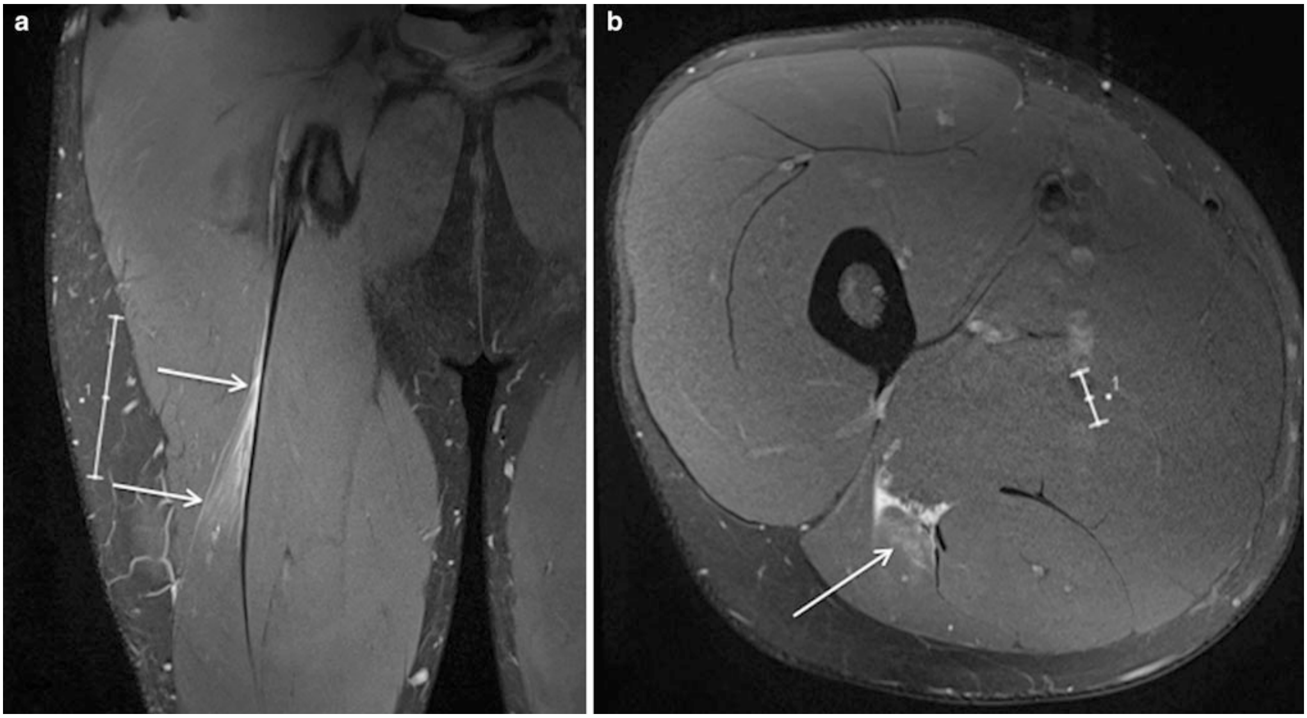

Fig. 3 Coronal (**a**) and axial (**b**) proton density weighted MR images with fat saturation in an Australian Rules football player with grade 1 muscle strain injury centred on the proximal muscle-tendon junction of the long head biceps of femoris, manifest as mild feathery intramuscular oedema and subfascial and perifascial oedema, without muscle fibre discontinuity or acute tendon injury (*arrows*). Note the presence of mild scarring of the intramuscular segment of the tendon related to remote injury

with either a non-fat suppressed PD or T1 sequence. Measures of the longitudinal lengths as well as percentage and volume of muscle injury (Connell et al. 2004) in MRI are strong predictors of the time to return to play. It has been suggested that persistence of oedema defines the period of increased vulnerability to develop a re-tear (Fleckenstein et al. 1989). MRI is also more sensitive in monitoring muscle healing compared with US (Fleckenstein et al. 1989).

As a consequence, MRI may be of benefit for the assessment of the nature and extent of the injury, particularly in elite athletes.

The normal MRI appearance of muscle is intermediate signal intensity on all sequences. There should be no signal hyperintensity on water sensitive fat-suppressed, inversion recovery or Dixon subtraction method techniques (Linklater et al. 2010) (Fig. 2).

Prior to imaging, a skin maker should be placed on the patient overlying the region of interest. The coverage of the study should include the muscle origin, extending below the region of abnormality. Selection of an appropriate coil should be based on the coverage required, so that the coil does not need to be repositioned during the study. Pulse sequences should include: long and short axis proton density (PD) and either a STIR or frequency selective fat suppression (T2 or proton density) or Dixon fat suppression technique. A single long axis T1 sequence is also performed in some centres for characterisation of haematomas and identification of muscle atrophy.

Muscle fibre tracking with diffusion tensor imaging (DTI) has been used to assess muscle damage (Zaraiskaya et al. 2006) and to measure pennation angle (Lansdown et al. 2007). Normal muscle on DTI demonstrates uniformity in bulk directionality and exhibits orderly arrangements (Hayashi et al. 2012). Disturbance of normal arrangement of muscle fibres is demonstrated on DTI after injury (O'Brien 2005). At present, DTI remains an investigation/research tool and does not play a role in the clinical MRI assessment of muscle injury (see also "Diffusion-weighted and diffusion-tensor imaging: Applications in skeletal muscles").

5.2.2 MRI Findings of Acute Muscle Strain/Tear

Grade I muscle strain demonstrates intramuscular signal hyperintensity on fluid sensitive sequences without discernible muscle fibre disruption. The oedema pattern is classically "feathery" in appearance (Blankenbaker and Tuite 2010). This represents oedema insinuating between intact muscle fascicles. The injury is most commonly seen adjacent to the muscle–tendon junction but may be peripheral-epimyseal. Fluid may also be identified tracking along the perifascial intermuscular region. In professional sport, the threshold for performing an MRI for muscle strain

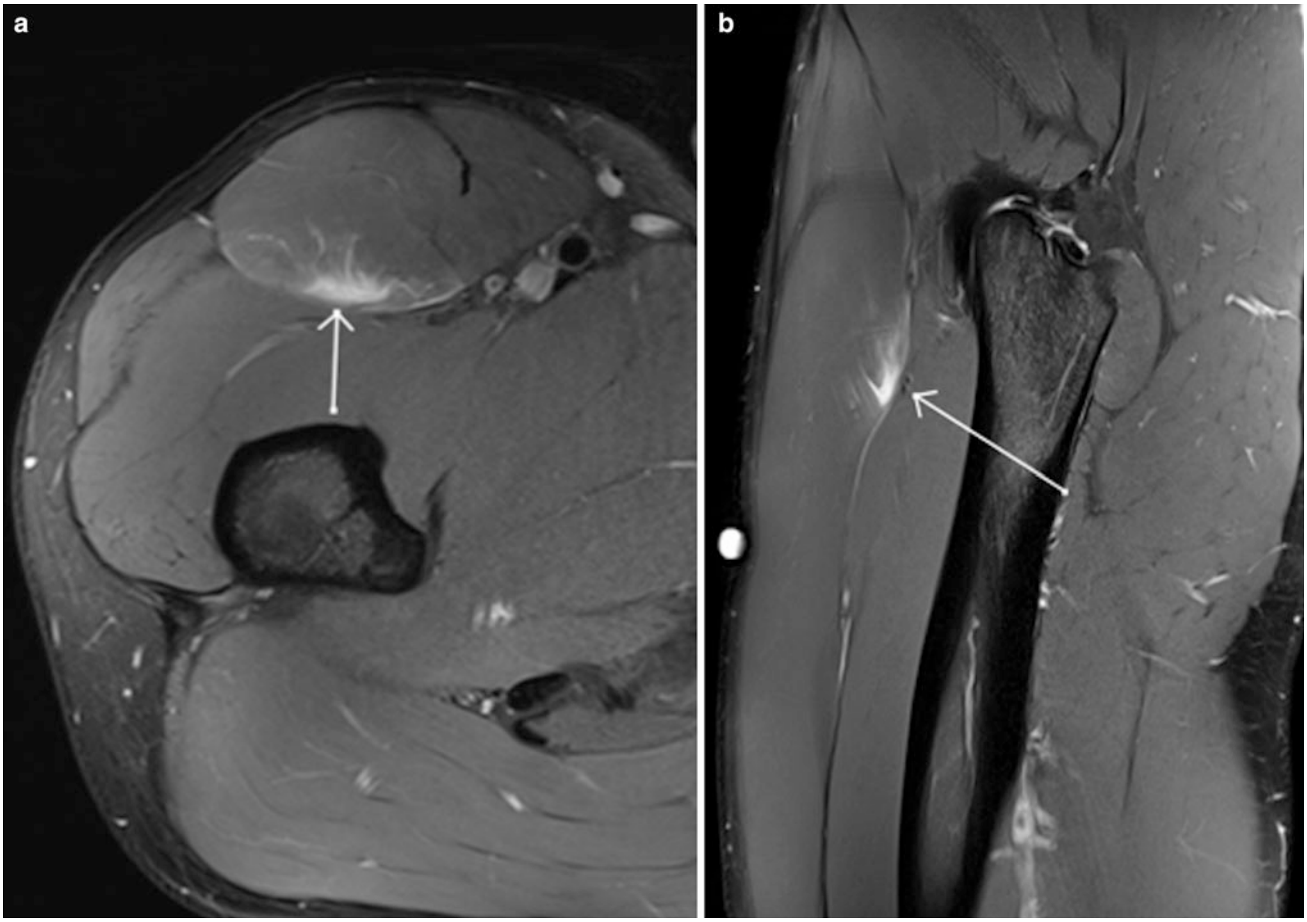

Fig. 4 Axial (**a**) and sagittal (**b**) proton density weighted MR images with fat saturation show a grade 1 epimyseal muscle strain injury of rectus femoris, manifest as eccentric-peripheral muscle oedema, without muscle fibre discontinuity (*arrows*)

injury is reducing. As a consequence, there are increasing instances where it is difficult to differentiate between post exercise oedema and a grade 1 strain (Figs. 3, 4). In general post exercise oedema demonstrates a ground glass-like, mild degree of signal hyperintensity and often demonstrates a somewhat patchy geographic distribution (Fig. 5).

In partial tears (grade 2), disruption of muscle fibres is identified. Oedema and haemorrhage is present within the muscle or at the muscle–tendon junction, often with perifascial extension (Kijowski 2011). Concomitant injury to the intramuscular component of the tendon may be evident, manifest as signal hyperintensity on fluid sensitive sequences. On longitudinal cross-section the tendon may demonstrate nonlinear, concertina-like morphology due to elongation. Higher grade injuries may be associated with macroscopic tendon fibre discontinuity (Kijowski 2011). A haematoma at the muscle–tendon junction may develop in patients with a partial tear and is generally not seen in the setting of a Grade 1 strain injury (El-Khoury et al. 1996). Intramuscular haematomas are not always indicative of a Grade 2 muscle strain injury as they may also be seen in the setting of a contusional muscle injury (Figs. 6, 7, 8).

Complete tears (grade 3) demonstrate complete discontinuity of muscle fibres, usually with associated tendon fibre discontinuity and an associated haematoma. Extensive adjacent intramuscular and perifascial oedema may be present. It may be difficult to determine whether there is a partial or a complete tear due to blood and oedema filling the defect between the torn muscles (Blankenbaker and Tuite 2010) (Fig. 9).

Acute and subacute muscle tears are usually best visualised on longitudinal sequences (Linklater et al. 2010). In the subacute phase, immature scar tissue forming at the point of injury is generally of intermediate signal intensity tissue and often best appreciated on proton density sequences. When the scar tissue remodels, the signal intensity becomes increasingly more hypointense on all pulse sequences (Linklater et al. 2010) (Fig. 10).

Important findings to identify and document on MRI in the setting of muscle injury includes: site of injury, the

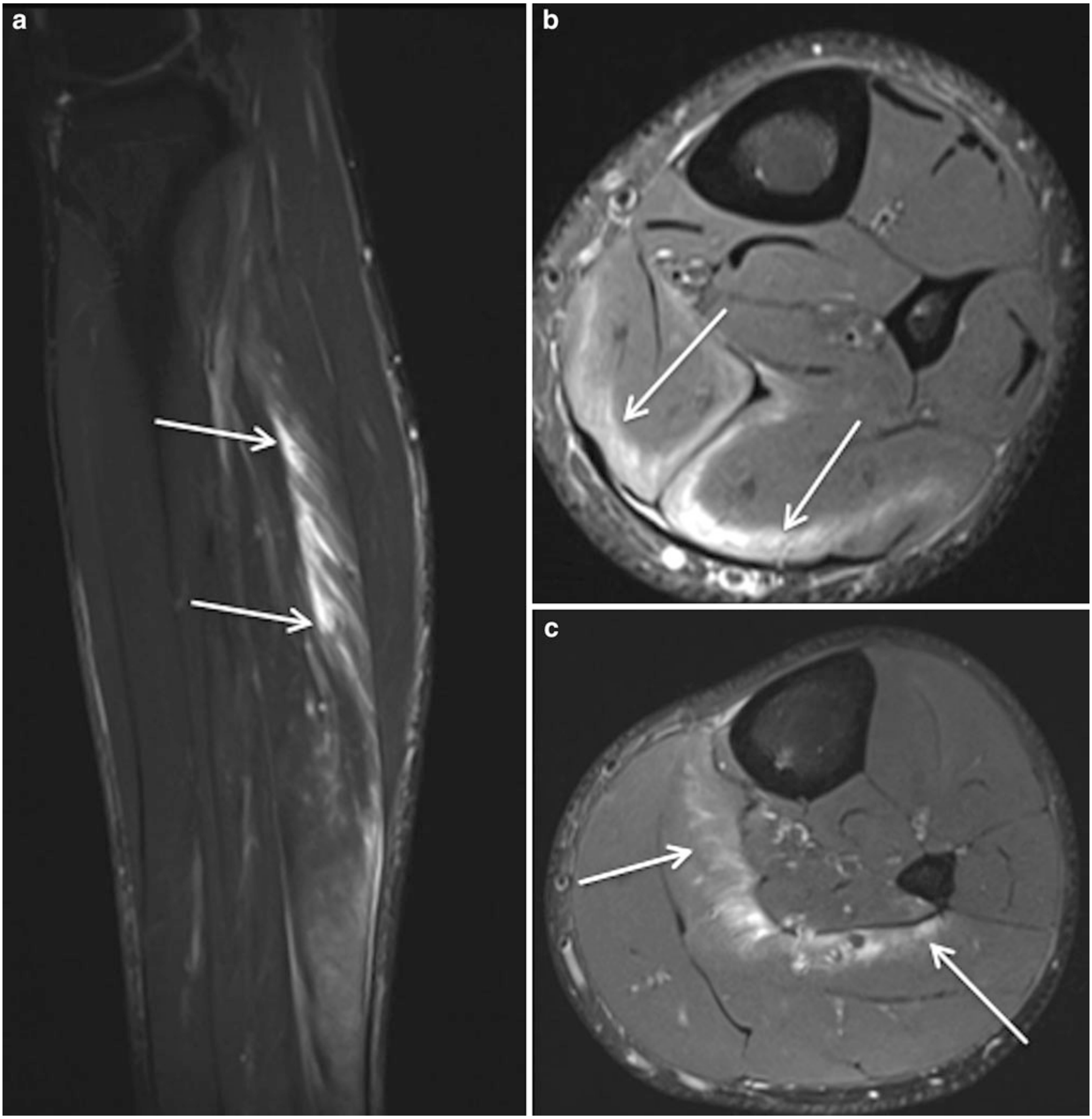

Fig. 5 Sagittal STIR MR image (**a**) and axial proton density weighted MR images with fat saturation (**b** and **c**) demonstrate extensive post exercise oedema within the soleus muscle in an Australian Rules football player, centred around the muscle tendon junctions, demonstrating a somewhat geographically marginated distribution (*arrows*). *Note*: The patient played an entire game 2 days after this MRI

presence/absence of fibre discontinuity, longitudinal extent and percentage cross-sectional oedema of muscle oedema, signal hyperintensity or frank fibre discontinuity within the intramuscular component of the tendon (Blankenbaker and Tuite 2010). Longer recovery times are associated with a larger volume of affected muscle, greater longitudinal extent and percentage cross-sectional area of muscle oedema, more cranially located injuries, and the presence of a haematoma (Askling et al. 2007; Connell et al. 2004; Gibbs et al. 2004; Malliaropoulos et al. 2010).

Healing muscle strains/tears demonstrate a reduction in the amount of oedema on fluid-sensitive sequences. Oedema post muscle injury may persist for weeks to months, even after return to sport and represents continuation of the healing process (Kijowski 2011). After the oedema has resolved, variable amounts of fatty atrophy and

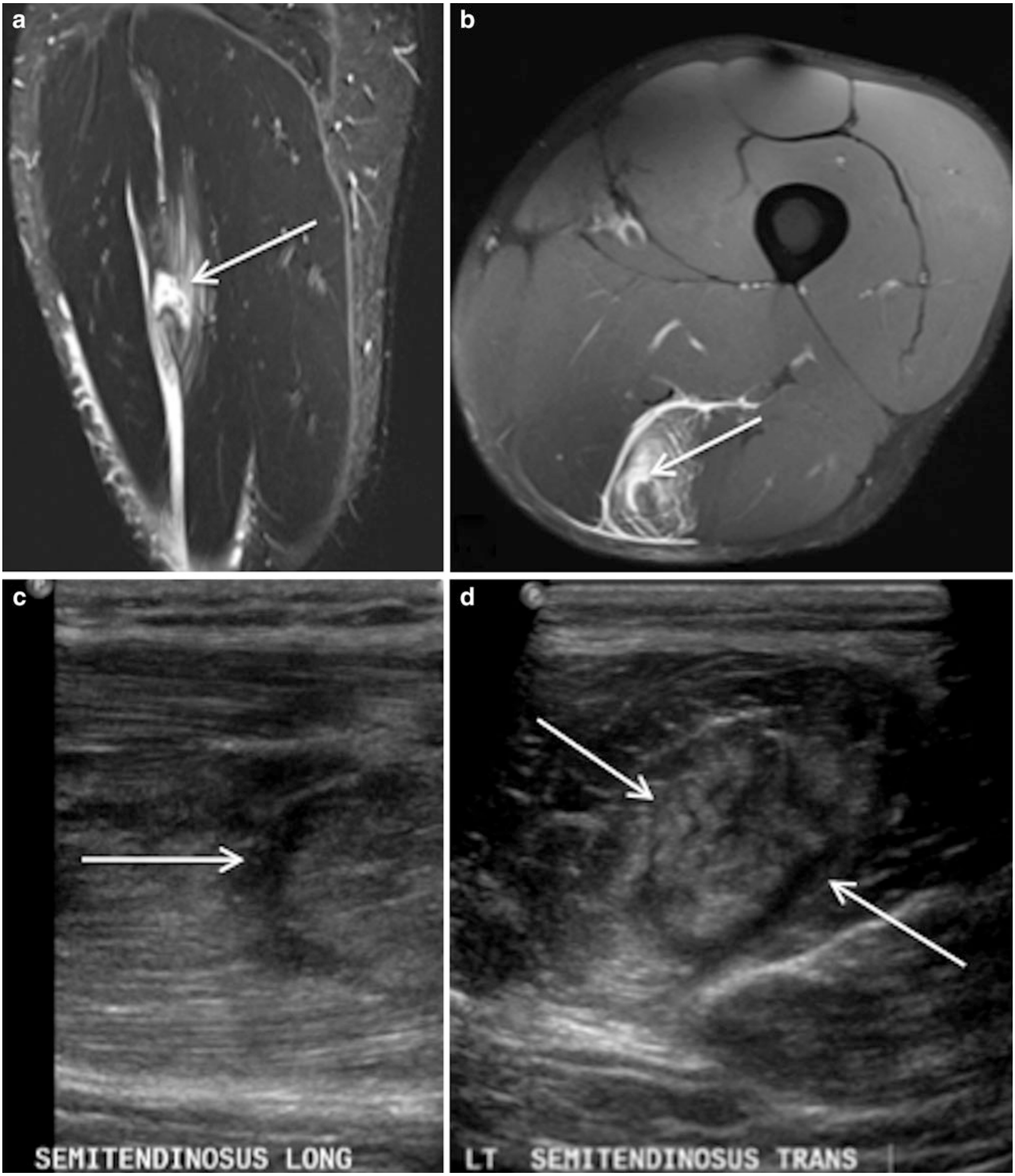

Fig. 6 Sagittal STIR MR image (**a**), axial proton density weighted MR image with fat saturation (**b**) and corresponding US images (**c** and **d**) in a professional rugby league player demonstrates a grade 2 injury of the semitendinosus muscle at the proximal margin of the intramuscular segment of the distal tendon, with fluid signal evident at the point of muscle fibre disruption and moderate surrounding intramuscular oedema (*arrows*). The area of muscle fibre discontinuity can also be appreciated on US. There was no associated tendon

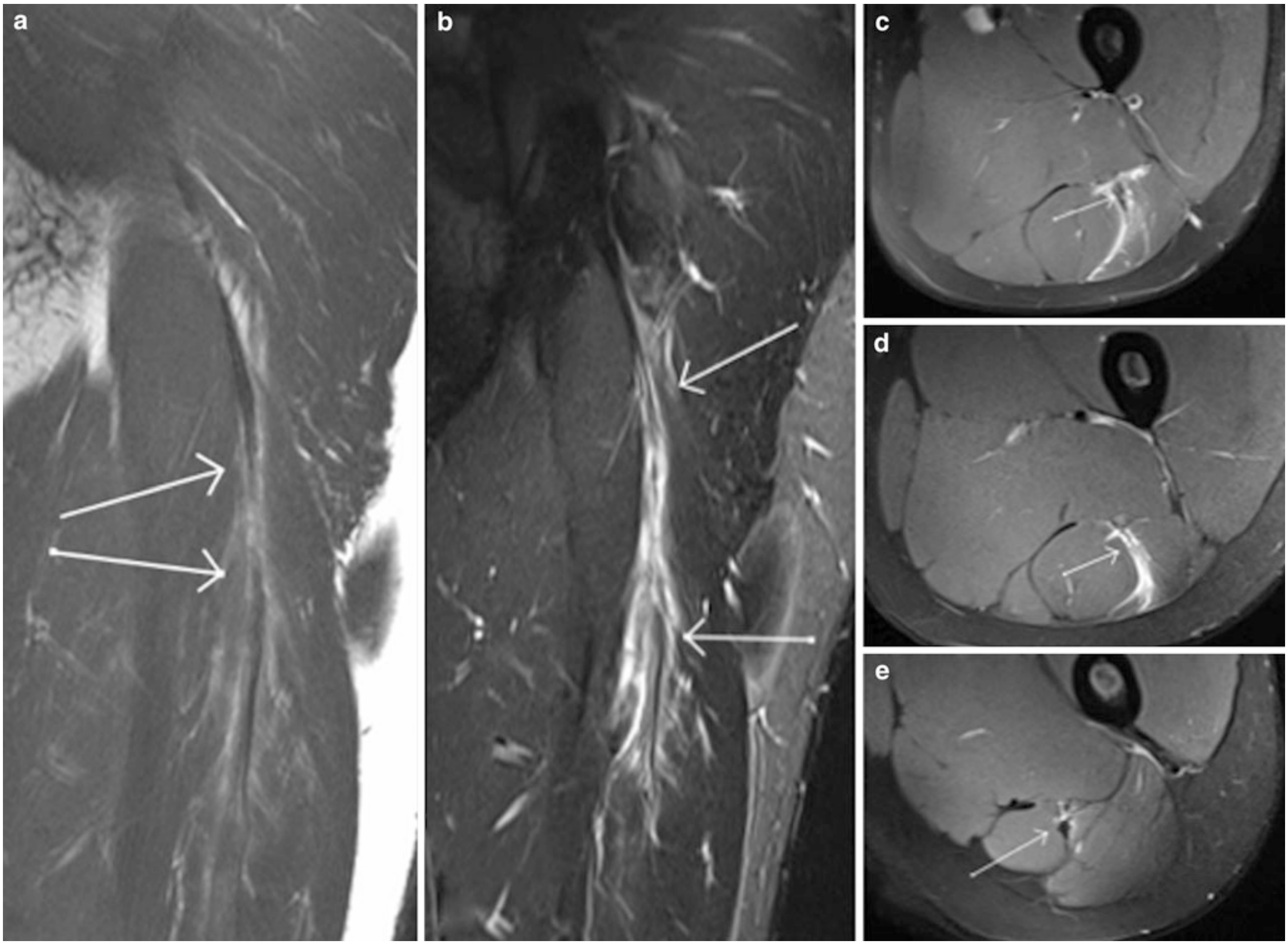

Fig. 7 Coronal STIR MR image (**a**), coronal T2 weighted MR image with fat saturation (**b**) and axial proton density weighted MR images with fat saturation (**c**–**e**) demonstrate an injury to the proximal aspect of the long head biceps femoris with frank tear of the intramuscular segment of the proximal tendon and adjacent feathery intramuscular oedema (*arrows*). This pattern of injury does not readily fit into the generally used classification system for muscle injuries which does not take into account the presence or absence of tendon injury

compensatory hypertrophy may be seen. T1 and T2 hypointense foci represent scar formation and residual blood degradation products (hemosiderin) (Blankenbaker and Tuite 2010; Linklater et al. 2010; Slavotinek 2010).

5.2.2.1 MRI Negative Muscle Strain

MRI negative strains have been described. These strains are associated with a better prognosis compared with MRI positive strains for time to return to sport and risk of recurrent injury (Schneider-Kolsky et al. 2006; Verrall et al. 2001, 2003).

5.2.3 Muscle Contusion

The MRI appearance of a contusion may be similar to a muscle strain/tear, however may have a variable appearance depending on the age of the blood products. The typical appearance in mild contusion is a feathery appearance of diffuse muscle oedema on fluid sensitive sequences. More severe cases of contusion demonstrate a haematoma. T1-weighted sequences may be used to differentiate between haemorrhage/haematoma and oedema and to estimate the age of the haematoma (Hayashi et al. 2012) (Fig. 11).

An acute haematoma is typically isointense to muscle on T1-weighted images and is hypointense on T2-weighted images. Methaemoglobin is the predominant component of a subacute haematoma (injury occurred less than 30 days prior), which is hyperintense relative to muscle on both T1-weighted and fluid-sensitive sequences. With further evolution of the blood products, a hypointense rim develops due to hemosiderin deposition and fibrosis and is visible on all pulse sequences (Blankenbaker and Tuite 2010) (Fig. 12). With evolution, a haematoma will reduce in size and will usually resolve within 6–8 weeks. An underlying

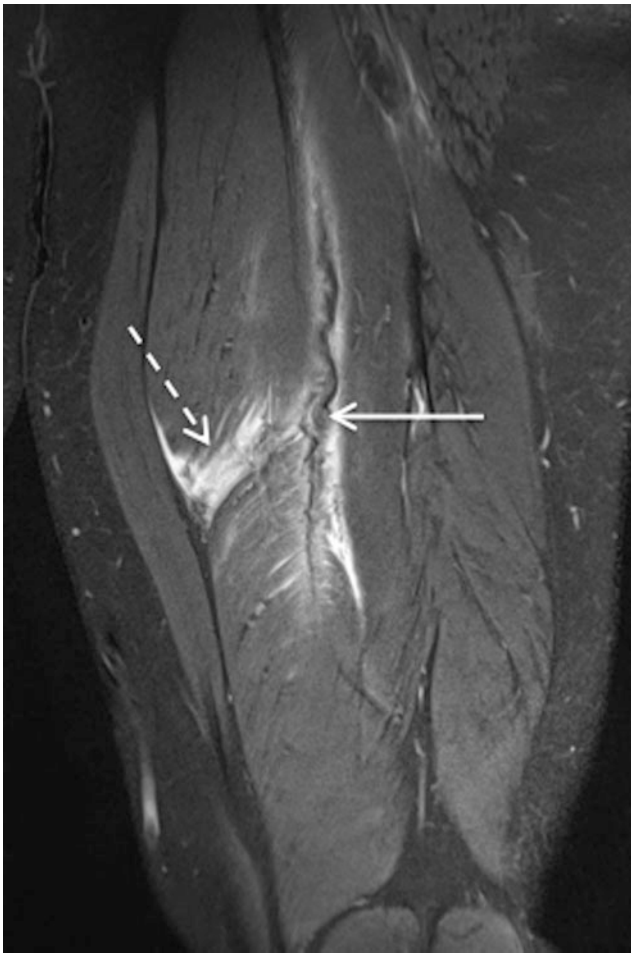

Fig. 8 Coronal proton density weighted MR image with fat saturation demonstrates a non retracted tear (*arrow*) of the intramuscular segment of the proximal tendon of the semimembranosus muscle, with mildly redundant morphology of the tendon at the proximal and to a lesser extent at the distal margin, with moderate adjacent intramuscular oedema and small focus of muscle fibre discontinuity (*dashed arrow*)

cause should be sought if a haematoma persists longer than 6–8 weeks (Blankenbaker and Tuite 2010).

5.2.4 Delayed Onset Muscle Soreness

On MRI, recently exercised muscle demonstrates increased signal intensity on fluid-sensitive sequences secondary to an increase in intracellular water. This usually resolves within minutes of cessation of activity but may persist to some degree for several hours without symptoms (Fleckenstein et al. 1988).

The typical appearance of DOMS on MRI is difficult to differentiate from a muscle strain (grade 1). As stated previously, the differentiation of these two diagnoses may be the clinical history of the onset and duration of symptoms. There is “feathery” oedema within the muscle and perifascial oedema, which may persist for up to 80 days (Shellock et al. 1991). Although the areas of signal abnormality have been reported to correlate well with sites of structural injury, but poorly with sites of patient symptomatology, the literature in this area is sparse (Nurenberg et al. 1992) (Figs. 13, 14).

Similarly, differentiation of DOMS and fatigue-induced muscle injury requires appropriate history from the patient. Patients suffering from DOMS complain of stiff, weak muscles and pain at rest, which resolves within 1 week.

Whereas aching, circumscribed muscle firmness, dull ache to stabbing pain which increases with continued activity is associated with fatigue-induced muscle injury. This entity may persist for a longer duration and predispose to acute injury (muscle strain/tear) (Mueller-Wohlfahrt et al. 2012). Further research is required to further define fatigue-induced muscle injury (Opar et al. 2012).

5.2.5 Acute Compartment Syndrome

On MRI, acute and chronic compartment syndrome is visualised as diffuse muscle oedema, petechial haemorrhage within the affected muscles and enlargement of the affected compartment (Elliott and Johnstone 2003; Elsayes et al. 2006). There is no indication for MR imaging of an acute compartment syndrome as this could delay fasciotomy. In cases where intracompartmental pressure elevation is minimal (30-40 mmHg), there may be no observable abnormality on MRI (Counsel and Breidahl 2010).

Chronic exertional compartment syndrome is often bilateral and relieved with rest. This entity is due to increased compartment pressure during exercise. The anterior and lateral compartments of the leg are most commonly affected. Less commonly, the compartments of the thigh, forearm and foot may be affected (Rybak and Torriani 2003; Verleisdonk 2002).

In exercising muscle, there is increased blood flow and increased permeability resulting in a shift in water content with the muscle. On MRI, this increased water content within muscle during exercise results in an increase in T1 and T2 relaxation times (Litwiller et al. 2007; Ringler et al. 2013). This is best assessed on proton density or T2-weighted sequences as increased signal hyperintensity relative to a resting state. In normal individuals, increased muscular water content is transient, peaking during exercise and returning to normal within minutes of cessation. In patients with chronic exertional compartment syndrome, signal hyperintensity within the muscle peaks after cessation of exercise, with a delay in return to the signal intensity and water content of a resting state (Litwiller et al. 2007; Ringler et al. 2013). Litwiller and colleagues in 2007 reported a threshold for the ratio of relative T2-weighted signal intensity in post exercise muscle compared to the resting state of 1.54 which had a diagnostic sensitivity of 96 %, specificity of 90 % and accuracy of 96 % for chronic exertional compartment

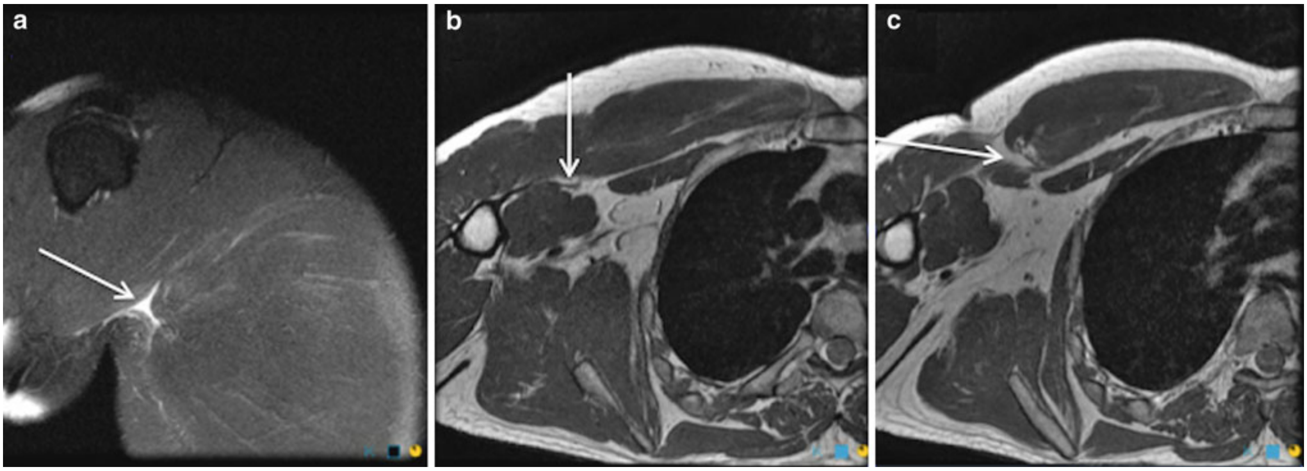

Fig. 9 Coronal proton density weighted MR image with fat saturation (**a**) and axial proton density weighted (**b** and **c**) images demonstrate a grade 3 muscle–tendon junction injury involving the sternal head of pectoralis major. The *arrow* in **a** denotes the small fluid collection at the site of tear. The *arrow* in **b** denotes the distal tendon edge, while the *arrow* in **c** shows the mild retraction of the muscle–tendon junction, with no discernible proximal tendon edge

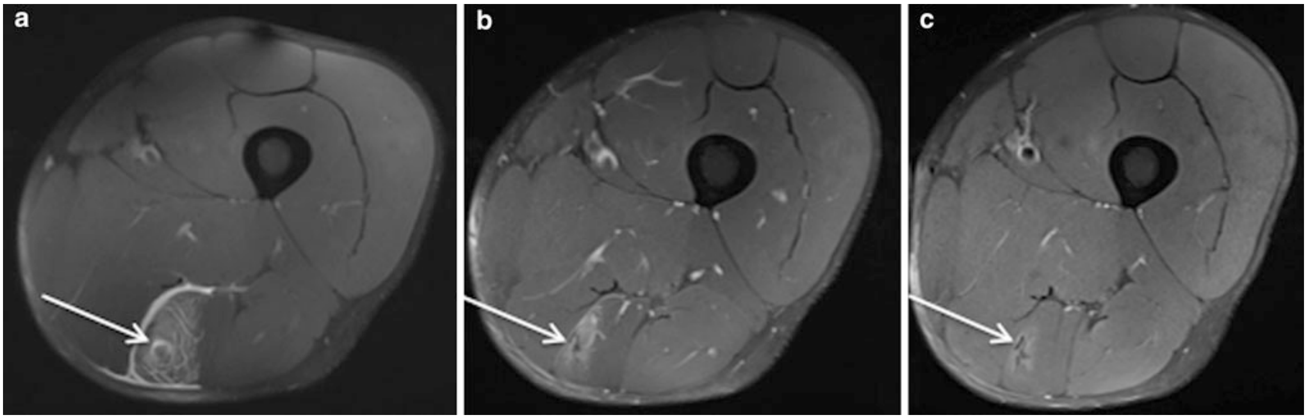

Fig. 10 Axial proton density weighted MR images with fat saturation (**a**–**c**) in a professional rugby league player. **a** Shows an acute semitendinosus muscle–tendon junction injury the day after the injury occurred, the *arrow* indicating a small focus of muscle fibre discontinuity, with surrounding feathery intramuscular oedema and thin layer of perifascial fluid. **b** 3 weeks post injury shows early scar formation and reduction in the extent of surrounding muscle oedema and resolution of the perifascial fluid. **c** 7 weeks post injury demonstrates maturation of scar tissue, with contraction of the scar and virtually complete resolution of the adjacent intramuscular oedema

syndrome (Litwiller et al. 2007). The degree of abnormal T2 signal also correlates well with increased intracompartmental pressures (Litwiller et al. 2007).

Other findings may include fascial thickening, fatty infiltration, muscle atrophy and fibrosis (Verleisdonk 2002) (Fig. 15).

5.2.6 Muscle Hernia

MRI may demonstrate a static contour deformity, oedema or focal out-pouching of the muscle through the fascial defect (Zeiss et al. 1989). However, muscle hernias are often more conspicuous with muscle contraction and in the lower extremity with weight bearing. Consequently US is often superior in providing assessment for muscle hernia (Fig. 16).

5.2.7 Myositis Ossificans/Heterotopic Ossification

MR imaging findings in the acute and subacute phase are often non-specific. The affected area appears ill defined with oedema and haemorrhage and increased signal intensity on fluid sensitive images and increased enhancement after contrast administration (Elsayes et al. 2006). Typical imaging features can be seen after about 6 weeks and reflects the zonal composition with a peripheral rim of ossification. MR imaging might be confusing as the mass may be inhomogeneous and surrounded by an extensive

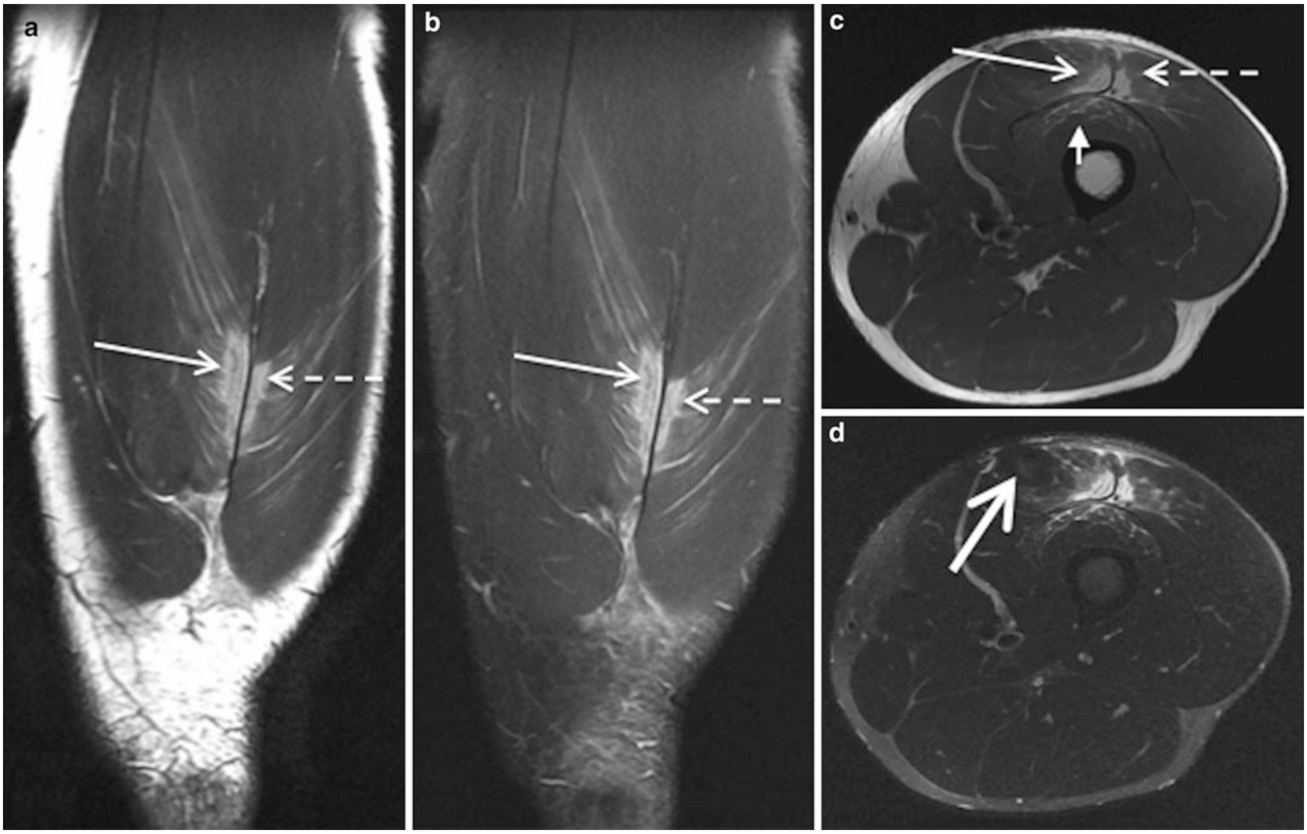

Fig. 11 Coronal proton density weighted MR images, with (**a**) and without fat saturation (**b**) and axial proton density (**c**) and STIR images (**d**) in a professional rugby league player, demonstrate a contusional injury involving the rectus femoris (*arrow*), vastus lateralis (*dashed arrow*) and vastus intermedius (*short arrow*) components of the quadriceps muscle group. Note the small haematoma at the epicentre of the injury, with somewhat geographic margins (thick arrow). The player returned to play at 2 weeks post injury

oedema. Typically, a small hypointense rim on T2- or T2*-weighted sequences can be seen. In this stage the rim is calcified and is best visualised on CT. The ossification then develops towards the centre. This pattern of calcification in myositis ossificans may be differentiated from osteosarcoma which typically demonstrates central ossification, which then develops peripherally (McCarthy and Sundaram 2005). In rare cases biopsy may be performed, especially when clinical history is equivocal (no trauma) to exclude especially a soft tissue or parosteal osteosarcoma (Fig. 17).

5.3 Ultrasound

5.3.1 Introduction and Technique

If a muscle injury is suspected in professional soccer-players, US may be used (in Europe) as a first-line modality because of the ease of availability of US onsite at the match/training. The advantages of US when compared with MRI include: lower cost, greater availability, short imaging time, no contraindications (e.g., pacemakers), the ability to perform dynamic imaging and the ability to easily compare with the contralateral side (Hayashi et al. 2012). Furthermore, US offers the opportunity to guide injections (e.g. platelet-rich plasma) to improve the healing process.

The disadvantages of US include a lower sensitivity, reliance on operator expertise/reliability, a limited field of view and difficulty identifying deep injuries, particularly in high-performance athletes with large muscles or in patients with increased adiposity (Connell et al. 2004). It is also more difficult to accurately quantify and follow-up the extent of large injuries. US has also been reported to have difficulty in differentiating between old and new tears (Connell et al. 2004).

An intermediate-frequency linear array probe (7–10 MHz) is optimal for imaging skeletal muscle (Woodhouse and McNally 2011). Harmonic and compound imaging and post-processing algorithms of the returned signal may be employed to enhance the signal-to-noise ratio and tissue contrast (Entrekin et al. 2001).

The muscle should be examined from origin to insertion in both transverse and longitudinal planes, with evaluation

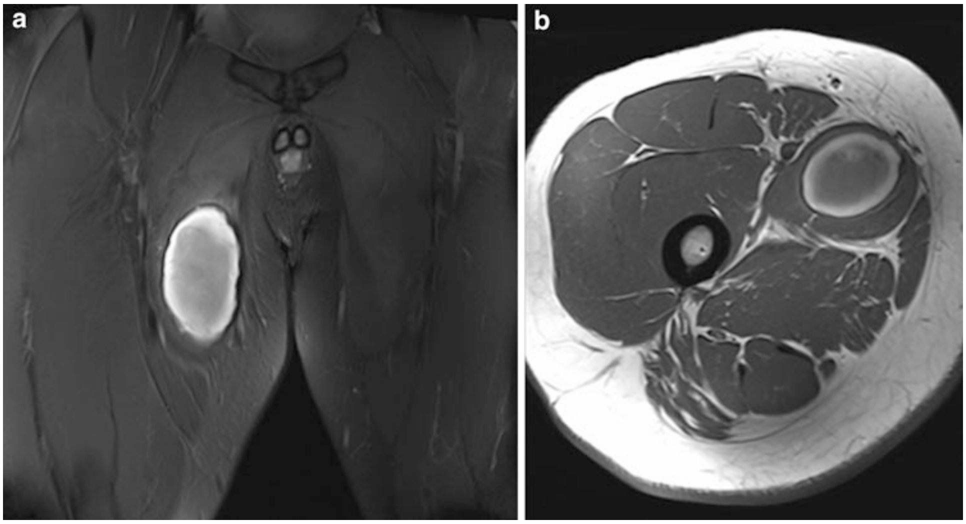

Fig. 12 Coronal proton density with fat saturation (**a**) and axial proton density weighted MR images (**b**) show a subacute haematoma within adductor longus following a muscle tear, with central hyperintensity and a hypointense peripheral rim

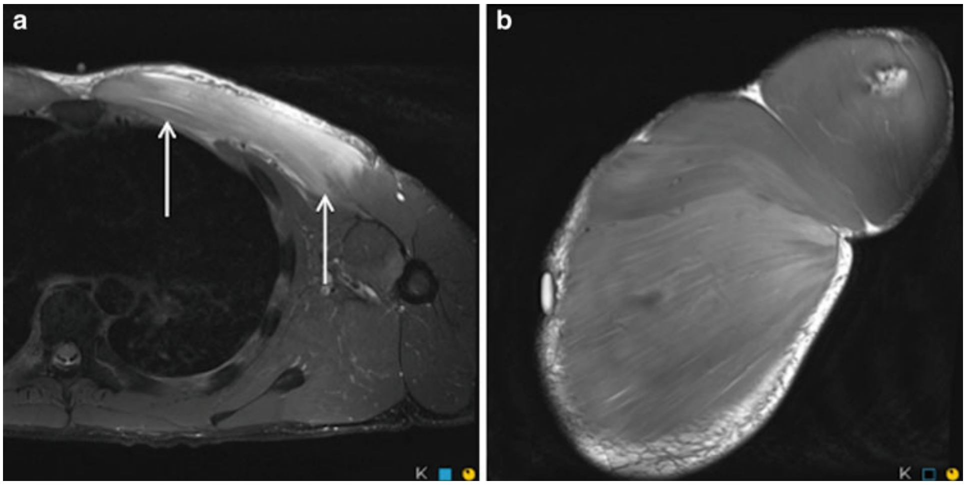

Fig. 13 Axial (**a**) and coronal (**b**) proton density weighted MR images with fat saturation demonstrate the appearance of delayed onset muscle soreness in a pectoralis major muscle in a professional boxer after performing an excessive number of decline bench presses (*arrows*). Note the widespread muscle oedema, predominantly involving the sternal head, with associated muscle swelling

of the enthesis, musculotendinous junction, intermuscular septa and epimysium (Woodhouse and McNally 2011). Dynamic examination (active and passive movement) may be performed to assess for subtle abnormalities, function and lesion stability. Colour or power Doppler interrogation of muscle may be used to assess vascularity in the region of abnormality.

5.3.2 Grading of Muscle Injuries

On US, the echogenicity of muscle fascicles is highly angle-dependent due to anisotropy. In general muscle fascicles are hypoechoic, while perimysium is linear and hyperechoic in appearance. Epimysium, fascia and tendons are also hyperechoic (Peetrons 2002) (Fig. 18).

Peetrons has described a sonographic grading system for muscle tears (Table 2).

On US, grade 1 tears may be hyperechogenic, hypoechogenic or may appear normal (Lee and Healy 2004). In grade 2 tears, interstitial oedema and haemorrhage, haematoma at the musculotendinous junction and perifascial fluid collections appear hypoechogenic. Disruption of muscle fibres may be visualised as areas of altered echogenicity, with loss of perimysial striation adjacent to the musculotendinous junction (Woodhouse and McNally 2011). Identification of a hypo- or anechoic haematoma is the key sign of a muscle tear on US (Peetrons 2002).

Although the classification of Peetrons is often used clinically it has its limitations, and a universal, standardised method of reporting muscle tears has not been established. A more appropriate approach is to document the approximate percentage of muscle fibres involved relative to the total cross-sectional area of the muscle (Woodhouse and McNally 2011) and to also take into account the presence and extent of injury to the intramuscular component of the tendon.

5.3.3 Muscle Contusion

Mild muscle contusions are visualised on US as focal muscle echotextural change. More severe contusions may

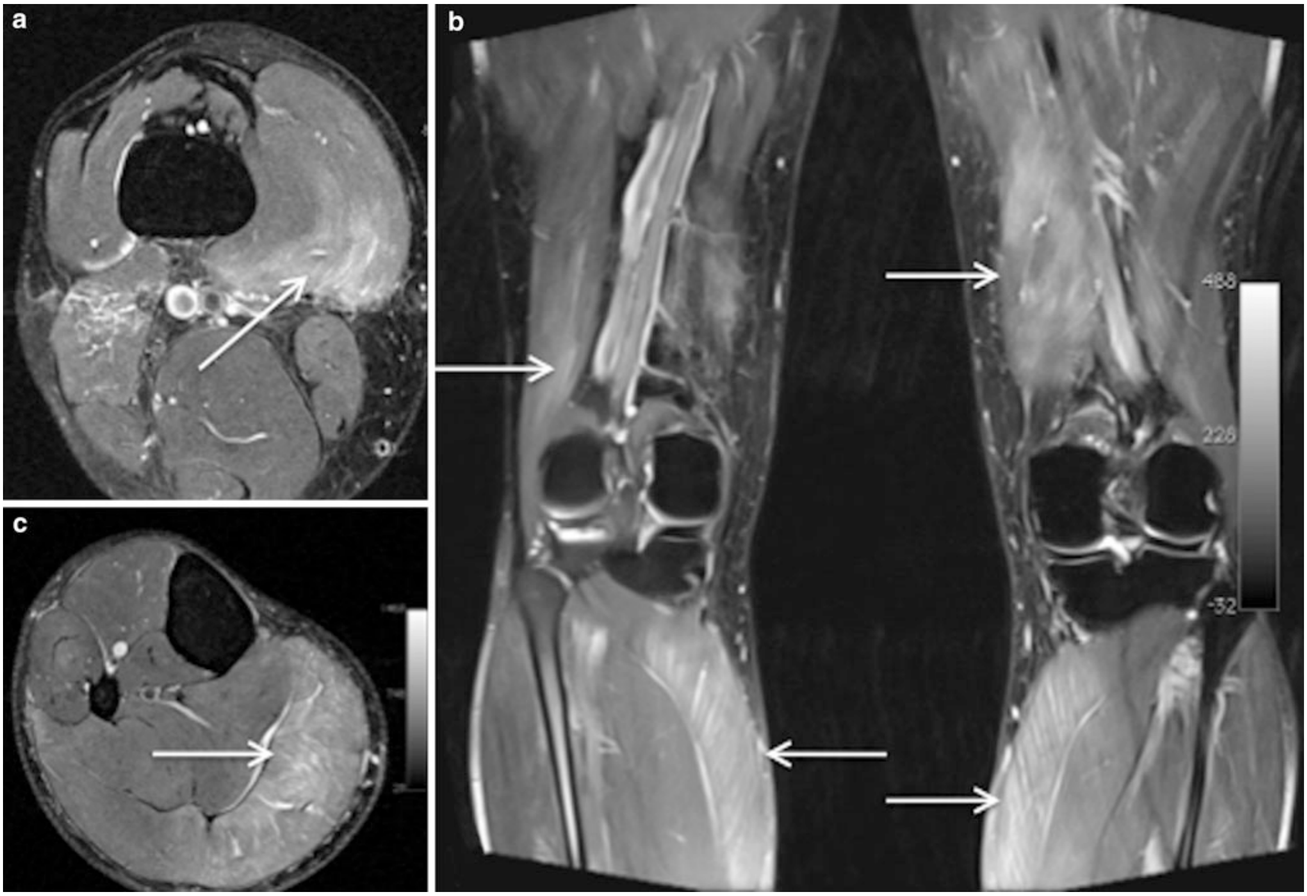

Fig. 14 Coronal (**a**) and axial (**b** and **c**) proton density weighted MR images with fat saturation in an athlete with delayed onset muscle soreness 4 days post triathlon. There is extensive lower limb oedema bilaterally, predominately involving the vastus medialis and the medial head of gastrocnemius (*arrows*) (Images courtesy of Dr Andrew Van Den Heever, Cape Town, South Africa)

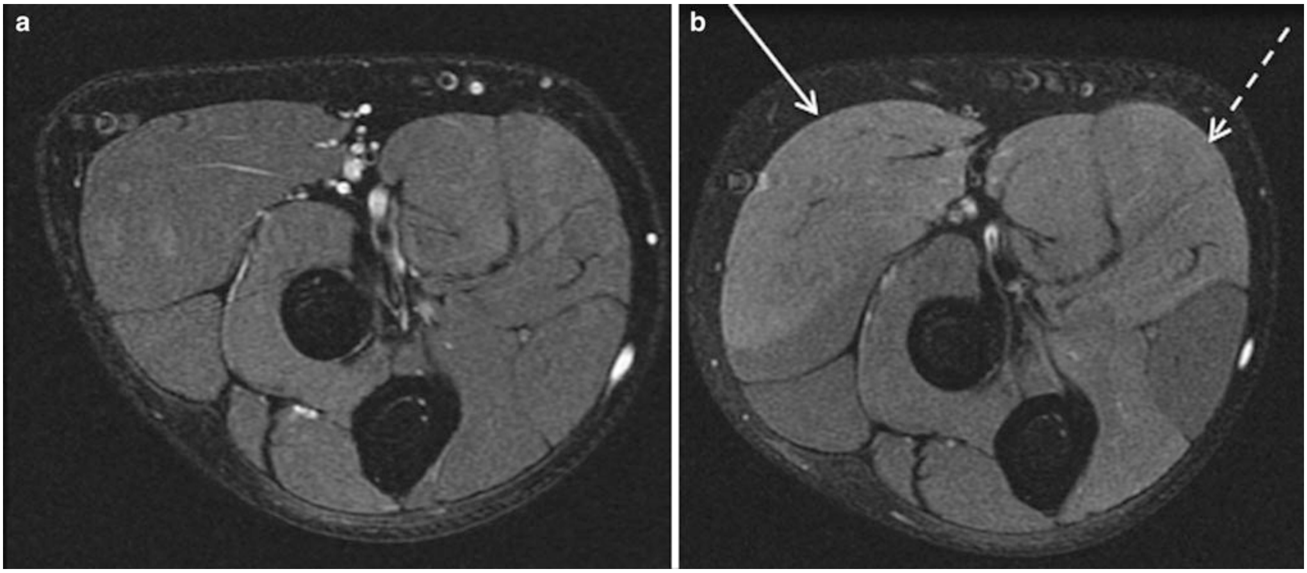

Fig. 15 Axial proton density weighted MR image with fat saturation (**a** and **b**) in a tennis player with an exercise induced compartment syndrome. **a** Shows the forearm prior to exercise. Post exercise (**b**) there is swelling and ground glass-like oedema within the brachioradialis and humeral head of pronator teres (*arrow*), while the remainder of the flexor pronator muscle group appears normal, with the exception of flexor carpi ulnaris (*dashed arrows*)

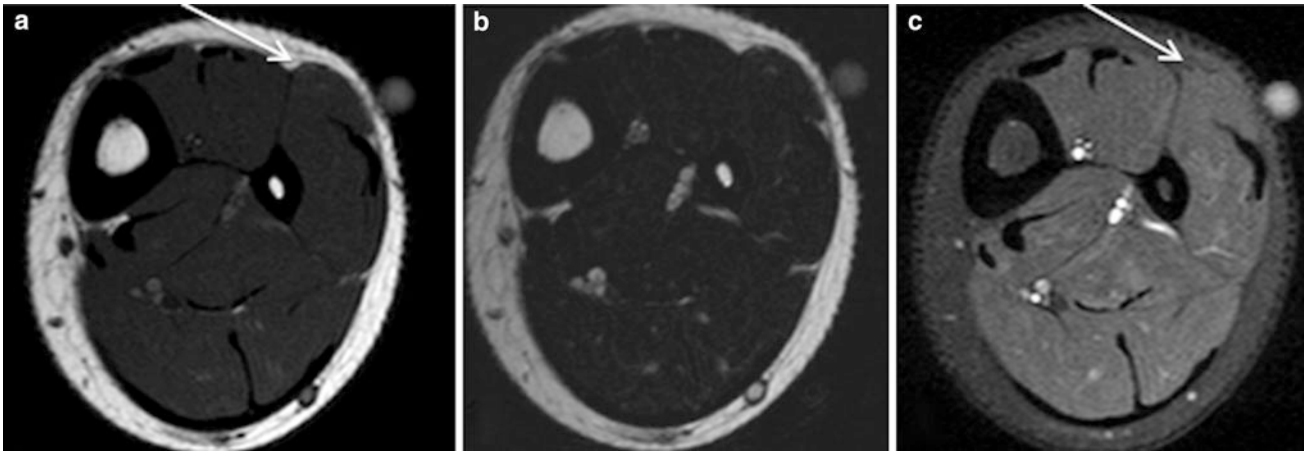

Fig. 16 A 16-year-old kickboxer with a suspected "tumour" of the lateral leg, location marked with a capsule. Axial T1 (**a**), T2 (**b**) and post contrast T1-weighted MR images with fat saturation demonstrates a muscle hernia of the peroneus longus muscle with outpouching of the muscle through the investing fascia antero-laterally. The hernia follows the imaging characteristics of muscles in all sequences. There was a history of direct trauma while kicking 1 year ago, presumably resulting in a tear of the investing fascia. The patient noted an increase in size during training/muscle activity

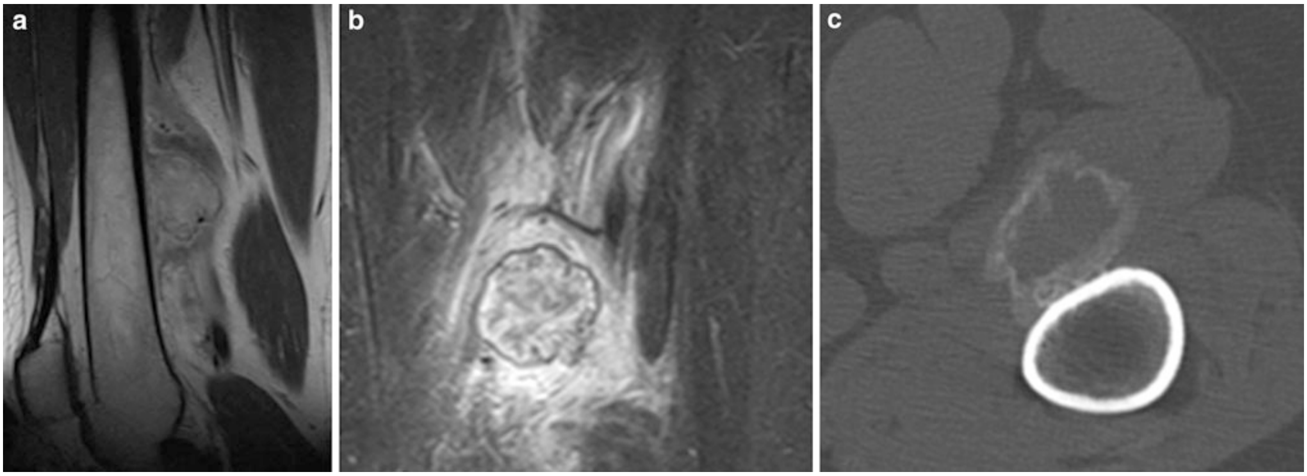

Fig. 17 Sagittal T2-weighted MR image (**a**), coronal STIR MR image (**b**) and axial CT image (**c**) show myositis ossificans immediately adjacent to the posterior aspect of the mid to distal shaft of the femur in a 32-year-old female patient who developed local pain and a palpable lesion following a recreational sports activity. Please note the hypointense rim of the lesion (*arrows*) and the peripheral but not central calcification

Fig. 18 Longitudinal (**a**) US image of a normal proximal rectus femoris muscle demonstrates a striated appearance (*arrow*). Corresponding transverse image shows both rectus femoris (*arrow*) and vastus intermedius (*dashed arrow*)

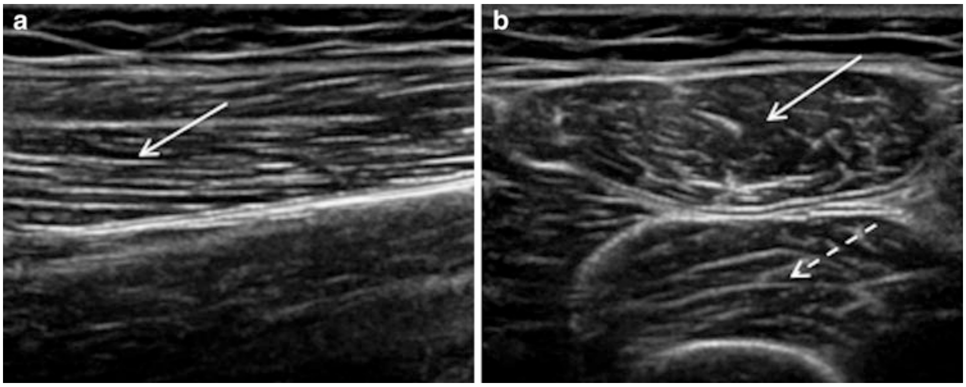

Table 2 Grading of muscle injuries on ultrasound

Grade	Sonographic findings
0	No sonographic abnormality identified
1	Muscle fibre disruption involving less than 5 % of the cross-sectional area of the muscle
2	Between 5 and 50 % of cross-sectional area involved
3	Complete muscle tear with retraction of fibres

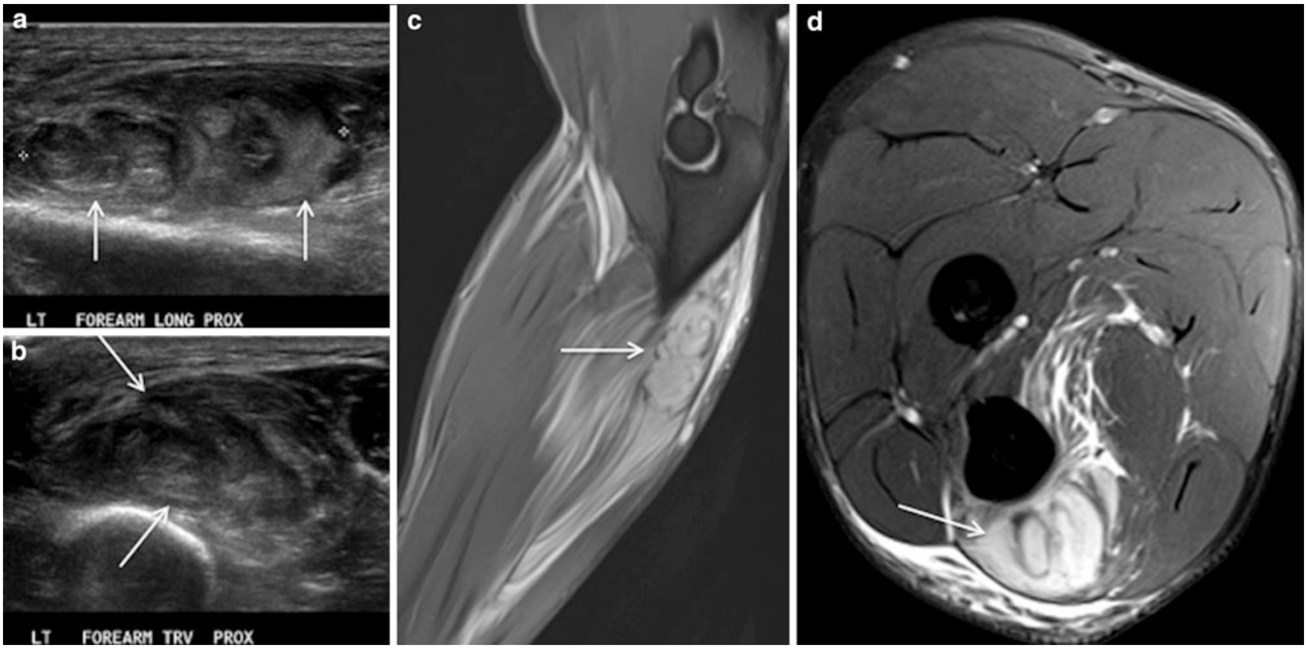

Fig. 19 Longitudinal (**a**) and transverse (**b**) US images and sagittal (**c**) and axial (**d**) proton density weighted MR images with fat saturation in a professional rugby league player demonstrate an acute haematoma following a contusional injury involving flexor digitorum profundus distal to the muscle–tendon junction (*arrows*). The player presented with acute pain due to increased intracompartmental pressure. A small volume of the haematoma was aspirated which provided symptomatic relief such that a fasciotomy was not required

demonstrate discontinuity of normal muscle architecture, with ill-defined anechoic, hypoechogenic or hyperechogenic material that may cross fascial boundaries (Lee and Healy 2004). With evolution, contusions become increasingly more hypoechoic and eventually may organise, resolve, or develop scar tissue (Woodhouse and McNally 2011).

5.3.4 Delayed Onset Muscle Soreness

US has been reported to be unable to diagnose DOMS and the changes identified on MRI (Dierking et al. 2000).

5.3.5 Acute Compartment Syndrome

US should not be used to diagnose acute compartment syndrome, however, may be used to exclude other differential diagnoses (Woodhouse and McNally 2011). In mild cases, diffusely increased echogenicity and tissue swelling may be identified. Muscles that have undergone ischaemic necrosis will appear more heterogeneous. Doppler studies are not helpful—arterial and venous flow may be demonstrated until such time that an acute compartment syndrome is clinically evident.

Fluid collections within a muscle compartment may be identified as a cause for an acute compartment syndrome and may be treated with percutaneous drainage using US guidance (Woodhouse and McNally 2011) (Fig. 19).

5.3.6 Muscle Hernias

US may be useful in the diagnosis of muscle hernias. A defect in the investing perimysium can be identified through which muscle herniates. This can be assessed dynamically using US. Scanning the patient during muscle contraction and when standing (with lower limb cases) increases the sensitivity of the study. Pressure applied by the US probe

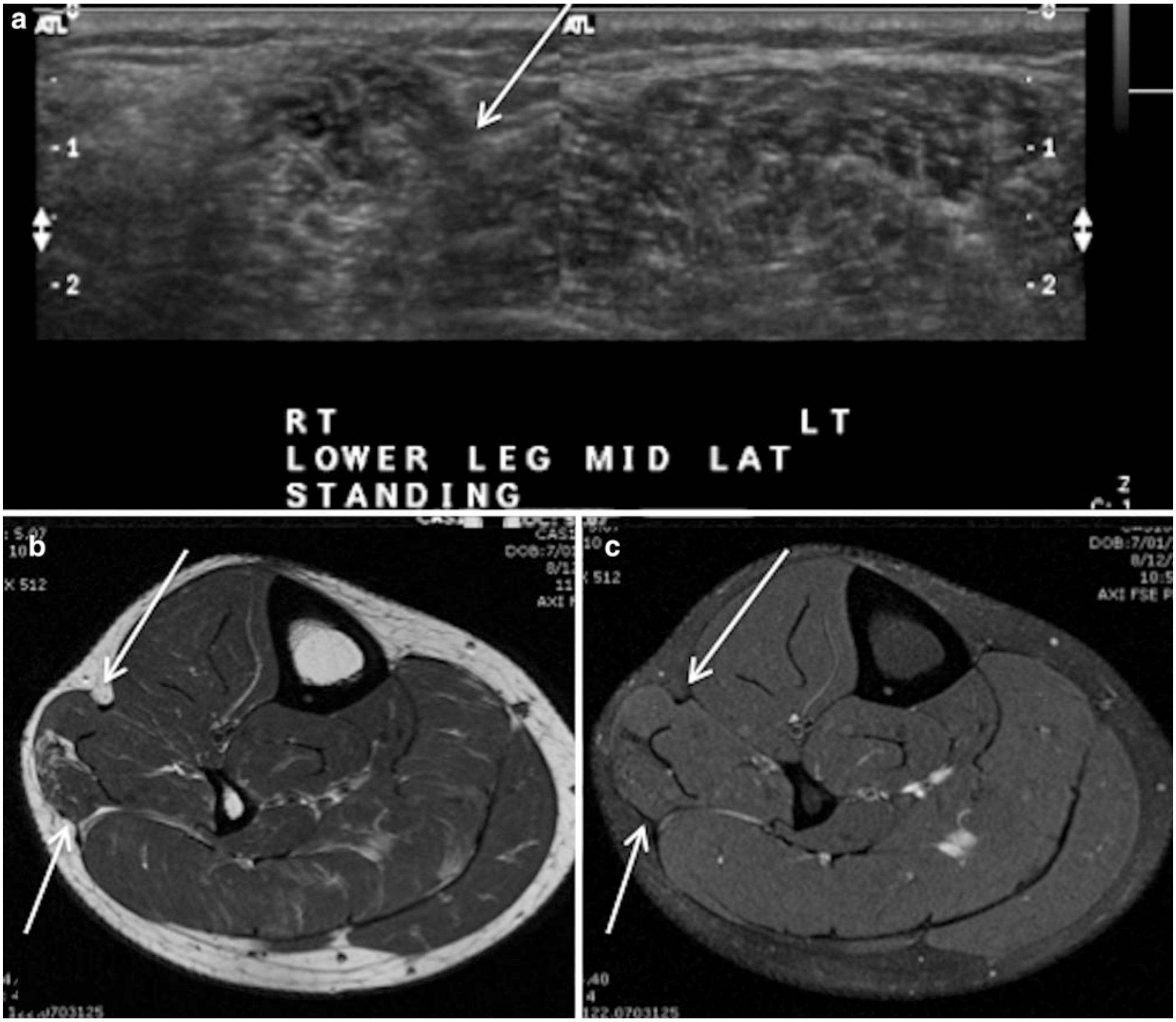

Fig. 20 US image comparing the right and left peroneal muscles (**a**), axial proton density weighted MR image (**b**) and proton density weighted MR image with fat saturation demonstrates a hernia of the right peroneus longus and brevis muscles. The *arrows* denote the margins of the broad defect in the investing fascia through which the muscle herniates

may reduce the hernia and therefore minimal probe pressure is recommended (Peetrons 2002). Multiple herniations may indicate an underlying chronic compartment syndrome (Woodhouse and McNally 2011) (Fig. 20).

5.3.7 Myositis Ossificans

In the early stage of post-traumatic myositis ossificans, a peripherally echogenic lesion may be seen on US. Internal vascularity will differentiate myositis ossificans from an abscess. US is capable of visualising calcification several weeks prior to plain film radiographs (Kramer et al. 1979; Peck and Metreweli 1988). Posterior acoustic shadowing from the calcification is not present initially, but develops later (Peetrons 2002). With evolution, the mass may become increasingly hypoechoic or heterogeneous (Woodhouse and McNally 2011).

6 Specific Muscle Injuries

Muscle injuries are not specific to certain sports, but some biomechanics are typical and therefore some injury patterns occur more often. For instance, tennis players most commonly suffer from injuries of the upper extremity,

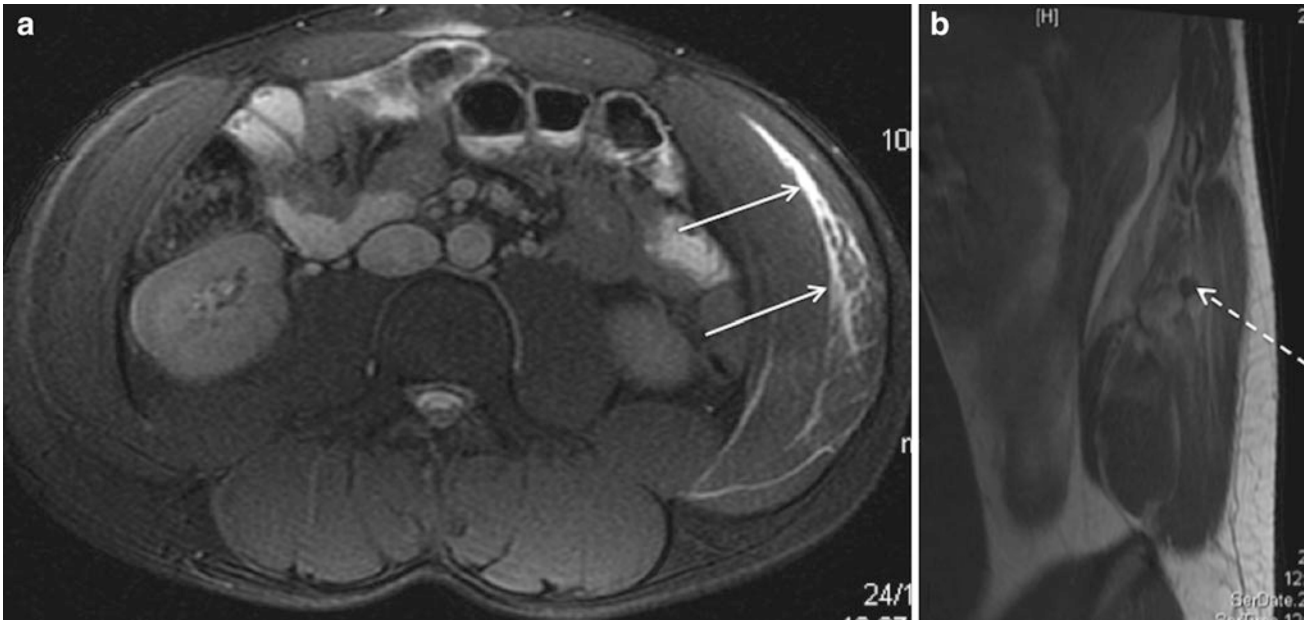

Fig. 21 Axial proton density weighted MR image with fat saturation (**a**) in a professional cricket player demonstrates an acute side strain, with feathery intramuscular oedema in the external oblique (*arrow*). Sagittal proton density weighted image (**b**) shows an associated costal cartilage fracture (*dashed arrow*). Images courtesy of Dr Shaun Fowler, Adelaide, Australia

particularly of the pronator teres complex followed by injuries of the rectus abdominis muscle. In contrast, injuries of the lower extremity account for about 92 % in soccer players (Ekstrand et al. 2011a, b). Muscle injuries involving the thigh are most common in track and field athletes (16 %), but are also present in team sports like rugby (10.4 %), basketball (17.7 %) and American football (22 %) (Mueller-Wohlfahrt et al. 2012).

6.1 Side Strain

Side strain is a term that describes a strain/tear of the internal oblique muscle at the rib or costal cartilage insertion (Connell et al. 2003). This injury most commonly occurs in cricket fast bowlers, javelin throwers, rowers, baseball pitchers and ice hockey players (Balius et al. 2012; Palmer et al. 1999; Stevens et al. 2010).

The superior attachment of the internal oblique muscle is the inferior margin of the ninth to twelfth ribs and the linea alba. There is also interdigitation of fibres with intercostal muscles. The inferior insertion includes the inguinal ligament, the anterior two-thirds of the iliac crest, thoracolumbar fascia and on the pubic crest as the conjoint tendon, with fibres of transversus abdominis (Standring 2005). The internal oblique muscle contains a high percentage of type II muscle fibres, which may be a predisposition to injury.

The mechanism of injury is a sudden eccentric contraction, resulting in an acute muscle strain/tear at the point of insertion at the undersurface of the ninth, tenth or, most commonly, the eleventh rib. Patients experience a sudden onset of pain and point tenderness in the region of the lower costal margin (Connell et al. 2003). Connell and colleagues (2013) identified detachment of muscle fibres from the cartilaginous cap or adjacent costal cartilage in six of ten subjects.

Cricket medium and fast bowlers sustain side strain on the side of the non-bowling arm, during the final delivery action, when the bowler's non-bowling is pulled down from a position of maximum elevation, with lateral trunk flexion (Humphries and Jamison 2004).

In baseball pitchers, side strain is proposed to occur during throwing in the late cocking and early acceleration stages, when the non-dominant arm is torqued backward from a hyperextended position, which allows the dominant arm to follow through and release the ball (Stevens et al. 2010).

In rowers, maximum tension of the internal oblique occurs when the shoulder is behind the hips and the scapula is fully retracted. At this point in the rowing technique, the athlete is susceptible to side strain (Connell et al. 2003).

On MRI, the sagittal oblique plane is most useful for assessment of side strain. Minimal fibre retraction occurs due to the wide origin and varied muscle fibres. Connell and colleagues also demonstrated muscle defects at the attachment at rib or costal cartilage ranged from 10 to 35 mm in size (Connell et al. 2003). At sites of osseous or chondral cartilage avulsion, stripping of the periosteum may result in significant haemorrhage (Fig. 21).

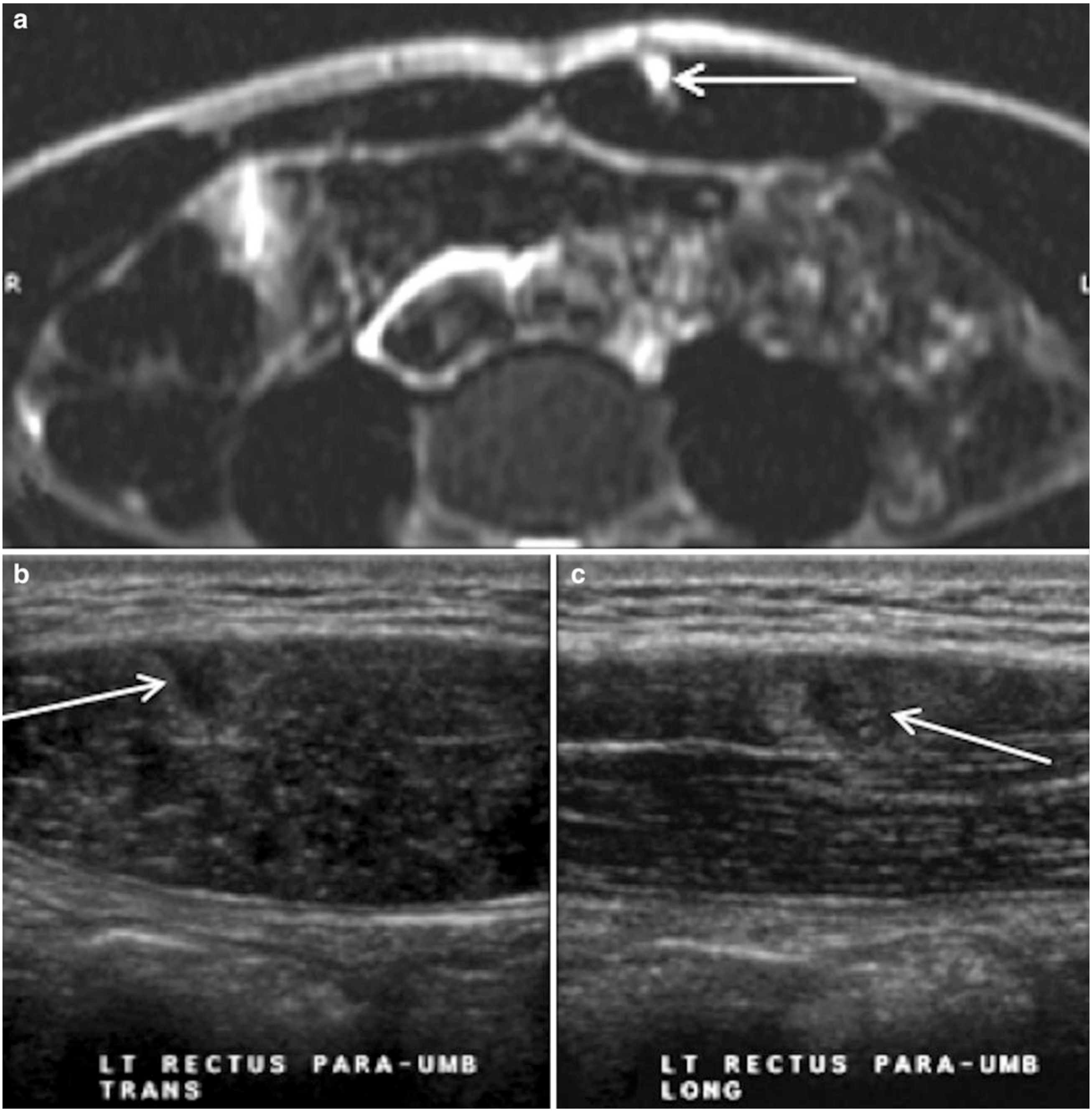

Fig. 22 Axial T2-weighted MR image (**a**) and transverse (**b**) and longitudinal (**c**) US images in a professional tennis player with a grade 2 left rectus abdominis muscle injury (*arrows*). Note the hypertrophy of the left rectus abdominis compared to the right side on the MR image. Images courtesy of Dr John Read, Sydney, Australia

6.2 Rectus Abdominis Strain

The rectus abdominis is a flat, paired muscle, separated in the midline by the linea alba. Inferiorly, a medial head attaches to the anterior surface of the pubic symphysis and the larger, lateral head to the upper border of the pubic crest. Superiorly the rectus abdominis inserts onto the fifth to seventh costal cartilages (Standring 2005).

Rectus abdominis muscle strain most commonly occurs while playing tennis, however, has also been described in volleyball and handball players and may be seen in elite divers (Aagaard and Jorgensen 1996; Balius et al. 2011, 2012; Connell et al. 2006; Maquirriain et al. 2007).

In tennis players, the rectus abdominis is more developed in muscle mass and volume on the non-dominant side compared with the dominant side (Connell et al. 2006).

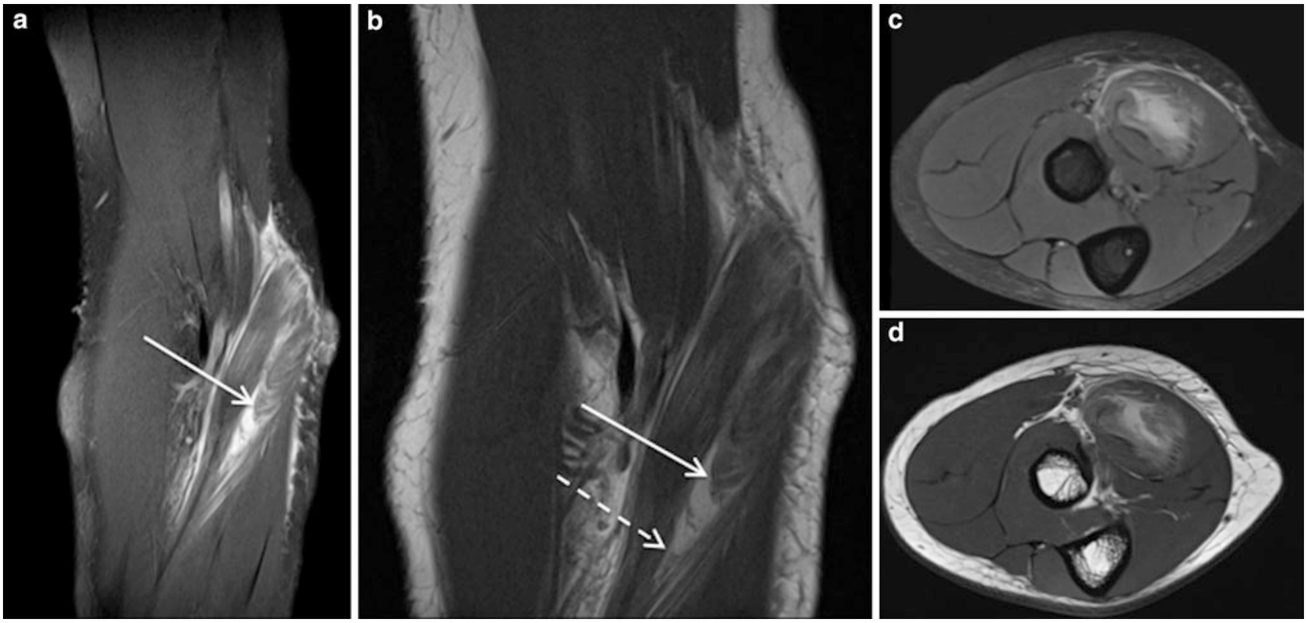

Fig. 23 Grade 2 pronator teres muscle tear in a professional tennis player. Coronal proton density weighted MR images, with (**a**) and without fat saturation (**b**) and axial proton density weighted MR images, with (**c**) and without fat saturation (**d**) show a partial tear of the humeral head of the pronator teres muscle adjacent to the muscle–tendon junction (*dashed arrow*), with up to 1 cm of retraction of muscle fibres (*arrows*). The injury occurred while performing a forehand

Strains occur during the cocking phase of the service motion due to eccentric overload, followed by the forced contraction of the non-dominant side of the rectus abdominis. The most common site of strain occurs on the non-dominant side, at an infraumbilical level, within the deep epimysium (Connell et al. 2006; Maquirriain et al. 2007) (Fig. 22).

6.3 Flexor Pronator Musculature

The term "tennis elbow" represents a lateral epicondylitis and may occur in tennis players of all standards. Flexor-pronator tendinosis or rupture is more common in higher level tennis players (Eygendaal et al. 2007). Pronator teres and flexor carpi radialis are the most common sites of pathologic change (Nirschl and Pettrone 1979; Vangsess and Jobe 1991).

Proposed mechanisms of injury in tennis players include an excessive wrist snap, "open stance hitting", opening too soon on serve and short arming of the stroke (Kibler 1994). Patients present with tenderness distal and lateral to the medial epicondyle which is exacerbated by resisted wrist flexion and forearm pronation.

MRI is an important modality to assess the site and extent of abnormality and to exclude other pathology, such as ulnar collateral ligament insufficiency (Fig. 23).

6.4 Hamstring Injuries

The hamstring muscle group is commonly injured in a multitude of sports, particularly those involving running with rapid acceleration/deceleration and changing direction. The hamstrings play an important, complex role in the gait cycle and act as both hip extensors and knee flexors. They also limit knee extension immediately prior to and during heel strike, working in tandem with the anterior cruciate ligament to prevent antero-posterior translation of the tibia in relation to the femur (Linklater et al. 2010).

There are a number of anatomical risk factors that predispose the hamstrings to injury. These include: the muscles cross two joints, contain a high proportion of type II fibres and have long proximal and distal tendons and muscle–tendon junctions that extend well into the muscle bellies. The length of the hamstring tendons provides a greater "spring" effect that enhances athletic performance, but also increases the risk of injury (Linklater et al. 2010).

The hamstrings are at risk of two different types of injury—acute high-energy tensile eccentric overload injuries seen in sprinters and footballers and lower energy tensile overload injuries, most commonly associated with dancing (Askling et al. 2007).

Eckstrand et al. (2011) demonstrated that hamstring strains were the single most common injury in professional

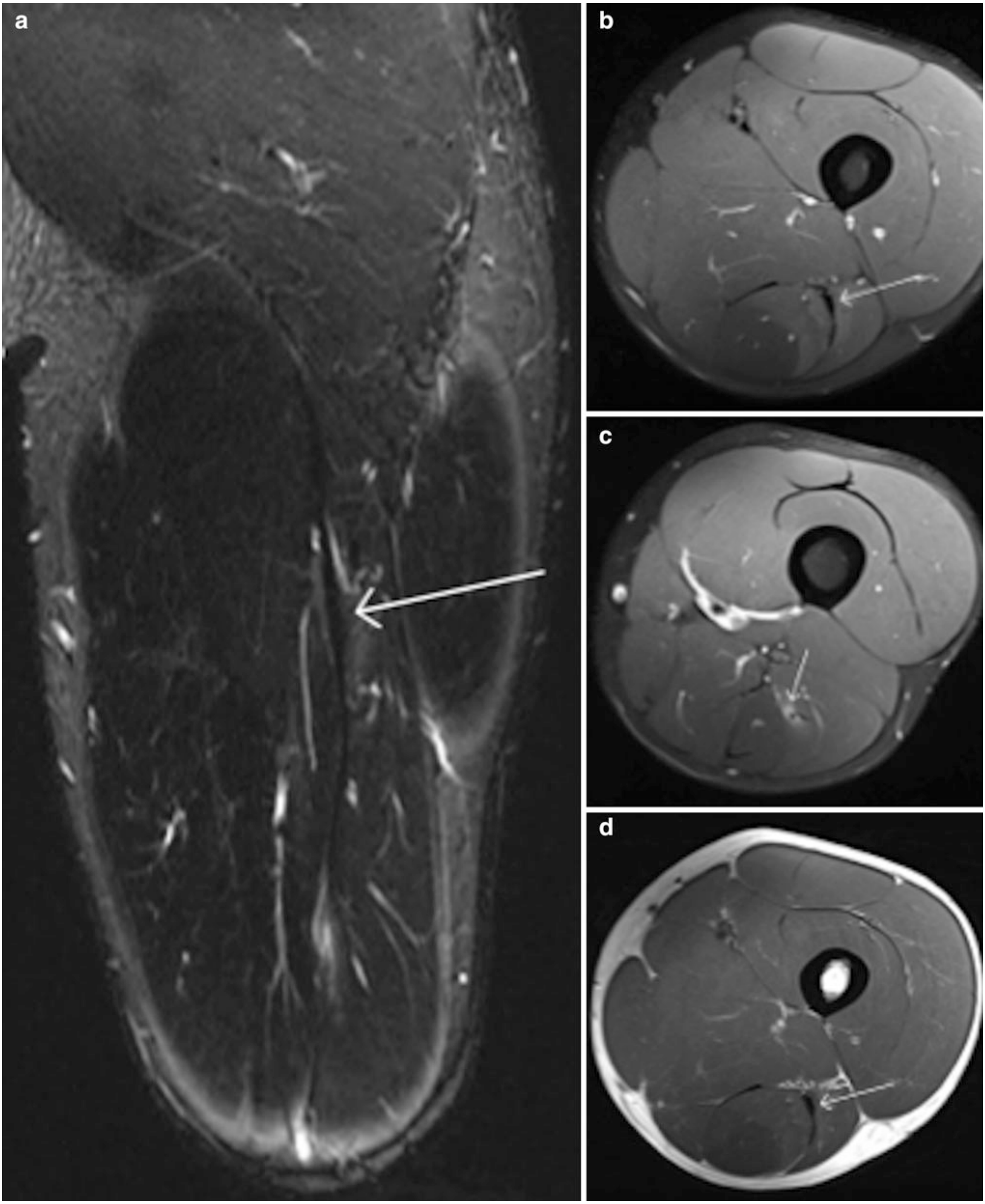

Fig. 24 Recurrent muscle injury. Coronal STIR image (**a**), axial proton density weighted image with fat saturation (**b** and **c**) and axial proton density weighted image (**d**) demonstrates a recurrent grade 1 strain injury of the long head biceps femoris muscle adjacent to the scarred intramuscular component of the proximal (*arrows*)

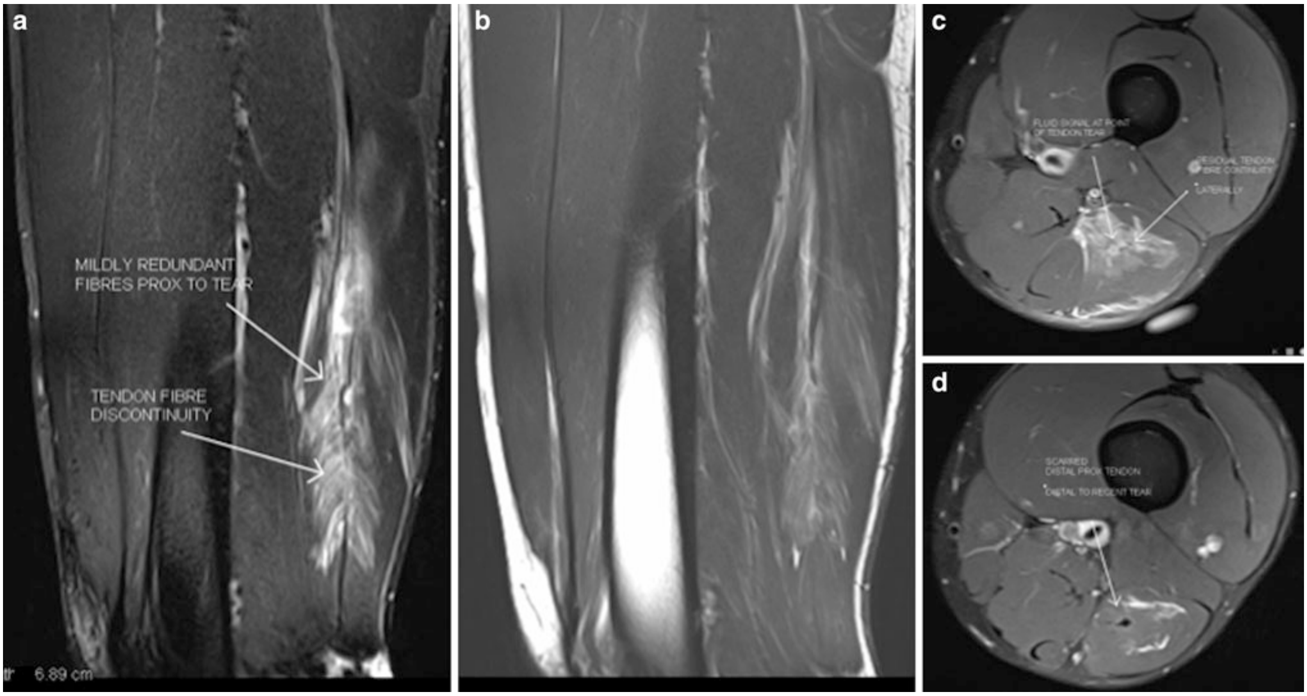
a
MILDLY REDUNDANT
FIBRES PROX TO TEAR
TENDON FIBRE
DISCONTINUITY
6.89 cm
b
c
FLUID SIGNAL AT POINT
OF TENDON TEAR
RESIDUAL TENDON
FIBRE CONTINUITY
LATERALLY
d
SCARRED
DISTAL PROX TENDON
DISTAL TO RECENT TEAR

Fig. 25 Recurrent muscle injury with central tendon tear. Sagittal STIR MR image (**a**) and proton density weighted MR image (**b**) and axial proton density weighted MR image with fat saturation (**c** and **d**) demonstrate a recurrent long head biceps femoris muscle–tendon junction injury with fibre discontinuity of the central-proximal tendon in a professional Australian Rules football player

Fig. 26 Calf strain. Coronal STIR MR image (**a**) and axial proton density weighted MR image with fat saturation (**b**) shows a grade 1 injury of the medial head of gastrocnemius in a professional Australian Rules football player, with feather intramuscular oedema but no muscle fibre discontinuity (*arrows*)

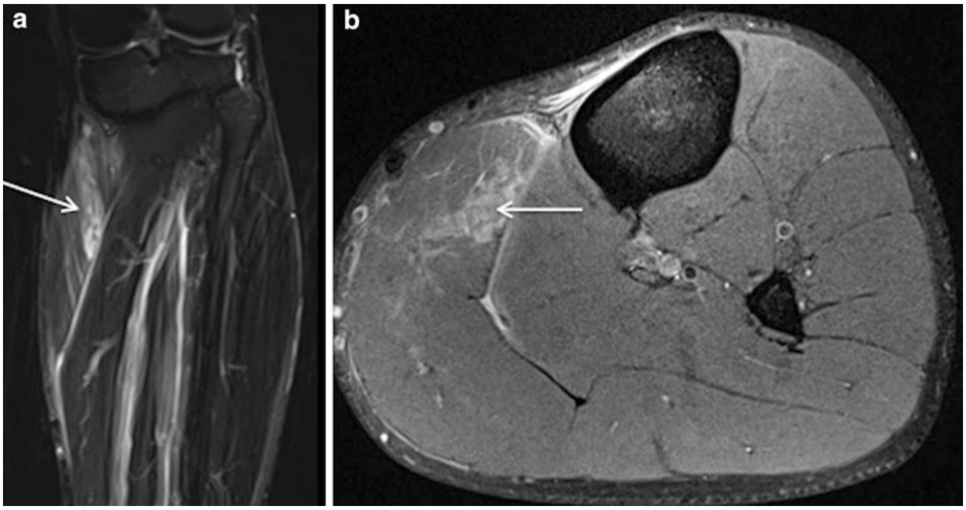

football players. Hamstring strains constituted 12 % of all injuries and was the cause of 12 % of all injuries in which there was an absence from play of >28 days. There is an annual incidence of five to six hamstring injuries per season in professional football and Australian Rules teams (Orchard and Seward 2003; Woods et al. 2004).

Recurrent muscle injury occurs in approximately 30 % of athletes (Connell et al. 2004). For 8 weeks following an initial muscle strain, there is a relative increase in risk of 6.3 for repeat injury (Megliola et al. 2006).

Immediately post injury, the site of tear is weaker than the surrounding tissue. Eventually, with scar formation and remodelling, the scar is stronger than the native muscle–tendon unit. Recurrent strains may then occur at sites adjacent to scar formation which is a presumed site of stress due to differences in elasticity and altered contractility (Koulouris and Connell 2005).

Scar tissue may be visualised on MRI as early as 6 weeks after initial injury and is low signal intensity on all pulse sequences (Connell et al. 2004). On US, scar tissue is

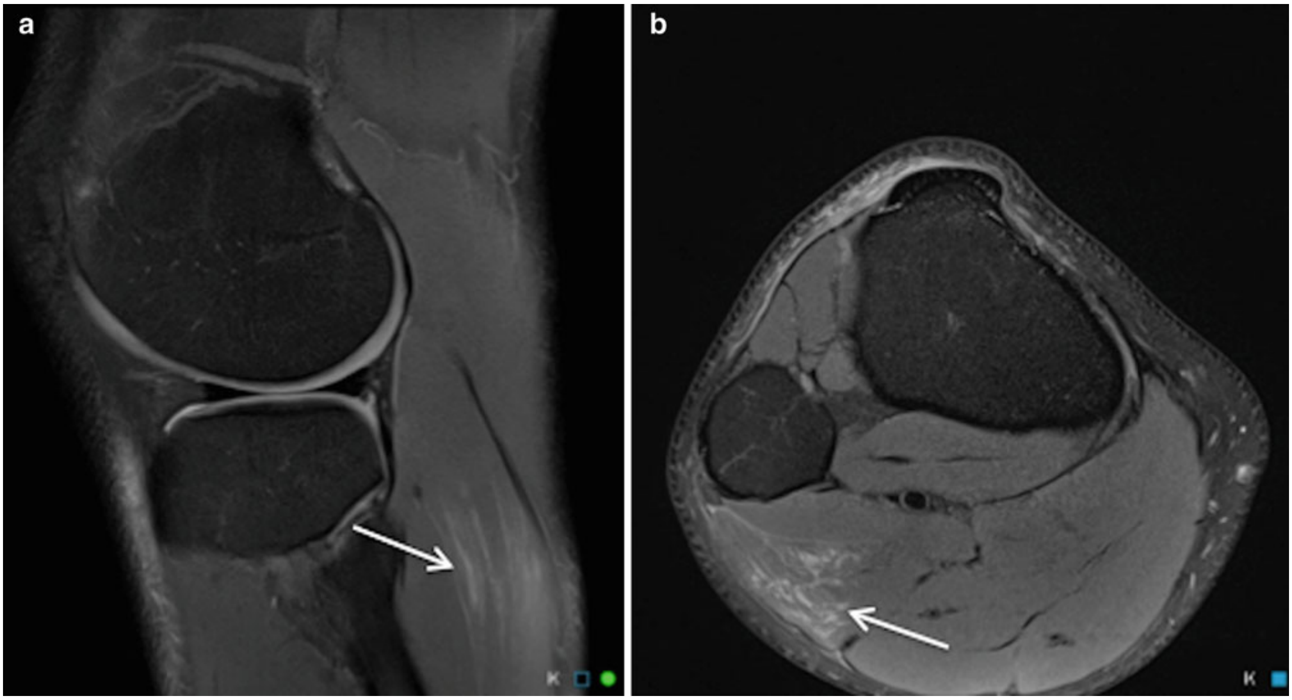

Fig. 27 Calf strain. Sagittal (**a**) and axial (**b**) proton density weighted MR images with fat saturation (**b**) show a grade 1 injury of the lateral head of gastrocnemius in a professional rugby league player, with feathery intramuscular oedema but no muscle fibre discontinuity (*arrows*)

heterogeneous in echotexture and is irregular in morphology (Koulouris and Connell 2005). Sidler et al. (Silder et al. 2008) demonstrated that two-thirds of previously injured subjects had residual scarring at the site of hamstring muscle–tendon junction injury which was present a minimum of 5 months after injury (Figs. 24, 25).

Koulouris et al. (2007a, b) demonstrated that with repeat hamstring muscle injury, the longitudinal length of the recurrent tear further increased on average compared with the dimensions of the original tear. Although not statistically significant in their study, the MR length of a strain had the strongest correlation association with a repeat hamstring injury. They hypothesised that injuries greater than 60 mm in length appear to have a higher likelihood of recurrence (Koulouris et al. 2007a, b).

6.5 Calf Muscle Complex

The triceps surae consists of the soleus and gastrocnemius muscles (medial and lateral heads). Distally, the medial and lateral heads of the gastrocnemius insert onto a broad aponeurosis. Further distally, the aponeurosis unites with the deep tendon of the soleus to form the Achilles tendon (O'Brien 2005).

Anatomically, there are multiple risk factors for gastrocnemius tears. It crosses two joints and contains a high density of type II fibres (Armfield et al. 2006; Bryan Dixon 2009). In contradistinction, the soleus crosses only the ankle joint and is largely comprised of type I fibres (Bryan Dixon 2009). The medial head of gastrocnemius has a more prolonged attachment and therefore may generate higher forces than the lateral head, thus also increasing the risk of injury to the medial head compared with the lateral head.

Koulouris et al. (2007a, b) however, produced conflicting result to the aforementioned anatomical risk factors. The authors identified a similar incidence of isolated tears in both the gastrocnemius and soleus. This conflicts with previous studies that demonstrated a higher incidence of gastrocnemius tears relative to soleus tears, in particular, the medial head (Brukner and Khan 2002). The deeper position of the soleus muscle compared with the gastrocnemius may reduce conspicuity of strains on US.

Furthermore, synchronous gastrocnemius-soleus strains may have been previously diagnosed as an isolated tear of the gastrocnemius. Two studies have demonstrated a high proportion of synchronous tears also not previously documented (Armfield et al. 2006; Koulouris et al. 2007a, b). Given, the gastrocnemius and soleus muscle function as a unit, with a common tendon (Achilles tendon), with failure of the gastrocnemius, greater forces may be imparted onto the soleus, which if sufficient, may increase the likelihood of a concurrent tear of the soleus (Koulouris et al. 2007a, b) (Figs. 26, 27, 28, 29, 30, 31).

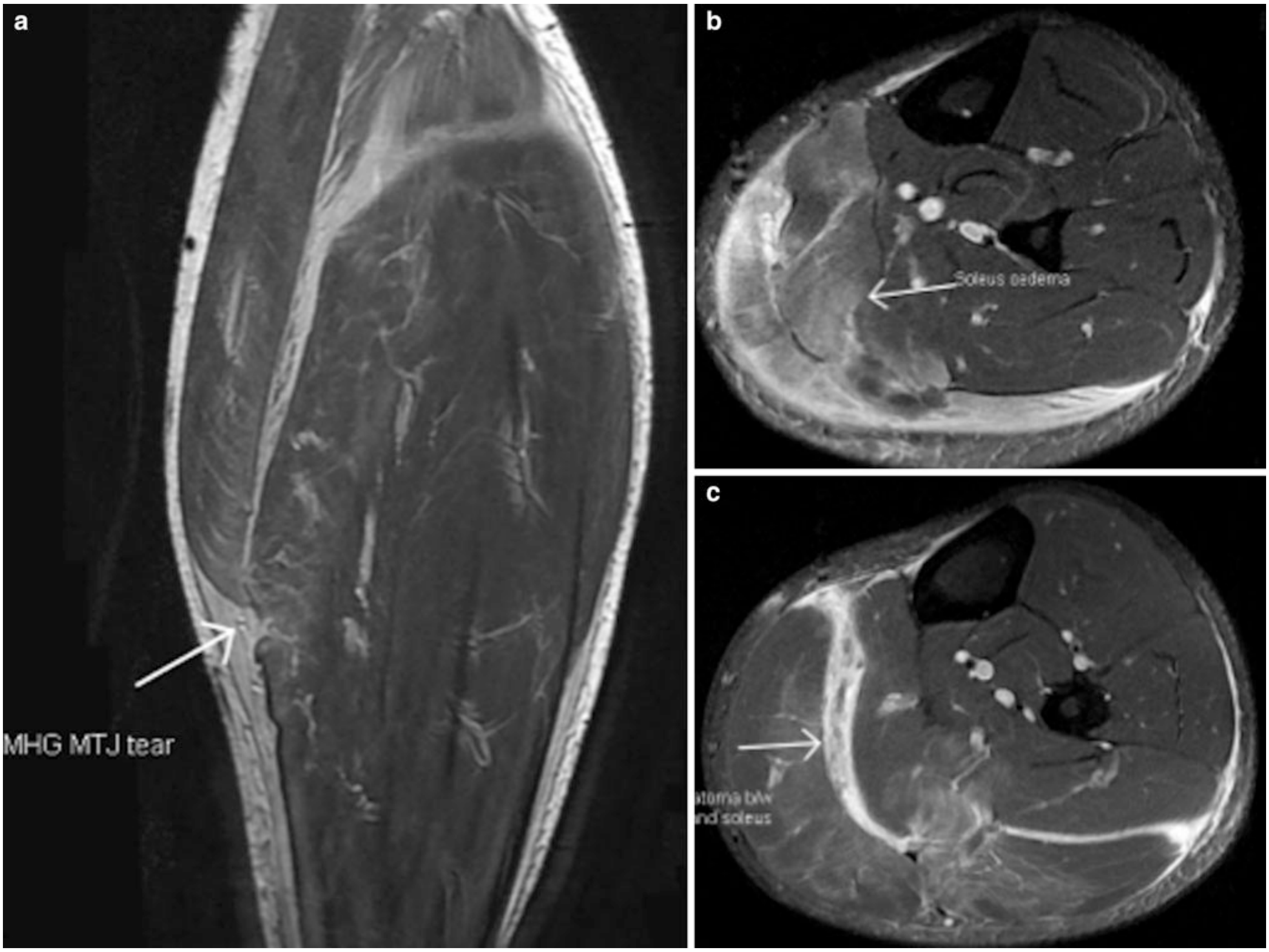

Fig. 28 Medial head gastrocnemius muscle tendon junction injury. Coronal proton density weighted (**a**) and axial proton density weighted image with fat saturation in a professional rugby league player show a partial tear at the aponeurotic insertion of the medial head of gastrocnemius (*arrow* in **a**), with mild muscle retraction and shallow fluid collection tracking proximally at the deep margin. Not concomitant intramuscular oedema in the lateral head of gastrocnemius and soleus (**b** and **c**). Muscle–tendon junction injury of the medial head of gastrocnemius and further grade 1 injuries of the lateral head of gastrocnemius and soleus is also visible (**b** and **c**)

6.6 Rectus Femoris Tears

Rectus femoris tears are common injuries that require repetitive kicking and/or sprinting and may occur proximally or distally (Brophy et al. 2010; Cross et al. 2004; Hawkins et al. 2001) (Figs. 32, 33). Distal tears involve the caudal musculotendinous junction where the muscle fibres can be seen inserting into a flat posterior tendon. Distal musculotendinous tears present as a palpable lump and may be diagnosed clinically (Bianchi et al. 2002).

Proximal intrasubstance tears involve the central aponeurosis, a distinct, sagittally oriented, proximal aponeurosis located in the mid-muscle belly substance (Hughes et al. 1995). These tears are difficult to diagnose clinically due to their deep location and lack of retraction (Bianchi et al. 2002). In cases of muscle retraction in intrasubstance tears, a discrete anterior thigh mass related to muscle retraction may be mistaken for a soft tissue neoplasm (Temple et al. 1998).

Rectus femoris is composed of two heads proximally. The direct (straight) head originates from the anterior inferior iliac spine, while the indirect (reflected) head originates from the superior acetabular ridge and hip joint capsule (Gyftopoulos et al. 2008). A few centimetres below their origins, the two heads form a conjoined tendon. The direct head constitutes the majority of the superficial component of the conjoined tendon and then more distally, blends with the anterior fascia that covers the ventral aspect of the proximal third of the rectus femoris muscle (Hasselman et al. 1995). The indirect head constitutes the

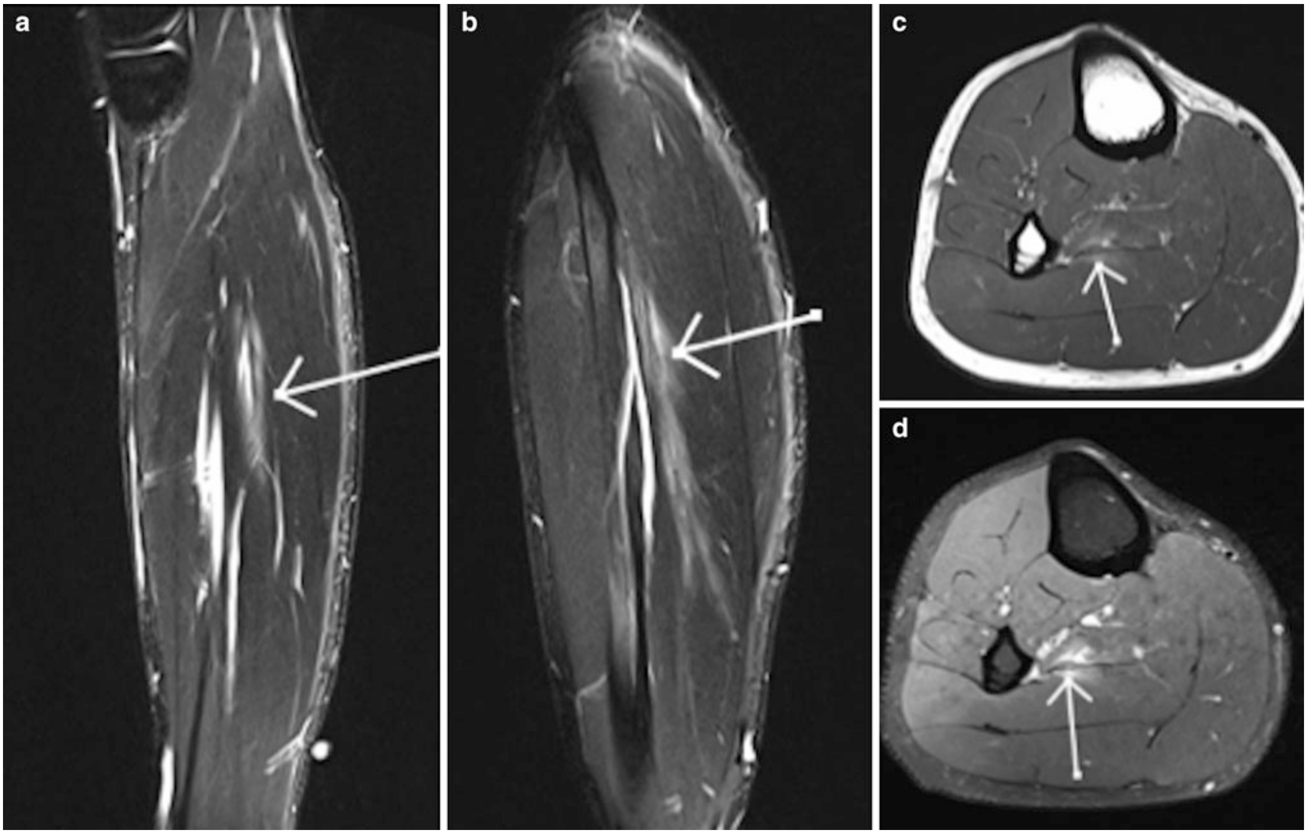

Fig. 29 Soleus strain in a professional Australian Rules football player. Sagittal STIR MR images (**a** and **b**), axial proton density weighted MR image (**c**) and axial proton density weighted MR image with fat saturation (**d**) show an injury at the proximal lateral-fibular muscle tendon junction, with mild focal intramuscular oedema and interstitial strain injury of the proximal tendon manifest as mild tendon signal hyperintensity (*arrows*)

Fig. 30 Calf strain. Sagittal STIR (**a**) and axial proton density weighted image (**b**) shows a retracted tear of the aponeurotic insertion of the medial head of gastrocnemius, with moderate fluid collection at the deep margin, tracking proximally and moderate adjacent intramuscular oedema (*arrows*)

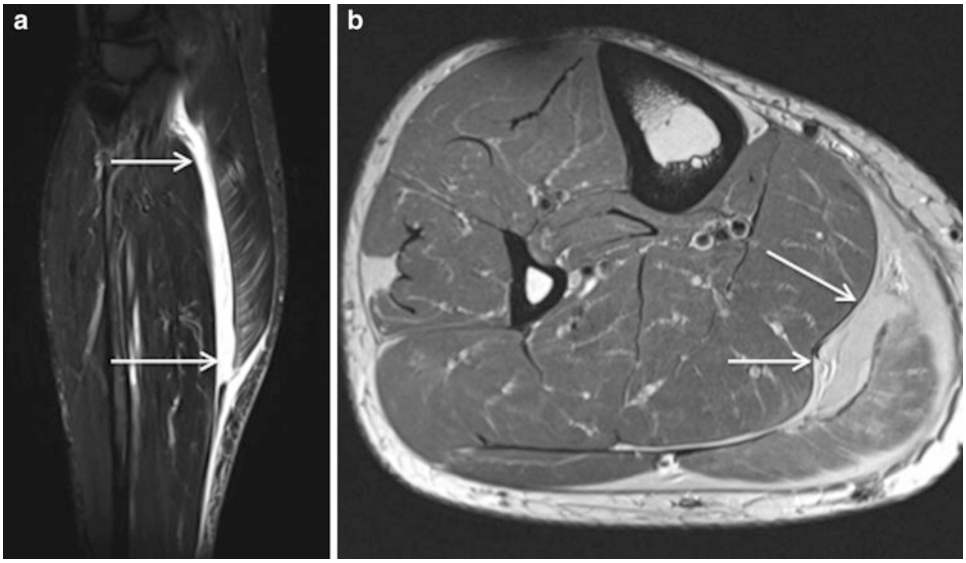

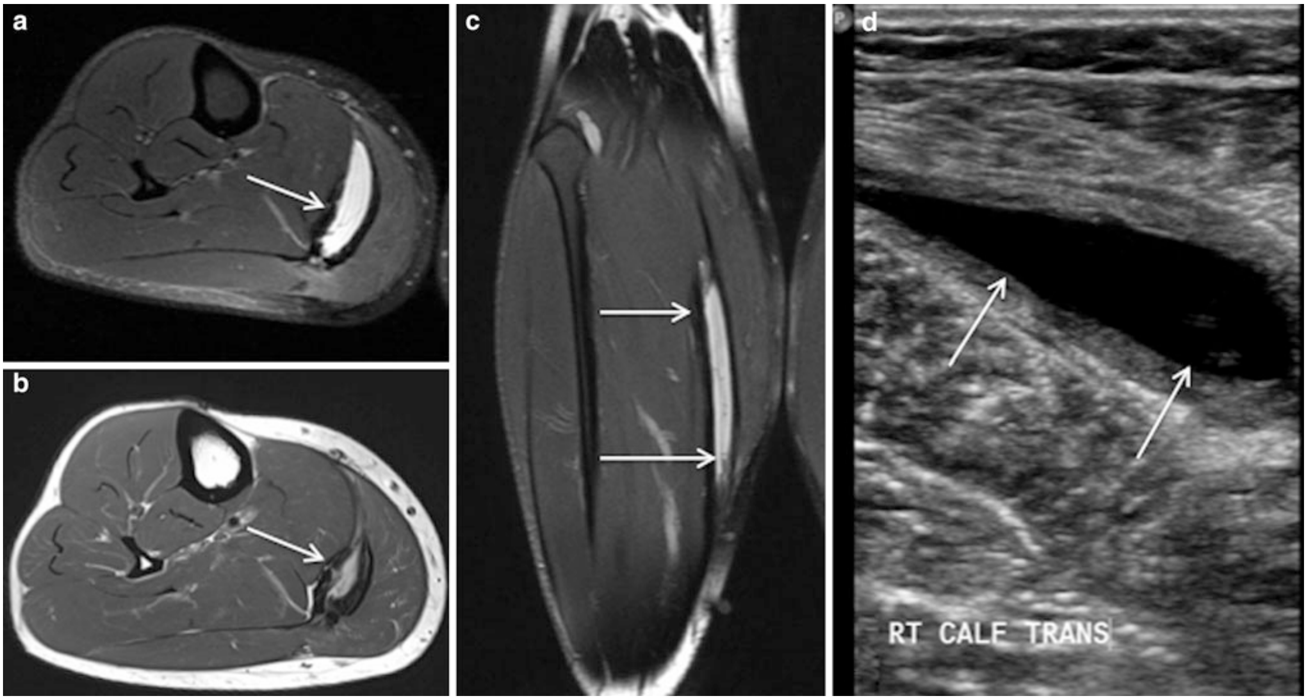

Fig. 31 Chronic calf strain. Axial proton density weighted MR images, with (**a**) and without fat saturation (**b**), coronal proton density weighted MR image with fat saturation (**c**) and US image (**d**) of a chronic incompletely healed tear of the aponeurotic insertion of medial head of gastrocnemius with a thick walled chronic haematoma and scar (*arrows*)

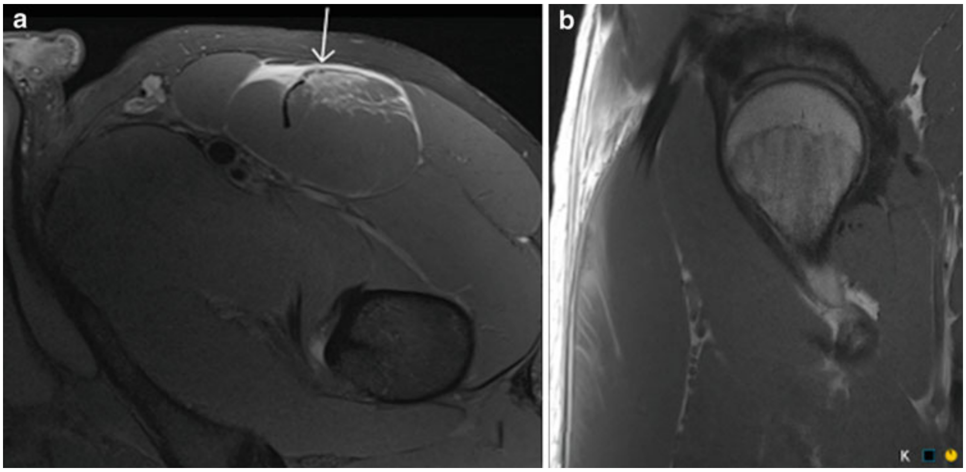

Fig. 32 Rectus femoris strain. Axial proton density weighted image with fat saturation (**a**) and sagittal proton density weighted image (**b**) in a professional soccer player demonstrate a grade 1 strain of the proximal muscle–tendon junction injury of rectus femoris, centred on the reflected head tendon, with feathery intramuscular oedema, subtle tendon signal hyperintensity indicating interstitial strain injury and shallow overlying subfascial fluid collection (*arrows*)

posterior component of the conjoined tendon and more distally forms a long, central intrasubstance aponeurosis and resultant musculotendinous junction within the muscle belly extending approximately two-thirds of the length of the muscle (Gyftopoulos et al. 2008).

Centrally located fibres arise from the lateral and medial aspect of the central aponeurosis form a bipennate muscle. The fibres which originate from the superficial aponeurosis give rise to a unipennate muscle and surround the more central bipennate fibres. This gives the rectus femoris “muscle within a muscle” (Bianchi et al. 2002).

Sprinters with acute injury involving the central tendon of the rectus femoris had a mean recovery time of 26.85 days, compared with injury to the peripheral tendon of the rectus femoris (9.17 days) and vasti muscles (4.42 days) (Cross et al. 2004).

Rectus femoris crosses two joints, has a high percentage of type II muscle fibres and commonly contracts while

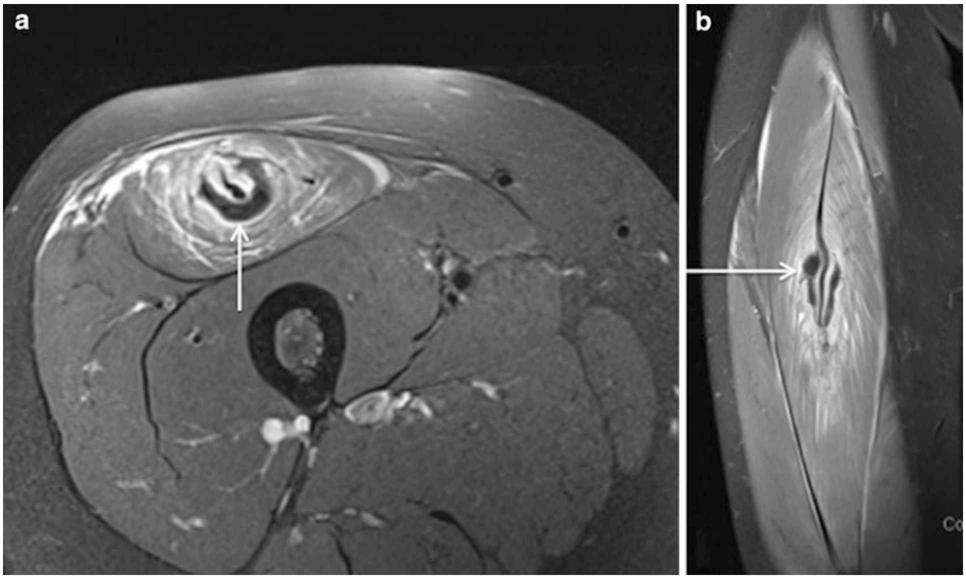

Fig. 33 Axial (**a**) and coronal (**b**) proton density weighted images with fat saturation show a crescentic/"bull's eye" haematoma adjacent to the muscle–tendon junction of the central-direct head proximal tendon of rectus femoris in a 12-year-old soccer player who had sustained a grade 2 muscle injury, the haematoma having formed at the site of muscle tear (*arrows*)

passively stretched, which increases the risk of muscle injury. A further predisposing factor in kicking sports is the increased stress on rectus femoris during foot strike with the ball (Cross et al. 2004).

Hasselman et al. (Hasselman et al. 1995) identified that intrasubstance tears of the rectus femoris macro- and microscopically demonstrate local haemorrhage and oedema at the site of disruption of the musculotendinous junction. Chronically, the haematoma organizes into a fatty, loose connective tissue encasement of the intramuscular tendon. Serous fluid arising from the haematoma may persist within the connective tissue sheath, forming a pseudocyst around the tendon (Hasselman et al. 1995).

The bull's-eye sign was coined by Hughes et al. (Hughes et al. 1995) which is signal hyperintensity surrounding the intrasubstance tendon (Bianchi et al. 2002). Gyftopoulos et al. (Gyftopoulos et al. 2008) demonstrated this sign in both acute and old injuries and pre and post administration of intravenous gadolinium. The authors postulated this sign represents evolving stages of injury and healing. In the acute phase, signal hyperintensity on fluid-sensitive images most likely represents oedema and haemorrhage. Cross et al. (Cross et al. 2004) proposed the term "acute bull's-eye lesion" for this imaging finding. In the subacute/chronic phase and post contrast signal hyperintensity may represent increased vascularity and scarring. In chronic injuries, atrophy and fatty infiltration of the musculotendinous junction may also demonstrate a bull's-eye sign (Gyftopoulos et al. 2008).

It has been postulated that chronic pain and dysfunction experienced by individuals post rectus femoris tear occus due to independent action of the indirect and direct heads of the proximal tendon, creating a shearing phenomenon (Hughes et al. 1995). This scenario is in contrast to what occurs during a contraction in the normal rectus femoris.

References

Aagaard H, Jorgensen U (1996) Injuries in elite volleyball. Scand J Med Sci Sports 6:228–232

Arciero RA, Shishido NS, Parr TJ (1984) Acute anterolateral compartment syndrome secondary to rupture of the peroneus longus muscle. Am J Sports Med 12(5):366–367

Armfield DR, Kim DH, Towers JD et al (2006) Sports-related muscle injury in the lower extremity. Clin Sports Med 25:803–842

Armstrong RB (1984) Mechanisms of exercise-induced delayed onset muscular soreness: a brief review. Med Sci Sports Exerc 16(6):529–538

Askling C, Tengvar M, Saartok T et al (2007) Acute first-time hamstring strains during high-speed running: a longitudinal study including clinical and magnetic resonance imaging findings. Am J Sports Med 35:197–206

Balius R, Pedret C, Pacheco L et al (2011) Rectus abdominis muscle injuries in elite handball players: management and rehabilitation. Open Access J Sports Med 2:69–73

Balius R, Pedret C, Galilea P et al (2012) Ultrasound assessment of asymmetric hypertrophy of the rectus abdominis muscle and prevalence of associated injury in professional tennis players. Skeletal Radiol 41:1575–1581

Beiner JM, Jokl P (2001) Muscle contusion injuries: current treatment options. J Am Acad Orthop Surg 9:227–237

Benjamin M, Kaiser E, Milz S (2008) Structure-function relationships in tendons: a review. J Anat 212(3):211–228. doi:10.1111/j.1469-7580.2008.00864.x

Best TM, Hunter KD (2000) Muscle injury and repair. Phys Med Rehabil Clin North Am 11:251–266

Bianchi S, C Martinoli, Waser NP et al. (2002) Central aponeurosis tears of the rectus femoris: sonographic findings. Skeletal Radiol 31:581–586. doi 10.1007/s00256-002-0559-z

Blankenbaker DG, Tuite MJ (2010) Temporal changes of muscle injury. Semin Musculoskelet Radiol 14(2):176–193

Brophy RH, Wright RW, Powell JW et al (2010) Injuries to kickers in American football: the National Football League experience. Am J Sports Med 38(6):1166–1173

Brukner P, Khan K (2002) Clinical sports medicine. Revised 2nd edn. McGraw-Hill, Australia

Bryan Dixon J (2009) Gastrocnemius vs. soleus strain: how to differentiate and deal with calf muscle injuries. Curr Rev Musculoskelet Med 2:74–77

Clanton TO, Coupe KJ (1998) Hamstring strains in athletes: diagnosis and treatment. J Am Acad Orthop Surg 6(4):237–248

Cleak MJ, Eston RG (1992) Delayed onset muscle soreness: mechanisms and management. J Sports Sci 10(4):325–341

Colosimo AJ, Wyatt HM, Frank KA et al (2005) Hamstring avulsion injuries. Oper Tech Sports Med 13:80–88

Comin J, Malliaras P, Baquie P et al (2013) Return to competitive play after hamstring injuries involving disruption of the central tendon. Am J Sports Med 41:111–115

Connell DA, Jhamb A, James T (2003) Side strain: a tear of internal oblique musculature. Am J Roentgen 181:1511–1517

Connell DA, Schneider-Kolsky ME, Hoving JL (2004) Longitudinal study comparing sonographic and MRI assessments of acute and healing hamstring injuries. Am J Roentgenol 183(4):975–984

Connell D, Ali K, Javid M et al (2006) Sonography and MRI of rectus abdominis muscle strain in elite tennis players. Am J Roentgen 187:1457–1461

Counsel P, Breidahl W (2010) Muscle injuries of the lower leg. Semin Musculoskelet Radiol 14:162–175

Cross TM, Gibbs N, Houang MT (2004) Acute quadriceps muscle strains: magnetic resonance imaging features and prognosis. Am J Sports Med 32(3):710–719

Davies JAK (1979) Peroneal compartment syndrome secondary to rupture of the peroneus longus. A case report. J Bone Joint Surg Am 61(5):783–784

Dierking JK, Bemben MG, Bemben DA et al (2000) Validity of diagnostic ultrasound as a measure of delayed onset muscle soreness. J Orthop Sports Phys Ther 30:116–122

Early JS, Ricketts DS, Hansen ST (1994) Treatment of compartmental liquefaction as a late sequela of a lower limb compartment syndrome. J Orthop Trauma 8:445–448. doi:10.1097/00005131-199410000-00015

Ekstrand J, Hägglund M, Waldén M (2011a) Epidemiology of muscle injuries in professional football (soccer). Am J Sports Med 39(6):1226–1232

Ekstrand J, Hägglund M, Waldén M (2011b) Injury incidence and injury patterns in professional football: the UEFA injury study. Br J Sports Med 45:553–558

Ekstrand J, Healy JC, Waldén M (2012) Hamstring muscle injuries in professional football: the correlation of MRI findings with return to play. Br J Sports Med 46:112–117

El-Khoury GY, Brandser EA, Kathol MH (1996) Imaging of muscle injuries. Skeletal Radiol 25(1):3–11

Elliott KG, Johnstone AJ (2003) Diagnosing acute compartment syndrome. J Bone Joint Surg (Br) 85(5):625–632

Elsayes KM, Lammle M, Shariff A et al (2006) Value of magnetic resonance imaging in muscle trauma. Curr Probl Diagn Radiol 35(5):206–212

Entrekin RR, Porter BA, Sillesen HH et al (2001) Real-time spatial compound imaging: Application to breast, vascular, and musculoskeletal ultra-sound. Semin Ultrasound CT MR 22:50–64

Exeter D, Connell DA (2010) Skeletal muscle: functional anatomy and pathophysiology. Semin Musculoskelet Radiol 14(2):97–105. doi:10.1055/s-0030-1253154

Eygendaal D, Rahussen FTG, Diercks RL (2007) Biomechanics of the elbow joint in tennis players and relation to pathology. Br J Sports Med 41:820–823. doi:10.1136/bjsm.2007.038307

Farber JM, Buckwalter KA (2002) MR imaging in nonneoplastic muscle disorders of the lower extremity. Radiol Clin North Am 40(5):1013–1031

Finni T, Hodgson JA, Lai AM et al (2003) Nonuniform strain of human soleus aponeurosis-tendon complex during submaximal voluntary contractions in vivo. J Appl Physiol 95:829–837

Fleckenstein JL, Canby RC, Parkey RW et al (1988) Acute effects of exercise on MR imaging of skeletal muscle in normal volunteers. Am J Roentgenol 151(2):231–237

Fleckenstein JL, Weatherall PT, Parkey RW et al (1989) Sports-related muscle injuries: evaluation with MR imaging. Radiology 172(3):793–798

Folsom GJ, Larson CM (2008) Surgical treatment of acute versus chronic complete proximal hamstring ruptures: results of a new allograft technique for chronic reconstructions. Am J Sports Med 36(1):104–109

Garrett WE (1996) Muscle strain injuries. Am J Sports Med 24:S2–S8

Gibbs NJ, Cross TM, Cameron M et al (2004) The accuracy of MRI in predicting recovery and recurrence of acute grade one hamstring muscle strains within the same season in Australian Rules football players. Am J Sports Med 7:248–258

Guillodo Y, Bouttier R, Saraux A (2011) Value of sonography combined with clinical assessment to evaluate muscle injury severity in athletes. J Athl Train 46(5):500–504

Gyftopoulos S, Rosenberg ZS, Schweitzer ME (2008) Normal anatomy and strains of the deep musculotendinous junction of the proximal rectus femoris: MRI features. Am J Roetgenol 190:W182–W186. doi:10.2214/AJR.07.2947

Hasselman CT, Best TM, Hughes C (1995) An explanation for various rectus femoris strain injuries using previously undescribed muscle architecture. Am J Sports Med 23(4):493–499

Hawkins RD, Hulse MA, Wilkinson C et al (2001) The association football medical research programme: an audit of injuries in professional football. Br J Sports Med 35:43–47

Hayashi D, Hamilton B, Guermazi A (2012) Traumatic injuries of thigh and calf muscles in athletes: role and clinical relevance of MR imaging and ultrasound. Insights Imaging 3(6):591–601

Holobinko JN, Damron TA, Scerpella PR (2003) Calcific myonecrosis: keys to early recognition. Skeletal Radiol 32:35–40

Huard J, Li Y, Fu FH (2002) Muscle injuries and repair: current trends in research. J Bone Joint Surg (Am) 84:822–832

Hughes C 4th, Hasselman CT, Best TM et al (1995) Incomplete, intrasubstance strain injuries of the rectus femoris muscle. Am J Sports Med 23:500–506

Humphries D, Jamison M (2004) Clinical and magnetic resonance imaging features of cricket bowler's side strain. Br J Sports Med 38:e21. doi:10.1136/bjsm.2003.005272

Hurme T, Kalimo H, Lehto M (1991) Healing of skeletal muscle injury. An ultrastructural and immunohistochemical study. Med Sci Sports Exerc 23:801–810

Jackson DW, Feagin JA (1973) Quadriceps contusions in young athletes. Relation of severity of injury with treatment and prognosis. J Bone Joint Surg (Am) 55:95–105

Järvinen TA, Kääriäinen M, Järvinen M et al (2000) Muscle strain injuries. Curr Opin Rheumatol 12(2):155–161

Järvinen TA, Järvinen TL, Kääriäinen M et al (2005) Muscle injuries: biology and treatment. Am J Sports Med 33(5):745–764

Jozsa LG, Kannus P (1997) Human tendons: anatomy, physiology, and pathology, 1st edn. Human Kinetics Publishers, Champaign, p. 105

Kääriäinen M, Kääriäinen J, Järvinen TL (1998) Correlation between biomechanical and structural changes during the regeneration of skeletal muscle after laceration injury. J Orthop Res 16(2):197–206

Kalimo H, Rantanen J, Jarvinen M (1997) Muscle injuries in sports. Baillieres Clin Orthop 2:1–24

Kibler WB (1994) Clinical biomechanics of the elbow in tennis: implications for evaluation and diagnosis. Med Sci Sports Exerc 26:1203–1206

Kijowski R (2011) Magnetic resonance imaging of muscle injury. In: Conference Proceedings

Kneeland JB (1997) MR imaging of muscle and tendon injury. Eur J Radiol 25:199–208

Koulouris G, Connell D (2005) Hamstring muscle complex: an imaging review. Radiographics 25(3):571–586

Koulouris G, Connell DA, Brukner Pl et al (2007a) Magnetic resonance imaging parameters for assessing risk of recurrent hamstring injuries in elite athletes. Am J Sports Med 35(9):1500–1506

Koulouris G, Ting AYI, Jhamb A et al (2007b) Magnetic resonance imaging findings of injuries to the calf muscle complex. Skeletal Radiol 36:921–927

Kramer FL, Kurtz AB, Rubin C et al (1979) Ultrasound appearance of myositis ossificans. Skeletal Radiol 4:19–20

Lansdown DA, Ding Z, Wadington M (2007) Quantitative diffusion tensor MRI-based fiber tracking of human skeletal muscle. J Appl Physiol 103:673–681

Larson RC, Sierra RJ, Sundaram M et al (2004) Calcific myonecrosis: a unique presentation in the upper extremity. Skeletal Radiol 33:306–309. doi:10.1007/s00256-003-0740-z

Lee JC, Healy J (2004) Sonography of lower limb muscle injury. AJR Am J Roentgenol 182:341–351

Linklater JM, Hamilton B, Carmichael J et al (2010) Hamstring injuries: anatomy, imaging, and intervention. Semin Musculoskelet Radiol. 14(2):131–161

Litwiller DV, Amrami KK, Dahm DL et al (2007) Chronic exertional compartment syndrome of the lower extremities: improved screening using a novel dual birdcage coil and in-scanner exercise protocol. Skeletal Radiol 36:1067–1075. doi:10.1007/s00256-007-0360-0

Mair SD, Seaber AV, Glisson RR et al (1996) The role of fatigue in susceptibility to acute muscle strain injury. Am J Sports Med 24:137–143

Malliaropoulos N, Papacostas E, Kiritsi O et al (2010) Posterior thigh muscle injuries in elite track and field athletes. Am J Sports Med 38:1813–1819

Maquirriain J, Ghisi JP, Kokalj AM (2007) Rectus abdominis muscle strains in tennis players. Br J Sports Med 41:842–848

McCarthy EF, Sundaram M (2005) Heterotopic ossification: a review. Skeletal Radiol 34(10):609–619

Megliola A, Eutropi F, Scorzelli A et al (2006) Ultrasound and magnetic resonance imaging in sports-related muscle injuries. Radiol Med 111(6):836–845

Milisano LP, Hunter GA (1992) Liquefaction and calcification of a chronic compartment syndrome of the lower limb. J Orthop Trauma 6:245–247

Mueller-Wohlfahrt H, Haensel L, Mithoefer K et al (2012) Terminology and classification of muscle injuries in sport: a consensus statement. Br J Sports Med 0:1–9. doi:10.1136/bjsports-2012-091448

Muramatsu K, Ihara K, Seki T (2009) Calcific myonecrosis of the lower leg: diagnosis and options of treatment. Arch Orthop Trauma Surg 129:935–939. doi:10.1007/s00402-009-0890-0

Nirschl RP, Pettrone FA (1979) Tennis elbow: the surgical treatment of lateral epicondylitis. J Bone Joint Surg (Am) 61:832–839

Noonan TJ, Garrett WE Jr (1992) Injuries at the myotendinous junction. Clin Sports Med 11(4):783–806

Nurenberg P, Giddings CJ, Stray-Gundersen J et al (1992) MR imaging-guided muscle biopsy for correlation of increased signal intensity with ultrastructural change and delayed-onset muscle soreness after exercise. Radiology 184(3):865–869

O'Brien M (2005) The anatomy of the Achilles tendon. Foot Ankle Clin 10:225–238

O'Donoghue DO (1962) Treatment of injuries to athletes. WB Saunders, Philadelphia

Olsen KM, Chew FS (2006) Tumoral calcinosis: pearls, polemics, and alternative possibilities. Radiographics 26:871–885. doi:10.1148/rg.263055099

Opar DA, Williams MD, Shield AJ (2012) Hamstring strain injuries: factors that lead to injury and re-injury. Sports Med 42:209–226

Orchard J (2001) Intrinsic and extrinsic risk factors for muscle strains in Australian football. Am J Sports Med 29:300–303

Orchard J, Seward H (2003) AFL injury report 2003. J Sci Med Sport 7:264–265

Palmer WE, Kuong SJ, Elmadbouh HM (1999) MR imaging of myotendinous strain. Am J Roentgenol 173:703–709

Pearl AJ (1981) Anterior compartment syndrome: a case report. Am J Sports Med 9(2):119–120

Peck RJ, Metreweli C (1988) Early myositis ossificans: a new echographic sign. Clin Radiol 39:586–588

Peetrons P (2002) Ultrasound of muscles. Eur Radiol 2002(12):35–43

Quintero AJ, Wright VJ, Fu FH et al (2009) Stem cells for the treatment of skeletal muscle injury. Clin Sports Med 28(1):1–11

Renwick SE, Naraghi FF, Worrell RV et al (1994) Cystic degeneration and calcification of muscle: late sequelae of compartment syndrome. J Orthop Trauma 8:440–444. doi:10.1097/00005131-199410000-00014

Ringler MD, Litwiller DV, Felmlee JP et al (2013) MRI accurately detects chronic exertional compartment syndrome: a validation study. Skeletal Radiol 42:385–392. doi:10.1007/s00256-012-1487-1

Rybak LD, Torriani M (2003) Magnetic resonance imaging of sports-related muscle injuries. Top Magn Reson Imaging 14(2):209–219

Ryu KN, Bae DK, Park YK et al (1996) Calcific tenosynovitis associated with calcific myonecrosis of the leg: imaging features. Skeletal Radiol 25:273–275. doi:10.1007/s002560050078

Schneider-Kolsky ME, Hoving JL, Warren P et al (2006) A comparison between clinical assessment and magnetic resonance imaging of acute hamstring injuries. Am J Sports Med 34(6): 1008–1015

Shellock FG, Fukunaga T, Mink JH (1991) Exertional muscle injury: evaluation of concentric versus eccentric actions with serial MR imaging. Radiology 179(3):659–664

Shelly MJ, Hodnett PA, MacMahon PJ (2009) MR imaging of muscle injury. Magn Reson Imaging Clin N Am 17(4):757–773

Silder A, Heiderscheit BC, Thelen DG et al (2008) MR observations of long-term musculotendon remodeling following a hamstring strain injury. Skeletal Radiol 37(12):1101–1109

Slavotinek JP (2010) Muscle injury: the role of imaging in prognostic assignment and monitoring of muscle repair. Semin Musculoskelet Radiol 14(2):194–200

Slavotinek JP, Verrall GM, Fon GT (2002) Hamstring injury in athletes: using MR imaging measurements to compare extent of muscle injury with amount of time lost from competition. Am J Roentgenol 179(6):1621–1628

Standring S (2005) Gray's anatomy: the anatomical basis of clinical practice, 39th edn. Elsevier, Edinburgh

Stauber WT (1989) Repair models and specific tissue responses in muscle injury. In: Leadbetter WB, Buckwalter JA, Gordon SL (eds) Sports induced inflammation: clinical and basic science concepts. American Association of Orthopaedic Surgeons, Rosemont, pp 205–213

Stedman TL (2000) Stedman's medical dictionary, 27th edn, Lippincott, Williams & Wilkins, Philadelphia

Stevens KJ, Crain JM, Akizuki KH et al (2010) Imaging and ultrasound-guided steroid injection of internal oblique muscle strains in baseball pitchers. Am J Sports Med 38:581–585. doi: 10.1177/0363546509350105

Temple HT, Kuklo TR, Sweet DE et al (1998) Rectus femoris muscle tear appearing as a pseudotumor. Am J Sports Med 26:544–548

Vangsess CT Jr, Jobe FW (1991) Surgical treatment of medial epicondylitis. Results in 30 elbows. J Bone Joint Surg 73:409–411

Verleisdonk EJ (2002) The exertional compartment syndrome: a review of the literature. Orthop Traumatol Rehabil 4(5):626–631

Verrall GM, Slavotinek JP, Barnes PG et al (2001) Clinical risk factors for hamstring muscle strain injury: a prospective study with correlation of injury by magnetic resonance imaging. Br J Sports Med 35(6):435–439; discussion 440

Verrall GM, Slavotinek JP, Barnes PG et al (2003) Diagnostic and prognostic value of clinical findings in 83 athletes with posterior thigh injury: comparison of clinical findings with magnetic resonance imaging documentation of hamstring muscle strain. Am J Sports Med 31(6):969–973

Viau MR, Pedersen HE, Salciccoioli GG et al (1993) Ectopic calcifcation as a late sequela of compartment syndrome. Report of two cases. Clin Orthop Relat Res 176:178–180

Wang JW, Chen WJ (2001) Calcific myonecrosis of the leg: a case report and review of the literature. Clin Orthop Relat Res 389:185–190. doi:10.1097/00003086-200108000-00026

Weishaupt D, Schweitzer ME, Morrison WB (2001) Injuries to the distal gastrocnemius muscle: MR findings. J Comput Assist Tomogr 25(5):677–682

Woodhouse JB, McNally EG (2011) Ultrasound of skeletal muscle injury: an update. Semin Ultrasound CT MR 32(2):91–100. doi: 10.1053/j.sult.2010.12.002

Woods C, Hawkins RD, Maltby S et al (2004) Football Association Medical Research Programme. The Football Association Medical Research Programme: an audit of injuries in professional football—analysis of hamstring injuries. Br J Sports Med 38(1): 36–41

Zaraiskaya T, Kumbhare D, Noseworthy MD (2006) Diffusion tensor imaging in evaluation of human skeletal muscle injury. J Magn Reson Imaging 24:402–408

Zeiss J, Ebraheim NA, Woldenberg LS (1989) Magnetic resonance imaging in the diagnosis of anterior tibialis muscle herniation. Clin Orthop Relat Res 244:249–253

MRI of Muscle Denervation in Central and Peripheral Nervous System Disorders

Mirko Pham, Marcel Wolf, Philipp Bäumer, Martin Bendszus,
and Gregor Kasprian

Contents

1 **Key points** 221
2 **Anatomy of Skeletal Muscle Innervation** 222
3 **Pathophysiology of Denervation and Reinnervation** 223
3.1 Early Denervation 223
3.2 Late Denervation 224
3.3 Reinnervation 224
4 **Diagnostic Potential of Detecting Muscle Denervation by MRI** 224
4.1 Radiculopathies 225
4.2 Plexopathies 225
4.3 Trunk Neuropathies 229
4.4 Multifocal Neuropathies and Motor Neuron Disease 232
5 **Advanced MRI Techniques** 236
5.1 Perfusion MRI of Denervated Muscle 236
5.2 Diffusion Tensor MRI of Denervated Muscle 236
5.3 MR Spectroscopy of Denervated Muscle 237
References 238

Abstract

High-resolution MR imaging of peripheral nerves, also termed MR-Neurography, is becoming more common and practical for lesion localization with the increasing availability of 3 T magnets. This book chapter reports on the role of MR imaging in peripheral neuropathies with particular emphasis of denervation related changes of the muscles supplied by affected nerves and gives a brief overview of the added value of MRI in neurogenic myopathies. In acute muscle denervation, an increase of intramuscular T2-signal and gadolinium-enhancement can be observed and reversal of these signal changes may indicate reinnervation and treatment success. In contrast to the denervation patterns in complete radiculopathies and plexopathies, in multifocal neuropathies the muscle T2 signal increase is distributed more heterogeneously involving muscles typically supplied by more than one nerve trunk. Furthermore, T2 signal increase in multifocal nerve lesions typically involves not entire muscle bellies but only confined zones within a muscle belly. Several advanced techniques such as diffusion tensor imaging or MRI perfusion have become available for muscle imaging. The latter, by dynamic measurement of contrast enhancement seems particularly promising in quantifying denervation related alteration of the muscle microvasculature.

1 Key points

1. In acute muscle denervation, an increase of intramuscular T2-signal and contrast medium uptake can be observed by increased T1-signal. While gadolinium-enhancement might indicate an increased capillary extravasation, the histological correlation with enlarged intramuscular capillaries suggested increase of regional blood volume in denervated muscle.
2. In severe cases of cubital tunnel syndrome (the second most common nerve entrapment syndrome after the

---

M. Pham (✉) · M. Wolf · P. Bäumer · M. Bendszus
Department of Neuroradiology, Heidelberg University Hospital,
INF 400, 69120 Heidelberg, Germany
e-mail: Mirko.Pham@med.uni-heidelberg.de

G. Kasprian
Division of Neuroradiology and Musculoskeletal Radiology,
Department of Biomedical Imaging and Image-guided Therapy,
Medical University of Vienna, Währinger Gürtel 18–20,
1090 Vienna, Austria

M.-A. Weber (ed.), *Magnetic Resonance Imaging of the Skeletal Musculature*, Medical Radiology. Diagnostic Imaging,
DOI: 10.1007/174_2013_928, © Springer-Verlag Berlin Heidelberg 2013
Published Online: 16 October 2013

carpal tunnel syndrome), STIR sequences may depict denervation of target muscles supplied by the ulnar nerve with reversal of these signal changes indicating reinnervation and treatment success.

3. Muscle denervation patterns in multifocal neuropathies seem to differ substantially from denervation patterns in complete radiculopathies, plexopathies or trunk neuropathies: The muscle T2 signal increase is distributed over several target muscle groups in the distribution of more than one single nerve root or nerve trunk and the denervation signal often involves not entire muscle bellies but only confined zones within a muscle belly.

2 Anatomy of Skeletal Muscle Innervation

Voluntary action through coordinated contraction of skeletal muscles is mediated from upper motor neurons in cerebral cortex through the descending corticospinal and corticobulbar pathways. At level of the brain stem (bulbar) or spinal column lower motor neurons convey electrical impulse conduction to the peripheral nervous system (PNS). Peripheral nerves emerge from the anterior and posterior intradural filaments which are connected as anterior and dorsal rootlets to gray matter of anterior and dorsal horns within the spinal column. Voluntary motor function is transmitted through motor neurons within anterior horn gray matter connected to large myelinated Aα—fibers. Other myelinated and unmyelinated fiber classes of peripheral nerve bear mainly somatosensory and autonomic functions and intermingle with the Aα—fiber type. At, or immediately distal to the spinal ganglion which is connected to the dorsal intradural filaments, the anterior/ventral, and posterior/dorsal filaments unite and enter the dural sheath to form at each spinal/radicular level one spinal nerve. Each spinal nerve further divides into a ventral and dorsal ramus, the latter supplying the back. The ventral ramus supplies the anterolateral parts of the body and extremities. The complex function of coordinated voluntary control of the extremities demands a particularly high density of motor and sensory neurons at cervical and lumbar cord levels forming two regions of caliber gain in the spinal column which are called "intumescentiae." At these cervical and lumbar intumescentiae also the caliber of the emerging spinal nerves is enlarged, with C7 and L5 being most prominent, in comparison with their counterparts at mid-thoracic level for example. Muscle innervation follows a well-organized somatotopic arrangement which follows the metameric arrangement of the spinal column and spinal nerves. Therefore, characteristic patterns of muscle denervation can be observed by clinical symptoms, findings on electromyography (EMG) and MRI as is the subject of this chapter. The correct interpretation of such denervation patterns represents indispensable diagnostic information for localizing peripheral nerve lesions to aid the differential diagnoses of peripheral neuropathies, which often is challenging. The somatotopic arrangement of muscle innervation is not intuitively comprehensible without knowledge of certain anatomical details. Although lesion localization by clinical observation of motor symptoms can rely to some degree on certain indicator muscles to infer at which level the PNS is affected, the association between indicator muscles and spinal nerve level or peripheral nerve is not straightforward. For example, the M. biceps brachii is typically affected by injury to the spinal nerve at C6 level, or as another example, the calf muscles (M. gastrocnemius and M. soleus) by injury to S1. However, a single muscle does not receive its innervation supply from one spinal level/nerve in isolation. That is, an overlapping supply from adjacent spinal nerve levels exists for skeletal muscles as it exists for dermatomes (Foerster 1933). The anatomical/structural correlate for overlapping myotomes and dermatomes mainly is the exchange of fascicles between adjacent spinal nerve levels. The predominance of fascicle exchange is located at the level of the cervicobrachial and lumbosacral nerve plexus. Proximal to the plexus or distally at peripheral nerve level, however, fascicle exchange may also occur to a significant degree. In addition, interindividual variability in spinal levels of muscle innervation especially occurs if spinal level contributions to plexus are shifted cranially or caudally as in the so-called pre- and postfixed plexus. For example, prefixation of the cervicobrachial plexus is associated with pronounced supply from upper roots (C3–C5) and less supply from lower levels (Pellerin et al. 2010). Distinct peripheral nerves eventually emerge from the plexus and further bifurcate into terminal nerve branches which enter the target muscle through its fasciae. The complexity of arrangement and distribution of terminal nerve branches entering certain target muscles is another source of potentially significant anatomical variability and the degree of variability seems to differ between certain target muscles. Terminal nerve branching patterns and intramuscular ramifications of these terminal branches are less well studied than peripheral nerve, plexus, or spinal nerve anatomy owing to the minute caliber of these branches which are at the limit of (micro-)dissectability (An et al. 2012). In recent work, Sihler staining or high-resolution 3D digitization could be used to investigate distal branching patterns of certain muscles of interest namely the human phrenic, intrinsic hand, and soleus muscle (Loh et al. 2003; An et al. 2012; Xie et al. 2012). Sihler staining to date seems to be the best available histological method of mapping nerve branching patterns in 3D and is based on the staining of nerve trunks and branches after several preparatory steps including maceration of surrounding tissue have been undertaken to enhance nerve visibility and contrast (Mu and Sanders 2010).

These investigations have given further important clues supporting the assumption that some degree of somatotopic arrangement is preserved to the distal end of the motor innervation path. Fascicular somatotopy within peripheral nerve trunks seems to be preserved, in that fascicles or certain axon bundles within a peripheral nerve trunk or branch that stem from adjacent spinal nerve levels will supply terminal muscular branches, which bifurcate close to the muscle belly or at intramuscular level, in rostrocaudal fashion. Such arrangement could be particularly well documented in flat shaped muscles such as the diaphragm which in large parts is stretched in two dimensions. These studies have also shown that intramuscular fine ramifications may overlap in a given muscular subvolume and that contributions to the terminal muscular branches may stem from different peripheral nerves: E.g., mixed innervation of extensor carpi radialis brevis muscle by terminal branches of radial and median nerve (Ravichandiran et al. 2012) or mixed innervation of brachialis muscle by musculocutaneous and radial nerve (Puffer et al. 2011).

Finally, from the intramuscular fine ramifications of the intramuscular terminal nerve branches individual myelinated motor axons will emerge and divide into 20–100 unmyelinated terminal fibers each innervating one single muscle fiber (Hirsch 2007). The anatomical and functional coherence between terminal fibers of one axon and their target muscle fibers is considered a motor unit.

3 Pathophysiology of Denervation and Reinnervation

Complete or partial denervation of skeletal muscle is accompanied by diverse pathophysiologic processes on a metabolic, biochemical, micro-, and macrostructural level. These processes occur either acutely or chronically and lead to tissue changes, which are not only limited to the neuromuscular unit itself. They also involve the vascular as well as the local connective tissue compartments. Ultimately, denervation may lead to a significant degree of functional deficit. In order to adequately interpret imaging findings in patients with neurogenic myopathy, knowledge about early and late pathophysiological responses to denervation and reinnervation is important.

Denervation associated changes of the musculature are dependent on the grade of injury to the affected peripheral nerve. There can be either a *selective degeneration* of motor neurons with consecutive partial muscle denervation, as best seen in spinal muscular atrophy. In the case of "*crush injury*" the nerve sheath may remain intact but axonal degeneration may occur ("axonotmesis"). The most severe form of nerve injury is *complete dissection* ("neurotmesis") of the peripheral nerve, involving discontinuity injury of the inner and outer nerve sheath (epi-, peri-, and endoneurium) and axons. In each of these scenarios, differences in the pathophysiologic mechanisms associated with de- and reinnervation have been observed [reviewed in (Willmott et al. 2012)].

3.1 Early Denervation

Acute and complete injury ("neurotmesis") to the motor fibers of a peripheral nerve leads to denervation of the muscle fibers of the affected neuromuscular unit. Due to the nerve lesion, the action potential dependent release of acetylcholine at the neuromuscular junction cannot be triggered. As a consequence the nerve terminals show rapid degeneration and disappear within the first day after denervation, whereas the postsynaptic membranes are well preserved (Sakakima et al. 2000). Soon thereafter, the muscular protein synthesis pattern changes leading to the expression of a new type of (tetrodotoxin-resistant) sodium channel, which is peaking 3–5 days after denervation (Lupa et al. 1995). At the same time embryonal forms of acetylcholine receptors are spread out all over the muscle membrane causing a superexcitability of the denervated muscle (Witzemann et al. 1991). These changes are the basis for a decrease in the resting state potential of the muscular postsynaptic membrane and subsequent occurrence of spontaneous depolarization of the affected skeletal muscle, visible as fibrillations. However, the timeline of the occurrence of fibrillation potentials as measured by EMG is variable. Dependent upon the distance between the site of nerve injury and the consecutively denervated muscle, fibrillation potentials can take between 10 days and 6 weeks to develop [reviewed in (Willmott et al. 2012)].

Soon after denervation the metabolic activity of muscle cells changes. Glycogenolysis and glycolysis enzyme activities are decreased leading to a lower ATP biosynthesis (Danon and Schliselfeld 2007) and reduced energy metabolism. Proteolysis outweighs the initially decreased and later increased protein synthesis resulting in an overall loss of myofibrillar components (Goldspink 1976; Furuno et al. 1990). These early changes explain the rapidly occurring loss of muscle mass and atrophy within the initial 14 days after denervation (O'Leary et al. 2012).

In addition to alterations of the neuromuscular unit itself, rapid changes of the local vasculature occur. A ten-fold increase in blood flow (Eisenberg and Hood 1994), accompanied by a significant increase in the mean capillary area within the first 2 days and peaking 4 weeks after denervation (Wessig et al. 2004), have been reported. Besides the overall increase in blood volume within the affected skeletal muscle, changes in the vascular permeability lead to an increased extracellular fluid space, as determined by T2- and diffusion-weighted MRI (Hazlewood et al. 1974; Polak et al. 1988; Kikuchi et al. 2003; Holl et al. 2008; Goyault et al. 2012). Besides increase of intramuscular T2-signal in acute denervation, contrast medium uptake can be observed by increased T1-signal (Bendszus and Koltzenburg 2001).

3.2 Late Denervation

Several weeks and months after acute denervation, 70–85 % of muscle tissue mass is lost (Gutmann 1962). Already in early stages after denervation, collagen fibrils are deposited between denervated myocytes (Wechsler and Hager 1961)—a process which becomes particularly pronounced in chronic and late denervation states. Massive deposition of interstitial collagen results in further separation of regenerative satellite from atrophic muscle cells. Muscle cells lose their nuclei, change the morphology of their mitochondria and their myofilaments become increasingly disorganized (Lu et al. 1997; Viguie et al. 1997). Moreover, atrophic myocytes accumulate lipid droplets and glycogen deposits within their cytoplasm (Lu et al. 1997). These processes are paralleled by a mass degeneration and death of capillaries with consequent devascularization of the muscle (Borisov et al. 2000). These degenerative muscle tissue changes significantly interfere with the regenerative potential of the skeletal muscle and further complicate successful late reinnervation.

3.3 Reinnervation

Restoration of the functional properties of denervated muscle is a complex process, which requires the interplay between several physiologic processes on a molecular level. However, regeneration of the causative peripheral nerve injury is the major determinant of the establishment of the functional properties of the skeletal muscle. Therefore, the grade and severity of peripheral nerve injury play an important role in the prognosis of functional recovery from denervation. In addition, time to muscle reinnervation seems to be the best prognostic indicator of final functional outcome (Krarup et al. 2002). Due to previously described tissue remodeling of long-term denervated skeletal muscle, late reinnervation often leads to unsatisfactory results with incomplete recovery of function. Thus, maintenance of physiologic properties of skeletal muscle by electric stimulation is a new and important therapeutic concept (Kern et al. 2002).

As soon as functional nerve terminals have reached the transiently denervated muscle, they form their active acetylcholine releasing zones exactly in the regions of the original postsynaptic folds (Letinsky et al. 1976). This indicates the influence of molecular factors, which govern the guidance of reinnervating axons and the reestablishment of a functional motor endplate. In particular the intactness and integrity of the basal lamina of the neuromuscular junction seem to be of utmost importance in this regenerative process. Both—the pattern of excitation by the regenerated peripheral nerve, as well as local neurotrophic factors controlling the physiological properties of the reinnervated muscle—are important factors in the functional consolidation of the neuromuscular unit. Finally, besides amelioration of the ultrastructure of distorted myofibrils (Sakakima et al. 2000) and recovery of muscle cell metabolism, also normalization of blood flow and capillary diameters occurs (Eisenberg and Hood 1994; Wessig et al. 2004).

4 Diagnostic Potential of Detecting Muscle Denervation by MRI

Cross-sectional radiologic imaging and in particular MRI can give significant diagnostic information in the workup of patients with suspected peripheral neuropathies or in motor neuron disorders of the central nervous system. Several quantitative and qualitative MRI measures reflect acute, intermediate and chronic structural, pathomorphological, and functional changes of denervated muscle. Spatial resolution and soft tissue contrast can be optimized in order to detect and delineate reliably single muscles, muscle bellies, or whole muscle groups on any chosen imaging plane. For the detection and correct anatomical localization of denervated muscle standard axial imaging planes with perpendicular orientation to the long axis of muscle are preferable. With the use of multiple surface array receive coils and parallel imaging techniques larger areas of coverage can be recorded during a single examination session. In this manner, target muscle groups in the territory of a given peripheral nerve, spinal nerve, or nerve plexus can be examined comprehensively. MRI is a reasonable auxiliary diagnostic examination which may complement EMG to detect denervation in deeply located muscles not amenable to reliable needle recordings. Another limitation of needle EMG is the small size of the sampling volume. Denervation signal may go undetected if only certain neuromuscular compartments are affected and not the entire target muscle or a larger bulk of the target muscle. Selective denervation sparing the muscle partially may be observed in selective fascicular nerve injury or may be the result of mixed or dual nerve supply. Several diagnostic signs may serve the recognition of muscle denervation. In the early acute stage, T2 signal increase in denervated muscles can be observed. In severe axonal injury this change is supposed to occur very

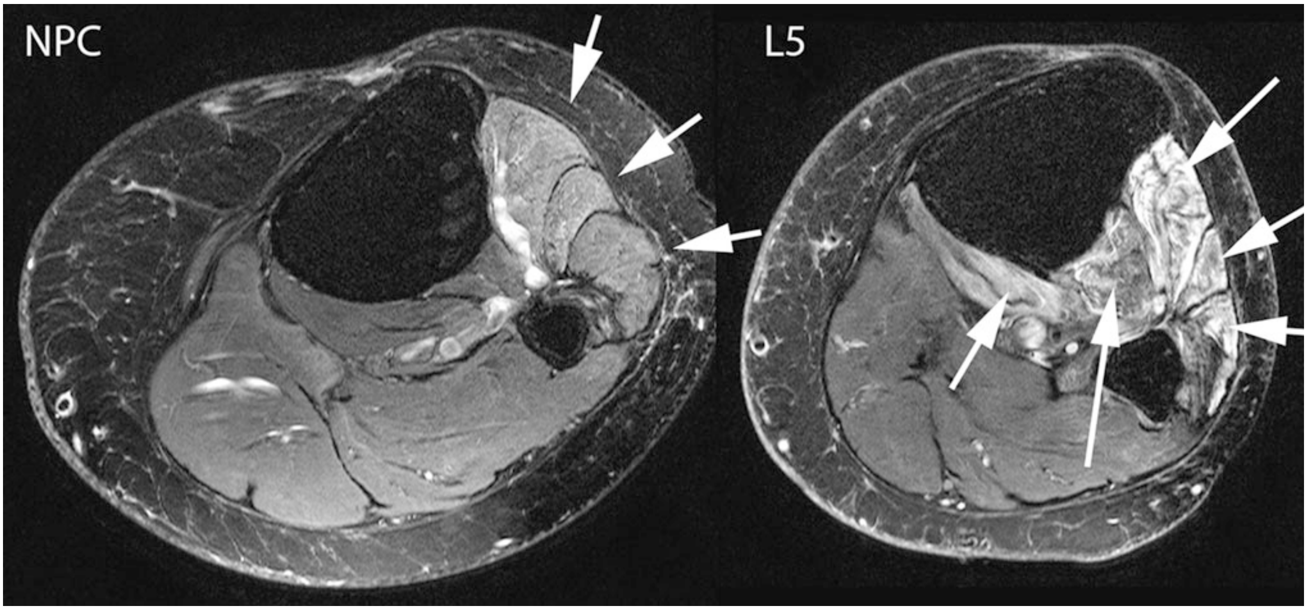

Fig. 1 *Left side* shows typical denervation pattern in NPC neuropathy including the extensors and peroneal muscles visible due to the prolonged T2 time of the muscle tissue (*arrows* on *left image*). In cases of L5 denervation as shown on the *right*, the posterior tibial muscle, and the popliteal muscle (*arrows* on *right image*) are additionally affected

early, during the first 48 h after injury and thus presumably earlier than any spontaneous electrical activity on EMG which in humans may have to be awaited for up to several weeks. This assumption is based on the experimental observation in rats showing T2 signal increase within 48 h of injury but has not been investigated in controlled fashion in humans yet (Wessig et al. 2004). Denervation without successful reinnervation is followed by muscle fiber degeneration and fatty atrophy. This chronic stage can be detected by hyperintense signal alteration on T1-weighted MRI and volume loss of affected muscles (Kamath et al. 2008). The correct interpretation of acute or chronic denervation related muscle injury on MRI relies on pattern recognition of affected muscle groups and on neuroanatomical knowledge about target muscles of certain PNS elements such as spinal nerves, plexus, or peripheral nerves.

4.1 Radiculopathies

Typical denervation patterns may be observed by muscle MRI in radiculopathies of various origins. For example, the complete denervation of target muscles in the territory of the L5 root just below knee level (M. tibialis anterior, M. extensor digitorum longus, M. peroneus longus et brevis, M. tibialis posterior, M. popliteus), points toward an L5 radiculopathy (Fig. 1). If, at the same level, the denervation pattern spares the M. tibialis posterior and popliteal muscle, a neuropathy of the common peroneal nerve would be likely (Bendszus et al. 2003). At more proximal level an L5 radiculopathy severe enough to be followed by muscle denervation would be associated with denervation change in typical proximal target muscles such as, e.g., the M. gluteus minimus (Fig. 2). In certain cases, specific imaging findings of the nerval structures themselves will aid the imaging differential diagnosis of radiculopathy or neuropathy. For example, an inflammatory radiculopathy or plexopathy will increase spinal nerve or plexus T2 signal and thereby facilitate correct lesion localization (Fig. 3).

4.2 Plexopathies

4.2.1 Anatomy of the Brachial Plexus

In order to understand and diagnose lesions to the brachial plexus adequately, knowledge of the anatomy of this complex region is necessary. The brachial plexus is formed by the ventral nerve roots of five spinal cord segments. The roots C5, C6, C7, C8, and Th1 always contribute to the formation of the upper extremity nerves. Furthermore, participation of the ventral nerve root C4 or the involvement of the nerve root Th2 can be observed. Frequencies of anatomical variations are different on the right or left side as well as in males and females (Uysal et al. 2003). Although diverse terminologies have been used, a contribution by C4 and absent or minimal contribution by Th2 has been most frequently defined as a "prefixed" condition, whereas a major contribution by Th2 and absent contribution by C4 has been described as

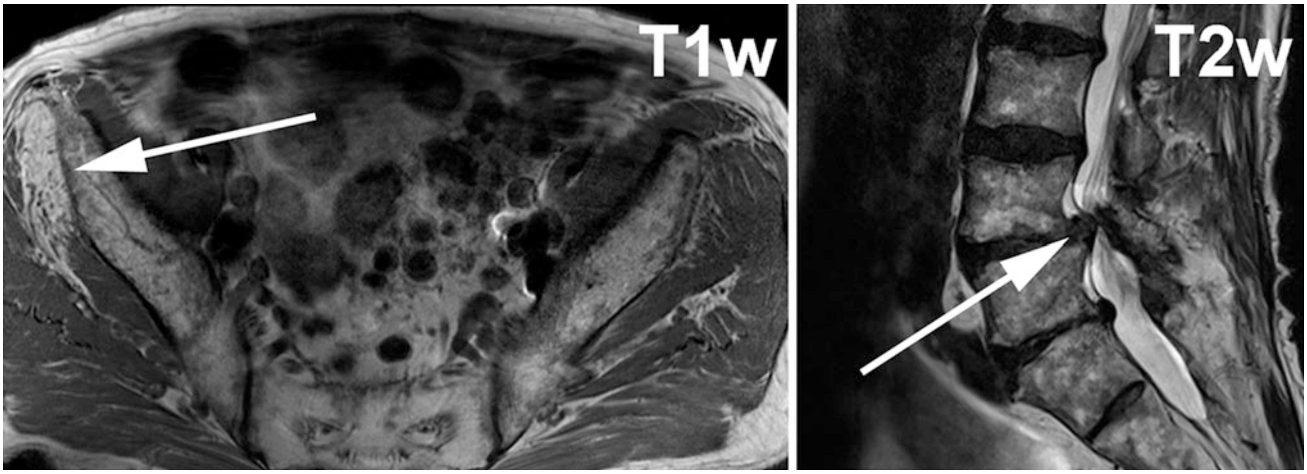

Fig. 2 *Left image* shows T1-weighted axial slice through gluteal region. On the *right side* of the patient (*solid arrow* on *left*) the gluteus minimus muscle shows strong T1w hyperintense signal alteration indicating fatty atrophy in the chronic stage of denervation. The gluteus minimus muscle receives its supply predominantly from L4 and L5. In this case right sided severe L5 radiculopathy was caused by disk sequestration at L4/L5 level on top of preexisting severe degenerative stenosis of the spinal canal (*right image*, *solid arrow*)

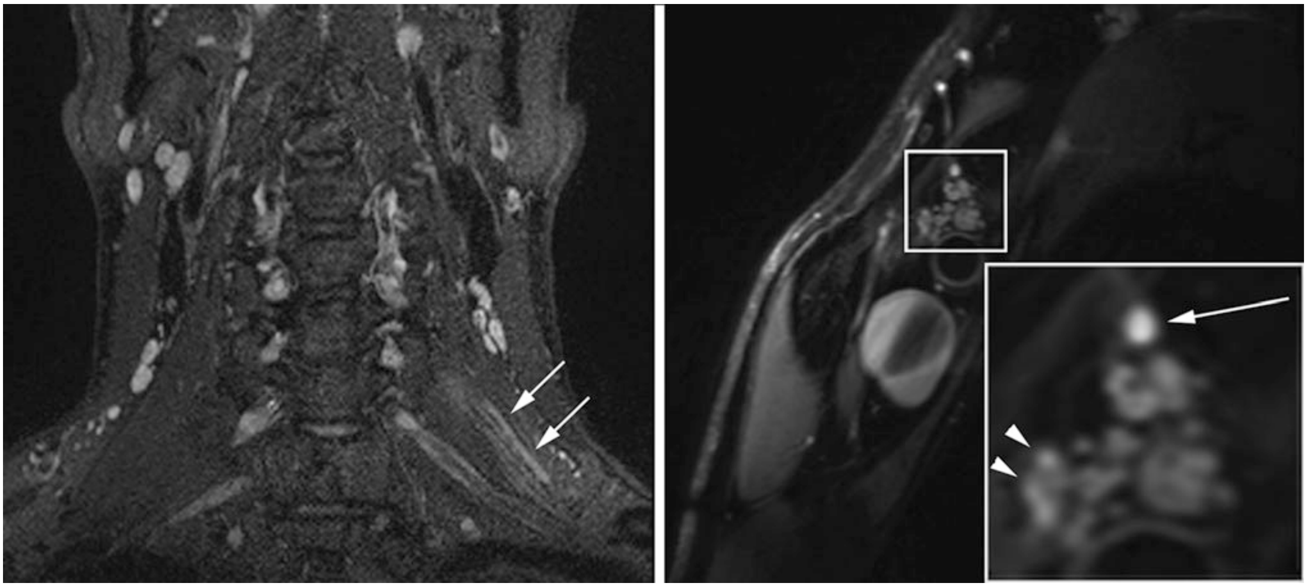

Fig. 3 Patient with inflammatory left radiculopathy of C5. Coronal SPACE (Sampling Perfection with Application optimized Contrasts using different flip angle Evolution) with fat-saturation by inversion-recovery reveals markedly hyperintense C5 spinal nerve (*arrows*). The sagittal-oblique T2-weighted fat-saturated image with high resolution through the plexus at a more distal level displays hyperintense nerve lesions in the posterior cord (*arrow*, *right image*) and the lateral cord (*arrowheads*, *right image*) in those fascicles emerging from C5 at more proximal level

"postfixed" brachial plexus [reviewed in (Pellerin et al. 2010)]. The "prefixed" condition can be encountered quite frequently [in up to 63 % (Kerr 1918)]. The postfixed condition is generally rather rare and has been observed in larger series in only up to 8 % (Kerr 1918; Loukas et al. 2007). A certain degree of Th2 contribution always occurs, either in the extrathoracic form (through the intercostobrachial nerve) or the intrathoracic form (through a communicating branch between Th2 and Th1 (Loukas et al. 2007). Clinically, Th2 participates in the sensory processing, mostly in the innervation sites of the medial and posterior antebrachial cutaneous nerves and thus is more of surgical than imaging interest. However, the detection and description of a postfixed brachial plexus are of clinical relevance, since it has been postulated to be more commonly associated with irregularities of the C7 transverse process and with cervical ribs.

In normal and pathological conditions MRI can be used to depict the integrity of the intradural portions of the ventral and posterior nerve rootlets using MR myelography. Since fibrous band like attachments between the epineurium of the spinal nerves C5, C6, and C7 and the cervical transverse processes protect these nerves from traction, they are less likely to be avulsed than C8 and Th1, which do not show these protective ligaments (Sunderland 1974).

The ventral nerve roots can be easily identified on short-tau inversion recovery (STIR) or neurography T2-weighted sequences, as their slightly hyperintense signal gives contrast against to the dorsally located scalenus medius muscle. The T2-weighted pulse sequences used in MR Neurography are typically fat-saturated and provide submillimeter in-plane resolution. Nerve lesions of various origins seem to be detectable in robust manner over a range of echo- and relaxation times including T2-weighted and proton-density weighted contrast. As the characteristic topographic anatomy with the brachial plexus nerve roots travelling dorsally to the anterior scalenus muscle is encountered in only 32 % of cases bilaterally, anatomic variations are described to occur frequently in this region, and may be addressed, when reporting a plexus imaging study (Harry et al. 1997). In 15 % the C5 and C6 nerve roots are found to pierce through the scalenus anterior muscle. In 3 % a small slip of the scalenus medius muscle travels anterior to one or two of the brachial plexus roots (Harry et al. 1997).

The differentiation of different trunks and later forming divisions of the supraclavicular part of the brachial plexus by imaging is extremely challenging. The upper trunk is formed by the nerve roots C5 and C6 at the lateral border of the scalenus medius muscle, the middle trunk of ventral nerve root C7, and the lower trunk of the roots C8 and Th1 posterior to the anterior scalenus muscle (Johnson et al. 2010). Each trunk divides into a ventral and dorsal division. The posterior divisions will form the posterior cord, which is the smallest of the three cords. The anterior divisions of the superior and middle trunk unite on the lateral side of the axillary artery to form the lateral cord. The anterior division of the middle trunk gives rise to the medial cord. Due to the limited dimensions of the infraclavicular space, clear imaging differentiation of the divisions may not be possible. However, the cords can be easily identified by MRI due to their topographic relationship with the axillary artery. The posterior cord branches into the axillary and radial nerves. The lateral cord gives rise to the musculocutaneous nerve and lateral root of the median nerve and the medial cord evolves into the ulnar, cutaneous antebrachii, and brachii medialis nerves as well as the medial root of the median nerve.

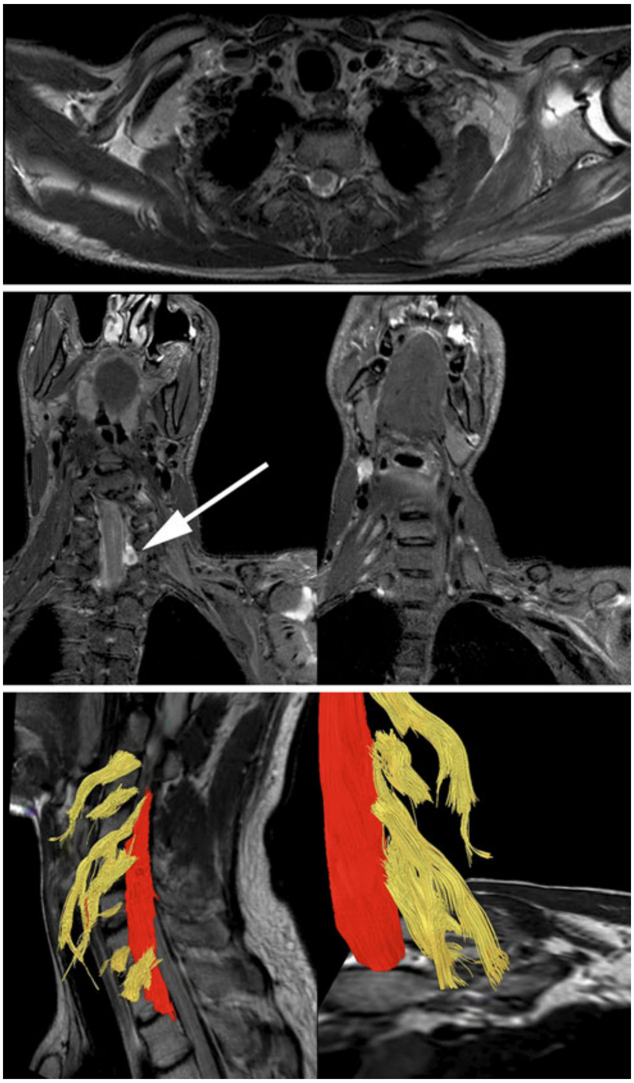

Fig. 4 Axial T2-weighted (*upper row*), paracoronal STIR (short tau inversion recovery) (*middle row*), and tractography images in a patient with a complete posttraumatic (fall from great height) brachial plexus paresis: In addition to the posttraumatic effusion of the glenohumeral joint, signal alterations of left sided subscapular and infraspinatus muscle are detected. The pattern of these signal alterations follows a characteristic distribution, typical for muscle denervation after brachial plexus injuries. The paracoronal STIR sequences show denervation edema of the middle and posterior scalenus muscles as well as the retracted distal nerve segments of the ruptured brachial plexus nerves. This finding is visualized in 3D by tractography (*lower row*). Moreover, diffusion tensor imaging (DTI) could not visualize the distal segments of the avulsed nerve root C7 and C8 (*arrow points* to pseudomeningocele), due to loss of anisotropy and Wallerian degeneration

4.2.2 Traumatic Plexopathies

Traumatic injuries of the brachial plexus are mainly caused by motor vehicle accidents, with the majority of them being motor cycle related. Less frequent causes for traumatic plexopathies are falls, iatrogenic injuries, sports injuries, penetrating, and gunshot wounds. More than two-thirds of patients are young male adults aged between 20 and 40 years. The injuries affect mostly the root and the trunk level of the brachial plexus. Isolated infraclavicular plexus injuries are a rarity (Barman et al. 2012).

Surgical posttraumatic plexus repair including nerve transfer aims to restore elbow flexion and shoulder abduction function (Yang et al. 2012). Preoperative imaging plays an important role in planning these procedures. Internationally, over 90 % of dedicated peripheral nerve surgeons consider (CT or MR) imaging as important diagnostic step in the workup of patients with traumatic brachial plexus injuries (Belzberg et al. 2004).

The imaging assessment of patients with traumatic plexopathies has to respect the diversity of injury mechanisms involved in traumatic plexus injuries. Traction injuries (axonotmesis and neurapraxia) to either the roots C5 and/or C6 as well as to the upper trunk are most frequently seen. Lower trunk injuries occasionally occur; however, middle trunk traction injuries are almost never encountered (Barman et al. 2012). The second type of injury mechanism is nerve rootlet avulsion—a "preganglionic" separation of the ventral (motor) and/or less frequently dorsal (sensory) rootlets from the spinal cord. This most severe form of injury mechanisms mainly involves the lower plexus nerve rootlets (C7, C8, and Th1) (Sunderland 1974) and is associated with no regenerative potential, as surgical repair of these rootlets is not successful. As third injury mechanism, rupture and complete discontinuity (neurotmesis) of extradural nerve roots or trunks can be sometimes observed (Fig. 4).

Besides excluding or confirming posttraumatic injuries to the bones and joints of the shoulder girdle, the spinal cord, vascular, and soft tissue structures, the main objective in imaging of traumatic brachial plexus injuries is the imaging differentiation of the described injury mechanisms. The identification of an avulsion (preganglionic) injury is of immense clinical importance. As electrophysiological examinations are frequently equivocal in differentiating pre- and postganglionic injuries (Barman et al. 2012), imaging offers important presurgical information (Martinoli et al. 2010).

Pseudomeningoceles are tears of the dural recessus within the neuroforamen and can be easily identified by their bright signal on T2-weighted sequences (Fig. 4). The presence of a pseudomeningocele is a quite sensitive indicator of nerve root avulsion (preganglionic injury). However, 20 % of nerve root avulsion injuries are not associated with pseudomeningoceles (Yoshikawa et al. 2006; Martinoli et al. 2010). Thus, direct visualization of the rootlets is necessary to confidently rule out or confirm a preganglionic nerve root injury. For a long time the invasive technique of CT myelography, was the only method to accomplish this task. Recent studies indicate equal sensitivity and specificity of MR myelography techniques, in particular 3D heavily T2-weighted sequences (3D CISS, TrueFISP, FIESTA, and the DRIVE) and CT myelography in detecting nerve root avulsions (Doi et al. 2002). Furthermore, the inability to identify intact anisotropic nerve structures distal to the avulsed nerve root by diffusion tensor imaging (DTI) and tractography may help to even further improve the capabilities of MRI in the differentiation of pre- and postganglionic injuries (Fig. 4).

Traction injuries manifest themselves as neuromas in continuity, with thickening of the affected nerve. In future, new techniques in peripheral nerve MR imaging, such as DTI and tractography may be able to assess the severity of the traction injury and moreover the presence or absence of intact fascicles within the lesioned nerve segments.

Complete rupture of a brachial plexus nerve is characterized by an abrupt ending of the disrupted nerve and retraction of the distal nerve segments. Using tractography no continuity with the distal nerve segments can be detected (Fig. 4).

Finally, the assessment of the brachial plexus is complete, if the pattern of nerve lesions is in congruency with the pattern of acute or chronic denervation signs of the depicted muscles.

Typically, the field of view of a brachial plexus examination (if a flexible body-array coil is used), includes the muscles listed in Table 1. Denervation of paraspinal (dorsal branch of cervical nerves) and scalenus (ventral branch of cervical nerves/root) muscles occurs in cases of very proximal spinal nerve lesions (Fig. 4). In nerve avulsion injuries, characteristically the multifidus (= deepest of paraspinal muscles) and the levator scapulae muscle show denervation changes. Thus, denervation edema or volume loss of these specific muscle groups are helpful indicators and reassuring signs for avulsion injuries (Uetani et al. 1997; Hayashi et al. 2002). Knowledge about the specific innervations of depicted muscles is essential in differentiating between muscle signal changes due to denervation and those caused by posttraumatic changes.

4.2.3 Perinatal Brachial Plexus Lesions

Although obstetric management of shoulder dystocia has significantly improved and the overall rate of cesarean sections has increased, the incidence of brachial plexus birth palsies lies still between 0.4 and 4.6 per 1,000 live births (Hoeksma et al. 2000; Foad et al. 2008). Thus, birth related brachial plexus injuries remain an epidemiologically significant burden. Generally, most perinatal plexus lesions are associated with transient functional deficits. However, a minority of patients will have to live with a sometimes remarkable degree of disability. The early clinical assessment of these cases is essential to provide timely surgical treatment in order to prevent major neurological deficits of the affected upper extremity. Since most treatment concepts favor early surgery in cases without clinical improvement up to the age of 6 months (O'Brien et al. 2006; Hale et al. 2010), the clinical examination of the injured neonates and

Table 1 Plexus and segmental innervation of shoulder girdle and proximal upper extremity muscles, which is usually visualized by MRI of the brachial plexus

Muscle	Nerve	Cord	Trunk	Root
Deltoid	Axillary	Posterior	Upper	C5, C6
Subscapular	Subscapular	Posterior	Upper, middle	C5, C6, C7
Supraspinatus	Suprascapular	–	Upper	(C4), C5, C6
Infraspinatus	Suprascapular	–	Upper	(C4), C5, C6
Teres minor	Axillary	Posterior	Upper	C5, C6
Teres major	Subscapular, thoracodorsal	Posterior	Upper, middle	C5, C6, C7
Pectoralis major	Medial pectoral	Medial	Upper, middle, lower	C6, C7, C8, T1
Pectoralis minor	Lateral pectoral	Lateral	Upper, middle	C5, C6, C7
Subclavius	Subclavian	–	Upper	C5, C6
Serratus	Long thoracic	–	Upper, middle, lower	C5, C6, C7, C8
Scalenus anterior, medius, posterior	Ventral branches, cervical nerves	–	–	C4, C5, C6
Paraspinal muscles: multifidus, semispinalis cervicis and capitis, splenius capitis and cervicis	Dorsal branches, cervical nerves	–	–	–
Trapezius, sternocleidomastoideus	Accessory nerve	–	–	–

infants remains the basis for further decision making. At this early time point, the role of electrodiagnostic testing and imaging is currently unclear. However, higher field strength and new developments in peripheral nerve MR imaging may add valuable morphologic information. Thus, future radiologists will be more frequently involved in the management of birth related plexus injuries.

The imaging approach in these patients should aim to solve the following tasks: (1) Detection of injuries to the spinal cord and of a preganglionic (=avulsion) injury of C5–Th2, (2) Visualization of the extent of nerve traction injuries and neuromas at the level of nerve roots, trunks, divisions, or cords, (3) Visualization of the degree and specific pattern of muscle denervation and consecutively, (4) The identification of early reactive bone/cartilage remodeling of the shoulder joint leading to glenohumeral deformities.

The assessment of nerve root avulsions remains challenging in the neonatal period. Although the presence of a pseudomeningocele (on MRI, CT, or myelography) shows a high sensitivity for nerve root avulsions, it is a rather nonspecific sign (Vanderhave et al. 2012). In some centers CT myelography continues to be the gold standard for the assessment of preganglionic injuries (Steens et al. 2011). However, in future the wide distribution of 3 T MR units and the use of noninvasive MR myelography sequences should allow a more specific evaluation of the preganglionic segments in these cases (Medina et al. 2006).

High-resolution STIR sequences in the orientation of the nerve roots and trunks are sensitively able to depict the involvement and extent of nerve lesions due to traction injuries and neuroma in continuity (Smith et al. 2008).

Moreover, atrophy patterns of the shoulder girdle muscles have to be evaluated. The subscapular and deltoid muscles are most frequently (in up to 87 and 89 % of patients) involved (Hogendoorn et al. 2010). Since the subscapular nerve arises from C5 to C7, subscapular muscle denervation in particular is characteristic for upper brachial plexus injuries. In addition the infraspinatus (in 71 %) and supraspinatus (in 74 %) muscles show signs of chronic denervation (Fig. 5) (Hogendoorn et al. 2010; Poyhia et al. 2005).

An imbalance in muscle strength may ultimately lead to an internal rotation contracture and progressive glenohumeral joint incongruence (Poyhia et al. 2005). In some cases, the glenohumeral deformity is early encountered and causes a significant osseous limitation in the range of motion of the shoulder joint. Thus, the radiological identification of this process is crucial for further physical therapy. Due to the optimal soft tissue contrast, MRI can depict remodeling processes in the nonossified humeral head early in the course of the disease (Fig. 5).

4.3 Trunk Neuropathies

In the following section MRI appearances of the most common nerve lesion patterns of the upper extremity will be described. However, this overview cannot cover the

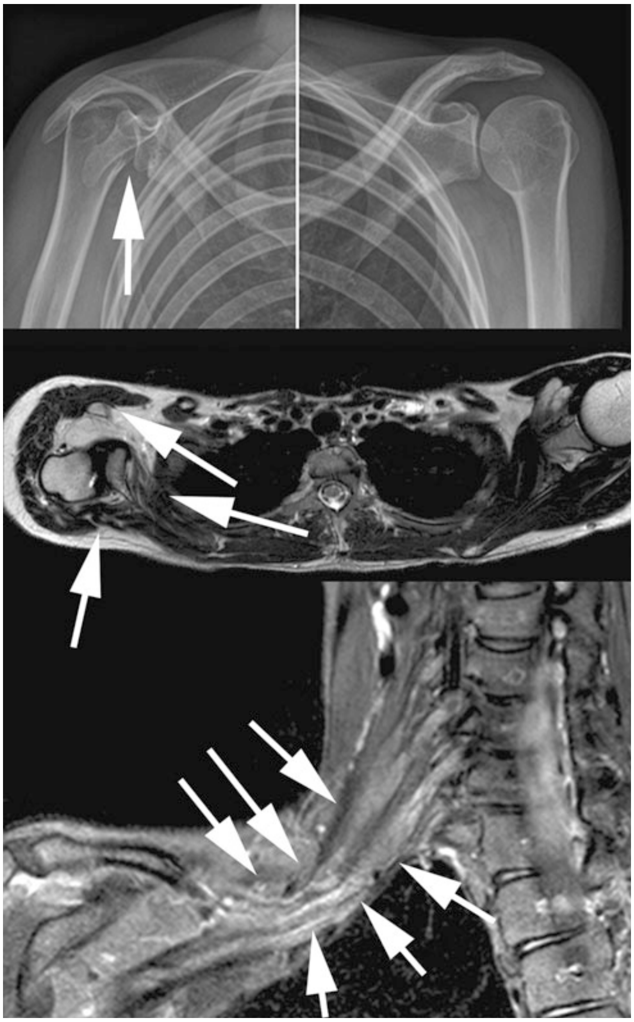

Fig. 5 Radiographs (*upper row*), axial T2-weighted, and paracoronal STIR (short tau inversion recovery) sequences in a 23-year-old patient with perinatal brachial plexus injury. There is subluxation of the humeral head (*solid arrow* in *upper image*) and remodeling of the right shoulder, typical for a glenohumeral deformity. Please note the significant atrophy of the subscapular and infraspinatus as well as right sided deltoid muscles (*solid arrows* in *middle image*). The paracoronal STIR image depicts extensive traction neuromas of the upper and middle trunk (*solid arrows* in *lower image*)

complexity of all upper extremity nerve lesions in every detail. For more detailed descriptions, the reader is referred to the cited reference articles.

4.3.1 Musculocutaneous Nerve Neuropathies

Isolated lesions to the musculocutaneous nerve are rare. They are mainly posttraumatic or exercise related, occasionally entrapment of the nerve is observed in the region, where the nerve penetrates the coracobrachial muscle.

In particular, MRI at 3 T promises to be a valuable tool in the identification and characterization of isolated musculocutaneous nerve lesions, as the nerve itself can be successfully visualized (Chhabra et al. 2012). The musculocutaneous nerve arises from the lateral cord and its motor innervations comprise the coracobrachial, biceps, and brachial muscles. However, denervation associated MR signal changes of the brachial muscle is frequently incomplete, since in the majority of cases [67–100 %, reviewed in (Puffer et al. 2011)] its inferolateral portion is supplied by the radial nerve.

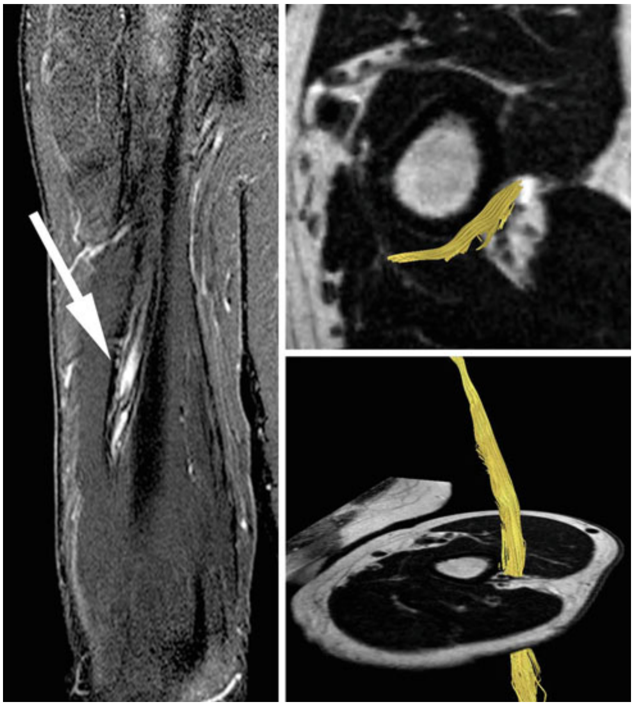

Fig. 6 Coronal STIR (short tau inversion recovery) sequence (*left*) and 3D tractography analysis of the radial nerve in a patient with Saturday night palsy (*right*). Please note the signal increase of the entrapped radial nerve at the spiral groove of the humerus (solid white arrow, *left*). However, tractography detects intact trajectories ruling out severe internal injury of radial nerve or true neuroma formation

4.3.2 Radial Nerve Neuropathies

The most frequent site of radial nerve injury is the spiral groove of the humerus. In this region, the nerve is mainly injured by two mechanisms: (1) Due to its close anatomical proximity to the humerus, upper extremity trauma causing fractures, frequently leads to radial nerve lesions. (2) Because of its attachment to the surrounding soft tissue at its penetration site through the lateral intermuscular septum, the radial nerve is particularly vulnerable to compression/entrapment injuries ("Saturday night palsy") in this region (Fig. 6).

Lesions of the radial nerve at this level lead to denervation of the hand extensor muscles. However, since its innervation occurs proximal to the spiral groove, the triceps muscle is generally not denervated in the typical upper arm radial nerve lesions.

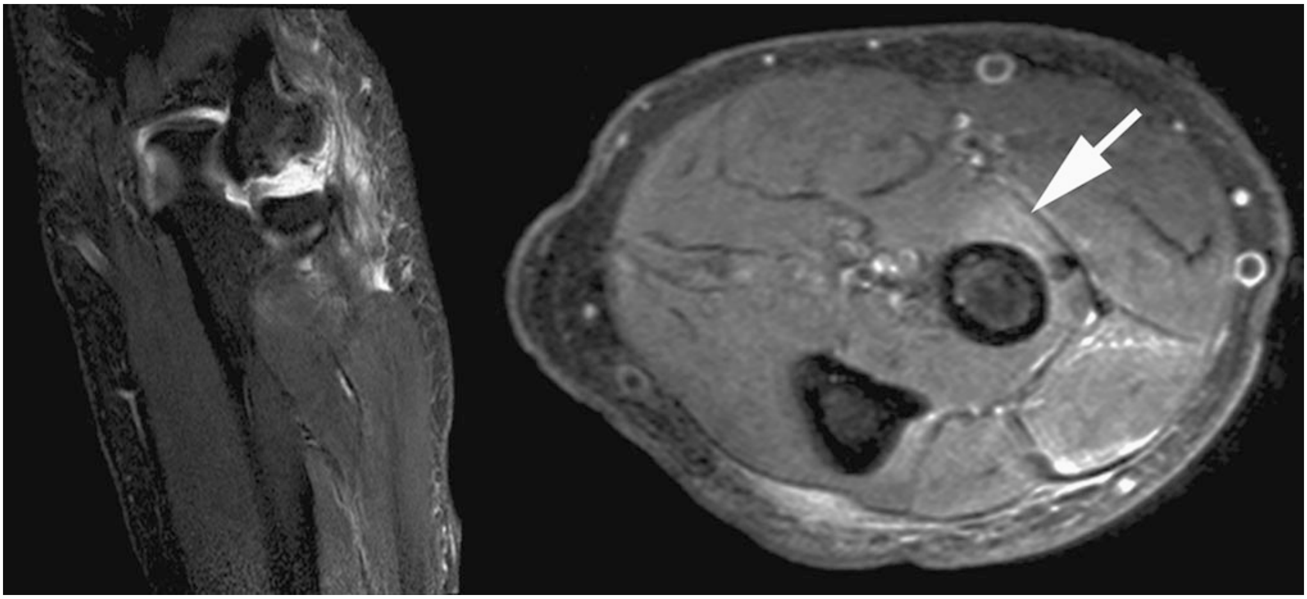

Fig. 7 Coronal STIR (short tau inversion recovery) and axial Proton Density sequences of the proximal forearm in a patient with lateral epicondylitis. Please note the extent of signal changes, affecting the proximal wrist extensor muscles and the supinator muscle (*arrow*). Moreover, increased signal intensity at the site where the posterior interosseous nerve pierces the supinator muscle (white solid arrow, Frohse Arcade, a fibrous arch over the posterior interosseus nerve and the most superior part of the superficial layer of the supinator muscle) is identified. These findings confirm the presence of an additional posterior interosseous nerve syndrome

The neurogenic "radial tunnel syndrome" affects the purely motor posterior interosseous branch of the radial nerve. Over a distance of 5 cm this radial nerve branch is crossed by potentially compressing fibrous bands, branches of the radial artery, and the edges of the supinator muscle (Rosenbaum 1999). The proximal edge of the supinator muscle is found to be tendinous in half of all individuals (Arcade of Frohse), and may represent a potential compression site (Spinner 1968). The isolated neurogenic posterior interosseous nerve (PIN) compression manifests clinically as radial deviation of the hand, weakness in the extension of the wrist and of all digits (in a complete lesion), and weak extension of fourth and fifth digits (in a partial lesion) without any sensory loss. The pure PIN compression has to be differentiated from the clinical presentation of the "disputed" radial tunnel syndrome, which is dominated by pain in the region of the lateral epicondyle and is observed in patients with recurrent epicondylitis (Werner 1979; Rosenbaum 1999). However, in both conditions denervation signs of the PIN innervated muscles occur and can be detected by MRI in more than 50 % of cases (Ferdinand et al. 2006) (Fig. 7). The most frequently affected muscle showing denervation edema in this condition is the supinator muscle (Ferdinand et al. 2006) (Fig. 7).

4.3.3 Ulnar Nerve Neuropathies

The most common site of ulnar nerve injury is the cubital tunnel. After the carpal tunnel syndrome, the cubital tunnel syndrome (CUS) is the second most common nerve entrapment syndrome. As the ulnar nerve passes the intramuscular medial septum and the medial head of the triceps muscle it may be compressed by a locally thickened ligament (sometimes also referred to as the Struther′s arcade) (Wehrli and Oberlin 2005). The cubital tunnel per se is an osteofibrous canal, which is formed by the bony retrocondylar sulcus of the medial epicondyle proximally. Then it is defined by the course of the nerve underneath a retinaculum proximally and further distally underneath the arcuate ligament of Osborne and finally it is covered by the deep aponeurosis of forearm flexor muscles (Assmus et al. 2009). In 10–23 % of cases muscle fibers support the retinaculum—referred to as epitrochleoanconeus muscle (Campbell et al. 1991; Husarik et al. 2009). The most distal point of potential entrapment of the ulnar nerve is the Loge de Guyon at the wrist. Recent MRI data at 3 T could impressively demonstrate the high sensitivity of MRI in detecting signal changes of the deep motor branch of the ulnar nerve in Guyon's-canal-syndrome (Kollmer et al. 2012).

However, the CUS is by far more common than the distal entrapment neuropathy of the ulnar nerve. The ulnar nerve physiologically shows de- and remyelinating changes as response to the exposure to significant mechanical forces, which are most accentuated in the region of the cubital tunnel (Bozentka 1998). Therefore, a clear distinction between subclinical CUS and changes within the normal spectrum of nerve lesions is difficult. This is also reflected by the controversial data on ulnar nerve signal changes in this region. A high accuracy in the definition of CUS was

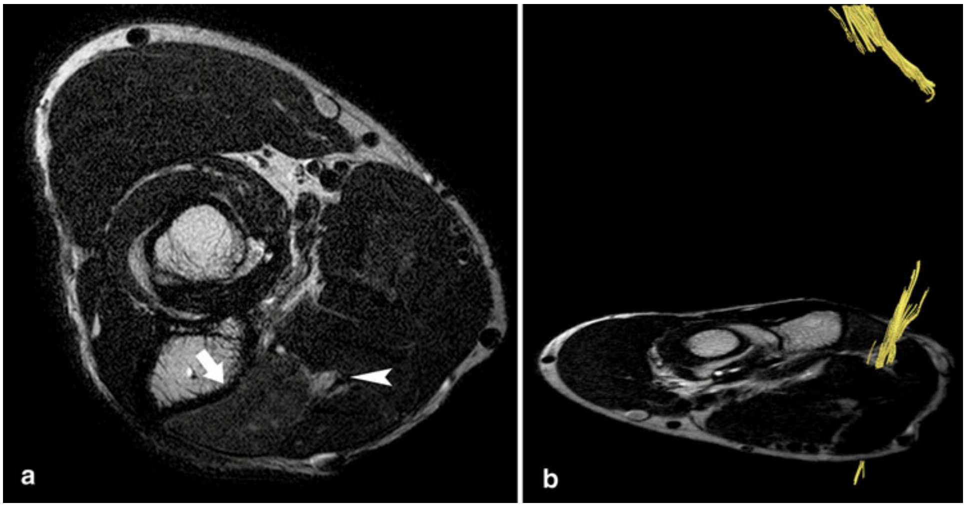

Fig. 8 Axial T2-weighted **a** sequence in a patient with severe cubital tunnel syndrome: please note the denervation edema of the flexor digitorum profundus muscle (*arrow*) and the increase in signal intensity of the ulnar nerve (arrowhead). Tractography **b** is unable to track the axonal trajectories of the ulnar nerve in the region of the cubital tunnel

reached in the so far largest study published on the use of MRI in CUS by measuring the T2-weighted signal intensity of the ulnar nerve (Baumer et al. 2011) (Fig. 8). Moreover, signal changes of the ulnar nerve did also correspond to the clinical severity of CUS (Baumer et al. 2011). As increases in ulnar nerve signal intensity may occur in the cubital tunnel of asymptomatic subjects (Husarik et al. 2009), the radiological assessment of ulnar nerve signal changes has to respect the clinical context and further imaging findings. In severe cases of CUS, STIR sequences may depict denervation edema of the flexor carpi ulnar and ulnar bulk of the deep forearm flexor muscles (Fig. 9). Moreover, reversal of these signal changes indicates reinnervation and treatment success (Fig. 9) (Viddeleer et al. 2012). In cases, where decompression surgery does not lead to improvement of clinical symptoms, the ulnar nerve may show widespread signal abnormalities, which are not confined to the cubital tunnel itself and may indicate a noncompressive etiology (Baumer et al. 2012). Finally, DTI and tractography may add further topographical information on the exact site of ulnar nerve compression and help to tailor the surgical approach (Fig. 9).

4.3.4 Median Nerve Neuropathies

Entrapment of the median nerve within the carpal tunnel constitutes the most common entrapment neuropathy. In most cases the clinical and electrophysiological diagnosis of the carpal tunnel syndrome (CTS) is not challenging. Imaging mainly serves to identify or rule out mass lesions such as lipoma, synovitis, neuroma, hamartoma, or deformities of the wrist, which negatively impact surgical outcome [reviewed in (Wilson and Allen 2012) and (Kim et al. 2007)]. Surgical complications after carpal tunnel release are reported to occur in the range of 3–19 % (Stutz et al. 2006). In these cases reevaluation by MRI is helpful, since scarring and postoperative fibrosis of the median nerve may be optimally objectified and extensive reexploration can be avoided (Campagna et al. 2009).

4.3.5 Lower Extremities

Trunk neuropathies of the lower extremities, in particular, the spontaneously occurring forms are relatively rare when compared to the upper extremities. A typical example of common peroneal neuropathy and how it can be differentiated from an L5 radiculopathy by merely identifying the corresponding denervation pattern is illustrated in Fig. 1. Other trunk neuropathies involve the sciatic nerve which is frequently involved secondarily following trauma such as hip replacement surgery, injection injury or in rare cases it may be associated with extrapelvic endometriosis (Pham et al. 2010, 2011). Isolated trunk neuropathies of the tibial nerve are uncommon as well but likewise present a distinct denervation pattern involving the tibial target muscles of the lower leg (Fig. 10).

4.4 Multifocal Neuropathies and Motor Neuron Disease

Predictable groups of target muscles will undergo denervation related MRI alterations, such as T2 signal increase, if complete nerve trunks are involved. For example, forearm and wrist extensors will be affected in a radial neuropathy involving the segment of the radial nerve distal to its branches to the triceps muscle. In contrast, multifocal mono- or polyneuropathies are disease entities associated with more complex lesion patterns of nerve and muscle with regard to the spatial extension and pattern of nerve lesions and denervated target muscles. Among the vast variety of

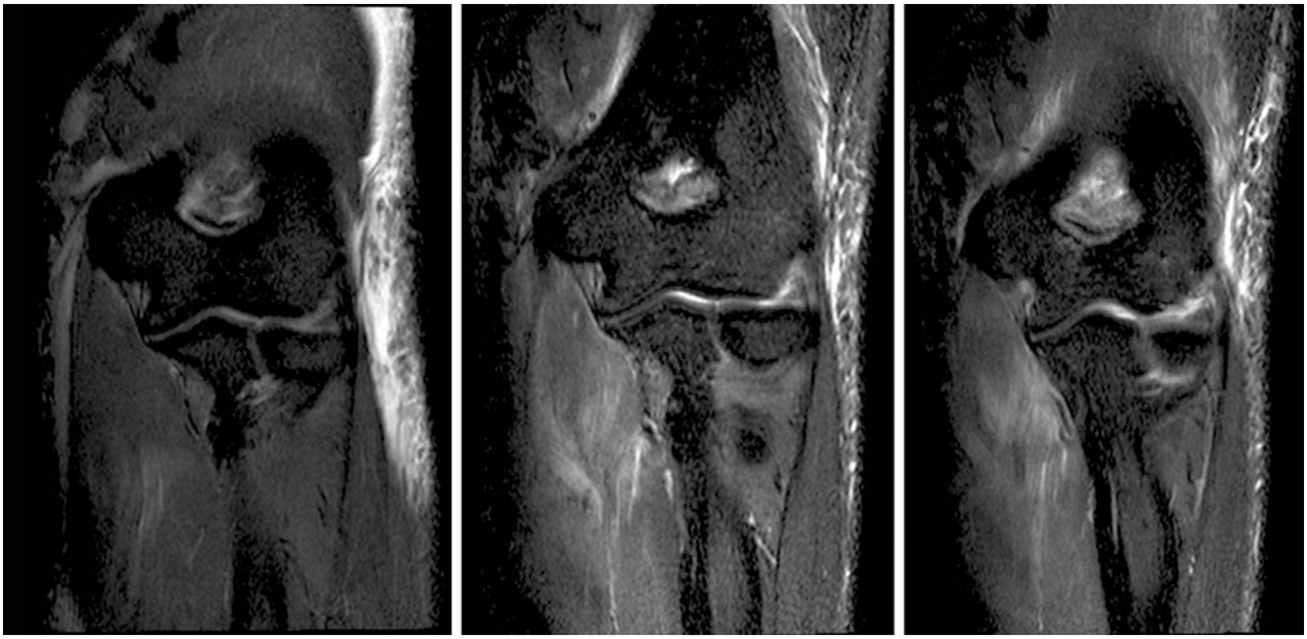

Fig. 9 Sequential coronal STIR (short tau inversion recovery) sequences 2 days after complete iatrogenic neurotmesis of the ulnar nerve during an arthroscopy procedure (*left*). The middle image shows a STIR sequence of the same patient 4 weeks after surgical repair, and 5 weeks after injury. The right image shows the follow up results 4 months after the lesion. Please note the maximum signal intensity changes of the denervated flexor digitorum profundus muscle to be present 5 weeks after denervation (*middle image*). Normalization/ reduction of denervation associated signal changes (*right image*) correlated well with clinical improvement after surgical repair and reinnervation

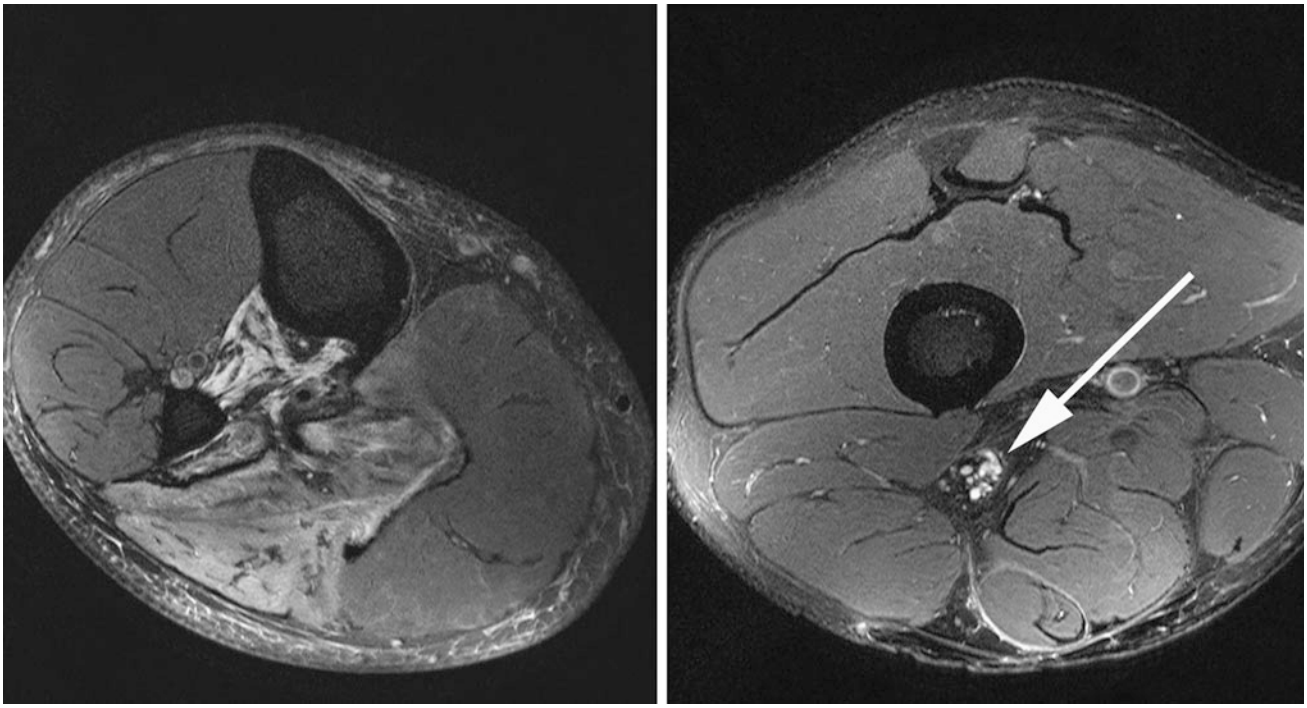

Fig. 10 Denervation pattern in tibial trunk neuropathy. On the left T2-w hyperintense denervation signal is seen in the posterior tibial, popliteal, and soleus muscles, and affects also the lateral part of the gastrocnemius muscles. Except for the medial belly of the gastrocnemius muscle which in this case of an incomplete neuroma in continuity (*right image*, *solid arrow*) is not affected, this represents a typical denervation pattern in a severe lesion of the tibial nerve trunk

multifocal polyneuropathies, multifocal motor neuropathy (MMN) is particularly well defined by clinical and electrophysiological criteria. Its main features are signatures of demyelination on nerve conduction studies, predominance of motor symptoms and mostly asymmetric limb involvement (Nobile-Orazio et al. 2005). Muscle denervation on EMG as indicated by positive sharp waves and fibrillation potentials is not a rare finding in MMN and points toward secondary axonal injury. It is also discussed if a predominantly axonal multifocal motor neuropathy coexists with the more established, typical demyelinating form of MMN (Nobile-Orazio 2005).

In the majority of patients referred to high-resolution MR Neurography with symptoms indicative of multifocal polyneuropathic involvement (these are irregular clinical symptom patterns often asymmetrically involving target muscles of more than one single peripheral nerve) multifocal fascicular nerve T2 lesions in fact can be observed with reliable lesion contrast (Figs. 11, 12). Larger diagnostic studies are still missing investigating the diagnostic and therapeutic relevance of these novel imaging findings with regard to improving classification schemes of multifocal peripheral nerve diseases and with regard to improve indication of any, mostly anti-inflammatory or immune-modulating, therapeutic intervention. The interpretation of these novel findings of nerve imaging is further complicated by the fact that the histopathological nerve alterations underlying MMN and other multifocal neuropathies are essentially unknown. The reason why histopathological analyses of relevant human nerve tissue of clinically symptomatic peripheral nerves are so scarce is obvious. Motor or mixed limb nerves cannot be sacrificed without acceptable functional disturbance in humans, in vivo. At least, biopsies of single motor nerve fascicles have been possible in few centers, however with the limitation that entire nerve cross-sections comprising all traversing fascicles still could not be obtained (Taylor et al. 2004). These few histopathological studies in fact could show a multifocality pattern also on the microscopic fiber level. MR Neurography in patients confirmed with MMN and in patients with suspected MMN or with a multifocality pattern of clinical symptoms frequently shows a multifocality pattern on an intermediate level of spatial resolution of the anatomical nerve structure. Nerve fascicles can be reliable depicted by MRI at 3 T magnetic field strength and show multifocal T2 signal increase affecting certain fascicles over confined longitudinal segments and sparing other fascicles (Figs. 11, 12). This novel observation of multifocal nerve fascicular lesion pattern, together with the scarce histopathological evidence of multifocal fiber loss in MMN as outlined above, may explain the complex muscle denervation patterns observable by imaging in multifocal neuropathies (Figs. 12, 13). Muscle denervation patterns in multifocal neuropathies substantially differ from denervation patterns in complete radiculopathies, plexopathies, or trunk neuropathies. Two distinguishing hallmarks are regularly observed. First, muscle T2 signal increase is distributed over several target muscle groups in the distribution of more than one single nerve root or nerve trunk (Fig. 13). Second, denervation signal often involves not entire muscle bellies but only confined zones within a muscle belly possibly reflecting a larger likelihood of selective fascicular nerve lesions instead of complete cross-sectional nerve lesions in MMN (Figs. 12, 13). Together with the observation of multifocal fascicular T2 lesions, this irregular pattern of patchy denervation signal may be a helpful diagnostic sign to differentiate multifocal polyneuropathies such as MMN from motor neuron disease such as amyotrophic lateral sclerosis. In motor neuron disease, especially during early clinical manifestation of the disease, it may be very challenging to establish the definite diagnosis. This difficulty is related to the fact that

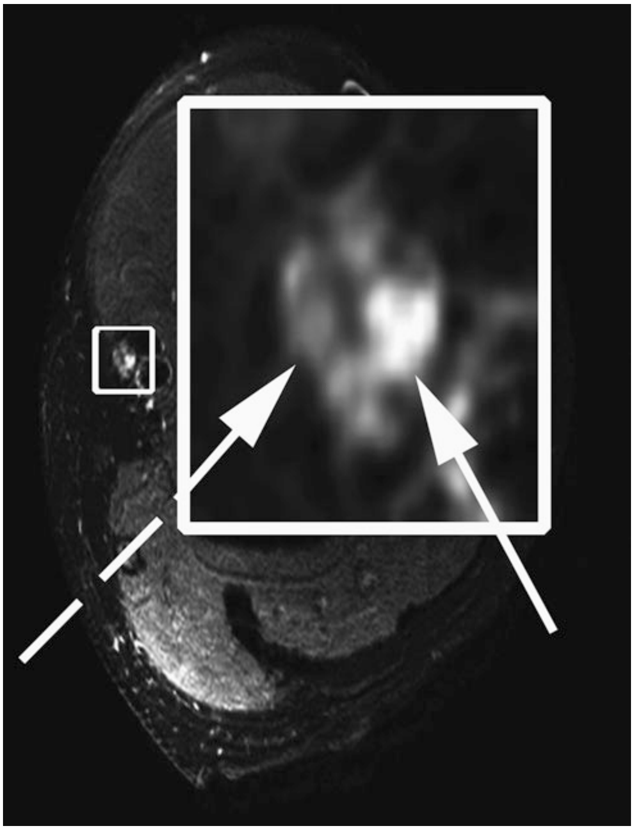

Fig. 11 Fascicular multifocal lesion pattern of multifocal motor neuropathy (MMN). Increased T2 signal of individual median nerve fascicles at upper arm level are shown (*solid arrow* in zoomed insert). Normal-appearing fascicles are indicated by dashed arrow. Fascicular multifocality may be observed in both the longitudinal direction along major nerve trunks and within the cross-section. Lesion multifocality on imaging demonstrates that lesioned fascicles alternate with normal-appearing fascicles. Such lesion distribution might explain why atypical patchy denervation patterns appear in the target muscles in patients with multifocal mono- or polyneuropathies

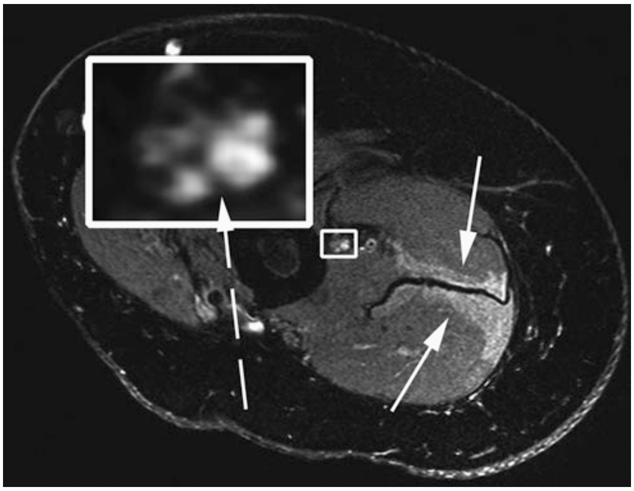

Fig. 12 Fascicular multifocal lesion pattern of multifocal motor neuropathy (MMN) and associated patchy denervation pattern in target muscle. Zoomed insert on *upper left* displays fascicular multifocal lesions of radial nerve within spiral groove (*dashed white arrow*). The triceps as typical target muscle of the radial nerve shows irregular patchy denervation pattern (*solid white arrows*) which usually is not observed in complete trunk neuropathies

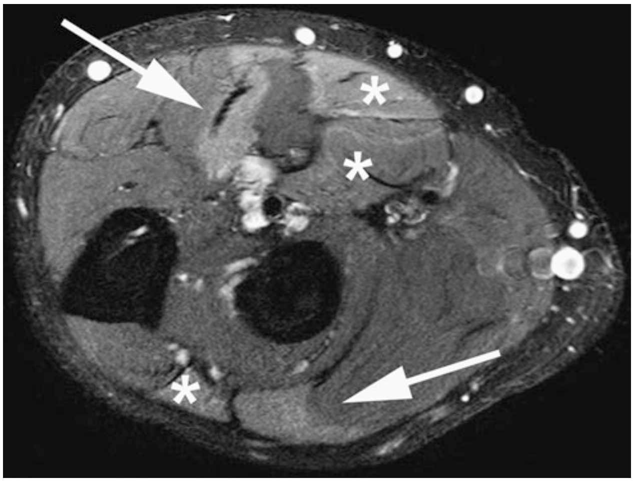

Fig. 13 Typical patchy denervation pattern in multifocal neuropathies. In this case of multifocal motor neuropathy (MMN) elevated T2 signal of muscle denervation extends over patchy areas not involving entire muscles bellies (*arrows*). Target muscles of more than one nerve trunk are affected (*asterisks*), in this case long extensors of wrist and hand (deep branch of radial nerve) and volar flexors innervated by the median nerve. Especially in the extensor digitorum muscle it becomes evident that only the ulnar aspect shows denervation signal while radial parts are inconspicuous

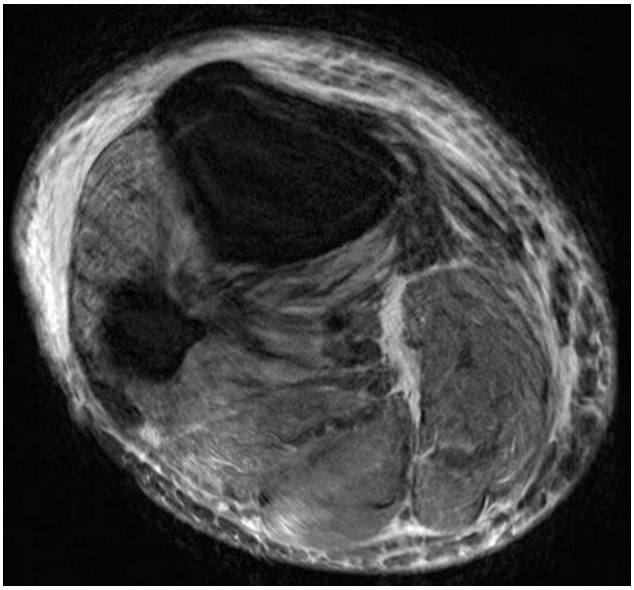

Fig. 14 Typical diffuse denervation pattern in a patient with confirmed amyotrophic lateral sclerosis (ALS). In contrast to the patchy denervation pattern observed in multifocal peripheral neuropathies motor neuron disorders are associated with a more diffuse distribution of elevated denervation T2 signal. The image quality is impaired due to motion artifacts from the involuntary permanent muscle fasciculations typical of ALS

upper and lower motor neurons may be affected in variable and asymmetric manner with the result of symptom patterns not discernible, e.g., from MMN. Diagnostic studies of these rare diseases with large enough sample sizes to characterize potentially helpful imaging findings are still missing. From the few cases observed, however, it seems that multifocal neuropathies such as MMN and motor neuron disease such as amyotrophic lateral sclerosis (ALS) each appear with distinguishing MR imaging features in both peripheral nerve and muscle. The multifocal fascicular T2 lesion pattern of MMN along with small patchy denervation fields in target muscles (Figs. 12, 13) seems to be very distinct from a homogeneous, diffuse muscle denervation pattern, and absence of multifocal T2 nerve lesions in ALS (Fig. 14).

4.4.1 MRI in Poliomyelitis and Post-Polio Syndrome

Motor neuron diseases as ALS and post-polio syndrome are characterized by prominent muscular weakness and severe motor disability (Abraham and Drory 2012). Post-polio syndrome is defined as a clinical syndrome of new pareses in individuals who had been affected by acute paralytic poliomyelitis years before. In a study on 16 patients with post-polio syndrome, post-polio syndrome manifested at a median age of 57.5 years in a median of 41 years after acute poliomyelitis. Muscles already affected during acute poliomyelitis were affected in all patients with post-polio syndrome but 37.5 % of patients developed paresis in muscles formerly not affected by acute poliomyelitis (Weber et al. 2004). MRI shows typical signs of muscle atrophy and lipomatous degeneration in the affected muscles (Tollback et al. 1996). In contrast to neurogenic

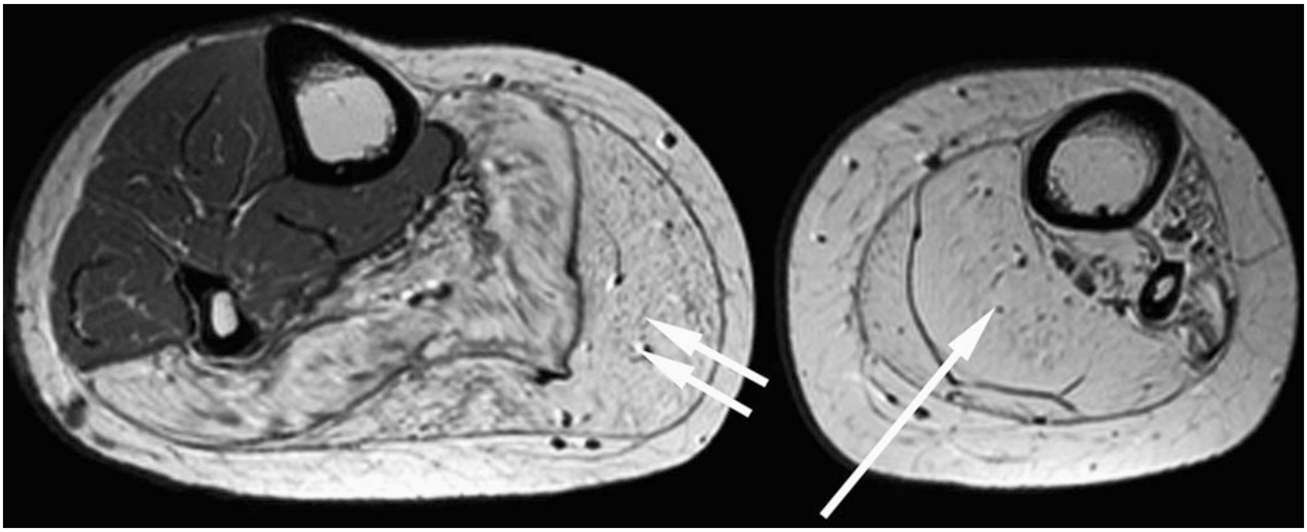

Fig. 15 Severe neurogenic fatty atrophy in the chronic stage after motor neuron disease. In this patient long-standing weakness predominantly of left lower leg was caused by poliomyelitis during childhood. Correspondingly, T1-weighted muscle MRI without fat-saturation shows complete substitution of muscle tissue with fat (*right image* with *single white arrow* pointing on left lower leg with nearly homogeneous hyperintense T1-w alteration caused by fatty atrophy). Progressive weakness of contralateral plantar flexion occurred during adulthood equally showing severe atrophy in contralateral (*right*) calf (*double arrow* on *left image*). The latter clinical and imaging findings are consistent with progressive neurogenic muscle atrophy and Post-Polio-Syndrome

atrophy after radiculopathy or peripheral nerve injury, the atrophy of muscle denervation after motor neuron degeneration usually is more severe. This observation is likely to be explained by incomplete fiber degeneration in root or peripheral nerve injury and possibly by residual cross-innervation from adjacent root levels or peripheral nerve branches (Fig. 15).

Using in vivo phosphorus magnetic resonance spectroscopy, the muscle metabolism of at-rest patients with varying degrees of post-polio residual paralysis was studied and compared with that of controls demonstrating that the phosphocreatine (PCr)/inorganic phosphate (Pi) and PCr/adenosine triphosphate ratios were lower in patients than in controls (Sharma et al. 2007).

5 Advanced MRI Techniques

5.1 Perfusion MRI of Denervated Muscle

Muscles undergoing denervation show distinct histological changes (Wessig et al. 2004). 24 h after a denervating injury of a motor nerve, slight dilatations of some capillaries of the affected target muscles are detectable, progressing on the following days. About 4 weeks after the denervating event, the muscle exhibits maximally enlarged capillaries, and subsarcolemmal vacuoles indicating early signs of muscular degeneration. In the following weeks muscle fibers undergo increasing degeneration. Atrophy and fatty metaplasia of the muscle fibers are seen in the late stage of muscle denervation. MRI is capable to indicate degeneration of muscles at early stage. In correlation to histology, with an enlargement of intramuscular capillaries, after about 24 h, MRI of denervated muscles shows increased T2-signal intensity and significant gadolinium-enhancement (Bendszus and Koltzenburg 2001; Wessig et al. 2004). While gadolinium-enhancement might indicate an increased capillary extravasation, the histological correlation with enlarged intramuscular capillaries suggested changes in regional blood volume in denervated muscle. Experimental data in rats support these two hypotheses, by showing increased blood flow and an expansion of the extracellular water volume in denervated muscles (Bendszus and Koltzenburg 2001; Wessig et al. 2004). Our own, yet unpublished data of dynamic contrast-enhanced MRI (see also Chap. 6 of this book) in patients with denervated muscles at calf level show a more rapid increase to a larger plateau of gadolinium uptake in denervated, compared to healthy muscles (Fig. 16), supporting the results of experimental studies, with increased blood flow and gadolinium-extravasation in denervated muscles.

5.2 Diffusion Tensor MRI of Denervated Muscle

By assessing the degree and directionality of water motion in a given tissue, the advanced MRI method of diffusion tensor imaging (DTI) is able to probe and visualize its microstructure. Besides three dimensional qualitative data,

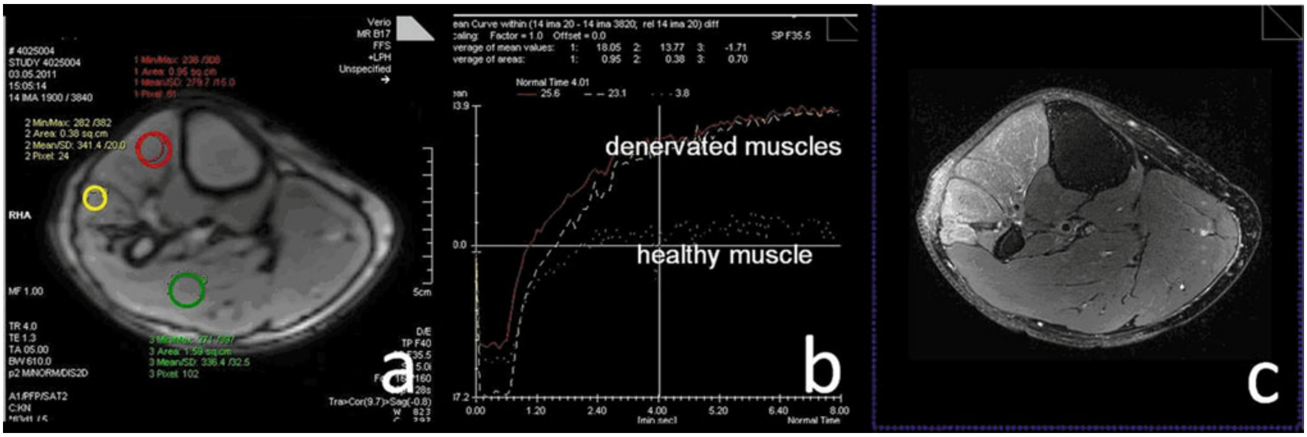

Fig. 16 Perfusion MRI of denervated and healthy muscle. On the *left* **a** three regions-of-interest are displayed: *red* anterior tibial muscle, *yellow* long peroneal muscle, *green* lateral soleus, and gastrocnemius muscle. In the *middle* **b** three signal-intensity-time-curves are displayed with two upper graphs (*red* and *yellow*) corresponding to anterior tibial and long peroneal regions, whereas the lower curve corresponds to the gastrocnemius/soleus region-of-interest (*green circle* on *left image*). Note the markedly elevated dynamic enhancement reflecting increased regional muscle perfusion and possibly also increased blood-muscle permeability. On the *right* **c** the typical pattern of a common peroneal neuropathy with denervation in the typical target muscles can be seen (increased T2 signal in tibial anterior, extensor digitorum, and long peroneal muscles)

DTI provides noninvasive measures of the integrity of a given tissue. The fractional anisotropy (FA) represents the most representative quantitative DTI parameter. A high FA value corresponds to highly restricted (anisotropic) diffusion, whereas low FA values reflect nonrestricted diffusion of water molecules [for a detailed technical review on the technique and application of DTI the reader is referred to (Mori and Zhang 2006)].

So far this technique has been mainly applied in the depiction of white matter pathways of the human central nervous system. Recently, it has also been applied in the characterization of the peripheral nervous system [for review see (Lehmann et al. 2010)]. Moreover, further postprocessing of DTI data ("tractography") allowed the visualization of the architecture of skeletal (Saotome et al. 2006; Budzik et al. 2007), cardiac (Sosnovik et al. 2009) and smooth musculature (Weiss et al. 2006) in 3D (see also Diffusion-weighted and diffusion-tensor imaging: Applications in skeletal muscles).

So far the DTI assessment of the denervated muscle is limited to observations in animal studies. There it could be demonstrated that DTI is capable of detecting subtle derangements in the structure and morphology of muscle fibers after subacute and chronic denervation (Saotome et al. 2006; Zhang et al. 2008).

The earliest DTI measurements of denervated muscles were performed by Saotome et al. (Saotome et al. 2006) 2 weeks after axonotomy in rats. At this time point none of the quantified muscle DTI parameters showed significant differences to the control group. At 4 weeks after axonotomy a significant increase in FA values of the denervated muscles was detected. These results were confirmed by Zhang et al. using a similar denervation model at 11.7 T and DTI quantification of denervated muscle 25 days after axonotomy (Zhang et al. 2008). Even at later time points (8 weeks after denervation) FA values were found to be significantly increased (Saotome et al. 2006). Both authors attributed these findings to muscle atrophy and loss of muscle fiber diameters.

So far, a systematic evaluation of DTI in the assessment of early acute denervation changes (24 h after denervation) is not available. According to the early changes in muscle perfusion after denervation, DTI parameters may indicate the increase in extracellular fluid spaces, similar to the phenomenon observed in muscle reperfusion after ischemia (Heemskerk et al. 2006). However, future animal and human muscle DTI studies will have to address the DTI properties of early denervation changes.

5.3 MR Spectroscopy of Denervated Muscle

In a small number of studies neurogenic muscle denervation has been investigated by MR Spectroscopy (for an overview on MR spectroscopy, see also MR Spectroscopy and Spectroscopic Imaging for Evaluation of Skeletal Muscle Metabolism: Basics and Applications in Metabolic Diseases). Following peripheral nerve damage, ^{31}P MR spectroscopy has been shown to detect metabolic changes in muscle both experimentally and in patients (Frostick et al. 1991, 1992). Likewise, ^{1}H MR spectroscopy of muscle detected metabolic changes in an experimental setting with nerve transsection and repair in rodents (Dort et al. 1997, 2001). Glucose and lactate levels increased after denervation while choline decreased. Levels returned to normal if nerves were repaired surgically. MR spectroscopy has also been investigated in patients with chronic denervation and advanced muscle atrophy (Schroder et al. 2006). Normal muscle could clearly be differentiated from atrophied musculature by the water/lipid ^{1}H signal intensity ratio. Further, ^{31}P resonance of phosphocreatine was shown to be an adequate marker for the differentiation of intact myocells with high-energy metabolism in contrast to regions dominated by terminal fiber necrosis.

References

Abraham A, Drory VE (2012) Fatigue in motor neuron diseases. Neuromuscul Disord 22(Suppl 3):S198–S202

An X, Yue B et al (2012) Intramuscular distribution of the phrenic nerve in human diaphragm as shown by Sihler staining. Muscle Nerve 45(4):522–526

Assmus H, Antoniadis G et al (2009) Diagnosis and therapy of cubital tunnel syndrome—state of the art. Handchir Mikrochir Plast Chir 41(1):2–12

Barman A, Chatterjee A et al (2012) Traumatic brachial plexus injury: electrodiagnostic findings from 111 patients in a tertiary care hospital in India. Injury 43(11):1943–1948

Baumer P, Dombert T et al (2011) Ulnar neuropathy at the elbow: MR neurography–nerve T2 signal increase and caliber. Radiology 260(1):199–206

Baumer P, Weiler M et al (2012) MR neurography in ulnar neuropathy as surrogate parameter for the presence of disseminated neuropathy. PLoS One 7(11):e49742

Belzberg AJ, Dorsi MJ et al (2004) Surgical repair of brachial plexus injury: a multinational survey of experienced peripheral nerve surgeons. J Neurosurg 101(3):365–376

Bendszus M, Koltzenburg M (2001) Visualization of denervated muscle by gadolinium-enhanced MRI. Neurology 57(9):1709–1711

Bendszus M, Wessig C et al (2003) MR imaging in the differential diagnosis of neurogenic foot drop. Am J Neuroradiol 24(7):1283–1289

Borisov AB, Huang SK et al (2000) Remodeling of the vascular bed and progressive loss of capillaries in denervated skeletal muscle. Anat Rec 258(3):292–304

Bozentka DJ (1998) Cubital tunnel syndrome pathophysiology. Clin Orthop Relat Res (351):90–94

Budzik JF, Le Thuc V et al (2007) In vivo MR tractography of thigh muscles using diffusion imaging: initial results. Eur Radiol 17(12):3079–3085

Campagna R, Pessis E et al (2009) MRI assessment of recurrent carpal tunnel syndrome after open surgical release of the median nerve. Am J Roentgenol 193(3):644–650

Campbell WW, Pridgeon RM et al (1991) Variations in anatomy of the ulnar nerve at the cubital tunnel: pitfalls in the diagnosis of ulnar neuropathy at the elbow. Muscle Nerve 14(8):733–738

Chhabra A, Lee PP et al (2012) High-resolution 3-Tesla magnetic resonance neurography of musculocutaneous neuropathy. J Should Elbow Surg 21(2):e1–e6

Danon MJ, Schliselfeld LH (2007) Study of skeletal muscle glycogenolysis and glycolysis in chronic steroid myopathy, non-steroid histochemical type-2 fiber atrophy, and denervation. Clin Biochem 40(1–2):46–51

Doi K, Otsuka K et al (2002) Cervical nerve root avulsion in brachial plexus injuries: magnetic resonance imaging classification and comparison with myelography and computerized tomography myelography. J Neurosurg 96(3 suppl):277–284

Dort JC, Fan Y et al (2001) Investigation of skeletal muscle denervation and reinnervation using magnetic resonance spectroscopy. Otolaryngol Head Neck Surg 125(6):617–622

Dort JC, Zochodne D et al (1997) Biochemical changes in denervated muscle identified by magnetic resonance spectroscopy. J Otolaryngol 26(6):368–373

Eisenberg HA, Hood DA (1994) Blood flow, mitochondria, and performance in skeletal muscle after denervation and reinnervation. J Appl Physiol 76(2):859–866

Ferdinand BD, Rosenberg ZS et al (2006) MR imaging features of radial tunnel syndrome: initial experience. Radiology 240(1):161–168

Foad SL, Mehlman CT et al (2008) The epidemiology of neonatal brachial plexus palsy in the United States. J Bone Joint Surg Am 90(6):1258–1264

Foerster O (1933) The dermatomes in man. Brain 56(1):1–39

Frostick SP, Dolecki MJ et al (1991) Denervation of the rabbit hind limb studied by 31-phosphorus magnetic resonance spectroscopy. J Hand Surg Br 16(5):537–545

Frostick SP, Taylor DJ et al (1992) Human muscle cell denervation: the results of a 31-phosphorus magnetic resonance spectroscopy study. J Hand Surg Br 17(1):33–45

Furuno K, Goodman MN et al (1990) Role of different proteolytic systems in the degradation of muscle proteins during denervation atrophy. J Biol Chem 265(15):8550–8557

Goldspink DF (1976) The effects of denervation on protein turnover of rat skeletal muscle. Biochem J 156(1):71–80

Goyault G, Bierry G et al (2012) Diffusion-weighted MRI, dynamic susceptibility contrast MRI and ultrasound perfusion quantification of denervated muscle in rabbits. Skeletal Radiol 41(1):33–40

Gutmann E (1962) Denervation and disuse atrophy in crosstriated muscle. Rev Can Biol 21:353–365

Hale HB, Bae DS et al (2010) Current concepts in the management of brachial plexus birth palsy. J Hand Surg Am 35(2):322–331

Harry WG, Bennett JD et al (1997) Scalene muscles and the brachial plexus: anatomical variations and their clinical significance. Clin Anat 10(4):250–252

Hayashi N, Masumoto T et al (2002) Accuracy of abnormal paraspinal muscle findings on contrast-enhanced MR images as indirect signs of unilateral cervical root-avulsion injury. Radiology 223(2):397–402

Hazlewood CF, Chang DC et al (1974) Nuclear magnetic resonance transverse relaxation times of water protons in skeletal muscle. Biophys J 14(8):583–606

Heemskerk AM, Drost MR et al (2006) DTI-based assessment of ischemia-reperfusion in mouse skeletal muscle. Magn Reson Med 56(2):272–281

Hirsch NP (2007) Neuromuscular junction in health and disease. Br J Anaesth 99(1):132–138

Hoeksma AF, Wolf H et al (2000) Obstetrical brachial plexus injuries: incidence, natural course and shoulder contracture. Clin Rehabil 14(5):523–526

Hogendoorn S, van Overvest KL et al (2010) Structural changes in muscle and glenohumeral joint deformity in neonatal brachial plexus palsy. J Bone Joint Surg Am 92(4):935–942

Holl N, Echaniz-Laguna A et al (2008) Diffusion-weighted MRI of denervated muscle: a clinical and experimental study. Skeletal Radiol 37(12):1111–1117

Husarik DB, Saupe N et al (2009) Elbow nerves: MR findings in 60 asymptomatic subjects—normal anatomy, variants, and pitfalls. Radiology 252(1):148–156

Johnson EO, Vekris M et al (2010) Neuroanatomy of the brachial plexus: normal and variant anatomy of its formation. Surg Radiol Anat 32(3):291–297

Kamath S, Venkatanarasimha N et al (2008) MRI appearance of muscle denervation. Skeletal Radiol 37(5):397–404

Kern H, Hofer C et al (2002) Denervated muscles in humans: limitations and problems of currently used functional electrical stimulation training protocols. Artif Organs 26(3):216–218

Kerr A (1918) The brachial plexus of nerves in man, the variations in its formations and branches. Am J Anat (23):285–395

Kikuchi Y, Nakamura T et al (2003) MR imaging in the diagnosis of denervated and reinnervated skeletal muscles: experimental study in rats. Radiology 229(3):861–867

Kim S, Choi JY et al (2007) Role of magnetic resonance imaging in entrapment and compressive neuropathy—what, where, and how to see the peripheral nerves on the musculoskeletal magnetic resonance image: part 2. Upper extremity. Eur Radiol 17(2):509–522

Kollmer J, Baumer P et al (2012) T2-signal of ulnar nerve branches at the wrist in guyon's canal syndrome. PLoS One 7(10):e47295

Krarup C, Archibald SJ et al (2002) Factors that influence peripheral nerve regeneration: an electrophysiological study of the monkey median nerve. Ann Neurol 51(1):69–81

Lehmann HC, Zhang J et al (2010) Diffusion tensor imaging to assess axonal regeneration in peripheral nerves. Exp Neurol 223(1): 238–244

Letinsky MS, Fischbeck KH et al (1976) Precision of reinnervation of original postsynaptic sites in frog muscle after a nerve crush. J Neurocytol 5(6):691–718

Loh EY, Agur AM et al (2003) Intramuscular innervation of the human soleus muscle: a 3D model. Clin Anat 16(5):378–382

Loukas M, Louis RG Jr et al (2007) T2 contributions to the brachial plexus. Neurosurgery 60(2 suppl 1):ONS13–ONS18, (discussion ONS18)

Lu DX, Huang SK et al (1997) Electron microscopic study of long-term denervated rat skeletal muscle. Anat Rec 248(3):355–365

Lupa MT, Krzemien DM et al (1995) Expression and distribution of sodium channels in short- and long-term denervated rodent skeletal muscles. J Physiol 483(Pt 1):109–118

Martinoli C, Gandolfo N et al (2010) Brachial plexus and nerves about the shoulder. Semin Musculoskelet Radiol 14(5):523–546

Medina LS, Yaylali I et al (2006) Diagnostic performance of MRI and MR myelography in infants with a brachial plexus birth injury. Pediatr Radiol 36(12):1295–1299

Mori S, Zhang J (2006) Principles of diffusion tensor imaging and its applications to basic neuroscience research. Neuron 51(5):527–539

Mu L, Sanders I (2010) Sihler's whole mount nerve staining technique: a review. Biotech Histochem 85(1):19–42

Nobile-Orazio E, Cappellari A et al (2005) Multifocal motor neuropathy: current concepts and controversies. Muscle Nerve 31(6):663–680

O'Brien DF, Park TS et al (2006) Management of birth brachial plexus palsy. Childs Nerv Syst 22(2):103–112

O'Leary MF, Vainshtein A et al (2012) Denervation-induced mitochondrial dysfunction and autophagy in skeletal muscle of apoptosis-deficient animals. Am J Physiol Cell Physiol 303(4):C447–C454

Pellerin M, Kimball Z et al (2010) The prefixed and postfixed brachial plexus: a review with surgical implications. Surg Radiol Anat 32(3):251–260

Pham M, Sommer C et al (2010) Magnetic resonance neurography for the diagnosis of extrapelvic sciatic endometriosis. Fertil Steril 94(1):351, e311–e354

Pham M, Wessig C et al (2011) MR neurography of sciatic nerve injection injury. J Neurol 258(6):1120–1125

Polak JF, Jolesz FA et al (1988) Magnetic resonance imaging of skeletal muscle. Prolongation of T1 and T2 subsequent to denervation. Invest Radiol 23(5):365–369

Poyhia TH, Nietosvaara YA et al (2005) MRI of rotator cuff muscle atrophy in relation to glenohumeral joint incongruence in brachial plexus birth injury. Pediatr Radiol 35(4):402–409

Puffer RC, Murthy NS et al (2011) The spectrum of denervation patterns on MRI reflects the dual innervation of the brachialis. Clin Anat 24(4):511–513

Ravichandiran M, Ravichandiran N et al (2012) Neuromuscular partitioning in the extensor carpi radialis longus and brevis based on intramuscular nerve distribution patterns: a three-dimensional modeling study. Clin Anat 25(3):366–372

Rosenbaum R (1999) Disputed radial tunnel syndrome. Muscle Nerve 22(7):960–967

Sakakima H, Kawamata S et al (2000) Effects of short-term denervation and subsequent reinnervation on motor endplates and the soleus muscle in the rat. Arch Histol Cytol 63(5):495–506

Saotome T, Sekino M et al (2006) Evaluation of diffusional anisotropy and microscopic structure in skeletal muscles using magnetic resonance. Magn Reson Imaging 24(1):19–25

Schroder L, Weber MA et al (2006) Metabolic imaging of atrophic muscle tissue using appropriate markers in 1H and 31P NMR spectroscopy. Neuroradiology 48(11):809–816

Sharma U, Kumar V et al (2007) In vivo (31)P MRS study of skeletal muscle metabolism in patients with postpolio residual paralysis. Magn Reson Imaging 25(2):244–249

Smith AB, Gupta N et al (2008) Magnetic resonance neurography in children with birth-related brachial plexus injury. Pediatr Radiol 38(2):159–163

Sosnovik DE, Wang R et al (2009) Diffusion MR tractography of the heart. J Cardiovasc Magn Reson 11:47

Spinner M (1968) The arcade of Frohse and its relationship to posterior interosseous nerve paralysis. J Bone Joint Surg Br 50(4):809–812

Steens SC, Pondaag W et al (2011) Obstetric brachial plexus lesions: CT myelography. Radiology 259(2):508–515

Stutz N, Gohritz A et al (2006) Revision surgery after carpal tunnel release—analysis of the pathology in 200 cases during a 2 year period. J Hand Surg Br 31(1):68–71

Sunderland S (1974) Meningeal-neural relations in the intervertebral foramen. J Neurosurg 40(6):756–763

Taylor BV, Dyck RJB et al (2004) Multifocal motor neuropathy: pathologic alterations at the site of conduction block. J Neuropathol Exp Neurol 63(2):129–137

Tollback A, Soderlund V et al (1996) Magnetic resonance imaging of lower extremity muscles and isokinetic strength in foot dorsiflexors in patients with prior polio. Scand J Rehabil Med 28(3):115–123

Uetani M, Hayashi K et al (1997) Traction injuries of the brachial plexus: signal intensity changes of the posterior cervical paraspinal muscles on MRI. J Comput Assist Tomogr 21(5):790–795

Uysal II, Seker M et al (2003) Brachial plexus variations in human fetuses. Neurosurgery 53(3):676–684 (discussion 684)

Vanderhave KL, Bovid K et al (2012) Utility of electrodiagnostic testing and computed tomography myelography in the preoperative evaluation of neonatal brachial plexus palsy. J Neurosurg Pediatr 9(3):283–289

Viddeleer AR, Sijens PE et al (2012) Sequential MR imaging of denervated and reinnervated skeletal muscle as correlated to functional outcome. Radiology 264(2):522–530

Viguie CA, Lu DX et al (1997) Quantitative study of the effects of long-term denervation on the extensor digitorum longus muscle of the rat. Anat Rec 248(3):346–354

Weber MA, Schonknecht P et al (2004) Postpolio syndrome. Neurologic and psychiatric aspects. Nervenarzt 75(4):347–354

Wechsler W, Hager H (1961) Electron microscopic findings in muscle atrophy after nerve section in white rats. Beitr Pathol Anat 125:31–53

Wehrli L, Oberlin C (2005) The internal brachial ligament versus the arcade of Struthers: an anatomical study. Plast Reconstr Surg 115(2):471–477

Weiss S, Jaermann T et al (2006) Three-dimensional fiber architecture of the nonpregnant human uterus determined ex vivo using magnetic resonance diffusion tensor imaging. Anat Rec A Discov Mol Cell Evol Biol 288(1):84–90

Werner CO (1979) Lateral elbow pain and posterior interosseous nerve entrapment. Acta Orthop Scand Suppl 174:1–62

Wessig C, Koltzenburg M et al (2004) Muscle magnetic resonance imaging of denervation and reinnervation: correlation with electrophysiology and histology. Exp Neurol 185(2):254–261

Willmott AD, White C et al (2012) Fibrillation potential onset in peripheral nerve injury. Muscle Nerve 46(3):332–340

Wilson D, Allen GM (2012) Imaging of the carpal tunnel. Semin Musculoskelet Radiol 16(2):137–145

Witzemann V, Brenner HR et al (1991) Neural factors regulate AChR subunit mRNAs at rat neuromuscular synapses. J Cell Biol 114(1):125–141

Xie P, Jiang Y et al (2012) The study of intramuscular nerve distribution patterns and relative spindle abundance of the thenar and hypothenar muscles in human hand. PLoS One 7(12):e51538

Yang LJ, Chang KW et al (2012) A systematic review of nerve transfer and nerve repair for the treatment of adult upper brachial plexus injury. Neurosurgery 71(2):417–429 (discussion 429)

Yoshikawa T, Hayashi N et al (2006) Brachial plexus injury: clinical manifestations, conventional imaging findings, and the latest imaging techniques. Radiographics 26(Suppl 1):S133–S143

Zhang J, Zhang G et al (2008) Magnetic resonance imaging of mouse skeletal muscle to measure denervation atrophy. Exp Neurol 212(2):448–457

MRI in Muscle Dystrophies and Primary Myopathies

Dirk Fischer and Mike P. Wattjes

Contents

1 **Introduction** ... 242

2 **MR Imaging Techniques** ... 242
2.1 Conventional MRI ... 242
2.2 Whole-Body MRI ... 243
2.3 Contrast-Enhanced MRI ... 243

3 **Image Analysis** ... 244
3.1 Fatty Degeneration ... 245
3.2 Muscle Edema ... 246
3.3 Pitfalls in Image Analysis ... 247

4 **Muscle Imaging as a Diagnostic Tool in Muscular Dystrophies** ... 247
4.1 Dystrophinopathies ... 247
4.2 Limb Girdle Muscular Dystrophies ... 248
4.3 Differential Diagnosis in Dystrophinopathies and LGMD ... 248
4.4 Myotonic Dystrophy ... 249
4.5 Facioscapulohumeral Muscular Dystrophy ... 249
4.6 Oculopharyngeal Muscle Dystrophy ... 250
4.7 Muscle imaging in Myotonic Dystrophies, FSHD, and OPMD ... 250

5 **Muscle Imaging as a Diagnostic Tool in Non-Dystrophic Myopathies** ... 250
5.1 Ryanodine Receptor 1-Related Myopathies, Central Core Disease ... 251
5.2 Selenoprotein 1-Related Myopathies, Multi Minicore Myopathy ... 251
5.3 Dynamin 2-Related Myopathies ... 251
5.4 ACTA1-Related Myopathies ... 251
5.5 MYH7-Related Myopathies ... 252
5.6 Differential Diagnosis in Congenital Myopathies ... 252

6 **Conclusions** ... 253

References ... 254

D. Fischer
Department of Neurology, University Hospital of Basel,
Basel, Switzerland

D. Fischer (✉)
Division of Neuropediatrics,
University Children's Hospital of Basel,
4005 Basel, Switzerland
e-mail: Dirk.Fischer@ukbb.ch

M. P. Wattjes
Department of Radiology and Nuclear Medicine,
VU University Medical Center,
Amsterdam, The Netherlands

Abstract

In the recent past substantial progress in the genetic assessment and the availability of advanced immunohistochemical staining techniques formed the beginning of a new era in characterization and classification of inherited muscle disorders. This was even more so since the introduction of imaging—and especially MRI—into routine diagnostic workup and research in inherited muscle disease. Muscle MRI can not only detect or exclude dystrophic changes but makes the extent and severity of muscle involvement visible and measurable. Recent research focuses on patterns of muscle pathology on whole body MRI. The detection of these patterns has widened the differential diagnosis of inherited muscle diseases even leading to the discovery of new disease entities in combination with genetic testing. The first part of this chapter gives an outline on the current neuromuscular MRI methods and their application for diagnosis and research in inherited muscular disease. In the second part we show how muscle MRI—especially due to newly detected involvement patterns—can lead to diagnostic algorithms as a guidance for diagnosis and differential diagnosis in hereditary myopathies.

Abbreviations

CT	Computed tomography
BMD	Becker muscular dystrophy
DM1	Myotonic dystrophy type I
DMD	Duchenne muscular dystrophy
FSHD	Facio-scapulo-humeral MD

M.-A. Weber (ed.), *Magnetic Resonance Imaging of the Skeletal Musculature*, Medical Radiology. Diagnostic Imaging,
DOI: 10.1007/174_2013_848, © Springer-Verlag Berlin Heidelberg 2013

Published Online: 6 July 2013

LGMD	Limb girdle muscular dystrophy
MD	Muscular dystrophy
MRI	Magnetic resonance imaging
OPMD	Oculo-pharyngeal MD
SNR	Signal-to-noise ratio
STIR	Short tau inversion recovery
T	Tesla
US	Ultrasound

Key Points

1. Magnetic resonance imaging (MRI) has become important in the diagnostic process of inherited and acquired muscle diseases.
2. Conventional MRI shows dystrophic (e.g., fatty degeneration) and nondystrophic (e.g., muscle edema) changes, identifies charateristic distribution patterns, and can be used for disease monitoring.
3. In the diagnostic work-up of patients with suspected inherited muscle diseases the detection and the assessment of the distribution of fatty muscle degeneration by T1-weighted sequences is crucial.
4. Muscle edema not only accompanies but may also precede degenerative findings such as fatty degeneration. Thus, muscle cell edema in dystrophic muscle diseases detected by MRI might be the first imaging manifestation of muscle tissue degeneration.
5. Muscular diseases with similar clinical appearance can be caused by different genetic defects. Muscle imaging can help to differentiate these genetic causes and guide genetic testing.

1 Introduction

Technical advances in genetics and histopathology including new immune-histochemical staining techniques have led to substantial progress in the diagnosis and classification inherited neuromuscular disorders. Inherited neuromuscular disorders represent a broad and heterogeneous spectrum of diseases and the clinical presentation particularly in the early disease course can be mild and inconclusive. Therefore, there is a need for additional (para) clinical tests that may aid in the diagnostic process with special regard to differential diagnosis. Beside the neurological examination, neurophysiology, histopathology (muscle biopsy), imaging, and particularly magnetic resonance imaging (MRI) have become important in the diagnostic process of inherited and acquired muscle diseases (Wattjes and Fischer 2013; Wattjes et al. 2010; Mercuri et al. 2007; Klotzenburg and Yousry 2007). In the first instance, imaging is used to detect or to exclude dystrophic muscle changes. However, in the past few years, the role of imaging went far beyond these purposes. MRI can detect early and preclinical changes of muscle degeneration such as muscle edema that might be important to select and guide further (interventional) diagnostic procedures like muscle biopsy (Poliachik et al. 2012). In addition, muscle MRI can assess the degree of muscle degeneration measures by visual rating scales or by quantitative MRI measures (Wattjes et al. 2010). Recently, it has been demonstrated that MRI is able to detect certain involvement and distribution pattern in inherited muscle diseases that might substantially contribute to the consideration of the correct differential diagnosis. Recent research activities have put great effort into the aim to noninvasively classify inherited muscle diseases and to quantify disease activity and progression.

2 MR Imaging Techniques

There are several MRI techniques available for the evaluation of inherited muscle diseases. Conventional MRI is the main tool for the assessment of dystrophic (e.g., fatty degeneration) and nondystrophic (e.g., muscle edema) changes, the identification of distribution pattern and disease monitoring. In addition, an abundance of advanced and quantitative MR methods have been introduced in the field of neuromuscular imaging which, however, have yet not been established in clinical practice and are limited to research purposes.

2.1 Conventional MRI

Conventional MRI techniques are well established in the field of neuromuscular imaging and have almost completely replaced computed tomography (CT) and to a certain degree also ultrasound, particularly regarding the evaluation of deeper muscles. The major advantages of MR compared to CT is the absence of ionic radiation, higher soft tissue contrast and the possibility of contrast manipulation by the use of different pulse sequences with or without fat suppression. Another relevant advantage of MRI, particularly when compared to ultrasound (US), is the operator independence and the ability to standardize the imaging protocol in terms of pulse sequences, spatial resolution, and repositioning. This is of special importance for longitudinal MR measurements such as disease and treatment monitoring. Although MRI can be performed in any anatomical plane (coronal, sagittal etc.), axial image acquisition is the most frequently used anatomical plane in clinical practice since it is easy to standardize. If necessary, the image acquisition can be performed in other anatomic orientation. In general, structural MRI for the evaluation of inherited (dystrophic

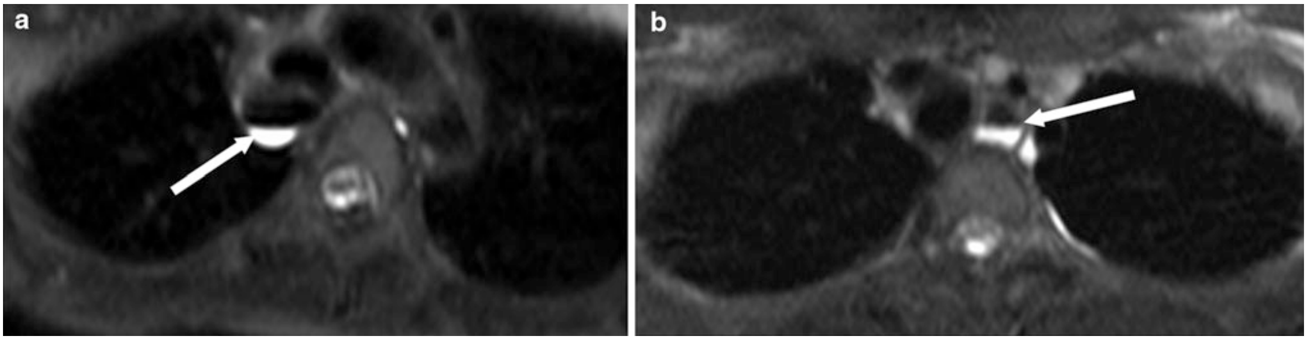

Fig. 1 Axial fat-suppressed T2-weighted images obtained from whole-body MRI protocol in a 37-year-old woman **a** and a 16-year-old boy with myotonic dystrophy type 1. Please note the dilatation of the esophagus with an air-fluid level (*arrows*). Both patients presented clinically with a gastrointestinal reflux (from Wattjes et al. (2010) Reprinted with permission from Springer

and nondystrophic) myopathies is performed as a multi-sequence protocol including

- Axial T1-weighted (turbo/fast) spin echo
- Axial T2-weighted (turbo/fast) spin echo with fat suppression pulse sequences.

Among the different available techniques of fat suppression including spectral fat suppression and relaxation time-dependent fat suppression (e.g., short tau inversion recovery, STIR), STIR sequences offer a stable and homogenous fat suppression and are therefore preferred and most frequently used.

Regarding sequence types, there are no specific guidelines for the use of conventional spin echo or turbo/fast spin echo sequences. However, turbo/spin echo sequences do offer some advantage in terms of scan time reduction, while maintaining good image quality with high signal-to-noise ratios (SNR) particularly when operating at higher magnetic field strengths.

There are no specific recommendations regarding sequence parameters. They have to be scanner optimized and are particularly depending on the magnetic field strength and other characteristics of the MR system and equipment used. The spatial resolution can be adjusted according to the purposes of the imaging study. MRI can be performed in a submillimeter resolution in particular when using high field ($\geq$3 T) MR systems. However, for the detection of dystrophic and edematous muscle changes in patients with muscular dystrophies a slice of thickness 5–8 mm, interslice gap 1–2 mm, and in-plane resolution of about 1–2 mm.

2.2 Whole-Body MRI

Initially imaging studies aiming to find charateristic pattern inherited muscle diseases used MRI protocols focussing only on certain anatomic regions such as the lower limbs (particularly the thighs) and the pelvis. Advances in the MRI acquisition particularly at higher magnetic field strengths have led to the introduction whole-body MRI protocols. In inherited muscle diseases such as muscle dystrophies and primary myopathies, whole-body MRI allows a evaluation of the entire muscles leading to a complete involvement pattern including clinically relevant anatomic regions such as the shoulder girdle, upper extremities, and the head and neck region (Kornblum et al. 2006; Quijano-Roy et al. 2012; Jarraya et al. 2012). In addition, whole-body MRI protocols allow the evaluation of organ systems beyond the skeletal muscle including the lungs, heart and abdominal organs. Particularly, organs containing muscle tissue like the esophagus may be involved in neuromuscular disorders like in myotonic dystrophies (Wattjes et al. 2010; Kornblum et al. 2006) (Fig. 1). "Whole-body MRI for evaluation of the entire muscular system" gives a comprehensive overview of the whole-body MRI applications of the musculoskeletal system.

2.3 Contrast-Enhanced MRI

Contrast-enhanced MRI is important in the diagnosis of neoplastic and inflammatory muscle diseases. In the diagnostic work-up of patients with muscle dystrophies, the use of contrast agents does not have added diagnostic value and is not recommended in the clinical routine setting. Current research is going on developing and testing specific contrast agents targeting affected muscle tissue and allowing the detection of (microstructural) muscle damage even in a preclinical stage are presently a matter of research. When available, such contrast agents may aid in the understanding of the pathophysiological mechanisms of muscle degeneration in inherited muscle diseases. Several new contrast agents are currently in a preclinical stage and are hoped to clinical application in the future may become available. A comprehensive summary of these new contrast agents and

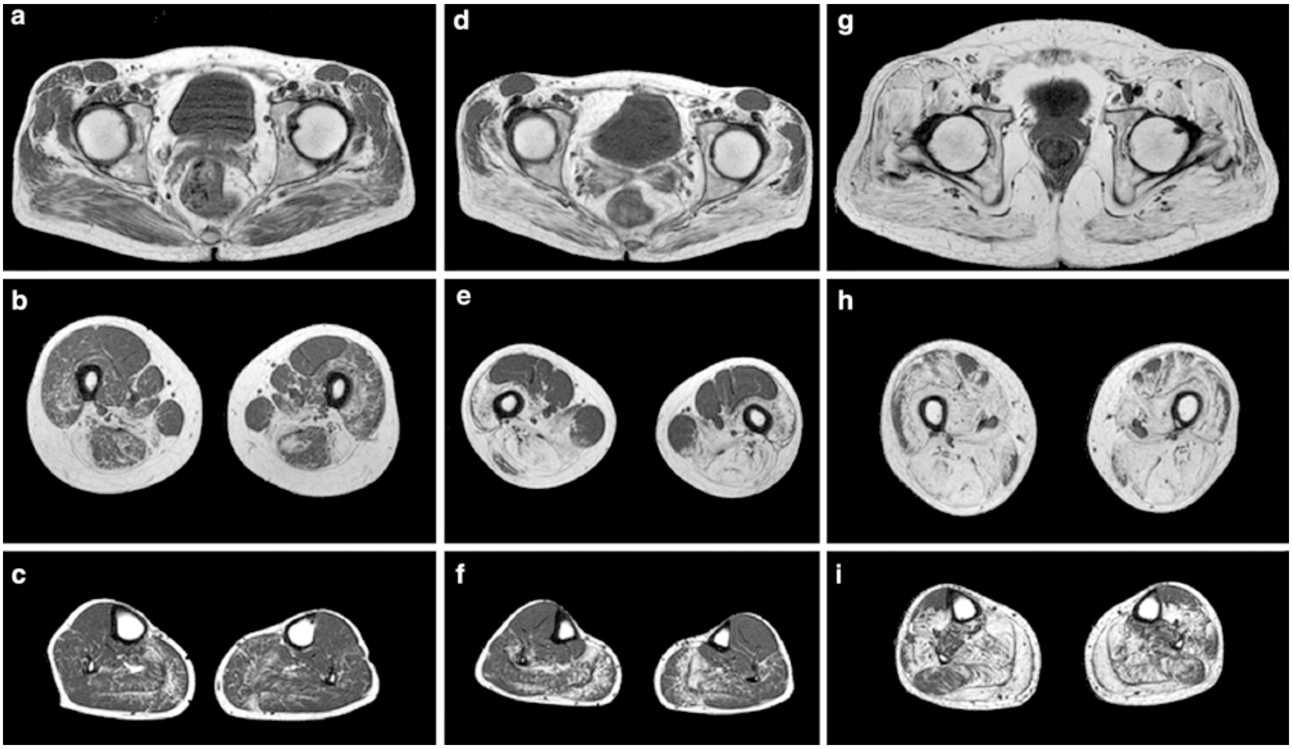

Fig. 2 Axial T1-weighted MRI obtained from three LGMD 2I patients on the pelvic (**a**, **d**, **g**,) thigh (**b**, **e**, **h**) and lower leg (**c**, **f**, **i**) levels demonstrating different degrees of fatty muscle degeneration. The MRI findings correspond well with the clinical phenotype. In the mild clinical phenotype (**a**, **b**, **c**) the fatty degeneration is most obvious in the adductor and biceps femoris muscles. In the patient with a rather moderate clinical phenotype (**d**, **e**, **f**) additionally changes are present in the semimembranosus and semitendinosus, vastus intermediolaterals, and in the gluteus maximus muscles. In the patient with severe clinical phenotype (**g**, **h**, **i**) an almost all muscles diffuse involvement can be observed. Reprinted from Fischer et al. (2005) with permission from Springer

the corresponding pharmacodynamics goes beyond the scope of this book chapter. Please consider the following references for further reading (Amthor et al. 2004; Straub et al. 2000; Schmidt et al. 2009).

3 Image Analysis

Image analysis of muscle tissue in patients with suspected and/or definite inherited muscle diseases should include the following parameters:

- Shape (normal configuration, deformation etc.)
- Size (normal, atrophic, and hypertrophic)
- Tissue architecture (homogenous, signs of (fatty) degeneration, and adjacent connective tissue)
- Focal lesions (calcifications, soft/mixed tissue lesions)
- Signal abnormalities (edema).

The muscle shape, size, and tissue architecture should be analyzed on T1-weighted images. The shape and size of the muscle is depending on individual parameters such as nutrition, exercise, age, sex, and hormone status. In addition, the tissue architecture of the skeletal muscle in terms of shape and inclusion of physiological fat tissue in and adjacent to the muscle strongly differs between muscle groups and anatomic locations.

The crucial parameter in the diagnostic work-up of patients with suspected inherited muscle diseases is the assessment of fatty muscle degeneration. Before approaching this important topic, the reader should be familiar with physiologic T1- and T2 signal intensities (relaxation times) of the two most relevant tissue types of the body: muscle and fat. The signal intensity of skeletal muscle tissue on T1-weighted images is slightly higher than the signal intensity of water and substantially lower than that of fat. On T2-weighted images, the signal intensity of muscle tissue is much lower compared to water and fat tissue. Due to its short T1-relaxation time, the signal intensity of fat tissue is bright on T1-weighted MR images (Figs. 2, 3). Fat shows also high signal intensities on T2-weighted images. T2-weighted images with fat suppression (e.g., STIR) allow to differentiate between fat and water. Water shows a high signal intensity on fat suppressed T2-weighted images leading to a high tissue contrast between fat/water and water (e.g. edema). This substantially improves the sensitivity in the detection intracellular and extracellular free water like in muscle edema (Fig. 3).

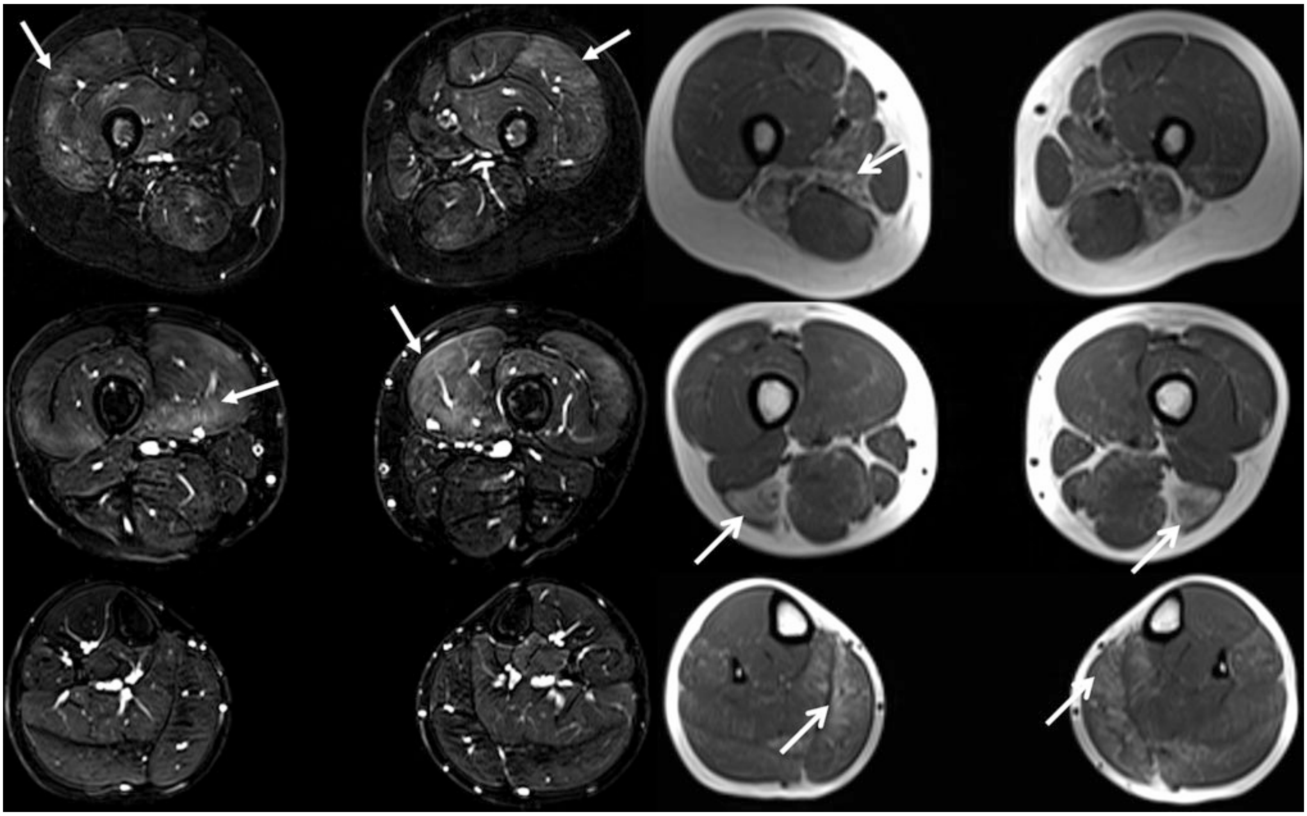

Fig. 3 Axial T1-weighted images (*right*) and fat suppressed T2-weighted images (*left*) at different levels of the lower extremities obtained from a 4-year-old female with a genetically unclassified muscular dystrophy. The focal areas of fatty degeneration involving different muscles/muscle groups (*open head arrows*) are clearly visible on the T1-weighted images. The areas of high signal hyperintensity on the T2-weighted images with fat suppression (*closed head arrows*) particularly reflect edematous (inflammatory) changes in terms of active muscle degeneration in muscles that do not show fatty degeneration at that time. From: Wattjes MP, "Conventional MRI" in Wattjes and Fischer (2013), with permission from Springer

3.1 Fatty Degeneration

Fatty degeneration (synonym: fatty replacement) is defined as the replacement of muscle tissue by fat. It can be a physiologic phenomenon like in normal aging muscle tissue (sarcopenia) but is more prominent in pathophysiologic conditions such as inactivity, disuse, denervation (chronic stage), drug use (steroids), and degenerative/dystrophic muscle diseases. However, the term fatty degeneration is more appropriate for primary degenerative disease processes like in chronic denervation and (inherited) dystrophic muscle diseases, whereas as the term fatty replacement should rather be used for normal muscle aging and other possibly reversible conditions.

Fatty degeneration as well as fatty replacement can present as focal lesions or as a diffuse process involving the entire muscle or even muscle groups. Since the volume of the muscle may decrease during muscle degeneration, fatty degeneration is frequently associated with atrophy. However, fat deposition may also lead to an increase in muscle volume and therefore to "pseudo hypertrophy", most frequently observed in the calf muscles (Fischer et al. 2005). Structured and reproducible assessment and grading of fatty muscle degeneration is crucial for the diagnosis and disease monitoring. In particular, patterns of muscle involvement may be of value in diagnostic and differential diagnostic considerations. Although quantitative MR methods such as the three-point Dixon method might be more accurately describe the degree of fatty degeneration (Glover and Schneider 1991; Wren et al. 2008), several semi-quantitative rating scales have been developed, established and validated in clinical practice allowing a fast and reproducible rating of fatty degeneration (Kornblum et al. 2006; Fischer et al. 2008; Mercuri et al. 2002). Table 1 gives an overview of the most established and used rating scales on fatty degeneration in inherited muscle diseases. Fig. 2 shows different stages of fatty degeneration.

Table 1 Overview of well-established rating scales on MRI concerning the visual rating of dystrophic changes (fatty degeneration) of striated muscle tissue

Grade	Mercuri et al. (2002)	Kornblum et al. (2006)	Fischer et al. (2008)
0		Normal appearance	Normal appearance
1	Normal appearance	Discrete moth-eaten appearance with sporadic T1w-hyperintense areas	Mild: traces of increased signal intensity on the T1-weighted MR sequences
2	Mild involvement: early moth-eaten appearance with scattered small areas of increased signal or with numerous discrete areas of increased signal with beginning confluence, comprising less than 30 % of the volume of the individual muscle	a. Moderate moth-eaten appearance with numerous scattered T1w-hyperintense areas b. Late moth-eaten appearance with numerous confluent T1w-hyperintense areas	Moderate: increased T1-weighted signal intensity with beginning confluence in less than 50 % of the muscle
3	Moderate involvement: late moth-eaten appearance with numerous discrete areas of increased signal with beginning confluence, comprising 30–60 % of the volume of the individual muscle	Complete fatty degeneration, replacement of muscle by connective tissue and fat	Severe: increased T1-weighted signal intensity with beginning confluence in more than 50 % of the muscle
4	Severe involvement: washed-out appearance, fuzzy appearance due to confluent areas of increased signal, or an end stage appearance, with muscle replaced by increased density connective tissue and fat, and only a rim of fascia and neurovascular structures distinguishable		End stage appearance, entire muscle replaced by increased density of connective tissue and fat

Reprinted with permission from Wattjes et al. (2010)

3.2 Muscle Edema

Skeletal muscle edema in MRI (synonym: myoedema) is defined as an increase in the amount of extracellular and/or intracellular water leading to a prolonged T2-tissue relaxation time and therefore to high signal intensities on T2-weighted images. Fat suppressed T2-weighted sequences are the most sensitive MR sequences in the detection of myoedema (Fig. 3). Similar to the assessment of fatty degeneration, muscle edema can present as focal areas of edema involving parts of a certain muscle, may involve the entire muscle and muscle groups or may present as diffuse edema involving major parts of the skeletal muscle system such as in systemic rhabdomyolysis. Compared to fatty degeneration, visual rating scales for the assessment and grading (quantification) of myoedema are less popular and not applied on regular basis in the clinical routine setting. One example of a rating scale in muscle edema by Poliachik and colleagues (2012) is presented in Table 2.

Table 2 Rating scheme on skeletal muscle edema according to Poliachik and colleagues (2012)

Rating scale on skeletal muscle edema (myoedema)
Myoedema absent
Slight, interfascicular myoedema
Slight, intrafascicular, and segmental myoedema of individual muscle
Slight, intrafascicular, and global myoedema of individual muscle
Moderate, intrafascicular, and segmental myoedema of individual muscle
Moderate, intrafascicular, and global myoedema of individual muscle

Reprinted with permission from Wattjes and Fischer (2013)

Myoedema is a rather unspecific finding on imaging and is not exclusively being found in degenerative muscle diseases accompanying fatty muscle degeneration. It can be observed in a broad and heterogeneous spectrum of diseases including muscle denervation (Chap. 11), autoimmune (aseptic) inflammatory myopathies (polymyositis, dermatomyositis) (Chap. 13), infectious muscle diseases or infections of the adjacent structures, muscle trauma (Chap. 10), treatment related (e.g., radiation), rhabdomyolysis (e.g., toxic, drug induced), and inherited myopathies/muscular dystrophies. Myoedema may also occur in physiologic conditions e.g., during or after exercise probably due to extracellular (intercellular) water accumulation.

In patients with inherited muscle diseases, the assessment of muscle edema is a crucial part of MR image analysis. Histopathological studies have conclusively shown that the corresponding histopathological findings include the loss of muscle fiber integrity leading to primarily intracellular water accumulation as a first sign of degeneration followed by degeneration of muscle fibers which will subsequently be replaced by fat and connective tissue in later disease stages. The exact pathophysiological mechanism is not well understood yet. However, results from immuno-histochemistry studies provided some arguments that inflammatory processes are involved in dystrophic muscle tissue with muscle edema. The development and degree of muscle edema in dystrophic muscle tissue can be initiated, aggravated, and accelerated by muscle exercise. From the clinical point of view, it is important to understand that muscle edema not only accompanies but also precedes degenerative findings such as fatty degeneration. Therefore, muscle cell edema in dystrophic muscle diseases detected by MRI might be the first imaging manifestation of muscle tissue degeneration. This is of particular importance since these findings on muscle MRI can guide muscle biopsy, in order to acquire muscle tissue with ongoing disease activity as a target tissue for diagnostic and treatment monitoring.

3.3 Pitfalls in Image Analysis

Fat depositions in the skeletal muscle have a broad differential diagnosis and do not exclusively represent fatty degeneration. In terms of the correct interpretation of fatty replacement and degeneration in the skeletal muscle, it is key to distinguish between real fatty muscle degeneration and other entities associated with increased fat deposition, such as soft tissues including lipomas, hemangiomas, and other soft tissue tumors containing lipomatous tissue. Another important pitfall is the increased amount of fat tissue in the muscle of older and/or immobile patients. From the clinical point of view, it is crucial to differentiate between muscle changes due to aging, misuse, and immobilization (e.g., atrophy and fatty replacement) in terms of sarcopenia and abnormalities due to a primary degenerative disease of the skeletal muscle such as late onset inherited muscle dystrophies or sporadic inclusion body myositis. In sarcopenia and "normal aging" skeletal muscle, atrophy and fatty replacement are rather homogenously and symmetrically distributed affecting almost the entire skeletal muscle. In immobilezed patients and patients with misuse, the underlying cause (e.g., degenerative changes of the spine, postoperative changes) must be assessed first to enable a correct interpretation. Degenerative muscle changes in patients with muscle dystrophies can be symmetrically but may also asymmetrical. Co-morbidity such as aging and misuse can make a correct estimation and differentiation of primary and secondary degenerative changes challenging.

As far as the assessment of muscle edema concerns, the greatest pitfall is the inhomogeneous and/or insufficient fat suppression of T2-weighted images due to magnetic field inhomogeneity particularly at the peripheral region of the field of view (Fig. 4). Identifying T2-hyperintense lesions in the skeletal muscle on fat suppressed T2-weighted images, the assessment of the adjacent tissues (e.g., subcutaneous fat) is useful. If the adjacent structures show inhomogeneous signal intensity and an insufficient suppression of the subcutaneous fat, these muscle changes should not be considered as "real" muscle edema. Other important reasons for insufficient fat suppression include susceptibility artifacts particularly close to material containing metal (e.g., joint prosthesis).

4 Muscle Imaging as a Diagnostic Tool in Muscular Dystrophies

Muscle imaging is increasingly used in neuromuscular disorders to identify the underlying disease in patients with progressive weakness. Often the distribution of weakness in the physical examination is characteristic for a larger group of muscular dystrophies (e.g., limb-girdle muscular dystrophy (LGMD) or distal myopathy) despite of their wide genetic heterogeneity including several underlying genetic defects. While genetic analyses and whole-genome sequencing a widely used the search for a causative genetic mutation is still time consuming and expensive. Dystrophic changes in affected muscles usually do not occur randomly but rather develop in a specific pattern, which is often characteristic for the underlying protein defect and sometimes even for the causative gene. Detecting a specific pattern of muscular involvement is therefore often used to narrow down the genes to be sequenced and evaluated. Several muscle imaging protocols have been described either for the lower limbs (Straub et al. 2012) or in some cases the whole body (Sect. 2.2) (Kornblum et al. 2006; Quijano-Roy et al. 2012; Jarraya et al. 2012). In addition to pattern description, muscle imaging is also used to guide muscle biopsy e.g., to target an involved area which is not yet completely replaced with fatty tissue. In this review we try to focus on common patterns. An exhaustive description of all possible disorders and patterns has been prepared in a larger volume (Wattjes and Fischer 2013).

4.1 Dystrophinopathies

Dystrophinopathies and LGMD both present with proximal pelvic girdle and shoulder girdle weakness. Duchenne muscular dystrophy (DMD, the severe form) and Becker muscle dystrophy (BMD) (less severe form, BMD) are both dystrophinopathies characterized by the absence or a defective dystrophin protein. DMD is the most common muscular dystrophy worldwide affecting about 1 in every 3,500 to 5,000 boys or between 400 and 600 live male births each year (Bushby et al. 2010). The pattern of muscle pathology in DMD is charaterized by it's initial and most severe involvement of the adductors magnus, the biceps femoris, and involvement of the quadriceps. A relative

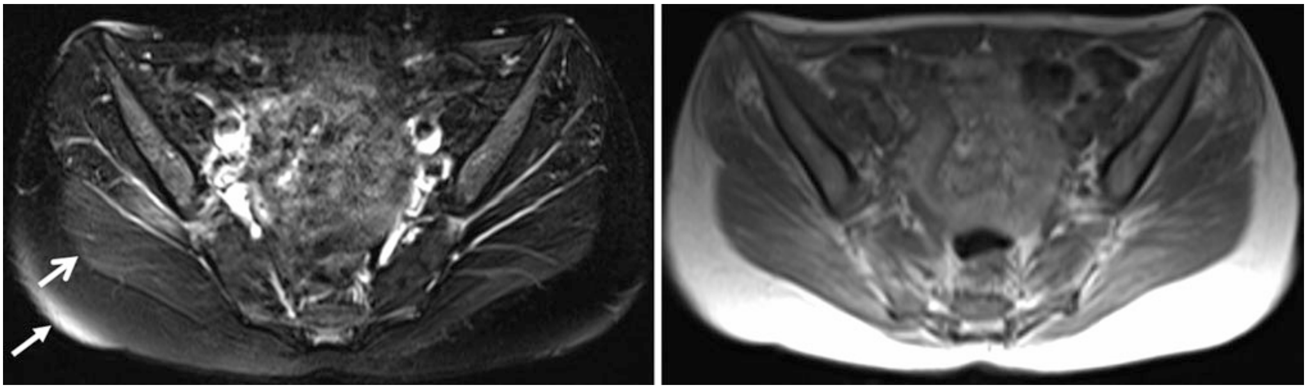

Fig. 4 Axial T1-weighted images (*right*) and fat suppressed T2-weighted images (*left*) at the pelvis region from a patient with suspected myotonic dystrophy. The areas with high signal intensities in the subcutaneous fat (*closed head arrow*) and in the adjacent gluteus maximus muscle (*open head arrow*) are based on inhomogeneous fat suppression and not on edema. These areas of inhomogeneous fat suppression can be frequently observed in the periphery of the field-of-view. From: Wattjes MP. "Conventional MRI" in Wattjes and Fischer (2013), with permission from Springer

sparing of the long adductor is also often detected (Fischmann et al. 2012). In BMD disease onset is at advanced age; however, it's distribution at onset is similar to DMD. Unlike DMD, affection of the semimembranosus usually precedes that of the quadriceps (ten Dam et al. 2012). Bilateral involvement of both heads of the gastrocnemius muscle is also observed.

4.2 Limb Girdle Muscular Dystrophies

Autosomal dominant and recessive LGMD are a heterogeneous group of genetic diseases with a wide spectrum of clinical involvement and severity. In contrast to the more common X-linked dystrophinopathies, onset is often later during late childhood, adolescence, or at adult age. LGMD patients usually show progressive weakness predominantly in the limb musculature, proximal more than distal. Onset, progression, and distribution of weakness and wasting can vary greatly between individual patients and genetic subtypes. Muscle imaging data are available in detail for LGMD2A, LGMD2B, LGMD2I, and LGMD2L. Patients with LGMD2A (calpainopathy) show a relative typical pattern of muscle involvement on MRI studies. Often there is moderate to severe atrophy of the gluteus maximus muscle. At the thigh the medial (adductor) and posterior compartment (hamstring) muscles are usually the most severely and the quadriceps muscle is the least affected. In particular, involvement of the adductor magnus and semimembranosus muscles is the most common finding. Sartorius and gracilis are usually spared. In the lower legs the first muscles to be involved are the medial head of the gastrocnemius muscle and the soleus muscle with relative sparing of lateral head of the gastrocnemius muscle (Fischer et al. 2005; Mercuri et al. 2005). Similar to LGMD2A, in LGMD2I muscle MRI has shown that changes occur predominantly in the medial and posterior compartments of both the thigh and the lower leg. Most severe changes occur in the biceps femoris long head muscle, adductor magnus muscle, semitendinosus muscle, and semimembranosus muscle with the gracilis muscle, sartorius muscle, vastus lateralis muscle, and the rectus femoris muscle being initially relatively spared. In the lower leg, predominant diffuse involvement is seen in the gastrocnemii muscles and the soleus muscle, often accompanied by pseudohypertrophy (Kornblum et al. 2006). Patients with mutations in the dysferlin gene can present with either more proximal (LGMD2B) or more distal muscle involvement (miyoshi myopathy). Over the course of the disease, these phenotypes often overlap and patients show both proximal and distal involvement, especially of the leg muscles. Almost every muscle can be affected in dysferlinopathies. In the thigh, muscle pathology generally seems to start in the adductor magnus muscle and later affects the semimembranosus and the vastus lateralis muscles. Similarly to many other LGMD, the rectus, gracilis, and sartorius muscles are usually spared. In the calf, the posterior compartment is predominantly affected, mainly the gastrocnemius medialis and lateralis and the soleus muscles (Kesper et al. 2009).

4.3 Differential Diagnosis in Dystrophinopathies and LGMD

Figure 5 shows a flowchart demonstrating an approach to how to discriminate between dystrophinopathies and different forms of LGMD using muscle imaging and clinical findings. We suggest when analysing muscle imaging findings in LGMD first to consider the degree of anterior compared to posterior thigh involvement. Most LGMD

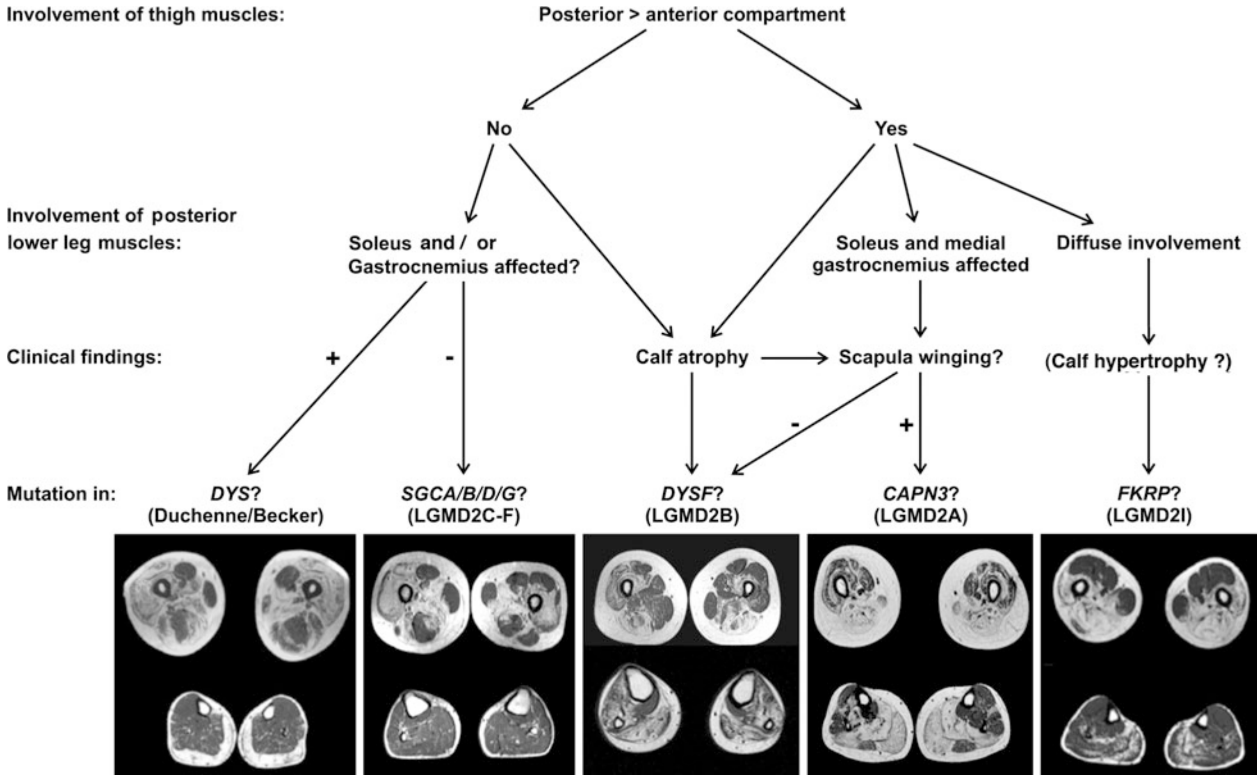
Involvement of thigh muscles:
Posterior > anterior compartment
No
Yes
Involvement of posterior lower leg muscles:
Soleus and / or Gastrocnemius affected?
Soleus and medial gastrocnemius affected
Diffuse involvement
Clinical findings:
+
-
Calf atrophy
Scapula winging?
(Calf hypertrophy ?)
-
+
Mutation in:
DYS? (Duchenne/Becker)
SGCA/B/D/G? (LGMD2C-F)
DYSF? (LGMD2B)
CAPN3? (LGMD2A)
FKRP? (LGMD2I)

Fig. 5 Algorithm for the differential diagnosis of dystrophinopathies and limb-girdle muscular dystrophies (LGMD) based on muscle imaging data of the lower limbs. For details please refer to the main text (Sect. 4.3). With permission from Springer (from Wattjes and Fischer (2013). Adapted from Wattjes et al. (2010))

patients show more pronounced muscle alterations in the posterior than in the anterior thigh compartment. In contrast, patients presenting with a limb-girdle pattern of muscle weakness caused by dystrophin mutations (such as female carriers or late onset patients with Becker type dystrophy) or sarcoglycanopathy often have a predominant affection of the quadriceps muscle. In a second step, the degree of lower leg involvement can seperate the two diseases. Dystrophinopathy often presents with early and marked changes in the gastrocnemii or soleus muscles, while these muscles are not affected in sarcoglycanopathy patients. Patients with dysferlinopathy most often show posterior thigh and posterior lower leg involvement with sparing of sartorius, gracilis, and biceps femoris but the pattern of muscle involvement can be variable. However, calf atrophy and absence of scapular winging are common clinical findings. LGMD2A and LGMD2I patients present with predominant posterior thigh and posterior lower leg involvement. LGMD2A patients usually show marked involvement of soleus and medial gastrocnemius muscles. Furthermore, calf atrophy and scapular winging are usually observed. In contrast, LGMD2I patients have a more diffuse involvement of the posterior lower leg muscles, while the tibialis anterior muscle is often spared or even hypertrophied.

4.4 Myotonic Dystrophy

Myotonic Dystrophy type I (DM1) also known as Steinert's Disease is the second most common muscular dystrophy after DMD, and probably the most common adult form of muscle dystrophy, affecting approximately one person in 8,000 worldwide. The classical adult-onset DM1 phenotype is characterized by facial and distal muscle weakness and wasting of forearm and lower leg ankle dorsiflexor muscles. Muscle imaging in DM1 patients shows most frequently an affection of the anterior thighs and the calf muscles. In lower legs of DM1 patients, involvement of the medial heads of gastrocnemius muscles as well as soleus muscles is a consistent finding. The thighs mainly show involvement of the vasti muscles, while the rectus femoris is relatively spared resulting in a characteristic semilunar pattern of involvement (Kornblum et al. 2006).

4.5 Facioscapulohumeral Muscular Dystrophy

Facioscapulohumeral Muscular Dystrophy (FSHD) is the third most common muscular dystrophy worldwide affecting approximately one person in 20,000. FSHD is usually passed on in an autosomal dominant fashion. As the name suggests, patients develop (asymmetric) weakness of the face, the shoulder, and the proximal arm usually beginning in their teenage years. MRI findings in FSHD show often asymmetric leg muscle affection which distal prominence. The tibialis anterior muscle is usually the most severely involved muscle, followed by the medial head of the gastrocnemius muscle. The peroneal muscles are usually spared. In the thighs, the hamstring and adductor muscles are most severely involved. The most severe changes are observed in the semimembranosus, biceps femoris, semitendinosus, and the adductor group muscles, while the vasti muscles are least affected (Kan et al. 2010).

4.6 Oculopharyngeal Muscle Dystrophy

Oculopharyngeal Muscle Dystrophy (OPMD) is a much rarer adult-onset muscular dystrophy usually inherited in an autosomal dominant fashion, mainly found in a French Canadian community. Usually patients become symptomatic in their 40's or 50's with drooping eyelids and difficulties swallowing. In contrast to chronic progressive external ophthalmoplegia (CPEO), the external eye muscles are not involved. Peripheral muscle involvement is predominantly in the proximal lower limbs. Lifespan is usually not diminished with most patients remaining independently and ambulatory. There are only few reports on muscle imaging in OPMD. Predominant involvement of the thighs is visibly especially in the adductor magnus and hamstrings, while the quadriceps is mainly involved in the deeper layers of the vastus intermedius muscle (Fischmann et al. 2011).

4.7 Muscle imaging in Myotonic Dystrophies, FSHD, and OPMD

Diagnosis of the more common muscular dystrophies as DM1, FSHD, and also OPMD, is usually not very difficult due to distinctive clinical findings. Therefore, in these muscular dystrophies the role of muscle imaging has yet to be defined. However, some characteristic imaging findings are presented in Fig. 6. Myotonic dystrophy type I is typically characterized by distal more than proximal muscle involvement showing predominant affection of the soleus, medial gastrocnemius and proximally the anterior thigh compartment with relative sparing of the rectus femoris. Myotonic dystrophy type II (or proximal myotonic myopathy = PROMM) often are often less affected and show no fatty degeneration. Affected patients show more involvement of the proximal muscles with an affection of the quadriceps and sparing of the rectus femoris and gracilis muscles. FSHD is often characterized by marked asymmetry with adductor magnus, hamstrings, rectus femoris, and tibial anterior being the most often affected muscles. OPMD patients show predominantly posterior thigh (adductor magnus, semimembranosus, and biceps femoris muscles) and posterior lower leg (soleus) muscle involvement.

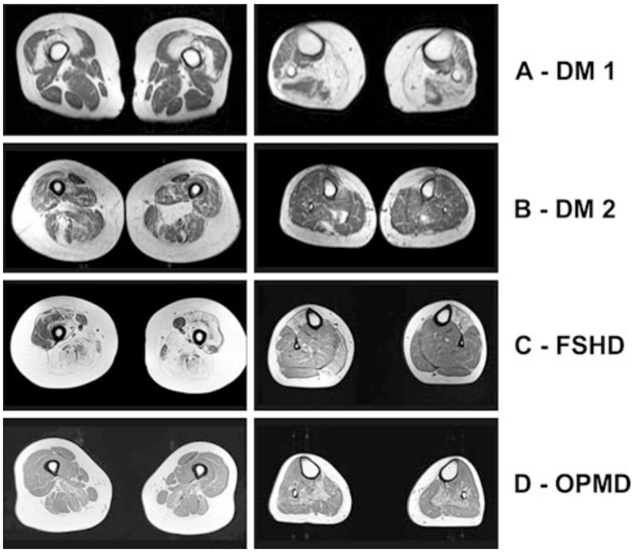

Fig. 6 Muscle MRI of lower extremities in different forms of muscular dystrophies. For details please refer to the main text (Sect. 4.7). With permission from Springer (from Wattjes and Fischer (2013). Adapted from Wattjes et al. (2010))

5 Muscle Imaging as a Diagnostic Tool in Non-Dystrophic Myopathies

Apart from muscular dystrophies, there are other nondystrophic often structural myopathies presenting with permanent but usually not or only very slowly progressive muscle weakness. These are often also referred to as congenital myopathies (CM), as onset is often congenital or within the first years of life. CM are a genetical heterogeneous group of myopathies, classified according to the predominant histopathological findings in skeletal muscle. However, considerable overlap between different histopathologically and genetically defined forms of CM has recently been observed. By comparison, the pattern of involved muscles seen on muscle imaging is often more specific, providing useful additional information in the differential diagnosis of these diseases. Therefore, muscle imaging can help to target the most appropriate genetic investigations. Here, we aim to give an overview on muscle imaging on the most common congenital myopathies. For more details please refer to the following recently published reviews (Wattjes and Fischer 2013; Quijano-Roy et al. 2011).

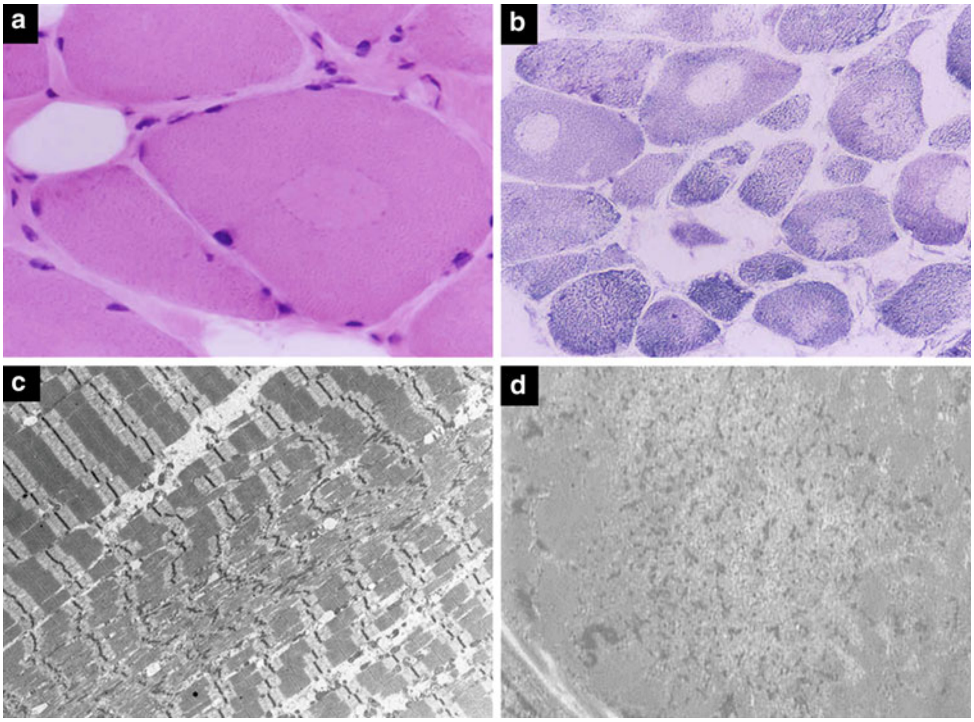

Fig. 7 Histological findings in *RYR1*-related central core disease. **a**, **b** Light microscope of muscle biopsy sections with typical central core lesions (*white arrows*) by hematoxilin-eosin staining (**a**) and NADH (**b**) (courtesy M. Olivé, Barcelona, Spain); **c**, **d** Electron microscopy of a patient with typical disruption of sarcomeres and streaming of (*dark*) Z lines (*white arrows*) (**c**) and severe sarcomere disorganization in a patient with fetal akinesia syndrome (Courtesy N.B. Romero, Paris, France). With permission from Springer (from Wattjes and Fischer (2013))

5.1 Ryanodine Receptor 1-Related Myopathies, Central Core Disease

Congenital myopathies with core lesions are probably one of the more common CM. "Core myopathies" show an important genetic overlap. Patients with mutations in the ryanodine receptor 1 gene (RYR1) present with limb-girdle weakness and usually show central cores on a diagnostic muscle biopsy (Fig. 7). The muscle imaging findings in RYR1-related CM show probably the most characteristic pattern of all CM. In RYR1 patients, the most involved pelvis muscle is the gluteus maximus. At the thigh, the most severe affection can be found in the adductor magnus, the vastus lateralis and intermedius, the semitendinosus, and the sartorius muscles. Sparing of the rectus femoris, adductor longus, gracilis, and biceps femoris muscles is common. In the lower legs, there is predominant affection of soleus, and peroneal muscles, while posterior tibial, gastrocnemius, and anterior tibial muscles are often preserved (Fischer et al. 2006a).

5.2 Selenoprotein 1-Related Myopathies, Multi Minicore Myopathy

Selenoprotein 1 (SEPN1) patients often present as a rigid spine myopathy and may have multi-minicore lesions in the muscle biopsy. On imaging, affection of sartorius and hamstring muscles and a relative sparing of the rectus femoris, adductor longus, and gracilis muscles is commonly observed. Involvement of medial and lateral gastrocnemius muscles usually exceeds soleus muscle affection. The anterior tibial muscle is unimpaired (Amthor et al. 2004).

5.3 Dynamin 2-Related Myopathies

Centronuclear myopathies (CNM) are a subgroup of congenital myopathies histogically defined by an increased presence of centrally located nuclei in affected muscle fibers (Fig. 8). DNM2-related CNM is the most common form of CNM, commonly presenting as autosomal dominant late childhood or early adult distal myopathy. Sporadic, severe early onset clinical forms have also been described. In patients with dynamin 2-related autosomal dominant centronuclear myopathy (DNM2-CNM), muscle imaging often shows predominant distal lower leg muscle affection. At the thigh, the adductor longus, vastus intermedius, and the posterior thigh compartment muscles are the most affected, while medial and lateral vasti, sartorius, and gracilis are relatively spared. At the lower legs, the medial gastrocnemius and soleus are often severely involved while the posterior tibial muscle is spared (Fischer et al. 2006b).

5.4 ACTA1-Related Myopathies

Mutations in the skeletal muscle actin gene, ACTA1, are responsible for different pathological types of CM comprising nemaline myopathy, cap myopathy, intranuclear rod

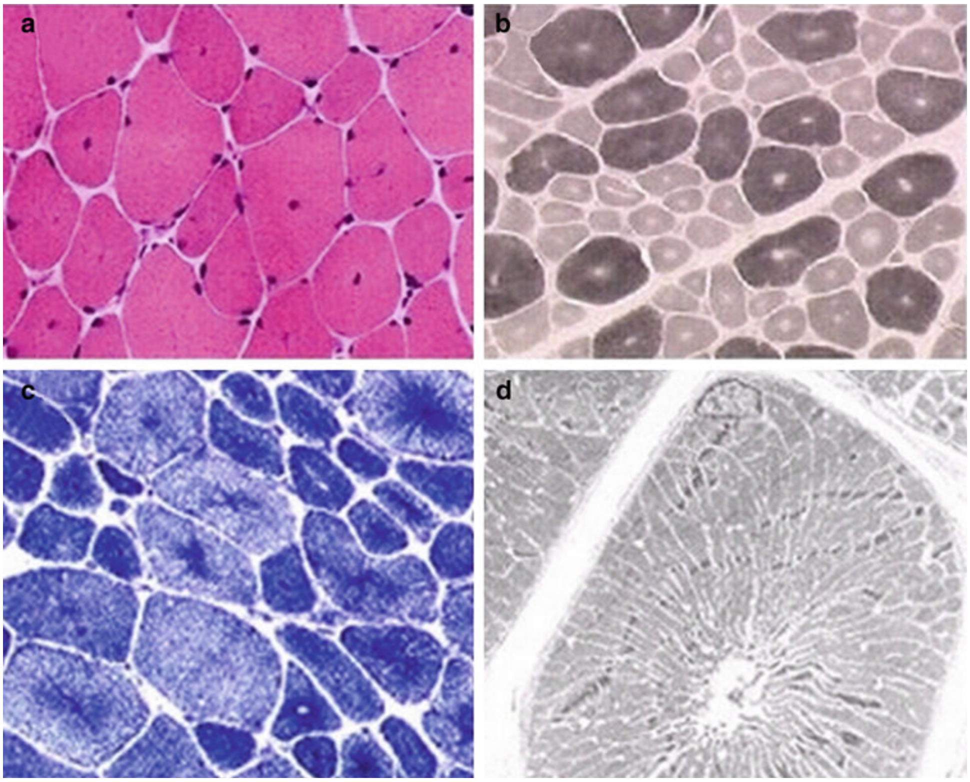

Fig. 8 Histological findings observed in *DYN2*-related centronuclear myopathy. Characteristic histopathological findings with myotube-like fibers that show an increased number of centralized nuclei (**a**; HE, original magnification 20×), presence of fiber type 1 predominance and atrophy (**b**; ATP 9.4), as well as radial distribution of sarcoplasmic strands seen on NADH (**c**) and electron microscopy (**d**). Courtesy of Norma Romero, Paris, France with permission of Oxford University Press (Fischer et al. 2006b)

myopathy, and congenital fiber type disproportion (CFTD). The clinical phenotypes are variable, also ranging from late childhood slowly progressive proximal weakness to severe, neonatal onset with facial, respiratory, axial, and limb weakness, resulting in early death. In patients with ACTA1-related nemaline myopathy, muscle imaging may show only minor and diffuse affection of the thigh muscles, mostly involving the sartorius and adductor magnus muscles. The vasti muscles are usually spared. In the lower legs, there is predominant affection of the tibial anterior, peroneal, and tibial posterior muscles. The soleus muscle is less involved, and the medial and lateral gastrocnemius muscles are spared (Wallgren-Pettersson and Laing 2006).

5.5 MYH7-Related Myopathies

Mutations in the slow beta-myosin heavy-chain (MYH7) gene have been identified in early childhood onset (slowly progressive) distal myopathy (type Laing). Pathological findings include myosin or hyaline body deposition. Distal big-toe and ankle dorsiflexion weakness is usually the first presenting sign, while proximal thigh and finger and wrist extensors may be involved later. On imaging, the tibial anterior muscle is the most severely involved muscle. Involvement of the peroneal group, the soleus, and tibial posterior muscles can follow. In the thigh, the vastus lateralis and vastus intermedius are the most affected muscles while the rectus femoris, adductor longus, sartorius, and gracilis muscles are spared (Muelas et al. 2010).

5.6 Differential Diagnosis in Congenital Myopathies

Figure 9 provides an algorithm for the differential diagnosis of CM based on muscle imaging data of lower extremities. We suggest starting with the distinction between predominant proximal and distal involvement. In the group with predominant proximal thigh involvement, the pattern observed in RYR1-patients is highly characteristic. Distinction of SEPN1-patients can be difficult but SEPN1-patients show more involvement of the medial and lateral gastrocnemius muscles than of the soleus muscle. DNM2-patients show some important differences compared to RYR1 and SEPN1 patients: relative sparing of the vasti and sartorius muscles and more affection of the adductor longus than adductor magnus muscles. Compared to the lack. Overall MTM1 patients have a very similar pattern to RYR1 patients, but the vastus lateralis is more affected than the vastus medialis in RYR1-patients while the opposite seems to be the case in MTM1 patients. Furthermore, the biceps femoris is involved early in MTM1 patients, but often spared in RYR1 patients and the tibial anterior

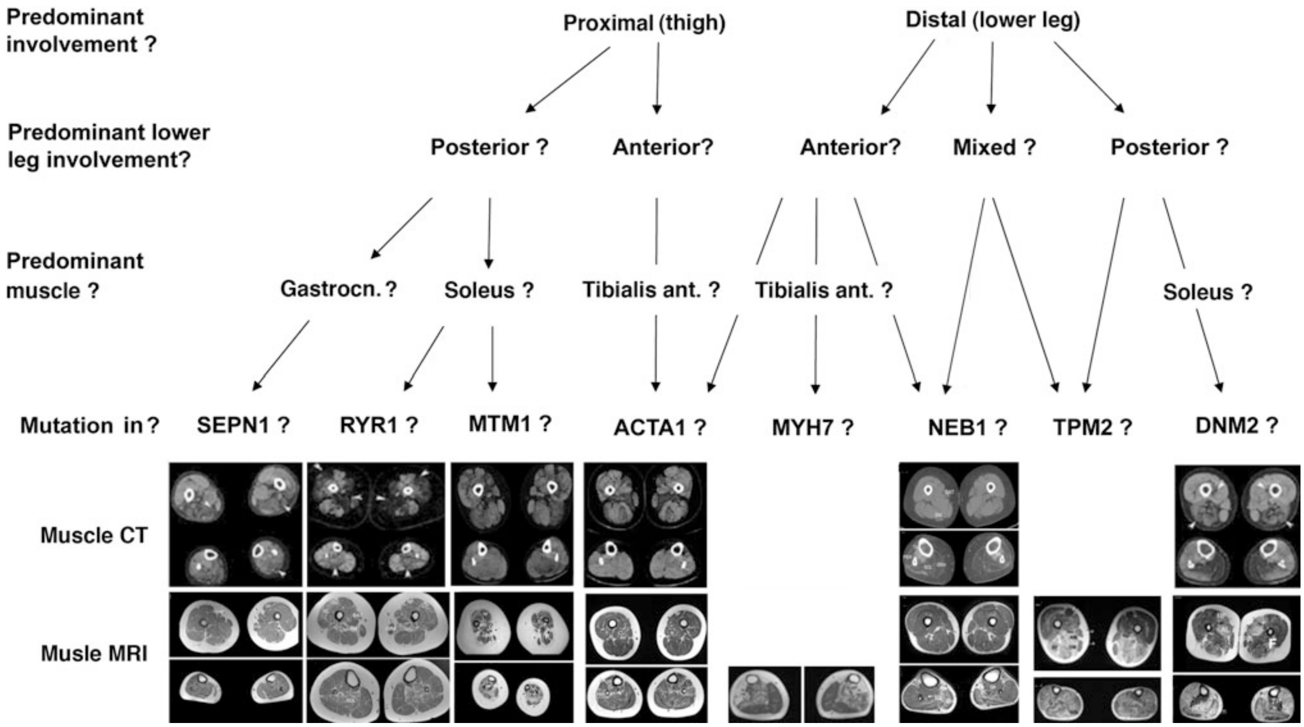

Fig. 9 MRI findings in congenital myopathies. For details please refer to the main text (Sect. 5.6). With permission from Springer (from Wattjes and Fischer 2013. Adapted from Wattjes and Fischer (2010) and Bevilacqua et al. (2009))

involvement can be seen in MTM1 but not in RYR1 patients. However, a reliable distinction cannot be made before further data are published. NEB patients show an affection of the tibial anterior muscle, which should help to make a distinction from RYR1 patients and SEPN1 patients, where it is spared.

In contrast, the second group of CM patients presents with predominant distal lower leg weakness. DNM2 patients often have isolated distal affection on muscle imaging with medial gastrocnemius and soleus muscles being often severely involved while the posterior tibial and anterior lower leg compartment muscles are spared. Other distal presenting CM related to NEB, ACTA1, and MYH7 gene mutations show predominant anterior lower leg involvement. ACTA1 patients show predominant distal anterior lower leg and mild diffuse thigh compartment involvement, while MYH7 gene-associated myopathies can spare the thigh muscles and show selective distal involvement of the tibial anterior, tibial posterior, and soleus muscles. In case of thigh muscle involvement, there is more posterior compartment affection than involvement of the vasti muscle in patients with ACTA1 and NEB mutations while the opposite has been observed in patients with MYH7 mutations. However, a reliable distinction among NEB, ACTA1, and MYH7 patients does not seem possible at this time.

6 Conclusions

The importance of diagnostic muscular imaging for pattern analysis is increasingly recognized in patients with inherited neuromuscular disorders and especially in primary disorders of the muscles, such as muscular dystrophies or congenital (structural) myopathies. Today muscle MRI is the modality of choice in the diagnostic work-up, often able to identify the muscle involvement and even to quantify the degree of pathological changes according to established rating scales. Diseases with similar clinical appearance can be caused by different genetic defects. Here, muscle imaging showing pathology beyond the scope of physical examination can guide the differential diagnostic work-up and genetic testing. Caution should be taken with described patterns which were identified in a limited number of patients, especially when patients are relatives. In the future, whole-body MRI protocols will probably be able identify additional important differences in other muscles that might increase the use of muscle MRI for the differential diagnosis. Finally, monitoring the natural history and therapeutic effects in future trials can be expected with quantitative MRI.

References

Amthor H, Egelhof T, McKinnell I et al (2004) Albumin targeting of damaged muscle fibres in the mdx mouse can be monitored by MRI. Neuromuscul Disord 14:791–796

Bevilacqua JA et al (2009) Necklace fibers, a new histological marker of late-onset. MTM1-related centronuclear myopathy. Acta Neuropathol 117(3):283–291

Bushby K, Finkel R, Birnkrant DJ et al (2010) Diagnosis and management of Duchenne muscular dystrophy, part 1: diagnosis, and pharmacological and psychosocial management. Lancet Neurol 9:77–93

Fischer D, Walter MC, Kesper K et al (2005) Diagnostic value of muscle MRI in differentiating LGMD2I from other LGMDs. J Neurol 252:538–547

Fischer D, Herasse M, Ferreiro A et al (2006a) Muscle imaging in dominant core myopathies linked or unlinked to the ryanodine receptor 1 gene. Neurology 67:2217–2220

Fischer D, Herasse M, Bitoun M et al (2006b) Characterization of the muscle involvement in dynamin 2-related centronuclear myopathy. Brain 129:1463–1469

Fischer D, Kley RA, Strach K et al (2008) Distinct muscle imaging patterns in myofibrillar myopathies. Neurology 71:758–765

Fischmann A, Gloor M, Fasler S et al (2011) Muscular involvement assessed by MRI correlates to motor function measurement values in oculopharyngeal muscular dystrophy. J Neurol 258:1333–1340

Fischmann A, Hafner P, Fasler S, Gloor M, Bieri O, Studler U, Fischer D (2012) Quantitative MRI can detect subclinical disease progression in muscular dystrophy. J Neurol 259:1648–1654

Glover GH, Schneider E (1991) Three-point Dixon technique for true water/fat decomposition with B_0 inhomogeneity correction. Magn Reson Med 18:371–383

Jarraya M, Quijano-Roy S, Monniers N et al (2012) Whole-body muscle MRI in a series of patients with congential myopathy related to TPM2 gene mutations. Neuromuscul Disord 22(2):S137–S147

Kan HE, Klomp DW, Wohlgemuth M et al (2010) Only fat infiltrated muscles in resting lower leg of FSHD patients show disturbed energy metabolism. NMR Biomed 23:563–568

Kesper K, Kornblum C, Reimann J, Lutterbey G, Schröder R, Wattjes MP (2009) Pattern of skeletal muscle involvement in primary dysferlinopathies: a whole-body 3.0-T magnetic resonance imaging study. Acta Neurol Scand 120:111–118

Klotzenburg M, Yousry T (2007) Magnetic resonance imaging of skeletal muscle. Curr Opin Neurol 20:595–599

Kornblum C, Lutterbey G, Bogdanow M, Kesper K, Schild H, Schröder R, Wattjes MP (2006) Distinct neuromuscular phenotypes in myotonic dystrophy types 1 and 2. A whole body highfield MRI study. J Neurol 253:753–761

Mercuri E, Talim B, Moghadaszadeh B et al (2002) Clinical and imaging findings in six cases of congenital muscular dystrophy with rigid spine syndrome linked to chromosome 1p (RSMD1). Neuromuscul Disord 12:631–638

Mercuri E, Bushby K, Ricci E et al (2005) Muscle MRI findings in patients with limb girdle muscular dystrophy with calpain 3 deficiency (LGMD2A) and early contractures. Neuromuscul Disord 15:164–171

Mercuri E, Pichiecchio A, Allsop J, Messina S, Pane M, Muntoni F (2007) Muscle MRI in inherited neuromuscular disorders: past, present and future. J Magn Reson Imaging 25:433–440

Muelas N, Hackman P, Luque H et al (2010) MYH7 gene tail mutation causing myopathic profiles beyond Laing distal myopathy. Neurology 75:732–741

Poliachik SL, Friedman SD, Carter GT, Parnell SE, Shaw DW (2012) Skeletal muscle edema in muscular dystrophy: clinical and diagnostic implications. Phys Med Rehabil Clin Am 23:107–122

Quijano-Roy S, Carlier RY, Fischer D (2011) Muscle imaging in congenital myopathies. Semin Pediatr Neurol 18:221–229

Quijano-Roy S, Avila-Smirnow D, Carlier RY, WB-MRI muscle study group (2012) Whole body muscle MRI protocol: pattern recognition in early onset NM disorders. Neuromuscul Disord 22(2):S68–S84

Schmidt S, Vieweger A, Obst M et al (2009) Dysferlin-deficient muscular dystrophy: gadofluorine M suitability at MR Imaging in a mouse model. Radiology 250:87–94

Straub V, Donahue KM, Allamand V, Davisson RL, Kim YR, Campbell KP (2000) Contrast agent-enhanced magnetic resonance imaging of skeletal muscle damage in animal models of muscular dystrophy. Magn Reson Med 44:655–659

Straub V, Carlier PG, Mercuri E (2012) TREAT-NMD workshop: pattern recognition in genetic muscle diseases using muscle MRI: 25–26 February 2011, Rome. Italy. Neuromuscul Disord 22(Suppl 2):S42–S53

ten Dam L, van der Kooi AJ, van Wattingen M, de Haan RJ, de Visser M (2012) Reliability and accuracy of skeletal muscle imaging in limb-girdle muscular dystrophies. Neurology 79:1716–1723

Wallgren-Pettersson C, Laing NG (2006) 138th ENMC workshop: nemaline myopathy, 20–22 May 2005, Naarden, The Netherlands. Neuromuscul Disord 16:54–60

Wattjes MP, Fischer D (eds) (2013) Neuromuscular imaging. Springer, Berlin

Wattjes MP, Kley RA, Fischer D (2010) Neuromuscular imaging in inherited muscle diseases. Eur Radiol 20:2447–2460

Wren TAL, Bluml S, Tseng-Ong L, Gilsanz V (2008) Three-point technique of fat quantification of muscle tissue as a marker of disease progression in Duchenne muscular dystrophy: preliminary study. Am J Roentgenol 190:W8–W12

MRI in Inflammatory Myopathies and Autoimmune-Mediated Myositis

Umesh A. Badrising, Hermien E. Kan, and Jan JGM Verschuuren

Contents

1 **Key Points** ... 256

2 **Introduction** ... 256

3 **Idiopathic Inflammatory Myopathies** ... 256
3.1 Clinical Presentation ... 256
3.2 Laboratory Findings ... 257
3.3 Histopathology and Pathogenesis ... 258

4 **Imaging in Idiopathic Inflammatory Myopathies** ... 259
4.1 Magnetic Resonance Imaging in Idiopathic Inflammatory Myopathies ... 259
4.2 Muscle Involvement Patterns in IIM on MRI ... 260
4.3 Other Magnetic Resonance Imaging Techniques in IIM ... 261
4.4 Other Imaging Modalities Used in IIM ... 262

5 **Other Idiopathic Inflammatory Myopathies** ... 264

6 **Therapy in Idiopathic Inflammatory Myopathies** ... 264

7 **Infectious Inflammatory Myopathies** ... 264

References ... 266

Abstract

In this chapter, dermatomyositis, polymyositis, inclusion body myositis, and the necrotizing myopathies are discussed in detail with regard to their clinical features, laboratory and histopathological findings, mimics and the imaging findings with magnetic resonance imaging, computed tomography, and ultrasound. With the focus on magnetic resonance imaging, its discriminating role between disorders during the diagnostic work-up, the evaluation of the extent and activity of the disease, and the gathering of information on fat replacement of muscles are considered. Furthermore, its use to locate the best site for a muscle biopsy to enhance the diagnostic yield of a histopathologically confirmed diagnosis and its use during the follow-up of patients in assessing the therapeutic effect of immunosuppressive and immunomodulating therapies and to detect signs of relapse are outlined.

Abbreviations

ATP	Adenosine triphosphate
CK	Creatine kinase
CT	Computed tomography
DM	Dermatomyositis
DWI	Diffusion weighted imaging
EMG	Electromyography
HIV	Human immunodeficiency virus
HLTV-I	Human T cell lymphotropic virus
HMGCR	3-hydroxy-3-methylglutaryl-coenzyme A reductase
IBM	Inclusion body myositis
IIM	Idiopathic inflammatory myopathies
JDM	Juvenile dermatomyositis
MAC	Membrane attack complex
MDA5	Melanoma differentiation matrix protein
MHC	Major histocompatibility complex

U. A. Badrising (✉) · H. E. Kan · J. JGM Verschuuren
Department of Neurology, K5-Q,
Leiden University Medical Centre, Albinusdreef 2,
P.O. Box 9600, 2300 RC, Leiden, The Netherlands
e-mail: u.a.badrising@lumc.nl

M.-A. Weber (ed.), *Magnetic Resonance Imaging of the Skeletal Musculature*, Medical Radiology. Diagnostic Imaging,
DOI: 10.1007/174_2013_860,

© Springer-Verlag Berlin Heidelberg 2013
Published Online: 30 June 2013

MRI	Magnetic resonance imaging
MRS	Magnetic resonance spectroscopy
MSA	Myositis specific antibody
MUAP	Muscle unit action potential
NM	Necrotizing myopathy
NXP-2	Nuclear matrix protein
PCr	Phosphocreatinine
PET	Positron emission tomography
Pi	Inorganic phosphate
PM	Polymyositis
SRP	Single recognition particle
STIR	Short tau inversion recovery

1 Key Points

1. MRI is useful to enhance the diagnostic yield of a muscle biopsy in inflammatory myopathies.
2. The key feature of inclusion body myositis is fatty infiltration, while edema is central in dermatomyositis, polymyositis, and necrotizing myopathy.
3. Whole body (STIR) MRI is best informative with regard to activity and extent of the disease and to detect the best location for a muscle biopsy.
4. MRI can be used to evaluate the effect of immunosuppressive treatment and relapses during follow-up.

2 Introduction

The inflammatory myopathies can be subdivided into infectious and non-infectious myopathies. Among the latter are the idiopathic inflammatory myopathies (IIM) comprising dermatomyositis (DM), polymyositis (PM), inclusion body myositis (IBM), and autoimmune necrotizing myopathy (NM). DM, PM, and NM are often associated with connective tissue disorders, and are then regarded as a part of an overlap syndrome. All IIM are rare sporadic disorders and their annual incidence is estimated at 1–9 per 100.000 inhabitants (Smoyer-Tomic et al. 2012; Furst et al. 2012; Lindberg et al. 1994). The infectious inflammatory myopathies comprise infections with viruses, bacteria, fungi, and parasites. The prevalence of these infections is related to geographical, cultural, dietary and hygienic differences, and food inspection regulations of governments.

This chapter will primarily focus on the non-infectious inflammatory myopathies as magnetic resonance imaging (MRI) is becoming a frequently used imaging modality in these disorders. Those infectious inflammatory myopathies in which imaging is of high importance or those that are of cardinal importance in the differential diagnosis will be addressed as well.

3 Idiopathic Inflammatory Myopathies

3.1 Clinical Presentation

Dermatomyositis has a female predominance (female–male ratio 2:1) and a peak incidence between 30 and 50 years of age. DM presents with an insidious onset (weeks to months) of progressive symmetrical limb muscle weakness, which is predominantly proximal, and neck flexor weakness. In some cases, muscle pain may be present, in particular exercise-induced pain.

Patients may show characteristic skin features such as a purplish discoloration of the eyelids (heliotrope rash) often associated with periorbital edema or a erythematous or violet-colored symmetrical rash over the extensor surfaces of the metacarpophalangeal and interphalangeal joints, elbows, knees, and medial malleoli (Gottron's sign). This rash may evolve into scaly lichenoid papular eruptions (Gottron's papules), but these papules may also be located on the volar side, and then referred to as inverse Gottron's papules. Another characteristic skin abnormality is the erythematous rash on sun-exposed areas such as the face, neck, anterior chest, and upper back ("V-sign" and "shawl-sign"). The nail beds may have dilated capillary loops with periungual hyperemia, and there can be skin ulcerations, livedo reticularis, alopecia, and lipodystrophy. In DM patients with the antisynthetase syndrome (arthritis, Raynaud's phenomenon, and interstitial lung disease) thickened and cracked skin (mechanics' hands) on the volar and dorsal parts of the hands can be present. Skin abnormalities usually precede or appear simultaneously with muscle weakness. The degree of muscle and skin involvement is part of a spectrum with amyopathic DM (also called DM sine myositis), patients with skin features of DM but without clinical evidence of weakness on one side and adermatopathic DM with isolated myositis at the other end. About 20 % of patients with amyopathic DM develop muscle weakness within 5 years during follow-up.

Proximal muscle weakness results into difficulty using the hands above the head and inability to get up from a deep chair or to climb stairs. This pattern of weakness is frequently seen in other myopathies as well. Dysphagia and to a lesser degree dysarthria may occur. In rare cases, cardiomyositis and interstitial lung fibrosis may be features.

DM may present in concurrence of a connective tissue disease. DM is associated with a higher risk of cancer, especially that of adenocarcinoma of the lung, colon and rectum, and of breast and ovarian cancer. The first years after developing DM are associated with the highest odds of a concurrent malignancy, but cancer may also precede DM. Risk factors for cancer include older age, male sex, dysphagia, and cancer associated myositis specific antibodies

(MSA). Therefore, screening for cancer is recommended after diagnosis, but a validated algorithm is lacking so far. This encompasses a thorough medical history and physical examination, including inspection of the skin for melanoma, breast palpation and rectal examination, laboratory testing, computed tomography (CT), scanning of chest and abdomen, colonoscopy in patients above 50 years, and mammography with pelvic ultrasound in women and ultrasound of testis in men under the age of 50. Repeat screening is recommended during 3 years at least annually (Titulaer et al. 2011). Different approaches have also been suggested, such as a yearly positron emission tomography (PET)/CT scan (Selva-O'Callaghan et al. 2010b).

Patients with DM have a mortality risk >10 % to die from disease related causes such as cancer, pulmonary complications, lethal adverse events of drugs used and cardiac complications, especially in the first years after onset.

Juvenile DM (JDM) is the only idiopathic inflammatory myopathy in non-adults. Subcutaneous calcinosis, joint contractures and multisystem involvement are common in JDM in contrast to the adult form. Necrotizing vasculitis of the bowel may cause perforation due to ischemia and necrosis. Nailfold capillary density is diminished in JDM and inversely correlated to disease activity of the muscle and skin.

Polymyositis is considered to be an overdiagnosed, but still a distinct, clinical entity (van der Meulen et al. 2003; Fernandez et al. 2013; Hoogendijk et al. 2004). Some physicians still use the Bohan and Peter criteria to diagnose PM (Bohan and Peter 1975), which do not discriminate inclusion body myositis or DM without a rash as separate disorders from PM, or use PM as an exclusionary diagnosis in patients who do not have a rash or other likely neuromuscular disorder. PM is more common in women and occurs in adults after the age of 20 years. As in DM, symmetric proximal muscle weakness of the limbs progresses subacutely in weeks to months. Muscle pain and tenderness, fever, non-destructive arthritis, mild facial weakness, neck flexor weakness, and dysphagia may accompany limb muscle weakness. PM patients are considered to have a higher chance of an emerging malignancy, but due to ill-defined inclusion criteria in the literature, this remains debatable. PM can be present in conjunction with a connective tissue disorder.

Inclusion body myositis is considered to be the most frequent myopathy after the age of 50 years. There is a male predominance (male–female ratio 2:1) and weakness is usually slowly progressive with mostly asymmetric weakness of distal or proximal muscles, mostly coexistent, with a preference for weakness of the forearm flexors, quadriceps muscles and pharyngeal muscles (Badrising et al. 2000; Needham et al. 2008). This leads to complaints of diminished grip strength, difficulty with rising from low chairs or walking stairs, falls due to buckling of the knees, and dysphagia. Weakness usually commences after the age of 40 and progresses with ventrally located muscles being affected more than dorsally located muscles and shoulder and hip abductors remaining least affected (Badrising et al. 2005). Mean muscle strength decline is estimated at 3.5–5.4 % per year (Badrising et al. 2002; Cox et al. 2011a; Cortese et al. 2013). Myalgia is not a feature of the disease. End-stage disease is accompanied by major disabilities leading to confinement to a wheel chair or bed, recurrent aspiration and cachexia. Life expectancy is not affected by the disorder on group level, but end of life measures are not uncommon at end-stage disease (Cox et al. 2011b; Benveniste et al. 2011).

IBM is associated with autoimmune disorders (Badrising et al. 2004; Koffman et al. 1998). There is no increased risk for malignancy (Cox et al. 2011a).

Autoimmune necrotizing myopathy has a subacute progressive onset of proximal muscle weakness and lacks a rash. Weakness is usually severe within 6 months (Medical Research Counsel scale $\leq$ 3) and can include dysphagia and respiratory failure. Myalgia is common. Data with regard to sex preponderance in prevalence are inconsistent, but in a large cohort of 64 patients a male predominance was found. It can occur after the age of 20, but the mean age of onset is around 57 years (Ellis et al. 2012). NM is associated with cancer preceding or following the myopathy (Bronner et al. 2003). Although the frequency of associated cancer is not clear, screening is advised as in DM. There is also an association with connective tissue disorders, statin-triggered autoimmunity, and viral infections such as acquired immunodeficiency syndrome and hepatitis C (Liang and Needham 2011). Statin-induced autoimmune NM may occur up to 10 years after initiation of a statin and can advance many months after discontinuation of a statin (Grable-Esposito et al. 2010).

3.2 Laboratory Findings

In DM patients, serum creatine kinase (CK) is elevated up to 50 times the upper limit of normal, but can be normal in <10 % of patients, regardless of its presentation within the clinical spectrum. The most common MSA in DM patients is the Jo-1 (histidyl t-RNA synthetase) antibody, associated with the antisynthetase syndrome. Less common anti-synthetase antibodies are anti-PL-7, anti-PL12, anti-EJ, anti-OJ, and anti-KS, occurring only in 1–3 % of patients. Usually no more than one antibody is found in a patient. Suspicion of interstitial lung disease, a major cause of morbidity and mortality, which is part of the antisynthetase syndrome, warrants pulmonary consultation, chest imaging, and pulmonary function testing. Anti-P155/140 antibody is associated with an increased risk of a malignancy in adult DM and with severe cutaneous juvenile DM. Anti-MJ directed toward the nuclear matrix protein (NXP-2) is associated with cancer in adult DM patients and is the most common MSA in juvenile DM. Anti-CADM-140 directed against the melanoma differentiation associated gene 5 (MDA5) is associated with DM with only mild inflammation in the muscle biopsy and clinically amyopathic DM. Highly specific for DM and suggestive of an encouraging outcome are anti-Mi-2 antibodies, which are more infrequent in Caucasians, and occur in 15–30 % of DM patients.

Electromyography (EMG) shows a myopathic pattern with low amplitude, short duration polyphasic motor unit action potentials (MUAPs) with spontaneous muscle fiber activity (fibrillations, positive sharp waves, and complex repetitive discharges) and early recruitment. In chronic patients, MUAPs become longer in duration.

In PM, serum CK is 5–50 times the upper limit of normal and correlates well with treatment response (decrease) or relapse (increase). Several anti-synthetase antibodies have been described in PM, but precise frequencies remain obscure as a result of differences in disease definition. In the "pure" PM form MSA are perhaps rare. They probably represent the presence of an overlap syndrome.

EMG findings in PM are similar to those of DM patients.

In IBM, serum CK levels may be normal or elevated up to 12 times the upper limit of normal. Recently, two study groups independently described an autoantibody targeted against cytosolic 5'-nucleotidase 1A (Mup44) present in 25–40 (33) % of IBM sera and it is only rarely found in other neuromuscular disorders and is absent in normal sera (Pluk et al. 2012; Salajegheh et al. 2011). In up to 30 % of patients, EMG shows a mild sensory neuropathy on nerve conduction studies. Needle EMG shows the pattern of a myopathy but can be confusing as some patients may show a mixed myopathic-neuropathic pattern with high amplitude MUAPs overshadowing the small ones leading to a wrong conclusion of a motor neuron disorder.

In NM, serum CK is more than 10-fold elevated. NM with rapidly progressive and severe weakness and an onset during fall has been related to anti signal-recognition particle (SRP) antibodies. This type of NM is regularly steroid-resistant (Miller et al. 2002; Fernandez et al. 2013). An Australian study detected no anti-SRP autoantibodies in stored serum of a retrospective NM series and casted doubt on the previous association (Ellis et al. 2012). In progressive statin-associated autoimmune myopathy antibodies against 3-hydroxy-3-methylglutaryl-coenzyme A reductase (HMGCR) can be found and used to discriminate from self-limited statin induced myopathy with improvement after discontinuation of the statin (Mammen et al. 2011). EMG shows small amplitude, short duration, polyphasic motor unit potentials with sometimes fibrillations, and positive sharp waves and complex repetitive discharges. Electrical myotonia is prominent according to some but has not been formally studied, and has been described in cases with self-limited statin induced myopathy (Dimachkie and Barohn 2012).

3.3 Histopathology and Pathogenesis

DM is considered to be a complement-mediated microangiopathy. The first histopathologic manifestation consists of the perivascular deposition of immune complexes of membrane attack complex (MAC) i.e. the C5b-9 of complement. Due to destruction of capillaries and ischemia muscle biopsies may show atrophic, degenerating, and regenerating myofibers often with a perifascicular distribution. Inflammatory infiltrates consist of B cells, macrophages and plasmacytoid dendritic cells and have a perimysial or perivascular location. They present a presumed antigen to naïve CD4 + T-lymphocytes. MAC deposition helps to discriminate DM from other myopathies. Invasion of non-necrotic fibers is not a feature of DM.

PM muscle biopsies are considered to signify a cell-mediated cytotoxic immune response against the muscle fiber. Besides atrophic, hypertrophic, necrotic, and regenerating fibers focal mononuclear infiltrates with a predominantly endomysial location and consisting of mainly CD8 + cytotoxic T cells that surround and invade non-necrotic fibers that express major histocompatibility complex (MHC) class I molecules on their sarcolemma are present. It is assumed that MHC-1 antigens express an undetermined peptide that acts as an autoantigen (Arahata and Engel 1986, 1988).

IBM muscle biopsies show the same features as in PM and therefore PM muscle biopsy features are not considered distinctive. Thirty-seven percent of patients with histopathological PM have the clinical features and clinical course of IBM patients (Chahin and Engel 2008). Apart from the inflammation the muscle biopsy in IBM shows degenerative changes such as "rimmed vacuoles," which are seen in fresh frozen muscle biopsy specimens stained with hematoxylin-eosin or Gomori trichrome. These vacuoles contain amorphous material. With electron microscopy tubulofilaments with a 15–21 nm diameter can be observed near rimmed vacuoles or the nucleus. Degenerative proteins such as hyperphophorylated tau and β-amyloid accumulate near these tubulofilamentous structures. The precise connection between the degenerative and inflammatory changes remains elusive.

NM is characterized by widespread necrosis, surrounded by macrophages, and regeneration of muscle fibers, which contradicts in abundance to the lack of inflammation and absence or minimal MHC-I staining of non-necrotic fibers.

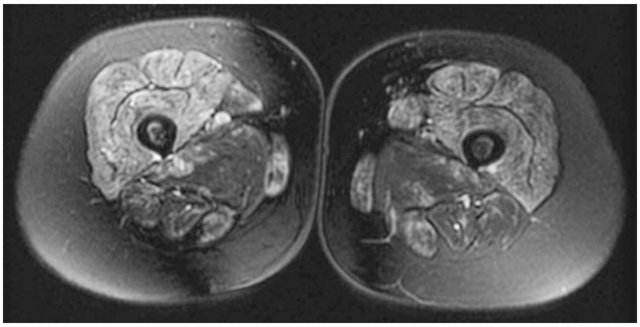

Fig. 1 Axial spectral presaturation with inversion recovery image of the thigh with more or less symmetric hyperintensities of mainly the anterior compartment in DM. Fat suppression is not uniform over the leg

4 Imaging in Idiopathic Inflammatory Myopathies

4.1 Magnetic Resonance Imaging in Idiopathic Inflammatory Myopathies

MRI in inflammatory myopathies is usually directed at assessment of muscle anatomy and fatty infiltration on T1-weighted images, and assessment of muscle edema as a sign of inflammation on fluid-sensitive sequences consisting of fat-suppressed T2-weighted images or short tau inversion recovery (STIR) images (Fig. 1). MRI is used as a noninvasive diagnostic tool but also as a longitudinal follow-up tool for therapeutic monitoring and outcome, and has the advantage that previous images of the same patient obtained in a similar scanner can mostly be reliably compared. A second important reason to perform MRI in IMM is to guide muscle biopsies. Blind muscle biopsies may be false-negative in 10–45 % of myositis patients (Bohan et al. 1977; Schweitzer and Fort 1995).

Thigh muscles that are affected on MRI in DM/PM patients show a significantly higher number of inflammatory cells in muscle tissue after a muscle biopsy compared to non-affected MRI muscles of the same patients, thus perhaps indicating an increase in the yield of a histological diagnosis after MRI-guided biopsy (Tomasova Studynkova et al. 2007).

The cost effectiveness of MRI in suspected PM is evaluated in a small study of 25 patients through comparing false-negative biopsies in patients with biopsies based upon MRI results versus untargeted biopsies. False-negative results are reported in one of 14 patients after MRI-guidance biopsies and in 5 of 11 without MRI guidance. MRI prior to biopsy has been associated with a medical costs reduction from 20,000 USD to 14,000 USD, which the authors presented as cost-effective. These costs are outdated and cannot be used at present as patients were admitted for many days, which was included in the price as were other ancillary investigations (Schweitzer and Fort 1995; Fleckenstein 1996). A 1994 study in the Washington DC area found that the cost of performing and interpreting an MRI ranged from 680 to 1030 USD whereas the costs for performing a muscle biopsy and interpretation ranged from 1520–2400 USD. The authors concluded that MRI might be more cost-effective than repeat biopsy (Adams et al. 1995). So far consensus is lacking on this subject.

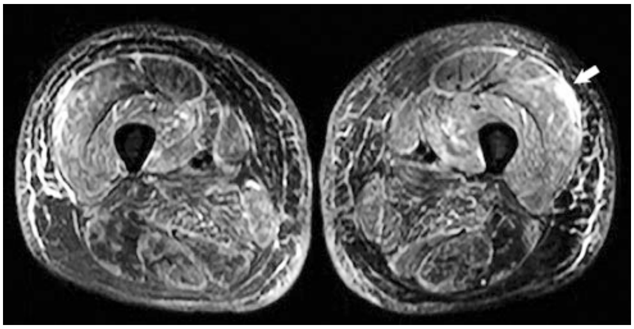

Fig. 2 Axial STIR images of the thigh in a different patient with DM with hyperintensities of mainly the anterior compartment and fascia with chemical shift artifact between skin and subcutis (*arrow*)

In IIM, STIR sequences are preferred over fat-saturated T2-weighted sequences due to their more uniform fat suppression (Fig. 2). Administration of gadolinium appears to have no advantages compared to T2-weighted images (Reimers et al. 1994) or in comparison to STIR and fat suppressed T2 images (Dion et al. 2002). MRI protocols in IIM commonly contain axial slices of several muscle groups aimed at the highest probability of finding diagnostically helpful features. The upper legs are preferentially studied, because they are often affected, and are an easy target for a muscle biopsy.

Increasingly, whole-body MRI becomes available to clinicians (see also MRI in Muscle Dystrophies and Primary Myopathies of this book). It has the advantage to detect areas of muscle inflammation in clinically unsuspected muscles, which may even be easily accessible for a muscle biopsy (Cantwell et al. 2005). Furthermore, it gives an overall picture of the anatomic distribution and size of lesions, and expands our knowledge about disease variability as muscles such as the intercostal muscles have now observed to be also affected by the disease process and inflammation can be visualized in cases of suspected amyopathic DM (Fig. 3). Whole-body STIR MRI can be done in 15–30 min, depending on respiratory triggering and the number of coronal slices needed on each level (O'Connell et al. 2002). Whole body T1-weighted MRI can be done even faster.

The hyperintensity observed on STIR or fat-suppressed T2-weighted images, is often regarded as muscle edema, an unspecific sign. It can be subtle, focal, diffuse, inhomogeneous, and with ill demarcated margins and be the result of

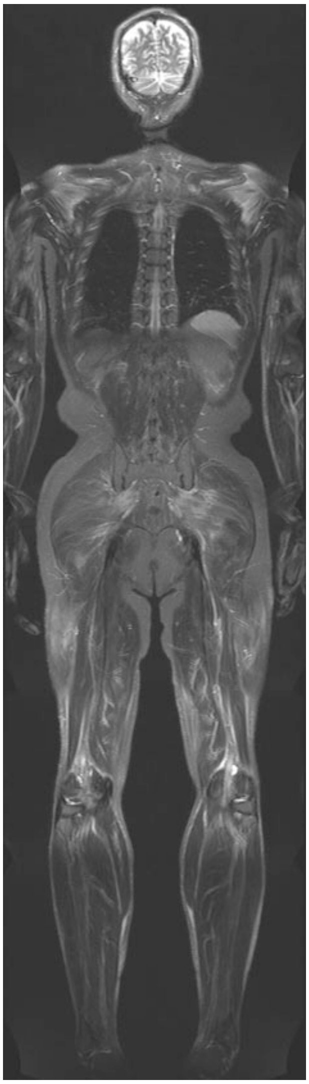

Fig. 3 Coronal STIR MR whole body image of a 56-year-old patient with DM. Symmetrical edema-like changes are present within the shoulder girdle and the thighs, as well as the gluteal muscles (image courtesy of Prof. Dr. M.-A. Weber, Heidelberg)

muscle injury, inflammation, interstitial fluid overload or (sub)acute denervation. Apart from inflammatory myopathies, muscle edema is also observed, diffuse or focal, in muscular dystrophies such as Duchenne's muscular dystrophy, fascioscapulohumeral dystrophy and myotonic dystrophy, metabolic myopathies, toxic myopathies, infectious myopathies, congenital myopathies such as minicore disease, muscle channelopathies such as hypokalemic periodic paralysis, rhabdomyolysis, sports injuries, after acute exercise, but also in neurogenic lesions, including neuropathies such as hereditary motor and sensory neuropathies and spinal muscular atrophy. Apart from metabolic myopathies these increased T2 signal intensities are usually infrequent, relative and unspecific (Schedel et al. 1992, 1995).

In a small series of DM and PM patients, MRI has been shown to have a sensitivity of 100 %, a specificity of 88 %, a positive predictive value of 77 %, and a negative predictive value of 100 %, as compared to histopathological diagnosis (Weber et al. 2006). Another larger study reported a sensitivity of 80 % (Reimers et al. 1994). So far, only studies in 0.5–1.5 T MRI have been published on the subject of IIM.

4.2 Muscle Involvement Patterns in IIM on MRI

The number of studies looking at MRI abnormalities in DM is limited. Focal or diffuse areas with high signal intensity on fat-suppressed T2-weighted images are the most common findings. These areas suggest edema or inflammation and are preferentially located in proximal muscles and tend to be more or less symmetrical. In unusual cases, however, a unilateral distribution can be seen (Reimers et al. 1994). Within these high signal intensity areas, signal intensities may fluctuate. There is a preference for involvement of the four heads of the quadriceps muscles and the dorsiflexors of the lower legs. Least affected muscles are the pectineus, obturatorius, thigh adductors, biceps femoris caput brevis, gracilis, soleus and caput laterale of the gastrocnemius (Reimers et al. 1994). There can be diffuse or focal subcutaneous edema, and edema may show a myofascial pattern in some muscles (Cantwell et al. 2005; O'Connell et al. 2002; Schulze et al. 2009; Yoshida et al. 2010).

In PM studies, the problem of uncertainty with regard to the correct diagnosis at inclusion reappears. Reported MRI studies may be hampered by unjustly including IBM patients or DM patients without a rash and consequently the results of these PM studies are less reliable. In those studies where IBM patients have been excluded inflammation is a more prominent feature than fatty infiltration (Cantwell et al. 2005; Dion et al. 2002; Reimers et al. 1994). Patients may have inflammation as a sole manifestation, thus in the absence of fatty infiltration. Both, however, are located preferentially in proximal limb muscles with a more or less symmetrical distribution. Most studies focused on abnormalities in the legs. Muscles with high signal intensity on fat-suppressed T2-weighed images are most frequently the vasti of the quadriceps, the anterior tibial and the caput laterale of the gastrocnemius. Fatty infiltration is preferentially observed in the hamstrings, vastus muscles of the quadriceps, and the gastrocnemius.

Least affected muscles by inflammation are the gracilis, peroneal, extensor digitorum, posterior tibial, flexor digitorum, and flexor hallucis longus muscles. Comparatively spared from fatty infiltration are the rectus femoris, gracilis, posterior tibial, and soleus muscles (Reimers et al. 1994). During treatment, inflammatory changes on MRI resolve but without a clear clinical correlation.

The MRI hallmarks of IBM are inflammation, fatty infiltration and (asymmetric) atrophy, with fatty infiltration

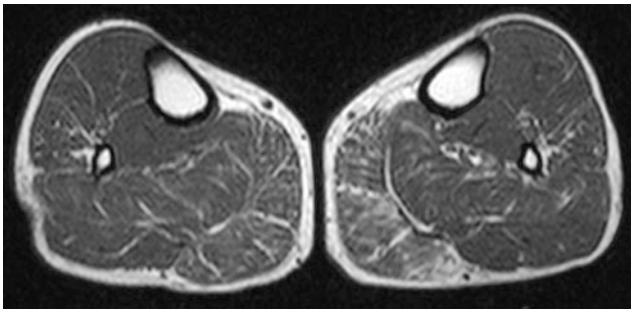

Fig. 4 Axial T1-weighted images of the lower legs showing the beginning of preferential and asymmetric fatty infiltration of the medial gastrocnemius muscle, most pronounced on the left side, in inclusion body myositis

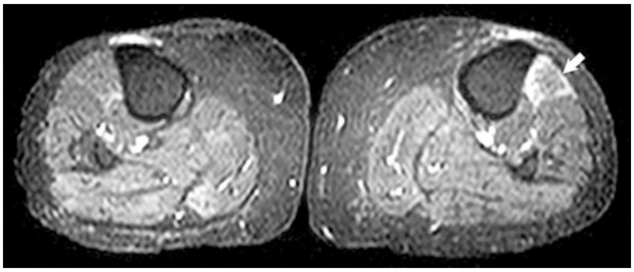

Fig. 5 Axial STIR images through the lower legs showing hyperintensity in the left anterior tibial muscle (*arrow*) in inclusion body myositis

as the most noticeable feature (Fig. 4). Inflammation is erratically present, most often in a patchy focal nature (Fig. 5). It is repeatedly found in the extensor carpi ulnaris, soleus and gastrocnemius muscles.

Fatty infiltration is more prominent in the legs than in the arms, and the lower legs have less muscle bulk left compared to the upper legs. The upper arms are more affected than the shoulder girdle muscles and in the forearm the deep finger flexors appear to be the most vulnerable to fatty infiltration. In the upper legs, the ventral muscles are more affected than the dorsal muscles and adductors, with sparing of the rectus femoris muscle (Phillips et al. 2001). In the lower legs, the medial part of the gastrocnemius muscle appears to be the most susceptible for fatty infiltration, and the lateral head is often spared (Cox et al. 2011a).

Asymmetry of muscle bulk usually follows the clinical pattern of muscle weakness distribution and that of fatty infiltration of muscle groups. Disease duration, the degree of muscle weakness, and functional disability scores correlate well with the level of fatty infiltration in IBM. Fatty infiltration is more usual and apparent in IBM than in PM. Inflammation is less obvious in IBM than in PM and does not relate to the level of weakness.

MRI in NM (Fig. 6) has hardly been reported and shows edema of the thigh muscles (100 %), muscle atrophy (75 %), fatty replacement (67 %), and fascial edema (25 %) in a selection of 16 patients with auto-immune associated necrotizing myopathy (Christopher-Stine et al. 2010).

4.3 Other Magnetic Resonance Imaging Techniques in IIM

Phosphorous magnetic resonance spectroscopy (MRS), ^{31}P MRS, is used to assess energy metabolism in muscle. With this technique, high energy phosphate metabolites phosphocreatinine (PCr), adenosine triphosphate (ATP), and inorganic phosphate (Pi) can be assessed as well as tissue pH (see also chap 8 of this book). In the quadriceps muscles of DM patients, elevated levels of the ratio of Pi/PCr are observed, which is attributed to lower levels of PCr. During exercise, PCr levels drop further compared to controls and the recovery of PCr after exercise is slower in these patients. In addition, the level of phosphorylated sugars is increased compared to control subjects (Park et al. 1990). These changes all indicate disturbed energy metabolism, both at rest and during exercise, and show problems with oxidative ATP production. Interestingly, these abnormalities are also found in mitochondrial dysfunction. The problems in DM are not thought to be due to impaired mitochondrial function, but are due to reduced oxygen supply by the vessels. Also in PM, problems with oxidative ATP production are found, which is in contrast to IBM, where PCr recovery after exercise is normal. In IBM, lower levels of PCr and increased levels of Pi are observed (Argov et al. 1998; Lodi et al. 1998; Cea et al. 2002).

Diffusion-weighted imaging (DWI) enables quantification of the apparent diffusion coefficient, a measure of random motion of water. Using sophisticated models, diffusion of water within the muscle fibers and in the capillary bed can be separated. Using this technique, skeletal muscles of DM and PM patients that appear normal on T1 and T2 weighted images also show no differences in diffusive properties compared to healthy muscles. Muscles with inflammation showed increased diffusion values, which agree with an increase in the amount of fluid in these muscles. In contrast, muscles with fat infiltration show decreased diffusion values, in agreement with a reduction in water content. Interestingly, modeling of the diffusion signal indicates that there is a reduced perfusion volume in muscles with inflammation, which could be due to a reduced capillary bed (Qi et al. 2008).

Magnetic resonance elastography is a method to measure muscle stiffness based upon the propagation of shear waves. A decrease of muscle stiffness is found in patients with PM/DM/JDM (McCullough et al. 2011). Wave attenuation, a viscoelastic parameter, is significantly different in healthy

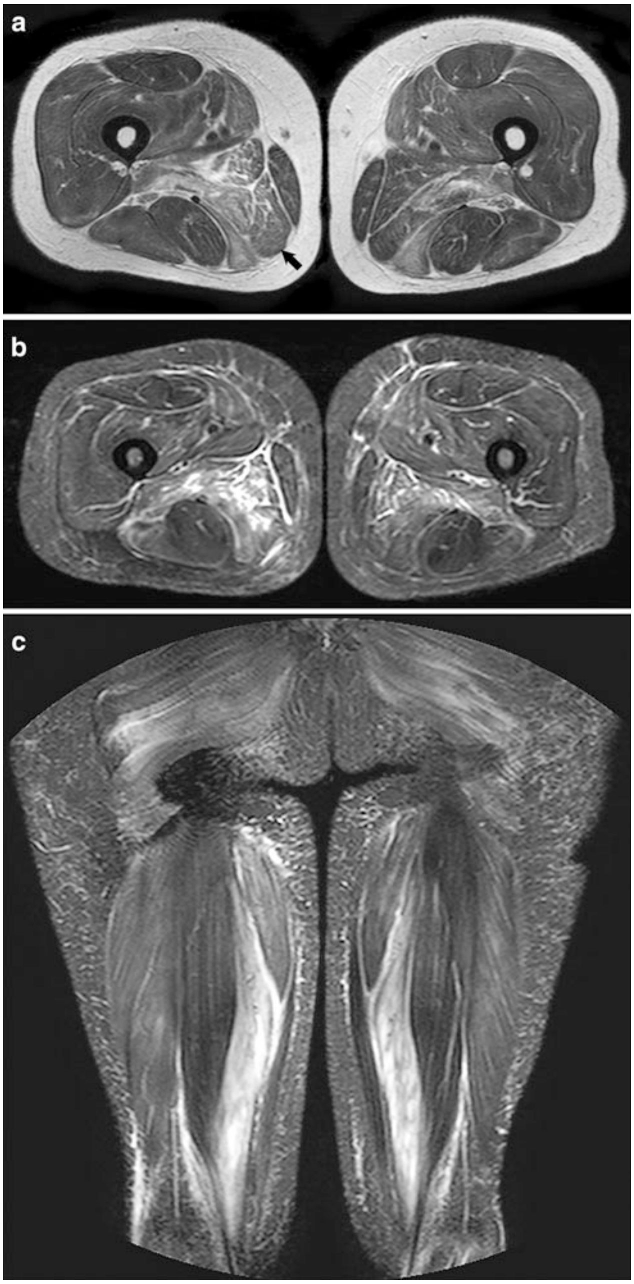

Fig. 6 **a** Axial T2-weighted images (without fat suppression) of the thigh in a patient with necrotizing myopathy with hyperintensities of preferentially the dorsomedial compartment (*arrow*) and fascia **b** Axial STIR images of the thigh of the same patient as in Fig. 5a **c** Coronal STIR images of the same patient as in Fig. 6a

muscles compared to muscle of patients with DM/PM (Domire et al. 2009).

Quantitative and semi-quantitative assessment with MRI has been done by measuring the T2 relaxation time as well as by visual or automated assessment of signal intensity values on fat saturated T2-weighted or STIR images. An increased T2 relaxation time gives rise to increased signal intensity on STIR or fat-suppressed T2-weighted images, but can also be quantitatively and semi-quantitatively assessed to enable a more objective and accurate measure of muscle edema. While this has significant advantages in terms of therapy follow-up or disease monitoring, in severely atrophied and fat infiltrated muscles it is impossible to measure the T2 relaxation time accurately. In the acute phase of DM and PM, semi-quantitative visual analysis of signal intensity correlates well with global disease activity and muscle disease activity (Tomasova Studynkova et al. 2007).

In response to treatment, MRI intensity parameters on STIR and T2-weighted fat-suppressed images improve (Reimers et al. 1994; Fujino et al. 1991). This improvement precedes improvement of muscle biopsy features in a second biopsy (Tomasova Studynkova et al. 2007). Another method based upon pixel intensity values is the myositis index, which uses a histogram of intensity values obtained from STIR images. This method appears to be equally sensitive to changes on MRI in PM, DM, and one patient with IBM as visual analysis (Bartlett et al. 1999).

Whether swift improvement of MRI abnormalities is predictive of a favorable outcome remains to be studied. In JDM, T2 values were measured and compared to inactive JDM. The T2 relaxation time is significantly increased in active JDM and correlates with muscle strength (Maillard et al. 2004).

In IBM, the increased T2 relaxation time of the quadriceps and hamstring muscles is related to the level of muscle weakness (Phillips et al. 2001). In adults, fat-corrected muscle T2 maps may become a useful marker of disease activity (Yao and Gai 2012).

4.4 Other Imaging Modalities Used in IIM

Computed tomography scanning in the inflammatory myopathies can be useful in muscle imaging in IBM, but is less informative in PM and least in DM and NM. CT has a good spatial resolution, but lacks the contrast resolution of MRI to distinguish smaller muscles from each other. In IBM, CT is able to detect fatty infiltration, muscle atrophy, and asymmetry, but inflammation is missed as is the case in the other types of immune-mediated myopathies. Although CT scanning is widely available, faster, less sensitive to motion artifacts and cheaper, it has the disadvantage of ionizing radiation exposure and is less informative compared to MRI, especially in detecting edema-like muscular changes. Therefore, MRI is the preferred imaging modality unless contraindications exist, such as certain metal implants like pacemakers and cochlear implants or claustrophobia, making it impossible to use. CT is superior in detecting muscle calcifications.

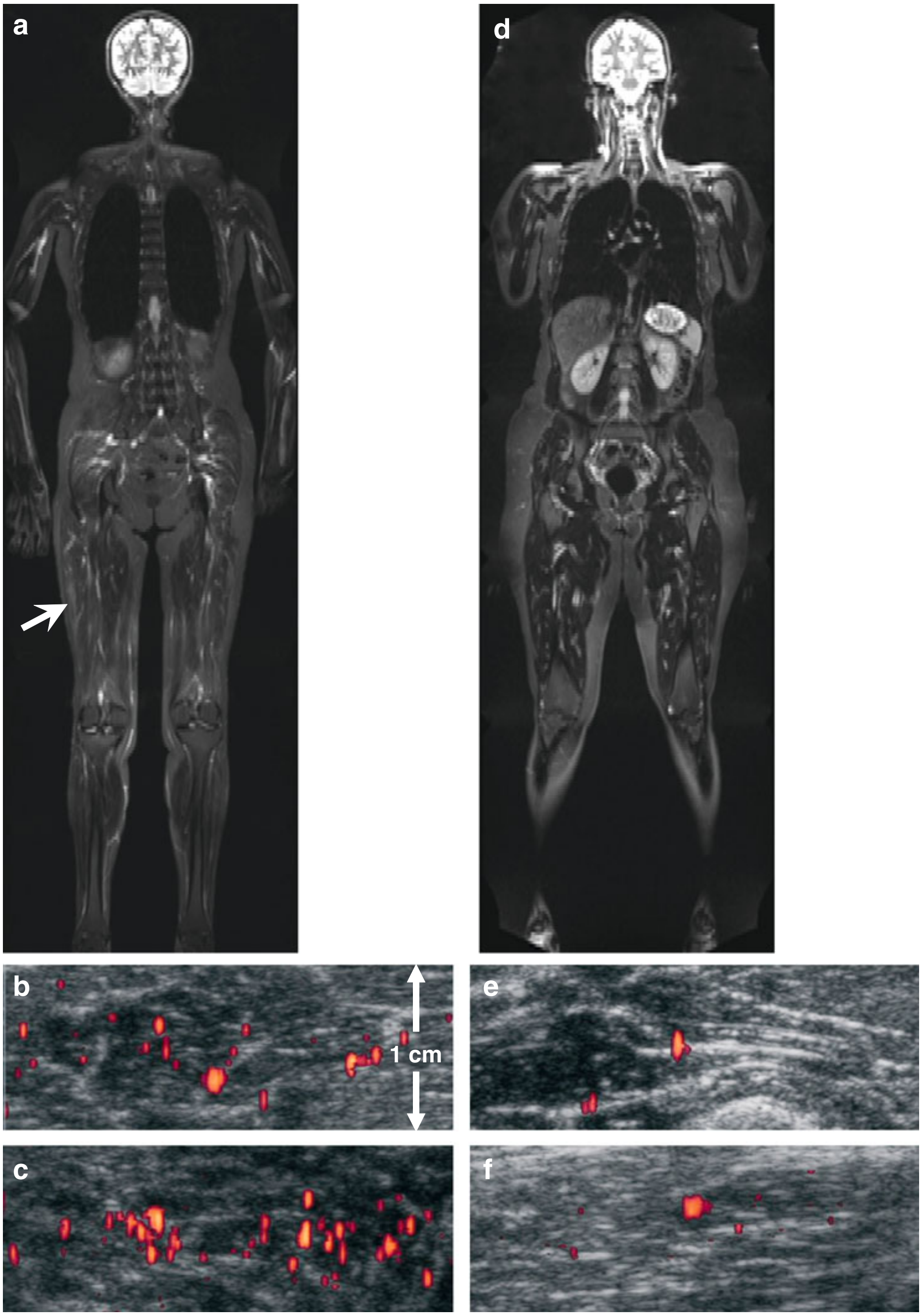

Fig. 7 **a**–**c** 64-year old woman with DM. **d**–**f** 36-year old woman with final diagnosis of collagenosis and exclusion of myositis on histologic analysis. **a** and **d** Whole-body MR imaging using a fat-suppressed T2-weighted short tau inversion recovery sequence. Transverse images of power Doppler sonography (7 MHz) after bolus injection of 10 mL Levovist in 1.5 cm depth (focus area) showing initial increase **b**, **e** and maximum plateau **c**, **f**) of microbubbles' replenishment. In DM, a focal area of moderate signal enhancement in the right vastus lateralis muscle is visible (*arrow* in **a**), whereas in the other patient, muscles are free of pathological signal alterations **d**. The corresponding contrast-enhanced power Doppler signals clearly visualize the higher concentration of microbubbles in muscle tissue of the woman with myositis **b**, **c** due to the higher muscle perfusion. Reprinted from Weber et al. (2006) J Neurol 253: 1625–1632 with permission from Springer

Muscle ultrasonography can be used to detect inflammation in muscles and has, in particular, been described in PM and DM patients. Affected muscles show increased echogenicity and the fasciae and septa become obscured and the normal architecture changes. Contrast-enhanced intermittent power Doppler ultrasound in PM and DM showed significant higher blood flow velocities, blood volume, and blood flow compared to patients without myositis, with blood flow being the best measure for DM and PM with a sensitivity of 73 %, a specificity of 91 %, a positive predictive value of 80 %, and a negative predictive value of 88 % (Weber et al. 2006) (Fig. 7). Ultrasound is compared with MRI often readily available, not distressing, and easy to do without contraindications and cheap. Reproducibility may vary between sonographers. Ultrasound can be used for muscle biopsy guidance as well to reduce the false-negative rate. MRI, however, gives a more global scope on involvement because more muscles and even deeply located muscles are investigated at once than with ultrasound. Calcifications can also be detected by ultrasound as bright echogenic foci with acoustic shadowing.

Scintygraphy has been used to assess myositis using technetium (Tc 99 m), gallium (Ga 67), and indium (In111) altumomab pentetate-labeled antimyosin antibodies. Uptake of antimyosin antibody in the legs correlates with myositis activity based on CK levels (Lofberg et al. 1998). Scintigraphy lacks the ability to distinguish between lesions in different muscle groups and does not reflect atrophy or fatty infiltration compared to MRI.

Swallowing video-fluoroscopy is the method of first choice to objectively assess dysphagia. Dysphagia is common in the idiopathic inflammatory myopathies. Obstruction due to cricopharyngeal dysfunction, vallecular and piriform sinus residues, pharyngeal weakness, diverticula and aspiration can be visualized.

18F-fluorodeoxyglucose-PET/CT has limited value in detecting active inflammation in PM and DM patients because of its low sensitivity; the diagnostic yield is lower than that of EMG, MRI, and muscle biopsy (Owada et al. 2012). However, it is useful in the detection of malignancies and one study group advocates that it is equally sensitive to conventional screening with CT scanning of the chest and abdomen, mammography, gynecological screening, ultrasonography, and tumor marker analysis (Selva-O'Callaghan et al. 2010a). However, cost and accessibility have to be weighed against personal convenience and distress of these investigations.

5 Other Idiopathic Inflammatory Myopathies

Granulomatous myositis can occur in isolated form, as part of sarcoidosis or secondary to a disorder associated with skeletal muscle granuloma such as inflammatory bowel disease, thymoma, myasthenia gravis, and lymphoma. It can be asymptomatic or present as a subacute or chronic myositis. The acute form presents with proximal muscle weakness, whereas the chronic form can evolve into a clinical picture that is indistinguishable from IBM (Le Roux et al. 2007; Larue et al. 2011). On MRI of the thigh, preferential affliction by fatty replacement in the adductors and semimembranosus muscles, with relative sparing of the rectus femoris and semitendinosus muscles has been described in chronic cases (Reimers et al. 1994), but given the small numbers of patients investigated is it still uncertain whether MRI may be helpful in discriminating between IBM and isolated granulomatous myositis.

Eosinophilic polymyositis occurs as part of the hypereosinophilic syndrome with an idiopathic rise of eosinophils causing infiltration and clinical signs and symptoms of the involved organs. There is slow onset of muscle aching with weakness of proximal muscles. There can be skin changes, Raynaud phenomenon, and small hemorrhages of the nail beds. Serum CK is elevated and the muscle biopsy shows predominantly eosinophilic infiltration, scattered necrosis, and regeneration of muscle fibers. MRI data are scarce, but suggest a diffuse and irregular hyperintensity of muscle on STIR images (Hundt et al. 1999; Layzer et al. 1977).

6 Therapy in Idiopathic Inflammatory Myopathies

The first line of treatment in DM and PM is administration of corticosteroids, based on empirical data, in order to improve muscle strength. High dose prednisolone is given during 6–8 weeks and then tapered off during a year. Pulsed oral dexamethasone compared with daily oral prednisolone is equally effective, but the latter has more side effects but a longer median time to relapse (van der Meulen et al. 2000). A second immunosuppressive agent (azathioprine, methotrexate, cyclophosphamide, cyclosporine A) is added in case of relapse, ineffective treatment, failure to lower the prednisolone dose in time, or in order to minimize side effects. Sometimes intravenous immunoglobulin is used. Treatment of a concurrent neoplasm can result in improvement or fading of clinical symptoms.

In IBM, none of the immunosuppressive or immunomodulating therapies tested have shown long-term benefit, neither improvement, nor stabilization of the disorder. Intravenous immunoglobulin may temporarily improve dysphagia.

Chronic obstructive dysphagia in the IIM can be treated with a cricopharyngeal myotomy. Botulinum toxin injections have been reported to be effective as well. Sometimes a percutaneous gastrostomy is needed to prevent cachexia and orally administered fluid or food aspiration.

7 Infectious Inflammatory Myopathies

The infectious inflammatory myopathies can be split up into viral, parasitic, fungal, and bacterial myopathies. Apart from infectious myositis via the direct infection of skeletal muscle, microorganisms may also cause myositis past immune mechanisms. Bacterial myositis ordinarily presents with focal infection of the muscle, whereas viruses and parasites present with a more diffuse clinical picture of widespread myalgia or multifocal muscle involvement.

Acute viral myositis is a disorder following a short illness, usually accompanied by fever, associated with a viral infection. The most common symptom is myalgia, but muscle tenderness and swelling, weakness, and a moderately elevated serum CK can accompany this disorder. Benign acute childhood myositis begins within a week after developing symptoms like malaise, fever, sore throat, headache, nausea or rhinorrhea, and usually starts with pain of the calves, gait difficulties, and sometimes leading to refusal to walk. It most commonly resolves within a week (Middleton et al. 1970; Rubin et al. 2010). It is related to an Influenza virus infection but has also been described after adenovirus, parainfluenza virus, respiratory syncytial virus, and herpes simplex virus infections. Muscle biopsies of the gastrocnemius muscle may show necrosis and mononuclear inflammatory infiltrates depending on the time between the biopsy and initial symptoms. Influenza virus myositis in adults is uncommon, but when present, weakness and tenderness are more diffuse compared to children.

Overall, acute viral myositis in adults is rarely described in large series, but has been associated in small series and case reports with many viruses, such as Epstein-Barr virus, echovirus, cytomegalovirus, human immunodeficiency virus (HIV) type I, adenovirus, herpes simplex virus, hepatitis B and C, dengue virus, and parainfluenza virus.

Subacute viral myositis, resembling adult-onset PM, typically occurs in retrovirus-related viral infections, such as HIV and human T-cell lymphotropic virus type I (HLTV-I). HIV polymyositis starts with proximal symmetric weakness of the legs, which extends to the proximal arm muscles, with or without muscle wasting. Serum CK is elevated 10–15 times the upper limit of normal. Muscle biopsy shows perivascular, perimysial or endomysial, predominantly mononuclear, infiltrates surrounding and invading non-necrotic muscle fibers, with necrosis and degeneration (Johnson et al. 2003). Muscle MRI shows hyperintensity on T2-weighted sequences and isointensity on T1-weighted images (Restrepo et al. 2004). HLTV-I polymyositis occurs in regions where HLTV-I is endemic such as in the Caribbean region (especially Jamaica and Haiti).

The most common parasitic infections of muscle are trichinosis, toxoplasmosis, and cysticercosis. Trichinosis, caused by the nematode *Trichinella spiralis*, is characterized by a period of nausea, anorexia, diarrhea, and abdominal pain followed by fever, muscle pain, and tenderness of particularly proximal muscles and muscle weakness. There can be skin involvement resembling that of DM. The infection is transferred through inadequately cooked meat of pork, bear, and walrus. The diagnosis can be confirmed by serum antibodies against Trichinella or by identification of *Trichinella* larvae in the muscle biopsy. Toxoplasmosis, caused by *Toxoplasma gondii*, can mimic polymyositis and DM, usually in immune-compromised hosts. The myositis can appear to be present alone with fever and lymphadenopathy or may be accompanied by other features such as pneumonia, hepatitis, uveitis, meningoencephalitis, hepatosplenomegaly, hepatitis, or chorioretinitis. The diagnosis can be established by serological tests, but can also be established by isolation of *T. gondii* from blood or demonstration of cysts or trophozoites in the muscle biopsy or other histological specimens. Muscle biopsy shows inflammation with lymphocytes, histiocytes, and giant cells in the perimysium and endomysium. Transmission of the infection usually occurs through ingestion of ill cooked meat and through contact with feces of cats. Cysticercosis is caused by *Taenia solium* and transmitted through ingestion of *T. solium* eggs excreted in the feces of human carriers of the tapeworm. Infestation of the muscle is often asymptomatic and accidentally discovered on radiographs of muscles with calcified cysts with a “puffed rice” presence. In rare cases, it may present as a pseudohypertrophic myopathy with symmetric enlargement and tenderness of muscles, in particular of the calf muscles. Muscle MRI, CT, and ultrasound investigations may all show cysts, however MRI is superior in detecting cysts and CT is superior in visualizing calcifications The scolex is best seen with ultrasound (Jankharia et al. 2005). Ultrasound reveals an intramuscular anechoic area with an eccentric echogenic intraregional focus suggestive of scolex. MRI shows oval cysts with hypointense signal on T1 and hyperintense signal on T2-weighted images. There is perilesional contrast enhancement, suggestive of edema, and the lesions are oriented along the muscle fiber direction (Tripathy et al. 2012). The diagnosis is confirmed by serological or histological testing. American trypanosomiasis, also called Chagas disease, may present with a PM/DM syndrome in the beginning of the disease. Diagnosis is made by demonstrating *T. cruzi* in the blood or in tissue. Transmission occurs through a bite from an infected vector, the *reduviid* bug, or through blood transmission. A travel history to an endemic region or eosinophilia in blood should give rise to the suspicion of a parasitic infection. Other parasites giving cause to myositis or myalgia are *Sarcocystis spp.*, *Entamoeba histolytica*, *Echinococcus spp.*, *Toxocara canis*, *Microsporidia spp.*, *Schistosoma spp.*, *Spirometra mansonoides*, *Plasmodium falciparum*, and *Onchocerca volvulus*.

Fungal myositis is especially seen in the immune-compromised host. The most common infections are with *Cryptococcus neoformans*, *Histoplasma capsulatum*, *Aspergillus spp.*, *Coccidiodes spp.*, *Pneumocystis jiroveci*, *Fusarium spp.*, and *Candida spp.*, *Candida spp.* gives rise to multiple diffuse microabscesses, which can be localized with ultrasound, CT, and MRI imaging for the purpose of muscle biopsy for diagnostic confirmation.

Bacterial muscular infections can be related to infection through extensio per continuitatem by nearby open wounds or penetrating trauma or through hematogenous spread. The etiology of the infection is related to the type of bacteria involved. In hematogenous dissemination, *Stafylococcus*

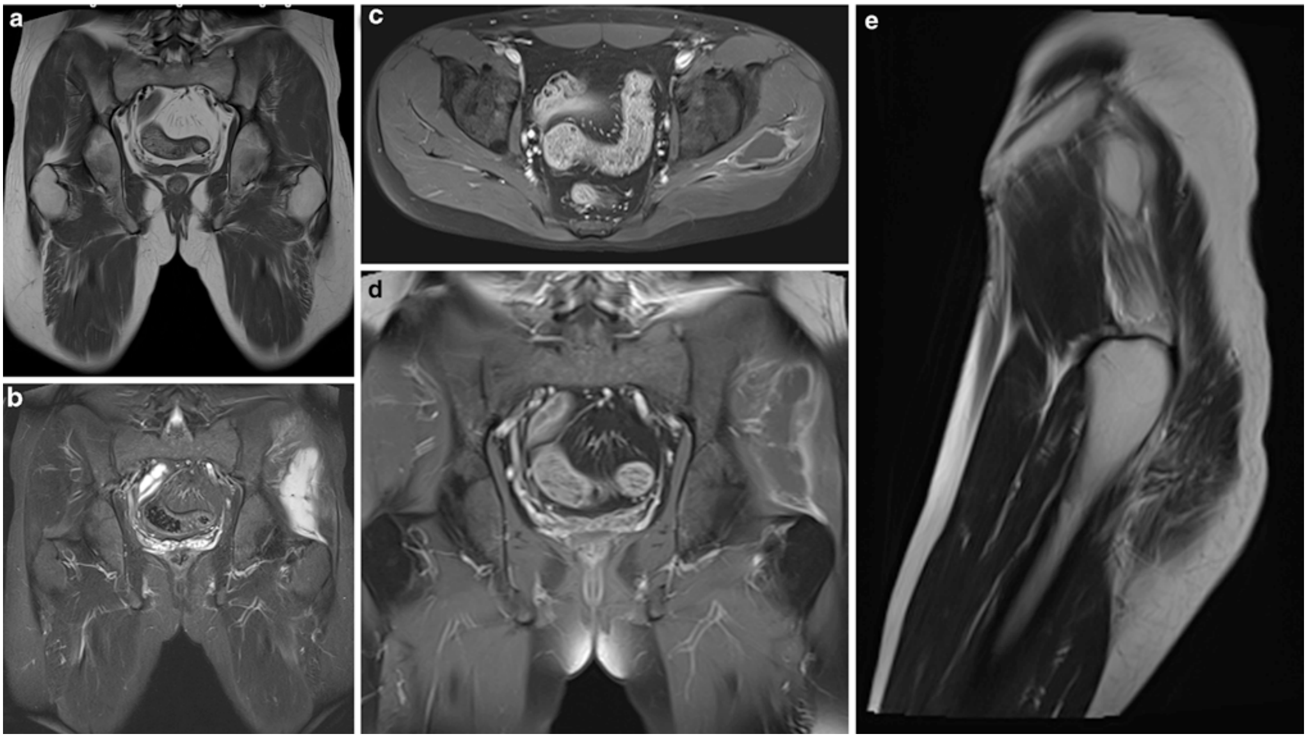

Fig. 8 A 23-year-old woman with muscle abscess formation in the left gluteal muscles. MRI images (coronal T1-weighted (**a**) and STIR images (**b**), axial (**c**) and coronal (**d**) fat-saturated contrast-enhanced T1-weighted images and sagittal T2-weighted (**e**) image) show a hyperintense area on STIR and T2-weighted images with a gadolinium enhanced rim on T1-weighted images (images courtesy of Prof. Dr. M.-A. Weber, Heidelberg)

aureus is the most common causative organism resulting in pyomyositis, or when located in the psoas muscle usually referred to as psoas abscess. Pyomyositis is increasingly diagnosed due to the increase of immune-compromised hosts as a result of more prevalent immune-deficiencies and greater use of chemotherapy and immunomodulating therapies. It usually develops gradually with local swelling, slight pain, and undulating temperatures during one or a few weeks followed by more obvious fever and muscle aching. This may be followed by sepsis. Pyomyositis is usually restricted to one muscle group, but can be more diffuse in a minority of patients. It can present in any muscle group. There is, however, a preference for the lower extremities, in particular the glutei and quadriceps muscles. The diagnosis can be made through imaging and aspiration of fluid from the abscess. CT scanning shows muscle enlargement and hypodense areas in the muscle with fluid collections in the center and with enhancement of the rim after administration of intravenous contrast fluid (Gordon et al. 1995). MRI images show hypointense areas with a gadolinium-enhanced rim on T1-weighted images (Fig. 8). More diffuse heterogeneous or homogeneous intermediate signal intensity on T1-weighted images and high signal intensity on T2 weighted images can be seen in muscle infection without an apparent fluid collection. Frequently, there is spread of infection to subcutaneous tissue, deep fascia, and bone marrow, all seen as low signal intensity on T1 and high signal intensity on T2-weighted images (Soler et al. 2000). CT scanning with contrast appears to be equally effective in detecting abscesses as Gadolinium-enhanced MRI (Gordon et al. 1995). Fat-suppressed T2-weigthed images appear to be as good as, but probably better than Gadolinium-enhanced T1-weighted images in detecting inflammatory changes in muscle (Miller et al. 1997). Diffuse bacterial infection of muscle without abscess formation, is rare in comparison to pyomyositis and psoas abscess. Many types of bacteria have been associated with acute bacterial myositis, such as for example *S. aureus* and group A and B streptococci, *Legionella* and *Borrelia burgdorferi*.

Acknowledgments The authors would like to thank Janneke van de Vlekkert for her contribution.

References

Adams EM, Chow CK, Premkumar A, Plotz PH (1995) The idiopathic inflammatory myopathies: spectrum of MR imaging findings. Radiographics 15(3):563–574

Arahata K, Engel AG (1986) Monoclonal antibody analysis of mononuclear cells in myopathies. III: Immunoelectron microscopy aspects of cell-mediated muscle fiber injury. Ann Neurol 19(2):112–125. doi:10.1002/ana.410190203

Arahata K, Engel AG (1988) Monoclonal antibody analysis of mononuclear cells in myopathies. V: Identification and quantitation of T8 + cytotoxic and T8 + suppressor cells. Ann Neurol 23(5):493–499. doi:10.1002/ana.410230511

Argov Z, Taivassalo T, De Stefano N, Genge A, Karpati G, Arnold DL (1998) Intracellular phosphates in inclusion body myositis—a 31P magnetic resonance spectroscopy study. Muscle Nerve 21(11): 1523–1525

Badrising UA, Maat-Schieman M, van Duinen SG, Breedveld F, van Doorn P, van Engelen B, van den Hoogen F, Hoogendijk J, Howeler C, de Jager A, Jennekens F, Koehler P, van der Leeuw H, de Visser M, Verschuuren JJ, Wintzen AR (2000) Epidemiology of inclusion body myositis in the Netherlands: a nationwide study. Neurology 55(9):1385–1387

Badrising UA, Maat-Schieman ML, Ferrari MD, Zwinderman AH, Wessels JA, Breedveld FC, van Doorn PA, van Engelen BG, Hoogendijk JE, Howeler CJ, de Jager AE, Jennekens FG, Koehler PJ, de Visser M, Viddeleer A, Verschuuren JJ, Wintzen AR (2002) Comparison of weakness progression in inclusion body myositis during treatment with methotrexate or placebo. Ann Neurol 51(3):369–372

Badrising UA, Maat-Schieman ML, van Houwelingen JC, van Doorn PA, van Duinen SG, van Engelen BG, Faber CG, Hoogendijk JE, de Jager AE, Koehler PJ, de Visser M, Verschuuren JJ, Wintzen AR (2005) Inclusion body myositis. Clinical features and clinical course of the disease in 64 patients. J Neurol 252 (12):1448–1454. doi:10.1007/s00415-005-0884-y

Badrising UA, Schreuder GM, Giphart MJ, Geleijns K, Verschuuren JJ, Wintzen AR, Maat-Schieman ML, van Doorn P, van Engelen BG, Faber CG, Hoogendijk JE, de Jager AE, Koehler PJ, de Visser M, van Duinen SG, Dutch IBMSG (2004) Associations with autoimmune disorders and HLA class I and II antigens in inclusion body myositis. Neurology 63(12):2396–2398

Bartlett ML, Ginn L, Beitz L, Villalba ML, Plotz P, Bacharach SL (1999) Quantitative assessment of myositis in thigh muscles using magnetic resonance imaging. Magn Reson Imaging 17(2):183–191

Benveniste O, Guiguet M, Freebody J, Dubourg O, Squier W, Maisonobe T, Stojkovic T, Leite MI, Allenbach Y, Herson S, Brady S, Eymard B, Hilton-Jones D (2011) Long-term observational study of sporadic inclusion body myositis. Brain 134(Pt 11):3176–3184. doi:10.1093/brain/awr213

Bohan A, Peter JB (1975) Polymyositis and dermatomyositis (first of two parts). New Engl J Med 292(7):344–347. doi:10.1056/NEJM197502132920706

Bohan A, Peter JB, Bowman RL, Pearson CM (1977) Computer-assisted analysis of 153 patients with polymyositis and dermatomyositis. Medicine 56(4):255–286

Bronner IM, Hoogendijk JE, Wintzen AR, van der Meulen MF, Linssen WH, Wokke JH, de Visser M (2003) Necrotising myopathy, an unusual presentation of a steroid-responsive myopathy. J Neurol 250(4):480–485. doi:10.1007/s00415-003-1027-y

Cantwell C, Ryan M, O'Connell M, Cunningham P, Brennan D, Costigan D, Lynch T, Eustace S (2005) A comparison of inflammatory myopathies at whole-body turbo STIR MRI. Clin Radiol 60(2):261–267. doi:10.1016/j.crad.2004.06.027

Cea G, Bendahan D, Manners D, Hilton-Jones D, Lodi R, Styles P, Taylor DJ (2002) Reduced oxidative phosphorylation and proton efflux suggest reduced capillary blood supply in skeletal muscle of patients with dermatomyositis and polymyositis: a quantitative 31P-magnetic resonance spectroscopy and MRI study. Brain 125(Pt 7):1635–1645

Chahin N, Engel AG (2008) Correlation of muscle biopsy, clinical course, and outcome in PM and sporadic IBM. Neurology 70(6):418–424. doi:10.1212/01.wnl.0000277527.69388.fe

Christopher-Stine L, Casciola-Rosen LA, Hong G, Chung T, Corse AM, Mammen AL (2010) A novel autoantibody recognizing 200-kd and 100-kd proteins is associated with an immune-mediated necrotizing myopathy. Arthritis and Rheumatism 62(9):2757–2766. doi:10.1002/art.27572

Cortese A, Machado P, Morrow J, Dewar L, Hiscock A, Miller A, Brady S, Hilton-Jones D, Parton M, Hanna MG (2013) Longitudinal observational study of sporadic inclusion body myositis: implications for clinical trials. Neuromuscular disorders: NMD. doi:10.1016/j.nmd.2013.02.010

Cox FM, Reijnierse M, van Rijswijk CS, Wintzen AR, Verschuuren JJ, Badrising UA (2011a) Magnetic resonance imaging of skeletal muscles in sporadic inclusion body myositis. Rheumatology 50(6):1153–1161. doi:10.1093/rheumatology/ker001

Cox FM, Titulaer MJ, Sont JK, Wintzen AR, Verschuuren JJ, Badrising UA (2011b) A 12-year follow-up in sporadic inclusion body myositis: an end stage with major disabilities. Brain 134(Pt 11):3167–3175. doi:10.1093/brain/awr217

Dimachkie MM, Barohn RJ (2012) Idiopathic inflammatory myopathies. Semin Neurol 32(3):227–236. doi:10.1055/s-0032-1329201

Dion E, Cherin P, Payan C, Fournet JC, Papo T, Maisonobe T, Auberton E, Chosidow O, Godeau P, Piette JC, Herson S, Grenier P (2002) Magnetic resonance imaging criteria for distinguishing between inclusion body myositis and polymyositis. J Rheumatol 29(9):1897–1906

Domire ZJ, McCullough MB, Chen Q, An KN (2009) Wave attenuation as a measure of muscle quality as measured by magnetic resonance elastography: initial results. J Biomech 42(4):537–540. doi:10.1016/j.jbiomech.2008.11.034

Ellis E, Ann Tan J, Lester S, Tucker G, Blumbergs P, Roberts-Thomson P, Limaye V (2012) Necrotizing myopathy: clinicoserologic associations. Muscle and Nerve 45(2):189–194. doi:10.1002/mus.22279

Fernandez C, Bardin N, De Paula AM, Salort-Campana E, Benyamine A, Franques J, Schleinitz N, Weiller PJ, Pouget J, Pellissier JF, Figarella-Branger D (2013) Correlation of clinicoserologic and pathologic classifications of inflammatory myopathies: study of 178 cases and guidelines for diagnosis. Medicine 92(1):15–24. doi:10.1097/MD.0b013e31827ebba1

Fleckenstein JL (1996) Re: Cost-effectiveness of MR imaging in evaluating polymyositis. AJR. Am J Roentgenol 167(2):531–532. doi:10.2214/ajr.167.2.8686645

Fujino H, Kobayashi T, Goto I, Onitsuka H (1991) Magnetic resonance imaging of the muscles in patients with polymyositis and dermatomyositis. Muscle and Nerve 14(8):716–720. doi:10.1002/mus.880140805

Furst DE, Amato AA, Iorga SR, Gajria K, Fernandes AW (2012) Epidemiology of adult idiopathic inflammatory myopathies in a U.S. managed care plan. Muscle and Nerve 45(5):676–683. doi:10.1002/mus.23302

Gordon BA, Martinez S, Collins AJ (1995) Pyomyositis: characteristics at CT and MR imaging. Radiology 197(1):279–286

Grable-Esposito P, Katzberg HD, Greenberg SA, Srinivasan J, Katz J, Amato AA (2010) Immune-mediated necrotizing myopathy associated with statins. Muscle and Nerve 41(2):185–190. doi:10.1002/mus.21486

Hoogendijk JE, Amato AA, Lecky BR, Choy EH, Lundberg IE, Rose MR, Vencovsky J, de Visser M, Hughes RA (2004) 119th ENMC international workshop: trial design in adult idiopathic inflammatory myopathies, with the exception of inclusion body myositis, Neuromuscul Disord : NMD 14(5):337–345. 10–12 Oct 2003, Naarden. The Neth. doi:10.1016/j.nmd.2004.02.006

Hundt W, Stabler A, Reiser M (1999) MRI findings of muscle involvement in idiopathic hypereosinophilic syndrome. Eur Radiol 9(3):525–528

Jankharia BG, Chavhan GB, Krishnan P, Jankharia B (2005) MRI and ultrasound in solitary muscular and soft tissue cysticercosis. Skeletal Radiol 34(11):722–726. doi:10.1007/s00256-005-0954-3

Johnson RW, Williams FM, Kazi S, Dimachkie MM, Reveille JD (2003) Human immunodeficiency virus-associated polymyositis: a longitudinal study of outcome. Arthritis and Rheumatism 49(2):172–178. doi:10.1002/art.11002

Koffman BM, Rugiero M, Dalakas MC (1998) Immune-mediated conditions and antibodies associated with sporadic inclusion body myositis. Muscle and Nerve 21(1):115–117

Larue S, Maisonobe T, Benveniste O, Chapelon-Abric C, Lidove O, Papo T, Eymard B, Dubourg O (2011) Distal muscle involvement in granulomatous myositis can mimic inclusion body myositis. J Neurol Neurosurg Psychiatry 82(6):674–677. doi:10.1136/jnnp.2009.190751

Layzer RB, Shearn MA, Satya-Murti S (1977) Eosinophilic polymyositis. Ann Neurol 1(1):65–71. doi:10.1002/ana.410010106

Le Roux K, Streichenberger N, Vial C, Petiot P, Feasson L, Bouhour F, Ninet J, Lachenal F, Broussolle C, Seve P (2007) Granulomatous myositis: a clinical study of thirteen cases. Muscle and Nerve 35(2):171–177. doi:10.1002/mus.20683

Liang C, Needham M (2011) Necrotizing autoimmune myopathy. Curr Opinion Rheumatol 23(6):612–619. doi:10.1097/BOR.0b013e32834b324b

Lindberg C, Persson LI, Bjorkander J, Oldfors A (1994) Inclusion body myositis: clinical, morphological, physiological and laboratory findings in 18 cases. Acta Neurolog Scand 89(2):123–131

Lodi R, Taylor DJ, Tabrizi SJ, Hilton-Jones D, Squier MV, Seller A, Styles P, Schapira AH (1998) Normal in vivo skeletal muscle oxidative metabolism in sporadic inclusion body myositis assessed by 31P-magnetic resonance spectroscopy. Brain 121(Pt 11): 2119–2126

Lofberg M, Liewendahl K, Lamminen A, Korhola O, Somer H (1998) Antimyosin scintigraphy compared with magnetic resonance imaging in inflammatory myopathies. Arch Neurol 55(7):987–993

Maillard SM, Jones R, Owens C, Pilkington C, Woo P, Wedderburn LR, Murray KJ (2004) Quantitative assessment of MRI T2 relaxation time of thigh muscles in juvenile dermatomyositis. Rheumatology 43(5):603–608. doi:10.1093/rheumatology/keh130

Mammen AL, Chung T, Christopher-Stine L, Rosen P, Rosen A, Doering KR, Casciola-Rosen LA (2011) Autoantibodies against 3-hydroxy-3-methylglutaryl-coenzyme A reductase in patients with statin-associated autoimmune myopathy. Arthritis Rheumatism 63(3):713–721. doi:10.1002/art.30156

McCullough MB, Domire ZJ, Reed AM, Amin S, Ytterberg SR, Chen Q, An KN (2011) Evaluation of muscles affected by myositis using magnetic resonance elastography. Muscle and Nerve 43(4): 585–590. doi:10.1002/mus.21923

Middleton PJ, Alexander RM, Szymanski MT (1970) Severe myositis during recovery from influenza. Lancet 2(7672):533–535

Miller T, Al-Lozi MT, Lopate G, Pestronk A (2002) Myopathy with antibodies to the signal recognition particle: clinical and pathological features. J Neurol Neurosurg Psychiatry 73(4):420–428

Miller TT, Randolph DA Jr, Staron RB, Feldman F, Cushin S (1997) Fat-suppressed MRI of musculoskeletal infection: fast T2-weighted techniques versus gadolinium-enhanced T1-weighted images. Skeletal Radiol 26(11):654–658

Needham M, James I, Corbett A, Day T, Christiansen F, Phillips B, Mastaglia FL (2008) Sporadic inclusion body myositis: phenotypic variability and influence of HLA-DR3 in a cohort of 57 Australian cases. J Neurol Neurosurg Psychiatry 79(9):1056–1060. doi:10.1136/jnnp.2007.138891

O'Connell MJ, Powell T, Brennan D, Lynch T, McCarthy CJ, Eustace SJ (2002) Whole-body MR imaging in the diagnosis of polymyositis. AJR. Am J Roentgenol 179(4):967–971. doi:10.2214/ajr.179.4.1790967

Owada T, Maezawa R, Kurasawa K, Okada H, Arai S, Fukuda T (2012) Detection of inflammatory lesions by f-18 fluorodeoxyglucose positron emission tomography in patients with polymyositis and dermatomyositis. J Rheumatol 39(8):1659–1665. doi:10.3899/jrheum.111597

Park JH, Vansant JP, Kumar NG, Gibbs SJ, Curvin MS, Price RR, Partain CL, James AE Jr (1990) Dermatomyositis: correlative MR imaging and P-31 MR spectroscopy for quantitative characterization of inflammatory disease. Radiology 177(2):473–479

Phillips BA, Cala LA, Thickbroom GW, Melsom A, Zilko PJ, Mastaglia FL (2001) Patterns of muscle involvement in inclusion body myositis: clinical and magnetic resonance imaging study. Muscle and Nerve 24(11):1526–1534

Pluk H, van Hoeve BJ, van Dooren SH, Stammen-Vogelzangs J, van der Heijden A, Schelhaas HJ, Verbeek MM, Badrising UA, Arnardottir S, Gheorghe K, Lundberg IE, Boelens WC, van Engelen BG, Pruijn GJ (2012) Autoantibodies to cytosolic 5'-nucleotidase IA in inclusion body myositis. Ann Neurol doi:10.1002/ana.23822

Qi J, Olsen NJ, Price RR, Winston JA, Park JH (2008) Diffusion-weighted imaging of inflammatory myopathies: polymyositis and dermatomyositis. J Magn Reson Imaging : JMRI 27(1):212–217. doi:10.1002/jmri.21209

Reimers CD, Schedel H, Fleckenstein JL, Nagele M, Witt TN, Pongratz DE, Vogl TJ (1994) Magnetic resonance imaging of skeletal muscles in idiopathic inflammatory myopathies of adults. J Neurol 241(5):306–314

Restrepo CS, Lemos DF, Gordillo H, Odero R, Varghese T, Tiemann W, Rivas FF, Moncada R, Gimenez CR (2004) Imaging findings in musculoskeletal complications of AIDS. Radiograph A Rev Publ Radiol Soc North Am 24(4):1029–1049. doi:10.1148/rg.244035151

Rubin E, De la Rubia L, Pascual A, Dominguez J, Flores C (2010) Benign acute myositis associated with H1N1 influenza A virus infection. Eur J Pediatr 169(9):1159–1161. doi:10.1007/s00431-010-1178-7

Salajegheh M, Lam T, Greenberg SA (2011) Autoantibodies against a 43 kDa muscle protein in inclusion body myositis. PLoS ONE 6(5):e20266. doi:10.1371/journal.pone.0020266

Schedel H, Reimers CD, Nagele M, Witt TN, Pongratz DE, Vogl T (1992) Imaging techniques in myotonic dystrophy. A comparative study of ultrasound, computed tomography and magnetic resonance imaging of skeletal muscles. Eur J Radiol 15(3):230–238

Schedel H, Reimers CD, Vogl T, Witt TN (1995) Muscle edema in MR imaging of neuromuscular diseases. Acta Radiolog 36(3): 228–232

Schulze M, Kotter I, Ernemann U, Fenchel M, Tzaribatchev N, Claussen CD, Horger M (2009) MRI findings in inflammatory muscle diseases and their noninflammatory mimics. AJR Am J Roentgenol 192(6):1708–1716. doi:10.2214/AJR.08.1764

Schweitzer ME, Fort J (1995) Cost-effectiveness of MR imaging in evaluating polymyositis. AJR Am J Roentgenol 165(6):1469–1471. doi:10.2214/ajr.165.6.7484589

Selva-O'Callaghan A, Grau JM, Gamez-Cenzano C, Vidaller-Palacin A, Martinez-Gomez X, Trallero-Araguas E, Andia-Navarro E, Vilardell-Tarres M (2010a) Conventional cancer screening versus PET/CT in dermatomyositis/polymyositis. Am J Med 123(6): 558–562. doi:10.1016/j.amjmed.2009.11.012

Selva-O'Callaghan A, Trallero-Araguas E, Grau-Junyent JM, Labrador-Horrillo M (2010b) Malignancy and myositis: novel autoantibodies and new insights. Curr Opin Rheumatol 22(6):627–632. doi:10.1097/BOR.0b013e32833f1075

Smoyer-Tomic KE, Amato AA, Fernandes AW (2012) Incidence and prevalence of idiopathic inflammatory myopathies among commercially insured, Medicare supplemental insured, and Medicaid enrolled populations: an administrative claims analysis. BMC Musculoskelet Disord 13:103. doi:10.1186/1471-2474-13-103

Soler R, Rodriguez E, Aguilera C, Fernandez R (2000) Magnetic resonance imaging of pyomyositis in 43 cases. Eur J Radiol 35(1):59–64

Titulaer MJ, Soffietti R, Dalmau J, Gilhus NE, Giometto B, Graus F, Grisold W, Honnorat J, Sillevis Smitt PA, Tanasescu R, Vedeler CA, Voltz R, Verschuuren JJ (2011) European federation of neurological S screening for tumours in paraneoplastic syndromes: report of an EFNS task force. Eur J Neurol 18 (1):19-e13. doi: 10.1111/j.1468-1331.2010.03220.x

Tomasova Studynkova J, Charvat F, Jarosova K, Vencovsky J (2007) The role of MRI in the assessment of polymyositis and dermatomyositis. Rheumatology 46(7):1174–1179. doi:10.1093/rheumatology/kem088

Tripathy SK, Sen RK, Akkina N, Hampannavar A, Tahasildar N, Limaye R (2012) Role of ultrasonography and magnetic resonance imaging in the diagnosis of intramuscular cysticercosis. Skeletal Radiol 41(9):1061–1066. doi:10.1007/s00256-011-1320-2

van der Meulen MF, Bronner IM, Hoogendijk JE, Burger H, van Venrooij WJ, Voskuyl AE, Dinant HJ, Linssen WH, Wokke JH, de Visser M (2003) Polymyositis: an overdiagnosed entity. Neurology 61(3):316–321

van der Meulen MF, Hoogendijk JE, Wokke JH, de Visser M (2000) Oral pulsed high-dose dexamethasone for myositis. J Neurol 247(2):102–105

Weber MA, Jappe U, Essig M, Krix M, Ittrich C, Huttner HB, Meyding-Lamade U, Hartmann M, Kauczor HU, Delorme S (2006) Contrast-enhanced ultrasound in dermatomyositis- and polymyositis. J Neurol 253(12):1625–1632. doi:10.1007/s00415-006-0318-5

Yao L, Gai N (2012) Fat-corrected T2 measurement as a marker of active muscle disease in inflammatory myopathy. AJR. Am J Roentgenol 198(5):W475–W481. doi:10.2214/AJR.11.7113

Yoshida K, Kurosaka D, Joh K, Matsushima S, Takahashi E, Hirai K, Noda K, Ukichi T, Furuya K, Yanagimachi M, Kingetsu I, Fukuda K, Yamada A (2010) Fasciitis as a common lesion of dermatomyositis, demonstrated early after disease onset by en bloc biopsy combined with magnetic resonance imaging. Arthritis Rheumatism 62(12):3751–3759. doi:10.1002/art.27704

MRI in Muscle Channelopathies

Karin Jurkat-Rott, Marc-André Weber, and Frank Lehmann-Horn

Contents

1 Key points 272
2 Introduction and Classification 272
3 Prevalence, Genetics and Pathophysiology 273
4 Clinical Features 276
5 Histopathology 278
6 Magnetic Resonance Imaging 278
7 Therapy 285
8 Conclusions and Future Perspectives 287
References 288

Abstract

Myotonia is an involuntary-slowed relaxation after a forceful voluntary muscle contraction which is experienced by the patient as muscle stiffness. Electrical hyperexcitability of the muscle fiber membrane is the basis of myotonia. The stiffness recedes with repeated contractions, a phenomenon called warm-up. Patients in whom muscle stiffness worsens with repetition or with cooling suffer from paradoxical myotonia or so-called paramyotonia. This type of myotonia is associated with episodes of flaccid limb muscle weakness similar to periodic paralysis. Patients with periodic paralysis experience episodic weakness spells with varying intervals of normal muscle function. Electrical inexcitability of the muscle fiber membrane is the basis of periodic paralysis. Two dominant episodic types of weakness with or without myotonia are distinguished by the serum K^+ level during the attacks of tetraplegia: hyper- and hypokalemic periodic paralysis. Independently of the severity and frequency of the paralytic episodes, many patients develop a chronic progressive myopathy in the forties, an age at which the attacks of weakness decrease. Although channelopathies such as myotonias and periodic paralyses are known for episodic symptoms, in most cases progressive focal or general muscular weakness is present. Routine protocols of proton (^{1}H) magnetic resonance imaging (MRI) show normal muscle morphology or may demonstrate edematous or lipomatous changes, atrophy or hypertrophy; however, these morphologic changes are not very disease-specific. The following chapter introduces examples of conventional and modern functional imaging methods like ^{23}Na MRI for evaluation of muscular channelopathies, in which an autosomal-dominant bequeathed defect of muscular Na^+ channels leads to a pathologic Na^+ influx that causes intermittent or permanent muscular paresis as well as muscular stiffness. ^{23}Na MRI by which aspects of muscular pathogenesis such as muscular Na^+ homeostasis can be visualized and

K. Jurkat-Rott (✉) · F. Lehmann-Horn
Department of Neurophysiology, Ulm University,
Albert-Einstein-Allee 11, 89081 Ulm, Germany
e-mail: karin.jurkat-rott@uni-ulm.de

M.-A. Weber
Department of Diagnostic and Interventional Radiology,
University Hospital of Heidelberg, Im Neuenheimer Feld 110,
69120 Heidelberg, Germany

M.-A. Weber (ed.), *Magnetic Resonance Imaging of the Skeletal Musculature*, Medical Radiology. Diagnostic Imaging,
DOI: 10.1007/174_2013_922,

© Springer-Verlag Berlin Heidelberg 2013
Published Online: 5 October 2013

monitored has effectively achieved value in the radiologic management of muscular Na^+ channel diseases, since ^{23}Na MRI is able to depict an intracellular muscular sodium accumulation simultaneous to development of muscular paresis. This sodium accumulation correlates well with the grade of paresis and is reproducible.

Abbreviations

^1H-MRI	Hydrogen magnetic resonance imaging
^{23}Na-MRI	Sodium magnetic resonance imaging
Cl^-	Chloride ion
ClC-1	Chloride channel of skeletal muscle, member 1 of the chloride channel family ClC
CLCN1	Gene encoding the muscular chloride channel, ClC-1
DMC	Dominant myotonia congenita, Thomsen myotonia
EMG	Electromyography
HyperPP	Hyperkalemic periodic paralysis
HypoPP	Hypokalemic periodic paralysis
K^+	Potassium ion
MRI	Magnetic resonance imaging
Na^+	Sodium ion
Nav1.4	Sodium channel of skeletal muscle, member 4 of the voltage-gated sodium channel family
PAM	K^+-aggravated myotonia, a Na^+ channel myotonia
PC	Paramyotonia congenita, Eulenburg disease
RMC	Recessive myotonia congenita, Becker myotonia
SCNA4	Gene encoding the muscular sodium channel, Nav1.4

1 Key points

1. Muscular ion channelopathies include the non-dystrophic myotonias and periodic paralyses. They have in common that muscle membrane potential is altered due to changes in ion conductivities. Generally, this means that gradients for Na^+ and Cl^- are different resulting in altered membrane excitability. These muscular diseases clinically manifest with myotonia or weakness associated with hyper- or hypokalemia.
2. Periodic paralysis occurs episodically with varying intervals of normal muscle function, because apparently, the underlying ion channel defects are usually well compensated and an additional trigger (e.g., exposure to cold) is often required for channel malfunction and thus triggers clinical symptoms.

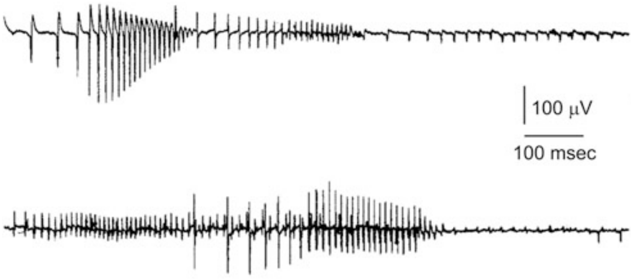

Fig. 1 Typical myotonic bursts on conventional electromyographic examination performed with a concentric EMG needle. The bursts consist of repetitive muscle action potentials that typically show a modulation of amplitude and frequency. Mostly the amplitude decreases and the frequency increases

3. Muscle channelopathies can be monitored by functional MRI techniques for testing of pathogenesis, estimating prognosis, and monitoring of treatment.
4. For instance, ^{23}Na magnetic resonance imaging can depict an intracellular muscular sodium accumulation simultaneous to development of muscular paresis in paramyotonia, hyperkalemic-, and hypokalemic periodic paralysis. The sodium accumulation correlates well with the grade of paresis and is reproducible in these muscular channelopathies.
5. In hyperkalemic- and hypokalemic periodic paralysis, anti-edematous treatment has the potential to alleviate the muscular edema and weakness.

2 Introduction and Classification

Defective ion channels can play a causal role in disease pathogenesis. This implication was first concluded from the observation of an abnormal ion conductance in muscle fibers biopsied from myotonic goats (Bryant 1969). In man, a similar conclusion was reached for patients with paramyotonia congenita and with periodic paralyses (Lehmann-Horn et al. 1987a, b). The term "ion channelopathies" was then coined in the 1990s (Hoffman et al. 1995), and defined for disorders that are caused by malfunction or altered regulation of ion channel proteins. Channelopathies can, therefore, be either hereditary or acquired (usually caused by auto-antibodies). Hereditary channelopathies can be categorized into those affecting the motor endplate (congenital myasthenic syndromes), the sarcolemma (myotonias and periodic paralyses), excitation–contraction coupling (malignant hyperthermia, central core and multi-minicore myopathy caused by ryanodine receptor-1 mutations), and in the membrane of the sarcoplasmic reticulum (proximal or distal muscular dystrophies due to recessive anoctamin-5 chloride channel mutations).

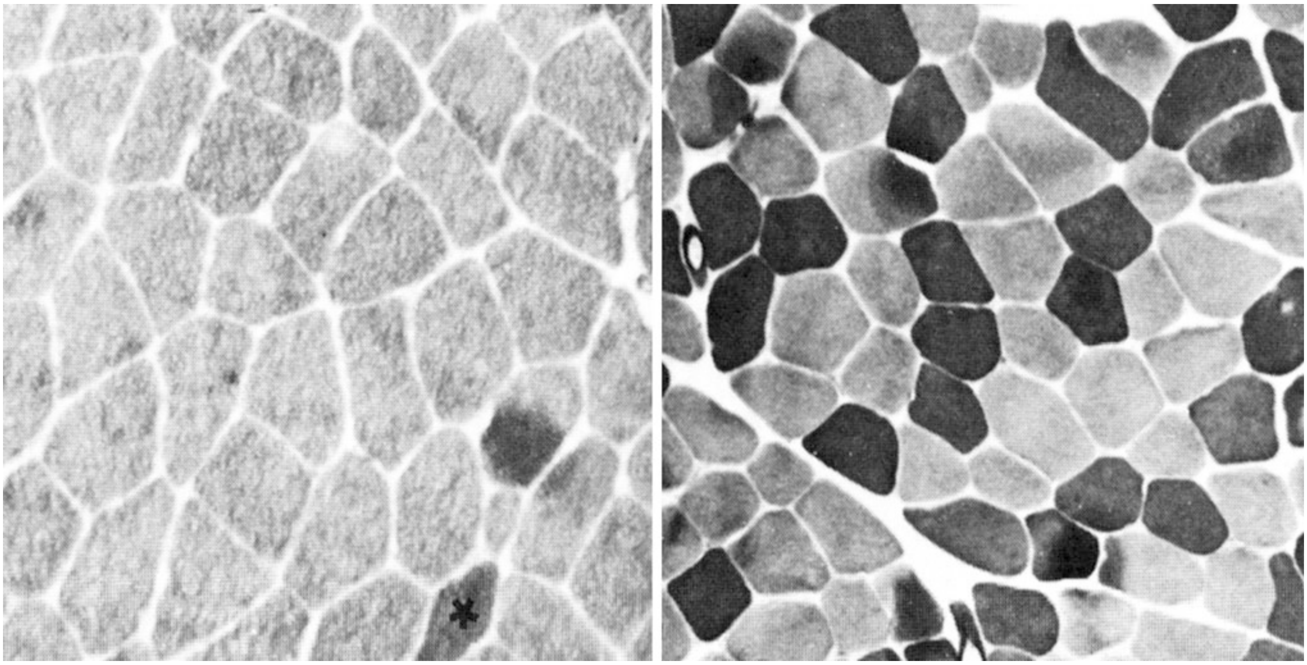

Fig. 2 Histopathologic images of muscle cross sections obtained from myotonia congenita patients. Preincubation of muscle slices at pH 4.6 yields in high ATPase activities (*dark*) of type 2B fibers while type 2A fibers show no activity (*bright*). In contrast to the control (*right*), myotonia patients exhibit almost no type 2B fibers (*left*; the only 2B fiber is marked by an *asterisk*)

In this chapter, we focus on sarcolemmal channelopathies, i.e., diseases resulting from disturbed excitation of the surface or the T-tubular membrane. The ability of the membrane to generate action potentials is either enhanced or decreased. This altered membrane excitability results in myotonia or in weakness and hyper- or hypokalemia.

Myotonia is an involuntary slowed relaxation after a forceful voluntary muscle contraction which is experienced by the patient as muscle stiffness. Electrical membrane hyperexcitability is apparent in the form of repetitive action potentials in the electromyography (EMG). The stiffness recedes with repeated contractions, a phenomenon called warm-up. Patients in whom muscle stiffness worsens with repetition or with cooling suffer from paradoxical myotonia or so-called paramyotonia. In this type of myotonia, the stiffness can be followed by flaccid limb muscle weakness. Patients with periodic paralysis experience episodic spells of weakness with varying intervals of normal muscle function. Electrical inexcitability of the muscle fiber membrane is the basis of periodic paralysis which is apparent in lack of activity in the EMG. Two dominant episodic types of weakness with or without myotonia are distinguished by the serum K^+ level during the attacks of tetraplegia: hyper- and hypokalemic periodic paralysis (Lehmann-Horn et al. 2004). Independently of the severity and frequency of the paralytic episodes, many patients develop a chronic progressive myopathy in the forties, an age at which the weakness episodes decrease (Jurkat-Rott et al. 2009).

3 Prevalence, Genetics and Pathophysiology

Although the two forms of myotonia congenita are distinguished by their mode of inheritance, they are caused by mutations in the same gene, *CLCN1*, i.e., the gene coding for the sarcolemmal voltage-gated Cl^- channel, ClC-1 (Koch et al. 1992). For this reason, they are also referred to as Cl^- channel myotonias. The prevalence of dominant Thomsen disease (DMC) is estimated at ~1:400,000, i.e., much lower than thought in the premolecular era (1:23,000) owing to the fact that many families with dominant myotonia are now identified as carriers of a Na^+ channel mutation which results in a different disease with very similar symptomatology, potassium (K^+)-aggravated myotonia (PAM). Other families were found to have recessive Becker myotonia (RMC) with pseudodominant inheritance (Jurkat-Rott et al. 2002). Conversely, the prevalence of Becker myotonia is now thought to be higher (1:25,000) than Becker's original estimate of 1:50,000 (Jurkat-Rott et al. 2002).

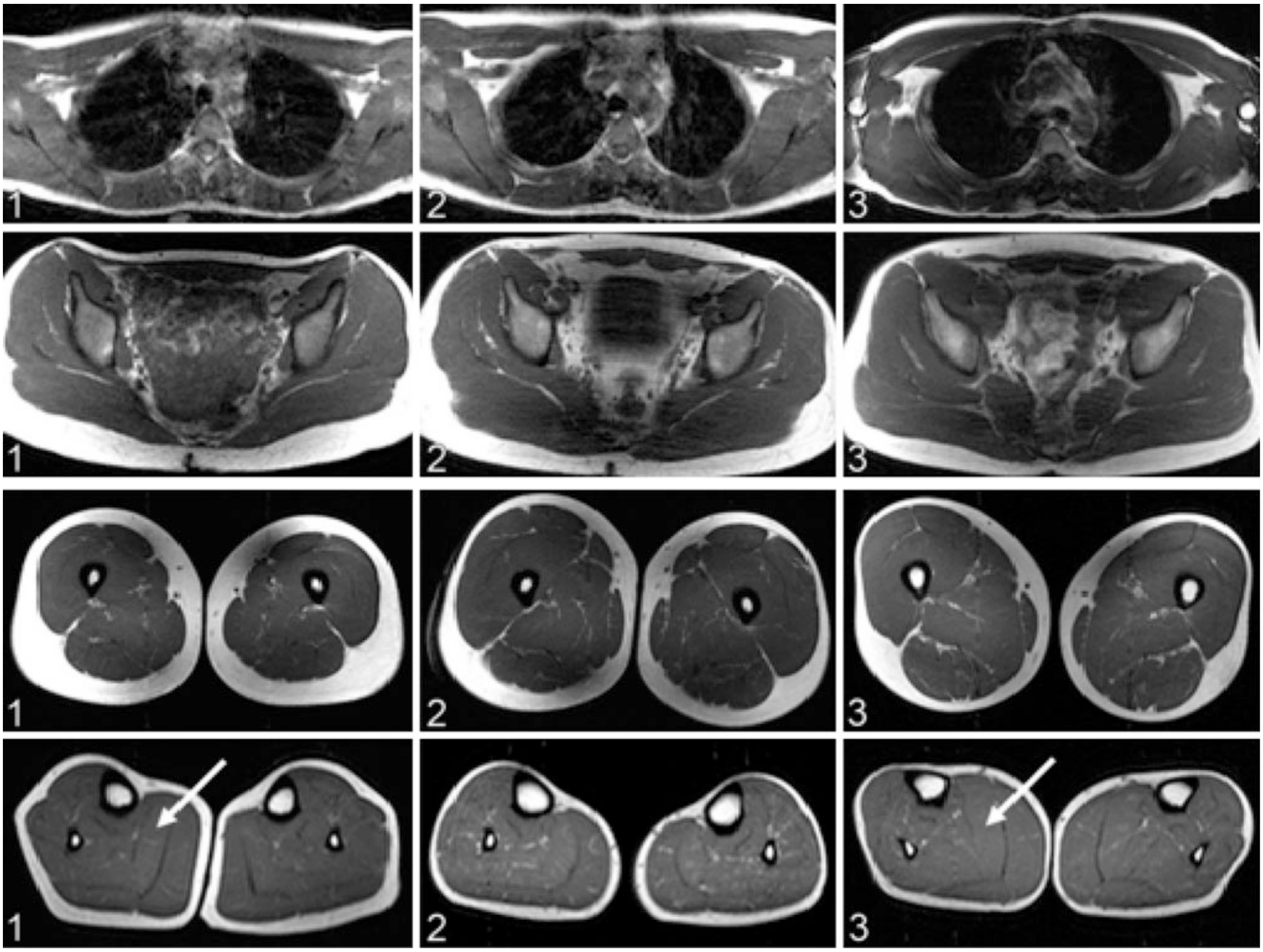

Fig. 3 Whole-body magnetic resonance imaging (MRI) findings in three recessive myotonia congenital (RMC) patients corresponding to columns 1–3. Axial sections of T1-weighted turbo spin-echo sequences at the level of the shoulder girdle (*top row*), pelvis (*second row*), thighs (*third row*), and calves (*bottom row*). In all patients, shoulder girdle and trunk muscles showed no trophic changes. Patients 1 and 3 had hypertrophy of the thigh and calf muscles (*arrows*). Lower leg muscles of patient 2 were comparatively hypotrophic, with neither fatty degeneration nor skeletal muscle edema. Reproduced with permission of Kornblum et al. (2010)

After-depolarizations of the muscle action potential are normally prevented by Cl^- conducted through homodimeric ClC-1 channels. If this muscle-specific high Cl^- conductance is decreased by 75 % or more, after-depolarizations are large and are able to initiate new bursts of action potentials (Bryant 1969). These so-called myotonic runs result in involuntary contractions or slowed relaxation. All DMC and RMC are loss-of-function mutations. In DMC, only one allele is mutated and a typical mutation reduces conductance of mutant/mutant and mutant/wildtype channel complexes, the latter in a dominant-negative fashion. In contrast, RMC mutations result in simple loss-of-function of the mutant/mutant complex only—thus, both alleles must be mutated, so that the Cl^- conductance falls below 25 % of its normal value.

K^+-aggravated myotonia (PAM) is caused by gain-of-function mutations in $Na_v1.4$, the voltage-gated Na^+ channel of skeletal muscle, encoded by the *SCN4A* gene (Heine et al. 1993). This channel is essential for the generation of the muscle action potential. The mutations cause a pathologically increased inward Na^+ current which can activate more Na^+ channels, thereby generating action potential bursts. This repetitive activity reflects a dominant-positive effect of the mutations which is more pronounced by pre-existing membrane depolarization by elevated serum K^+ in PAM or cold environment in paramyotonia congenita (PC) (Lerche et al. 1993, 1996).

Hyperkalemic periodic paralysis (HyperPP) is caused by mutations in the voltage-gated sodium channel $Na_v1.4$ as well (Fontaine et al. 1990; Rojas et al. 1991). Most mutations

Fig. 4 **a**, **c**, **e**, Transverse T1-weighted spin-echo (516/15) and, **b**, **d**, **f**, transverse T2-weighted turbo spin-echo (3000/104) MR images of both lower legs in a family with paramyotonia congenita (R1448C mutation). Images of the 54-year-old father (**a**, **b**) show a symmetrically fatty infiltration of both gastrocnemius muscles (*arrows*) and edema in both soleus muscles (*asterisks*). The 0.3 % saline reference phantom is also visible. Images of the 25-year-old son (**c**, **d**) show muscle edema, a precursor and possible causative mechanism of muscle degeneration, bilaterally symmetrical in the medial head of both gastrocnemius muscles, whereas the youngest family member, a 17-year-old daughter (**e**, **f**), has not yet developed morphologic changes. Reproduced with permission of the Radiological Society of North America (RSNA) from Weber et al. (2006b)

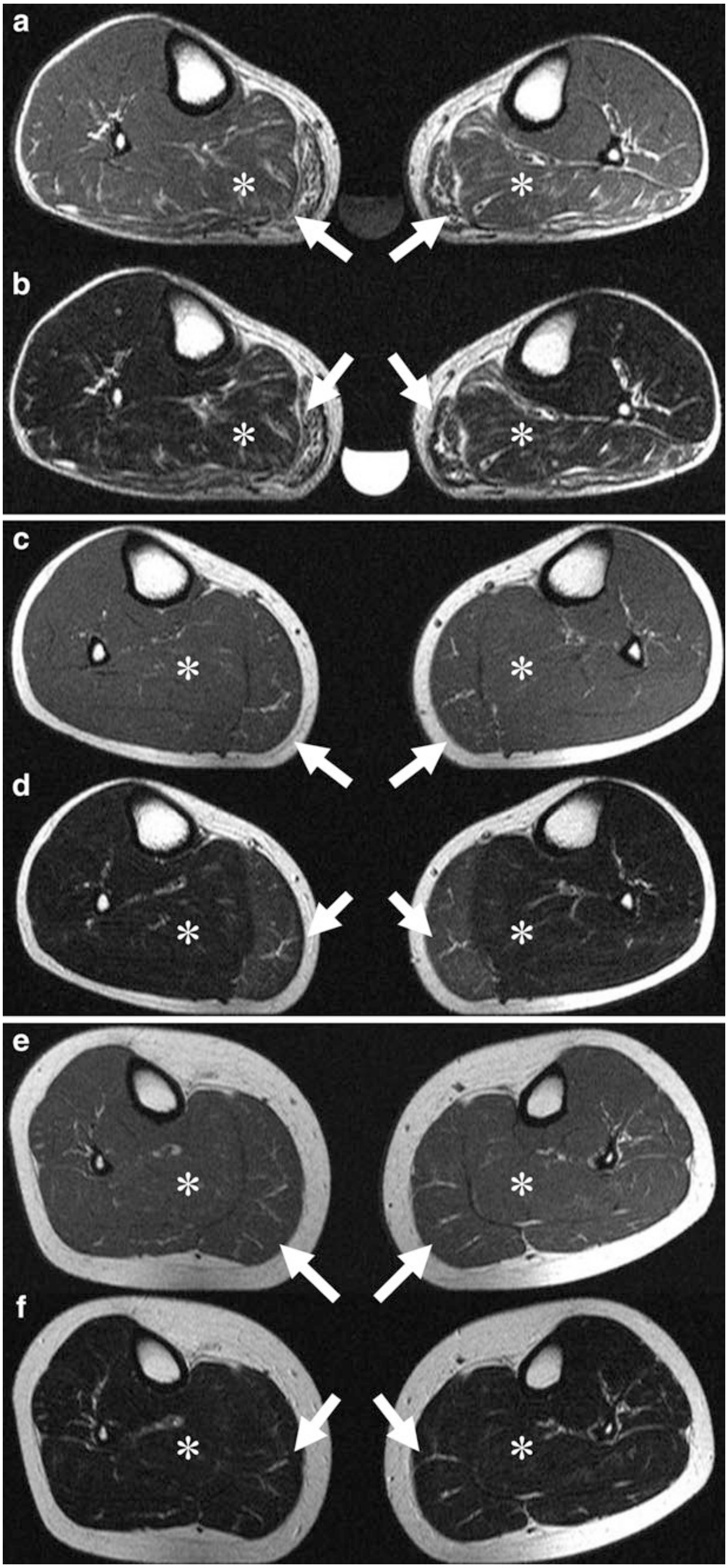

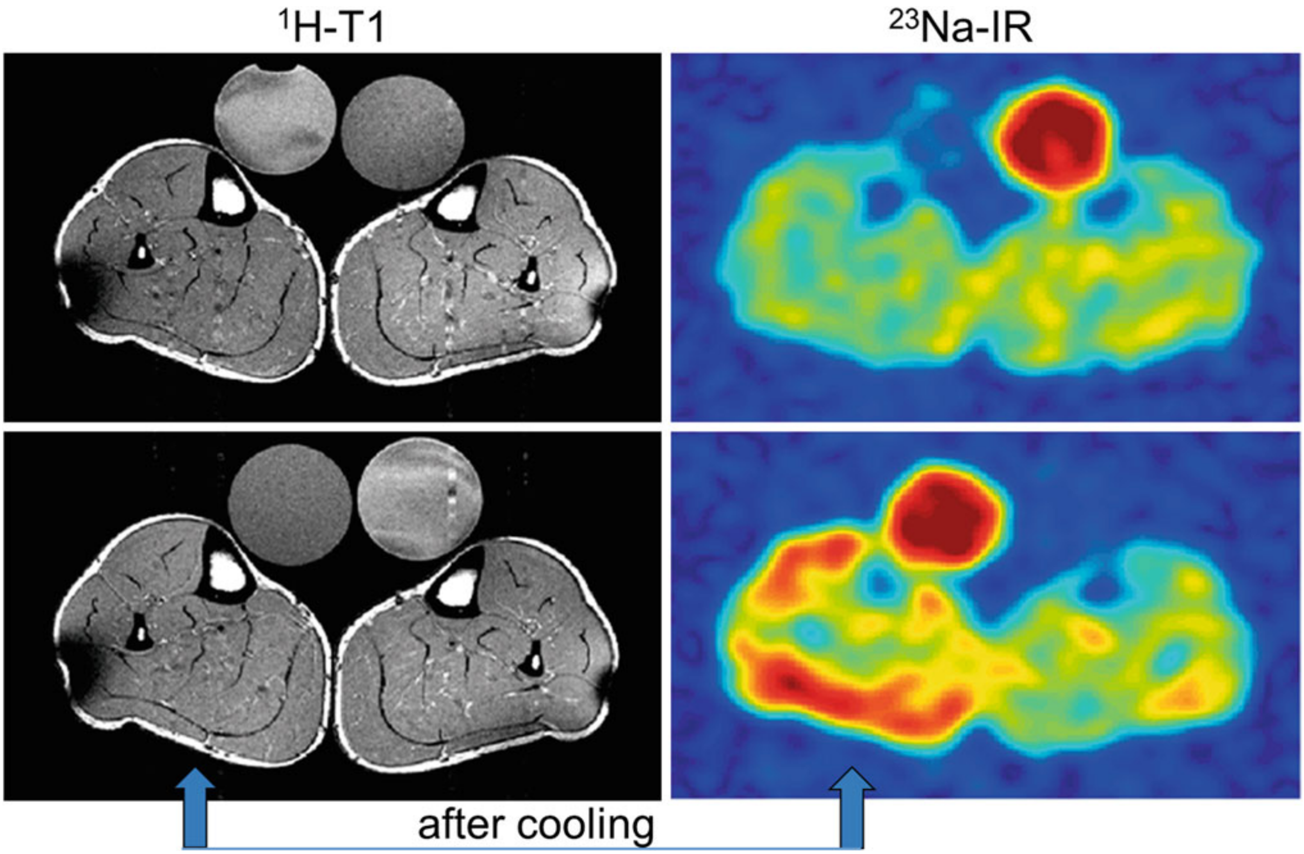

Fig. 5 ^{1}H-MR and ^{23}Na-MR images of a PC patient before and after cooling of the lower leg (*arrow*). While the T1-weighted ^{1}H-MR signal is unaltered, the ^{23}Na inversion recovery (Na-IR) signal is markedly increased in the muscles of the cooled leg (*blue* low intensity, *red* high intensity)

destabilize the inactivated state which causes channel reopenings and a persistent current corresponding to a gain-of-function defect. The resulting long-lasting membrane depolarization inactivates wildtype channels whereby the muscle is rendered inexcitable. It also increases the driving force for K^+ which increases efflux and serum levels of this ion.

In contrast to the gain-of-function changes in HyperPP, hypokalemic periodic paralysis (HypoPP) is associated with a loss-of-function defect of $Na_v1.4$ or $Ca_v1.1$, the latter being the main subunit of the voltage-gated L-type Ca^{2+} channel complex located in the T-tubular system (Fontaine et al. 1994; Jurkat-Rott et al. 1994, 2000). Both genetic variants are clinically similar, and in both channel types, the mutations are located exclusively in the S4 segments, the voltage sensors of the channel. Functionally, the inactivated state is stabilized in the Na^+ channel mutants, while the channel availability is reduced for the Ca^{2+} channel mutants. Additional currents through an aberrant pore in the S4 segment (the voltage sensor) have been described that allow a persistent inward Na^+ flow which depolarizes the membrane and make the fibers inexcitable similar to HyperPP (Jurkat-Rott et al. 2012).

4 Clinical Features

Myotonia is characterized by muscle stiffness due to involuntary electrical after-activity following voluntary strong muscle activity. If the myotonia is severe, transient weakness can occur. The myotonia decreases with continued activity, a phenomenon called warm-up. Also the transient weakness, if present at all, resolves (Lehmann-Horn et al. 2004). On the contrary, paradoxical myotonia as seen in paramyotonia worsens with exercise in the cold. Paradoxical myotonia of the eyelid muscles may also occur in the warmth; it is indicative of sodium channel myotonia (Lehmann-Horn et al. 2004). This type of myotonia can be aggravated by ingestion of potassium (potassium-aggravated myotonia). On electromyographic examination,

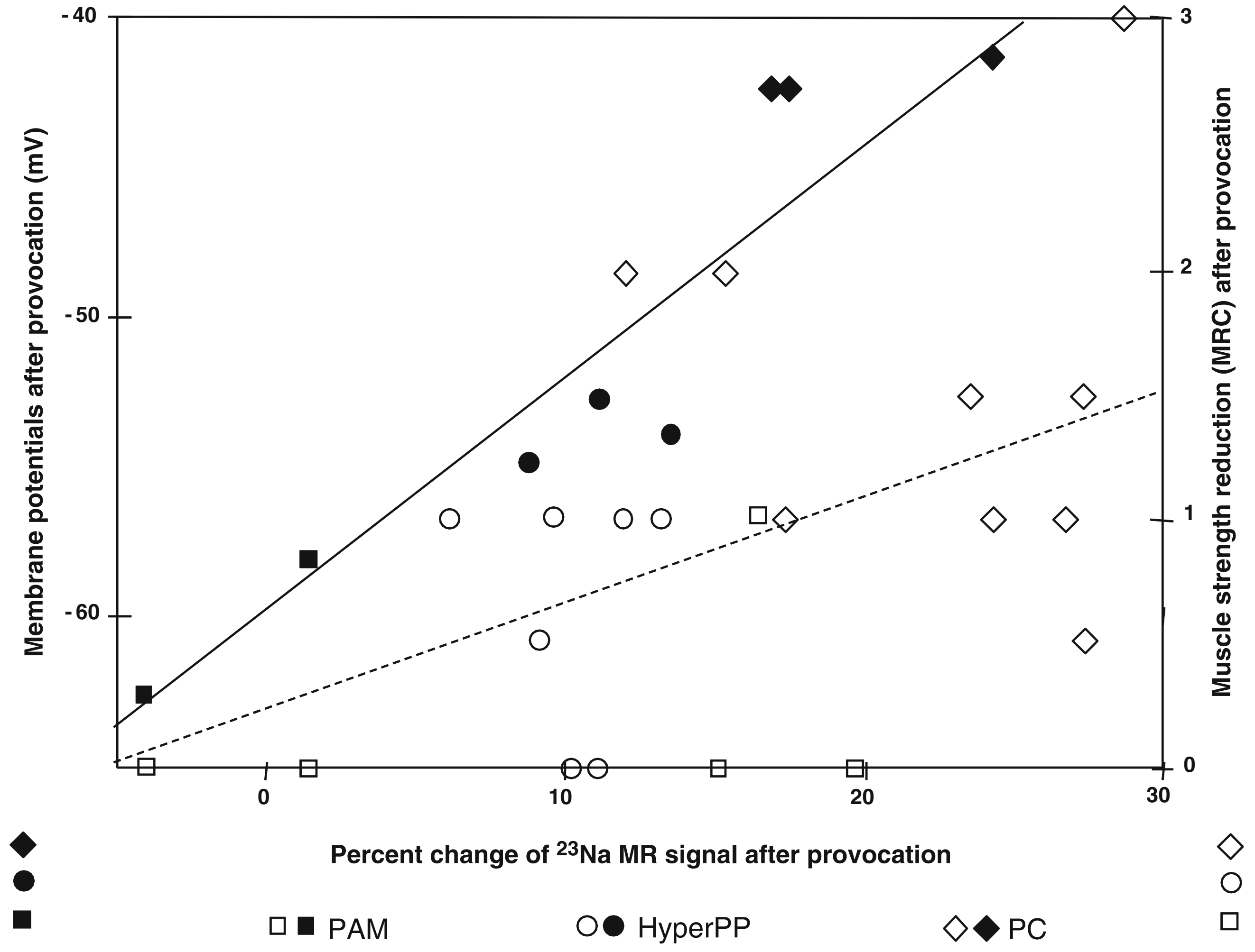

Fig. 6 Analysis of the correlation between ^{23}Na signal increase, membrane potential, and muscle strength reduction. The filled symbols represent the mean resting membrane potentials of the muscle fibers taken from the eight patients (three PC, three HyperPP, two PAM) versus the muscular ^{23}Na signal increase of these patients. The *open symbols* show the decrease in muscle strength of all patients who underwent a provocation test (nine PC, seven HyperPP, five PAM) versus the muscular ^{23}Na signal increase of these patients. The degree of the membrane depolarization correlates with the percent change of the muscular ^{23}Na signal after provocation according to the function $y = 0.825x—60.3$ (*continuous line*) and yields a correlation coefficient of $r = 0.92$ after Pearson. The muscle strength reduction is much less correlated with the muscular ^{23}Na signal ($r = 0.48$; $y = 0.043 x + 0.24$, dashed line for plantarflexion). Reproduced with permission of Weber et al. (2006a)

myotonic muscles exhibit myotonic runs, i.e., action potentials characterized by a modulation of frequency and amplitude (Fig. 1). In mild cases, myotonia may not be evident on clinical examination, yet EMG may reveal the typical myotonic bursts. This is termed latent myotonia. In general, myotonia and corresponding muscle hypertrophy are more prominent in Becker than in Thomsen's disease and myotonia fluctuans (Lehmann-Horn et al. 2004).

Periodic paralysis occurs episodically with varying intervals of normal muscle function. Apparently, the underlying ion channel defects are usually well compensated and an additional trigger is often required for channel malfunction. Two dominant episodic types of weakness with or without myotonia are distinguished by the serum K^+ level during attacks: HyperPP and HypoPP. Intake of K^+ and glucose has opposite effects in the two disorders: while K^+ triggers attacks and glucose is a remedy in HyperPP, glucose-induced hypokalemia provokes attacks in HypoPP which are ameliorated by K^+ intake (Lehmann-Horn et al. 2004). Due to additional release of K^+ from muscle in HyperPP and uptake of K^+ by muscle in HypoPP, the resulting dyskalemia can be so severe that cardiac complications arise. During an attack, death can also occur due to respiratory insufficiency (Jurkat-Rott et al. 2009). Independently of the severity and frequency

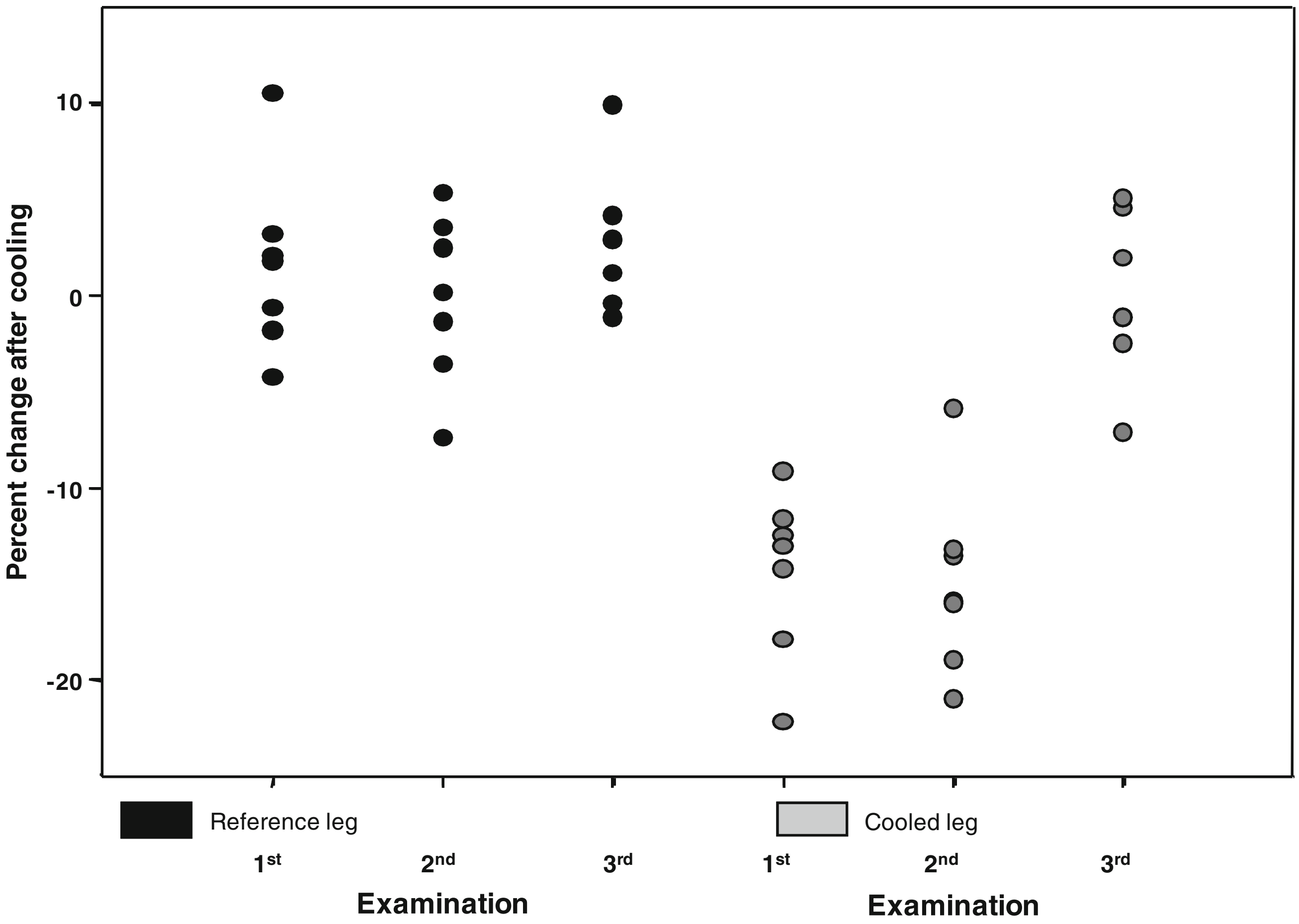

Fig. 7 Graph shows results in seven patients with paramyotonia congenita before (first and second examination) and after (third examination) blockage of pathologic Na^+ channels. Percentage change of muscular ^{23}Na signal intensity after cooling (measured by means of ^{23}Na free induction decays with a time delay between end of the radiofrequency pulse and start of acquisition (echo time) of 0.2 ms) is shown for each patient. There is a decrease in the extracellular-to-intracellular Na^+ concentration ratio in the cooled leg at the first and second examination (without mexiletine). At the third examination, concomitant with an improvement in muscle strength, there is an increase in the concentration ratio to values comparable to those in the reference leg. Reproduced with permission of Weber et al. (2006b)

of the paralytic episodes, many patients develop a chronic progressive myopathy in their forties, an age at which the attacks of weakness decrease.

5 Histopathology

Myotonic muscle fibers may have normal appearance, however, slight myopathic changes with increased occurrence of central nuclei and pathological variation of fiber diameter may be found. Both hypertrophy of type 2A fibers and absence of type 2B fibers can be identified (Jurkat-Rott and Lehmann-Horn 2013) (Fig. 2).

In both types of familial periodic paralysis, dilations of components of the T-tubular system and the sarcoplasmic reticulum occur. Dilation, proliferation, and regeneration result in vacuolization (Engel 1970). Contractions of nearby myofibrils and focal increases in muscle glycogen have also been noted, suggesting that the changes in several organelles accounted for the permanent myopathy of the disease. In otherwise unaffected fibers, collections of multiple closely packed tubules giving a honeycomb appearance may be viewed in cross sections, mostly at the end of fiber. These tubular aggregates are located between longitudinally running myofibrils or beneath the sarcolemma and may contain an internal circular membrane that is not normally seen in the T-tubule or the sarcoplasmic reticulum from which they originate (Jurkat-Rott and Lehmann-Horn 2013; Engel 1970).

6 Magnetic Resonance Imaging

Myotonia congenita and PAM patients do not generally present with pathological imaging findings. In potassium-aggravated myotonia, normal T1- and T2-weighted MR images of the lower legs were observed in a study of six

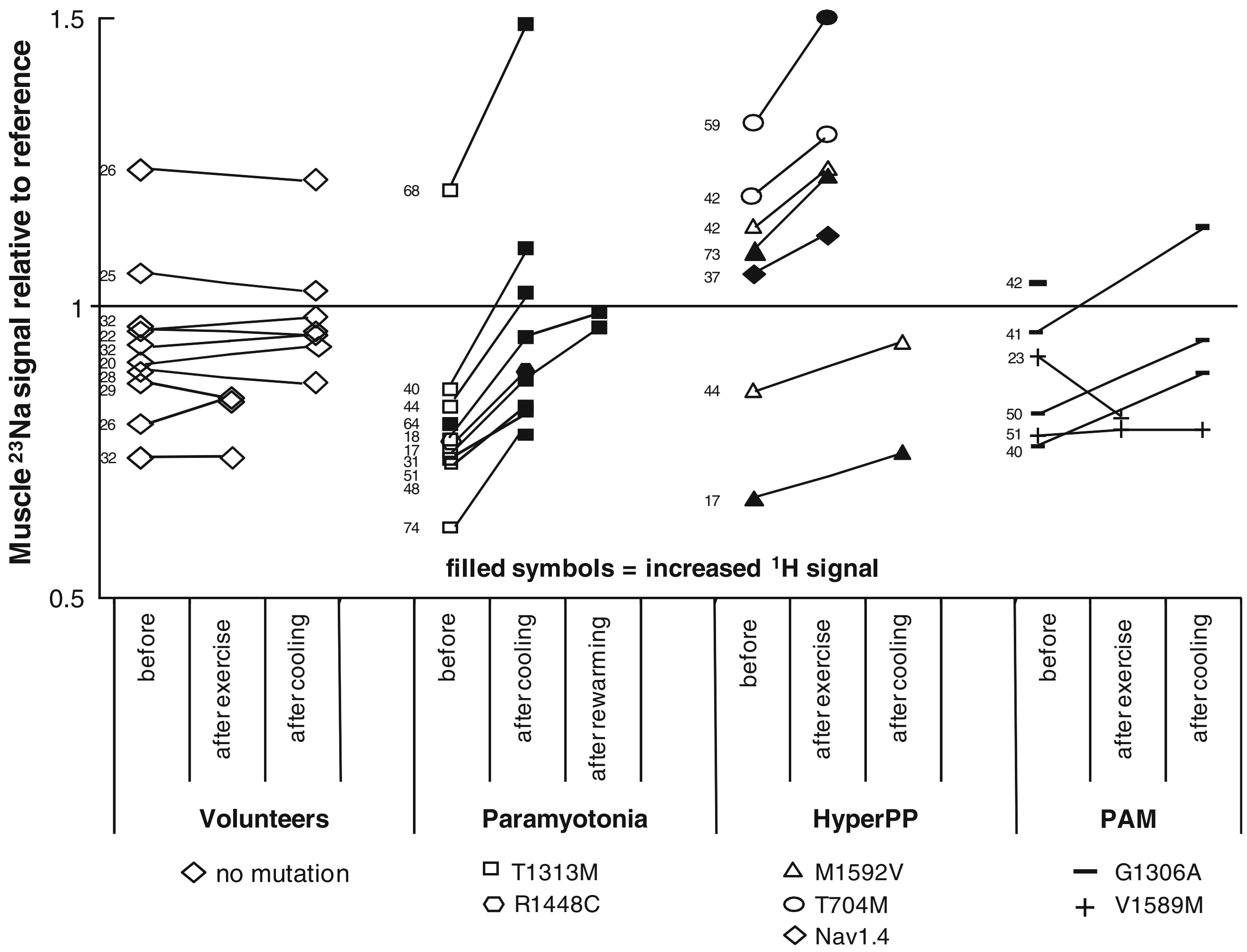

Fig. 8 Muscular ^{23}Na signal intensity relative to reference prior to and after provocation. Muscular ^{23}Na MRI signal intensities of regions-of-interest from the lower legs are shown in relation to the signal of the phantom prior to and after provocation. The figures give the age of the individuals in years. PC and HyperPP patients exhibited a striking increase in the muscle ^{23}Na signal intensity after provocation whereas volunteers showed no significant changes. This increase could also be observed in all PAM patients after cooling. A muscle edema was caused by cooling in all PC patients. The 17-year-old HyperPP patient presented with a unilateral calf edema after he had experienced an attack of paresis and aching muscles of this calf two days before. Reproduced with permission of Weber et al. (2006a)

patients (median age, 43 years) (Weber et al. 2006a). In a recent study, three severely affected RMC patients were examined using a multisequence (T1-weighted, T2-weighted, fat suppressed T2-weighted sequences) whole-body 3 Tesla MRI (Kornblum et al. 2010). In agreement with (Weber et al. 2006a), none of the patients showed skeletal muscle signal changes indicative of fatty muscle degeneration or edema. However, two patients showed muscle bulk hypertrophy of thighs and calves in line with the clinical appearance (Fig. 3) (Kornblum et al. 2010). The authors concluded that chloride channel myotonia and even serious and prolonged transient weakness alone do not result in MRI skeletal muscle signal changes, while MRI fatty skeletal muscle changes and edema that can be seen in myotonic dystrophy type 1 (Kornblum et al. 2006) are not the result of chloride channel dysfunction but clearly consequences of the dystrophic disease process. Therefore, imaging can be used to differentiate DMC and RMC from myotonic dystrophy in which there is reduced muscle mass and edema. Likewise, the prominent muscle bulks in myotonia congenita are due to genuine muscle hypertrophy and not to pseudo-hypertrophy as possible differentiation to other muscular dystrophies (Kornblum et al. 2010). In myotonic dystrophy type 1, a characteristic distribution of muscle involvement with frequent and early degeneration of the medial heads of gastrocnemius muscles, and a perifemoral semilunar pattern of quadriceps muscle affection sparing the rectus femoris has been reported using 3 Tesla MRI

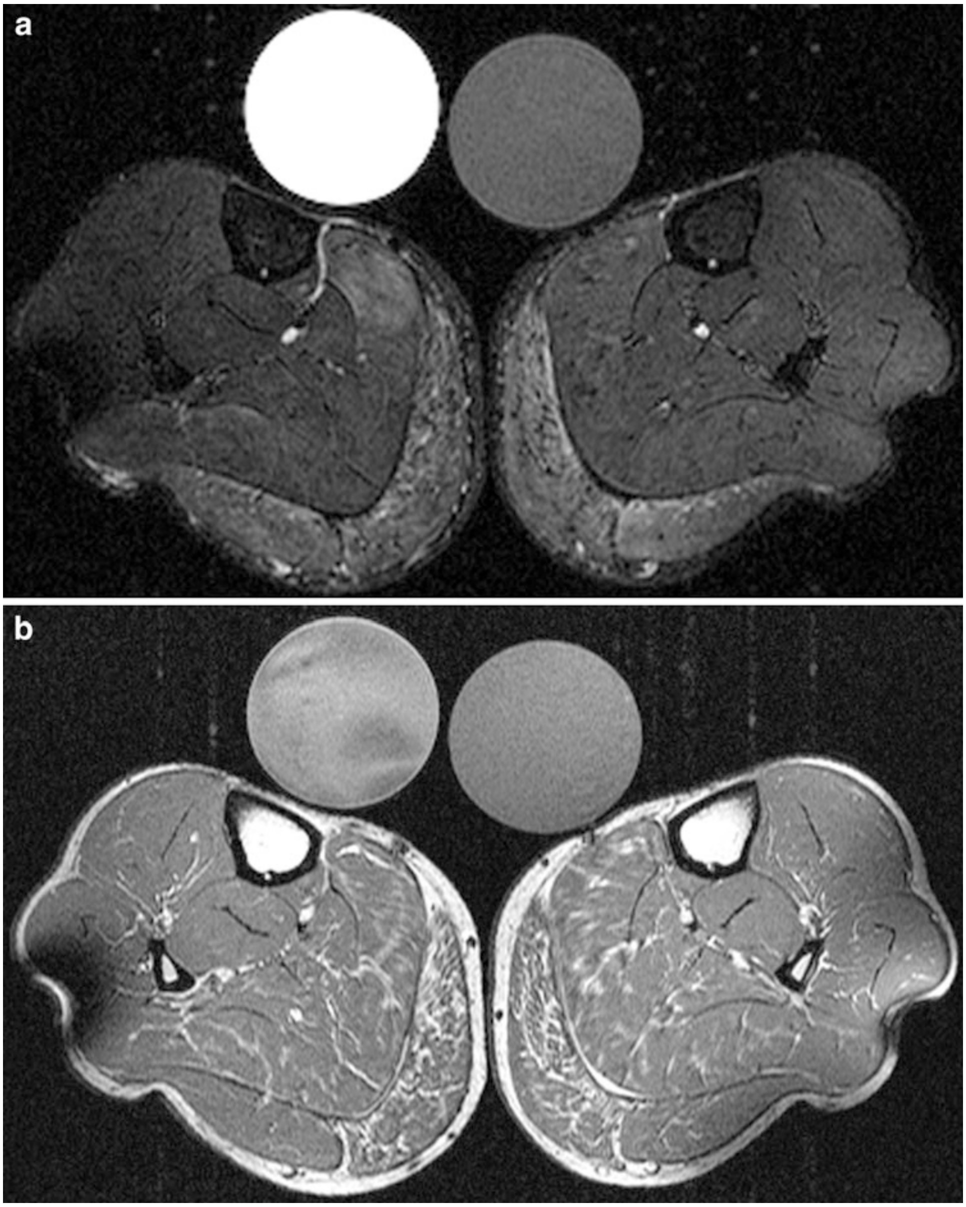

Fig. 9 ^{1}H MRI of the lower legs of a HyperPP patient at age 39. Fat-saturated axial T2 short tau inversion recovery (STIR) sequence visualizes edematous changes most pronounced within the gastrocnemius muscle of both calves (**a**). The axial T1-weighted sequence demonstrates fatty changes most pronounced within both gastrocnemius muscles. The soleus muscle is less affected on both sides (**b**). Two different reference tubes filled with 51.3 mmol/l sodium are also visible

(Kornblum et al. 2006). The most frequently affected muscles in myotonic dystrophy type 1 were the medial heads of gastrocnemius, soleus, and vastus medialis muscles.

In PC, approximately 38 % of patients show normal muscle on T1-weighted and T2-weighted 1.5 Tesla MR imaging examinations of the lower legs (Weber et al. 2006b). In 12.5 % (two male R1448C patients of 25 and 42 years), a bilaterally symmetric homogeneous edema was observed at rest before any exercise or other provocation scheme that was confined to the medial head of the gastrocnemius muscle (Fig. 4) (Weber et al. 2006b). Edema-like muscular changes in the triceps surae muscles were evidenced in 10 % of PC patients (median age 45 years) in another cohort (Weber et al. 2006a). Up to 50 % of older patients (mean age 55 ± 13 years; mutation, R1448H in 1, T1313 M in 3, and R1448C in 4 patients) showed a bilaterally symmetric increased signal intensity of the medial head of the gastrocnemius muscle on T1- and T2-weighted images that was interpreted as a fatty infiltration. There was no distinct muscle atrophy in any of the so far studied 16 paramyotonia patients (Weber et al. 2006b). Highly specific for PC is ^{23}Na MRI which can visualize and monitor aspects of muscular pathophysiology, such as a disturbed muscular Na^+ homeostasis. For example, cooling of the lower leg muscles of PC patients, opens non-inactivating Na^+ channels and depolarizes the muscle fibers and thereby causes muscle stiffness followed by muscle weakness that lasts several hours even after immediate rewarming (Weber et al. 2006a). ^{23}Na MRI is able to depict a myoplasmic sodium accumulation (Fig. 5) which

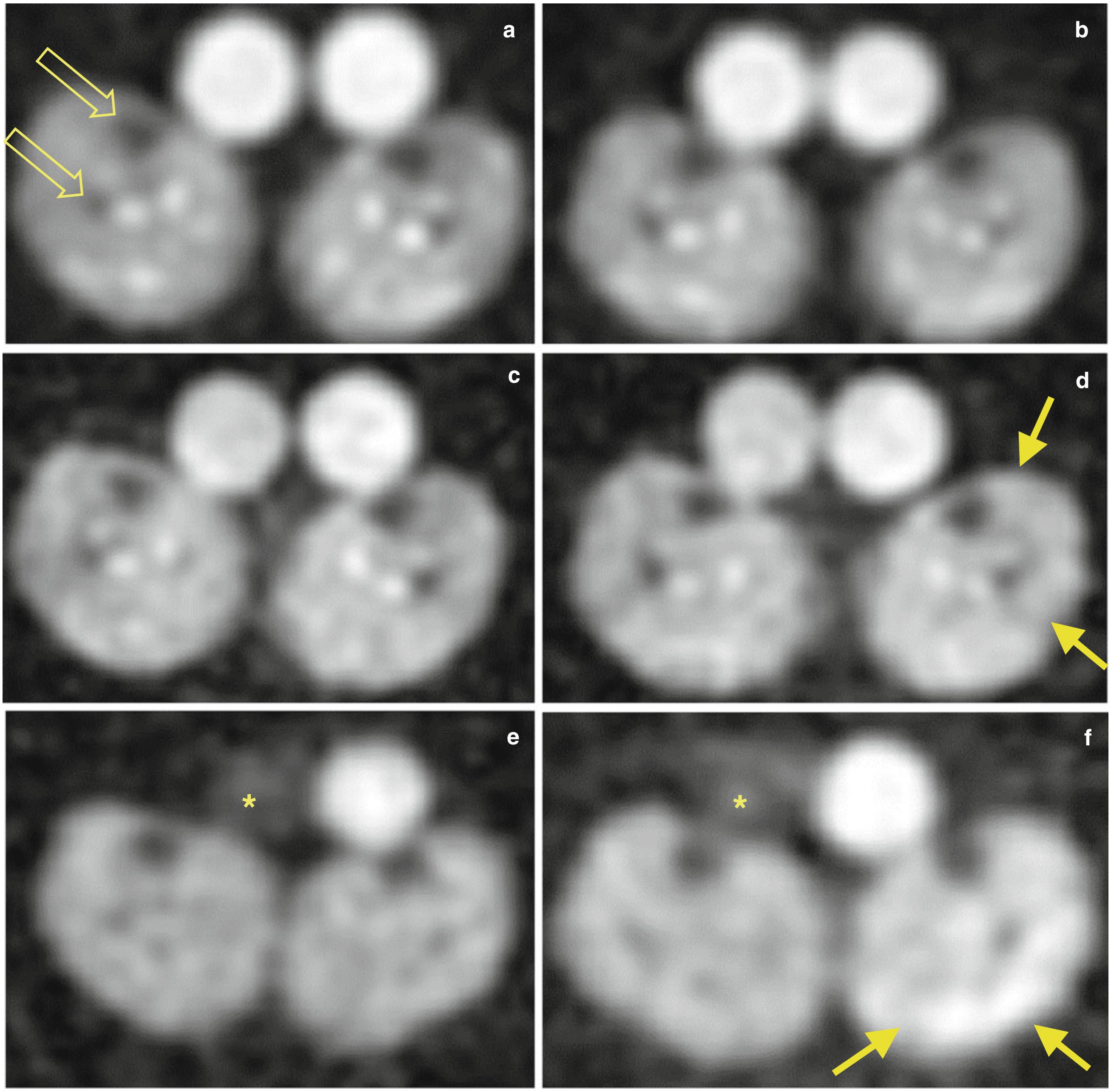

Fig. 10 Axial ^{23}Na MRI of both lower legs in the same patient of Fig. 9 prior and post provocation by cooling of the left lower leg. No relevant changes of the overall sodium concentration are evident as assessed by a spin density image contrast, prior (**a**) and post provocation (**b**). ^{23}Na T1-weighted image contrast prior (**c**) and post provocation (**d**): after provocation, a slight signal increase within the left calf is ascertainable (*arrows* in **d**). ^{23}Na inversion recovery sequence prior (**e**) and post provocation (**f**): the signal increase in the left calf is clearly visible (*arrows* in **f**), and is probably caused by a pathologically increased sodium influx through the mutant Na^+ channels as demonstrated by functional expression of these channels. The *open arrows* in **a** point to the tibial and fibular bones with low ^{23}Na signal. With the ^{23}Na IR sequence, the ^{23}Na signal emitted from vasogenic oedema and vessels was sufficiently suppressed. Note that the signal of the reference tube containing free 51.3 mM Na^+ solution on the right side is suppressed in the ^{23}Na IR sequence (*asterisks* in **e**, **f**), while the contralateral reference tube on the left side filled with 51.3 mM Na^+ in 5 % agarose gel is well visible

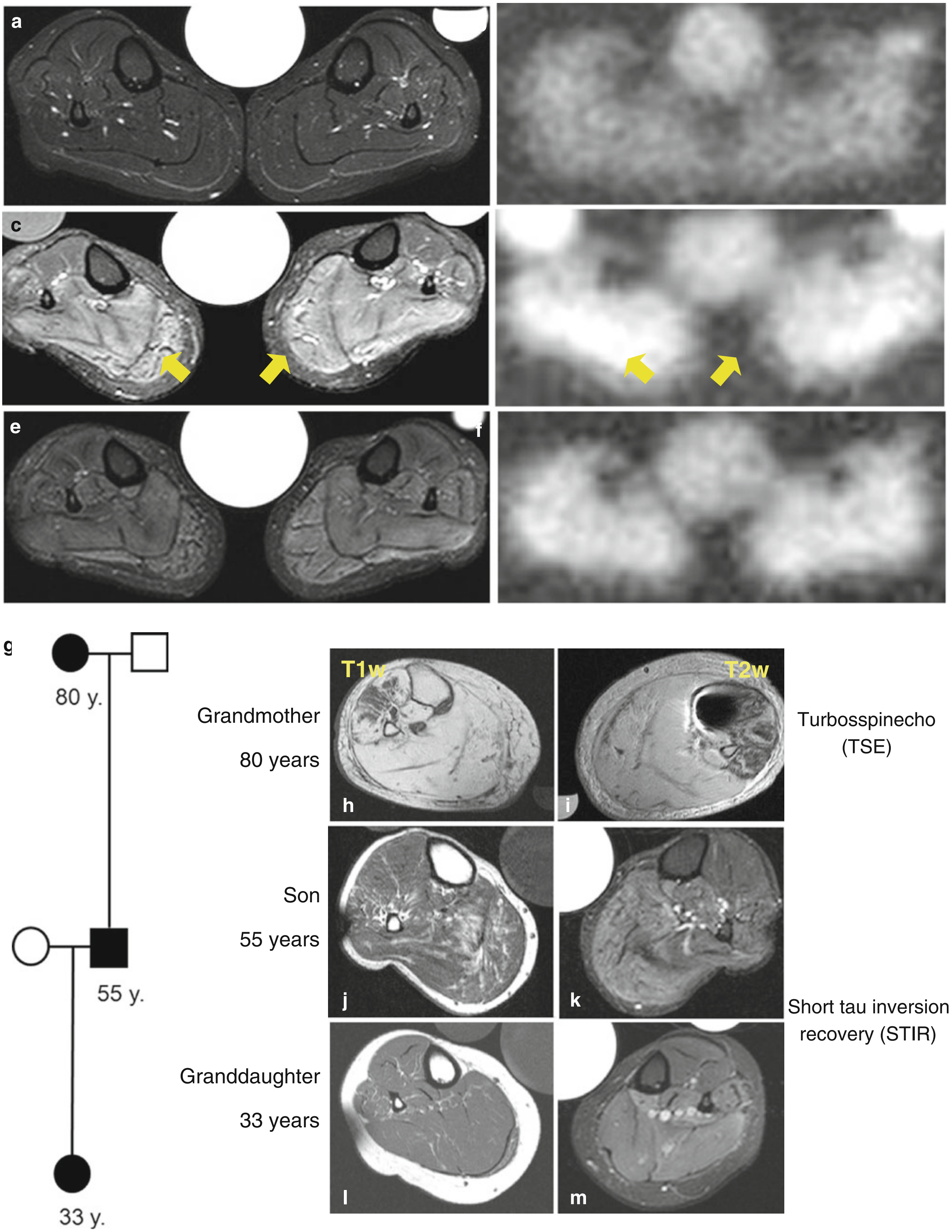
a
c
e
f
g
80 y.
55 y.
33 y.
Grandmother
80 years
Son
55 years
Granddaughter
33 years
T1w
T2w
h
i
j
k
l
m
Turbosspinecho
(TSE)
Short tau inversion
recovery (STIR)

◀**Fig. 11** ^{1}H and ^{23}Na measurements in the calf muscles of HypoPP patients. **a**–**f**: T2-weighted STIR ^{1}H *(left)* and ^{23}Na-MR images (*right*) from a healthy control (**a**, **b**) and the propositus of a HypoPP family, a 37-year-old female harboring the Cav1.1-R1239H mutation (**c**–**f**). The images in (**c**) and (**d**) were taken before treatment and the images in (**e**) and (**f**) were taken after treatment with 250 mg/d acetazolamide for 4 weeks. Note the very high proton intensities in STIR (**c**) and the elevated Na^{+} concentration before treatment (**d**, *arrows* pointing at highest ^{23}Na and ^{1}H signal intensities) and their improvement after treatment. The central reference contains 0.3 % NaCl solution; occasional side tubes containing 0.3 % NaCl in 1 % agarose (*left*) and 0.6 % NaCl in H_2O (*right*) were additional standards. (**g**–**i**): Axial T1-weighted MR images (**h**, **j**, **l**) and T2-weighted images (**i**, **k**, **m**) from family members of the patient, the pedigree is given in (**g**): the female's 80-year-old grandmother whose limb muscles were almost completely replaced with fat (**h** and **i**), the female's 33-year-old sister (**l**, **m**), and the 55-year-old uncle (**j**, **k**). In the youngest family member, no fatty changes (**l**) but already a pronounced muscular edema can be appreciated (**m**), whereas the middle-aged family member presents already with fatty degeneration (**j**) and persistent edema most pronounced in the triceps surae muscle (**k**)

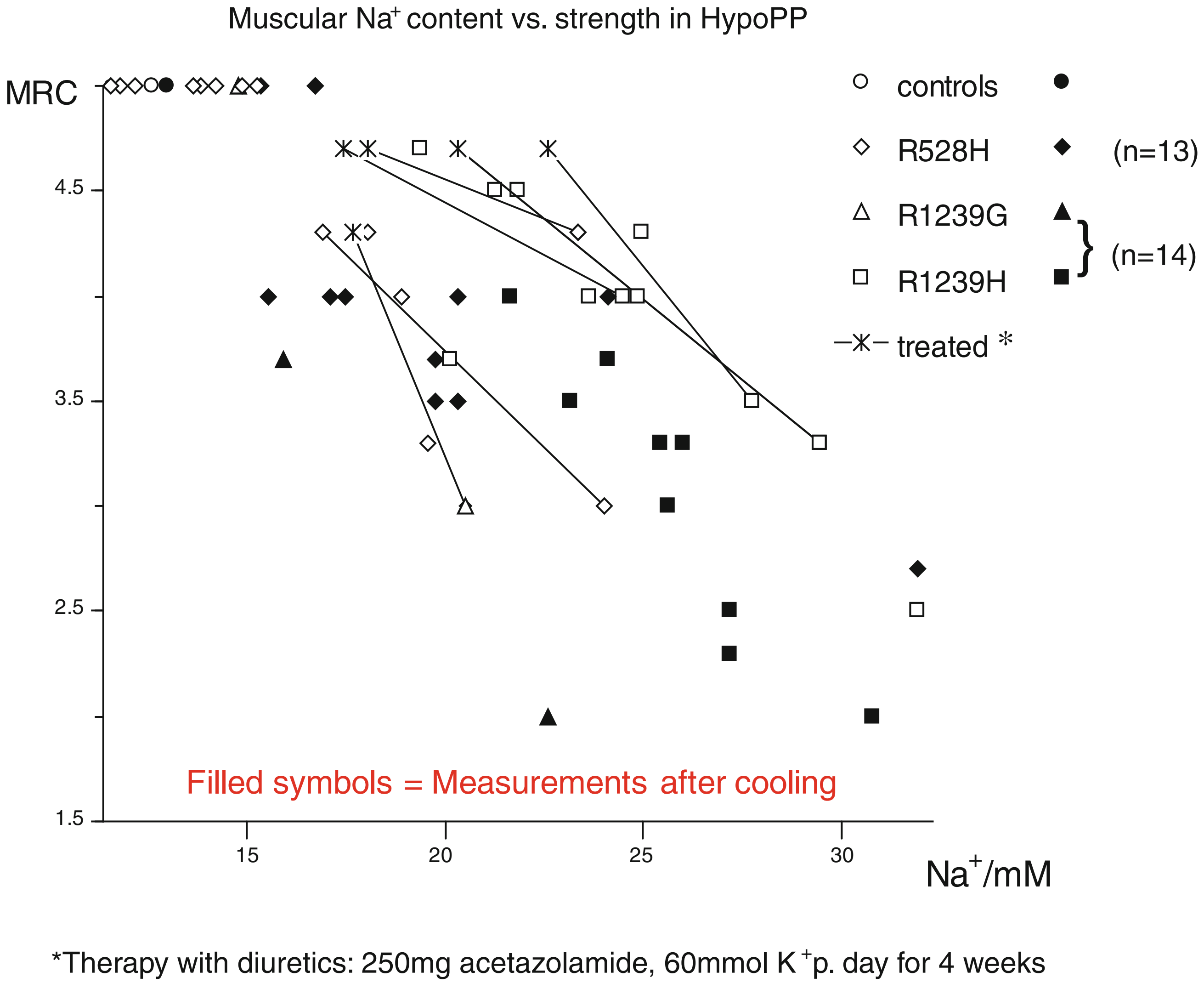

Fig. 12 Correlation of muscle strength and muscular sodium content as measured by ^{23}Na MRI in patients with hypokalemic periodic paralysis (HypoPP) which are also reported in Jurkat-Rott K et al. Proc Natl Acad Sci USA 2009;106:4036-4041 (Jurkat-Rott et al. 2009). The muscular sodium values obtained with a ^{23}Na 1.5 Tesla MRI of the lower legs and the values of plantar flexor muscle strength measured according to the Medical Research Council of Great Britain (MRC) grading scale show a clear correlation. The mean value from 12 healthy controls is shown as open circle. Local cooling increased the ^{23}Na signal intensities and weakness in all provoked patients with HypoPP but not in healthy controls. Following therapy of six patients with 250 mg acetazolamide and 60 mmol K^{+} per day for 4 weeks, a decrease in muscular edema, a 22 % decrease in muscular Na^{+} content, and a 33 % increase in muscle strength could be observed (Jurkat-Rott et al. 2009)

correlates well with the grade of paresis (Fig. 6) (Weber et al. 2006a) and is reproducible (Weber et al. 2006b). Therefore, ^{23}Na MRI is the method of choice for this disease. Na^{+} channel blockers such as mexiletine are able to prevent the myoplasmic sodium accumulation (Fig. 7) (Weber et al. 2006b).

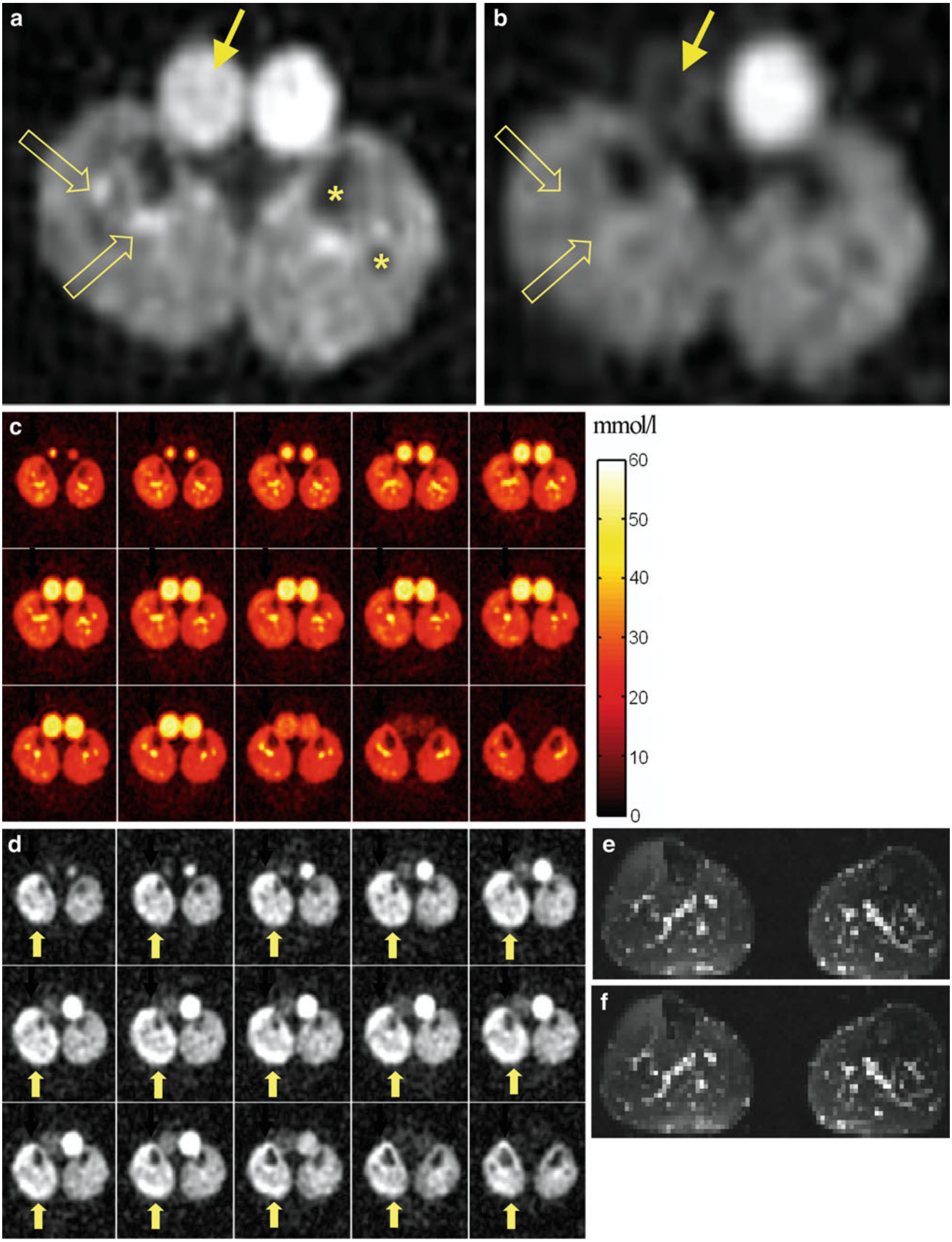
a
b
*
*
c
mmol/l
60
50
40
30
20
10
0
d
e
f

◀**Fig. 13** Twenty-two-year-old man with paramyotonia congenita. **a**, **c**: Spin density contrast (^{23}Na-concentration measurement, TE/TR = 0.2 ms/100 ms; voxel size: 5 × 5 × 5 mm^3; 8 min 20 s); **b**, **d**: Inversion recovery (IR) ^{23}Na 3 Tesla MR-sequence (TE/TR = 0.3 ms/124 ms; TI = 34 ms; voxel size: 6 × 6 × 6 mm^3, 10 min 20 s). **e**, **f**: 3 Tesla ^{1}H MR images using an axial 3 Tesla short tau inversion recovery (STIR) sequence before and after provocation of muscle stiffness and paresis by ice-bags placed around the right lower leg for 25 min. **a**, **b**: Situation of both lower legs before provocation. Compared to the spin density contrast, there is a suppression of vessels in the IR sequence (*open arrows* in **a**, **b**), also the reference tube containing free 51.3 mM Na$^+$ solution on the right side is suppressed in the ^{23}Na IR sequence (*arrows* in **a**, **b**), while the contralateral reference tube on the left side filled with 51.3 mM Na$^+$ in 5 % agarose gel is well visible. The *asterisks* mark the tibial and fibular bone. Sequential images of the multislice ^{23}Na concentration (**c**) and ^{23}Na IR sequence (**d**) demonstrating in this paramyotonia congenita patient after provocation of the right lower leg a homogeneous increase in the intracellular muscular sodium content caused by a pathologically increased sodium influx through the mutant Na$^+$ channels (**d**). The total sodium concentration was changed to a much lesser degree, since in PC there is a shift from the extracellular towards the intracellular sodium concentration after provocation. There is no muscle edema visible after provocation (**f**). However, there is an elevated intracellular sodium concentration in the right calf muscles 15 min after provocation (*arrows* in **d**). The signal intensity after provocation persisted also 1.5 h later after rewarming of the lower-leg. In PC patients cooling induced a significant increase in the muscular ^{23}Na-IR signal (**d**) and a corresponding decrease of muscle strength. 15 min after provocation, the signal intensity increase was 34 % in the right lower leg muscles on the ^{23}Na-IR MR images in this patient (**d**) and 40 % 1.5 h later after rewarming of the provoked lower leg

In HyperPP, increased signal intensities on T2-weighted 1.5 Tesla ^{1}H MRI were visible in the triceps surae muscles of 43 % of the patients prior to any provocation (Fig. 8) (Weber et al. 2006a). In a more recent series using 3 Tesla MRI, eight of twelve HyperPP patients exhibited edema-like changes prior to any provocation on STIR images (Amarteifio et al. 2012). Seven of the twelve HyperPP patients showed fatty infiltration/degeneration, i.e., high signal intensities within their lower leg muscles on T1-weighted images (Amarteifio et al. 2012). HyperPP patients suffering from permanent weakness presented with a high degree of lipomatous changes compared to the group without permanent weakness and healthy volunteers (Amarteifio et al. 2012). A specific pattern of lipomatous changes was noticeable: the highest degree of fatty atrophy was observed in the triceps surae muscle (gastrocnemius followed by the soleus muscle). The peroneal muscles showed concomitantly with the lowest degree of edema-like changes also the lowest degree of fatty atrophy/degeneration (Fig. 9) (Amarteifio et al. 2012). In the hip muscles, the ischiocrural muscles are particularly affected. ^{23}Na MRI displayed significantly higher intracellular muscular sodium signal intensities normalized to a reference phantom containing 51.3 mM Na$^+$ in HyperPP patients with permanent weakness than in those without permanent weakness or healthy volunteers (0.83 vs. 0.67 vs. 0.53). Cooling induced or aggravated muscle weakness in the patients and further increased the sodium signal intensity significantly from 0.75 to 0.86 (Fig. 10). High sodium signal intensities were associated with an osmotic edema. In five patients with permanent weakness, treatment with acetazolamide or hydrochlorothiazide reduced the muscular ^{23}Na signal intensity from 0.85 to 0.64 and increased muscle strength (Amarteifio et al. 2012).

In HypoPP, a cohort of 25 patients with permanent weakness, 21 displayed fatty muscle degeneration, and 18 displayed edema in a ^{1}H-MRI of the lower legs (Jurkat-Rott et al. 2009). The degree of fatty muscle degeneration increased with age. The correlation between water content and Na$^+$ yielded a linear coefficient of determination (R^2) of 0.63. In HypoPP, there is also intramuscular ^{23}Na accumulation. The sodium overload causes muscle edema and weakness in these patients (Fig. 11) and it now can be treated specifically with acetazolamide (Fig. 12) or eplerenone (Jurkat-Rott et al. 2009). Without such continuous treatment, the myoplasmic sodium overload results in a severe osmotic edema that is cytotoxic and causes a lipomatous muscle degeneration and continuous weakness (Fig. 11). Depending on the degree of structural alterations (dilations of the T-tubular system and the sarcoplasmic reticulum, vacuoles, and other myopathic changes), the recovery to be gained by medication will be substantial or minor.

7 Therapy

Myotonia can partially be managed by keeping the muscles in the “warmed-up” state by continuous slight movements. However, particularly Becker myotonia patients require long-term medication. The myotonic stiffness responds to class 1 anti-arrhythmic drugs which show use-dependence and block the repetitive activity (Mohammadi et al. 2005). Of the many drugs tested that can be administered orally, flecainide and propafenone are the drugs of choice. They preferentially block the non-inactivating mutant sodium channels that reopen abnormally frequently. Thus, they have a much greater beneficial effect in sodium channel myotonias than in chloride channel myotonia. Patients with myotonia permanens need long-term continuous therapy. The drugs are also very effective in preventing and reducing the degree of cold-induced stiffness and weakness in PC. Carbonic anhydrase inhibitors are an alternative treatment for patients with sodium channel myotonias but may induce weakness in PC patients and exacerbate chloride channel myotonia.

For HyperPP attacks of weakness, the reduction of serum potassium levels by stimulation of the Na$^+$/K$^+$ pump, e.g., by continuous mild exercise or carbohydrate ingestion of salbutamol inhalation helps relieve the attacks of weakness.

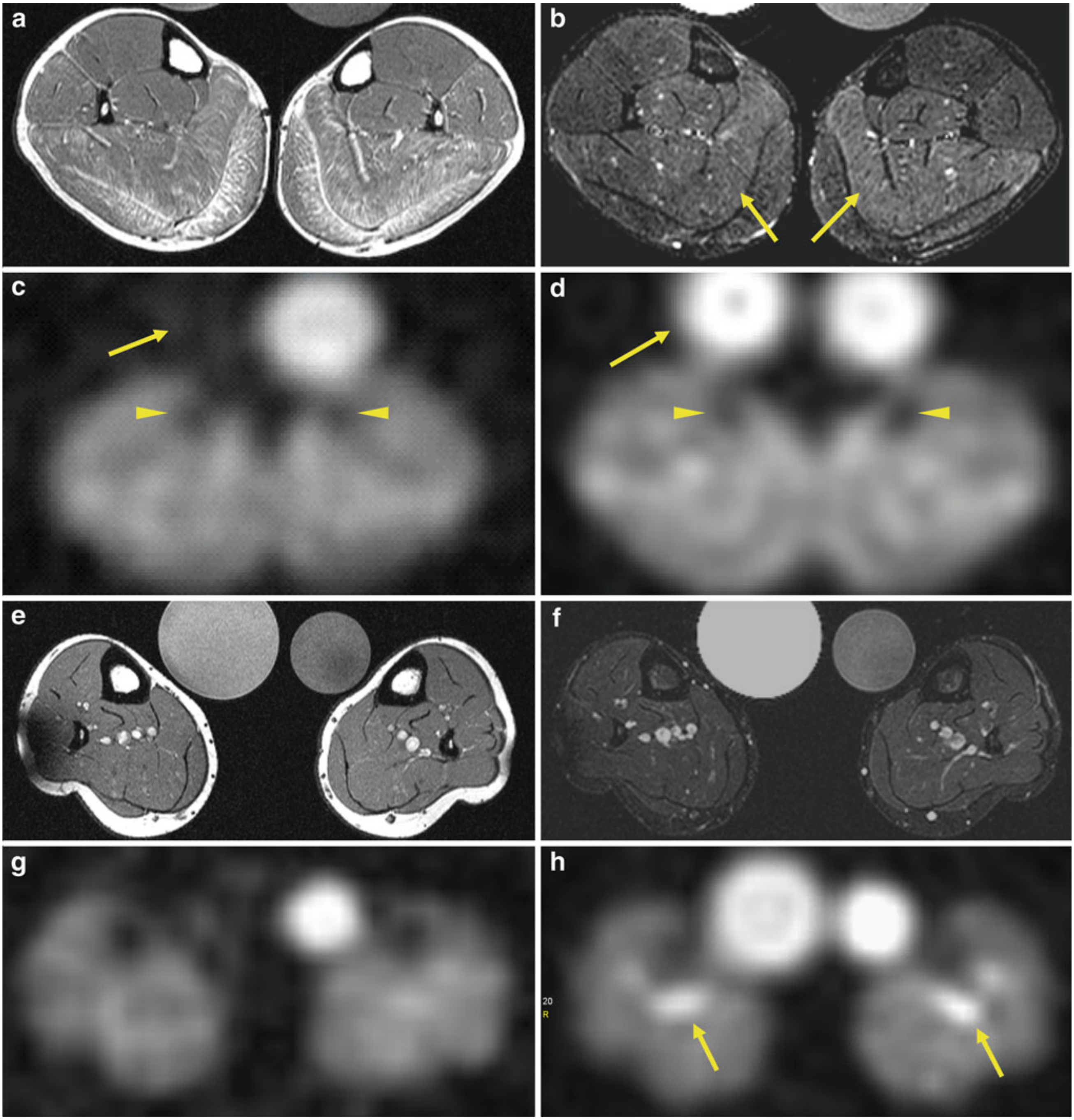

Fig. 14 Edema-like changes and increased muscular sodium are present in Duchenne muscular dystrophy (DMD). MRI of both calves of a 10-year-old boy with DMD (**a**–**d**), a 16-year-old healthy volunteer (**e**–**h**), and a 22-year-old woman with DMD (**i**–**l**); **a**, **e**, **i**: T1-weighted, **b**, **f**, **j**: short tau inversion recovery (STIR), **c**, **g**, **k**: ^{23}Na inversion recovery (IR), and **d**, **h**, **l**: ^{23}Na tissue sodium concentration (TSC) images. There is fatty degeneration of the triceps surae muscles in the boy (**a**) and muscular edema of both soleus muscles (*arrows* in **b**) compared with normal findings in the volunteer (**e**–**f**). ^{23}Na IR (**c**) and TSC ^{23}Na MRI (**d**) reveal elevated signal in both soleus muscles compared with those of the volunteer (**g**, **h**). The arrowheads point to the tibial bones (**c**, **d**). Note that the signal of vessels is bright on TSC ^{23}Na MRI (*arrows* in **h**) and that the signal of the reference tube containing free 0.3 % NaCl solution (*arrow* in **c**) is suppressed in the ^{23}Na IR sequence, while the contralateral reference tube filled with Na^+ in agarose gel is well visible. In the woman with DMD (*asterisk* on right soleus muscle in **i**–**l**), fatty infiltration mainly affects the peroneus muscles (*arrow* in **i** and **j**) in contrast with all boys studied (mainly triceps surae muscle). Reproduced with permission of Weber et al. (2011)

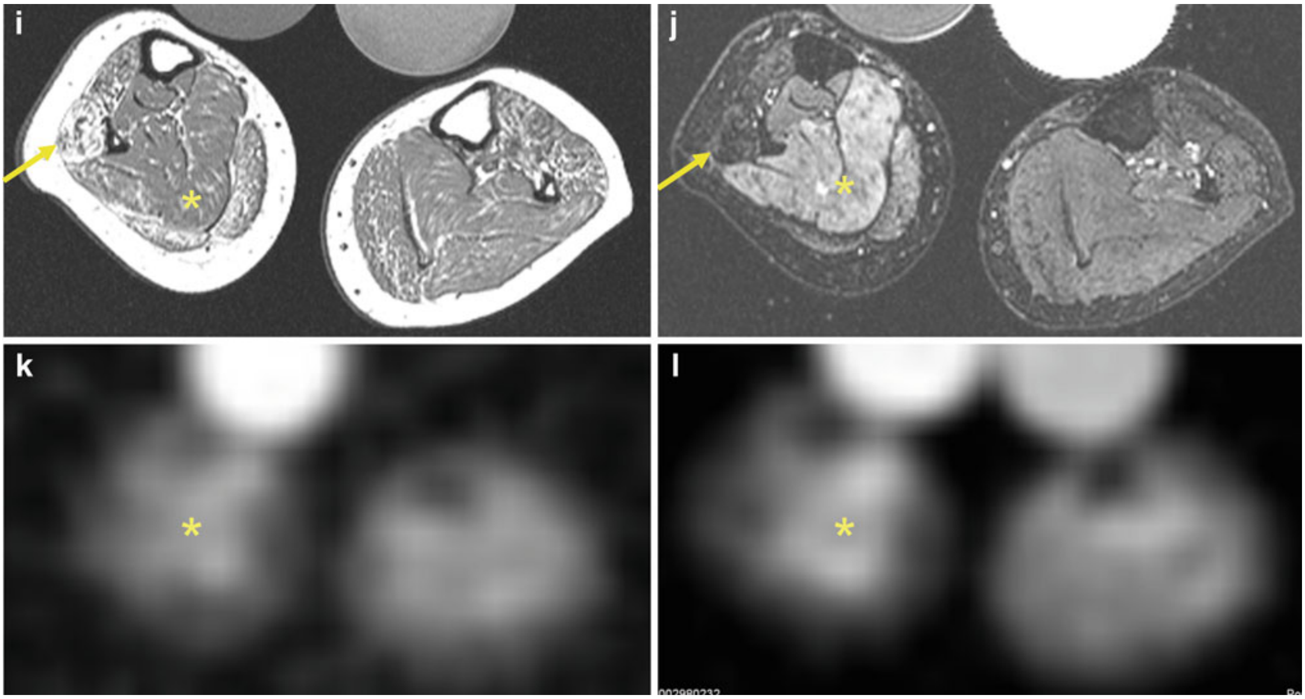

Fig. 14 continued

Permanent stabilization of serum K^+ at low levels by thiazide diuretics is also a possibility. Alternatively, carbonic anhydrase inhibitors are the second choice and may be effective via myoplasmic acidification (Jurkat-Rott and Lehmann-Horn 2007).

In patients with HypoPP, all substances which decrease serum K^+ levels either by shifting potassium into the cells or by excretion by the kidney should be avoided, i.e., high carbohydrate/salt meals, bicarbonate and K^+-extruding diuretics, sedentary lifestyle and strenuous physical exercise. Weakness episodes should be treated orally with KCl. Carbonic anhydrase inhibitors are the prophylactic medication of choice. K^+-sparing diuretics, such as triamterene, amiloride, and particularly the selective aldosterone antagonist eplerenone may be administered as well.

8 Conclusions and Future Perspectives

The implementation of an inversion recovery (IR) sequence with ^{23}Na MRI (Nagel et al. 2011) allowed us to better differentiate intracellular from extracellular sodium (Fig. 13). However, while the IR prepared Na^+ measurement enables weighting of the measurement toward intracellular ^{23}Na, it would still have significant contributions from extracellular pool and it does not provide a clear separation between intra- and extracellular ^{23}Na but nevertheless the ^{23}Na IR sequence allows for an suppression of the ^{23}Na signal emitted by extracellular edema and vessels (see also "Skeletal Muscle MR Imaging Beyond Protons:With a Focus on Sodium MRI in Musculo skeletal Applications" of this book). Using this technique, a markedly increased intracellular sodium concentration was detected in periodic paralysis patients with permanent weakness at rest, while in paramyotonia muscle a transient intracellular sodium overload occurred during transient weakness provoked by cooling (Amarteifio et al. 2012; Nagel et al. 2011) (Fig. 13). The muscle edema displayed in the periodic paralysis patients by STIR ^{1}H-MRI is likely to be of osmotic rather than inflammatory origin. The increased myoplasmic sodium seems to initiate and to be indicative of the permanent weakness which precedes fatty muscle degeneration.

The development of ^{23}Na MRI at high magnetic field strengths of 3 to 7 Tesla permits greater signal to noise and maybe will hopefully allow for a more precise quantification of intracellular ^{23}Na homeostasis in healthy volunteers as well as in patients. We expect that this technique will help to elucidate the pathophysiology of muscular edema-like changes in the periodic paralyses and in other muscular dystrophies, such as Duchenne (Fig. 14) (Weber et al. 2011,

2012) (see also "Skeletal Muscle MR Imaging Beyond Protons: With a Focus on Sodium MRI in Musculoskeletal Applications" of this book).

Acknowledgments The authors thank Dr. Armin M. Nagel, Department of Medical Physics in Radiology, German Cancer Research Center Heidelberg, for his contribution. Prof. Dr. Frank Lehmann-Horn and PD Dr. Karin Jurkat-Rott receive grants from the non-profit Else Kröner-Fresenius-Stiftung, the German Federal Ministry of Education and Research (BMBF, IonoNeurOnet), and the Baden-Wuerttemberg Ministry of Science (Competence Center on Rare Disease). Prof. Dr. Frank Lehmann-Horn is an endowed Senior Research Professor of Neurosciences of the non-profit Hertie-Foundation. Parts of the ^{23}Na MRI work were supported by a research grant from the Medical Faculty of Heidelberg University. Finally, we are grateful to the patients and their families for their participation and to the Deutsche Gesellschaft für Muskelkranke e.V. for their support.

References

Amarteifio E, Nagel AM, Weber MA, Jurkat-Rott K, Lehmann-Horn F (2012) Hyperkalemic periodic paralysis and permanent weakness: 3-T MR imaging depicts intracellular 23Na overload—initial results. Radiology 264:154–163

Bryant SH (1969) Cable properties of external intercostal muscle fibres from myotonic and nonmyotonic goats. J Physiol (Lond) 204:539–550

Engel AG (1970) Evolution and content of vacuoles in primary hypokalemic periodic paralysis. Mayo Clin Proc 45:774–814

Fontaine B, Vale Santos JM, Jurkat-Rott K et al (1994) Mapping of the hypokalaemic periodic paralysis (HypoPP) locus to chromosome 1q31-32 in three European families. Nat Genet 6:267–272

Fontaine B, Khurana TS, Hoffman EP et al (1990) Hyperkalemic periodic paralysis and the adult muscle sodium channel alpha-subunit gene. Science 250:1000–1002

Heine R, Pika U, Lehmann-Horn F (1993) A novel SCN4A mutation causing myotonia aggravated by cold and potassium. Hum Mol Genet 2:1349–1353

Hoffman EP, Lehmann-Horn F, Rüdel R (1995) Overexcited or inactive: ion channels in muscle diseases. Cell 80:681–686

Jurkat-Rott K, Lehmann-Horn F (2007) Genotype-phenotype correlation and therapeutic rationale in hyperkalemic periodic paralysis. Neurotherapeutics 4:216–224

Jurkat-Rott K, Müller-Höcker J, Pongratz D et al (2002) Chapter 5: diseases associated with ion channel and ion transporter defects: Chloride and sodium channel myotonias. In: Karpati G (ed) Structural and molecular basis of skeletal muscle diseases. ISN Neuropath Press, Basel, pp 90–94

Jurkat-Rott K, Lehmann-Horn F, Elbaz A, Heine R, Gregg RG, Hogan K, Powers P, Lapie P, Vale-Santos JE, Weissenbach J, Fontaine B (1994) A calcium channel mutation causing hypokalemic periodic paralysis. Hum Mol Genet 3:1415–1419

Jurkat-Rott K, Mitrovic N, Hang C et al (2000) Voltage-sensor sodium channel mutations cause hypokalemic periodic paralysis type 2 by enhanced inactivation and reduced current. Proc Natl Acad Sci USA 97:9549–9554

Jurkat-Rott K, Groome J, Lehmann-Horn F (2012) Pathophysiological role of omega pore current in channelopathies. Front Pharmacol 3:112. Epub 2012 Jun 11

Jurkat-Rott K, Lehmann-Horn F (2013) Chapter 11: Sarcolemmal ion channelopathies. In: Goebel HH, Sewry CA, Weller RO (eds) Muscle disease: pathology and genetics, 2nd edn. International Society of Neuropathology. John Wiley and Sons Ltd., Hoboken, New Jersey, pp 118–125

Jurkat-Rott K, Weber MA, Fauler M et al (2009) K + -dependent paradoxical membrane depolarization and Na + overload, major and reversible contributors to weakness by ion channel leaks. Proc Natl Acad Sci USA 106:4036–4041

Koch MC, Steinmeyer K, Lorenz C et al (1992) The skeletal muscle chloride channel in dominant and recessive human myotonia. Science 257:797–800

Lehmann-Horn F, Rüdel R, Ricker K (1987a) Membrane defects in paramyotonia congenita (Eulenburg). Muscle Nerve 10:633–641

Lehmann-Horn F, Küther G, Ricker K et al (1987b) Adynamia episodica hereditaria with myotonia: a non-inactivating sodium current and the effect of extracellular pH. Muscle Nerve 10: 363–374

Lehmann-Horn F, Rüdel R, Jurkat-Rott K (2004) Chapter 46: Nondystrophic myotonias and periodic paralyses. In: Engel AG, Franzini-Armstrong C (eds) Myology, 3rd edn. McGraw-Hill, New York, pp 1257–1300

Lerche H, Heine R, Pika U et al (1993) Human sodium channel myotonia: slowed channel inactivation due to substitutions for a glycine within the III/IV linker. J Physiol (Lond) 470:13–22

Lerche H, Mitrovic N, Dubowitz V et al (1996) Paramyotonia congenita: The R1448P sodium channel mutation in adult human skeletal muscle. Ann Neurol 39:599–608

Kornblum C, Lutterbey GG, Czermin B et al (2010) Whole-body high-field MRI shows no skeletal muscle degeneration in young patients with recessive myotonia congenita. Acta Neurol Scand 121:131–135

Kornblum C, Lutterbey G, Bogdanow M et al (2006) Distinct neuromuscular phenotypes in myotonic dystrophy types 1 and 2: a whole body highfield MRI study. J Neurol 253:753–761

Mohammadi B, Jurkat-Rott K, Alekov AK et al (2005) Preferred mexiletine block of human sodium channels with IVS4 mutations and its pH-dependence. Pharmacogenet 15:235–244

Nagel AM, Amarteifio E, Lehmann-Horn F, Jurkat-Rott K, Semmler W, Schad LR, Weber MA (2011) 3 Tesla sodium inversion recovery magnetic resonance imaging allows for improved visualization of intracellular sodium content changes in muscular channelopathies. Invest Radiol 46:759–766

Rojas CV, Wang JZ, Schwartz LS et al (1991) A Met-to-Val mutation in the skeletal muscle Na + channel alpha-subunit in hyperkalaemic periodic paralysis. Nature 354:387–389

Weber MA, Nagel AM, Wolf MB, Jurkat-Rott K, Kauczor HU, Semmler W, Lehmann-Horn F (2012) Permanent muscular sodium overload and persistent muscle oedema in Duchenne muscular dystrophy a possible contributor of progressive muscle degeneration. J Neurol 259:2385–2392

Weber MA, Nagel AM, Jurkat-Rott K, Lehmann-Horn F (2011) Sodium (23Na) MRI detects elevated muscular sodium concentration in Duchenne muscular dystrophy. Neurology 77:2017–2024

Weber MA, Nielles-Vallespin S, Essig M et al (2006a) Muscle Na^{+} channelopathies—MRI detects intracellular ^{23}Na accumulation during episodic weakness. Neurology 67:1151–1158

Weber MA, Nielles-Vallespin S, Huttner HB et al (2006b) Evaluation of patients with paramyotonia at 23Na MR imaging during cold induced weakness. Radiology 240:489–500

MRI in Muscle Tumors and Tumors of Fasciae and Tendon Sheaths

F. M. Vanhoenacker, M. E. A. P. M. Adriaensen-van Roij,
and A. M. De Schepper

Contents

1 **Key points** 289
2 **Introduction** 290
3 **Benign Muscle Tumors** 290
3.1 Leiomyoma 290
3.2 Rhabdomyoma 291
3.3 Other Benign STT with Intramuscular Location 292
4 **Malignant Muscle Tumors** 295
4.1 Leiomyosarcoma 296
4.2 Rhabdomyosarcoma 297
5 **Pseudotumoral Lesions of Muscle** 298
5.1 Myositis Ossificans 298
5.2 Focal Myositis 300
5.3 Calcifying Myonecrosis 301
5.4 Intramuscular Abscess 301
6 **Tumor and Tumor-like Conditions of Fasciae and Tendon Sheaths** 301
6.1 Tendon Sheath Cyst 301
6.2 Giant Cell Tumor of Tendon Sheath 302
6.3 Fibroma of the Tendon Sheath 303
6.4 Lipoma of Tendon Sheath 303
6.5 Tenosynovial Chondromatosis 303
6.6 Superficial Fibromatoses 303
6.7 Nodular Fasciitis 306
7 **Conclusion** 306
References 307

Abstract

This chapter aims to discuss the relevant clinicopathological and imaging characteristics of tumor and tumor-like soft tissue lesions involving smooth muscle and skeletal muscle. Special emphasize is placed on MR imaging. The discussion is basically focused on those intramuscular tumors that show histologically muscle differentiation. Benign muscle tumors (rhabdomyoma and leiomyoma) are relatively rare and account for less than 2 % of benign soft tissue tumors. Malignant tumors with muscle differentiation (rhabdomyosarcoma and leiomyosarcoma) are more frequent than their benign counterparts, and represent 2–12 and 8–9 % of soft tissue sarcomas, respectively. Other histological types of soft tissue tumors (STT) may arise in muscle and MR imaging is usually not specific for prediction of histology. There are—however—some intramuscularly located tumors (e.g., usual lipoma) that may be characterized with confidence on MR imaging. Lesions with more or less specific imaging features are mostly benign, whereas malignant STT do not have specific imaging features. Although histologically not belonging to the group of muscle tumors (according to the World Health Organization Classification), the imaging features of characteristic STT located within the muscle will be briefly reviewed. Furthermore, this chapter will deal with the most frequent muscular pseudotumors. Finally, tumor (like) conditions of fasciae and tendon sheaths will be discussed.

1 Key points

- Soft tissue tumors (STT) of muscle are relatively rare.
- In contradistinction to other histological types of STT, malignant tumors with histologically myogenic differentiation are more frequent than benign muscle tumors of the soft tissues.

F. M. Vanhoenacker (✉) · A. M. De Schepper
Department of Radiology, University Hospital Antwerp,
Wilrijkstraat 10, B-2650 Edegem, Belgium
e-mail: filip.vanhoenacker@telenet.be

F. M. Vanhoenacker
General Hospital Sint-Maarten Duffel-Mechelen,
Rooienberg 25, 2570 Duffel, Belgium

F. M. Vanhoenacker
Faculty of Medicine and Health Sciences,
University of Ghent, Ghent, Belgium

M. E. A. P. M. Adriaensen-van Roij
Department of Radiology, Atrium Medical Center Parkstad,
Henri Dunantstraat 5, 6419 PC, Heerlen, The Netherlands

M.-A. Weber (ed.), *Magnetic Resonance Imaging of the Skeletal Musculature*, Medical Radiology. Diagnostic Imaging,
DOI: 10.1007/174_2013_849, © Springer-Verlag Berlin Heidelberg 2013
Published Online: 24 May 2013

- Rhabdomyosarcoma is the most common malignant pediatric STT, the embryonal subtype being by far the most frequent.
- MR imaging of muscle tumors is nonspecific, but it is the preferred technique for local staging.
- Radiographs or CT scan, although rarely diagnostic, may demonstrate intralesional calcifications.
- Histological confirmation is mandatory in any case of suspected malignancy.

2 Introduction

Benign muscle tumors are relatively rare and account for less than 2 % of benign soft tissue tumors (Kransdorf 1995a). Malignant tumors with muscle differentiation are more frequent than their benign counterparts. Rhabdomyosarcoma and leiomyosarcoma represent 2–12 and 8–9 % of soft tissue sarcomas, respectively (Kransdorf 1995b).

This chapter aims to discuss the relevant clinicopathological and imaging characteristics of tumor and tumor-like soft tissue lesions involving smooth muscle and skeletal muscle. Special emphasize is placed on MR imaging. The discussion is basically focused on those intramuscular tumors that show histologically muscle differentiation (Fletcher et al. 2013) (Table 1). One should consider that other histological types of soft tissue tumors may arise in muscle and that MR imaging is usually not specific for prediction of histology. Therefore, histological confirmation is always required particularly if there is any suspicion for malignancy.

There are—however—some intramuscularly located tumors (e.g., usual lipoma) that may be characterized with confidence on MR imaging. Lesions with more or less specific imaging features are mostly benign, whereas malignant soft tissue tumors (STT) do not have specific imaging features. Although histologically not belonging to the group of muscle tumors (according to the World Health Organization Classification 2013; Table 1), the imaging features of characteristic STT located within the muscle will be briefly reviewed.

Furthermore, this chapter will deal with the most frequent muscular pseudotumors.

Finally, tumor-like conditions of fasciae and tendon sheaths will be discussed.

Muscle tumors involving the gastrointestinal system, the retroperitoneum, uterus, and other organ systems different from the musculoskeletal system are excluded.

Table 1 World health organization classification of muscle tumors (from Fletcher et al. 2013, Fourth revision)

Skeletal muscle tumors
Benign
Extracardiac rhabdomyoma : adult, fetal, and genital type
Malignant
Embryonal rhabdomyosarcoma
Alveolar rhabdomyosarcoma
Pleomorphic rhabdomyosarcoma
Spindle cell/sclerosing rhabdomyosarcoma
Smooth muscle tumors
Benign
Deep leiomyoma
Malignant
Leiomyosarcoma (excluding skin)

3 Benign Muscle Tumors

3.1 Leiomyoma

3.1.1 Definition, Clinical Findings, and Histology

Superficial leiomyoma

Cutaneous leiomyomata (leiomyoma cutis) arise from the arrector pili muscle of the skin. They present as clustered papules or less commonly as single painful nodules. The size ranges from a few millimeters up to 2 cm.

Lesions arising from the deep dermis of the scrotum, nipple, areola, and vulva are designated as genital leiomyoma (Kransdorf and Murphey 2007).

Angioleiomyoma is a rare benign tumor, arising from the muscularis media of small vessels (Hachisuga et al. 1984). It is currently classified as a pericytic tumor rather than a true smooth muscle tumor (Fletcher et al. 2013). There are three histopathological subtypes: solid, cavernous, and venous.

The lesion is most common in adults, with two-thirds occurring in the fourth through sixth decades of life. The tumor is typically small (less than 2 cm) and often slowly growing. It may be localized in the dermis, the subcutaneous fat, or the superficial fasciae of the extremities (Vanhoenacker et al. 2009) (Fig. 1).

It is painful in over half of the cases (Ramesh et al. 2004). Classically, tenderness and pain, which is often paroxysmal in nature and precipitated by light touch or changes in temperature, are the presenting features in 50–70 % of cases (Gupte et al. 2008).

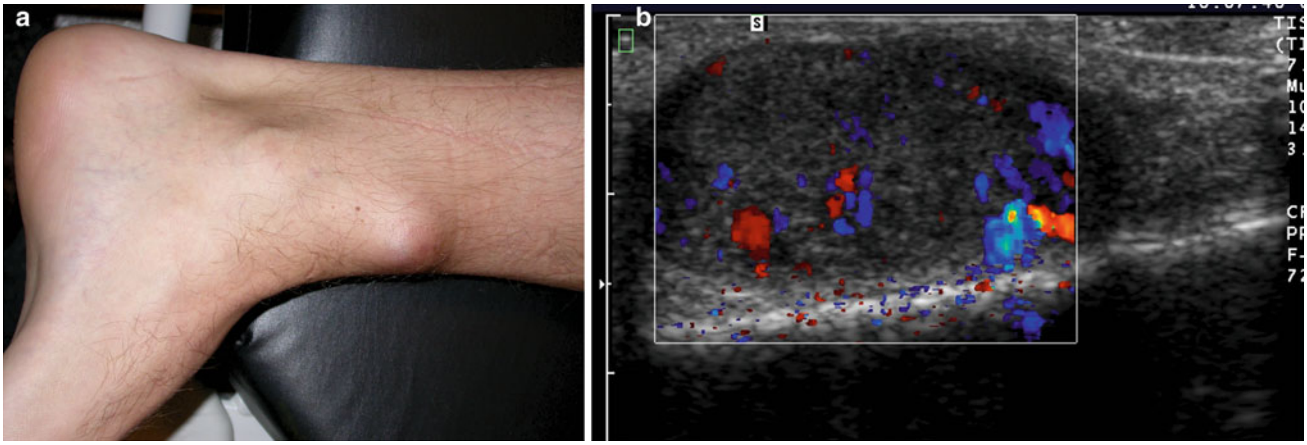

Fig. 1 Angioleiomyoma. **a** Photograph of a 34-year-old man presenting with a slowly growing mobile soft tissue mass at the left lower leg. **b** Longitudinal ultrasound showing a well-defined hypoechoic lesion within the subcutaneous tissue. The lesion is vascular on power Doppler

Deep leiomyoma

Leiomyomata of the deep soft tissue are very rare in comparison with superficial leiomyomata. Furthermore, long-term follow-up showed that deep leiomyoma may demonstrate aggressive behavior, leading to the assumption that these lesions could be potentially malignant (Weiss 2002). Therefore, histological confirmation of the lesion is mandatory to make a reliable diagnosis (Billings et al. 2001).

There are two distinct subtypes: the deep leiomyoma of extremities (the somatic leiomyoma) and the retroperitoneal or abdominal leiomyoma (Kransdorf and Murphey 2007).

The lesions are typically large at presentation (more than 5 cm) and have a rich vascularization (Davies et al. 2010; Kransdorf and Murphey 2007).

3.1.2 Imaging Findings

Superficial leiomyoma

Cutaneous leiomyomata are dermatological-based lesions which are rarely referred for imaging (Davies et al. 2010).

Conventional radiographs of angioleiomyoma are mostly inconclusive. Rarely, they may show scalloping of the cortex of the adjacent bone or intralesional dystrophic calcifications (Vanhoenacker et al. 2009).

On ultrasound, the tumor is homogeneously hypoechoic, with well-defined margins and without contact with the superficial fascia. Typically, the tumor is oval shaped with the longest axis parallel to the extremity axis. Color Doppler reveals hypervascularity (Vanhoenacker et al. 2009) (Fig. 1b).

The three histopathological subtypes (solid, cavernous, and venous subtypes) all display similar MR appearance (Fig. 2).

On T1-weighted images (WI), the lesion appears either homogeneously or heterogeneously isointense to skeletal muscle. On T2-WI, it is mainly hyperintense with few low signal intensity (SI) foci. The smooth muscle cells and patent vessels are believed to correspond to the hyperintense areas, whereas the low SI foci correlate with fibrous tissue or intravascular thrombi within the mass (Gupte et al. 2008). The lesion shows vivid enhancement after administration of intravenous gadolinium contrast. Hyperintense areas on T2-WI show strong enhancement, whereas the low SI foci on T2-WI enhance less (Ramesh et al. 2004) (Fig. 2).

Deep leiomyoma

Radiographs or CT may occasionally show intralesional calcifications of variable morphology (either sandlike, plaquelike, or large mulberry pattern) (Davies et al. 2010; Kransdorf and Murphey 2007).

MR imaging is nonspecific. Because of the large size, the heterogeneous T2-signal, and high vascularity resulting in marked enhancement, the lesion may mimic a malignant STT (Davies et al. 2010; Kransdorf and Murphey 2007).

3.2 Rhabdomyoma

3.2.1 Definition and Clinical Findings

Rhabdomyoma is a rare benign tumor composed of striated muscle cells (Davies et al. 2010). There are two broad categories, cardiac and extracardiac rhabdomyoma. Cardiac rhabdomyoma is associated with the tuberous sclerosis complex. Extracardiac rhabdomyoma is further subdivided into adult, fetal, and genital subtypes.

The adult subtype is a slowly growing painless mass most typically seen in the neck and rarely in the somatic skeletal muscle (Kransdorf and Murphey 2007).

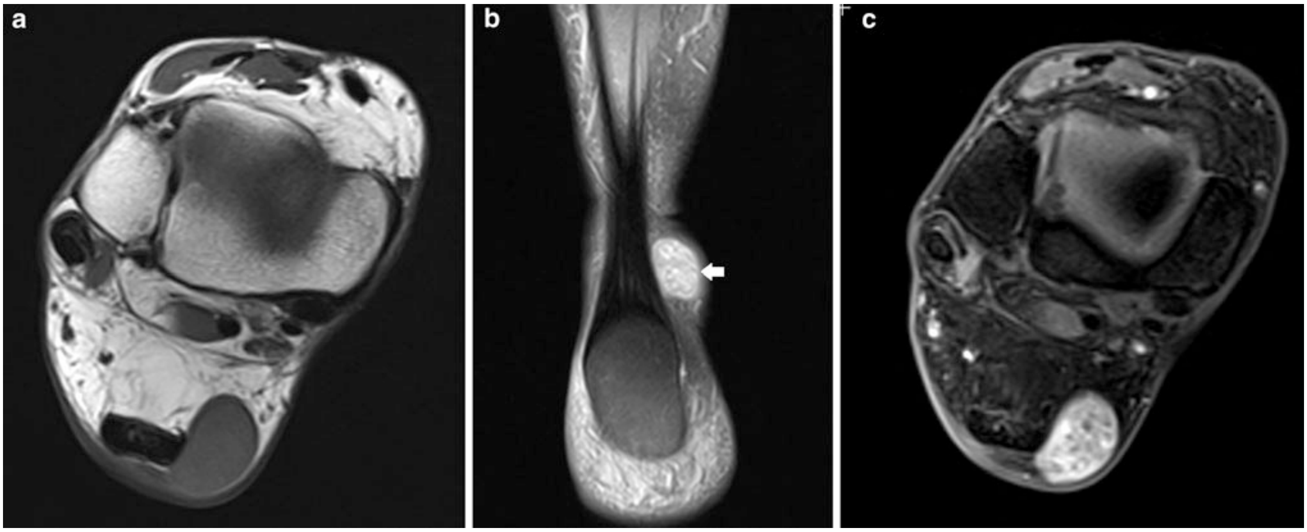

Fig. 2 Angioleiomyoma. **a** Axial T1-Weighted Image (WI). Well-delineated subcutaneous lesion abutting the medial aspect of the Achilles tendon. The lesion is isointense compared to muscle. **b** Coronal fatsuppressed (FS) T2-WI. Note lesion heterogeneity with areas of high and low signal intensity (*white arrow*). **c** Axial FS T1-WI after intravenous (IV) administration of gadolinium contrast. There is marked but slightly inhomogeneous enhancement

The less frequent fetal subtype has a predilection for the postauricular region (Fletcher et al. 2013). The median age of presentation is 4 years (Davies et al. 2010; Kransdorf and Murphey 2007).

3.2.2 Imaging

Cardiac rhabdomyoma are usually detected on echocardiography as solitary or multiple hyperechoic mass(es) within the myocardium, whereas reports of ultrasound (US) features of extracardiac rhabdomyoma are scarce. Maglio et al. (2012) reported a case of nonspecific oval hypoechoic mass in the neck of an adult patient. MR imaging reveals a well-delineated mass isointense or hyperintense compared to skeletal muscle on T1- and T2-WI. Central necrosis and hemorrhage is rarely seen. After administration of intravenous gadolinium contrast, there is marked homogeneous or heterogeneous enhancement (Davies et al. 2010; Kransdorf and Murphey 2007).

3.3 Other Benign STT with Intramuscular Location

3.3.1 Intramuscular Lipoma

3.3.1.1 Definition

Lipomas are well-capsulated masses composed of mature adipose cells.

Although lipomas are most frequently superficially located, they may also be located intramuscularly.

3.3.1.2 Imaging

Radiographs are usually normal, but a low to intermediate density may be seen in larger lesions.

On ultrasound, intramuscular lesions are often more difficult to distinguish from the surrounding muscle fibers. The reflectivity is highly variable ranging from hypo- to hyperreflective compared to subcutaneous fat (Fig. 3a).

CT shows a homogeneous mass with low density (−60 to −130 HU). Intramuscular lesions may contain thin fibromuscular septa. There is no significant contrast uptake.

On MRI, the lesion has similar signal characteristics as subcutaneous fat on all pulse sequences. Fat-suppression techniques show homogeneous suppression. Minor (less than 2 mm) internal septa and a low SI capsule may be seen. After administration of intravenous gadolinium contrast, there is no contrast enhancement, except for the peripheral fibrous capsule or the subtle internal septa (Vanhoenacker et al. 2006) (Figs. 3 and 4).

Table 2 summarizes the most useful criteria to differentiate between a usual lipoma and a liposarcoma.

3.3.2 Intramuscular Myxoma

3.3.2.1 Definition

Myxoma is histologically characterized by the presence of abundant, avascular, and myxoid stroma in which a small number of cells are embedded. Most myxomas are intramuscularly located (82 %). It is a tumor of adults. Areas most frequently involved are the large muscles of the thigh (Fig. 5), shoulder, buttocks, and upper arm. There is an association with polyostotic fibrous dysplasia (bones involved are usually in the vicinity of the myxoma) in Mazabraud's syndrome (De Schepper and Bloem 2007) (Fig. 6).

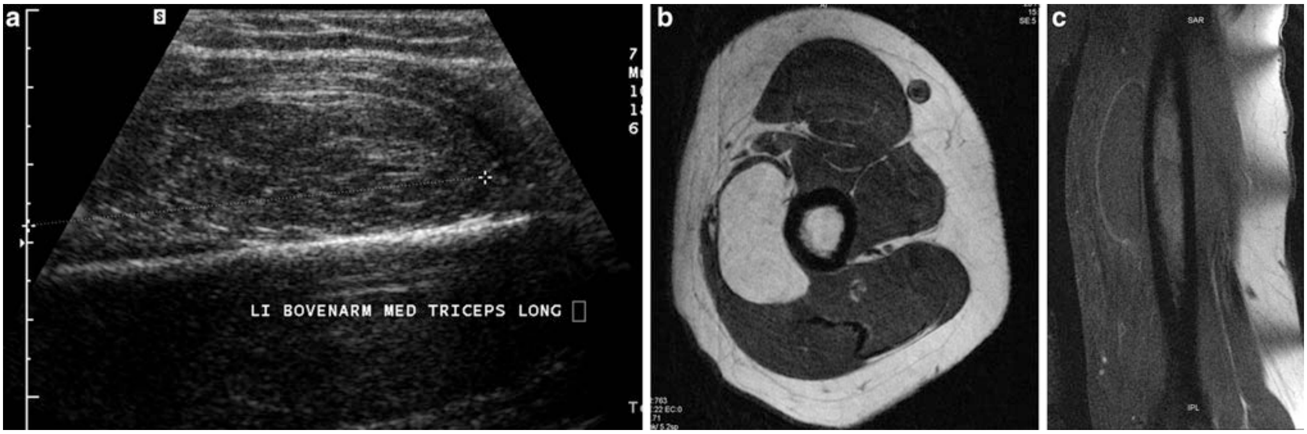

Fig. 3 Intramuscular lipoma in the left triceps muscle. **a** Longitudinal ultrasound showing a slightly hyperechoic lesion within the medial head of the triceps muscle. The lesion is difficult to distinguish from the surrounding muscle fibers. **b** Axial T1-WI. In contradistinction to the ultrasound findings, the lesion is well demarcated from the surrounding muscle and is isointense to subcutaneous fat. **c** Coronal FS T1-WI after IV administration of gadolinium contrast. There is fat suppression of the lesion and there is only faint peripheral enhancement of the compressed capsule

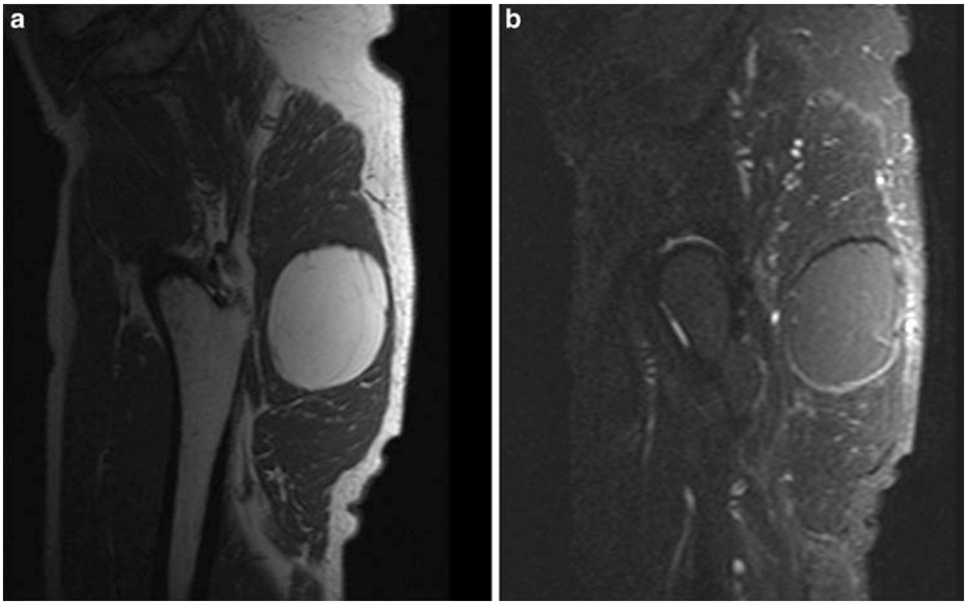

Fig. 4 Intramuscular lipoma in the gluteus maximus muscle. **a** Sagittal T1-WI. The lesion is isointense to subcutaneous fat except for some subtle intralesional strands of low signal, corresponding to small residual muscle fibers. **b** Sagittal FS T1-WI after IV administration of gadolinium contrast. There is fat suppression of the lesion and there is no significant contrast enhancement

3.3.2.2 Imaging

Ultrasound shows a well-delineated solid or mixed hypoechoic lesion with fluid-filled clefts or internal cystic foci reflecting myxoid stroma. Usually, there is retroacoustic sound enhancement. A small amount of hyperechoic fat or edema may surround the upper and lower poles of the lesion (Zamorani and Valle 2007). On MRI, myxomas present as very low signal intensity lesions on T1-weighted images (lower than signal intensity of normal muscle) and as high signal intensity lesions on T2-WI (higher than signal intensity of fat). A small rim of fat corresponding to focal atrophy of surrounding muscle may be seen on T1-WI (Luna et al. 2005). On T2-WI, perilesional strands of high signal may be seen due to leakage of myxomatous tissue in surrounding muscle (Nishimoto et al. 2004). There may be moderate, central enhancement after administration of intravenous gadolinium contrast, having a “smoke”-like appearance (Fig. 5) (Peterson et al. 1991).

3.3.3 Desmoid Tumors (desmoid type fibromatosis)

3.3.3.1 Definition and Clinical Findings

Extra-abdominal desmoids are rare benign soft tissue tumors arising from connective tissue of muscle, overlying fascia, or aponeurosis. They have been designated previously as

Table 2 Differential diagnostic criteria on MRI between lipoma/liposarcoma

	Lipoma	Liposarcoma
Location	Subcutaneous fat or muscle	Deep location (intramuscular, retroperitoneum)
Size	Less than 5 cm	Larger than 5 cm
Shape	Round, oval or fusiform	Multilobulated
Contents	Homogeneous fat-like or thin internal (fibromuscular) septa less than 2 mm	Inhomogeneous with intralesional non fat containing noduli or septa thicker than 2 mm
Enhancement	No enhancement	Intralesional foci of enhancement

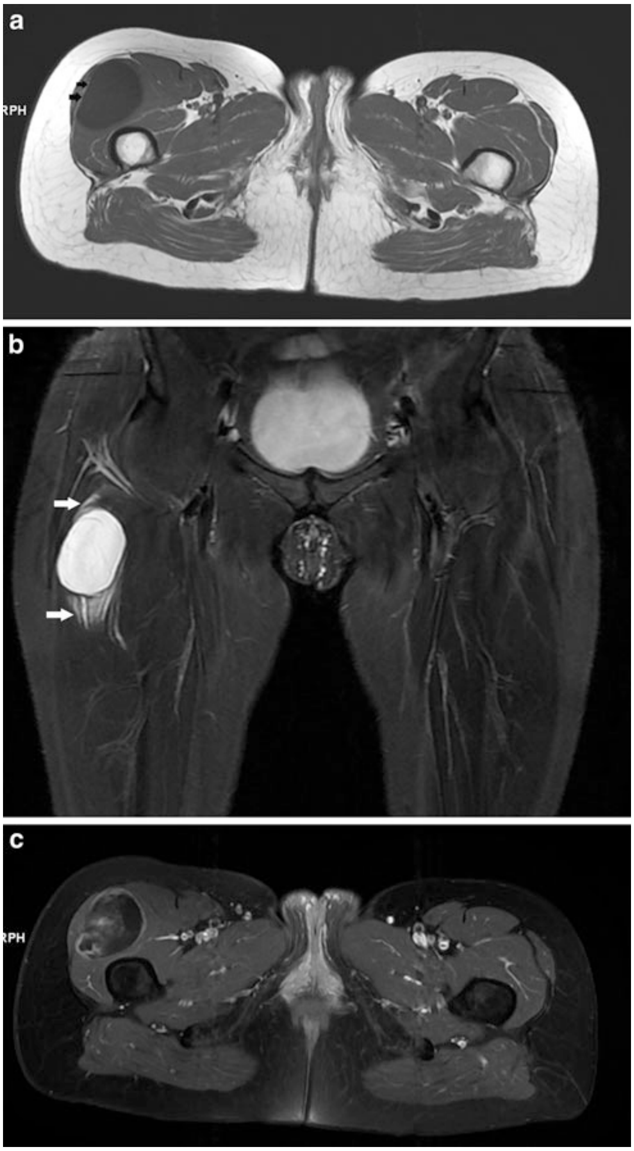

Fig. 5 Intramuscular myxoma in the right quadriceps muscle. **a** Axial T1-WI. The lesion is hypointense compared to muscle. Note a small peripheral rim of fat at the lateral aspect of the lesion, demarcating the lesion from the tensor fasciae latae muscle (*black arrows*). **b** Coronal FS T2-WI. The lesion is of high signal. Perilesional strands of high signal are caused by leakage of myxomatous tissue in surrounding muscle (*white arrows*). **c** Axial FS T1-WI after IV administration of gadolinium contrast. Note a "smoke"-like enhancement pattern

desmoid tumor, aggressive fibromatosis, or musculoaponeurotic fibromatosis. The term "desmoid" means band-like or tendon-like lesions (De Schepper and Vandevenne 2006). Currently, the term desmoid type fibromatosis is used (Fletcher et al. 2013). The lesions can be regarded as deeply seated fibromatosis in contradistinction to palmar fibromatosis which is superficially located. Desmoids are infiltrative tumors, known for their frequent recurrences. Complete surgical excision is often difficult.

The most commonly encountered locations are upper arm (28 %), chest wall and paraspinal area (17 %), thigh (12 %), neck (8 %), knee (7 %), pelvis or buttock (6 %), and lower leg (5 %). Desmoids occur most frequently in patients in the second to fourth decades of life, with a peak incidence between the ages of 25–35 years (Murphey et al. 2009). The lesion is typically deeply seated and poorly circumscribed. Slow insidious growth is the rule and most lesions are painless (Murphey et al. 2009).

3.3.3.2 Imaging

Plain radiographs are often normal. A nonspecific soft-tissue mass may be apparent in patients with larger lesions. Calcification is uncommon. Underlying pressure erosion or cortical scalloping may be seen.

Ultrasound may demonstrate a nonspecific poorly defined, hypoechoic soft-tissue mass. Large lesions may demonstrate posterior acoustic shadowing. Increased vascularity is seen on Doppler-ultrasound (Murphey et al. 2009; Chew and Vanhoenacker et al. in press) (Fig. 7a).

On CT, the lesion has variable attenuation and enhancement (up to 110 HU). The attenuation is usually similar to that of skeletal muscle, but lesions with more prominent collagen content may reveal mildly higher attenuation. Low attenuation is rare and is associated with myxoid components. The margins are often indistinct (Murphey et al. 2009).

On MRI, the lesion may be well demarcated or ill defined. The signal intensity of desmoid type fibromatosis is variable, and depends on the extent of collagen and degree of cellularity of the lesion. Low signal intensity areas on T2-WI correspond histologically to hypocellular and collagen-rich portions of the tumor, whereas more cellular areas with a large extracellular space are of high signal on

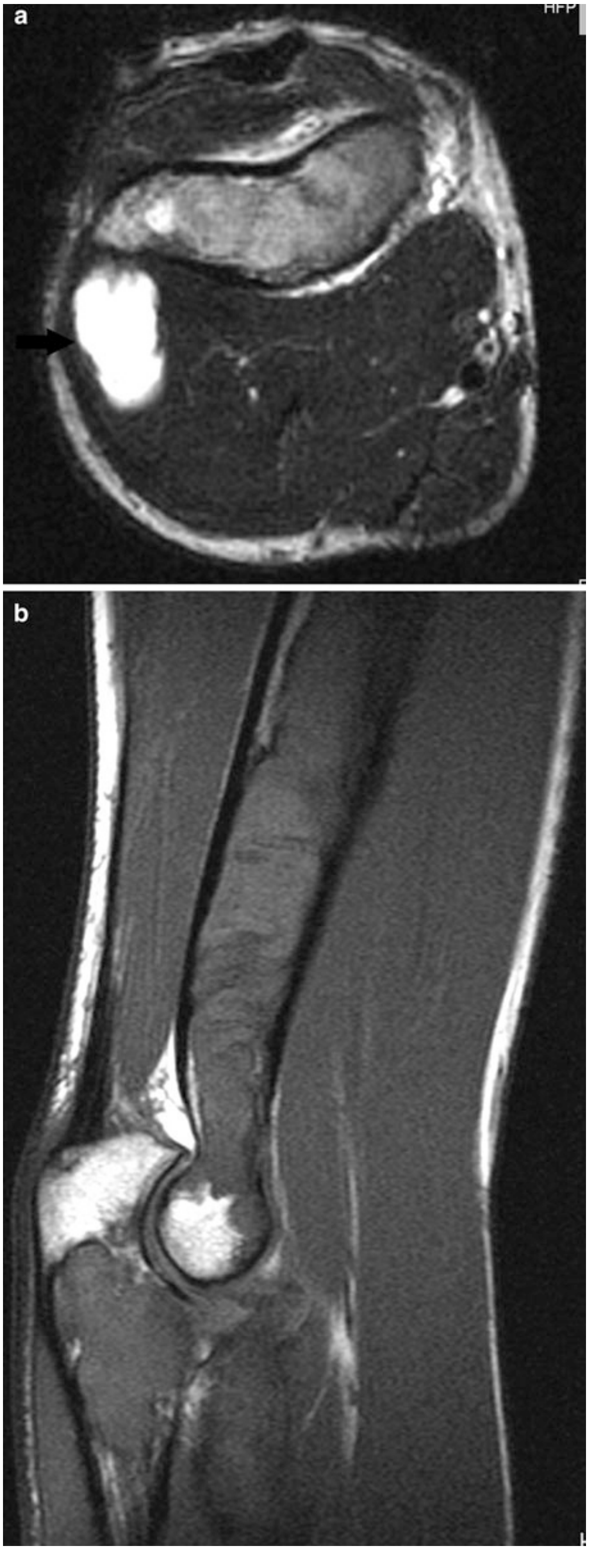

Fig. 6 Intramuscular myxoma associated with Mazabraud syndrome. **a** Axial T2-WI. Well-delineated intramuscular lesion within the lateral head of the right biceps muscle. The lesion is hyperintense compared to fat. **b** Sagittal T1-WI of the right elbow. Note bone expansion and abnormal bone marrow SI isointense to skeletal muscle within the distal humerus and proximal diaphysis of the ulna, in keeping with fibrous dysplasia

T2-WI. In addition, high T2 signal may be seen in myxoid portions.

Postcontrast MR images typically reveal heterogeneous and often moderate to marked enhancement of these lesions. Hypocellular, collagenized bands do not enhance and therefore are often accentuated at postcontrast MR imaging (Murphey et al. 2009) (Fig. 7).

3.3.4 Intramuscular Haemangioma and Vascular Malformations

Vascular anomalies of the soft tissues comprise a heterogeneous spectrum of lesions, encompassing hemangiomas, and vascular malformations. Although the term “hemangioma” should be strictly reserved for a group of benign endothelial neoplasms consisting of cellular proliferation and hyperplasia occurring in children (Flors et al. 2011), the terms hemangioma and vascular malformation are often used interchangeably in daily practice.

Hemangiomas may involve superficial (cutis and subcutis) and deep compartments (such as intramuscular location).

Plain radiographs and CT may show intralesional phleboliths.

US shows a complex ill-defined mass within the affected muscle, characterized by a mixtures of hypo-or anechoic (corresponding to blood-filled cavities) and hyperechoic (reflecting fat) components. Intralesional phleboliths may appear as bright dots with retroacoustic shadowing. Doppler imaging may distinguish high-flow and slow-flow vascular malformations (Zamorani and Valle 2007).

On MRI, hemangiomas are characterized by their high signal intensity on T2-WI and intermediate (between that of muscle and fat) signal intensity on T1-WI. They are frequently multilobular, resembling a “bunch of grapes”. Fluid–fluid levels may be seen in cavernous hemangiomas. A peripheral fat induction phenomenon is a frequent feature of intramuscular hemangiomas. High-flow lesions may show signal voids on all pulse sequences. After administration of intravenous gadolinium contrast they exhibit a serpiginous, marked enhancement. In low-flow venous hemangiomas, large venous convolutes are associated with late enhancement (De Schepper and Bloem 2007) (Fig. 8).

4 Malignant Muscle Tumors

Malignant tumors with muscle differentiation are summarized in Table 1.

Extrauterine leiomyosarcomata account for 9 % of all soft tissue tumors and are typically seen in adults (Davies et al. 2010).

Rhabdomyosarcoma is the most common soft tissue tumor in children (Navarro 2011).

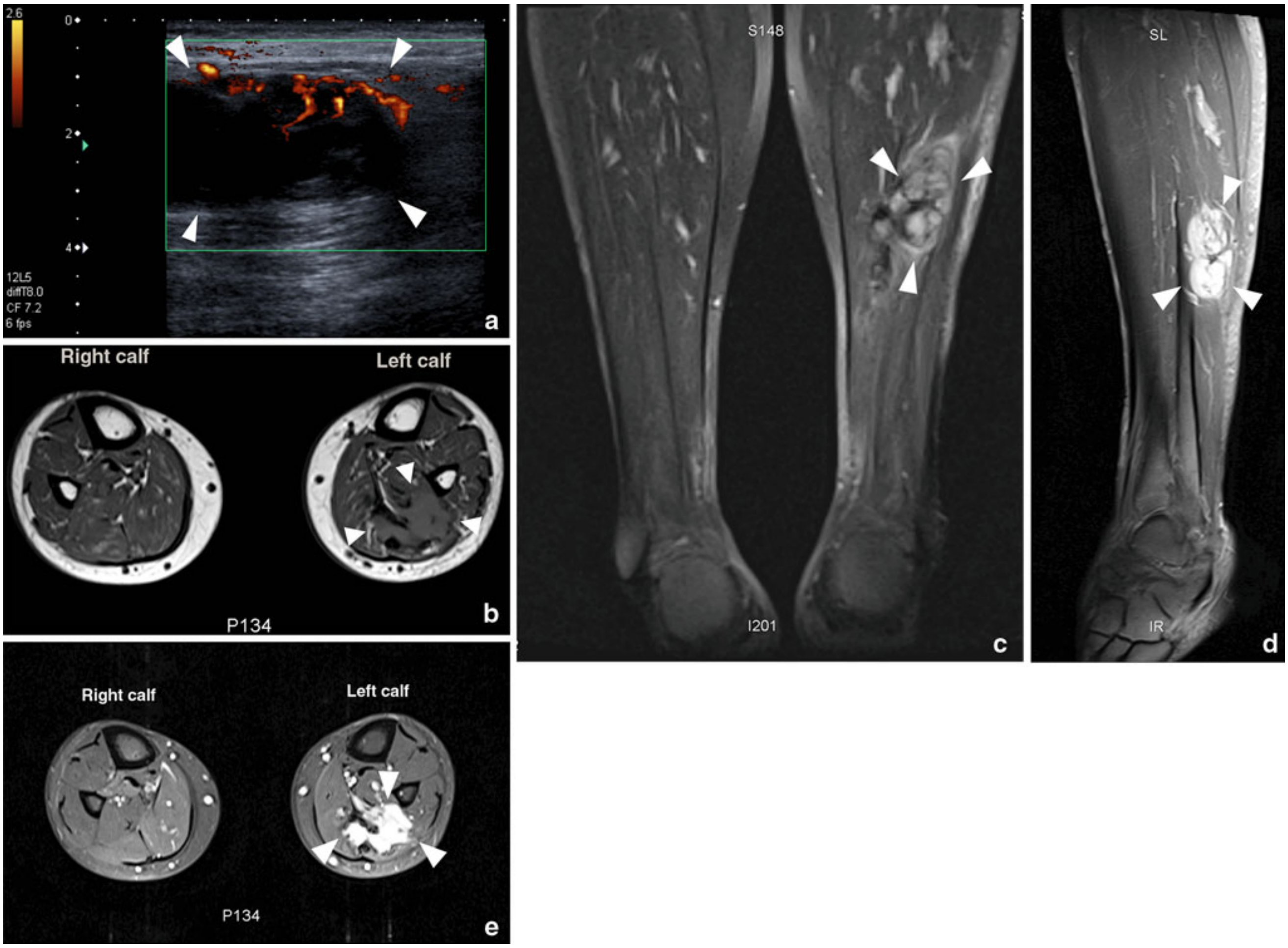

Fig. 7 Intramuscular desmoid of the calf muscles. **a** Ultrasound with power Doppler. A solid hypoechoic lesion (*arrowheads*) with peripheral neovascularity and posterior acoustic shadowing is identified. **b** Axial T1-WI. Infiltrative lesion (*arrowheads*) within the left lateral gastrocnemius lesion. The lesion invades the soleus muscle anteriorly and the medial gastrocnemius medially. The lesion is of intermediate signal. **c** Coronal FS T2- WI. The lesion (*arrowheads*) is hyperintense. Note its central hypointensity and irregular superior margins. Central hypointensity likely correlated to dense fibrous tissue. **d** Sagittal FS T1-WI after IV administration of gadolinium contrast. There is avid enhancement of the lesion (*arrowheads*). Note the irregular infiltrative superior margins. **e** Axial FS T1-WI after IV administration of gadolinium contrast. There is avid enhancement of the infiltrative lesion (*arrowheads*). (Used with permission from Chew NS et al. JBR-BTR in press)

Many malignant soft tissue tumors that are identified on imaging to arise in muscle do not show muscle differentiation histologically. On MRI, these lesions are often indistinguishable from STT with myogenic differentiation.

Table 3 summarizes the important MR parameters which may suggest malignancy, irrespective of the histological composition of the lesion.

4.1 Leiomyosarcoma

4.1.1 Definition and Clinical Findings

Extrauterine leiomyosarcomata typically occur in adults. There are four main subtypes, including cutaneous, subcutaneous, deep soft tissue, and vascular leiomyosarcoma. Cutaneous leiomyosarcoma has a far better prognosis than the subcutaneous type.

Deep soft tissue leiomyosarcomata are most common in the retroperitoneum and only in 12–41 % in the extremities, particularly in the thigh (Paal and Miettinen 2001; McLeod et al. 1984).

Vascular leiomyosarcomata arise in large vessels, most commonly in the inferior vena cava or lower extremity veins (Figs. 9 and 10). The lesions may cause vascular obstruction (Blanfield et al. 2003; Killoran et al. 2003).

4.1.2 Imaging

Leiomyosarcoma mostly presents as large, spindle-shaped masses with variable signal intensities, central necrosis, and

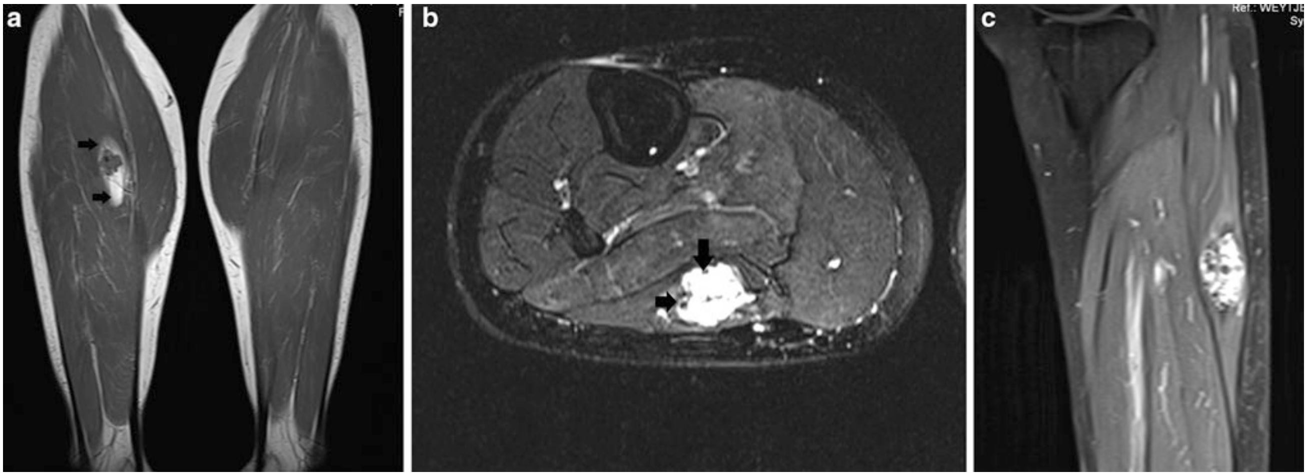

Fig. 8 Intramuscular hemangioma in the right lateral gastrocnemius muscle. **a** Coronal T1-WI. The lesion is predominantly isointense compared to muscle with some intralesional low SI foci (phleboliths). Note a peripheral rim of high signal intensity, due to fat induction (*black arrows*). **b** Axial FS T2-WI. The lesion is predominantly hyperintense with some low-signal intensity foci, in keeping with phleboliths (*black arrows*). **c** Sagittal FS T1-WI after IV administration of gadolinium contrast. There is marked enhancement of the lesion, except for the intralesional phleboliths. Note the lobulated appearance of the contour of the lesion, resembling a bunch of grapes

marked peripheral and septal enhancement (van Vliet et al. 2009).

Plain films or CT may demonstrate intralesional calcifications in 12–17 % (Bush et al. 2003). Bone involvement is seen in up to 10 % (van Vliet et al. 2009; Seynaeve et al. 2006).

Intravascular leiomyosarcoma may be confused with deep vein thrombosis on ultrasound (Davies et al. 2010). Leiomyosarcomata have no specific MR imaging features (Figs. 9 and 10) except for vascular leiomyosarcoma, which mostly occurs within the inferior vena cava. MR is able to differentiate intraluminal leiomyosarcoma from an intraluminal thrombus containing subacute blood. The latter will be of high T1-signal (Davies et al. 2010).

Table 3 General MR imaging features that may suggest malignancy (modified from De Schepper and Bloem 2007)

Large volume (any lesion exceeding 3 cm)
Ill-defined margins
Inhomogeneity on all pulse sequences
Intralesional hemorrhage
Intralesional necrosis
Extensive and peripheral enhancement pattern (with papillary projections) on static contrast examination
Rapid enhancement with steep slope on dynamic contrast examination
Extracompartmental extension
Invasion of adjacent bones and neurovascular bundles

4.2 Rhabdomyosarcoma

4.2.1 Definition, Histopathology, and Clinical Findings

Rhabdomyosarcoma is the most common soft tissue tumor in children, accounting for 5–8 % of all childhood cancers (Gurney et al. 1996). It is very rare in adults.

There are three main histological subtypes: embryonal, alveolar, and pleomorphic; each corresponding with a different prognosis. The embryonal subtype is most common in children, whereas the alveolar subtype is most common in young adults and adolescents (Newton et al. 1988). A rare clinicopathologic subtype is the so-called sclerosing rhabdomyosarcoma, which shows some overlapping features with the alveolar subtype (Chiles et al. 2004).

Embryonal rhabdomyosarcomata are most frequent in the head and neck (47 %) and the genitourinary system (28 %) and only rarely involve the extremities (6 %). There is an increased incidence in Beckwith–Wiedemann syndrome (Meyer and Spunt 2004).

Alveolar rhabdomyosarcoma is more aggressive than embryonal rhabdomyosarcoma and has a poorer prognosis. The outcome is also affected by age, stage, and location. Tumors located in the extremities have a poorer prognosis (Fletcher et al. 2002).

Pleomorphic rhabdomyosarcoma occurs almost exclusively in adults, typically in the deep soft tissues of the extremities, particularly the thigh (Allen et al. 2007). The prognosis is poor.

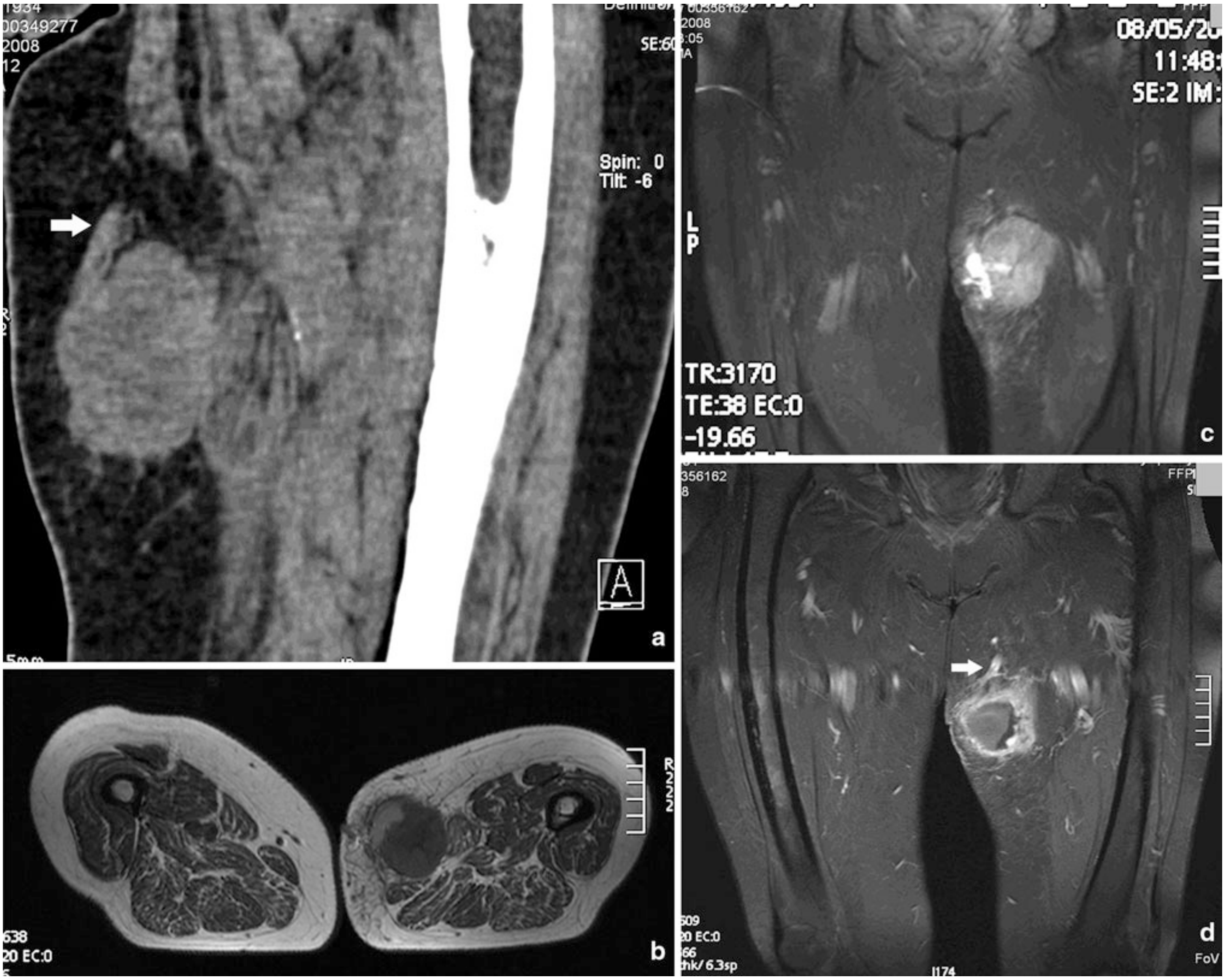

Fig. 9 High-grade leiomyosarcoma in the left thigh. **a** Coronal reformatted CT image. Large subcutaneous soft tissue mass abutting the adductor muscles. Note the intimate relationship with an adjacent subcutaneous vein (*white arrow*). **b** Axial T1-WI. **c** Coronal FS T2-WI. The mass is of inhomogeneous signal intensity on both pulse sequences. **d** Coronal FS T1-WI after IV administration of gadolinium contrast. There is marked inhomogeneous enhancement of the lesion. An intimate relationship with an adjacent subcutaneous vein is present (*white arrow*)

4.2.2 Imaging

Plain radiographs and CT may show local bone invasion, which is seen in about 25 % of cases. Bone metastasis may occur and are usually lytic and more rarely mixed (Davies et al. 2010; Kransdorf and Murphey 2007).

US of rhabdomyosarcoma is nonspecific (Zamorani and Valle 2007).

MR imaging features are nonspecific; isointense to muscle on T1-WI and heterogeneous hyperintense on T2-WI, often with necrotic foci. Marked enhancement is the rule, particularly in the alveolar subtype which has a prominent vascularity (Allen et al. 2007) (Fig. 11).

5 Pseudotumoral Lesions of Muscle

5.1 Myositis Ossificans

5.1.1 Definition and Clinical Findings

Myositis ossificans (MO) is a benign condition of heterotopic bone formation, which can mimic soft-tissue malignancies. A history of trauma is present in about 60 % of cases. In the acute stage, the most frequent complaint is pain, tenderness, and soft tissue swelling.

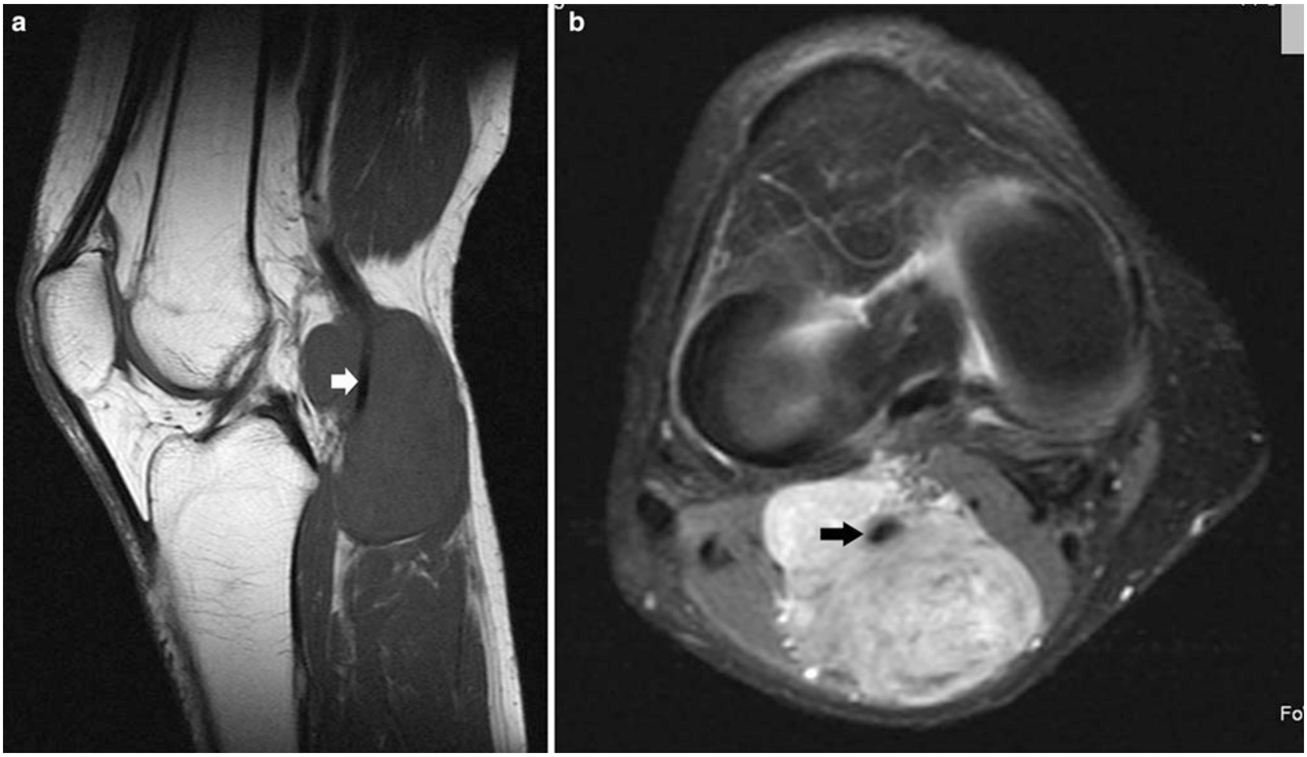

Fig. 10 Leiomyosarcoma of the right knee. **a** Sagittal T1-WI. **b** Axial FS T2-WI. Huge mass encasing the popliteal vessels (*arrows*)

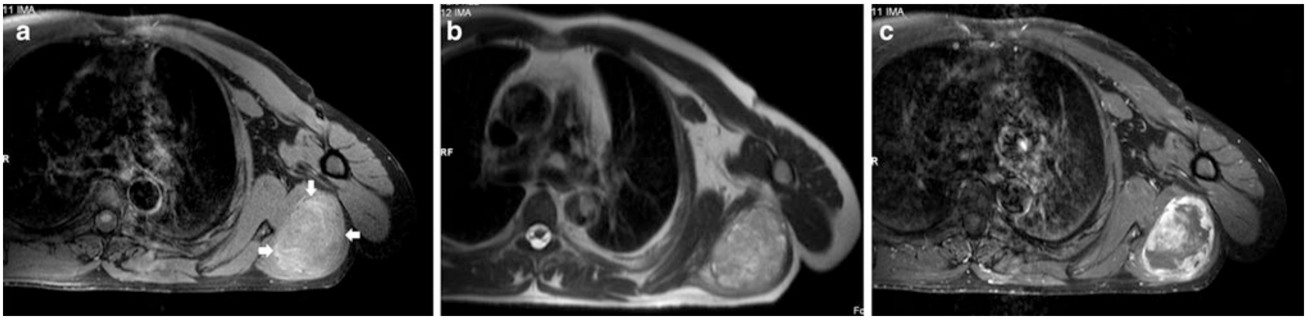

Fig. 11 Pleomorphic rhabdomyosarcoma in the left deltoid muscle. **a** Axial FS T1-WI. **b** Axial FS T2-HASTE. Large inhomogeneous mass on both pulse sequences. **c** Axial FS T1-WI after IV administration of gadolinium contrast. There is marked heterogeneous enhancement

5.1.2 Imaging

Imaging findings are time dependent. In the early/active stage (less than 2–4 weeks), plain films may show a nonspecific soft tissue mass. Faint peripheral calcifications may appear after 7–10 days of presentation (Fig. 12). This subtle peripheral calcification may be more obvious on ultrasound or CT. MRI shows a focal mass that is isointense to slightly hyperintense to muscle on T1-WI. On T2-WI, the lesion is hyperintense. Contrast enhancement may vary from peripheral rim enhancement to a more diffuse pattern.

In the subacute/intermediate stage (4 weeks to 6 months), a well-defined peripheral calcification and coarser central calcification become apparent on plain radiographs and CT. The ossification pattern is centripetal (Fig. 13a). MRI shows a peripheral rim of low signal on all pulse sequences, corresponding to calcifications. The signal of the center of the lesion varies according to the degree of calcification. The peripheral hyperintensity on T2-WI due to perilesional edema decreases gradually after 4 weeks (Fig. 13b).

In the chronic or mature stage (after 6 months), the calcification–ossification front further develops following a "zoning" or centripetal pattern, with lamellar bone at the periphery proceeding toward the center (Tyler and Saifuddin 2010; Wang et al. 2003). The lesion is densely calcified or ossified on plain films and CT, and therefore highly reflective on ultrasound with accompanying posterior

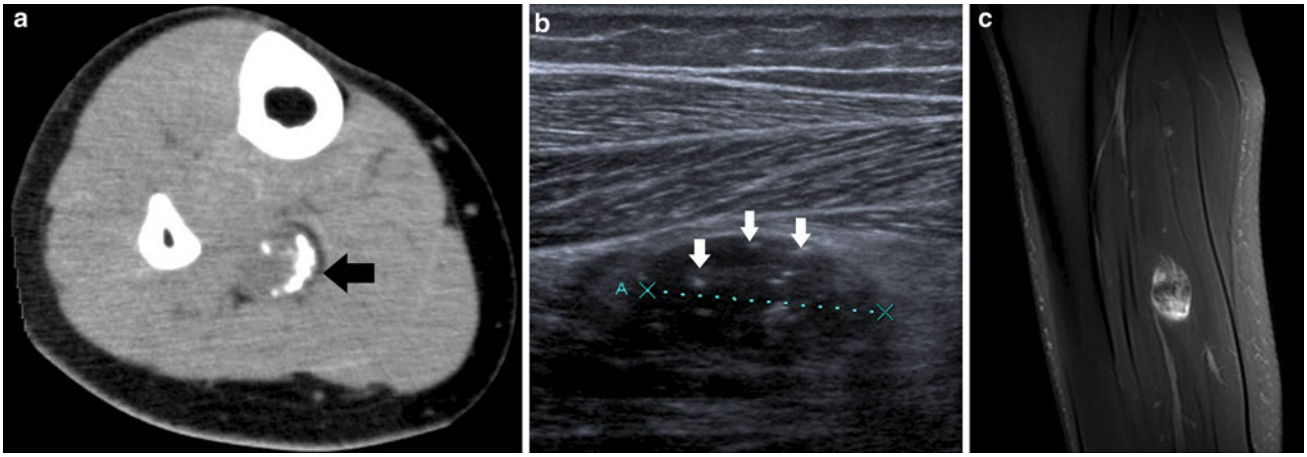

Fig. 12 Early myositis ossificans of the calf muscles. **a** Axial CT. Intramuscular soft tissue mass with subtle peripheral calcifications (*black arrow*) **b** Ultrasound. Intramuscular hypoechoic lesion with subtle peripheral reflections in keeping with faint calcifications (*white arrows*) **c** Sagittal FS T1-WI after IV administration of gadolinium contrast. There is heterogeneous enhancement

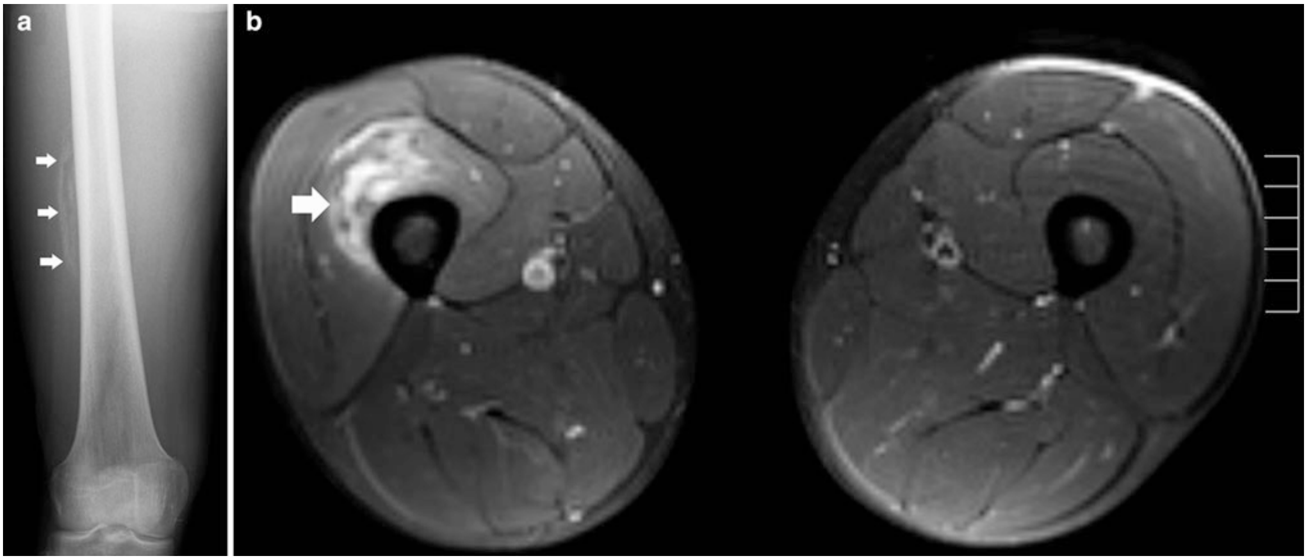

Fig. 13 Subacute myositis ossificans of right vastus intermedius muscle. **a** Plain radiograph of the right femur showing peripheral calcifications adjacent to the lateral aspect of the right femoral diaphysis (*white arrows*) **b** Axial FS T2-WI showing an irregular delineated hyperintense lesion within the right vastus intermedius muscle, containing hypointense strands at the periphery, in keeping with subtle calcifications (*white arrow*)

acoustic shadowing. On MRI, most lesions are of low SI on all pulse sequences, although areas isointense to normal bone marrow may be seen due to intralesional bone marrow formation. Perilesional edema is absent on T2-WI (Tyler and Saifuddin 2010; Wang et al. 2003).

5.2 Focal Myositis

5.2.1 Definition and Clinical Findings

Focal myositis is a rare, usually self-limiting soft tissue pseudotumor (Auerbach et al. 2009).

The process is usually limited to one muscle, but one-third of patients with focal myositis evolve to polymyositis (Flaisler et al. 1993). Focal myositis usually presents with a painful intramuscular mass, which can grow rapidly in a few weeks.

5.2.2 Imaging

Ultrasound and MRI demonstrate focal enlargement of the muscle, with typical sparing of the internal muscle fibers (Vanhoenacker et al. 2010). T2-WI show a heterogeneous increased signal within the affected muscle (Fig. 14). Administration of contrast is of limited value because the enhancement is variable (Bashir and O’Donnell 2010).

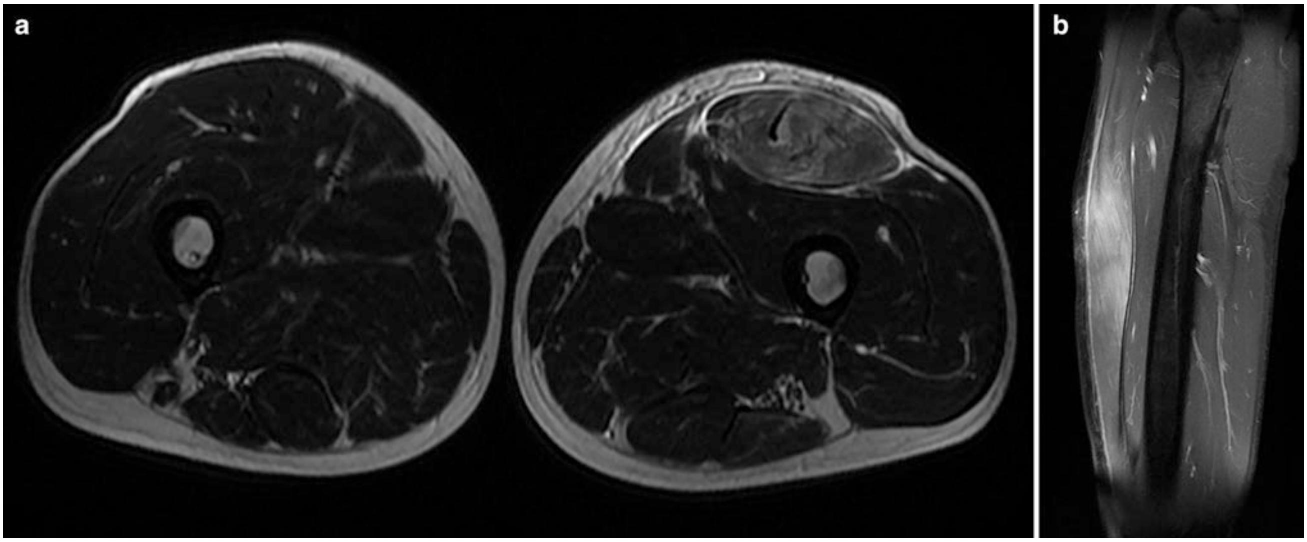

Fig. 14 Focal myositis of the rectus femoris muscle. **a** Axial FS T2-WI. **b** Sagittal FS T2-WI. Diffuse hyperintense signal in the rectus femoris muscle with sparing of the muscle fibers

5.3 Calcifying Myonecrosis

5.3.1 Definition and Clinical Findings

Calcifying myonecrosis is a condition characterized by latent formation of a dystrophic calcified mass occurring 10–64 years after an initial injury of the lower leg. It typically presents as a slowly enlarging mass in one or more compartments, but location within the anterior compartment of the lower leg is most frequent. It has been suggested that the lesion is a late sequela of compartment syndrome, in which necrotic muscle undergoes central liquefaction and peripheral calcification. Neurovascular compromise seems to be the most important etiopathogenetic factor. Calcifying myonecrosis can also occur after common peroneal nerve injury. The mass may enlarge slowly because of repeated intralesional hemorrhage with time.

5.3.2 Imaging

Plain radiographs show a well-defined mass with linear pattern of calcifications organized around the periphery of the lesion (Fig. 15a). Sonographic examination demonstrates peripheral, echogenic foci with acoustic shadowing consistent with calcification. The central part of the lesion is hypoechoic and often liquified. CT and MRI more readily identify the typical compartmental distribution. CT shows the predominantly rim-like morphology of the calcifications (Fig. 15b) and may sometimes depict scattered calcifications within the mass, calcium-fluid levels or longstanding, smooth pressure erosions affecting the outer cortex of adjacent bone.

On MRI, peripheral calcifications are of low-signal intensity on both T1-WI (Fig.15c) and T2-WI. On T2-WI, the mass is often heterogeneous in signal, with areas of bright signal intensity consistent with fluid, while other areas demonstrate intermediate signal intensity. On T1-WI, the central fluid region shows as a homogeneous low signal intensity area. Contrast-enhanced CT and/or MRI may demonstrate peripheral enhancement due to anastomosizing small blood vessels around the mass (Peeters et al. 2010) (Fig. 15d).

5.4 Intramuscular Abscess

An intramuscular abscess may mimic a soft tissue mass. A soft tissue abscess usually corresponds with low to intermediate signal on T1-WI, high signal on T2-WI demonstrates peripheral rim enhancement following administration of intravenous gadolinium contrast (Vanhoenacker et al. 2011). Diffusion weighted imaging (DWI) is an additional tool in the differential diagnosis of a central necrotic tumor versus an abscess. Diffusion restriction is not a characteristic feature of tumor necrosis, whereas restricted diffusion is typically seen in thick pus collections. On CT, intralesional gas may be present (Fig. 16).

6 Tumor and Tumor-like Conditions of Fasciae and Tendon Sheaths

6.1 Tendon Sheath Cyst

A tendon sheath cyst consists of a special subtype of a ganglion cyst located on the course of a tendon sheath. The

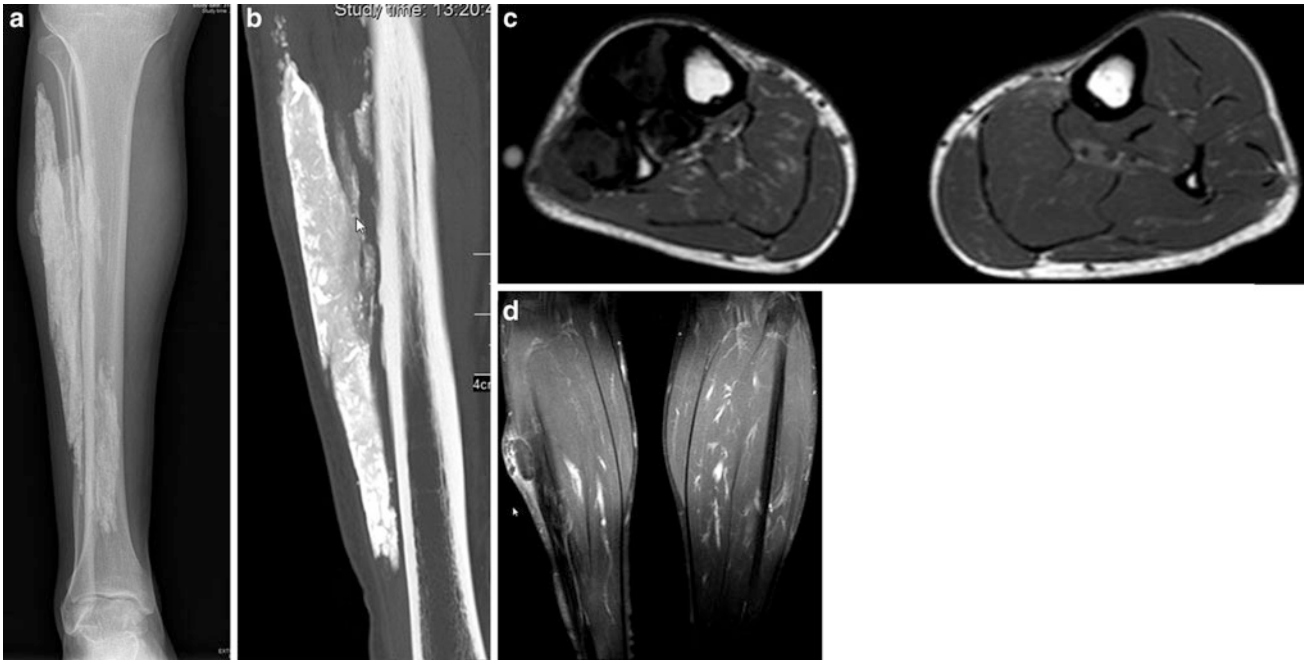

Fig. 15 Calcifying myonecrosis of the anterior and peroneus compartment. **a** Plain radiograph and **b** CT scan showing typical plaque-like intramuscular calcifications **c** Axial T1-WI. The lesion is hypointense compared to muscle **d** Coronal FS T1-WI after IV administration of gadolinium contrast. Note subtle peripheral enhancement due to anastomosizing small blood vessels around the mass

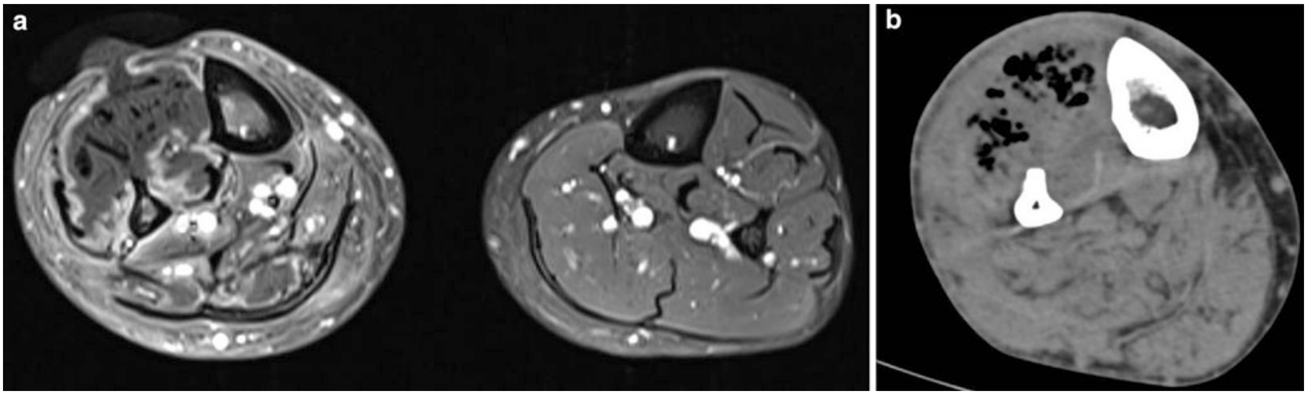

Fig. 16 Intramuscular abscess in the right lower leg. **a** Axial T1-WI after IV administration of gadolinium contrast. Note peripheral rim enhancement of the lesion in all compartments of the right lower leg. There are intralesional foci of low signal intensity, suspicious for intralesional gas bubbles. **b** Axial CT scan of the right lower leg confirming intralesional gas

diagnosis is readily made on ultrasound or MRI based on its typical fluid content. No enhancement is seen.

6.2 Giant Cell Tumor of Tendon Sheath

6.2.1 Definition and Clinical Findings

GCTTS are benign proliferative lesions of synovial origin and represent a localized extra-articular form of pigmented villonodular synovitis (Nguyen et al. 2004). Histologically, they are composed of histiocytes, macrophages, multinucleated giant cells, and hemosiderin due to repeated hemorrhage (Wan et al. 2010).

The lesions are most common in the fingers.

6.2.2 Imaging

In longstanding lesions, pressure erosion may be seen at the adjacent cortical bone.

Ultrasound shows a hypoechoic, solid mass with well-defined margins usually located near tendons. Hypervascularity can be seen on color or power Doppler imaging, particularly if there associated pressure erosions of the underlying cortex (Wan et al. 2010; Zeinstra et al. 2012).

MR images typically show a well-defined mass adjacent to or enveloping a tendon, with a signal intensity similar to

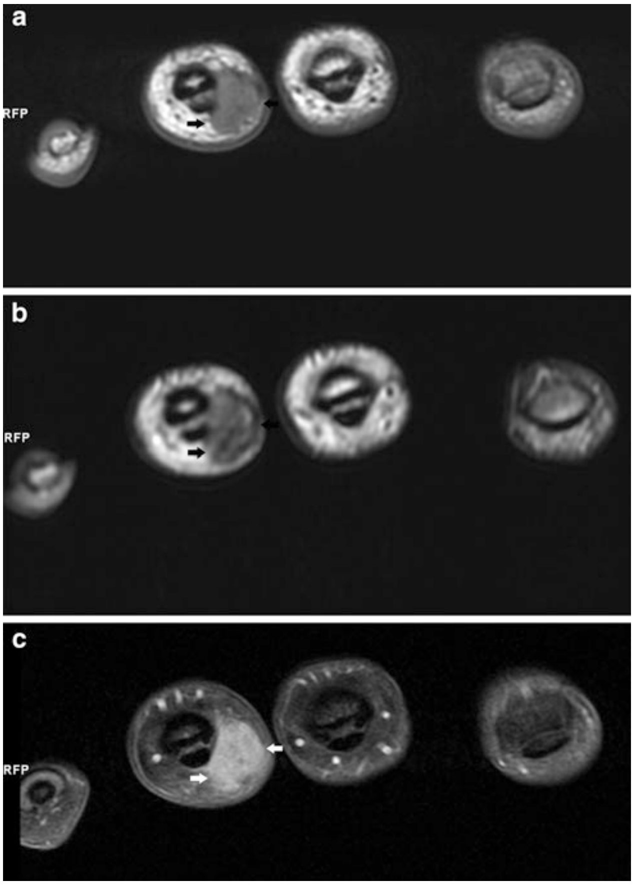

Fig. 17 Giant Cell Tumor of Tendon Sheath of the 4th finger of the left hand. **a** Axial T1-WI. **b** Axial T2-WI. The lesion is located near the flexor tendon of the fourth finger and is hypointense on all pulse sequences (*arrows*). Black intralesional spots on T2-WI correspond to hemosiderin deposits. **c** Axial FS T1-WI after IV administration of gadolinium contrast. Marked enhancement is seen (*white arrows*)

or less than that of skeletal muscle on T1-WI. On T2-WI, the signal intensity is predominantly low, with a variable degree of heterogeneity. Blooming artifact is seen on gradient-echo sequences due to the presence of hemosiderin (Wan et al. 2010). GCTTS usually enhance after administration of intravenous gadolinium contrast (Fig. 17).

6.3 Fibroma of the Tendon Sheath

6.3.1 Definition and Clinical Findings

A fibroma of the tendon sheath is a circumscribed tumor, rarely larger than 2 cm in diameter. The thumb is the most commonly involved digit (Nguyen et al. 2004). Histologically, the lesion is composed of scatters benign fibroblasts with dense collagen (Wan et al. 2010).

The mean age of presentation is 42 years (Nguyen et al. 2004). Lesions are typically located on the flexor surfaces, occurring most often in men (75 %) (Fox et al. 2003).

6.3.2 Imaging Findings

Ultrasound shows a nonspecific hypoechoic mass adjacent to the tendon sheath. The lesion is usually hypointense on MR sequences, and no or minimal enhancement is seen. Increased capillary vascularity near the lesion surface may cause minor peripheral enhancement. The MR imaging findings vary when areas of increased cellularity or myxoid change occur within the lesion. Myxoid changes within the lesion may cause an intermediate to high SI on T2-WI, whereas areas of increased cellularity may enhance (Fox et al. 2003) (Fig. 18).

6.4 Lipoma of Tendon Sheath

This is a lipomatous mass spreading along the tendon sheaths, preferentially located at the wrist. On MRI, a peritendinous fatty mass is seen, with SI characteristics of a lipoma.

6.5 Tenosynovial Chondromatosis

6.5.1 Definition and Clinical Features

Compared to synovial chondromatosis of joints, chondromatosis of the tendon sheath is a rare neoplastic disorder accounting for only 1.5 % of benign soft-tissue tumors. Tenosynovial chondromatosis occurs at almost any age, but most commonly in 30–60-year-old patients. The lesion occurs most commonly in the hands and feet (Hondar Wu et al. 2006).

6.5.2 Imaging Features

Plain films demonstrate calcifications in 33–80 % of tenosynovial chondromatosis. The pattern of calcifications is variable, including curvilinear, punctuate, mixed, dystrophic, and focal dense pattern (Hondar Wu et al. 2006) (Fig. 19).

On MRI, the signal intensity varies along with the degree of calcified matrix within the lesion. Highly calcified lesions are of low signal intensity on both pulse sequences, whereas noncalcified lesions are of intermediate signal intensity on T1-WI and of high signal on T2-WI (Fig. 19). The high signal is due to a high water content of the mucopolysaccharide component or due to myxoid changes (Hondar Wu et al. 2006). Following administration of intravenous contrast administration, septal or peripheral enhancement may be observed, corresponding to fibrovascular tissue surrounding the avascular nodules (Ergun et al. 2010).

6.6 Superficial Fibromatoses

Fibromatoses are nonneoplastic, fibroblastic proliferations that can be divided into deep fibromatosis (aggressive

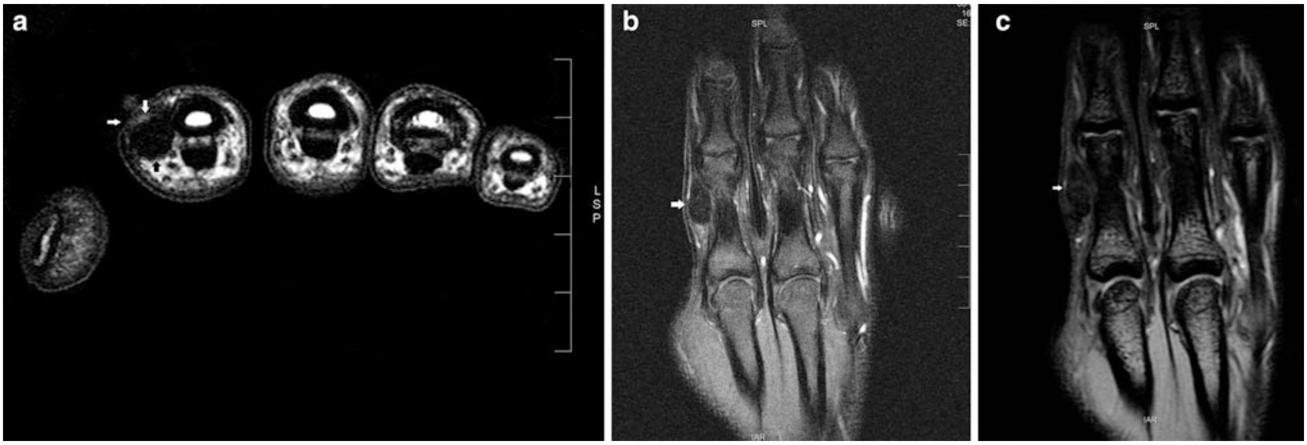

Fig. 18 Typical MR characteristics of a fibroma of the tendon sheath of the index finger. **a** Axial FS T2-WI and **b** Coronal FS T2-WI. The lesion is of low signal intensity (*arrows*). **c** Coronal gradient echo T2*-WI. There is absence of blooming artifact (*arrow*)

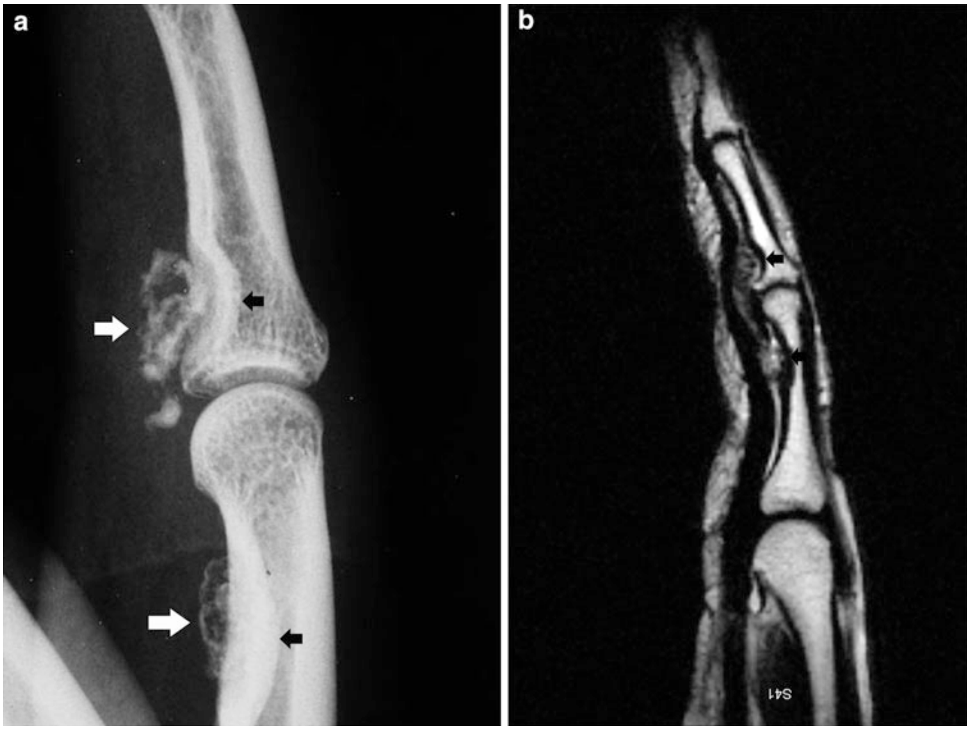

Fig. 19 Tenosynovial chondromatosis of the finger. **a** Plain radiograph. Chondroid-like calcifications adjacent to the flexor side of the proximal and middle phalanx (*white arrows*). There is scalloping of the adjacent cortical bone (*black arrows*). **b** Sagittal T2-WI. The lesions are of variable signal intensity corresponding to calcified and noncalcified chondroid areas. Note the intimate relationship with the flexor tendons and the presence of cortical erosions (*arrows*)

fibromatosis or desmoid tumors; see Sect. 2.3.3) or superficial (palmar and plantar) fibromatosis.

Palmar Fibromatosis

Palmar fibromatosis, also called Dupuytren contracture, most commonly occurs in patients over 65 years of age, and is bilateral in 40–60 % of the cases. The disease is seen almost exclusively in Caucasians and is rare in populations of African or Asian descent.

The etiology of palmar fibromatosis is not completely understood, but it is thought to be multifactorial, including associations with trauma, microvascular injury, immunologic processes, and genetic factors (Murphey et al. 2009).

Patients present clinically with painless, subcutaneous nodules (Murphey et al. 2009). These nodules may progress slowly to fibrous cords or bands that attach to and cause traction on the underlying flexor tendons, resulting in flexion contractures of the digits. The fourth and fifth digits are most commonly involved. Patients commonly have related diseases such as plantar fibromatosis (5–20 %), Peyronie disease, and knuckle pad fibromatosis.

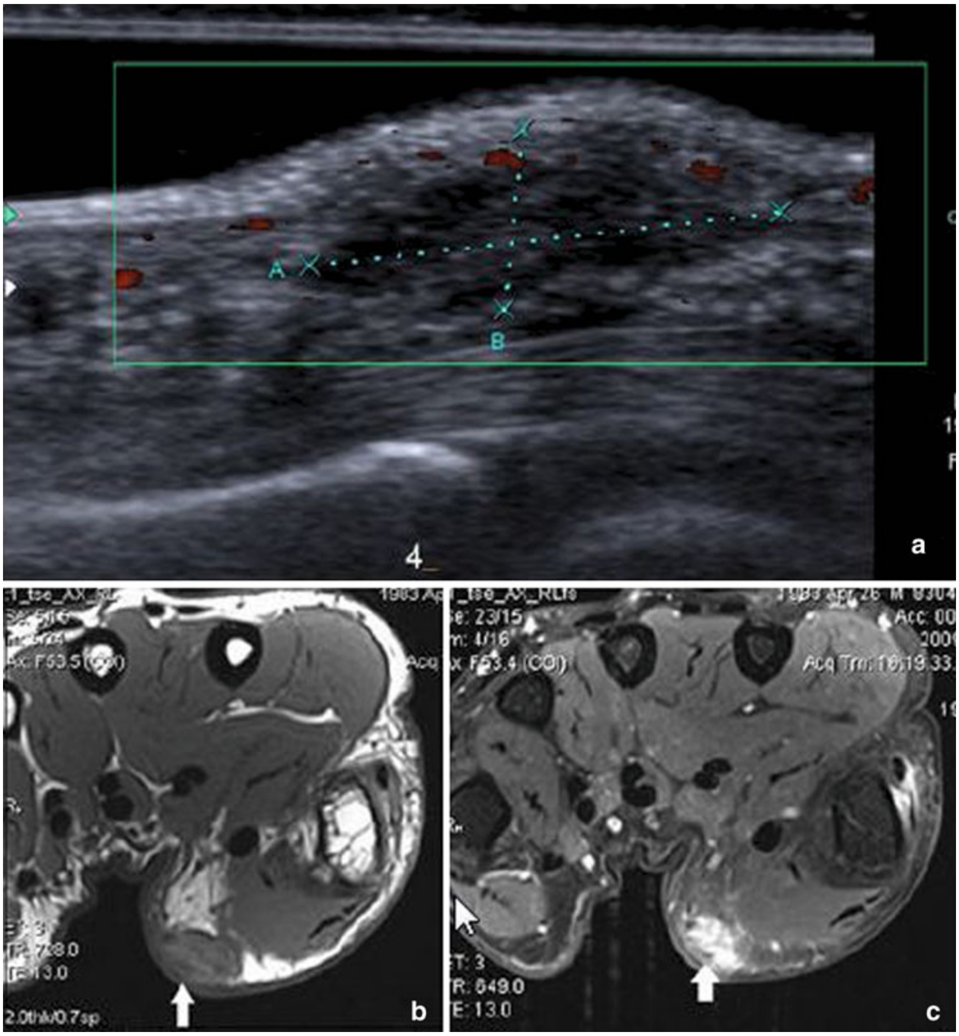

Fig. 20 Palmar fibromatosis. **a** Longitudinal Doppler ultrasound. Hypoechoic nodule adjacent to the flexor tendon of the palm of the hand (*third ray*). **b** Axial T1-WI in another patient shows a hypointense lesion at the palmar aspect of the thumb (*arrow*). **c** Axial FS T1-WI after IV administration of gadolinium contrast shows diffuse enhancement (*arrow*). (Used with permission from Vanhoenacker et al. (2011))

Plain radiographs are typically normal, other than the flexion contractures.

Ultrasound reveals hypervascular, hypoechoic nodules in the palmar subcutaneous tissues, and superficial to the flexor tendons.

On MR imaging, there are multiple nodular or cordlike, superficial soft-tissue masses that arise from the proximal palmar aponeurosis and extend superficially in parallel with the flexor tendons. The signal intensity of palmar fibromatosis is variable along with the cellularity and the collagen content of the lesion. Lesions of low-signal intensity on all pulse sequences are relatively hypocellular and contain abundant dense collagen. In contradistinction, the lesions of intermediate signal intensity on both T1- and T2-WI are more cellular or mixed with less abundant collagen (Murphey et al. 2009). After administration of intravenous gadolinium contrast, hypercellular lesions show more vivid enhancement than hypocellular lesions (Murphey et al. 2009) (Fig. 20).

Plantar Fibromatosis

Plantar fibromatosis, also called Ledderhose disease, is located at the medial aspect of, and superficial to the plantar aponeurosis of the foot. It can be bilateral (20 %) and multiple (32 %). A male predominance is reported.

On ultrasound examination, plantar fibromatosis typically appears as a poorly defined mass in the deep aponeurosis (Fig. 21a) in the medial aspect of the foot (Van Hul et al. 2011).

MR signal intensity pattern depends on the amount of fibrous versus cellular tissue and the age of the lesion. Most lesions are nonhomogeneous and of predominantly low SI

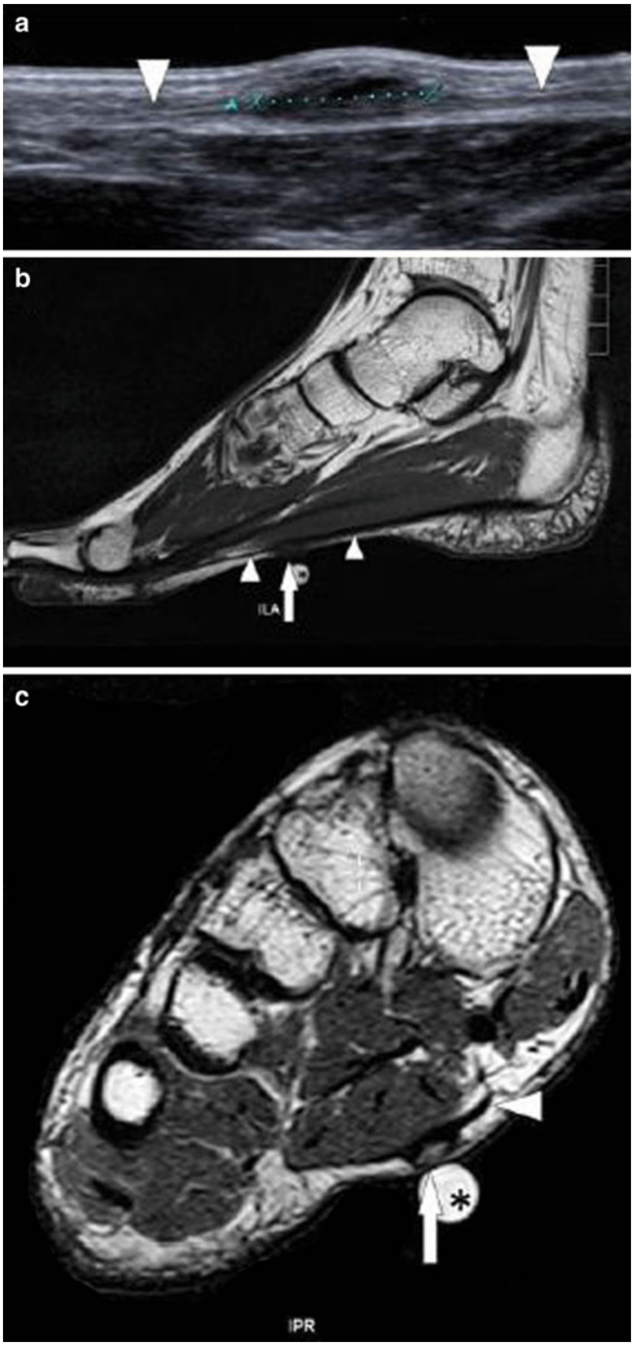

Fig. 21 Plantar fibromatosis. Patient with a painless subcutaneous nodule at the medial aspect of the foot sole. **a** Ultrasound image along the sagittal plane displays a hypo-echogenic ill-defined lesion at the medial bundle of the plantar aponeurosis, with a length of 11 mm. **b** Sagittal T1-WI and **c** Coronal T2-WI clearly demonstrate the relationship between the lesion (*arrow*) and the plantar aponeurosis (*arrowheads*). The fibromatosis is isointense to muscle on T1-WI and slightly hyperintense on T2-WI. The nodular extracorporeal structure (*asterisk*) is an imaging marker placed on the skin for easy lesion localization. (Used with permission from Van Hul et al. (2011))

(Fig. 21b-c). Young lesions enhance moderately, older lesions to a lesser degree (Morrison et al. 1994; Van Hul et al. 2011).

6.7 Nodular Fasciitis

6.7.1 Definition and Clinical Features

Nodular fasciitis is a benign nonneoplastic soft tissue lesion composed of fibroblastic–myofibroblastic cells that occur mainly on the volar aspect of the upper arm in patients in their third to fourth decade of life. The lesion may be either located within subcutis, fascia, or muscle. The fascial type is the most common.

Ossifying fasciitis is a rare histopathological variant of nodular fasciitis, composed of metaplastic bone with calcification and chondroid differentiation. This lesion may easily be misinterpreted as malignancy, clinically and histologically, because it presents as a rapidly growing mass originating from subcutaneous or deep fascial tissues (Kim et al. 2007).

6.7.2 Imaging Features

The MR signal intensity pattern reflects the histological composition of the lesion. Lesions with a high cellularity and/or myxoid content are iso- to hyperintense to skeletal muscle on T1-WI and hyperintense to fat on T2-WI. Lesions with a more fibrous histology are hypointense on all pulse sequences. More specific for nodular fasciitis is the “inverted target sign” which consists of a peripheral area of increased SI on T1-WI, low SI at the periphery on T2-WI, and marked enhancement of the peripheral zone after contrast administration (Wang et al. 2002).

7 Conclusion

There exists a myriad of soft tissue tumors and tumor-like conditions with variable biological behavior (ranging from benign to malignant) that may involve muscles, fasciae, and tendon sheaths.

MRI is the preferred imaging technique for defining the precise extent of a soft tissue lesion within muscles, fasciae or tendon sheaths. With the exception of some typical benign appearing soft tissue lesions (e.g., intramuscular lipoma), intramuscular tumors with histologically myogenic differentiation cannot reliably distinguished from other histological groups of soft tissue tumors on MRI alone. Therefore, biopsy and histological confirmation is mandatory in most clinical scenarios, particularly if there is any suspicion for malignancy on MRI. It should be emphasized that for tumors with smooth or skeletal muscle differentiation, malignant tumors are more frequent than their benign counterparts.

References

Allen SD, Moskovic EC, Fisher C, Thomas JM (2007) Adult rhabdomyosarcoma: cross-sectional imaging findings including histopathologic correlation. AJR Am J Roentgenol 189(2):371–377

Auerbach A, Fanburg-Smith JC, Wang G, Rushing EJ (2009) Focal myositis: a clinicopathologic study of 115 cases of an intramuscular mass-like reactive process. Am J Surg Pathol 33:1016–1024. doi:10.1097/PAS.0b013e31819e63fe

Bashir WA, O'Donnell P (2010) The myositides: the role of imaging in diagnosis and treatment. Semin Musculoskelet Radiol 14:217–226. doi:10.1055/s-0030-1253163

Billings SD, Folpe AL, Weiss SW (2001) Do leiomyoma of deep soft tissue exist? An analysis of highly differential smooth muscle tumors of deep supporting two distinct subtypes. Am J Surg Pathol 25(9):1134–1142

Blansfield JA, Chung H, Sullivan TR, Jr Pezzi CM (2003) Leiomyosarcoma of the major peripheral arteries: case report and review of the literature. Ann Vasc Surg 17(5):565–570

Bush CH, Reith JD, Spanier SS (2003) Mineralization in musculoskeletal leiomyosarcoma: radiologic-pathologic correlation. AJR Am J Roentgenol 180(1):109–113

Chew NS, Vanhoenacker FM (in press) Aggressive fibromatosis: is PET-CT useful in lesion characterization? JBR-BTR

Chiles MC, Parham DM, Qualman SJ et al (2004) Soft tissue sarcoma committee of the children's oncology group. Sclerosing rhabdomyosarcomas in children and adolescents: a clinicopathologic review of 13 cases from the intergroup rhabdomyosarcoma study group and children's oncology group. Pediatr Dev Pathol 7(6):583–594

Davies CE, Davies AM, Kindblom LG, James SL (2010) Soft tissue tumors with muscle differentiation. Semin Musculoskelet Radiol 14(2):245–256. doi:10.1055/s-0030-1253165

De Schepper AM, Bloem JL (2007) Soft tissue tumors: grading, staging, and tissue-specific diagnosis. Top Magn Reson Imaging 18(6):431–444. doi:10.1097/rmr.0b013e3181652220

De Schepper AM, Vandevenne JE (2006) Tumors of connective tissue. In: De Schepper AM, Vanhoenacker F, Parizel PM, Gielen J (eds) Imaging of soft tissue tumors, 3rd edn. Springer, Berlin Heidelberg New York, pp 167–202

Ergun T, Lakadamyali H, Derincek A, Cagla Tarhan N, Ozturk A (2010) Magnetic resonance imaging in the visualization of benign tumors and tumor-like lesions of hand and wrist. Curr Probl Diagn Radiol 39:1–16. doi:10.1067/j.cpradiol.2009.01.002

Flaisler F, Blin D, Asencio G, Lopez FM, Combe B (1993) Focal myositis: a localized form of polymyositis? J Rheumatol 20:1414–1416

Fletcher CDM, Bridge JA, Hogendoorn P, Mertens F (2013) World health organization classification of tumours of soft tissue and bone, 4th edn. IARC Press, Geneva

Flors L, Leiva-Salinas C, Maged IM, Norton PT, Matsumoto AH, Angle JF, Hugo Bonatti M, Park AW, Ahmad EA, Bozlar U, Housseini AM, Huerta TE, Hagspiel KD (2011) MR imaging of soft-tissue vascular malformations: diagnosis, classification, and therapy follow-up. Radiographics 31(5):1321–1340. doi:10.1148/rg.315105213

Fox MG, Kransdorf MJ, Bancroft LW, Peterson JJ, Flemming DJ (2003) MR imaging of fibroma of the tendon sheath. AJR Am J Roentgenol 180:1449–1453

Gupte C, Butt SH, Tirabosco R, Saifuddin A (2008) Angioleiomyoma: magnetic resonance imaging features in ten cases. Skeletal Radiol 37(11):1003–1009. doi:10.1007/s00256-008-0518-4

Gurney JG, Davis S, Severson RK, Fang JY, Ross JA, Robison LL (1996) Trends in cancer incidence among children in the U.S. Cancer 78(3):532–541

Hachisuga T, Hashimoto H, Enjoji M (1984) Angioleiomyoma: a clinicopathologic reappraisal of 562 cases. Cancer 54:126–130

Hondar Wu HT, Chen W, Lee O, Chang CY (2006) Imaging and pathological correlation of soft-tissue chondroma: a serial five-case study and literature review. Clin Imaging. 2006 30(1):32–36

Killoran TP, Wells WA, Barth RJ, Goodwin DW (2003) Leiomyosarcoma of the popliteal vein. Skeletal Radiol 32(3):174–178

Kim JH, Kwon H, Song D, Shin OR, Jung SN (2007) Clinical case of ossifying fasciitis of the hand. J Plast Reconstr Aesthet Surg 60(4):443–446

Kransdorf MJa (1995a) Benign soft-tissue tumors in a large referral population: distribution of specific diagnoses by age, sex, and location. AJR Am J Roentgenol 164(2):395–402

Kransdorf MJb (1995b) Malignant soft-tissue tumors in a large referral population: distribution of specific diagnoses by age, sex, and location. AJR Am J Roentgenol 164(2):129–134

Kransdorf MJ, Murphey MD (2007) Imaging of soft tissue tumors, 2nd edn. Lippencott Williams & Wilkins, Philadelphia, pp 298–327

Luna A, Martinez S, Bossen E (2005) Magnetic resonance imaging of intramuscular myxoma with histological comparison and a review of the literature. Skeletal Radiol 34:19–28

Maglio R, Francesco S, Paolo M, Stefano V, Francesco D, Giovanni R (2012) Voluminous extracardiac adult rhabdomyoma of the neck: a case presentation. Case Rep Surg 2012:984789. doi:10.1155/2012/984789

McLeod AJ, Zornoza J, Shirkhoda A (1984) Leiomyosarcoma: computed tomographic findings. Radiology 152(1):133–136

Meyer WH, Spunt SL (2004) Soft tissue sarcomas of childhood. Cancer Treat Rev 30(3):269–280

Morrison W, Schweitzer M, Wapner K, Lackman R (1994) Plantar fibromatosis: a benign aggressive neoplasm with a characteristic appearance on MR images. Radiology 193:841–845

Murphey MD, Ruble CM, Tyszko SM, Zbojniewicz AM, Potter BK, Miettinen M (2009) From the archives of the AFIP: musculoskeletal fibromatoses: radiologic-pathologic correlation. Radiographics 29(7):2143–2173. doi:10.1148/rg.297095138

Navarro OM (2011) Soft tissue masses in children. Radiol Clin N Am 49:1235–1259. doi:10.1016/j.rcl.2011.07.008

Newton WA Jr, Soule EH, Hamoudi AB et al (1988) Histopathology of childhood sarcomas, intergroup rhabdomyosarcoma studies I and II: clinicopathologic correlations. J Clin Oncol 6(1):67–75

Nguyen V, Choi J, Davis KW (2004) Imaging of wrist masses. Cur Probl Diagn Radiol 33:147–160

Nishimoto K, Kusuzaki K, Matsumine A, Seto M, Fukutome K, Maeda M, Hosoi S, Uchida A (2004) Surrounding muscle edema detected by MRI is valuable for diagnosis of intramuscular myxoma. Oncol Rep 11:143–148

Paal E, Miettinen M (2001) Retroperitoneal leiomyoma of deep soft tissue: a clinicopathologic and immunohistochemical study of 56 cases with a comparison to retroperitoneal leiomyosarcomas. Am J Surg Pathol 25(11):1355–1363

Peeters J, Vanhoenacker FM, Camerlinck M, Parizel PM (2010) Calcific myonecrosis. JBR-BTR 93(2):111

Peterson KK, Renfrew DL, Feddersen RM et al (1991) Magnetic resonance imaging of myxoid containing tumors. Skeletal Radiol 20:245–250

Ramesh P, Annapureddy SR, Khan F, Sutaria PD (2004) Angioleiomyoma: a clinical, pathological and radiological review. Int J Clin Pract 58:587–591

Seynaeve PC, De Visschere PJL, Mortelmans LL, De Schepper AM (2006) Tumors of muscular origin. In: De Schepper AM, Vanhoenacker F, Parizel PM, Gielen J (eds) Imaging of soft tissue tumors, 3rd edn. Springer, Berlin Heidelberg New York, pp 293–310

Tyler P, Saifuddin A (2010) The imaging of myositis ossificans. Semin Musculoskelet Radiol 14:201–216. doi:10.1055/s-0030-1253161

van Vliet M, Kliffen M, Krestin GP, van Dijke CF (2009) Soft tissue sarcomas at a glance: clinical, histological, and MR imaging features of malignant extremity soft tissue tumors. Eur Radiol 19(6):1499–1511. doi:10.1007/s00330-008-1292-3

Van Hul E, Vanhoenacker F, Van Dyck P, De Schepper A, Parizel PM (2011) Pseudotumoural soft tissue lesions of the foot and ankle: a pictorial review. Insights Imag 2(4):439–452. doi:10.1007/s13244-011-0087-2

Vanhoenacker F, Vanwambeke K, Bosmans J (2010) Pseudotumeur inflammatoire de la ceinture scapulaire. Ortho-rhumato 8:13–14

Vanhoenacker FM, Camerlinck M, Somville J (2009) Imaging findings of a subcutaneous angioleiomyoma. JBR-BTR 92(2):80–82

Vanhoenacker FM, Eyselbergs M, Van Hul E, Van Dyck P, De Schepper AM (2011) Pseudotumoural soft tissue lesions of the hand and wrist: a pictorial review. Insights Imag 2(3):319–333. doi:10.1007/s13244-011-0076-5

Vanhoenacker FM, Marques MC, Garcia H (2006) Lipomatous tumors. In: De Schepper AM, Vanhoenacker F, Parizel PM, Gielen J (eds) Imaging of soft tissue tumors, 3rd edn. Springer, Berlin Heidelberg New York, pp 227–261

Wan JM, Magarelli N, Peh WC, Guglielmi G, Shek TW (2010) Imaging of giant cell tumour of the tendon sheath. Radiol Med 115:141–151. doi:10.1007/s11547-010-0515-2

Wang XL, De Schepper AM, Vanhoenacker F et al (2002) Nodular fasciitis: correlation of MRI findings and histopathology. Skeletal Radiol 31:155–161

Wang XL, Malghem J, Parizel PM, Gielen JL, Vanhoenacker F, De Schepper AM (2003) Pictorial essay. Myositis ossificans circumscripta. JBR-BTR 86:278–285

Weiss SW (2002) Smooth muscle tumors of soft tissue. Adv Anat pathol 9(6):351–359

Zamorani MP, Valle M (2007) Muscles and tendon. In: Bianchi S, Martinoli C (eds) Ultrasound of the musculoskeletal system. Springer, Berlin Heidelberg New York, pp 45–96

Zeinstra JS, Kwee RM, Kavanagh EC, van Hemert WL, Adriaensen ME (2012) Multifocal giant cell tumor of the tendon sheath: case report and literature review. Skeletal Radiol. doi:10.1007/s00256-012-1552-9

Index

A
Achilles tendon rupture, 166, 179, 180
Amyotrophic lateral sclerosis (ALS), 5–7, 16, 17, 100, 153, 234, 235
Aponeuroses, 33, 189

B
Becker muscle dystrophy (BMD), 18, 21, 149, 247, 248
Blood oxygenation level-dependent (BOLD) MRI, 87–91, 93, 94–96, 100, 109
  BOLD effect in muscle tissue, 88
  Clinical applications of BOLD MRI, 94
  Comparison of ASL and BOLD MRI for muscle perfusion, 100

C
Calcific/calcifying myonecrosis, 187, 192, 301, 302
Cardiomyopathy, 4, 6, 20, 21
Carpal tunnel syndrome (CTS), 222, 231, 232
Chronic inflammatory demyelinating polyneuropathy (CIPD), 66
Chronic unloading, 166, 180, 181
Creatine phosphokinase (CK), 4, 8–9, 257, 258, 264, 265
Compartment syndrome, 15, 36, 41, 42, 46, 47, 87, 88, 90, 96, 187, 191, 192, 199, 203, 205, 206, 301
Computed tomography, 3, 14, 28, 29, 56, 242, 255, 257, 262
Congenital myopathies (CM), 4, 6, 19, 20, 250–253, 260
  ACTA1-related myopathies, 251
  Centronuclear myopathies (CNM), 251
  congenital myopathies with core lesions, 251
  multi minicore myopathy, 251, 272
  MYH7-related myopathies, 252
Cubital tunnel syndrome (CUS), 36, 39, 221, 231, 232

D
Delayed onset muscle soreness, 41, 42, 44, 45, 187, 189, 191, 199, 202, 203, 205
Denervation, 8, 15–17, 21, 61, 153, 189, 221–225, 228, 230–236, 245, 246
Desminopathy, 64
Diabetes mellitus, 5–7, 15, 87, 90, 96, 144, 148
Duchenne muscular dystrophy (DMD), 7, 9, 10, 15, 16, 21, 121, 124, 149, 247–249, 286

E
Electromyography, 4, 8, 9, 16, 18, 19, 21, 83, 222–224, 234, 258, 273, 277

F
Facioscapulohumeral muscular dystrophy (FSHD), 7, 150, 249, 250
Fasciculations, 5, 6, 13, 16, 17

G
Glycogen storage disorder myopathies, 20

H
Hepatomegaly, 4, 6

I
Idiopathic inflammatory myopathies, 18, 19, 47, 61, 256, 259–262, 264
  clinical presentation, 4, 190, 231, 242, 256
  dermatomyositis, 4, 18, 19, 47, 48, 61, 62, 150, 151, 255, 256
  eosinophilic polymyositis, 264
  granulomatous myositis, 264
  histopathology and pathogenesis, 258
  imaging in idiopathic inflammatory myopathies, 259
  inclusion body myositis, 9, 10, 18, 47, 62, 151, 247, 256, 257, 261
  laboratory findings, 257
  polymyositis, 4, 14, 18, 19, 47, 60, 62, 150, 151, 255–257, 264, 265, 300
  therapy in idiopathic inflammatory myopathies, 264
Infection, 5, 14, 47–49, 264–266
Infectious inflammatory myopathies, 256, 264
  pyomyositis, 266
Ion channel disorders, 6, 115, 124, 127, 260, 271–273, 277, 278, 287
  periodic paralysis, 6

L
Lambert–Eaton myasthenic syndrome, 6
Limb girdle muscle dystrophy (LGMD), 10, 20, 63, 64, 66, 150, 244, 247–249

M.-A. Weber (ed.), *Magnetic Resonance Imaging of the Skeletal Musculature*, Medical Radiology. Diagnostic Imaging,
DOI: 10.1007/978-3-642-36724-3, © Springer-Verlag Berlin Heidelberg 2014

M

Magnetic resonance imaging (MRI), 3, 4, 10, 11, 14, 15, 17–19, 21, 33, 34, 36, 38, 55–58, 61, 66, 69–71, 88, 91, 105, 116, 121, 124, 127, 136–138, 143, 167, 173, 174, 178, 179, 182, 187, 189, 193, 194, 198, 199, 209, 224, 229, 235, 242, 244, 250, 253, 255, 256, 259, 261, 264, 266, 271, 278, 279, 292, 294, 296, 300, 303, 306
  ^{17}O MRI, 128
  ^{23}Na MRI, 118
  2D and 3D strain and strain rate measurements in skeletal muscles, 181
  ^{35}Cl MRI, 127
  ^{39}K MRI, 127
  applications of ^{23}Na MRI in muscular channelopathies and muscle dystrophies, 121
  Arterial spin labeling (ASL), 87–89, 96–101
  clinical applications of ASL, 100
  Diffusion tensor imaging (DTI), 33, 48, 69, 70, 72, 73, 75–78, 81, 83, 194, 227, 228, 236, 237
  diffusion tensor indices in the normal MSK system, 76
  diffusion-weighted imaging, 11, 71, 73, 83
  displacement imaging (DENSE imaging), 168
  displacement imaging (spin tag imaging), 167
  Dynamic contrast enhancement (DCE), 87, 101, 103, 105, 107, 109
  Dynamic contrast enhanced (DCE)-MRI, 87, 101, 236, 88, 102, 104, 105, 107, 109
  dynamic MR imaging, 166
  dynamic susceptibility MRI, 105
  fiber tractography, 74, 75, 78, 80
  imaging pulse sequences for diffusion-weighted magnetic resonance imaging, 71
  MR sequences for muscle MRI, 57
  muscle fiber tracking, 69, 70, 73
  muscle model of diffusion, 75
  normal skeletal muscle MR appearances, 58
  post-processing of diffusion-weighted images, 74
  Short inversion time inversion recovery (STIR), 10, 11, 15, 17, 36, 48, 55, 56, 58–63, 65, 121, 196–198, 210, 214, 227, 229–231, 259, 260
  sodium MRI as a biomarker of cartilage degeneration, 124
  velocity encoded-phase contrast MR (VE-PC MR) imaging, 167
  velocity encoded-phase contrast (VE-PC) MR musculoskeletal imaging, 173
  whole-body MRI (WB-MRI), 13, 55, 56, 59, 70, 243, 253, 259
Magnetic resonance spectroscopy (MRS), 135–144, 146, 147–152, 154, 155, 236, 256, 261
  ^{13}C-MR spectroscopy, 138, 141, 144, 146
  ^{1}H-MR spectroscopy, 141, 152
  ^{31}P-MR spectroscopy, 139, 144, 153
  basics of MR spectroscopy in the musculoskeletal system, 137
  glycogen storage diseases, 146
  inflammatory myopathies, 150
  insulin resistance, 136, 144, 152, 154, 155
  Intramyocellular lipids (IMCL), 141, 144–146, 153, 154
  Malignant hyperthermia (MH), 151, 272
  McArdle's disease, 146, 147
  mitochondrial myopathies, 147–149, 151
  muscular dystrophies, 149
  muscular energy metabolism, 143, 153, 154
Mononeuropathy, 5
Motor neuron disease, 5–7, 232, 234, 235
Multifocal motor neuropathy (MMN), 8, 234
Muscle biopsy, 4, 6, 9–11, 19, 57, 83, 242, 247, 251, 255, 256, 258, 259, 262–265
Muscle channelopathies, 35, 115, 121, 124, 260, 271, 272
  Cl^{-} channel myotonias, 273
  clinical features, 276
  histopathology, 278
  Hyperkalemic periodic paralysis (HyperPP), 274
  Hypokalemic periodic paralysis (HypoPP), 283
  K^{+}-aggravated myotonia (PAM), 273, 274, 278
  magnetic resonance imaging, 3, 4, 27, 28, 69, 70, 87, 88, 116, 179, 189, 242, 256, 278
  paramyotonia congenita, 274, 275
  prevalence, genetics and pathophysiology, 273
  therapy, 285
Muscle contusion, 187, 189, 191, 198, 202
Muscle denervation, 8, 15–17, 21, 61, 153, 189, 221–225, 228, 230–236, 245, 246
  diffusion tensor MRI of denervated muscle, 236
  MR spectroscopy of denervated muscle, 237
  perfusion MRI of denervated muscle, 236
Muscle fiber or myofiber, 27, 28
Muscle fibers classification, 27, 28
Muscle hernia, 41, 45, 191, 200, 205
Muscle hypertrophy, 6, 15, 17, 277, 279
Muscle strains and tears, 41, 42
Muscle tear
  diffusion-weighted and diffusion tensor imaging in muscle injury, 83
  fibrous scar, 44
  grade 1 injury, 190
  grade 1 strain, 187
  grade 2 partial tear, 187
  grade 3 complete tear, 187
  grading of muscle injuries on ultrasound, 205
  haematoma, 195, 216
  imaging modalities and technique, 192
  MRI findings of acute muscle strain/tear, 194
  muscle healing, 191
  recurrent muscle injury, 210
  reinjury, 43
  specific muscle injuries, 206
Muscle tumors, 11, 15, 35, 42, 49, 289, 290
  desmoid tumors (desmoid type fibromatosis), 293
  intramuscular haemangioma and vascular malformations, 295
  intramuscular lipoma, 42, 50, 292
  intramuscular myxoma, 292
  leiomyoma, 289, 290
  leiomyosarcoma, 289, 296
  pseudotumoral lesions of muscle, 298
  rhabdomyoma, 289, 291
  rhabdomyosarcoma, 289, 290, 295, 297
Muscle–tendon junction (musculotendinous or myotendinous junction), 33, 189
Muscle weakness, 4, 18, 61, 63, 121, 149, 150, 249, 250, 256, 261, 262, 264, 265, 280
Muscular dystrophies, 4, 7, 9, 13, 17, 19, 21, 149, 243, 247, 250, 253, 260, 287
Muscular hematoma, 34, 36
Myasthenia gravis, 4–6, 8, 9, 153, 264
Myonecrosis or ischemic myositis, 15

Myopathy, 4, 6–8, 15, 17, 18, 21, 22, 57, 154, 278
  acquired myopathies, 4, 15
  hereditary myopathies, 4, 21
Myositis ossificans, 15, 41, 44, 45, 192, 200, 201, 206, 298
Myotilinopathy, 64
Myotonia, 6, 258, 271–273, 276, 277, 285
Myotonic dystrophy, 6, 7, 121, 150, 249, 260, 279

N
Neuromuscular junction, 4, 5, 7, 8, 153, 188, 223, 224
Neuropathy, 5, 6, 37, 148, 225, 258
Nodular fasciitis, 306

O
Oculopharyngeal Muscle Dystrophy (OPMD), 150, 250
Osteoarthritis (OA), 115, 124, 128

P
Peripheral arterial occlusive disease (PAOD), 87, 90, 94, 101, 104
Peripheral nerve, 4, 65, 83, 221, 223, 225, 234
  MR-Neurography, 221, 227, 234
Plexopathies
  anatomy of the brachial plexus, 225
  traumatic plexopathies, 227, 228
  perinatal brachial plexus lesions, 228
Polyneuropathy, 5, 8, 66, 234
Post-polio syndrome, 235, 236

R
Radial tunnel syndrome, 231
Radiculopathies, 221, 222, 225, 234

S
Saturday night palsy, 230
Skeletal muscle, 10, 28, 29
  accessory muscles, 35–37, 39
  anatomical variant, 28, 35, 36, 37
  anatomy, 27–29, 30, 33, 34, 42, 188
  atrophy, 15, 17, 19
  endomysium, 71, 76
  epimysium, 34, 71
  fatty degeneration, 56, 242, 246, 247
  hypertrophy, 15, 17
  imaging, 4, 10, 13, 33
  innervation, 222
  isometric contraction, 30, 31, 33, 171
  isotonic contraction, 29, 31
  macroscopical anatomy, 27, 29
  microscopical anatomy, 27, 28
  muscle edema, 11, 242, 246
  muscular contraction, 27, 30
  pathophysiology of denervation and reinnervation, 223
  perimysium, 28, 34, 71, 188
  pseudohypertrophy, 7, 15
  strain and strain rate mapping, 168
Spinal muscular atrophy, 5, 10, 223, 260

T
Tendon sheaths, 289, 290, 301
Tendons, 31, 33, 166, 189, 209
Tumors of fasciae and tendon sheaths, 289
  fibroma of the tendon sheath, 303, 304
  giant cell tumor of tendon sheath, 302, 303
  lipoma of tendon sheath, 303
  superficial fibromatoses, 303
  tendon sheath cyst, 301
  tenosynovial chondromatosis, 303, 304

U
Ultrasound/ultrasonography, 3, 4, 12, 35, 94, 167, 264
  contrast-enhanced ultrasound, 13, 95, 96
  muscle anisotropy, 35, 42

W
Whole-body MRI (WB-MRI), 13, 55, 56, 59, 70, 243, 253, 259
  comprehensive neuromuscular WB MRI protocol, 56, 58
  limitations of neuromuscular WB MRI, 61
  possible clinical applications of neuromuscular WB MRI, 61
  3T versus 1.5T WB MRI, 60
  why WB MRI for the evaluation of muscle diseases, 57